DOCTOR OF PHILOSOPHY

Nonlinear Dynamics of Microcirculation and Energy Metabolism for the Prediction of Cardiovascular Risk

Smirni, Salvatore

Award date:
2018

Nonlinear Dynamics of Microcirculation and Energy Metabolism for the Prediction of Cardiovascular Risk

---

by

Salvatore Smirni

A thesis submitted in fulfilment of the requirements for the degree of Doctor of Philosophy

Supervised by

Professor Faisel Khan and **Dr Michael P. MacDonald**

School of Medicine

Division of Molecular and Clinical Medicine

July 2018

Table of Contents

Acknowledgements

Firstly, I would like to thank my supervisors Professor Faisel Khan and Dr Michael P. MacDonald for the exceptional support and guidance provided throughout my doctoral studies at the University of Dundee. Their precious suggestions have been relevant in the process of doctoral training and education, enhancing my growth as interdisciplinary scientist with expertise at the cutting-edge between biomedicine and physics. I would also like to thank my supervisors for the human and friendly relationship that we have established throughout my doctoral studies.

I would like to thank all my colleagues and friends from the Division of Molecular and Clinical Medicine, from the PHOQUS doctoral program, and from the host institutions/companies that I have visited during my doctoral studies. All of them have made the creation of a friendly work environment possible, including people with diverse background and nationalities that have enriched my life experience both professionally and personally. I would like to express my gratitude especially to Hala Bagabir for her support and continued help throughout my stay at the School of Medicine, and Alison McNeilly for her precious help with the experimental work at the animal facility in Ninewells Hospital. Additionally, I would like to thank all the people that somehow have contributed to the progress of this research study, providing the tools for the fulfillment of the bureaucratic requirements for performing animal and human experimental work according to the current regulations.

I would like to express a special thanks to my fiancée Federica that has fully supported me during my doctoral studies, always staying by my side especially in the most difficult periods. Without her help and patience the completion of this work would not have been possible. Many thanks also to all my family that have always been present and helpful despite the long distance between the UK and the south of Italy. Finally, thanks to all my friends that have always given their valuable support throughout these years even from far away. Thanks to anyone else that I have forgotten to mention.

List of abbreviations

$\Delta\Psi_m$	Mitochondrial membrane potential
1P	One-photon
2P	Two-photon
ACh	Acetylcholine
AF	Autofluorescence
A_i	Absolute wavelet amplitude
a_i	Relative wavelet amplitude
AMI	Average mutual information
APA	Apamin
ATP	Adenosine triphosphate
AU	Arbitrary units
AUC	Area under the curve
AVAs	Arteriovenous anastomoses
BL	Baseline flow
BMI	Body mass index
BP	Blood pressure
BV	Blood volume
BZ	Biological zero
Ca^{2+}	Calcium
CC	Cross-correlation
CHD	Coronary heart disease
ChTX	Charybdotoxin
CIV	Current-induced vasodilation
cmOCT	Correlation mapping OCT
COXs	Cyclooxygenases
$C_\phi(\omega_k)$	Phase coherence
CVD	Cardiovascular disease
CWT	Continuous wavelet transform
CYPs	Cytochromes P450
D	Fractal dimension
D_2	Correlation dimension
DBP	Diastolic BP

deoxyHb	Deoxygenated Hb
DOCT	Doppler OCT
ECG	Electrocardiograph
ECs	Endothelial cells
EDHF	Endothelial-derived hyperpolarizing factor
EEMD	Empirical mode decomposition
EETs	Epoxyeicosatrienoic acids
E_i	Absolute wavelet energy
e_i	Relative wavelet energy
eNOS	Endothelial nitric oxide synthase
ER	Endoplasmic reticulum
f	Wavelet peak's frequency
FAD^+	Oxidised flavin adenine dinucleotide
$FADH_2$	Reduced flavin adenine dinucleotide
FL	Fluorescence lifetime
FLIM	Fluorescence lifetime imaging microscopy
FRS	Framingham risk score
FFT	Fast Fourier transform
GMG	Half-gaussian modified gaussian
H	Hurst index
H_0	Entropy
H_2O_2	Hydrogen peroxide
Hb	Haemoglobin
HeNe	Helium neon
HFD	High fat diet
H_i	Information dimension
HRV	Heart rate variability
I_m	Blood perfusion
I_{mn}	Nutritive blood flow
IR	Infra-red
K^+	Potassium
Keap-$1^{-/-}$	Kelch-like ECH-associated protein 1 KO
KO	Knock-out
LDF	Laser Doppler flowmetry

LDI	Laser Doppler imaging
LDL	Low-density lipoproteins
LFS	Laser fluorescence spectroscopy
LHT	Local thermal hyperaemia
L-NMMA	N^G-monomethyl-L-arginine
LSCI	Laser speckle contrast imaging
M	Milestone
MO	Metabolic oscillator
MPLSM	Multi-photon laser scanning microscopy
NAD(P)$^+$	Oxidised nicotamide adenine dinucleotide
NAD(P)H	Reduced nicotamide adenine dinucleotide
N_{er}	Erythrocytes concentration
NIR	Near infra-red
NIRS	Near infra-red spectroscopy
NO	Nitric oxide
Nrf2$^{-/-}$	Nuclear factor erythroid 2–related factor 2 KO
$O_2^{\bullet-}$	Superoxide anion
O_2ER	Oxygen extraction
OCT	Optical coherence tomography
OMAG	Optical microangiography
ONOO$^-$	Peroxynitrite
OPS	Orthogonal polarisation spectral imaging
OXPHOS	Oxidative phosphorylation
oxyHb	Oxygenated Hb
ϕ	Phase
p	p-value
PAM	Photoacoustic microscopy
pCO_2	Carbon dioxide partial pressure
PE	Phenylephrine
PFK	Phosphofructokinase
PGs	Prostaglandins
PIV	Pressure-induced vasodilation
PK	Absolute perfusion peak
PO	Pulse oximetry

pO_2	Oxygen partial pressure
PORH	Post-occlusive reactive hyperaemia
PROCAM	Prospective cardiovascular Munster
PTFE	Oscillating fluoroplastic disk
PU	Perfusion arbitrary units
r	Pearson's correlation coefficient
RBCs	Red blood cells
ROS	Reactive oxygen species
RR	Redox ratio
RS	Reflectance spectroscopy
S_aO_2	Arterial oxygen saturation
SBP	Systolic BP
SCORE	European systematic coronary risk evaluation
SD	Standard deviation
SDF	Sidestream dark-field imaging
SE	Standard error
Sik KI	Salt-inducible kinases knock in
SNP	Sodium nitroprusside
SO_2	Oxygen saturation
S_pO_2	Pulse oximeter arterial oxygen saturation
SR	Sarcoplasmic reticulum
STFT	Short time Fourier transform
S_vO_2	Venous oxygen saturation
svOCT	Speckle variance OCT
T	Temperature
$tcpO_2$	Transcutaneous oxygen partial pressure
TEA	Tetraethylammonium
UV	Ultra-violet
V_a	RBCs velocity
VO_2	Oxygen consumption
VSMCs	Vascular smooth muscle cells
WPCO	Wavelet phase coherence
WT	Wild type
ρ	Spearman's correlation coefficient

List of figures and tables

1. Literature review and aims

Figures:

2. Material and methods

Figures:

Tables:

3. Nonlinear dynamics of microcirculation and cell energy metabolism in the *Nrf2*$^{-/-}$ mouse model

Figures:

Tables:

4. Nonlinear dynamics of microcirculation and cell energy metabolism in human individuals

Figures:

Tables:

Declaration

I hereby declare to be the author of this thesis, the work of which is entirely a record carried out by myself. Unless otherwise stated, all references cited in this dissertation have been consulted. None of the work or material contained within this thesis has been previously submitted and accepted for a higher education degree. Where use has been made of the works of other people (third parties), it has been fully referenced or acknowledged accordingly, and it has been made for the only purpose of discussion with respect to the general guidelines acceptable to publishers on the re-use of limited amounts of journal article content.

Signature of the candidate:

Salvatore Smirni Dundee, 22 July 2018

Supervisors' statement

I certify that Salvatore Smirni has fulfilled the conditions of ordinance and of the relevant regulations, such that he is qualified to submit this thesis in application for the higher degree of Doctor of Philosophy.

Signatures of the supervisors:

Professor Faisel Khan Dundee, 22 July 2018

Dr Michael P. MacDonald Dundee, 22 July 2018

Abstract

The peripheral skin microcirculation reflects the overall health status of the cardiovascular system and can be examined non-invasively by laser methods to assess early cardiovascular disease (CVD) risk factors, i.e. oxidative stress and endothelial dysfunction. Examples of methods used for this task are the laser Doppler flowmetry (LDF) and laser fluorescence spectroscopy (LFS), which respectively allow tracing blood flow and the amounts of the coenzyme NAD(P)H (nicotamide adenine dinucleotide) that is involved in the cellular production of ATP (adenosine triphosphate) energy. In this work, these methods were combined with iontophoresis and PORH (post-occlusive reactive hyperaemia) reactive tests to assess skin microvascular function and oxidative stress in mice and human subjects. The main focus of the research was exploring the nonlinear dynamics of skin LDF and NAD(P)H time series by processing the signals with the wavelet transform analysis. The study of nonlinear fluctuations of the microcirculation and cell energy metabolism allows detecting dynamic oscillators reflecting the activity of microvascular factors (i.e. endothelial cells, smooth muscle cells, sympathetic nerves) and specific patterns of mitochondrial or glycolytic ATP production. Monitoring these dynamic factors is powerful for the prediction of general vascular/metabolic health conditions, and can help the study of the mechanisms at the basis of the rhythmic fluctuations of micro-vessels diameter (vasomotion). In this thesis, the microvascular and metabolic dynamic biomarkers were characterised *in-vivo* in a mouse model affected by oxidative stress and a human cohort of smokers. Data comparison, respectively, with results from control mice and non-smokers, revealed significant differences suggesting the eligibility of these markers as predictors of risk associated with oxidative stress and smoke. Moreover, a relevant link between microvascular and metabolic oscillators was observed during vasomotion induced by α-adrenergic (in mice) or PORH (in humans) stimulations, suggesting a possible role of cellular Ca^{2+} oscillations of metabolic origin as drivers of vasomotion which is a theory poorly explored in literature. As future perspective, further exploration of these promising nonlinear biomarkers is required in the presence of risk factors different from smoke or oxidative stress and during vasomotion induced by stimuli different from PORH or α-adrenergic reactive challenges, to obtain a full picture on the use of these factors as predictors of risk and their role in the regulation of vasomotion.

Preface

This work is completely based upon a research project carried out at the School of Medicine of the University of Dundee (Scotland), and funded by the European Union's Seventh Framework Programme (FP7/2007-2013) under REA grant agreement n° 608133. Additional experiments were carried out at other academic institutions or companies that were involved in the project as associated partners. In particular, results of a collaboration with the *Tissue Optics and Microcirculation Imaging* group of the National University of Ireland (Galway) were published in two papers, which are enclosed in the appendix at the end of the thesis.

The dissertation is structured in 5 chapters and a final appendix:

- *Chapter 1 – Literature review and aims*. This section contains an introduction to the topic and the tasks of the research. A complete overview on the non-invasive methods for assessing skin microvascular function and oxidative stress, and a description of the rationale and the procedures for studying the nonlinear dynamics of microcirculation and energy metabolism are provided.
- *Chapter 2 – Material and methods*. This section provides a detailed description of the workflow for the implementation of the methodology used in this work, and of the protocols that were applied on mice and human subjects.
- *Chapter 3 – Nonlinear dynamics of microcirculation and cell energy metabolism in the Nrf2$^{-/-}$ mouse model*. This section contains the results and discussion related to the role of the nonlinear markers of microcirculation and energy metabolism in mouse skin vasomotion and their potential application as predictors of risk associated with oxidative stress.
- *Chapter 4 – Nonlinear dynamics of microcirculation and cell energy metabolism in human individuals*. This section contains the results and discussion related to the role of the nonlinear markers of microcirculation and energy metabolism in human skin vasomotion and their potential application as predictors of risk associated with smoke.
- *Chapter 5 – Conclusions and future perspectives*. This section brings together all the findings of this research work with concluding remarks and an outline tracing all the points that need to be addressed in the future.
- *Appendix*. This section contains the manuscripts, part of this doctoral project, which have been published or submitted to peer-reviewed journals.

1 Literature review and aims

1.1 Cardiovascular Disease burden and risk factors

Cardiovascular disease (CVD) is the leading cause of death worldwide. Although the pathology affects especially older adults, the molecular events involved in the onset and progression of CVD start early in life making it necessary to implement a primary prevention from childhood [1, 2]. Many factors are involved in the development of CVD, including vascular cell dysfunction caused by the excess of circulating nutrients, the resulting inflammation, oxidative stress, thrombosis, and insulin resistance [1]. These processes damage the blood vessel wall and are associated with cellular genetic pathways supporting the beginning and progression of CVD [1]. Identification of CVD risk factors is powerful for the prediction of individuals who have a higher probability of developing the disease [1]. CVD risk factors can be categorised in traditional and non-traditional factors. The most important traditional factors are hypertension, elevated low-density lipoproteins (LDL) and cholesterol, obesity, glucose metabolism and insulin resistance, family history of CVD, age, sex, nutrition/diet, physical inactivity, tobacco exposure, perinatal exposures, diabetes mellitus, and chronic/end-stage kidney disease [1]. These factors have been combined into the Framingham Risk Score (FRS), which is a group of multivariate algorithms for the estimation of the probability to develop CVD over a range of time [2, 3]. Although this is a widely used method for the assessment of CVD risk, alternative functions have been developed such as the SCORE (European Systematic Coronary Risk Evaluation) and the PROCAM (Prospective Cardiovascular Munster) model [3].

Nevertheless, the contribution of the traditional risk factors is frequently not enough to explain CVD morbidity and incidence, making the evaluation of the absolute risk difficult [1, 2]. For this reason, cardiovascular research is focusing on the exploration of novel, non-traditional risk factors that might be added to the existing risk functions [1, 2, 3]. Assessment of endothelial microvascular function [4], oxidative stress [5], genomics, proteomics and metabolomics [1] represent examples of promising modalities for the investigation of new CVD risk factors.

1.2 The microcirculatory system

The microcirculation is a network of small resistance arterioles, capillaries and venules in all the organs of the body, which are involved in the exchange of oxygen, nutrients, hormones and metabolism end-products between blood and the surrounding tissue [6, 7]. A general scheme of the microcirculatory system is provided in Fig. 1.

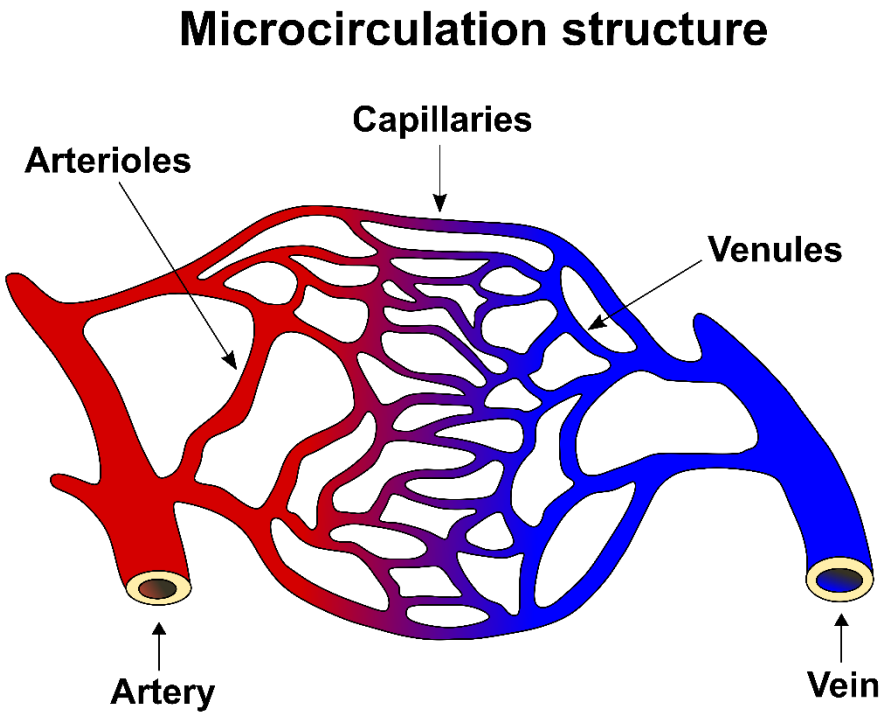

Fig. 1 Basic structural unit in the microcirculation. The microvascular network is made of small blood vessels for the distribution of nutritive blood in the surrounding tissue. The arterioles branch out from large arteries to deliver the oxygenated nutritive blood from the heart towards the capillaries. The arterioles diameter is lower than 100 µm and varies depending on the tissue, for example arterioles size in the skin is about 17-26 µm [8]. The capillaries are the smallest vessels in the microcirculation (5-10 µm), where the exchange of nutrients between blood and tissue takes place through several mechanisms of cellular transport. The venules are small vessels (7-50 µm) connected to the capillaries for the delivery of deoxygenated blood back to the heart through large veins.

In this circuit, arterioles are implicated in the regulation of blood delivery to the tissue through different adaptive mechanisms such as myogenic response, flow-induced vasodilation and metabolic neural control [7]. The main function of capillaries is the exchange of nutrients and metabolic bio-products between blood and tissue, and venules contribute to the maintenance of capillary hydrostatic

pressure ensuring a stable exchange of substances with the tissue and the delivery of deoxygenated blood back to the heart [6].

Endothelial cells (ECs) in the most internal layer of the blood vessels (endothelium) play a major role in the activity of microvascular arterioles, mainly consistent with the modulation of the vascular smooth muscle cells (VSMCs) located in the median layer of the blood vessels (tunica media) (Fig. 2) [6, 7]. The close cell-cell interaction between ECs and VSMCs through chemical mediators such as nitric oxide (NO) and prostaglandins (PGs), or through the endothelial-derived hyperpolarizing factor (EDHF) [communication by gap junctions or release of potassium K^+ and epoxyeicosatrienoic acids (EETs)] leads to arteriole relaxation and contraction for the adaptation of the vascular myogenic tone and blood flow in response to local tissue metabolic requirements, blood pressure (BP) or stress conditions (Fig. 2) [7, 9, 10]. The circular layers of VSMCs are also connected to a control system of peripheral sympathetic nerves (Fig. 2), which modulate the smooth muscle activity in response to local nervous stimuli [6, 7]. Micro-vessel functionality is essential to maintain the normal organs' perfusion, and deficiency in this task may lead to the onset of various diseases [6].

1.3 Mediators in the microcirculation related to the development of CVD

Abnormal cellular conditions, e.g. oxidative stress and altered metabolism, can cause an impairment of the microvascular network function associated with failure in the preservation of arterial blood pressure and organs perfusion, leading to the pathogenesis of several illnesses such as CVD [6, 11]. Oxidative stress is a transient or permanent imbalance in the amount of reactive oxygen species (ROS), e.g. hydrogen peroxide (H_2O_2), NO, and superoxide anion ($O_2^{\bullet -}$), which alters the cellular homeostasis and cannot be controlled by cellular antioxidant agents [5]. These highly reactive oxygen-containing molecules are mainly produced in the mitochondria, the endoplasmic reticulum (ER) or the peroxisomes cell compartments, and have harmful effects on the mitochondrial respiratory electron transport chain and ATP energy production [5, 12]. Blocking of the respiratory chain leads to alteration of the cellular redox state, and intracellular accumulation of the reduced form of the intermediate product of energy metabolism NAD(P)H (nicotamide adenine dinucleotide) [12].

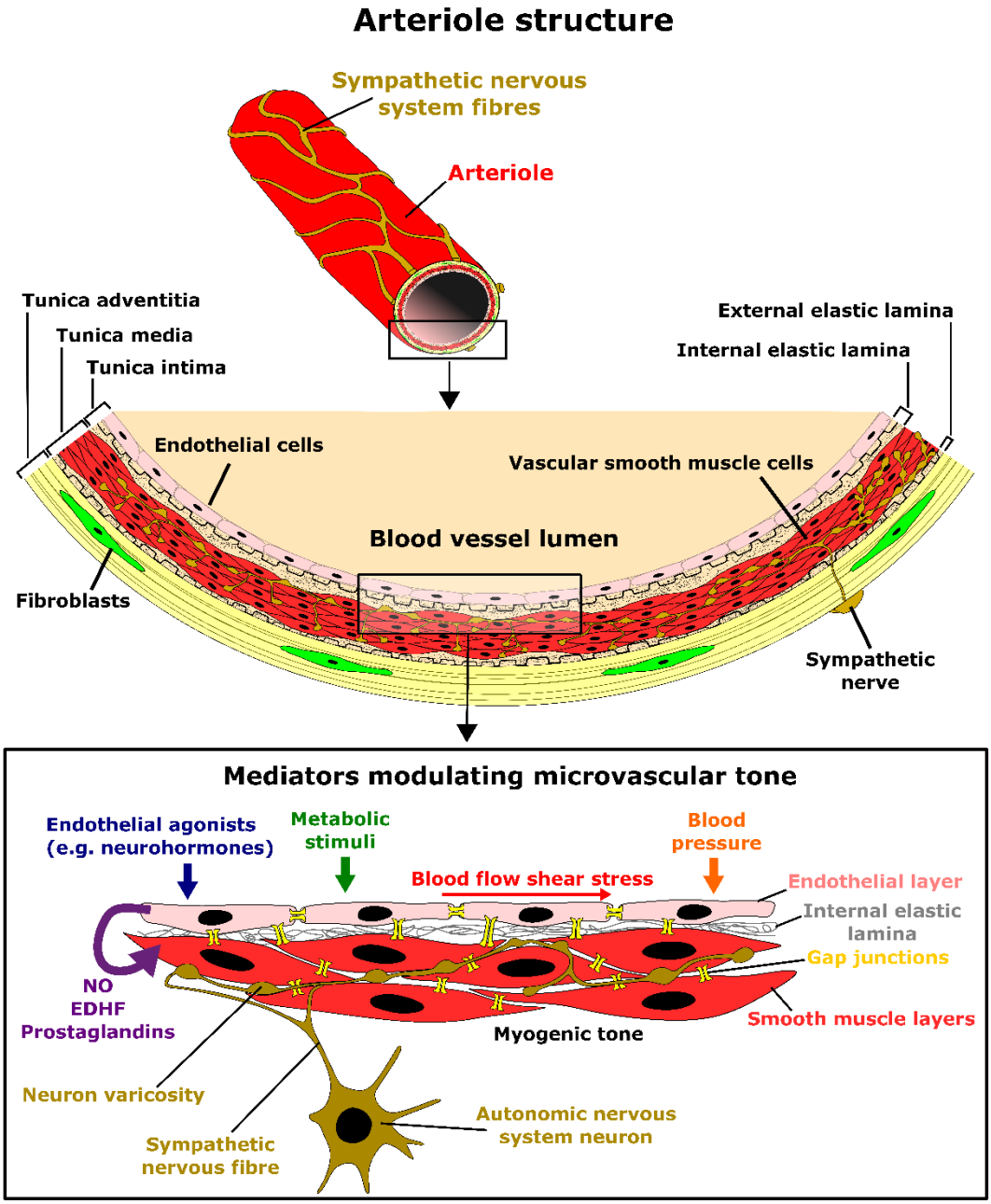

Fig. 2 Arteriole structure and adaptive mechanisms. The arteriole structure consists of three main layers defined as tunica intima, tunica media and tunica adventitia. The tunica intima is the most internal bed, which is made of a single stratum of ECs facing the vessel lumen. The tunica media consists of an internal elastic lamina at the interface with the endothelium made of structural proteins (i.e. elastin), and several layers of VSMCs which control the vessel's diameter by contraction and relaxation processes. The smooth muscle is innervated by sympathetic nervous fibres of the autonomic nervous system. The tunica adventitia is the most external layer of the arterioles, consisting of fibroblasts and stem mesenchymal progenitor cells included in an extracellular matrix of collagen and elastic fibres. The adventitia is involved in the processes of vessel elongation and repair. The modulation of arteriole myogenic tone is essential to ensure organ perfusion, and it involves adaptive mechanisms mainly associated with the release of vasoactive substances (i.e. NO, PGs and EDHF) or electric signals (EDHF via gap junctions) from the ECs to the VSMCs in response to metabolic, mechanical and chemical stimuli.

An important molecular optical property of NAD(P)H coenzyme is the endogenous natural autofluorescence (AF), which may be used for the non-invasive real-time monitoring of NAD(P)H concentrations to evaluate the mitochondrial function and oxidative stress [12]. There is growing evidence for a common pathway involved in the induction of oxidative stress, elevated blood pressure (BP) and inflammation resulting in endothelial microvascular dysfunction, which is a pivotal phenomenon involved in the development and progression of cardiovascular pathologies such as hypoxia, ischaemia, hypertension, coronary disease, and microvascular complications of diabetes [9, 13]. Microvascular dysfunction is characterised by the reduction of the endothelium-dependent vasodilation due to the simultaneous rise of the amount of endothelium-derived contracting factors, e.g. endothelin-1, and reduction of active vasodilators levels, e.g. NO. Oxidative stress and endothelial dysfunction precede structural changes in blood vessels and CVD clinical manifestations, thus they represent powerful candidates for the early preclinical assessment of cardiovascular risk [11, 14]. Indeed, there is a growing recognition that the microcirculation contributes to the onset of atherosclerotic cardiovascular disease. For example, the reduction of flow reserve in the coronary micro-vessels is widely considered an independent prognostic factor for adverse cardiovascular events (e.g. myocardial infarction) [15, 16, 17, 18, 19, 20, 21], and impaired microvascular function predicts the conduit artery atherosclerosis and its risk factors [11, 22]. Additionally, many studies have linked microvascular dysfunction with a variety of diseases or risk factors, i.e., obstructive sleep apnea [23], cardiomyopathy [17, 24, 25], heart failure [26, 27], ageing [28], physical inactivity [29], smoking tobacco [30]. Dysfunction in the microcirculation is considered also the cause for no-reflow phenomenon [31], damage from cardioplegic arrest [32], coronary microvascular spasm [33] and angiogenesis [34, 35].

1.4 Skin model to study microcirculation and oxidative stress

1.4.1 Rationale for using skin

Although the high potential of microvascular function and oxidative stress as predictors of CVD risk, the examination of microvascular function from the central coronary microcirculation is difficult, relying on the use of invasive procedures such as coronary angiography [11, 36]. The problem may be addressed by using

the peripheral microcirculation as a surrogate marker of central coronary arteriolar dysfunction. Assessment of peripheral arteriole function may be performed from readily accessible sites such as skin, eye, limbs and mucosal tissue by non-invasive techniques [11, 14, 36]. Although these procedures are not largely used in clinical practice, several studies have demonstrated that the peripheral microcirculation reflects the general health conditions of the central microvasculature [11, 36]. For instance, correlations between CVD risk factors and femoral [37] or retinal [38] endothelial function have been reported [11], and the cutaneous microcirculation has been shown to be correlated with markers of systemic endothelial function, i.e. plasma NO (positive correlation) and plasma endothelin-1 (negative correlation) [39]. Hansell *et al.* [40] have reported a significant correlation between vasodilator vascular responses to acetylcholine (ACh) in small cutaneous micro-vessels and the brachial artery, indicating a systemic nature of endothelial function and the link between skin microvascular dysfunction and large artery endothelial dysfunction. Furthermore, cutaneous microcirculation and coronary function have been shown to be in a high relationship [36], and impaired skin microvascular endothelium-dependent vasodilation induced by ACh has been found associated with coronary heart disease (CHD) risk [41]. Additional studies have reported an association between skin microvascular dysfunction and a wide range of CVD risk factors including hypertension [42], diabetes [43, 44] and ageing [45].

All this evidence makes skin microvascular activity a potential index of coronary micro-vessel dysfunction, which could be used as a surrogate marker for the prediction of CVD risk. However, further investigation is needed to better elucidate the reasons for the link between the peripheral microcirculation, the activity of large conduit arteries and adverse cardiovascular events. A possible explanation could be that small micro-vessels are the initial site for endothelial damage in individuals at risk of CVD [14]. Moreover, micro-vessels play a crucial role in the maintenance of tissue homeostasis (by supplying nutrients and oxygen) and the regulation of vascular resistance and of the local parenchymal tissue in every organ [11]. Therefore, deficiency in these fundamental tasks may have a negative impact on the overall cardiovascular system.

Skin accessibility has also been exploited for the *in-vivo* monitoring of oxidative stress [46]. Cutaneous NAD(P)H autofluorescence was found to be increased

during hypoxia, ischaemia or general conditions leading to blocking of the electron transport chain and improper delivery of oxygen to the tissue [47]. Assessment of skin NAD(P)H autofluorescence has also been proposed as an indirect tool to measure an index of widespread atherosclerosis [48]. Therefore, the concurrent use of non-invasive methods measuring *in-vivo* cutaneous microcirculation and skin AF of NAD(P)H is promising to address the preclinical evaluation of CVD risk in the future, through the early detection of endothelial dysfunction and oxidative stress [9, 14]. However, as mentioned above, although there is powerful potential application of using skin several aspects still need to be addressed such as understanding how much the skin peripheral microcirculation reflects the central cardiovascular system function [14, 49], and overcoming limitations due to the complex and inhomogeneous stratification of skin which is characterised by a spatial variety of optical properties [46].

1.4.2 Skin anatomy

Skin is the outer covering part of the body whose main functions are the protection of organs from external agents, and thermoregulation and homeostatic maintenance of the body. Skin is organised in three primary layers defined as epidermis, dermis and hypodermis (Fig. 3). The epidermis is the outermost cutaneous bed, characterised by a variable thickness between 0.07-1.4 mm [50]. It is organised in multiple sub-layers lacking blood vessels and serving mainly as a protective barrier from the external environment [9]. The dermis stratum below the epidermis is made of connective tissue and functional components, including the microvascular vessels, nerves, hair follicles and sebaceous or sweat glands [51]. The dermal layer has a thickness between 1.5-5 mm [9], and is responsible for the skin mechanical properties [51]. The hypodermis or subcutaneous tissue is the most internal skin bed, characterised by high content of adipose tissue for the storage of energy in the form of fat [52].

The skin microvascular network is divided into two horizontal plexuses. The upper plexus at the epidermal-dermal junction is named papillary dermis and contains finger-like capillary loops (Fig. 3) [9]. The lower plexus is a network of horizontal arterioles and venules located at the interface between the dermal and subcutaneous layers and connected to the upper system by ascending and descending micro-vessels (Fig. 3) [9]. The various regions of the body display diversity in the cutaneous microcirculation anatomic structure, which can be

mainly classified in arteriovenous anastomoses (AVAs) containing or lacking areas [9]. The AVAs are microvascular functional structures characterised by the direct exchange of blood between arterioles and venules, bypassing the capillaries [53, 54].

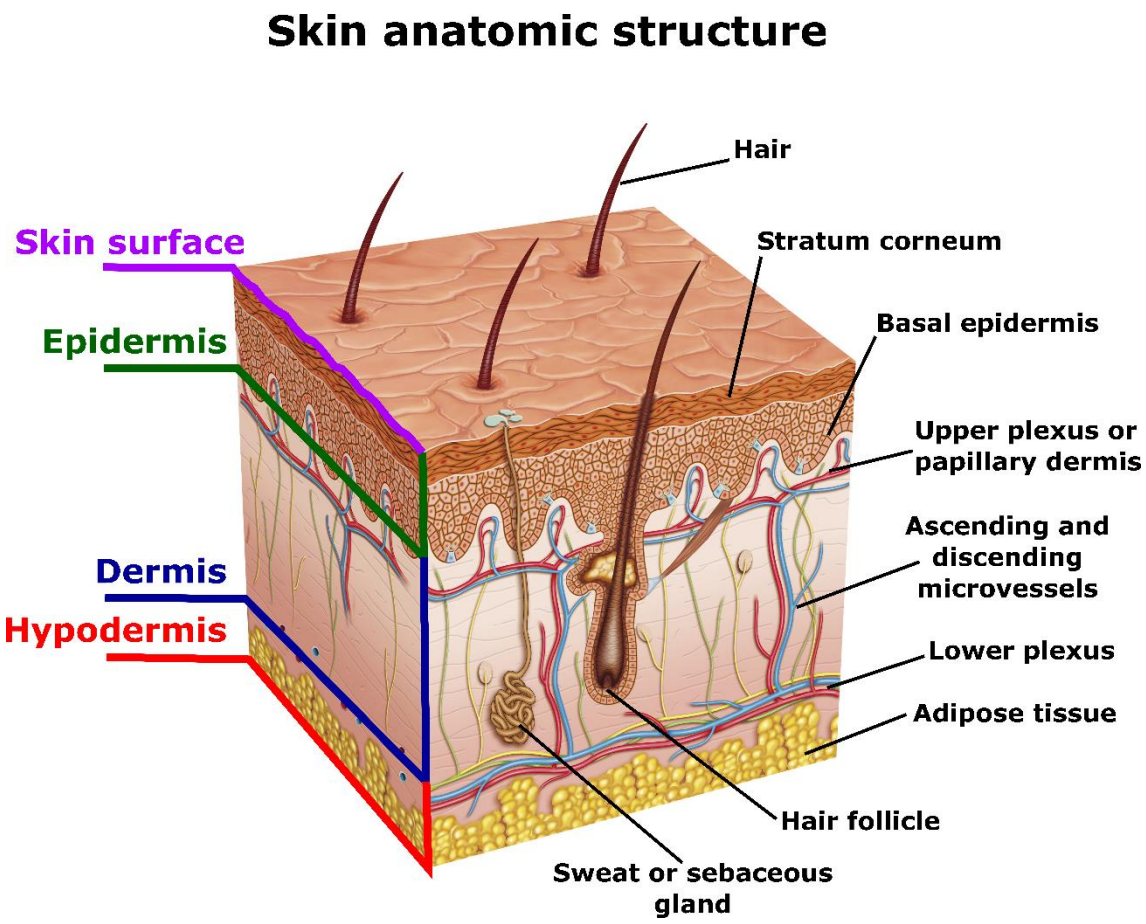

Fig. 3 Cutaneous anatomic structure. The picture was reproduced and adapted from http://anatomymedicalook.com/unlabeled-skin-diagram/unlabeled-skin-diagram-unlabeled-diagram-of-the-skin-anatomy-structure. Skin is made of three main layers defined as epidermis, dermis and hypodermis. The superficial epidermal layer protects the body from the external environment. For instance, the outermost stratum corneum functions as a permeable barrier selecting the molecules that pass into and out of the skin [55]. The production of melanin pigments by melanocyte cells in the basal epidermis protects the dermis and hypodermis from external UV (Ultraviolet)-B radiations [56]. The median dermal layer contains functional components (micro-vessels, sweat or sebaceous glands, nerves, hair follicles) embedded in a connective tissue responsible for the structural support and elasticity of the cutaneous tissue [51]. The connective tissue is composed of fibroblast cells, structural proteins (collagen and elastin), and hydrophilic gels [51]. The most internal hypodermal layer is rich in adipocyte cells and blood vessels, and exerts several functions such as thermoregulation, protection of the internal tissue from external wounds, and energy storage in the form of fat [52].

AVAs containing regions contribute to the maintenance of the thermoregulatory homeostasis [9, 53, 57], and are characterised by a heterogeneous density of capillary loops and arterioles across the vascular beds that ensure higher blood perfusion and intravascular pressure [9, 57]. In contrast, zones without AVAs show lower blood flow in the micro-vessels [57]. The palmar surface of the finger tips and in general hairless skin areas are examples of regions rich in AVAs, and the lower forearm's medial surface is an example of an area without AVAs [9].

1.4.3 Skin optical properties

As mentioned above, the non-invasive laser methods for the assessment of skin microcirculation and autofluorescence are limited by the complex cutaneous structure. Propagation of light through the skin is characterised by reflection, transmission, absorption and scattering events, which affect the light penetration depth depending on the used wavelength and on the thickness and anatomy of the examined skin area. When a laser beam hits the skin, the light is partially reflected and partially transmitted in the epidermal and dermal layers or deeper [58]. The transmitted light is partially scattered by heterogeneous biological structures with different refractive index (e.g. collagen and elastin fibres in the dermal connective tissue), and partially absorbed by several chemical and biological chromophores with different absorption coefficients (μ_a) (Fig. 4) [58].

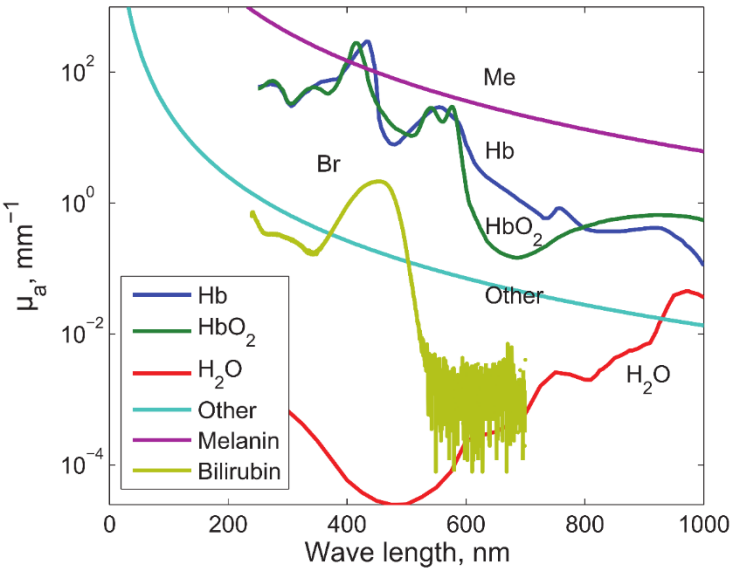

Fig. 4 Absorption coefficients (μ_a) of skin chromophores (figure reproduced from [59]). Haemoglobin (Hb) in the blood, water, melanin and bilirubin represent the main light absorbers in the cutaneous tissue. The graph shows that the μ_a of each chromophore varies according to the wavelength. Therefore, the complex signal detected when skin is irradiated by a light source may be affected differently, depending on the wavelength of the laser used to illuminate the tissue.

A part of the light after attenuation by absorption and scattering events is backscattered to the skin surface [58], where it is detected as a complex output signal resulting from the contribution of various biological, chemical and structural components in the tissue which interacted with light.

1.5 Non-invasive methods for the evaluation of cutaneous microcirculation

1.5.1 Assessment of skin microvascular function

Functional changes in the microcirculation precede the occurrence of structural microvascular abnormalities [11, 14], thus endothelial dysfunction represents a predictor of cardiovascular pathologic conditions more powerfully than structural information provides. Many studies have focused on the examination of skin microvascular function in both humans and animal models, by using non-invasive methods coupled with reactive tests to measure endothelial function [9, 14, 49].

The techniques mostly used for this purpose are the laser Doppler and laser speckle contrast imaging (LSCI), which are able to provide real-time functional data concerning the relative changes in skin blood perfusion [9, 49]. However, the use of these technologies in clinical practice is still limited by lack of standardisation [9, 49].

Laser Doppler

The laser Doppler methods provide an index of skin blood perfusion I_m calculated as the product between the average red blood cells (RBCs) velocity V_a and their concentration N_{er} [9, 49],

$$I_m = N_{er} \cdot V_a \ . \quad (1)$$

The blood perfusion is expressed in perfusion arbitrary units (PU). The principle of the technique is based on the detection of the Doppler shift in wavelength observed when a monochromatic and coherent beam of red or infra-red (IR) laser light is backscattered by moving RBCs [9, 14, 49]. This is an indirect measurement of skin blood perfusion, and there is evidence of a linear relationship between the detected laser Doppler signal and the actual blood flow [9, 49]. The laser Doppler methods are commonly classified into two categories:

- *Laser Doppler flowmetry (LDF)*. The LDF technology is based on the use of a laser single-point probe (Fig. 5) placed at direct contact with the skin surface,

which measures blood flow in a small tissue volume (1-5 mm^3) with a high sampling frequency and the ability to detect fast relative variations [9, 14, 49]. An advantage of LDF is the constant measurement of blood flow in the examined location that allows obtaining continuous time series of blood perfusion suitable for the study of microvascular nonlinear dynamics (Fig. 6) [14]. However, the method is characterised by low reproducibility due to the spatial variability of skin perfusion related to the heterogeneous cutaneous anatomy [9, 14, 49]. The problem may be addressed by using integrated probes composed of multiple collecting fibres to cover a larger skin area and increase the spatial resolution, through the calculation of the average signal from different scattering volumes [9, 14, 49].

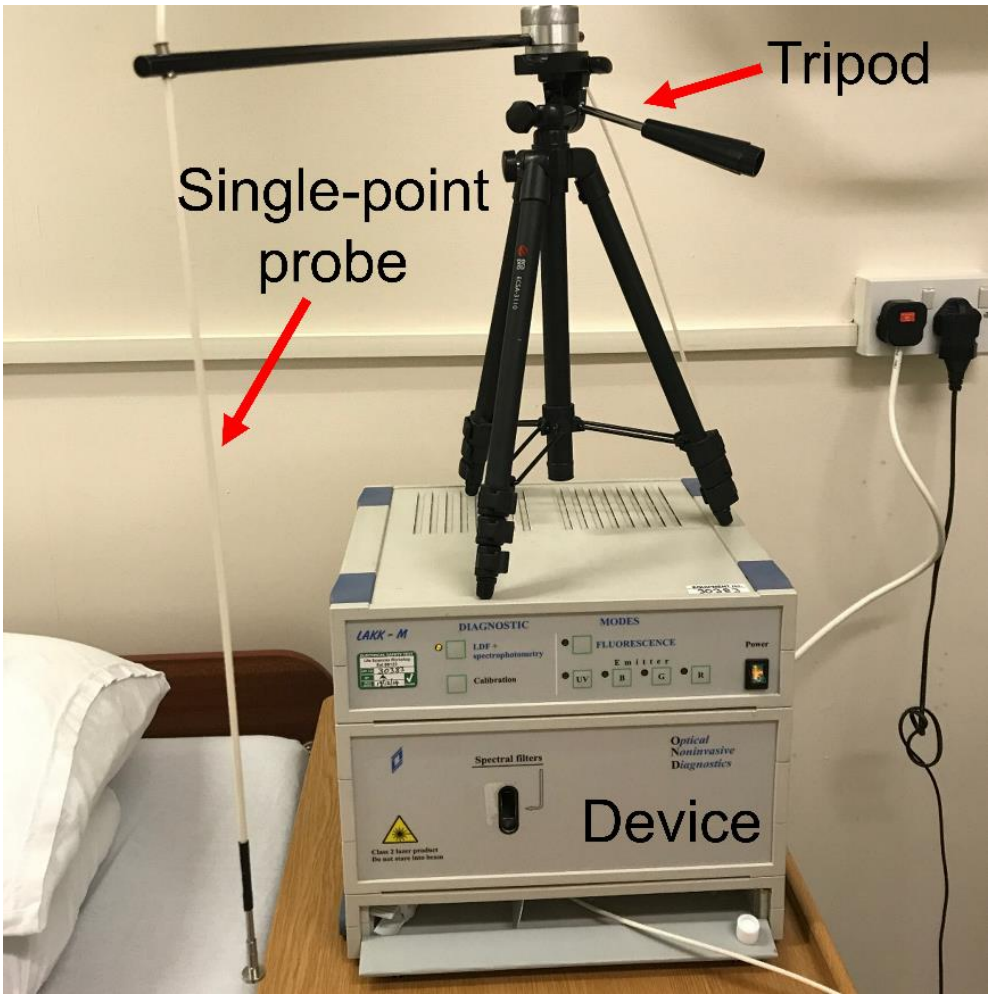

Fig. 5 Example of LDF instrument. *LAKK-M* device (*Spe Lazma Ltd*, Russia). The system is provided with a single-point multimode optical probe that must be placed at direct contact with the skin for recording LDF blood flow traces. A tripod is used to fix the probe perpendicularly to the cutaneous sample.

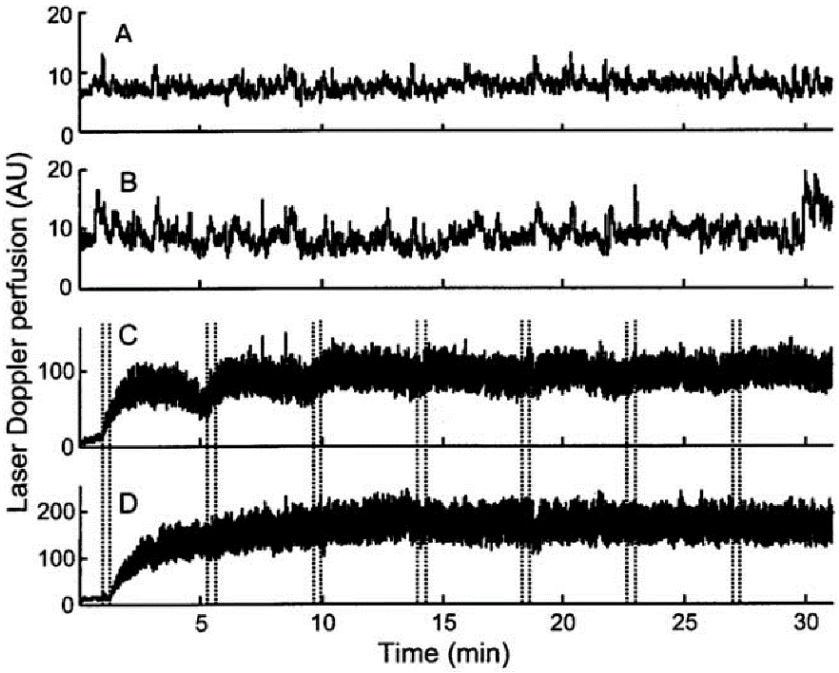

Fig. 6 LDF recordings (figure reproduced from [60]). (**a-b**) Examples of baseline LDF continuous time series measured from the human upper arm and forearm, respectively. (**c**) LDF signal recorded during stimulation of the endothelium-dependent vasodilation by iontophoresis delivery of acetylcholine (ACh). (**d**) LDF time series measured during stimulation of the endothelium-independent vasodilation by iontophoresis delivery of sodium nitroprusside (SNP). The data were collected by using a commercial single-point probe (*MP1*, *Moor Instrument Ltd*, UK). The amplitudes of the signals are expressed in arbitrary units (AU). Iontophoresis stimulation was performed by the application of a 100 μA current at intermittent intervals of 20 seconds highlighted by the vertical lines.

- *Laser Doppler imaging (LDI)*. The LDI technology provides 2D images by using the laser Doppler principle [9, 14, 49]. In this case, the light source is positioned at a specific distance above the skin surface (Fig. 7) and the system is provided with a computer-driven mirror, which reflects the laser beam scattered by the tissue to progressively scan the area of interest [9, 14, 49]. The final output is a 2D image mapping skin blood flow by using coloured pixels which represent perfusion values (Fig. 8) [9, 14, 49]. The advantage of the method is the reduction of spatial variability by scanning a large skin area [9, 14, 49]. However, LDI is slower than LDF leading to the inability of recording rapid variations in blood flow [9, 14, 49]. Moreover, LDI allows only discrete perfusion measurements at given time points, thus it can be used successfully only for the study of the maximum response to a given stimulus but it is not suitable for the investigation of microvascular nonlinear dynamics [14].

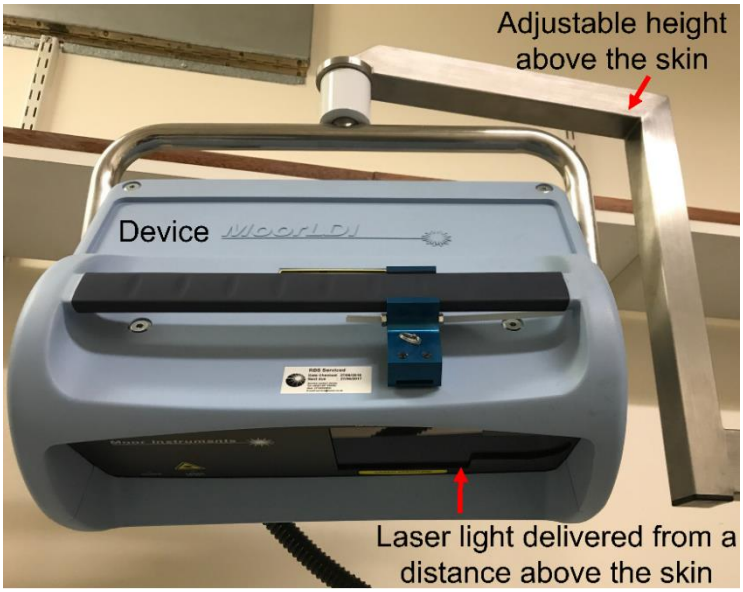

Fig. 7 Example of LDI instrument. *MoorLDI* device (*Moor Instruments Ltd*, UK). The system is fixed on a support provided with a handle to adjust the height of the device at a specific distance above the cutaneous sample from which the laser light is irradiated to image blood perfusion maps.

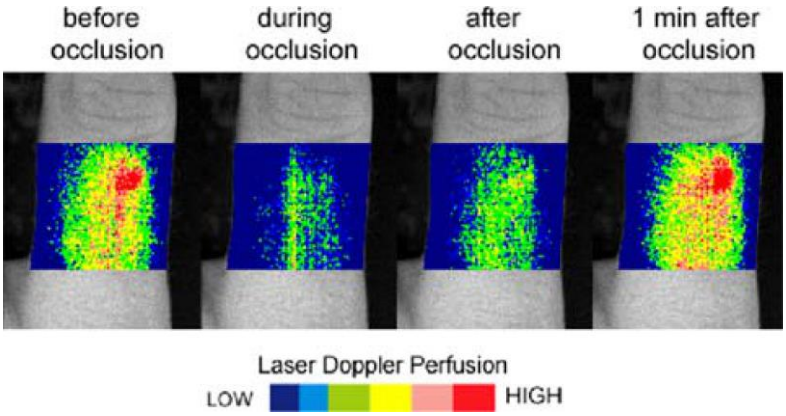

Fig. 8 Examples of LDI images (figure reproduced from [53]). The false-colour images show sequential LDI maps obtained from the human finger during the different stages of the post-occlusive reactive hyperaemia (PORH) test: baseline, occlusion of blood flow from the upper arm, and post-occlusion. The colour of the pixels reflects the level of skin blood flow, ranging from blue low perfusion regions to red high perfusion areas. The maps clearly show colour changes corresponding to a reduction of blood flow during occlusion, and an increase of perfusion after occlusion.

LSCI

Laser speckle contrast imaging is a non-contact technique based on the analysis of the speckle contrast pattern generated when a beam of light hits the opaque skin surface [9, 49]. Moving RBCs induce changes in the speckle pattern with a reduction in the contrast as the blood cells velocity increases [9, 49]. Therefore,

the analysis of the reduction in speckle contrast provides a perfusion index proportional to the velocity and concentration of RBCs [9, 49]. The LSCI technology provides a high reproducible index of blood flow with high spatial and temporal resolution, thus including the advantages of both LDI and LDF [9, 49]. However, the technique has lower penetration depth (~300 μm) in the skin than laser Doppler (~1-1.5 mm) and is more sensitive to movement artefacts [9, 49].

Furthermore, although it seems that LSCI signal and blood flow are in a linear relationship, a small number of experiments supporting this evidence has been performed [9, 49]. LSCI devices must be placed at a specific distance above the skin for performing blood perfusion measurements, and are characterised by a design similar to that of the LDI system displayed in Fig. 7. Fig. 9 shows an example of blood perfusion image obtained by LSCI.

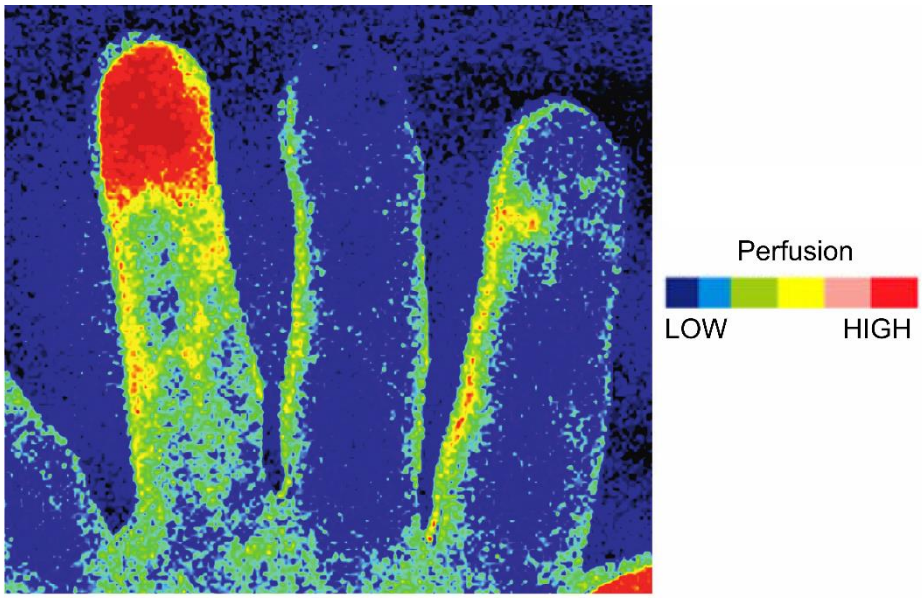

Fig. 9 Evaluation of blood perfusion by LSCI (image reproduced and adapted from [9]). Example of laser speckle contrast imaging of blood perfusion from the fingers of a patient affected by the Raynaud's phenomenon. As seen in the LDI method, LSCI provides coloured maps with low perfusion areas in blue and high blood flow regions in red. The image shows the perfusion levels after stimulation of the ring finger with iontophoresis of acetylcholine, and the middle finger with sodium chloride. The increase in blood flow due to vasodilation is clearly visible (red area).

Functional tasks

The laser Doppler and LSCI methods provide only relative measurements of blood perfusion, which means that basal levels of perfusion cannot be used reliably to make a significant evaluation of microvascular function and comparisons between different subjects. For this reason, the techniques must be

combined with functional tasks for the assessment of skin micro-vessels reactivity to allow a reliable examination of microvascular function. Several reactive tests have been developed for the assessment of blood flow changes in response to mechanical, thermal and electrical stimuli or to the local administration of pharmacological drugs [9, 49]. Examples of reactive tests are represented by post-occlusive reactive hyperaemia (PORH) and iontophoresis delivery of vasoactive drugs [9, 14, 49].

PORH. The PORH functional task consists in monitoring the increase of skin blood perfusion after a temporary period of ischaemia artificially induced by mechanical arterial occlusion, to measure an index of general microvascular function [9, 49]. This kind of micro-vessel response is defined as post-occlusive reactive hyperaemia and involves multiple mediators for the adaptation of the myogenic tone, including major players such as the sympathetic nerves in the microcirculation and EDHF (NO-independent), and a small contribution of the endothelial NO-dependent pathway [9, 49]. The most common procedure to perform PORH test is placing an inflation cuff on the upper part of the arm while recording blood flow from the volar forearm or the fingertip locations [9, 49]. The cuff is then inflated at a pressure 10 mmHg higher than the systolic blood pressure (SBP) of the subject, generally for a period of 5 min or more [9, 49]. The PORH response can be evaluated as the post-occlusion absolute perfusion peak (PK), as the area under the curve (AUC) of the post-ischaemia peak, or expressing the post-occlusion peak as a function of the baseline flow (BL) (Fig. 10) [49]. Skin PORH has been found to be decreased in a variety of cardiovascular diseases [9, 49].

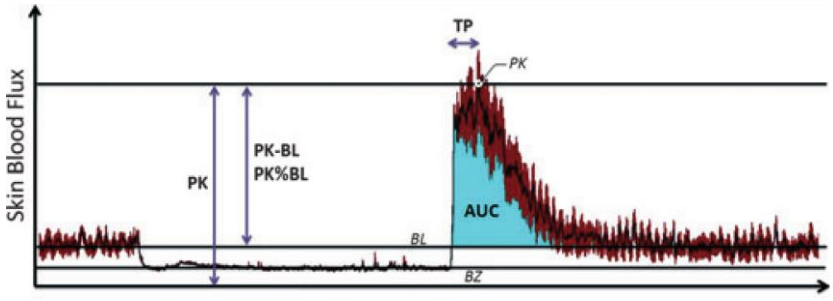

Fig. 10 Typical PORH curve (figure reproduced from [49]). The graph describes LDF blood flux changes in the human forearm during the different steps of PORH test. The decrease of flow during the occlusion and the PORH response peak after the release of the pressure are clearly visible. The PORH response may be evaluated by using the raw peak response (PK), the area under the curve (AUC), or relating the PK to the baseline flow (BL). BZ is the biological zero that represents the residual flow signal observed when blood perfusion is blocked by arterial occlusion.

Iontophoresis. The iontophoresis functional task is designed to evaluate microvascular blood perfusion changes in response to the local administration of vasoactive drugs across the skin [9, 14, 49]. The method is based on the non-invasive transdermal delivery of an ionic pharmacological agent solution through the application of an electric current, while the blood flow is measured by laser Doppler [9, 14, 49]. The equipment to perform iontophoresis is composed by a reference electrode and a ring-shaped chamber provided with an internal electrode (Fig. 11) [14]. The two electrodes are connected to a controller ensuring that the polarity of the chamber electrode has the same charge of the vasoactive drug [14]. The experimental setup is completed by the attachment of the chamber and the reference electrode on the skin of the testing subject or animal, and finally filling the chamber with a solution of the vasoactive agent [14]. Under the influence of the applied electric current, the charges of the chamber electrode will repel the charges of the drug inducing the transfer of the molecule into the skin [14]. The current used for iontophoresis is weak, generally up to a maximum of 100 µA [14].

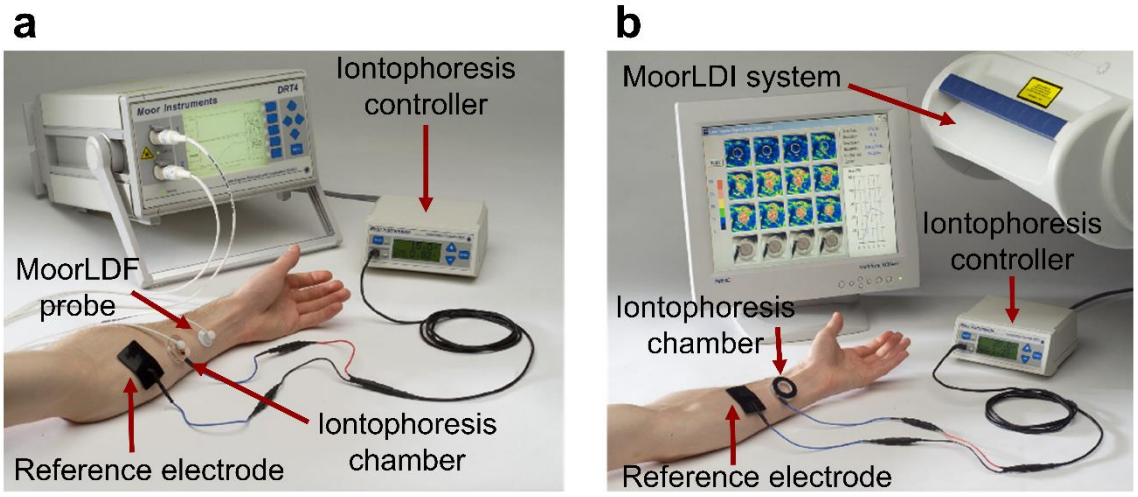

Fig. 11 Iontophoresis equipment. (**a**) Example of combination of the iontophoresis equipment with the *MoorLDF* probe (*Moor Instruments Ltd*, UK). (**b**) Example of combination of the iontophoresis equipment with the *MoorLDI* system (*Moor Instruments Ltd*, UK). Both of the reference electrode and the ring-shaped chamber must be attached to the skin and to an iontophoresis controller, for allowing the transdermal administration of a drug ionic solution by application of an electric current.

The drugs mostly used to study endothelial function are the vasodilators acetylcholine (ACh) and sodium nitroprusside (SNP), which allow respectively the evaluation of endothelium-dependent and endothelium-independent vasodilation

[9, 14, 49]. Fig. 6c-d show examples of LDF recordings during the stimulation of vasodilation by iontophoresis delivery of ACh and SNP, respectively. ACh stimulates vasodilation mainly by endothelial NO-dependent modulation of VSMCs, even though the possible concurrent contribution to the response of endothelial NO-independent mediators such as the EDHF and PGs is not clear [9, 14, 49]. In general, the decrease in microvascular vasodilation induced by ACh is related to endothelial dysfunction but care must be taken when reporting data [14]. For example, the decrease in the vasodilator capacity may cause a reduction in the mean flux, which might be misinterpreted as endothelial dysfunction [14]. Reporting data as a percentage of the maximum vasodilation peak may help to avoid results misinterpretation [14]. SNP is a NO donor able to induce an endothelium-independent vasodilation by the direct stimulation of VSMCs relaxation [14]. The increase of NO bioavailability induced by the external contribution of SNP allows bypassing the endothelium-mediated vasodilation, providing an endothelium-independent control [14]. When ACh-mediated vasodilation is reduced without decrease in the control SNP-mediated vasodilation, data may be interpreted as the presence of endothelial dysfunction [14]. In contrast, the reduced response to SNP is harder to interpret because it might be related to either the decrease in blood vessels vasodilator capacity, or the reduction of NO bioavailability associated with oxidative stress and vascular dysfunction [14].

The combination of iontophoresis and laser Doppler has been used extensively in many studies reporting significant associations between reduced response to ACh in the cutaneous microcirculation and CVD risk factors or cardiovascular pathologic conditions, as well as correlations with systemic biomarkers of endothelial function [14]. Therefore the methodology may find a wide range of applications such as assessment of preclinical risk factors, diagnosis of vascular pathologic conditions, and monitoring the progression of CVD [14]. However, the technique suffers from lack of standardised protocols leading to contrasting literature evidence, the results are not reproducible from different cutaneous locations and are affected by the different skin resistance between subjects [14].

Pressure-induced vasodilation (PIV), local thermal hyperaemia (LTH) or local cooling, current-induced vasodilation (CIV), and microdialysis or intradermal injections represent other examples of reactive tests based respectively on

mechanical, thermal, electric and pharmacological challenges [9, 49]. However, these methods will not be discussed here because they are not crucial for the work object of this dissertation.

1.5.2 Factors affecting the assessment of microvascular function

The assessment of microvascular reactivity by Laser Doppler or LSCI combined with functional tasks requires some preliminary arrangements, to avoid the influence of several factors that may affect skin blood perfusion changes confounding the results. For example, the temperature (T) in the room where the experiment is performed can influence blood perfusion changes, thus it is recommended to use a room with controlled T and start the recordings after a period of acclimatisation of the testing subject [9, 57]. Research studies related to skin perfusion must be designed ensuring that the subjects from different groups are matched for age and gender. The reason for this is the major probability of impaired vascular reactivity in elder subjects compared to young individuals, and the different physiology between men and women, i.e. because of hormone level variations across the menstrual cycle [9]. The skin location used for the measurements also affects the results. For instance, the volar forearm is a location associated with high nutritive blood flow, the absence of AVAs and low perfusion due to the low density of blood vessels [57]. In contrast, the finger tips are areas rich in AVAs characterised by higher blood vessels density [9, 57]. Using the finger pad may help to reduce the spatial variability and also to record a higher perfusion signal [9, 57]. However, the finger tips present high density and regulatory activity of the sympathetic nerves [57], which might confound the results especially when the task is the study of nonlinear dynamics and oscillations of blood flow. Therefore, care must be taken to choose the appropriate skin location based on the objectives of the research. Blood perfusion can also be influenced by circadian rhythms associated with a variable flow during different hours of the day. Therefore, it is suggested to test all the individuals participating in a study at the same time of the day [57]. Another factor that might be taken into account when using the PORH test is the biological zero (BZ), which represents the residual flow signal observed when blood perfusion is blocked by arterial occlusion through a pressure cuff (Fig. 10) [9]. The reports about the BZ are controversial, and a link with the Brownian motion of residual RBCs in the venules or macromolecules in the vascular tissue has been hypothesised [9].

Whether the BZ should be considered to correct perfusion data or to gain additional information is unclear [9]. However, several studies have shown that data correction with the BZ introduces more bias, especially when data are expressed as a function of the baseline [9].

1.5.3 Evaluation of microvascular structure

Skin microcirculation can also be assessed by a wide range of techniques such as optical microscopy, 3D photoacoustic imaging, and optical coherence tomography (OCT). However, these technologies are commonly appropriate to gain structural information, and further implementation is required to extend their application to the assessment of microvascular function and nonlinear dynamics. The main focus of this work is the investigation of the skin microvascular and energy metabolism nonlinear dynamics, thus only a general brief description of the methods for the assessment of microcirculation structure will be given to complete the overview concerning the non-invasive tools for the study of the cutaneous microcirculation health conditions.

Optical microscopy methods

Examples of optical microscopy techniques for the assessment of skin microvascular structure are represented by videocapillaroscopy, orthogonal polarisation spectral imaging (OPS) and sidestream dark-field imaging (SDF).

Videocapillaroscopy allows the *in-vivo* observation of capillaries through a microscope that transmits an image to a video camera, providing information about the capillary density and structure in the nail fold [49]. The technique shows several limitations such as low-contrast images and the requirement of trans-illumination or fluorescent dyes, which makes the method invasive [49].

OPS and SDF overcome the limitations of the videocapillaroscopy since they exploit a green light source for the non-invasive illumination of the tissue and the detection of the photons scattered from the skin to obtain a good resolution image [49]. The green light is absorbed by the haemoglobin (Hb) in the RBCs providing a contrast tool, where blood cells are dark and the remaining microvascular tissue that does not absorb green light is visualised in the white or grey field (Fig. 12) [53]. OPS and SDF are limited by artefacts due to the high sensitivity to subject's movements or to the pressure applied by the probes during the examination [49].

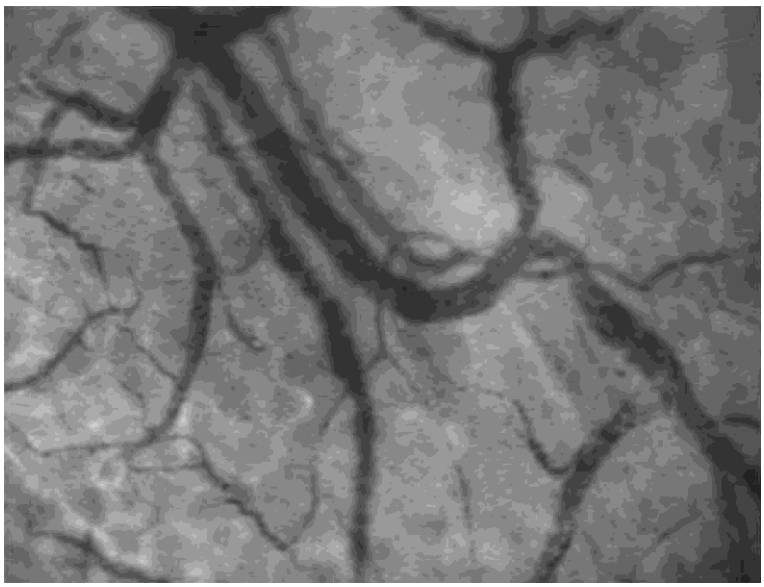

Fig. 12 Example of SDF image (figure reproduced from [6]). Image of the sublingual microcirculation obtained by sidestream dark field imaging method, showing capillaries and venules from the imaged region.

3D Photoacoustic imaging

This technology requires the combination of pulsing lasers and ultrasound receivers. The principle of operation is based on the detection by the receiver of the pressure acoustic waves generated in all directions when the pulsed light is absorbed by chromophores in the tissue [61, 62]. The detected waves allow the reconstruction of a 3D map of the chromophores location [61, 63].

The major benefit of this methodology is the low scattering of ultrasound waves, which allows exploiting a full light penetration depth [64]. The technique also allows to gain *in-vivo* functional information about the total Hb and oxygen saturation (SO_2) in the skin microcirculation, by tracing haemoglobin absorption at different wavelengths [65]. However, overall, the technology is limited by the low acoustic resolution leading to poor microvascular structural images, even though more advanced photoacoustic methods, e.g. PAM (photoacoustic microscopy), have improved this aspect [66]. Moreover, the requirement of a coupling medium to allow direct contact with the skin may affect the activity of the microcirculation providing confusing results.

OCT

Optical coherence tomography is a non-invasive and non-contact imaging method that overcomes some limitations of the photoacoustic technology. OCT is based on the employment of a broadband light source to create a low

coherence gate for the selection of the backscattered light from different skin tissue depths, to generate an *in-vivo* structural image [67]. The main advantage of this method is the ability to provide cross-sectional images similar to conventional optical biopsies with micrometer structural resolution [68, 69]. However, a disadvantage is represented by the low penetration depth (~1-2 mm) compared to photoacoustic [70]. Although the original application of OCT in the microcirculation field was mainly aimed to obtain structural information, the technology has been implemented to also gain functional information by adding contrast mechanisms based on the Doppler shift (DOCT) [71] and the speckle variance (svOCT) [72] principles, or by using processing techniques based on the separation of static and flow dynamic regions (OMAG, optical microangiography) [73] and on correlation mapping (cmOCT) [74]. However, these techniques have not yet been implemented for the study of nonlinear dynamics in the microcirculation, and are limited by high sensitivity to motion or long times required for post-processing. For these reasons, the conventional laser Doppler and LSCI techniques still represent the preferred choice for the study of microvascular function and nonlinear dynamics.

1.6 Non-invasive techniques for the study of skin oxygenation

Another approach to gain functional information about the skin microcirculation is represented by monitoring real time the cutaneous oxygenation. Indeed, poor tissue oxygenation may indicate the presence of vascular dysfunction. Several non-invasive methods to detect *in-vivo* the amount of oxygen are based on the measurement of the differential light absorption of oxyhaemoglobin (oxyHb) and deoxyhaemoglobin (deoxyHb), while other non-invasive techniques are based on the detection of the transcutaneous oxygen partial pressure ($tcpO_2$) through electrodes.

Overall, the laser techniques for the assessment of oxygenation may be classified into three categories:

- Conventional pulse oximetry (PO).
- Reflectance spectroscopy (RS).
- Near infra-red spectroscopy (NIRS).

PO

Pulse oximetry is the traditional method for the indirect measurement of arterial oxygen saturation (S_pO_2) [75]. The technique is based on the simultaneous irradiation of the tissue with both red and IR light, allowing to distinguish the oxyHb and deoxyHb haemoglobin forms [75]. OxyHb absorbs more the infra-red light while deoxyHb absorbs more the red light [75]. The absorbance ratio between the two forms of haemoglobin is used by manufacturing companies to make a calibration against direct measurements of arterial oxygen saturation (S_aO_2) to setup the pulse oximeter oxygen saturation (S_pO_2) [75].

The traditional PO probes are provided with emission (LEDs or lasers) and detection sensors on the opposite surface of the tested sample, allowing the estimation of oxygen saturation from the light transmitted through the sample [75]. An example is represented by the classic pulse oximeters used in the fingers [75].

PO provides only the estimation of the arterial oxygen saturation, based on the principle of the periodic contraction and relaxation of arterial blood vessels induced by pulse activity. Therefore, the calculation of the difference between the maximum and minimum haemoglobin absorption ratio from an area with pulsatile blood flow, e.g. the finger, will be equivalent to the arterial oxygen saturation.

Although S_pO_2 may be useful for clinical applications, it reflects mostly the lung function rather than the local tissue oxygenation. Therefore, conventional pulse oximetry is not an eligible method to gain functional information about the oxygen amount and uptake in the skin microcirculation.

RS

Reflectance spectroscopy is able to provide continuous measurements of the local level of oxygen in the tissue. The method is based on the reflectance principle, which allows determining the percentage oxygen saturation (SO_2) from the light backscattered by the skin tissue [75, 76, 77]. The examination of the wavelength of the backscattered light provides information on the differential absorption of bound and unbound haemoglobin [77]. The absorption is proportional to the relative concentrations of the chromophores in the local tissue, thus it represents an indirect measurement of the metabolic status and microvascular activity in the examined location [77]. RS devices are provided with emission and detection sensors integrated into adjacent locations of a single-point probe [76, 77]. The sensors are separated by a short distance to provide

both high spatial (mm^3) and high temporal (40 Hz) resolution [76], and they are connected to the light source and the spectrometer through optical fibres [75, 76, 77]. This kind of probe may be applied in several skin locations of the body, i.e. the forearm, the hand and the foot. The light source of RS devices may vary depending on the application and is generally selected according to the desired wavelength range [77]. The assessment of oxygen saturation *in-vivo* requires the use of low power laser sources (1-5 mW) to avoid damage to the skin. For this reason, most biomedical RS devices are provided with laser sources in the visible spectral range, which allow measuring only the superficial SO_2 due to the low penetration depth of visible light. Different kinds of device have been developed using the white light (e.g. *moorVMS-Oxy*, *Moor Instruments Ltd*, UK), or multiple laser sources with specific wavelengths in the visible range (e.g. *LAKK-M*, *Spe Lazma Ltd*, Russia). The white-light reflectance spectroscopy is based on the employment of a white LED which emits in the 450-700 nm spectral range [76], and takes advantage of the major red colour of oxygenated blood and the more prominent blue colour of deoxygenated blood to estimate Hb absorption [77]. The backscattered light in the 500-650 nm range is then processed to extract oxyHb and deoxyHb molar concentrations through the application of the Beer-Lambert law [57, 76],

$$\mu_a(\lambda) = \Sigma\, \varepsilon_i(\lambda) \cdot c_i\,, \tag{2}$$

where $\varepsilon_i(\lambda)$ is the molar extinction coefficient of each chromophore, c_i is the molar concentration of each chromophore, and $\mu_a(\lambda)$ is the absorption coefficient which can be deduced from the reflected (I) and incident (I_o) lights. The percentage oxygen saturation is finally computed by the following formula [57, 76],

$$SO_2 = \frac{[oxyHb]}{[oxyHb]+[deoxyHb]} \cdot 100\%\,, \tag{3}$$

where [oxyHb] is the concentration of oxygenated haemoglobin, and [deoxyHb] is the concentration of deoxygenated haemoglobin. More specific details on how the individual terms of equation 3 can be extracted from the analysis of the backscattered light are provided in the papers by Dunaev *et al.* [57], Liu *et al.* [76], Heusmann *et al.* [78] and Kohl-Bareis *et al*. [79, 80].

The *LAKK-M* device is based also on the reflectance spectroscopy principle to determine SO_2 by using the equations 2-3 [57]. However, in this case the backscattered light generated by simultaneous illumination of skin with green

(532 nm) and red (630 nm) lasers are used to determine the differential absorption of oxyHb and deoxyHb fractions [57]. SO_2 measured by the RS method is representative of the average oxygenation of small arterioles, capillaries and venules in the skin microcirculation, and it is closer to the venous oxygen saturation (S_vO_2) rather than the arterial oxygen saturation.

NIRS

The near infrared spectroscopy is a method designed for the study of the local deep tissue oxygenation. The main difference with the reflectance spectroscopy is the use of a low power (5-10 mW) light source in the red and IR spectral regions (650-1000 nm), which penetrates deeper in the tissue (1.5-2 cm) and allows monitoring the haemodynamics associated with oxygen metabolism in organs under the skin, i.e. skeletal muscle or brain [81, 82]. NIRS principle is similar to the pulse oximetry, based on the distinction of the major optical absorbance of oxyHb and deoxyHb respectively in the IR and red spectral ranges [81, 82]. However, NIRS differs from PO because it provides accurate continuous measurements of deep SO_2 which are representative of the local microcirculation in the examined sample rather than the general arterial oxygen saturation.

The method is characterised by a principle of operation similar to the reflectance spectroscopy with the employment of emission and detection sensors placed in adjacent sites of a probe, and the determination of haemoglobin concentration by the examination of the reflected light. However, the NIRS probes are designed with a separation distance between emission and detection sensors around 2-4 cm [81] which is larger compared to RS probes, and the algorithms used for the signal processing and the estimation of SO_2 are different.

Advantages of the NIRS method are the large tolerance to subject's motion compared to PO and RS technologies, higher temporal resolution and good intra-subjects reproducibility [81, 82]. Limitations are represented by the sensitivity to biological tissue heterogeneity, and requirement of signal processing to remove instrumental errors, and physiological noise (e.g. skin perfusion) [81, 82]. Several studies have shown that the NIRS signal measured from the skeletal muscle microcirculation is well related with a variety of cardiovascular pathologies, e.g. heart failure, coronary artery disease and peripheral artery disease [82]. Therefore, the method is eligible as a tool for investigating CVD risk factors.

tcpO₂

This non-invasive method to monitor cutaneous oxygenation is based on the use of two electrodes (a platinum cathode and a reference silver anode) for measuring the partial pressure of oxygen (pO_2) through the skin. The small $tcpO_2$ sensor is applied to the skin surface using an airtight self-adhesive ring [83]. The electrodes are included in an electrolyte solution and separated from the cutaneous tissue through a membrane permeable to oxygen. The principle of the technique is the outward diffusion of oxygen from the skin to the permeable membrane and the detection of the electric current produced by the reduction of O_2 at the cathode, which is proportional to the amount of oxygen in the capillary bed of the cutaneous region under investigation. To allow the measurement of pO_2 values representative of the arterial pO_2, the diffusion of oxygen across the skin is more enhanced by heating the electrodes to warm up the skin at a temperature of 44-45°C [83]. This induces cutaneous maximal vasodilation, a decrease of vascular resistance, and compensatory arteriolarisation of capillary blood leading to increasing pO_2 and decrease of carbon dioxide partial pressure (pCO_2) toward arterial levels [83]. The time required to warm up the skin obtaining $tcpO_2$ values proportional to the arterial pO_2 is around 15-20 min, and the tolerance of the sensor at one cutaneous site is limited to 4 hours [83].

As in the case of pulse oximetry, the $tcpO_2$ method is more useful for clinical applications reflecting the general function of the respiratory system or the general ability of the vascular system to deliver oxygen to the peripheral tissue. However, although $tcpO_2$ and pulse oximetry measurements are correlated variables, they provide different measurements mainly due to the different principle of operation and shortcomings of these methodologies. For example, the $tcpO_2$ monitor reacts slowly to sudden changes in tissue oxygenation, and pulse oximeters are highly sensitive to subject's movement.

1.7 Non-invasive assessment of skin autofluorescent markers of energy metabolism

1.7.1 Autofluorescence (AF)

The term autofluorescence is referred to the emission of light in the UV, visible or near-IR spectral regions detected when natural fluorophores in a biological system are excited by irradiation through light at a specific wavelength [84]. This

optical property characterises many biological molecules involved as substrates in important morpho-functional processes of living systems, providing the great opportunity of monitoring *in-vivo* specific biological processes based on detecting the changes in the AF emission properties of the substrate of interest [84]. Examples of natural fluorophores are represented by the reduced NAD(P)H and oxidised flavin adenine dinucleotide (FAD^+) coenzymes, porphyrins, structural proteins (e.g. elastin and collagen), vitamin A, riboflavin, thiamin, lipofuscins, ceroid pigments, β-carotene, and aminoacids (i.e. tryptophan) [84].

Evaluating the AF signal from a live biological system may find important biomedical diagnostic applications. Indeed, the biological fluorophores can be eligible as biomarkers for the detection of alterations in the structural and functional features of cells and tissues [84], which are reflected in the AF emission spectrum. Fig. 13 shows the spectral profile of the natural fluorophores mostly used in biomedical research [84].

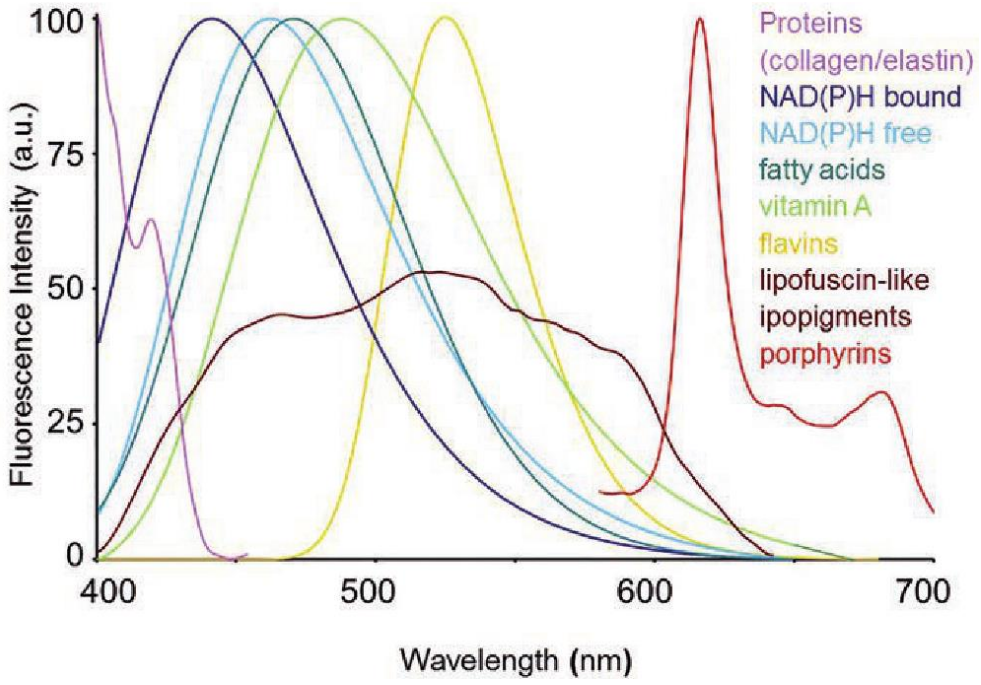

Fig. 13 AF emission profile of natural fluorophores used in biomedical research (figure reproduced from [84]). The spectra were measured by micro-spectrofluorimetry from *in-vitro* molecular solutions of the fluorophores (bound/unbound NAD(P)H, vitamin A, flavins, porphyrins), except for the spectra of the insoluble proteins collagen and elastin and the lipopigments that were measured respectively from connective tissue and hepatic portal of the liver cryostatic section. The wavelength of the excitation light was 366 nm. The graph clearly shows an overlap between emission spectra of different fluorophores at similar spectral regions, making it difficult for the assessment of the specific contribution of each fluorophore to AF spectra measured from the *in-vivo* tissue.

Although the powerful biomedical applications, as visible in Fig. 13 several natural fluorophores are characterised by an AF emission profile overlapping with the emission spectral region of other fluorophores, which makes it difficult the identification of the specific contribution of each biomarker to AF spectra measured from the *in-vivo* tissue. Excitation of the biological tissue at different wavelengths leads to the generation of complex AF spectral profiles, requiring further post-processing analysis for making reliable assumptions on the biological processes reflected by the AF spectrum. In addition, other factors affecting the AF spectral profile are also the optical properties of the different biological tissues (absorption, reflection, and scatter) from which depend the propagation of the excitation light and its interaction with the different components of the biological tissue, the fluorescence yield, and the overall signal collected at the tissue surface [84]. For these reasons, researchers are still working on the development of methods for characterising better the contribution of the biological fluorophores to the AF signal detected at the tissue surface. These methods are mainly based on Monte Carlo simulations to determine the effect of the tissue optical properties on AF spectra and the spatial resolution of the measurements, and analytical procedures, i.e. the spectral curve fitting for differentiating the relative overlapping contribution of different fluorophores to the total AF spectrum [84] (Fig. 14).

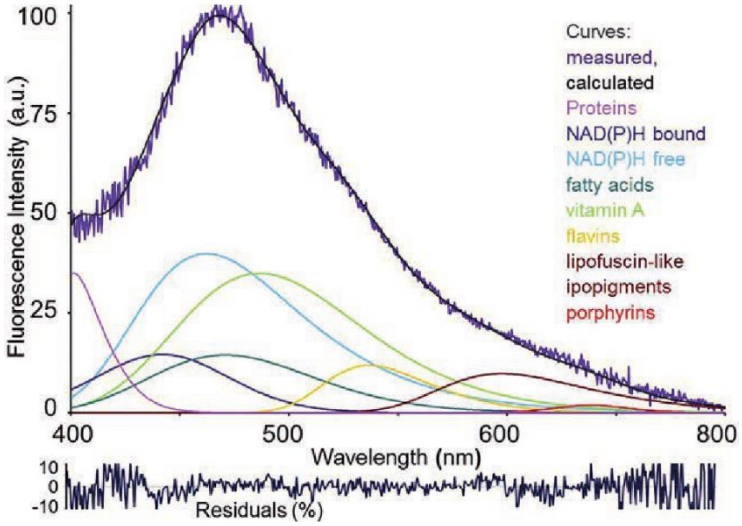

Fig. 14 Example of curve-fitting analysis of an *in-vivo* AF spectrum from rat liver (figure reproduced from [84]). The graph shows the AF curve measured experimentally, the fitting curve estimated as the sum of the overlapping contribution of the natural fluorophores, and the spectral function of each fluorophore. The curve-fitting analysis was based on using an iterative non-linear algorithm (Marquardt-Levenberg) for the estimation of the true absolute minimum value of the sum of squared deviations of a combination of half-Gaussian Modified Gaussian (GMG) spectral functions related to the spectral AF emission profile of each fluorophore.

Moreover, the recent advent of multi-photon technologies based on the excitation of different fluorophores using multiple photons has allowed the implementation of techniques for a better spatial resolution, separation of the AF emission profiles, and quantification of different fluorophores. These novel technologies represent the clue for the future progress in this field of research and the improvement of the existent instrumentation for a better *in-vivo* monitoring of AF.

1.7.2 Assessment of NAD(P)H AF for monitoring cutaneous metabolism

As described in sections 1.3 (page 24) and 1.4 (paragraph 1.4.1, page 26), it is possible to take advantage of the natural endogenous autofluorescence of NAD(P)H for monitoring *in-vivo* the cutaneous metabolic status and as an indication of the oxidative stress level. NAD(P)H is an intracellular coenzyme involved in cytosolic and mitochondrial cell energy metabolic redox reactions, acting as an oxidising/reducing agent able to donate electrons [12]. Energy in the cells is produced in the form of ATP (adenosine triphosphate) by the cytosolic glycolysis and the mitochondrial oxidative phosphorylation (OXPHOS) (Fig. 15). Oxidation of NAD(P)H in $NAD(P)^+$ by the mitochondrial electron transport chain and the use of glycolysis products are essential to produce ATP through the OXPHOS [12]. The increased amount of ROS and oxidative stress has a harmful effect on the respiratory chain, leading to the increase of the reduced NAD(P)H, and changes in the $NAD(P)^+$:NAD(P)H ratio and the mitochondrial activity with a negative impact on ATP production [12]. Therefore, real-time monitoring of these coenzymes levels can provide information on the mitochondrial metabolic status associated with physiological or diseased conditions of the biological tissue [85].

Laser fluorescence spectroscopy (LFS)

The autofluorescence of NAD(P)H and other biological cell fluorophores in the skin, i.e. the coenzyme FAD^+ and the structural proteins collagen and elastin, can be stimulated non-invasively by laser fluorescence spectroscopy (LFS) [84, 85]. LFS is an optical method using a monochromatic laser source with power between 1-5 mW and excitation wavelengths ranging from UV, visible and IR spectral regions to identify AF emission peaks proportional to the tissue concentration of specific biomarkers [12, 46, 84, 85, 86, 87].

LFS biomedical systems for the *in-vivo* evaluation of skin AF are provided with a single-point probe that integrates sensors for both the irradiation of the tissue and the detection of the fluorescent signal [88].

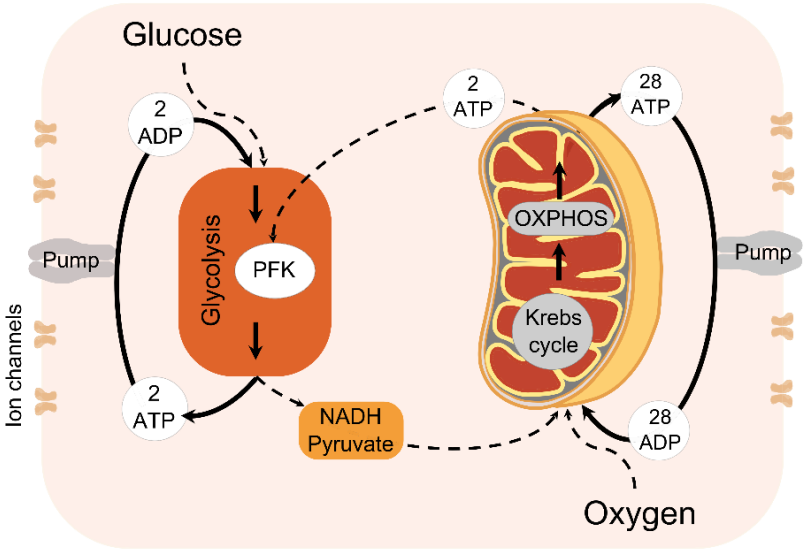

Fig. 15 Simple scheme of cell energy metabolism (figure reproduced from [89]). The overall process of energy production in the cells is defined as cell respiration. The energy is produced by the glycolysis and oxidative phosphorylation (OXPHOS) processes, which occur respectively in the cytosolic and mitochondrial cellular compartments. In these processes the activity of NAD^+, $NADP^+$ and flavin adenine dinucleotide (FAD^+) coenzymes are crucial for oxidation and reduction reactions to transport electrons that represent an energy source to form ATP molecules. Glycolysis and OXPHOS are coupled oscillatory processes which can influence reciprocally under the driving effect of glucose and oxygen concentrations, respectively. Energy production starts in the cytosol with the glycolysis process, which allows the conversion of the glucose substrate into pyruvate with the production of 2 net molecules of ATP and NADH. The pyruvate produced during glycolysis is then employed as the substrate which enters the mitochondrial Krebs cycle. The cycle consists of a series of reactions for the release of more ATP and NADH, which are used to create a chemical gradient across the mitochondrial membrane by the activity of the electron transport chain. The chemical gradient is finally used as energy source to produce ATP (28 to 30 net molecules) during OXPHOS, which has much higher efficiency compared to glycolysis. OXPHOS represents the preferential path for cell energy production in normal aerobic conditions when the tissue is well oxygenated. Anaerobic conditions due for example to disease have a negative impact on the functionality of the OXPHOS process that requires oxygen, and as a consequence enhance the production of energy by glycolysis to prevent the accumulation of pyruvate and NADH in the cytoplasm. Although glycolysis is less efficient than OXPHOS, it provides ATP rapidly and represents a quick energy source for pathologic cells, e.g. cancer cells.

The probe must be placed in direct contact with the skin to perform the analysis [88]. The light source and the detector (spectrometer) of LFS devices are connected respectively to the irradiation and detection sensors in the single-point probe through optical fibres [88]. The most common unit of measurement used to assess endogenous autofluorescence is in arbitrary units (AU), making it possible to provide only relative assumptions related to the fluorophores

concentrations in the local tissue environment [12, 47, 90]. Since absolute concentrations of the fluorophores cannot be obtained, LFS systems need to be calibrated carefully before each experiment to reduce the variation of the signal between different measurements. Generally, LFS devices are already provided with a standard procedure for the calibration of the signal [85], which is variable depending on the method implemented by the manufacturer. For example, the LFS probe of the *LAKK-M* device (*Spe Lazma Ltd*, Russia) is calibrated through a procedure based on the use of the skin location chosen for the analysis as a template for the calibration of the probe.

Considering the relative nature of the measurements, care must be taken when presenting LFS data to make comparisons between groups of subjects. Expression of the data as percentage relative changes in response to a functional task may be a suitable method, as well as the employment of a multi-parametric approach which combines the autofluorescence measurements with the assessment of other variables in the biological tissue, i.e. blood perfusion, oxygen saturation and blood volume.

LFS systems can stimulate NAD(P)H autofluorescence using UV light between 260-380 nm, and the signal is detected at emission wavelengths between 420-490 nm [12, 85, 91]. The oxidised $NAD(P)^+$ form is not fluorescent, thus the detected signal corresponds to the light emitted from the reduced NAD(P)H form [12]. FAD^+ autofluorescence can be induced by LFS employing light sources in the UV and blue spectral regions (365-460 nm) with emission wavelengths around 530-550 nm [12, 91, 92]. Absorption of UV light by blood has a major impact on the *in-vivo* monitoring of FAD^+ with reduction of the AF signal intensity six times greater than NAD(P)H fluorescence [85, 92]. Therefore, it is advisable the use of a blue excitation laser for those studies more focused on the detection and investigation of FAD^+. LFS allows stimulating also the autofluorescence of structural proteins such as collagen and elastin, which are abundant in the connective tissue of the dermal cutaneous layer. A limitation in the assessment of collagen and elastin fluorescence is represented by the similar emission wavelength (390-460 nm collagen, 400-450 nm elastin) after excitation with UV light [46, 87]. Therefore, the UV AF signal in the 400-450 nm wavelength is characterised by the overlapping contribution of these two structural proteins.

Advantages and shortcomings of LFS method

The main benefits of LFS are the minimally invasive nature of the measurements from an easily accessible site (skin) without the requirement of exogenous dyes [12], the low cost of the technology and the portability. However, the method presents several disadvantages. For example, LFS UV AF spectra derive from the overlapping contributions of several endogenous autofluorescent biomolecules, making the interpretation of the contribution from every single fluorophore difficult [12, 84]. In addition, the signal is highly affected by the heterogeneous skin structure [46], events in the cutaneous microenvironment (e.g. vascular changes in blood volume) [85], the absorption of UV light by cutaneous chromophores, i.e. Hb and melanin [12], and artefacts generated by subject's movement or pressure of the probe applied on the skin surface.

Moreover, LFS suffers from spatial and temporal resolution leading to the impossibility to distinguish cytosolic and mitochondrial NAD(P)H, even though some studies have reported that NAD(P)H AF measured by LFS originates mostly from the mitochondria [85]. A possible approach to overcome this problem may be monitoring the mitochondrial activity by the calculation of the redox ratio (RR) index. RR is the ratio between NAD(P)H and FAD^+ AF spectral peaks and represents an index of the balance between the reduced NAD(P)H and the oxidised FAD^+, which reflects the activity of the mitochondrial electron transport chain. However, a better approach would be implementing the time-resolved AF spectroscopy method, based on the combination of LFS measurements with the fluorescence lifetime (FL) technique that allows tracing the decay rate of the AF signal [93]. FL measures the mean time that a fluorophore is in an excited state before returning to its ground state by emitting a photon [94]. The technique is sensitive to conformational changes of the fluorophore, i.e., due to protein binding [94]. Therefore, considering that the fluorescence of free (cytosolic) NAD(P)H has a lower decay time compared to the protein-bound (mitochondrial) form of the coenzyme, FL is powerful to provide a time-resolved differentiation between bound and unbound NAD(P)H [94, 95, 96]. Similarly, also FAD^+ is characterised by a different FL between its free (longer decay time) and bound (shorter decay time) forms that can be distinguished using the FL method [94, 95]. Another FL-based technology for the *in-vivo* imaging of bound and unbound NAD(P)H or FAD^+ is the fluorescence lifetime imaging (FLIM). The technique provides two-

dimensional images where the contrast is based on the FL of individual fluorophores rather than their emission spectra [97]. The advantage of FLIM over the time-resolved AF spectroscopy is that the FL of the fluorophores is both temporally and spatially resolved, providing the location of cytosolic/mitochondrial NAD(P)H in specific regions of the sampled image. Moreover, Blacker *et al.* [98] have demonstrated that FLIM may potentially differentiate non-phosphorylated NADH and phosphorylated NADPH, which is not possible by LFS. Additional advantages of the FL-based methods over LFS are the independence of fluorescence lifetime from the concentration of the fluorophore, absorption or thickness of the sample, photo-bleaching and excitation intensity [96, 97]. However, FL-based methods are sensitive to the pH, the viscosity and the refractive index in the environment surrounding the fluorophore [97]. Moreover, the traditional FL-based methods employ a one-photon (1P) excitation laser source with consequent ambiguous depth resolution and impossibility to monitor the fluorophore activity at single-cell level.

The evaluation of NAD(P)H AF *in-vivo* with 3D sub-cellular and depth spatial resolution may be achieved by using the mutiphoton laser scanning microscopy (MPLSM) [99, 100], based on the use of near infra-red (NIR) two-photon (2P) excitation light to stimulate the AF of fluorophores of interest [99, 100]. The use of NIR light compared to UV 1P excitation is advantageous due to lower cellular photo-damage and photo-toxicity, reduced photo-bleaching, higher cell viability, lower scattering allowing deeper penetration into the tissue, and better separation of the AF emission profiles of different fluorophores [99, 100]. Balu *et al.* [100] have shown that MPLSM may be used successfully in combination with arterial occlusion to monitor non-invasively *in-vivo* NAD(P)H AF from epidermal cells of the human forearm. However, MPLSM alone does not allow to distinguish cytosolic and mitochondrial NAD(P)H [100]. For this reason, MPLSM has been frequently combined with FLIM [94, 96, 101] to assess NAD(P)H activity ensuring at the same time the differentiation between glycolytic or mitochondrial NAD(P)H, high temporal resolution, and high 3D spatial structural resolution allowing the comparison of different tissue layers. Moreover, the development of multiphoton FLIM systems for the rapid acquisition of data through the use of multiple scan beams and spinning discs is promising for the future, to allow studying dynamic natural processes in the cells [97], e.g., NAD(P)H metabolic oscillations.

1.8 Nonlinear dynamics of LDF signal to find predictors of vascular function

1.8.1 Rationale for the study of LDF nonlinear dynamics

An advantage of the LDF method compared with other modalities for the measurement of the peripheral blood perfusion is the opportunity to monitor the nonlinear dynamics of the cutaneous microcirculation. The expression “nonlinear dynamics” is referred to the oscillatory behaviour which characterises blood flow time series. Several studies have demonstrated that the LDF signal can be processed in the time-frequency domain, to characterise oscillatory components which reflect the physiological activity of different biological mediators contributing to the microcirculation (i.e. heart rate, respiratory rate, VSMCs, ECs and sympathetic nerves activities) [102, 103]. Monitoring the LDF oscillatory components in combination with reactive tests provides information about the functionality of central and local key factors involved in the regulation of the microcirculation, especially the endothelial cells which are the most important mediators associated with the health status and adaptation of the micro-vessels. Therefore, the main advantage of nonlinear dynamics studies is the possibility to reveal ‘hidden’ information related to specific microvascular components that would be lost by calculating the simple average value of the LDF signal.

1.8.2 Continuous wavelet transform

The pioneer investigators that characterised the LDF oscillatory components were Stefanovska and co-authors [103]. They implemented the use of the continuous wavelet transform (CWT) method for the processing of cardiovascular signals in the time-frequency domain [102, 103]. The main problem associated with the study of the oscillatory components of a LDF signal is the time-varying nature of the frequencies due to the changing period which characterises LDF time series. In addition, the wide range of frequencies where the specific peaks of the oscillatory components are located (5-2000 × 10^{-3} Hz) leads to difficulties in time and frequency resolution. The conventional method used to study the frequency of a signal is the fast Fourier transform (FFT). However, the technique is not suitable for the study of time-varying signals because it provides only one picture of the frequency domain of the entire signal, leading to the inability to trace time variations of the frequencies [102]. The short time Fourier transform (STFT)

was introduced to overcome the lack of time resolution, based on the use of a short temporal window which is shifted along the time series to obtain information about the time variations, and the detection of the frequency components by FFT within the window that has been chosen [102]. However, this methodology is still not appropriate to detect the oscillatory components of time-varying signals with a broad range of frequencies, i.e. the LDF signal (5-2000 × 10^{-3} Hz), because the time-frequency resolution of STFT is optimal only for narrow frequency windows leading to the inability to detect the low-frequency components [102]. For these reasons, Stefanovska and co-authors have implemented the CWT analysis to identify the LDF oscillatory components.

The CWT is a scale-independent method which uses a wide frequency window suitable for the study of time-varying signals, providing a low-frequency resolution greater than FFT [102]. Fig. 16 shows the comparison of the spectral analysis of the oscillations of a heart rate variability (HRV) signal performed either using FFT (Fig. 16a) or CWT (Fig. 16b) analyses [102]. The graphs clearly show that the wavelet transform analysis provides a better frequency resolution in the low-frequency region, allowing the identification of additional oscillatory peaks compared to FFT.

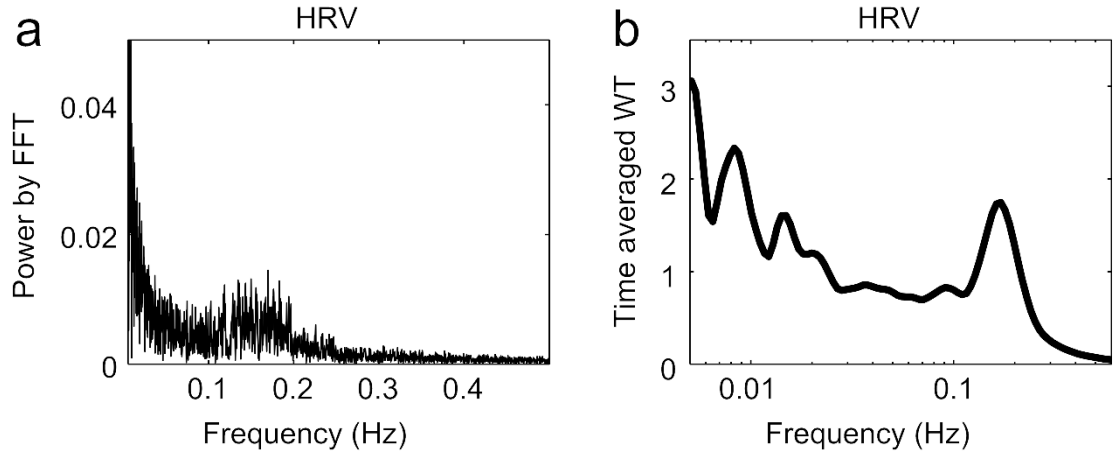

Fig. 16 Comparison of the frequency resolution achieved using FFT or CWT (figure reproduced from [102]). (**a**) FFT energy spectrum obtained from the analysis of an HRV signal. The spectrum is plotted on a linear scale. (**b**) CWT time-averaged energy spectrum obtained from the wavelet analysis of the same HRV signal. The spectrum is plotted on a semi-log scale. WT = Wavelet Transform. Although the comparison provided in this figure is unfair due to the fact that the graph (a) is plotted on a linear scale while the graph (b) is shown on a semi-log scale, the figure clearly displays that CWT allows the identification of more oscillatory peaks than FFT, especially in the low-frequency region between 3-40 × 10^{-3} Hz.

To perform the CWT analysis a mother wavelet is required to define a set of functions of various scales, which provide a basic window scaled and shifted in the time domain of the signal [102]. The mother wavelet employed for the CWT analysis of LDF signals is the Morlet wavelet ψ reported in equation 4 [102],

$$\psi(u) = \frac{1}{\sqrt{\pi}} e^{-iu} e^{-u^2/2}. \quad (4)$$

The use of the Morlet window function is advantageous because it provides optimal time resolution for high frequencies, optimal frequency resolution for the low-frequency components, and it allows an easy conversion of the used scale to frequency [102]. The Morlet window is scaled by a factor *s* and a centred time *t* in the time domain to obtain a set of non-orthogonal basic functions $\Psi_{s,t}$ from which the CWT can be calculated [102],

$$\Psi_{s,t}(u) = |s|^{-1/2} \psi\left(\frac{u-t}{s}\right), \quad (5)$$

The CWT spectrum of a signal *g(u)* is then obtained by the equation 6,

$$\tilde{g}(s,t) = \int_{-\infty}^{\infty} \overline{\Psi}_{s,t}(u) g(u) \mathrm{d}u, \quad (6)$$

where $\overline{\Psi}$ is the complex conjugate of Ψ which removes any specific scale making the method independent from frequency scales, and $\tilde{g}(s,t)$ represents the wavelet spectral function from which the absolute wavelet energy E_i, the absolute wavelet amplitude A_i, and the instantaneous phase ϕ of a specific oscillator can be extracted at the frequency scale *s* and time *t* [102]. The time-averaged E_i and A_i at a specific frequency range from f_{i2} to f_{i1} which defines a specific oscillator, can be calculated according to the equations 7 and 8, respectively [102],

$$E_i(f_{i1}, f_{i2}; t_1, t_2) = \frac{1}{(f_{i2}-f_{i1})(t_2-t_1)} \int_{1/f_{i1}}^{1/f_{i2}} \int_{t_1}^{t_2} \frac{1}{s^2} |\tilde{g}(s,t)|^2 \mathrm{d}s\mathrm{d}t, \quad (7)$$

$$A_i(f_{i1}, f_{i2}; t_1, t_2) = \frac{1}{(f_{i2}-f_{i1})(t_2-t_1)} \int_{1/f_{i1}}^{1/f_{i2}} \int_{t_1}^{t_2} \frac{1}{s^2} |\tilde{g}(s,t)| \mathrm{d}s\mathrm{d}t, \quad (8)$$

where (t_1,t_2) is the time window over which the time-averaged E_i is calculated. E_i is the area underneath the curve of the CWT power spectrum, expressed in arbitrary units (AU), which represents the average energy per unit time of the signal at the specific frequency range under investigation. A_i is the maximal mean energy in the frequency interval of interest expressed in AU. To allow reliable

comparisons of the E_i or A_i of an oscillator between signals from different subjects, these parameters are normalised by estimating the ratio between the E_i or A_i values extracted from the frequency range of the oscillator (f_{i2}, f_{i1}) and their values derived within the total frequency interval of the wavelet spectrum, obtaining dimensionless values of the time-averaged relative wavelet energy e_i and amplitude a_i,

$$e_i(f_{i1}, f_{i2}) = \frac{E_i(f_{i1}, f_{i2})}{E_{tot}}, \tag{9}$$

$$a_i(f_{i1}, f_{i2}) = \frac{A_i(f_{i1}, f_{i2})}{A_{tot}}. \tag{10}$$

Finally, e_i and a_i are normalised by the number of frequencies n_f in the interval (f_{i1}, f_{i2}) of the specific oscillator,

$$e_i = \frac{e_i(f_{i1}, f_{i2})}{n_f(f_{i1}, f_{i2})}, \tag{11}$$

$$a_i = \frac{a_i(f_{i1}, f_{i2})}{n_f(f_{i1}, f_{i2})}. \tag{12}$$

In simple words, the energy and amplitude extracted from the wavelet spectrum represent a measure of how much of the signal is located at a specific frequency at the time *t*. Translating this concept from a physiological point of view, the wavelet energy and amplitude of the LDF oscillators indicate how much each physiological component is contributing to the overall signal at a specific time, which could be referred to a task (e.g. PORH response) that provides information on the functionality of the components. Moreover, the extraction of the phase of each oscillator may help to study the synchronisation, coupling or interaction between the different physiological components contributing to LDF signal.

Fig. 17 displays examples of the CWT time-frequency domain (Fig. 17a) and the CWT time-averaged spectrum (Fig. 17b) of the LDF signal. The time-frequency domain graph provides an overview of how the wavelet energy of the signal is distributed in frequency and time. The time-averaged plot allows the wavelet amplitude peaks corresponding to the different LDF oscillators to be distinguished. As visible in the plot, six intervals have been identified ranging from low (5×10^{-3} Hz) to high (2000×10^{-3} Hz) frequencies, which are associated with cardiac (I), respiratory (II), myogenic (III), neurogenic (IV) and endothelial (V-VI) physiological activities for the regulation of the microcirculatory blood flow.

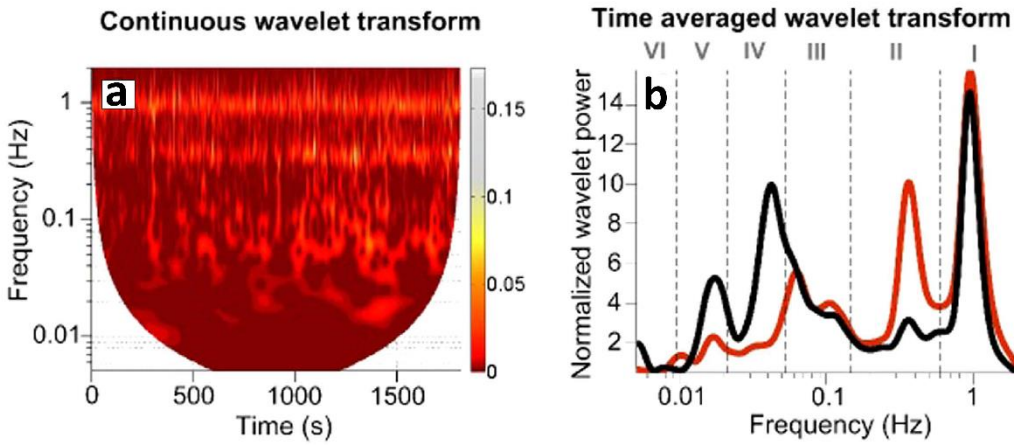

Fig. 17 CWT of LDF time series (figure reproduced and adapted from [104]). (**a**) Example of CWT scalogram from a LDF time series. The graph represents how the CWT spectral energy is distributed in the time-frequency domain, by using a colour map which refers to the magnitude of the energy. In this case, as shown by the colour bar on the right, the dark red colour corresponds to lower wavelet energy and the brighter areas to high wavelet energy. A high power continuous band is clearly visible in the cardiac beat frequency (~1000 × 10^{-3} Hz), which confirms the basic contribution of heart rate to the peripheral microcirculation. (**b**) Comparison of time-averaged CWT amplitudes of LDF signals measured from a healthy skin region (red line) and from a melanoma cutaneous lesion (black line) of the same subject. The graph allows to distinguish the wavelet amplitude peaks of the LDF oscillatory components, corresponding to six different frequency intervals: cardiac (I), respiratory (II), myogenic (III), neurogenic (IV) and endothelial (V-VI) physiological activities. Comparing the wavelet amplitudes of two LDF signals is powerful to distinguish healthy and diseased vascular conditions, gaining information on the function of specific vascular components. In this case for instance, relevant differences between the wavelet amplitudes of the two signals can be observed in the intervals V and IV, indicating a different functionality of the endothelial and neurogenic components between micro-vessels from healthy and melanoma lesion skin regions.

1.8.3 Physiological origin of the LDF CWT oscillations

The physiological origin of the six oscillatory components of LDF time series has been clarified by performing several experiments, which involved the application of the CWT analysis to electrocardiograph (ECG), heart rate variability (HRV) and LDF signals measured simultaneously, or to the LDF signal recorded during the iontophoresis of vasoactive drugs (e.g. ACh, SNP) [60, 102, 103, 105, 106, 107, 108]:

(I) 600-2000 × 10^{-3} Hz, a component related to the heart rate. The physiological origin of this oscillation was determined by the simultaneous measurement of ECG, HRV and LDF signals [109]. The ECG basic frequency corresponds

to the heart rate and is generally located around 1000 × 10^{-3} Hz, it may vary from 600 × 10^{-3} Hz in athletes to 1600 × 10^{-3} Hz in individuals with cardiovascular dysfunction [102, 109]. All the three measured signals showed a CWT component located at the same frequency around 1000 × 10^{-3} Hz, demonstrating that the cardiac pumping activity is reflected also in the peripheral microcirculation [109].

(II) 145-600 × 10^{-3} Hz, a component corresponding to the respiratory rate. The cardiac beat is modulated by the respiration with a general breathing frequency around 200-300 × 10^{-3} Hz which is visible in the HRV signal [102, 109]. Both of HRV and LDF signals measured simultaneously showed a CWT component located around 200 × 10^{-3} Hz, providing direct evidence of the effect of breathing activity in the peripheral microvasculature [109].

(III) 52-145 × 10^{-3} Hz, a component representing the VSMCs myogenic activity. This oscillation reflects the local myogenic control of vascular tone and blood perfusion, mediated by the spontaneous contraction and relaxation of the smooth muscle cells in the micro-vessels wall in response to blood pressure changes [102, 109]. The oscillatory activity is induced by cellular Ca^{2+} (calcium) fluctuations throughout the VSMCs plasma membrane and sarcoplasmic reticulum (SR) [109, 110]. The oscillation is visible in both the HRV and LDF signals around 100 × 10^{-3} Hz, and the myogenic origin has been demonstrated through studies in isolated vessels based on the measurement of spontaneous oscillations in the vessels diameter (vasomotion) or in Ca^{2+} concentrations, which exhibited a frequency between 70-100 × 10^{-3} Hz [102, 109]. Moreover, the CWT analysis of LDF signal displayed significant changes of the myogenic oscillation in response to exercise and local cooling [102].

(IV) 21-52 × 10^{-3} Hz, a component related to the neurogenic activity of the local sympathetic nerves in the microcirculation. The autonomous nervous system contributes to the regulation of micro-vessels vasoconstriction at rest by the release of mediators modulating VSMCs activity [102]. The neurogenic component has been detected in blood pressure, LDF and HRV signals at ~30-40 × 10^{-3} Hz [102, 109]. The neurogenic origin has been proved indirectly through several studies showing the disappearance of the oscillation in this frequency range after blockade of local and ganglionic

nerves in sympathectomised human tissue, or after denervation in rats [102, 109]. Furthermore, significant changes of the CWT neurogenic oscillation amplitude have been observed on transplanted compared to intact skin and under the effect of local anaesthesia [102].

(V) 9.5-21 × 10^{-3} Hz, a component associated with the ECs NO-dependent regulatory activity. The endothelial cells constitute the most internal layer (endothelium) of the blood vessels facing the vascular lumen (Fig. 2). The endothelial activity is stimulated by the concentration of metabolic mediators in the blood such as oxygen and carbon dioxide, which influence the regulation of the vascular tone [102]. Based on the concentration of metabolites in the blood, ECs are stimulated to mediate the relaxation or contraction of VSMCs by the release of agonist substances, i.e. NO, PGs, EDHF, endothelin-1, etc. which modulate VSMCs activity (Fig. 2). As discussed in section 1.5 (paragraph 1.5.1, page 35), the iontophoretic local delivery of the vasodilators ACh and SNP in the skin microcirculation stimulates respectively the endothelium-dependent and endothelium-independent vasodilation of the micro-vessels [9, 14, 49]. ACh induces vasodilation mainly by enhancing the endothelial release of NO, in addition to the concurrent contribution from endothelial NO-independent mediators such as the EDHF and PGs [9, 14, 49]. Several studies that combined the CWT analysis of the cutaneous LDF signal with the iontophoresis of the vasodilator ACh reported significant changes in the oscillation around 9.5-21 × 10^{-3} Hz after the inhibition of the endothelial NO synthesis by N^G-monomethyl-L-arginine (L-NMMA), suggesting a possible endothelial NO-dependent origin of this LDF oscillatory component [102].

(VI) 5-9.5 × 10^{-3} Hz, a component related to the NO-independent ECs modulatory activity. The origin of this oscillation has not been completely clarified. It has been reported a difference in the wavelet amplitude of this component between healthy individuals and heart failure patients during iontophoresis of ACh [102], and a major increase of the amplitude with ACh stimulation compared to the amplitude with SNP in healthy subjects [105]. These findings suggest an endothelial origin of the oscillation [102, 105]. However, the inhibition of the endothelial NO synthesis by L-NMMA did not show a difference between ACh and SNP response, suggesting that the

activity of other endothelium-derived NO-independent mediators might be associated with the oscillation in the 5-9.5 × 10^{-3} Hz interval, i.e. PGs or EDHF [105]. Kvandal *et al.* [105] performed an experiment where PGs synthesis was inhibited by aspirin and the difference between ACh and SNP response was not affected in both the oscillatory intervals V and VI, suggesting a more likely involvement of the EDHF rather than PGs in the oscillatory activity between 5-9.5 × 10^{-3} Hz.

The study of the LDF oscillatory components by CWT has found different kinds of applications, such as the investigation of vasomotion or the use of LDF oscillators as predictors of cardiovascular risk.

1.8.4 CWT for the study of vasomotion

The term vasomotion refers to spontaneous rhythmic variations in the diameter of the microcirculatory blood vessels, which are responsible for changes in the myogenic vascular tone and blood flow [110, 111]. The physiological role of this phenomenon is not clear, and it has been associated with both pathologic and healthy vascular conditions [110, 111]. The oscillations in vessel diameter observed during vasomotion are determined by the local contraction and relaxation of the VSMCs due to Ca^{2+} fluctuations throughout the plasma membrane and the SR [110, 111]. Vasomotion can be investigated directly by technologies measuring the micro-vessels diameter, i.e. the intravital video-microscopy [112, 113, 114]. However, the phenomenon can be studied also indirectly by the use of LDF in combination with the CWT analysis [111]. The use of CWT for the investigation of vasomotion is advantageous because it does not take into account only the oscillatory activity of VSMCs but it allows the examination of other mediators which can modulate and drive the smooth muscle activity, e.g. endothelial cells.

1.8.5 CWT for the study of CVD risk factors

Several studies have reported significant changes in the spectral energy of the CWT oscillatory components in relation to sex, age or pathologic conditions, suggesting the eligibility of LDF oscillators as markers of cardiovascular dysfunction. For example, Shiogai *et al.* [102] described a decrease of the endothelial, myogenic and respiratory wavelet energies with aging, and greater endothelial wavelet amplitudes in young women compared to young men. These

data were interpreted assuming that lower wavelet amplitudes might be associated with reduced vascular function [102]. The spectral amplitudes of the endothelial wavelet components were found to be reduced during iontophoresis delivery of ACh also in patients affected by congestive heart failure compared to healthy subjects [115].

1.8.6 Limitations in the study of LDF oscillatory components

The coupling between vascular oscillators has been suggested as possible description of the cardiovascular system [102, 109]. However, the main disadvantage related to the assessment of blood flow oscillations is that they are highly time-varying and not constant, making the direct assessment of the interactions between different oscillators difficult [116, 117]. The problem may be addressed by using specific methods to study the interactions between the oscillators. For example, the extraction of the wavelet phase coherence (WPCO) as a function of time and frequency is a relevant analysis to study the functional coupling between different signals or oscillators, providing information on the behaviour and interaction between different components of the nonlinear system [118, 119]. Moreover, a better interpretation of the data may be achieved through a multi-parametric approach, by integrating the study of vascular oscillators with a quantification of the complexity of cardiovascular signals, based on computing a set of parameters such as entropy and the dimension that are considered potential predictors of CVD risk [116, 117, 120, 121].

1.8.7 Wavelet phase coherence (WPCO) analysis

Functional coupling and synchronisation of cardiovascular oscillators may be studied by several methods such as the analysis of synchronisation or coupling direction [118]. However, the limitation when using these techniques is the requirement of well-separated oscillators, which could be distinguished by decomposition from the background noise and the other oscillators of the signal, or that can be sampled independently [118]. Unfortunately, in the case of the LDF cardiovascular oscillators this is possible only for the cardiac and respiratory components which can be measured independently, e.g. by ECG or HRV. In contrast, low-frequency LDF oscillators cannot be decomposed from the background noise or sampled independently [118]. For these reasons, wavelet phase coherence analysis has been implemented, which provides information on

the phase ϕ relationship between oscillators in the same frequency interval of two time series recorded simultaneously [118]. The main advantage of WPCO analysis is the possibility to gain information on the coupling/synchronisation between oscillators in time-frequency regions with relevant background noise [118]. Another advantage is the chance to study the interaction between oscillators involved in the regulation of different biological mechanisms, i.e. the WPCO has been used to examine the interaction between cutaneous blood perfusion and temperature oscillators [118].

The method is based on the use of the continuous wavelet transform that has been described in the equations 4-6, from which the phase $\phi_{k,n}$ can be extracted for each time t_n and frequency ω_k [118]. Considering the CWT of two different signals $x_1(t)$ and $x_2(t)$ measured simultaneously, the phases $\phi_{1k,n}$ and $\phi_{2k,n}$ can be extracted for the two time series and their relative difference calculated as [118],

$$\Delta\phi_{k,n} = \phi_{2k,n} - \phi_{1k,n}. \quad (13)$$

From the phase difference it is possible to calculate the coefficients $cos\ \Delta\phi_{k,n}$ and $sin\ \Delta\phi_{k,n}$ that can be time-averaged for the entire length of the signals, allowing the definition of the time-averaged wavelet phase coherence C_ϕ function at the frequency ω_k [118],

$$C_\phi(\omega_k) = \sqrt{(cos\Delta\Phi_{k,n})^2 + (sin\Delta\Phi_{k,n})^2}\ . \quad (14)$$

The $C_\phi(\omega_k)$ function returns values between 0 and 1, where $C_\phi(\omega_k) \approx 0$ indicates absence of phase coherence (no interaction/coupling), $C_\phi(\omega_k) \approx 1$ represents complete coherence (perfect interaction/coupling), and $0 < C_\phi(\omega_k) < 1$ is associated with partial coherence (partial interaction/coupling) [118].

1.8.8 Assessment of the complexity of a signal

In the last 25 years, several studies approached the vascular system as a natural spatially distributed, complex and nonlinear system. The behaviour of the vascular system was characterised according to chaos theory, which provides methods for the computation of a set of mathematical, statistical and physical parameters describing the complexity of the system, defined as attractors [102].

Examples of attractors are represented by the Hurst index (H), fractal dimension (D), entropy (H_0), information dimension (H_i) and correlation dimension (D_2) [102, 120]. These variables describe how a dynamic nonlinear system evolves over

time, by iterations predicting the behaviour of the system at intervals subsequent to an initial current state [122]. For example, this is the case of entropy that is a measure of the quantity of information required for the prediction of the future status of the dynamic system [102]. The fractal dimension describes the complexity of a nonlinear physiological signal by characterising fractions of the system showing the self-similarity property, which is the ability to reproduce the entire structure of the analysed signal [102, 123]. The Hurst index allows the evaluation of the complexity by quantifying the scaling properties of the nonlinear system [102]. According to the assumptions above, increased values of fractal dimension and entropy correspond to a greater complexity of the signal [102].

The assessment of attractors can help to get more insight about the functionality of the microvascular system, by providing information on the ability of the system to assume a particular state at a specific time or in response to functional tasks [122, 123]. For instance, the complexity analysis of blood pressure and HRV signals revealed major complexity in young individuals compared to aged people, and more complexity in women versus men [102]. Based on this evidence, it has been proposed that a loss of complexity in the physiological system might be related to a dysfunction or impaired coupling between the components [116, 121].

Attractors of cardiovascular signals may be quantified by several methods, which are all based on the initial integration of the signal *g(i)* according to equation 15, where *i = 1,…,N* , and *N* is the length of the time series [102],

$$y(i) = \sum_{j=1}^{i} [g(j) - \bar{g}], \tag{15}$$

where,

$$\bar{g} = \frac{1}{N} \sum_{j=1}^{N} g(j). \tag{16}$$

The integration of the signal is necessary to make the time series unbound, which is a fundamental requirement to reveal the scaling and dimensional properties of the system [102]. The next step is computing the standard deviation *S(N)* and the range *R(N)* that can be used for the calculation of the Hurst index and the fractal dimension [102],

$$S(N) = \left[\frac{1}{N} \sum_{t=1}^{N} \{g(i) - \bar{g}\}^2 \right]^{1/2}, \tag{17}$$

$$R(N) = \max_{1 \le i \le N} y(i) - \min_{1 \le i \le N} y(i). \tag{18}$$

The Hurst index *H* can be then extracted from the following equation [102],

$$R/S = (cN)^H, \quad (19)$$

where *c* is a coefficient equal to 0.5.

The Hurst index provides information on scaling properties for the prediction of the persistence of a signal, with values between 0.5 and 1 indicating a persistent behaviour and values $0 < H < 0.5$ associated with anti-persistent behaviour [102]. The fractal dimension *D* can be finally calculated from the Hurst index because the two parameters are linked by the following relation [102],

$$D = 2 - H. \quad (20)$$

The dimension of nonlinear systems can be assessed also by using several other methods, including statistical physics techniques [102]. Other ways to express the complexity of dynamic systems are represented by the calculation of the correlation dimension D_2, information dimension H_i and entropy H_0. The equations for the computation of these parameters are discussed in several papers from Grassberger and Procaccia that introduced methods and algorithms for the calculation of dimensional attractors and entropy [124, 125, 126, 127]. However, the mathematical details for computing these parameters will not be discussed, as the most important aspect related to this dissertation is understanding overall why attractors are important for the study of vascular function and evaluating their applicability as predictors of CVD risk.

1.9 Nonlinear nature of the glycolytic and mitochondrial intermediate product of energy metabolism NAD(P)H

1.9.1 Cellular metabolic oscillations

As discussed in section 1.7 (paragraph 1.7.2, page 47), NAD(P)H is involved in the mitochondrial and cytosolic reactions responsible for cellular energy production in the form of ATP. Dysfunction in the cell metabolic processes of energy production enhances the onset of several pathologies. An example is represented by the impairment of the electron transport chain induced in the presence of oxidative stress, which may evolve in a variety of illness including CVD and cancer. Recently, scientists have drawn particular attention on the oscillatory nature of energy metabolism. According to the latest reports,

monitoring the dynamics of cell energy metabolism may be powerful to predict specific cell and tissue metabolic states that might be associated with healthy and altered conditions, or with transition states [89]. The hypothesis is that by examining the dynamic properties of cell energy metabolism, specific patterns can be observed which may help to identify and predict the potential switch of the cell/tissue from a normal to a diseased phenotype [89].

The basic concept for the study of metabolic dynamics is assuming the oscillatory time-dependent nature of energy metabolism due to the continuous production and consumption of ATP in the cells [89]. Metabolic oscillations have been previously investigated in a variety of cellular specimens, i.e. yeast [128, 129], cardiac myocytes [130] and β-cells [131, 132]. They can be classified in glycolytic and mitochondrial oscillations detectable indirectly by the assessment of fluctuations in the autofluorescence of NAD(P)H stimulated by 1P [128, 129, 131, 133] or 2P [130, 134] excitation, or fluctuations of the mitochondrial membrane potential $\Delta\Psi_m$, respectively [89]. Limited research has described metabolic oscillations also in live tissue from animal models. For example, mitochondrial fast oscillations have been detected in *in-vivo* rat by intra-vital 2P microscopy measurements of NAD(P)H from the cutaneous salivary glands [135], and circadian diurnal metabolic oscillations of NAD(P)H have been studied from the stem cells of the basal epidermal skin layer of live mice by combination of 2P excitation and FLIM [136]. Nonetheless, skin metabolic oscillations have never been investigated *in-vivo* in humans or animal models (e.g. mouse) by using autofluorescence single-point readouts.

Recent reports have suggested that glycolytic oscillations derive from the activity of the enzyme phosphofructokinase (PFK), and might be driven by external glucose availability and uptake [89, 128, 133, 137]. On the other hand, the mitochondrial oscillations may be mediated by Ca^{2+} fluctuations in response to oxidative stress that destabilise the mitochondrial membrane potential $\Delta\Psi_m$ [129, 131, 134]. The external oxygen necessary for sustaining the electron transport chain has been proposed as the force driving mitochondrial oscillations [89]. The interaction and coupling between glycolytic and mitochondrial oscillators are strictly linked and can be regulated differently depending on the cellular metabolic state [89]. For example, in the presence of oxygen normal cells use mitochondrial ATP as the primary source of energy, while altered cells (e.g.

potential cancerous cells) switch to a preferential glycolytic ATP production [89]. As a consequence, it can be supposed that specific patterns of glycolytic and mitochondrial oscillations should reflect and help the identification of particular metabolic states [89]. The interaction between glycolytic and mitochondrial oscillators may be affected also by environmental conditions. For instance, it has been reported a driving force of the glycolytic on mitochondrial fluctuations in absence of oxygen, reflecting the switch of cells to an altered metabolic state which promotes the preferential production of ATP through the glycolysis process [89]. In contrast, during normoxic conditions mitochondrial metabolic oscillations drive glycolytic fluctuations [89].

1.9.2 Potential applications of metabolic oscillators

As discussed in the first part of this chapter (section 1.3, page 22), one of the factors involved in the onset of CVD at the cellular level is metabolic dysfunction in the mitochondrial electron transport chain. Therefore, the study of metabolic oscillators in the microcirculation may have the potential to find specific oscillatory patterns associated with the early alteration in the metabolic state of vascular cells due to oxidative stress and endothelial dysfunction. Metabolic oscillators may represent novel preclinical predictors of CVD risk, providing information on intrinsic altered conditions that are not visible at phenotypic level and which may reflect the potential of the tissue to switch towards a diseased state.

Another interesting application may be the investigation of the role of metabolic oscillators in vasomotion. In the previous section (section 1.8, paragraph 1.8.4, page 59), vasomotion has been described as a spontaneous oscillatory phenomenon affecting micro-vessels which are characterised by rhythmic fluctuations in the vessels diameter. Vasomotion is mainly determined by the contraction and relaxation of VSMCs, even though modulation of VSMCs by ECs may also play a relevant role in this phenomenon [138, 139, 140]. Ca^{2+} oscillations in VSMCs and ECs have been considered as the main factor driving vasomotion at a cellular level [110, 111]. Specifically, three cellular oscillators have been proposed as causal mechanisms to explain the Ca^{2+} fluctuation at the basis of this phenomenon: cytosolic oscillator, membrane oscillator and metabolic oscillator [110, 111].

The activity and interaction of cytosolic and membrane oscillators during vasomotion have been proved extensively [110, 111, 141, 142, 143, 144], with

evidence of oscillatory release of Ca^{2+} induced respectively through the SR [110, 142, 143] and by the opening activity of Ca^{2+} or K^{+} channels in the cell plasma membrane [110, 111, 144]. In contrast, although the presence of a metabolic oscillator has been hypothesised, little focus has been given to the investigation of this mechanism which has never been considered crucial for vasomotion [110, 111]. However, recent studies have proved the involvement of the glycolytic enzyme PFK in reactions responsible for Ca^{2+} oscillations of glycolytic origin [89, 145, 146], and oscillations of the mitochondrial membrane potential associated with Ca^{2+} fluctuations have been observed [129, 131, 134]. These recent findings show the presence in the cells of Ca^{2+} fluctuations of metabolic origin. Thus, a possible role of metabolic oscillators for driving vasomotion cannot be excluded. Considering that the physiological role and the mechanisms of vasomotion are still not completely understood, the possible involvement of metabolic oscillators may help to further elucidate this phenomenon.

Although the potential applications of cellular metabolic oscillators, further implementation of the present technologies is still needed to improve the *in-vivo* assessment of energy metabolism oscillatory dynamics. As already discussed in paragraph 1.9.1 (page 64), most of the studies on glycolytic and mitochondrial oscillations have been performed in *in-vitro* or *ex-vivo* cells, while limited research has described the metabolic oscillations in live tissue. The combination of FLIM and multi-photon technologies shown in the work by Stringari *et al.* [136] allows the measurement of free (glycolytic) and bound (mitochondrial) NAD(P)H with high spatial and temporal resolution, thus representing a powerful tool for the detection of metabolic oscillations at sub-cellular level. However, although several *in-viv*o applications of these technologies have been reported [94, 96, 101], they are still not well implemented for human clinical studies and for providing continuous NAD(P)H time series from *in-vivo* tissue to study metabolic oscillations. The development of faster multiphoton FLIM systems based on the use of multiple scan beams and spinning discs [97], and the development of commercial systems with a better design to facilitate the scan of all the regions of the human body [100] are promising modalities to improve the *in-vivo* study of the dynamic natural processes in the cells associated with the oscillatory turnover between NAD(P)H and $NAD(P)^{+}$.

1.10 Aims of the thesis (objectives, hypotheses)

1.10.1 Thesis aims

The assessment of oxidative stress and endothelial dysfunction in the microcirculation represent novel powerful modalities for the early preclinical evaluation of CVD risk. Several studies have demonstrated that oxidative stress and endothelial function in the peripheral skin microcirculation reflect the health conditions of the central cardiovascular system, and can be detected easily by the combination of non-invasive laser methods with reactive tests.

Therefore, the first objective of this research was the **development of protocols for the concurrent non-invasive assessment of cutaneous oxidative stress and microvascular function**, by simultaneous LFS measurements of NAD(P)H, LDF recordings of blood flow and RS oxygen measurements during PORH and iontophoresis functional tasks.

The investigation of nonlinear dynamics of LDF signals reveals information related to the functionality of specific microvascular components characterised by an oscillatory activity, i.e. endothelial and vascular smooth muscle cells. Moreover, recently the focus has been committed to the study of energy metabolism dynamics, which may reveal specific oscillatory patterns of cell metabolic oscillators defining the potentiality of the tissue to switch towards normal or diseased phenotypes. The assessment of LDF and energy metabolism nonlinear dynamics may find powerful applications for both the study of vasomotion and the prediction of CVD risk.

Therefore, the second objective of this research was the **implementation of methods for the simultaneous *in-vivo* detection of LDF blood flow oscillators and NAD(P)H metabolic oscillations**.

The final goal of the study was the application of the implemented protocols and methods for the **investigation of microvascular and cell energy metabolism nonlinear dynamics** in a relevant physiological mouse model characterised by increased oxidative stress ($Nrf2^{-/-}$, nuclear factor erythroid 2–related factor 2 knock-out) due to the knock-out (KO) of the transcription factor Nrf2 that is a major activator of the cellular antioxidant defence, and in a cohort of healthy human subjects and smokers.

This is the first attempt of studying skin metabolic oscillations from live mouse and human cutaneous tissue by using label-free single-point autofluorescence readouts, as well as the first attempt of studying the interactions between metabolic and microvascular oscillators.

1.10.2 Specific objectives and hypotheses of the research in animal models

The specific aims for this part of the work were:

1. Study the role of the endothelial oscillatory activity in cutaneous vasomotion.
2. Investigate the relationship between metabolic oscillators and vasomotion.
3. Evaluate the difference in cutaneous blood flow and metabolic oscillatory patterns between normal mice and animals with increased oxidative stress.

The first hypothesis is that both endothelial and metabolic oscillators may play an important role to enhance skin vasomotion for the adaptation of microvascular tone in response to specific stimuli. The second hypothesis is that both microvascular and metabolic oscillators show different oscillatory patterns between normal and $Nrf2^{-/-}$ mice, thus representing powerful markers to distinguish healthy and oxidative stress phenotypes.

1.10.3 Specific objectives and hypotheses of the research in human subjects

The specific aims for this part of the study were:

1. Assessing the potential application of microvascular and metabolic oscillators as preclinical predictors of CVD risk.
2. Study the relationship between metabolic oscillators and vasomotion in humans.

The first hypothesis is that microvascular and metabolic oscillators show different patterns between healthy subjects and individuals with higher CVD risk (smokers), thus they might find application as early preclinical predictors of risk. The second hypothesis is that cell energy metabolism dynamics are correlated with microvascular oscillations, suggesting a role of cell metabolic oscillators in human cutaneous vasomotion.

2 Material and methods

2.1 Timeline of the project and milestones

Table 1 shows a graphic representation of the various steps and milestones during the 36 months duration of the research project for the implementation and application of the methodology used in this study.

Table 1 Timeline of the research project and milestones (M). Twenty milestones related to various activities were achieved during the 36 months duration of the project: acquisition of theoretical background, technical training, development of the methodologies, obtaining of ethical approvals for animal and human work, subject recruitment, data collection, data analysis.

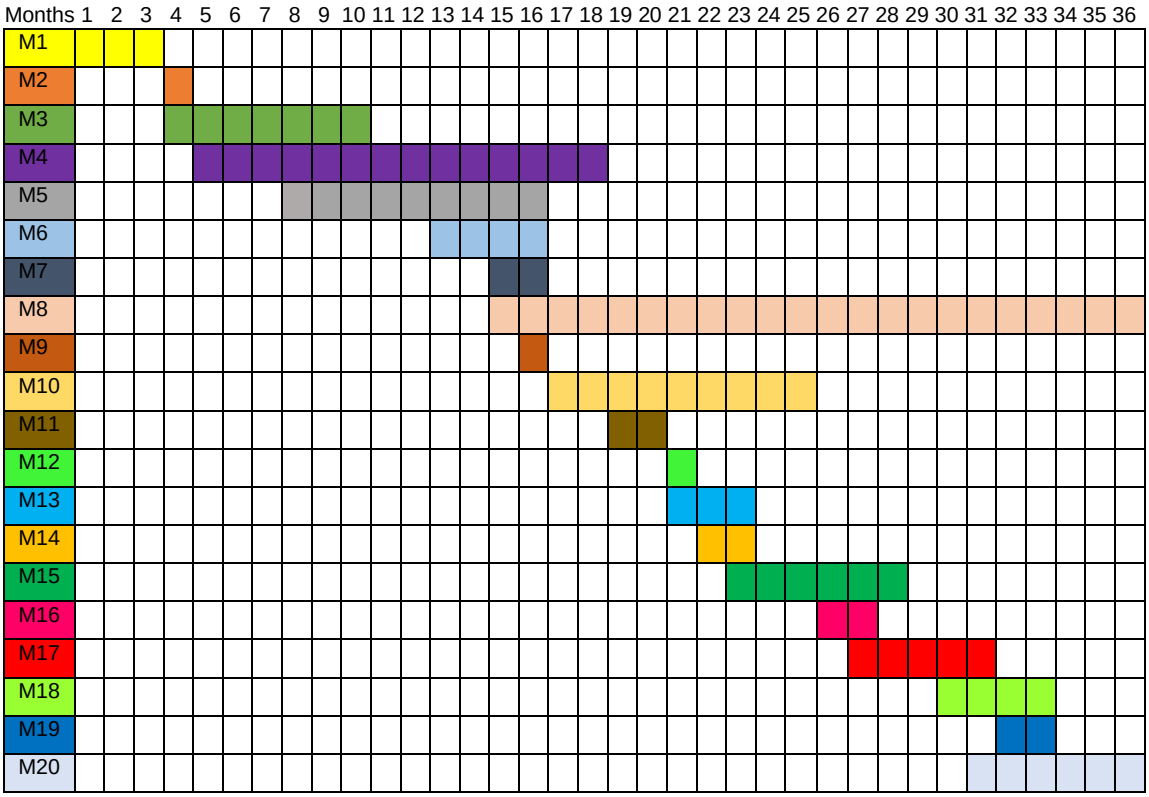

Milestone 1 (M1) – Initial acquisition of literature background on the burden of CVD, biophotonics and non-invasive laser methods for the examination of skin microvascular function and skin autofluorescence of oxidative stress biomarkers. (Months 1-3, August-October 2014).

Milestone 2 (M2) – Secondment period at Aston University (Birmingham, England): Introduction to the components, principles of operation and practical use of the laser fluorescence spectroscopy (LFS), laser Doppler flowmetry (LDF) and reflectance spectroscopy (RS) modalities of the *LAKK-M* commercial biomedical device (*Spe Lazma Ltd*, Russia). (Month 4, November 2014).

Milestone 3 (M3) – Theoretical and practical training on the application of experimental procedures on mouse models (e.g. handling and shaving mice, performing iontophoresis reactive test and laser scans on live mouse skin), and obtaining approvals of the experimental plan on mouse models from the University of Dundee Ethical Review Process (Project Licence PPL N$_o$. 60/4265, Personal Licence N$_o$. IACEC4BB2). (Months 4-10, November 2014-May 2015).

Milestone 4 (M4) – Evaluation of the robustness of NAD(P)H autofluorescence measurements by LFS in *in-vitro* molecular solutions and *in-vivo* human and mouse tissue, and development of a ratiometric normalisation method to reduce blood volume (BV) effects. (Months 5-18, December 2014-January 2016).

Milestone 5 (M5) – Obtaining approvals of the experimental plan on human subjects from the University of Dundee Research Ethics Committee (UREC, Study Protocol N$_o$. 15064). (Months 8-16, March-November 2015).

Milestone 6 (M6) – Optimisation of the examination of microvascular function with LDF method, by comparison with the LDI technique and preliminary testing on three different mouse models (Months 13-16, August-November 2015).

Milestone 7 (M7) – Initial acquisition of literature background related to the examination of microvascular nonlinear dynamics and identification of blood flow oscillators by continuous wavelet transform (CWT) spectral analysis of LDF signal. (Months 15-16, October-November 2015).

Milestone 8 (M8) – Collaboration with a research group from St. Andrews University (Scotland) to obtain Monte Carlo simulations of *LAKK-M* device measurements for gathering information on the skin tissue depth and microvascular bed from which the analysed signals were originating. (Months 15-36, October 2015-August 2017).

Milestone 9 (M9) – Draft of protocols for the concurrent evaluation of oxidative stress and microvascular function, respectively by LFS recordings of NAD(P)H autofluorescence and LDF/RS recordings of blood flow and oxygen saturation in combination with reactive tests, i.e. iontophoresis delivery of phenylephrine (PE) in mice and PORH test in humans. The protocols were designed based on the outcomes of M4, M6 and M7. (Month 16, November 2015).

Milestone 10 (M10) – Experimental application of the protocol implemented for testing human subjects (M9) to a cohort of 20 healthy individuals for determining

the basal normal ranges of microvascular and metabolic biomarkers. (Months 17-25, December 2015-August 2016).

Milestone 11 (M11) – Experimental application of the protocol implemented for testing mouse models (M9) on 5 wild-type (WT) and 6 $Nrf2^{-/-}$ mice to compare the dynamics of microvascular and metabolic markers between normal animals and mice affected by high oxidative stress. (Months 19-20, February-March 2016).

Milestone 12 (M12) – Secondment at *Moor Instruments Ltd* (Axminster, England) company: Exploration of commercial equipment for the imaging of cutaneous microcirculation and skin oxygenation. (Month 21, April 2016).

Milestone 13 (M13) – Acquisition of literature background on the potential application of "attractors" as predictors of CVD risk, exploration of the *LDF 3.1.1.404* software (*Spe Lazma Ltd*, Russia) as tool for the estimation of various attractors from LDF time series, and implementation of a R-Studio script code for plotting the LDF attractor in the phase-space. (Months 21-23, April-June 2016).

Milestone 14 (M14) – Obtaining ethics approvals from UREC to extend the human study to smokers. (Months 22-23, May-June 2016).

Milestone 15 (M15) – Acquisition of strong literature background on:

(1) Vasomotion.
(2) The oscillatory nature of cell glycolytic and mitochondrial metabolic reactions of NAD(P)H for the production of ATP energy.
(3) The possible link between vasomotion and cellular metabolic oscillators.
(4) The wavelet phase coherence (WPCO) analysis as a tool for the investigation of the interaction between oscillators identified in the same frequency interval of different signals measured simultaneously.
(Months 23-28, June-November 2016).

Milestone 16 (M16) – Secondment at the National University of Ireland Galway (NUIG): Validation of correlation mapping optical coherence tomography (cmOCT) method for the concurrent study of structural and functional dynamics of cutaneous microcirculation (Months 26-27, September-October 2016).

Milestone 17 (M17) – Implementation of methods for performing the nonlinear dynamics analysis of metabolic and microvascular signals measured simultaneously from mice models (M11) and human individuals (M10):

(1) Reconstruction of continuous NAD(P)H and RR time series by piecewise cubic spline interpolation of discrete autofluorescence data points.
(2) Continuous wavelet transform (CWT) spectral analysis of LDF, NAD(P)H and RR time series for the characterisation and examination of blood flow and metabolic oscillators.
(3) Exploration of the use of the open-source code for performing the WPCO analysis provided by the research group lead by Professor Stefanovska, available from the Lancaster University website (http://py-biomedical.lancaster.ac.uk).
(Months 27-31, October 2016-February 2017).

Milestone 18 (M18) – Experimental application of the protocol implemented for testing human subjects (M9) to a cohort of 20 healthy smokers for establishing early skin microvascular and metabolic dynamic biomarkers of vascular dysfunction, through the comparison with previous data collected from the healthy control group (M10). (Months 30-33, January-April 2017).

Milestone 19 (M19) – Application of the nonlinear dynamics analysis (M17) and statistical analysis on data collected from WT and $Nrf2^{-/-}$ mice (M11) for the study of dynamic markers of microcirculation and cell energy metabolism in mice models. (Months 32-33, March-April 2017).

Milestone 20 (M20) – Application of the nonlinear dynamics analysis (M17), analysis of the attractors (M13), and statistical analysis on data collected from non-smoker (M10) and smoker (M18) healthy individuals for the study of dynamic markers of microcirculation and cell energy metabolism in human subjects. (Months 31-36, March-August 2017).

2.2 Optical measurements

2.2.1 Multifunctional device for data collection (*LAKK-M*)

Non-invasive optical measurements were performed by using the multifunctional commercial biomedical device *LAKK-M* (*Spe Lazma Ltd*, Russia) (Fig. 18). The system combines laser Doppler flowmetry (LDF), laser fluorescence spectroscopy (LFS) and reflectance spectroscopy (RS) methods for the *in-vivo* evaluation of cutaneous blood perfusion, autofluorescent biomarkers and oxygen saturation, respectively. The apparatus is provided with 5 narrow-band semiconductor laser sources at the following wavelengths:

- 1064 nm (power ~2-5 mW), IR continuous wave laser for LDF recordings.
- 365 nm (power ~1 mW), continuous wave laser for the measurement of AF emission induced by UV light.
- 532 nm (power ~2-4 mW), green multimode laser working in continuous wave mode for the measurement of AF stimulated by green light and in pulsed mode for RS recordings.
- 630 nm (power ~2-4 mW), red multimode laser working in continuous wave mode for the measurement of AF stimulated by red light and in pulsed mode for RS recordings.
- 480 nm (power ~2-4 mW), continuous wave laser for the measurement of AF stimulated by blue light.

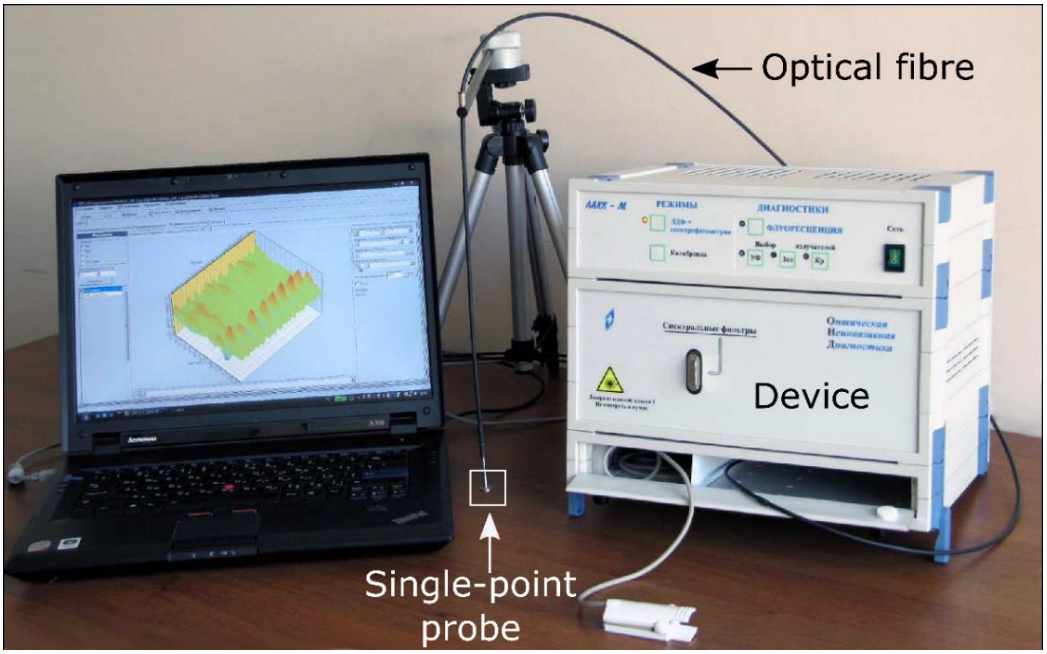

Fig. 18 *LAKK-M* device (picture reproduced and adapted from *Spe Lazma Ltd* user's manual). The apparatus is provided with a flexible optical fibre including a single-point probe at the tip. To perform the measurements the optical fibre must be fixed in a tripod ensuring a position of the probe perpendicular to the skin surface. The probe must be placed at direct contact with a specific site of interest in the skin surface.

The laser beams are delivered to the cutaneous sample through a flexible optical fibre provided at the extremity with a single-point probe (diameter ~4 mm) targeting a tissue volume of ~1-3 mm^3. The probe includes specific sensors for the delivery of the different laser beams, and detectors for the collection of the light coming from the tissue (Fig. 19). The general principles of operation for *LAKK-M* measurements are described in Fig. 20.

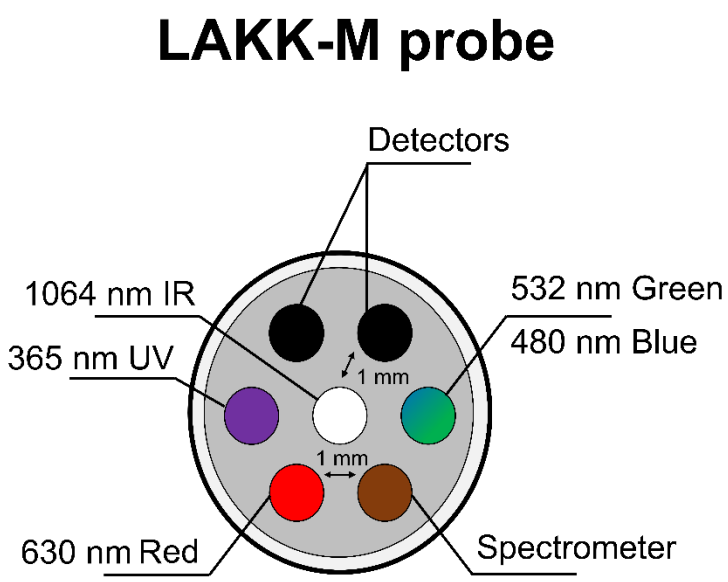

Fig. 19 Scheme of the *LAKK-M* single-point probe. The apparatus is provided with a multimodal single-point probe which includes 7 sensors: 4 irradiating sensors (IR, UV, green/blue, red laser sources), 2 detectors and a spectrometer. The distance between each irradiating sensor and the correspondent detector is around 1 mm. The probe is designed to test a skin tissue volume around 1-3 mm^3.

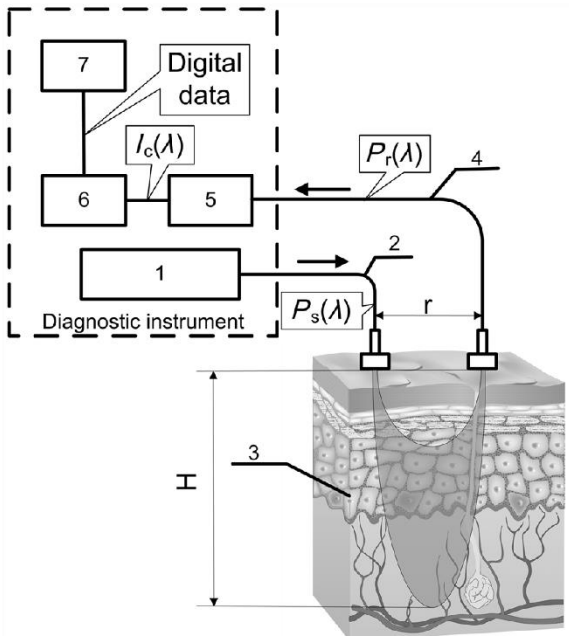

Fig. 20 General operation scheme of *LAKK-M* device (figure reproduced from [147]). (1) Optical radiation source with wavelength λ and power $Ps(\lambda)$. (2) Optical fibre to transfer the radiation from the laser source to the skin. (3) The radiation interacts with the skin tissue through absorption and scattering events. (4) The backscattered radiation emitted from the tissue with power $Pr(\lambda) < Ps(\lambda)$ is transmitted to a photodetector by an optical fibre system. (5) The photodetector converts the $Pr(\lambda)$ power into voltage $Ic(\lambda)$. (6) The electric signal $Ic(\lambda)$ is filtered and digitised in an electronic block. (7) The digital data is transferred to a computer for mathematical processing.

2.2.2 LDF and RS recordings

The *LAKK-M* system allows concurrent LDF and RS measurements to be performed according to the principles that have been discussed in sections 1.5 (paragraph 1.5.1, page 29) and 1.6 (page 41), respectively. Before collecting measurements the single-point probe was calibrated through a fluoroplastic oscillating disk located at the bottom of the device which simulates Brownian motion (Fig. 21). The LDF signal was obtained by the irradiation of the skin with the IR (1064 nm) laser source at a sampling frequency of 20 Hz. The blood perfusion I_m, calculated according to equation 1 (section 1.5, paragraph 1.5.1, page 29), was expressed in arbitrary perfusion units (PU). Fig. 22 shows an example of LDF blood perfusion continuous time series obtained by *LAKK-M*.

Fig. 21 *LAKK-M* system calibration before LDF and RS analyses (picture reproduced from the *Spe Lazma Ltd* user's manual). The calibration method is insensitive to environmental vibration artefacts, based on the detection of the Doppler shift generated in a layered structure with tissue-like optical properties. The layers are made of an oscillating fluoroplastic disk (PTFE) and a fixed light transparent upper plane-parallel plate used to create a constant component of the signal by the passage of the radiation through the transparent plate.

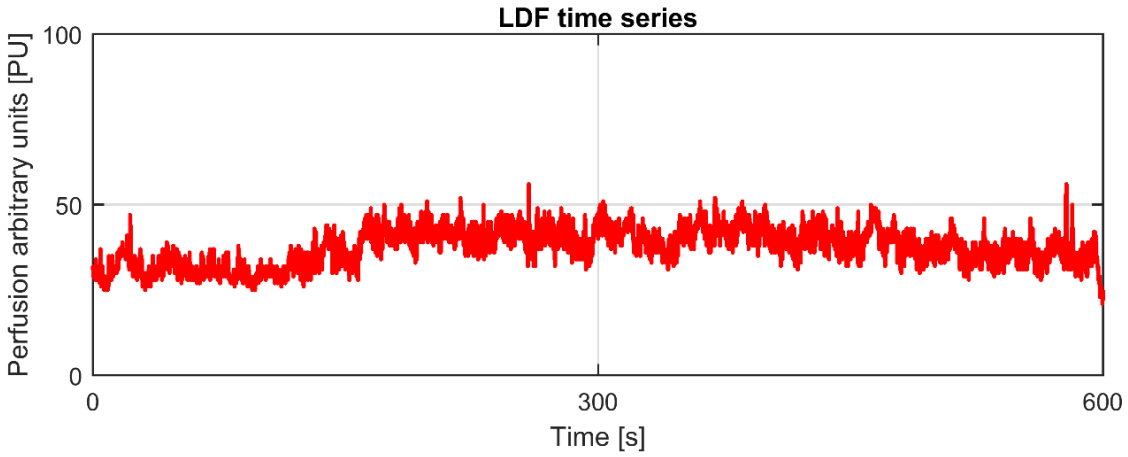

Fig. 22 LDF time series. Example of 10 min LDF recording from the human volar forearm collected by *LAKK-M* single-point probe. The technique allows to monitor continuously blood perfusion dynamics and is suitable for the study of nonlinear dynamics by wavelet analysis.

Oxygen saturation (SO_2) was obtained by RS, through the simultaneous irradiation of the skin with green (532 nm) and red (630 nm) lights which are absorbed differently by oxygenated and deoxygenated Hb fractions. The percentage SO_2 (equation 3, section 1.6, page 42) is extracted from green and red backscattered lights by the application of the Beer-Lambert law (equation 2, section 1.6, page 42). The software associated with the *LAKK-M* system (*LDF 3.1.1.404*) allows extracting raw data of the LDF signal for subsequent processing by using additional software (e.g. Matlab). In contrast, the software does not allow the extraction of SO_2 raw data for customised analysis.

2.2.3 Workflow to evaluate the reliability of LDF measurements

The workflow of this research study included preliminary experiments to evaluate the robustness and reliability of *LAKK-M* LDF measurements for monitoring skin blood perfusion (M6):

(1) Comparison of LDF measurements with blood perfusion recordings obtained using a standard optimised LDI protocol available at the School of Medicine of the University of Dundee.
(2) Examination of microvascular function by applying the LDF technique on three mouse phenotypes for which different microvascular reactivity was expected.

LDF vs LDI

The *LAKK-M* LDF perfusion measurements were compared with LDI recordings obtained using the *MoorLDI* imaging commercial system (*Moor Instruments Ltd*, UK), for which established optimised protocols were available at the facilities of the School of Medicine of the University of Dundee. The principles of LDI method have been already discussed in section 1.5 (paragraph 1.5.1, page 31). Fig. 23 displays a scheme of the experimental setup for the collection of LDI measurements from mice skin during iontophoresis transcutaneous delivery of vasoactive drugs. Fig. 24 shows the LDI protocol used to assess the microcirculation from the mouse flank. The protocol was consistent with the collection of 22 temporal LDI perfusion maps at a sampling rate of a map every 32 s, while challenging micro-vessels with iontophoresis administration of vasoactive drugs. The first 3 maps were imaged without administration of pharmacological agents to determine the baseline perfusion, then 6 maps were acquired during constriction of micro-vessels induced by iontophoresis

administration of 1% PE, 6 maps were acquired during vasodilation of micro-vessels induced by delivery of 2% ACh, and the last 7 maps were imaged to monitor the restoration of baseline perfusion after stopping ACh delivery.

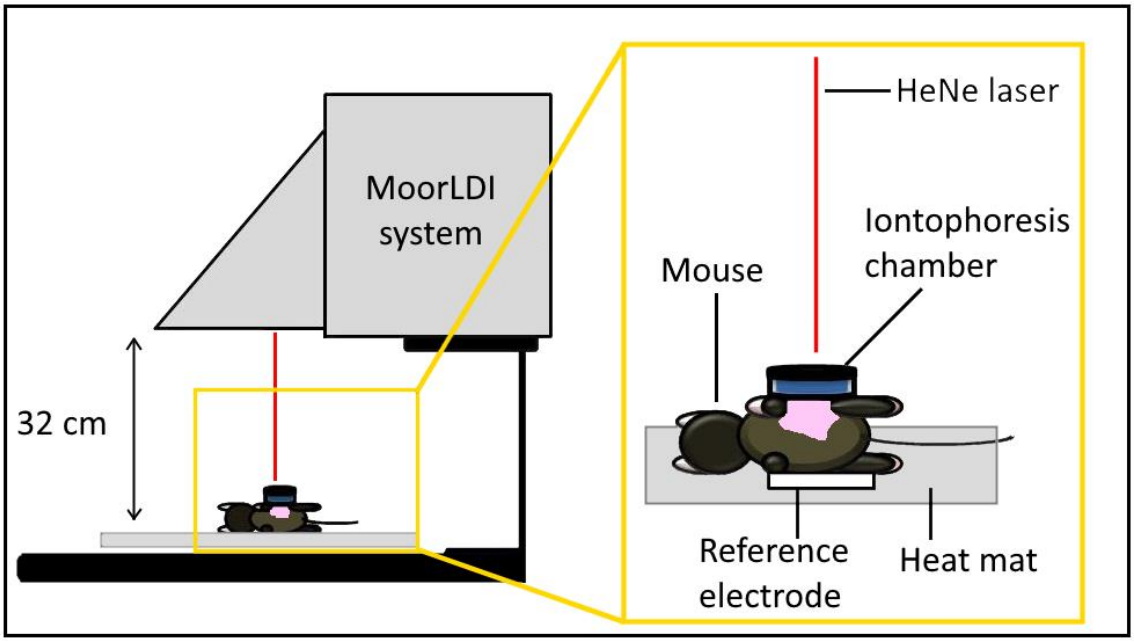

Fig. 23 Scheme of the experimental setup for LDI data acquisition. LDI is a method sensitive to light absorption from hair or pigmentation in the skin. Thus, the flank of the tested mice was shaved 48 hours prior to performing the experiments by using an electric shaver and removing the remaining hair with depilatory cream (*Veet*®, *Reckitt-Benckiser*) to obtain an intact hair-free skin. Before the experiments mice were anaesthetised through a standard Boyle's Apparatus to prevent movement artefacts, and were laid on a heat mat at 37°C with the flank facing the upper side. A general light anaesthesia was maintained by delivering 1.5-2% isoflurane (*Abbott Laboratories*) in oxygen (1.5 L/min) through an inhalation nose cone. An iontophoresis chamber (*ION6* probe, *Moor Instruments Ltd*, UK) of 20 mm internal diameter was attached to the mouse flank using double-adhesive tape, and a reference electrode was placed underside of the animal. The iontophoresis chamber was filled with a 2 ml solution of vasoactive drug and sealed with a clear Perspex cap (*Moor Instruments Ltd*, UK). The delivery of the vasoactive drug was induced by the application of a continuous 100 µA anodal current through an iontophoresis controller (*MIC2*, *Moor Instruments Ltd*, UK) connected to the electrodes. LDI images were acquired using the commercial system *MoorLDI* (*Moor Instruments Ltd*, UK), which employs a stable helium-neon (HeNe) laser source (633 nm, 2 mW nominal power) coupled with a diode laser source (780 nm, 1 mW nominal power) to irradiate the skin sample. The laser was positioned 50 cm above the mouse skin, and the internal mirror distance was accounted for a height of 32 cm from laser hood to tissue. The light scattered from the moving RBCs and the static scattering from the skin surface were detected through an imaging lens, focused on two photodetectors, and finally processed as a photocurrent to provide skin perfusion coloured maps.

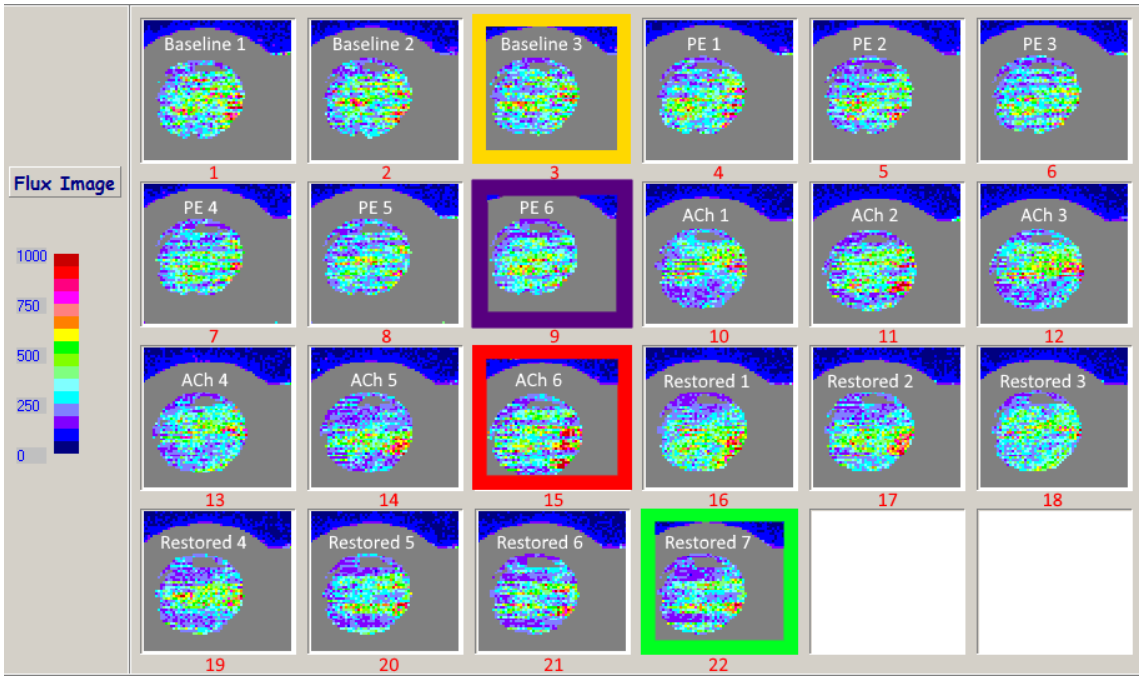

Fig. 24 Protocol to examine microvascular function by LDI during iontophoresis. LDI coloured maps of skin blood perfusion imaged in resting conditions (maps 1-3), during PE-induced vasoconstriction (maps 4-9), during ACh-induced vasodilation (maps 10-15), and during the restoration of baseline flow (maps 16-22). The coloured pixels of the images reflect the degree of blood perfusion in the cutaneous tissue, expressed in arbitrary perfusion units (PU) ranging from 0 (dark blue, low-perfusion) to 1000 (dark red, high-perfusion). The average perfusion values were extracted from the maps by using the LDI software *v5.3* (*Moor Instruments Ltd*, UK).

Considering that LDI provides only discrete measurements of blood perfusion, the comparison with LDF was performed by acquiring 10 s LDF measurements from the same skin location at specific key steps of the test and evaluating the relative trends of the average perfusion values obtained with the two techniques.

A total of 4 discrete time points were chosen to compare LDI and LDF measurements, which are highlighted by the coloured squares in Fig. 24:

(1) Baseline perfusion (yellow square, LDI map 3). At this time point the LDI was paused, to allow removing the Perspex cap and placing quickly the *LAKK-M* single-point probe in the skin inside the chamber to collect a 10 s LDF trace. Then, the LDF probe was removed and the experiment was continued by applying a 100 µA current to administrate the 1% PE solution. At this point LDI recordings were restarted.

(2) Perfusion after PE delivery (purple square, LDI map 9). At this time point the delivery of PE and LDI recordings were paused, to allow again placing quickly the LDF probe in the skin inside the chamber for collecting a 10 s LDF trace.

Then, both of the LDF probe and the PE solution were removed from the chamber. The skin was quickly washed with sterilised water and the chamber filled with a 2% ACh solution. The experiment was continued by applying a 100 µA current to deliver ACh. At this point LDI recordings were restarted.

(3) Perfusion after ACh delivery (red square, LDI map 15). At this time point the delivery of ACh and LDI recordings were paused, to allow a 10 s LDF trace to be collected. Then, both of the LDF probe and the ACh solution were removed from the chamber, the skin was quickly washed with sterilised water and the chamber filled with water solution. The experiment was continued by restarting LDI recordings to monitor the restoration of baseline perfusion.

(4) Restoration of baseline perfusion (green square, LDI map 22). This was the final time point of the experiment. After the acquisition of the last LDI map, the LDF single-point probe was placed quickly in the skin inside the chamber and a 10 s trace was collected.

The experiments were repeated in duplicate from the skin of 5 WT mice (10 experiments), collecting a total of 40 pairs of discrete LDF and LDI mean perfusion values (4 time points for each experiment) that were used to estimate the Pearson's correlation coefficient *r*. The correlation analysis performed by R-Studio software provided a robust positive correlation coefficient between LDF and LDI data (r=0.8, $p < 0.001$, number of samples n=40).

Fig. 25 shows the trends of the average relative perfusion (dimensionless values obtained as a function of the baseline perfusion) measured by LDF and LDI. Both of the methods were able to detect the expected trend of relative perfusion, showing a decrease of flow after vasoconstriction induced by PE, an increase of flow after administration of ACh, and restoration of the baseline flow after stopping the delivery of ACh. Although the two techniques provided quite similar results, the values of relative perfusion were different during ACh time point with higher perfusion values (9% higher) detected by the LDI technique. This observation could be due to different reasons:

(1) Because it was not possible to collect LDI and LDF data simultaneously, it may be possible that during the time period passing between the last ACh LDI recording (Fig. 24, map 15), the application of the LDF probe to the skin, and the collection of the LDF measurement the effect of ACh was already diminished, thus explaining the lower perfusion detected by LDF.

(2) As displayed in Fig. 26, the LDI scans reflect the average blood perfusion in the entire skin area inside the iontophoresis chamber providing better reproducibility of measurements compared to the LDF single-point recordings. This could also explain the detection of different perfusion values with the two methods during ACh time point, which is the reason why LDI is the preferred choice when the goal is evaluating the maximal blood flow peak response.

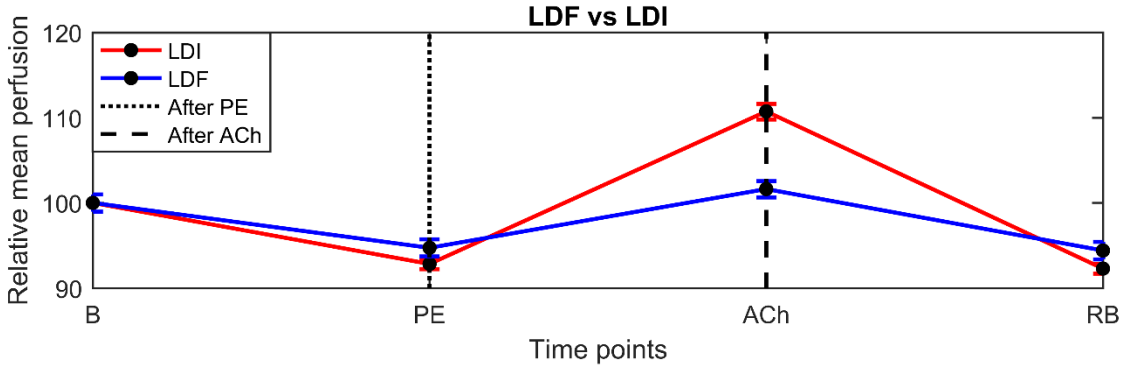

Fig. 25 Comparison of LDI and LDF measurements. Relative mean blood perfusion values measured in duplicate from 5 WT mice (n=5, n. of experiments=10) by LDI and LDF methods during the different time points of iontophoresis test. Data are expressed as a function of the baseline (dimensionless units) and presented as line plots of the mean values with error bars corresponding to the standard deviation (SD). Red line = LDI. Blue line = LDF. B = Baseline. PE = Phenylephrine. ACh = Acetylcholine. RB = Restored baseline.

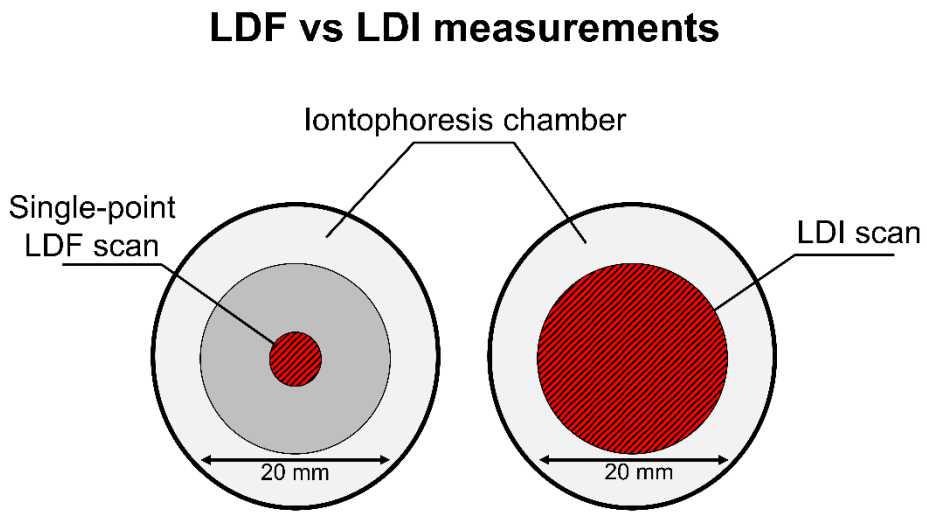

Fig. 26 Spatial distribution of LDF and LDI scans. LDI and LDF recordings cover skin areas of different size. As shown on the left side of the image, LDF provides recordings reflecting the mean perfusion of a single cutaneous point inside the iontophoresis chamber, while LDI (right side of the image) measures the average perfusion of the whole skin area inside the chamber. The slow sampling of a larger skin area typical of LDI recordings allows reducing the variability of perfusion measurements caused by the heterogeneous structure of skin, providing a better data reproducibility. In contrast, single-point measurements provide the advantage of fast continuous recordings suitable to track the non-linear oscillatory behaviour of the microcirculation.

Based on the results obtained from these preliminary experiments, the *LAKK-M* LDF recordings were considered sufficiently reliable to evaluate skin blood perfusion. Indeed, the measurements showed a relevant correlation with the standard LDI recordings used at the University of Dundee for assessing endothelial function in mice. Moreover, although the single-point nature of LDF recordings might be a shortcoming leading to inaccurate detection of the maximal perfusion peak response, this does not represent a major problem in this work that is aimed at investigating the nonlinear dynamics of the microcirculation. Indeed, LDF is more suitable than LDI for assessing the oscillatory behaviour of blood flow due to the high sampling frequency of continuous perfusion traces.

Examination of microvascular function by LDF in different mouse models

To confirm further the reliability of *LAKK-M* LDF measurements for the study of microcirculation function, the probe was also tested on three different mouse models that are expected to display different patterns of microvascular reactivity:

- WT mice (n=4), characterised by a normal functioning microvascular system.
- $Nrf2^{-/-}$ mice (n=4), characterised by impaired antioxidant defence and increased oxidative stress that should impact negatively the microcirculation.
- *Kelch-like ECH-associated protein 1* KO ($Keap\text{-}1^{-/-}$) mice (n=4), characterised by overexpression of the Nrf2 transcription factor and enhanced antioxidant defence that should impact positively the microcirculation.

The experiments were performed combining the LDF probe with iontophoresis, as displayed in Fig. 27. Also in this case mice were shaved and anaesthetised prior to performing the experiments, and the iontophoresis equipment was set up with the same modalities described in Fig. 23. However, in this case the chamber was not sealed with the Perspex cap to allow placing the LDF probe in direct contact with the skin. A continuous LDF signal was recorded during the iontophoresis test that was divided into three steps: baseline (1 min and 30 s), vasoconstriction induced by delivery of 1% PE (3 min), vasodilation induced by delivery of 2% ACh (6 min). The relative mean perfusion values were estimated for each time point of the test and compared between the three groups of mice.

The results displayed clearly different microvascular patterns between groups, reflecting the expected functional trends for the examined phenotypes (Fig. 28). $Nrf2^{-/-}$ knock-out animals displayed a major vasoconstriction during PE

administration and lower vasodilation during ACh delivery compared to both WT and Keap-1$^{-/-}$ animals, confirming the negative impact of oxidative stress on microvascular function. Moreover, Keap-1$^{-/-}$ mice showed the highest relative increase of blood perfusion in response to ACh stimulation, confirming the positive effect of enhanced antioxidant defence on the functional dynamics of the microcirculation. These preliminary results confirmed further the reliability of *LAKK-M* LDF measurements for the assessment of microvascular function.

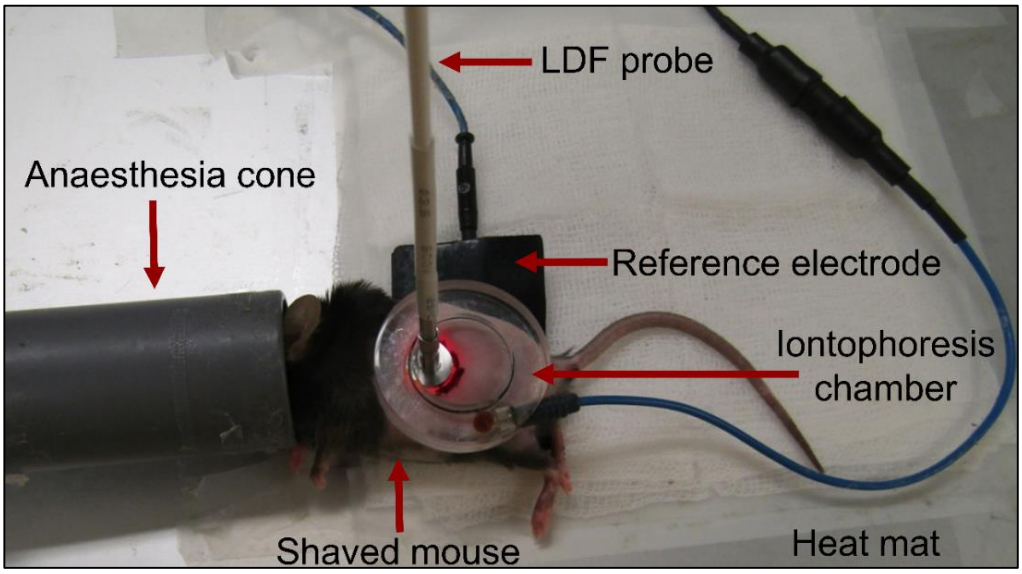

Fig. 27 Experimental setup to test microvascular function by *LAKK-M* LDF probe. The probe was placed in direct contact with the skin. A continuous 10 min and 30 s perfusion recording was collected during iontophoresis. The test was divided in 3 steps: baseline, transdermal delivery of 1% PE, and delivery of 2% ACh. Mice were anaesthetised and laid in a heat mat at 37°C prior to performing the test. The anaesthesia was maintained during the test by an inhalation nose cone.

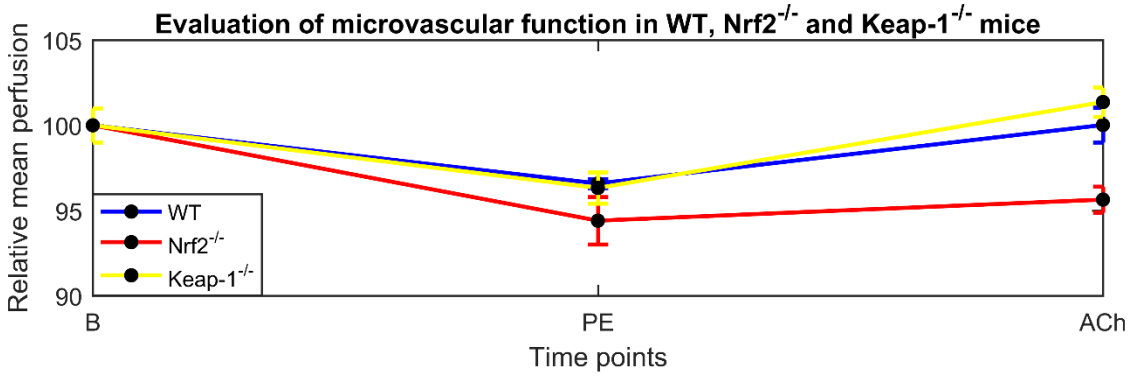

Fig. 28 Microvascular function in WT, Nrf2$^{-/-}$ and Keap-1$^{-/-}$ mice. Relative blood perfusion values measured in duplicate by LDF from WT (n=4, n. of experiments = 8), Nrf2$^{-/-}$ (n=4, n. of experiments = 8) and Keap-1$^{-/-}$ (n=4, n. of experiments = 8) mice during iontophoresis test. Data are expressed as a function of the baseline (dimensionless units) and presented as line plots of the mean values with error bars corresponding to the SD. Blue line = WT. Red line = Nrf2$^{-/-}$. Yellow line = Keap-1$^{-/-}$. B = Baseline. PE = Phenylephrine. ACh = Acetylcholine.

2.2.4 LFS measurements

As discussed in paragraph 2.2.1 (pages 72-73), the *LAKK-M* device allows the measurement of UV, blue, green and red autofluorescence by the employment of 365 nm, 480 nm, 532 nm and 630 nm laser sources, respectively. The calibration of LFS laser was performed by using the skin location chosen for the measurement as template. NAD(P)H skin autofluorescence was assessed by using the UV laser source, which is able to induce also the autofluorescence of structural proteins (e.g. collagen and elastin) and FAD^+ (Fig. 29). Therefore, the detected UV autofluorescence spectrum was the result of the overlapping contribution from different fluorophores with the central AF peak reflecting mainly NAD(P)H emission. Raw data of the UV spectra were processed by Matlab R2015a (*The MathWorks Inc.*) software to extract the amplitude of each fluorophore's emission peak expressed in arbitrary units.

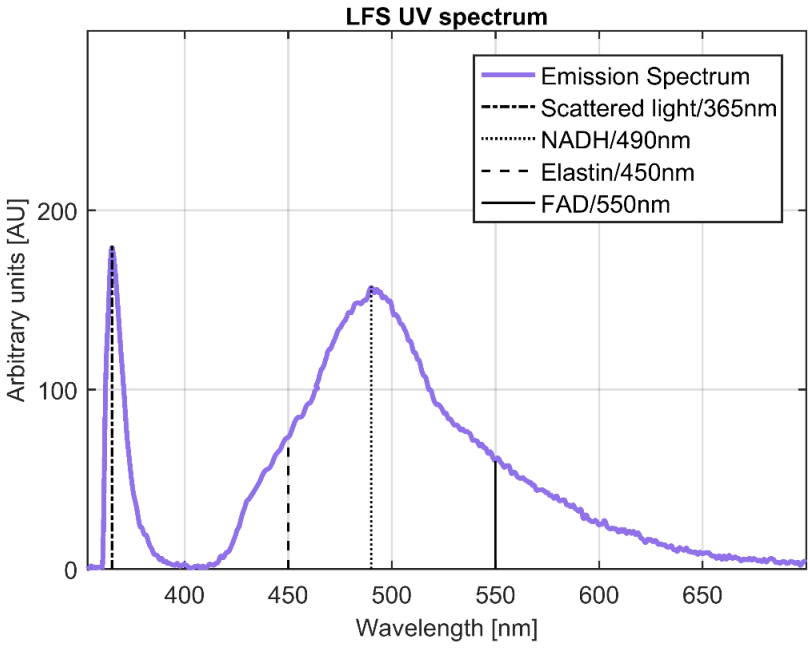

Fig. 29 Typical UV AF measured by *LAKK-M* LFS probe. Example of UV autofluorescence spectrum measured for 10 s from the flank of a mouse. The fluorescence amplitudes of the biomarkers were extracted at the following emission wavelengths: NAD(P)H 490 nm, FAD^+ 550 nm, elastin 450 nm. Data were expressed in arbitrary units (AU).

A disadvantage of the *LAKK-M* device is the impossibility to run simultaneously LFS and LDF/RS measurements. Therefore, to perform simultaneous recordings of AF, blood perfusion and oxygen saturation two single-point probes of two different *LAKK-M* devices were combined, a probe to measure LDF/RS signals and another probe to collect contemporary AF spectra.

Another aspect to consider is the discrete nature of LFS measurements which does not allow obtaining time series of NAD(P)H. For this reason, to monitor the changes of the biomarker over time, several discrete spectral measurements were collected in a specific time window and the fluorescence amplitude of NAD(P)H was extracted at 490 nm from each spectrum.

In addition, as discussed in the section 1.7 (paragraph 1.7.2, page 50), NAD(P)H cutaneous AF is affected by UV light absorption from Hb in the blood, leading to sensitivity of the signal to changes in blood volume (BV). To reduce BV influence, the NAD(P)H autofluorescence peak was normalised by the 1:1 ratio with the fluorescence amplitude of elastin (450 nm),

$$NAD(P)H_{normalised} = \frac{NAD(P)H_{amplitude}}{Elastin_{amplitude}} \quad (21)$$

Elastin is a structural protein that should maintain constant amounts in the tissue during the time-window while the recordings are collected (20-25 minutes). Thus, when evaluating the relative change of the $NAD(P)H_{normalised}$ (dimensionless variable) over time this should reflect the trend of NAD(P)H with a reduced effect of BV. The spectral emission region around 450 nm should contain also an overlapping contribution of collagen. However, this does not represent a major problem because collagen is also a structural protein of the cutaneous tissue characterised by a non-variable biological turnover in the short time frame of 20-25 minutes employed in this study for data collection.

The redox state of the skin tissue was assessed by calculating the redox ratio (RR), defined as the ratio between NAD(P)H and FAD^+ autofluorescence peaks,

$$RR_{index} = \frac{NAD(P)H_{amplitude}}{FAD^+{}_{amplitude}} \quad (22)$$

RR (dimensionless variable) is an index of the balance between the reduced NAD(P)H and the oxidised FAD^+, reflecting the mitochondrial activity. More specific details on the reasons for normalising NAD(P)H AF by elastin and FAD^+ AF are provided in the section 2.3 (paragraph 2.3.2, page 99).

An alternative better method the normalisation could have been done was performing the same calculations described in equations 21-22 by using data on the contributions of NAD(P)H, FAD^+ and elastin to the UV AF spectrum extracted with a more precise technique. A possible approach to achieve this goal could be computing the contribution of the fluorophores to the emission spectrum through

the curve-fitting analysis described in Fig. 14 of paragraph 1.7.1 (page 46). However, the implementation of the curve-fitting technique was not part of the main objectives of this project and will be certainly considered as future perspective to improve the methodology, allowing a better differentiation of the overlapping contributions of different natural dyes to the UV emission spectrum.

2.2.5 Workflow to evaluate the robustness of LFS measurements

An important aspect when evaluating autofluorescence is to determine the reliability, accuracy and reproducibility of the measurements. Indeed, LFS recordings are notoriously fickle measurements affected by several factors in the biological tissue, i.e. the location used for data collection, the temperature, the physiological state of the tested subject, and the absorption of light by absorbers in the cutaneous tissue. Therefore, the workflow for the design of the protocols used in this study was consistent with preliminary experiments to determine the reliability of *LAKK-M* LFS recordings for the final purpose of this research, which was the assessment of nonlinear dynamics of cellular energetic metabolism by the examination of NAD(P)H oscillatory behaviour. The preliminary work to determine the reliability of LFS recordings and possible normalisation techniques to improve the assessment of AF included different kind of experiments:

(1) Evaluation of the reproducibility of the technique for measuring NAD(P)H fluorescence in both *in-vitro* molecular solutions and *in-vivo* cutaneous tissue.
(2) Preliminary experiments comparing UV LFS recordings between WT and $Nrf2^{-/-}$ mice to evaluate the potential of the technique to distinguish between normal conditions and increased degree of oxidative stress in the skin.
(3) Monte Carlo modelling studies for determining the spatial resolution of autofluorescence single-point measurements.
(4) Application of correction methods to reduce the negative effect of natural skin absorbers, i.e. Hb, on AF recordings (section 2.3, paragraph 2.3.2, page 99).

Reproducibility of LFS measurements in-vitro

The variability of LFS recordings *in-vitro* was examined by measuring the UV fluorescence of molecular solutions of NADH. Specifically, 1 mM of fresh solution was prepared at a T of 4°C mixing w/v β-NADH (*Sigma-Aldrich*) with a solvent. The solvent used to prepare the solution was a *Trizma*® base buffer (*Sigma-Aldrich)* that according to the guidelines from *Sigma-Aldrich* allows obtaining stable solutions of β-NADH. 0.1 mM, 0.01 mM, 0.001 mM and 0.0001 mM 10-fold

serial dilutions were prepared from the starting 1mM solution as shown in Fig. 30. 300 µl of each solution/dilution and of the solvent (control) were analysed in triplicate using the matte black cuvette (*Spe Lazma Ltd*, Russia) described in Fig. 31, which is specifically designed for performing *in-vitro* fluorescence analysis using the *LAKK-M* LFS probe.

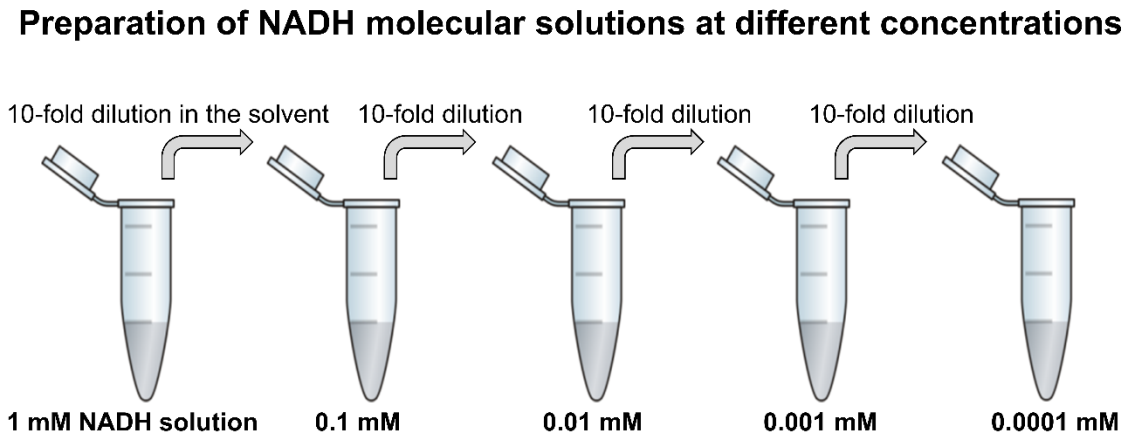

Fig. 30 Preparation of NADH solutions at different concentrations. Scheme of the 10-fold serial dilutions of β-NADH obtained starting from a 1 mM fresh solution. The *Trizma*® base solvent at pH 9 was used to produce stable solutions. The eppendorf tubes were covered with aluminium foil to avoid molecular photo-degradation induced by environmental light.

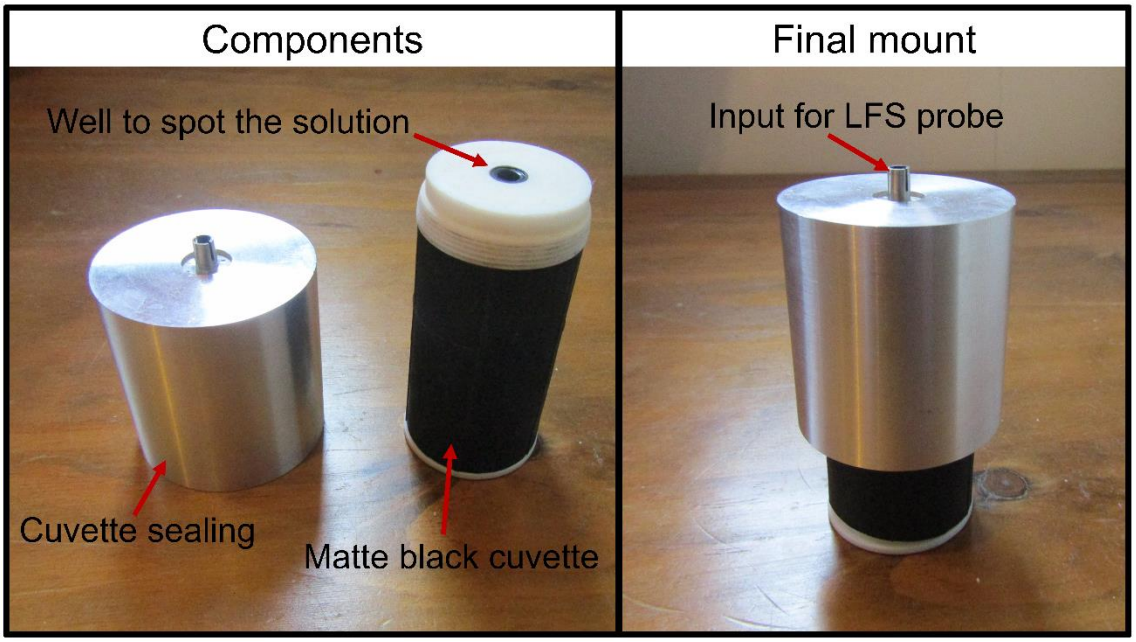

Fig. 31 Black cuvette for *in-vitro* fluorescence measurements. The image shows the matte black cuvette that was used to measure the fluorescence of *in-vitro* β-NADH solutions. The cuvette included a well for spotting the solution, and a cuvette sealing for protecting the sample from the external environmental light. The sealing was provided with a hole at the top, which was specifically designed with the same size of the *LAKK-M* single-point LFS probe to allow the insertion of the probe for collecting the fluorescence measurements.

For each analysed solution, five 10 s NADH fluorescence spectra were collected over 5-min (1 spectrum per min) by irradiating the solution inside the cuvette with the LFS 365 nm UV light. The well of the cuvette was washed three times with sterilised water between subsequent analyses to remove residuals of the solution examined previously. Fig. 32 displays the results of *in-vitro* fluorescence recordings of NADH, the peak was found at 490 nm for the 1 mM, 0.1 mM and 0.01 mM solutions (Fig. 32a-c), while a shift of the peak to 460 nm was observed for the 0.001 mM and 0.0001 mM solutions (Fig. 32d-e). A possible explanation for the shift of NADH emission peak may be that the fluorophore absorbs its own fluorescence at high concentrations. A control solution of the solvent (*Trizma*® base) was analysed prior to the examination of NADH solutions, to make sure that any contamination from external fluorophores was absent. No fluorescence peaks were observed in the control solution (Fig. 32f). The variability of NADH fluorescence measurements repeated over 5-min was estimated as the ratio between the standard deviation (SD) and the mean of NADH emission peak, revealing a coefficient of variation between 1-6% that is close to the 2-4% random error reported in the literature for LFS measurements on non-alive gauges performed by using the *LAKK-M* device [148]. The *in-vitro* experiments revealed also that the LFS is able to distinguish correctly different concentrations of NADH, at least for the range of concentrations tested in this study (0.0001-1 mM). Data on the sensitivity of LFS to different NADH concentrations are shown in Fig. 33.

Reproducibility of LFS measurements in-vivo

The variability of LFS measurements *in-vivo* was examined by measuring the UV AF from human subjects at two different skin locations: the forearm and the palmar side of the middle finger. Specifically, 10 s sequential UV spectra were collected over a temporal period of 10-min (1 spectrum per min) in resting conditions. The experiments were performed in a room with controlled T (23 ± 1°C), while the subject was resting in a clinical bed with the arm laid in a soft cushion. The forearm location was tested from 53 individuals and the middle finger from 10 individuals. The variability of the measurements over 10-min was estimated as the ratio between the SD and the mean of the AF emission peaks, revealing a coefficient of variation between 1-8% from the forearm and between 9-20% from the middle finger.

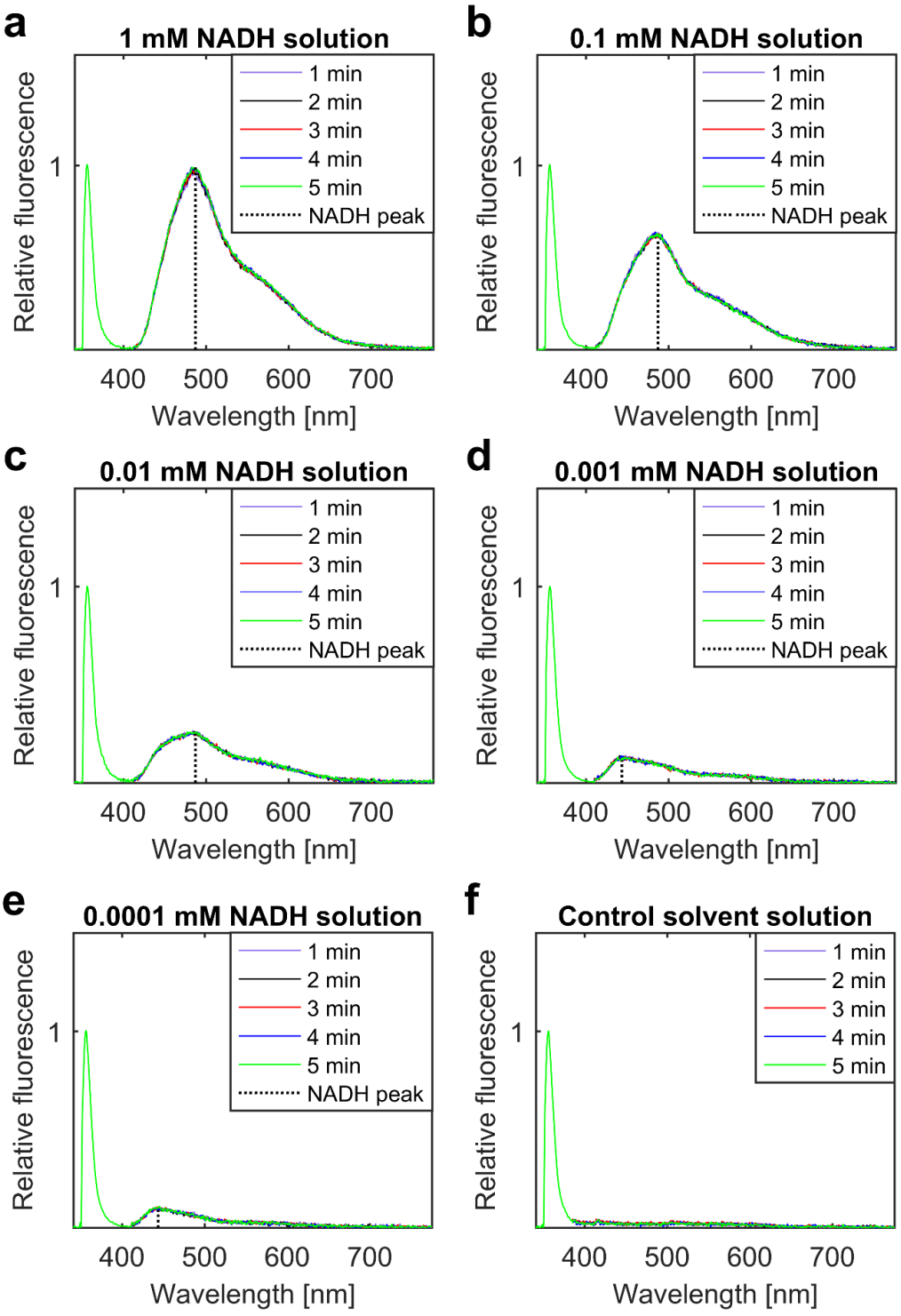

Fig. 32 UV fluorescence of NADH molecular solutions. 300 µl of each solution were tested over 5 min (experiment repeated in triplicate). (**a**) Fluorescence of 1 mM β-NADH. (**b**) Fluorescence of 0.1 mM β-NADH. (**c**) Fluorescence of 0.01 mM β-NADH. (**d**) Fluorescence of 0.001 mM β-NADH. (**e**) Fluorescence of 0.0001 mM β-NADH. (**f**) Fluorescence of a control solution of Trizma® base. The control solution did not show any fluorescence peak from external contaminations. NADH peak was located at 490 nm for 0.01-1 mM solutions and at 460 nm for 0.0001-0.001 mM solutions. Data are expressed as function of the backscattered light (dimensionless units). The variability over 5 min for the fluorescence recordings of each NADH solution was respectively 4-6% (a), 3-4% (b), 2-6% (c), 1-6% (d), 2-5% (e).

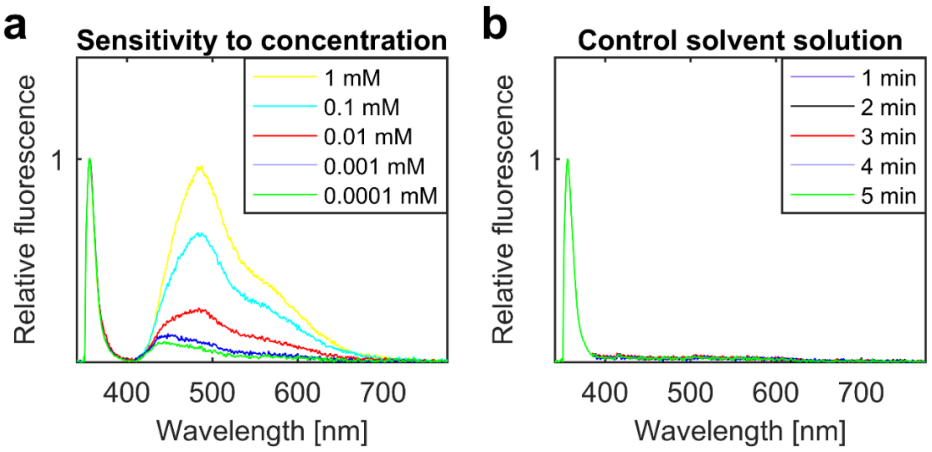

Fig. 33 Sensitivity of LFS optical measurements to NADH concentration. (**a**) β-NADH UV fluorescence spectra measured from solutions at different concentrations: 1 mM (yellow), 0.1 mM (light blue), 0.01 mM (red), 0.001 mM (blue), 0.0001 mM (green). The graph clearly shows a trend of fluorescence amplitude matching with the analysed concentrations, characterised by sequential increasing peaks from 0.0001 mM to 1 mM solutions. However, the increase of the spectral amplitude is nonlinear, probably due to the high concentration of NADH in a small testing volume (300 µl) for the 1 mM, 0.1 mM and 0.01 mM solutions. This may cause absorption of its own fluorescence by NADH and a consequent nonlinear increase of the emitted fluorescence. (**b**) Analysis of a control *Trizma*® base solution at pH 9. No contaminant fluorescence peaks were detected. Data are expressed as function of the backscattered light (dimensionless units).

Fig. 34 shows examples of sequential UV AF spectra measured from the two analysed locations over a period of 10-min. The results from these experiments clearly outlined that LFS measurements from the *in-vivo* tissue are characterised by a major variability compared to measurements from *in-vitro* molecular solutions, making it difficult the accurate quantification of the concentration of the autofluorescent biomarkers and the biological interpretation of the data. Indeed, several environmental factors affect the AF signal, e.g. the heterogeneous anatomy of the skin characterised by different thickness and functional structures depending on specific locations, and the absorbance of UV light by melanin in the skin and Hb in the blood of cutaneous micro-vessels. The LFS measurements were more stable from the forearm location (Fig. 34a-34c), which showed less variability compared to the middle finger (Fig. 34b-34d) over a period of 10-min. The higher variability observed from the middle finger could be due to a major number of physiological environmental factors affecting the autofluorescence signal at this location. Indeed, the palmar side of the fingers is rich of AVAs, capillaries and sympathetic nerves that can cause fast and frequent changes of blood perfusion and blood volume highly affecting LFS signal.

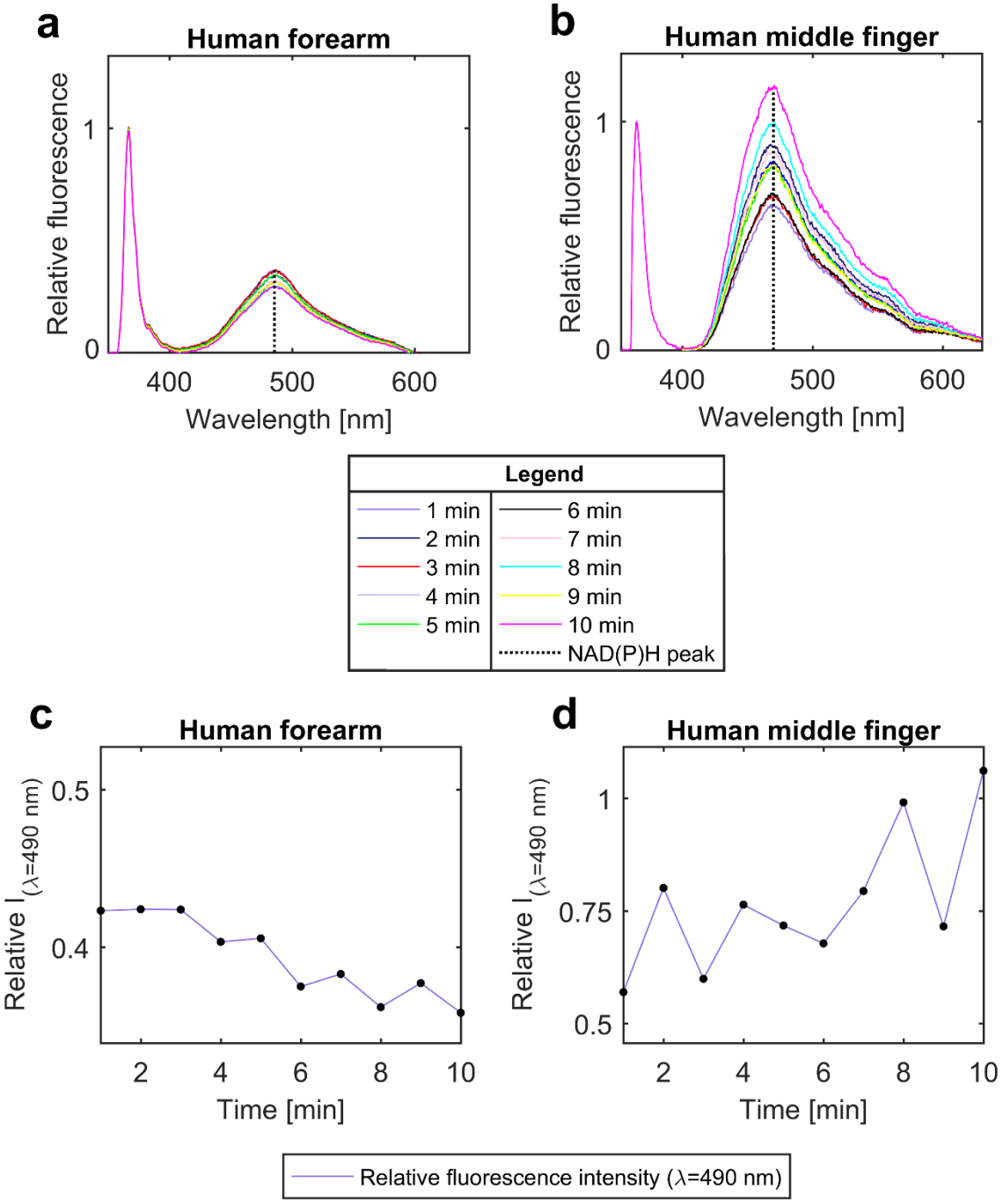

Fig. 34 UV autofluorescence from *in-vivo* human skin. (**a**) Example of AF spectra collected over 10 min (1 spectrum per min) from the forearm. (**b**) Example of AF spectra collected over 10 min (1 spectrum per min) from the middle finger. Data are expressed as function of the backscattered light (dimensionless units). The panel (**c**) shows the fluorescence intensity peak (λ = 490 nm), extracted from the spectra in the panel (**a**), expressed as function of time. The panel (**d**) shows the fluorescence intensity peak (λ = 490 nm), extracted from the spectra in the panel (**b**), expressed as function of time. The graphs clearly outline less variability of LFS measurements from the forearm location (1-8%) compared to the middle finger (9-20%). The spectra from the middle finger were characterised by a major intensity of the signal and a shift of the central peak from 490 nm to 480 nm compared to the AF spectra from the forearm.

Moreover, the middle finger location is more sensitive than the forearm to artefacts due to the pressure of the probe applied at direct contact with the skin or movements of the fingers. The AF signal was characterised by a major intensity in the middle finger compared to the forearm, probably due to higher content of melanin in the forearm which is an absorber of UV light.

The central AF peak was located at 490 nm in the spectra from the forearm, which should reflect mainly the autofluorescence of NAD(P)H, even though the spectrum is characterised by the overlapping contribution of the autofluorescence signal from other biological fluorophores (i.e. FAD^+, elastin, collagen). The central AF peak was located at 480 nm in the UV spectra from the middle finger, showing that the peak may be shifted in different cutaneous sites due to the effect of biological factors affecting the signal (e.g. changes of BV, anatomy, etc.).

Another aspect to consider, which is crucial for the final purpose of this work, is that part of the variability over time of the *in-vivo* skin AF signal is due to the natural turnover of the fluorophores in the biological tissue. For example, the coenzyme NAD(P)H which is the fluorophore contributing more to the UV LFS signal is fluctuating continuously in the biological tissue due to its involvement in the production of ATP energy in the cells, consistent with cyclic redox reactions converting the reduced NAD(P)H in the oxidised NAD^+ (non-fluorescent) and vice-versa. Therefore, part of the variability of NAD(P)H autofluorescence measured *in-vivo* reflects the natural oscillatory behaviour of this fluorophore.

Considering that one of the main goals of this research was the *in-vivo* assessment of cutaneous NAD(P)H nonlinear dynamics, the temporal collection of LFS measurements was an optimal approach to achieve this objective allowing tracking the oscillatory behaviour of this cellular coenzyme over time. However, to allow obtaining an acceptable reliable assessment of NAD(P)H oscillatory dynamics several points were addressed, aimed at reducing the variability of the autofluorescence signal associated with the negative effect of environmental factors (i.e. blood volume), and at implementing the methodology for the characterisation of NAD(P)H oscillations. This was achieved in different steps:

1. First, choice of the location for collecting LFS recordings. Based on the results reported above in Fig. 34, the forearm location was chosen as preferential site for assessing NAD(P)H dynamics in human subjects. Indeed, the recordings from the forearm were more stable, characterised by less variability over time

probably reflecting a lower effect of blood volume changes compared to the middle finger due to lower density of micro-vessels and sympathetic nerves. Moreover, although the intensity of the signal from the forearm location was reduced, which could be a shortcoming when the goal is the absolute quantification of NAD(P)H concentrations, this is not a major problem for the purpose of evaluating the oscillatory behaviour of the fluorophore over time.

2. Second, development of a method for reconstructing a continuous NAD(P)H AF signal from the discrete UV spectra collected over time (see section 2.3, paragraph 2.3.1, page 96). This was a key step to allow the characterisation of NAD(P)H oscillations by performing the continuous wavelet transform (CWT) analysis, which can be applied exclusively on continuous signals.
3. Third, application of a multi-parameter approach for assessing the effect of blood volume on the temporal changes of NAD(P)H AF signal. Specifically, simultaneous recordings of LFS and skin blood flow signals were performed during PORH test to examine the effect of a massive increase of blood volume on NAD(P)H autofluorescence (see section 2.3, paragraph 2.3.2, page 99).
4. Fourth, comparison of data from subjects with white and dark coloured skin for assessing the effect of melanin on the temporal changes of NAD(P)H autofluorescence signal (see section 2.3, paragraph 2.3.2, page 99).
5. Fifth, application of a 1:1 ratiometric correction of NAD(P)H autofluorescence signal by elastin autofluorescence in order to reduce the effect of blood volume and improve the assessment of NAD(P)H temporal dynamics (see section 2.3, paragraph 2.3.2, page 104).
6. Sixth, estimation of the redox ratio index to allow tracking the mitochondrial cellular energetic dynamics (see section 2.3, paragraph 2.3.2, page 104).

Evaluation of LFS potential to detect oxidative stress

Preliminary experiments comparing UV LFS baseline recordings between different mouse phenotypes were performed to explore the potential of the technique to distinguish between normal conditions and increased degree of oxidative stress in the skin. The groups of mice used for this purpose were:

- WT normal mice (n=4).
- $Nrf2^{-/-}$ KO animals (n=4) affected by impaired antioxidant defence.
- Sik *(Salt-inducible kinases)* knock-in (KI) mice (n=4), characterised by a protective anti-inflammatory phenotype.

Specifically, for each experiment 10 s UV autofluorescence LFS baseline spectra were collected over 10 min at a rate of 1 spectrum per min. The experiments were carried out in duplicate for each mouse under general isofluorane anaesthesia to avoid movement artefacts. Fig. 35 shows the experimental setup used for performing the recordings. The mean spectrum representative of the baseline AF was estimated by averaging the 10 spectra collected during the experiment.

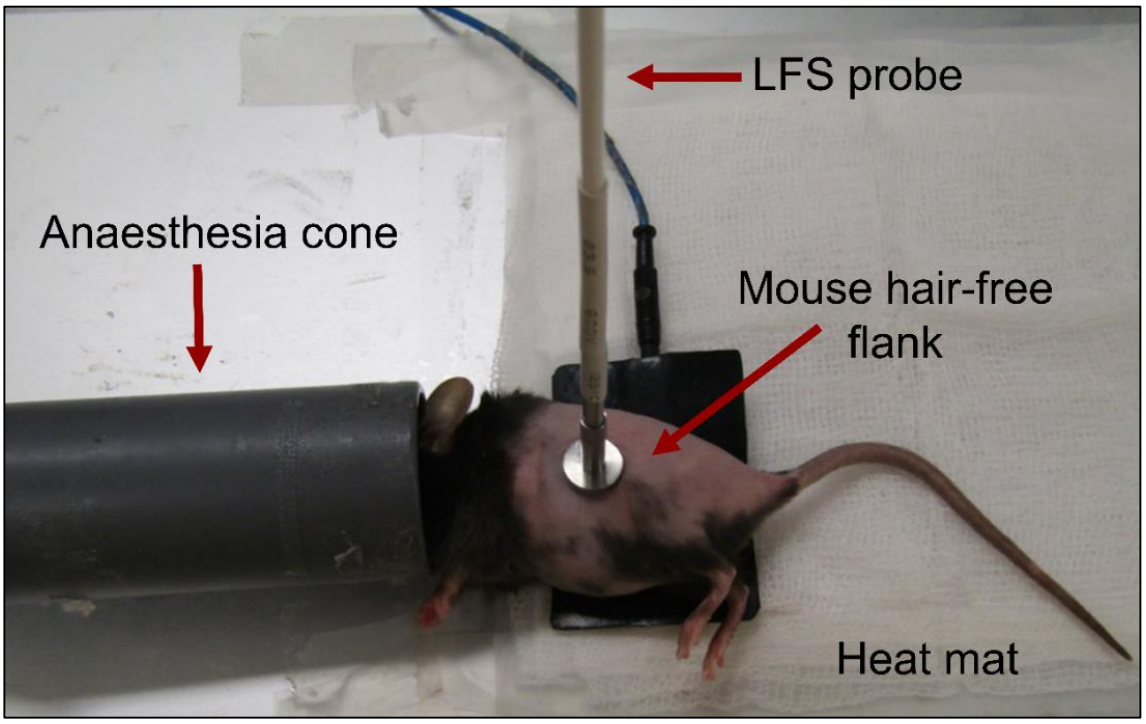

Fig. 35 Experimental setup to explore the potential use of LFS method for assessing cutaneous oxidative stress. The single-point probe was placed at direct contact with the skin in the flank of the mouse that was shaved 48 hours prior to performing the test. Multiple 10 s UV baseline spectra were collected over a 10 min time period (1 spectrum per min) by irradiation of the skin with the 365 nm LFS laser source. Mice were anaesthetised and laid in a heat mat at 37°C prior to performing the experiment. The anaesthesia was maintained during the experiment through an inhalation nose cone. Four mice were tested for each group repeating the experiment in duplicate (a total of 8 experiments for each group of mice).

Fig. 36 shows the comparison of the UV average baseline spectra between the three groups of examined mice. The results clearly outline a greater AF emission peak in Nrf2$^{-/-}$ KO animals compared to both WT and Sik KI anti-inflammatory phenotypes, which reflects the higher degree of oxidative stress in Nrf2$^{-/-}$ mice associated with accumulation of the reduced form of NAD(P)H. These preliminary findings confirmed the potential and reliability of LFS technique for evaluating cutaneous oxidative stress.

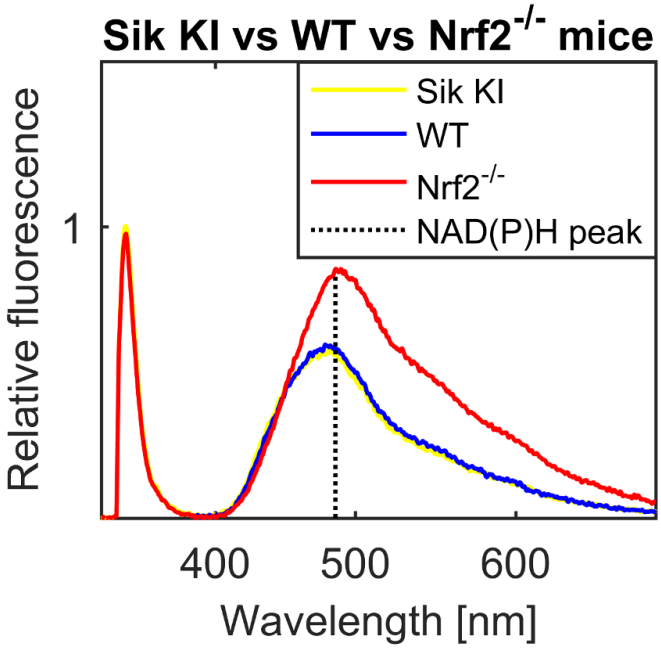

Fig. 36 Comparison of baseline AF between Sik KI, WT and Nrf2$^{-/-}$ mice. Mean baseline UV autofluorescence estimated for each group of mice by averaging the spectra obtained from duplicate experiments (n=4, n. of experiments = 8, n. of spectra collected for each experiment = 10). Data are expressed as a function of the backscattered light (dimensionless units). Yellow line = Sik KI mice. Blue line = WT mice. Red line = Nrf2$^{-/-}$ mice. The maximal emission peak was located at 490 nm, which should reflect mainly NAD(P)H contribution to the AF signal.

Spatial resolution of LFS measurements

A limitation of LFS method is the impossibility to determine the specific contribution to the AF signal coming from different cell types in the cutaneous tissue. The reason for this shortcoming is the uncertain spatial resolution of LFS recordings and the heterogeneous anatomy of the cutaneous tissue, which is made of multiple cell types that are part of the different skin layers and of the functional structures in the skin, i.e. micro-vessels. According to the literature, the 365 nm UV-A laser light might penetrate at a skin depth corresponding to the upper dermal layer in human subjects [149, 150]. Mouse skin structure includes an epidermal layer thinner than human epidermis [151], thus in this case the UV-A light might reach a tissue depth corresponding to the median dermal layer. As described in the section 1.4 (paragraph 1.4.2, page 26), the dermis contains functional microvascular structures (capillaries and arterioles). Therefore, a relevant part of the AF detected by LFS might take origin from the microcirculation that was the main tissue of interest in this study.

To get information on the spatial resolution of the 365 nm laser of the LFS device used in this study, the penetration depth of the *LAKK-M* UV laser source

was simulated in a 5 layer human skin model including various absorbers and scatterers in each stratum. This experiment was part of a collaborative work with a research group from the University of St. Andrews (Scotland), based on performing Monte Carlo simulations of LFS *LAKK-M* measurements for gathering information on the skin tissue depth from which the detected signal was originating. The simulation was performed by adopting the exact parameters related to the UV laser source and geometry of the *LAKK-M* probe: 365 nm source wavelength, 0.4 mm beam radius, 0.4 mm detector radius, 1 mm probe-detector center separation. The specific properties of the skin model used in the simulation are listed in Table 2.

Table 2 Parameters of the human skin model used to simulate the *LAKK-M* UV light propagation. The skin model used in the experiment was made of 5 layers: stratum corneum, epidermis, papillary dermis, reticular dermis and hypodermis. Various absorbers and scatterers at specific concentrations were distributed in each layer: water, blood (including both oxygenated and deoxygenated Hb fractions), melanin (including both eumelanin and pheomelanin), bilirubin, β-carotene, and a baseline absorber. Data were provided by Mr Lewis McMillan and Dr Kenneth Wood from the Astronomy group at the University of St. Andrews (Scotland).

Skin layer	Thickness	Absorbers
Stratum corneum	0.030 mm	5% water, baseline absorber
Epidermis	0.080 mm	20% water, 0.5% melanin, 2.1×10^{-4} g/L β-Carotene, baseline absorber
Papillary dermis	0.180 mm	50% water, 0.05 g/L bilirubin, 7×10^{-5} g/L β-Carotene, 6% blood, baseline absorber
Reticular dermis	1.800 mm	70% water, 0.05 g/L bilirubin, 7×10^{-5} g/L β-Carotene, 4.5% blood, baseline absorber
Hypodermis	2.900 mm	70% water, 7% blood, baseline absorber

The blood oxygenation level considered in the experiment was 75%, the skin type used was the Fitzpatrick skin type I, and the age of the modelled skin was ~30 years. The thickness of the tissue model described in Table 2 is similar to that of the skin at 1/3 length of the forearm. Indeed, as shown by my research group in a recent paper [152], the thickness of the superficial epidermal skin layer at 1/3 length of the forearm imaged by cmOCT technique was ~0-100 μm, followed by the epidermal-dermal junction (papillary dermis) at a depth of ~100-200 μm. Thus, considering that the human *LAKK-M* data in this thesis were collected from 1/3 of the forearm, the results of this Monte Carlo simulation can be used to discuss implications associated to the AF measurements performed in this study.

The results of the simulation are displayed in Fig. 37, showing a penetration depth of the 365 nm light around 0.2 mm (human dermal-epidermal junction), even though the graph suggests that ~99% of the photons are coming from a depth of 0.1 mm. Based on these observations, it can be stated that most of the AF signal measured by *LAKK-M* from the human forearm location is of epidermal origin with a partial smaller contribution of the papillary dermis region where the capillaries are located. Considering that mouse skin is characterised by a thinner epidermis than humans, it can be hypothesised a major contribution of the upper dermis to the AF signal in mouse models compared to humans.

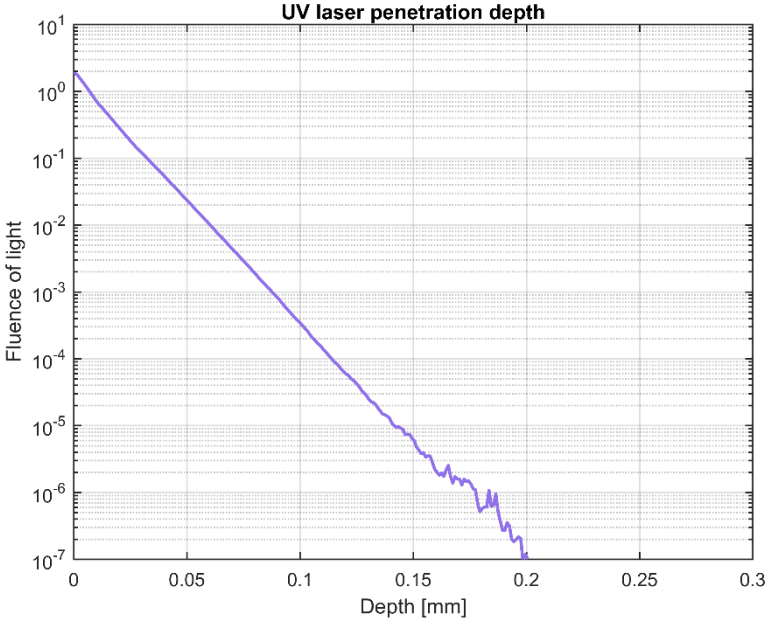

Fig. 37 UV laser penetration depth. Monte Carlo modelling of the *LAKK-M* 365 nm laser penetration depth. The result shows a penetration depth up to 0.2 mm with most of the light coming from a depth of 0.1 mm. Data were provided by Mr Lewis McMillan and Dr Kenneth Wood from the Astronomy group at the University of St. Andrews (Scotland).

2.3 Nonlinear dynamics analysis of LDF and LFS time series

2.3.1 Reconstruction of NAD(P)H and RR signals by spline interpolation

The LDF method is able to provide blood flow signals (Fig. 22) suitable for the study of nonlinear dynamics by application of the CWT spectral analysis. This is due to the fast sampling rate of perfusion values that in the case of the *LAKK-M* device are acquired at a sampling frequency of 20 Hz (one sample every 0.05 s). In contrast, LFS allows obtaining only single discrete AF spectra (Fig. 29). Thus, for the study of nonlinear cellular metabolic dynamics, NAD(P)H and RR signals were reconstructed from the discrete UV spectra collected over time in order to

obtain the same temporal sampling rate (one sample every 0.05 s) as the LDF data. The reconstruction was carried out by using the software Matlab R2015a (*The MathWorks Inc.*). The technique employed for the reconstruction was the piecewise cubic spline interpolation, a methodology that was also tested successfully by my research group for reconstructing continuous blood flow signals at a specific temporal sampling rate from discrete experimental data points [152, 153].

Piecewise cubic spline interpolation

The spline interpolation is a mathematical process employing a piecewise low-degree composite polynomial, defined spline, to approximate a continuous function *g* by interpolation of equally spaced discrete data points of *g* [153]. The main benefit of spline interpolation is the optimal accuracy in the approximation of *g* over wide ranges, reducing the occurrence of errors during the approximation process such as the generation of oscillatory artefacts (Runge's phenomenon) that can occur when using a single high-degree polynomial [153]. The spline interpolation addresses the shortcomings of the polynomial interpolation by subdividing the interval [a, b] where the function *g* is continuous in smaller sub-intervals, and approximating *g* in every sub-interval employing low-degree polynomial pieces that define a composite spline function *s* [153].

In this dissertation, a cubic spline *s* was employed that is optimal for the reconstruction of continuous natural processes, and requires four coefficients to define a piecewise polynomial between each pair of discrete data points, as shown by equation 23 [153],

$$p_3(x) = a_1x^3 + a_2x^2 + a_3x + a_4, \quad (23)$$

where p_3 is the piecewise cubic polynomial, and a_1, a_2, a_3 and a_4 are the four coefficients defining p_3. The curve obtained from the approximation process is composed of a number of pieces reconstructed between each pair of data points equal to *1-n*, where *n* is the number of data points [153].

In this work, the time series were reconstructed by using the *cftool* in Matlab. Specifically, discrete values of $NAD(P)H_{normalised}$ (equation 21) or RR_{index} (equation 22) extracted from sequential AF spectra measured over time were used for the reconstruction, applying an interval of 60 s between each pair of consecutive data points that corresponds to the sampling frequency used during the experiments for the temporal acquisition of the spectra (1 spectrum per min).

The 4 coefficients defining the piecewise cubic polynomial of each pair of discrete data points (equation 23) were extracted from the *cftool* and saved in the Matlab workspace for the subsequent estimation of the reconstructed curve by using the Matlab function *ppval*. Fig. 38 shows examples of $NAD(P)H_{normalised}$ and RR_{index} signals reconstructed by applying the procedure described above.

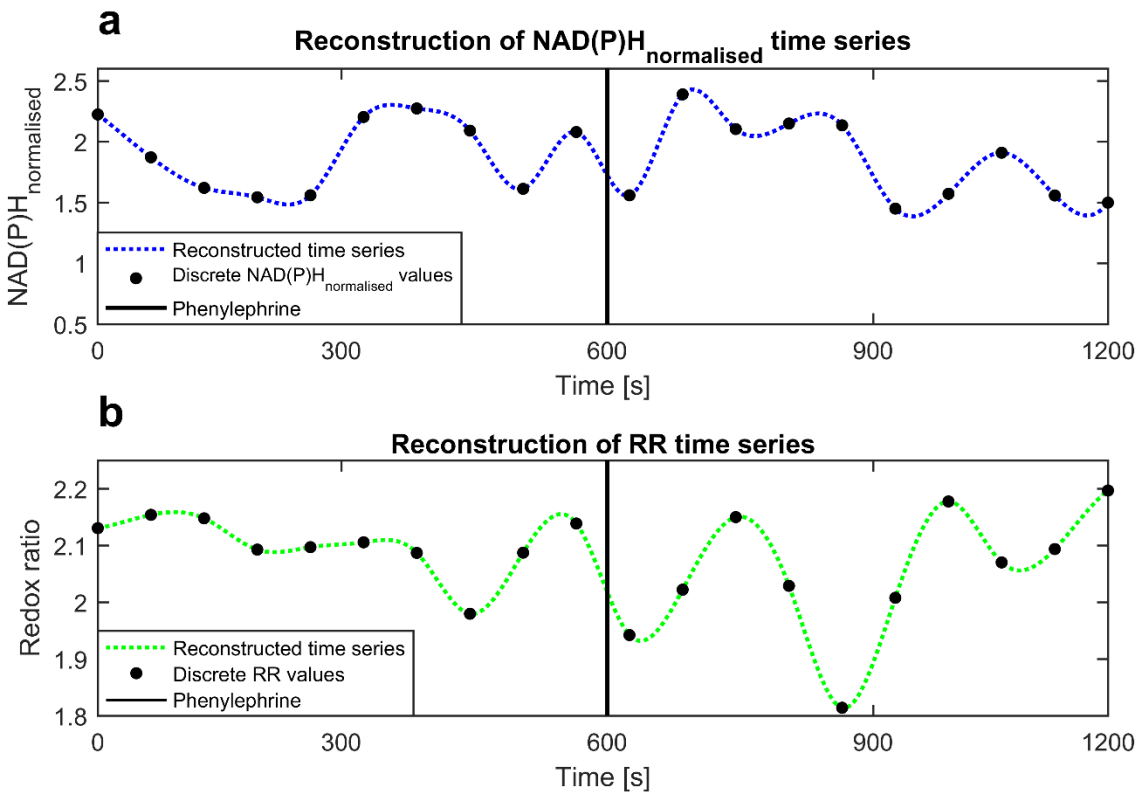

Fig. 38 Examples of signals reconstructed by spline interpolation. (**a**) 20 min NAD(P)H signal reconstructed from 20 sequential UV spectra (1 per min) collected from the flank of a mouse during iontophoresis of PE. The discrete data points represent dimensionless $NAD(P)H_{normalised}$ values estimated by correction of NAD(P)H AF peak by elastin AF (equation 21). The curve covers the time-window of 20 min used to sample the UV spectra. (**b**) 20 min RR signal reconstructed from 20 sequential UV spectra (1 per min) collected from the flank of a mouse during iontophoresis of PE. The discrete data points represent dimensionless RR values estimated by ratiometric correction of NAD(P)H AF peak by FAD^+ AF (equation 22). The curve covers the time window of 20 min used to sample the UV spectra. Considering that the *n* data points used for the reconstruction were 20, each curve in this graph is composed of 19 reconstructed pieces (*n-1*).

As discussed previously, the advantage of spline interpolation is that the approximation process does not generate oscillatory artefacts between each pair of data points [153]. Therefore, by applying this method it was ensured that the results of the subsequent CWT spectral analysis were representative of the real fluctuations of NAD(P)H and RR detected by discrete LFS AF measurements, without the effect of artefacts introduced during the reconstruction. Nonetheless,

a shortcoming of this technique is poor accuracy in the reconstruction of the right and left ends of the function [153] because of the presence of a single known discrete data point at each extremity. Thus, to prevent the generation of artefacts at the edges of the signal, the time series was broken off at the right and left extremities making sure that the beginning and ending points of the curve were corresponding respectively to the initial and final experimental discrete data points employed in the reconstruction process [153].

Finally, it should be noted that here the spline interpolation was not applied as a numerical analysis to fit a model but the technique was employed as a technical procedure for obtaining continuous time series, which is a mandatory condition to allow the application of the CWT spectral analysis [13]. However, a limitation of using reconstructed time series was the possibility to study only low-frequency dynamics, due to the slow sampling frequency of the discrete data points used for the reconstruction (1 spectrum per min).

2.3.2 Normalisation of NAD(P)H AF signal to remove artefacts and improve the evaluation of the temporal dynamics

As discussed in section 1.7 (paragraph 1.7.2, page 50), the UV autofluorescence measured from *in-vivo* skin is highly affected by physiological and biological factors in the cutaneous tissue such as natural absorbers of UV light, i.e. Hb in the blood of micro-vessels and skin pigmentation (melanin) [46, 85]. As a consequence, the evaluation of the temporal dynamic changes of NAD(P)H AF may be inaccurate and unreliable, especially due to the variability and artefacts of the signal associated with the temporal fluctuations of blood volume (BV).

Here, the effect of Hb on the dynamic changes of AF signal was tested by applying a multi-parameter approach. Specifically, simultaneous recordings of skin LFS signal and blood flow were performed in combination with the PORH reactive test to monitor how NAD(P)H AF emission is affected by massive changes of BV. Indeed, the PORH response is characterised by a substantial increase of blood flow and BV that is optimal to assess the effect of Hb UV light absorption on the AF signal. The effect of melanin was assessed by testing people with different coloured skin. As shown in Fig. 39, the study was designed by enrolling a total of 16 subjects (8 with white skin and 8 with dark skin), which signed an informed consent form before being tested. All the subjects were first examined as single group, to assess the effect of BV on the AF signal. Finally,

the subjects were divided in two groups with different coloured skin (8 subjects with white skin and 8 with dark skin), to compare data with the purpose of evaluating the effect of melanin on the AF signal. Fig. 40 shows the experimental setup used to collect simultaneous LFS and LDF recordings. The test was divided in three steps: baseline (10 min), occlusion of flow through the brachial artery (5 min), monitoring PORH response after stopping the occlusion (10 min).

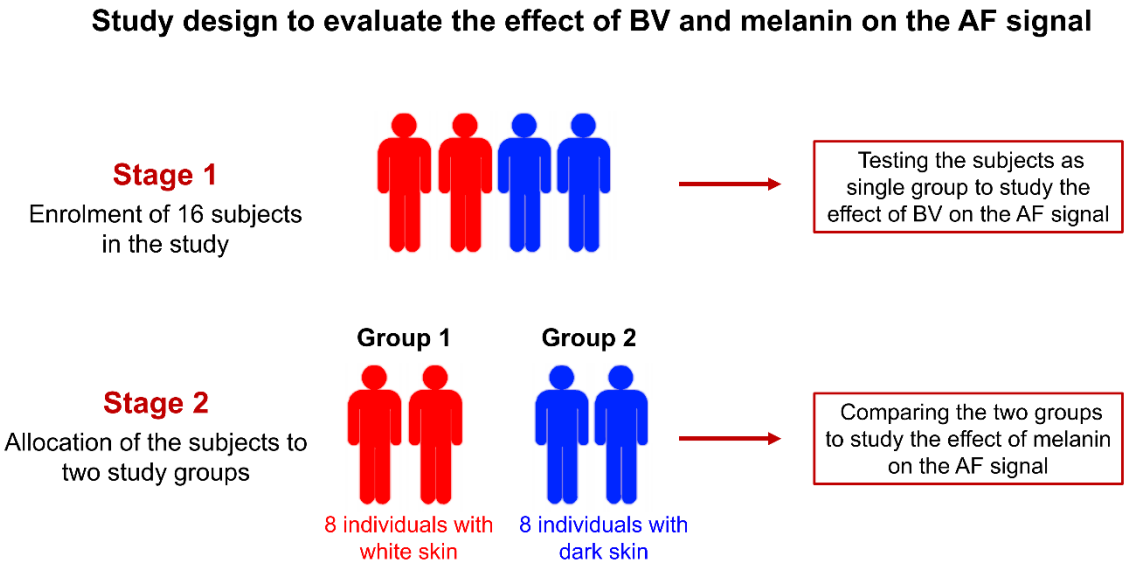

Fig. 39 Study design to assess BV and melanin effect on the AF signal. 16 healthy individuals (8 with white skin and 8 with dark skin) were enrolled in the study by signing an informed consent form. The subjects were initially tested as single group by collecting simultaneous LFS and LDF data during a 25-min PORH test to assess the effect of BV on the AF signal. Finally, the subjects were allocated in two different groups (white vs dark skin) to compare data with the aim of evaluating the effect of melanin on the AF signal.

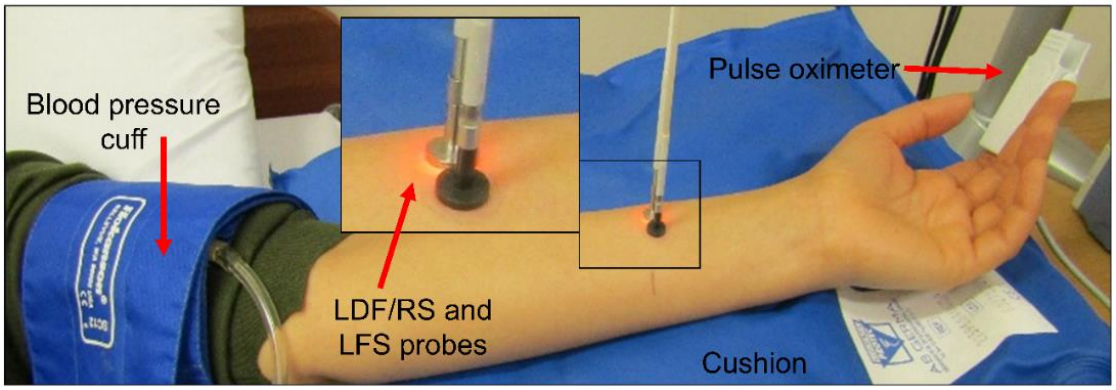

Fig. 40 Experimental setup for multi-parameter data collection in human subjects. LDF and LFS probes were placed gently in two adjacent locations at 1/3 length of the left forearm by using double adhesive tape. A pressure cuff was placed in the upper part of the arm to occlude blood flow through the brachial artery during PORH test by inflating the cuff at 200 mmHg. Subjects were tested in a room with controlled temperature while resting in a clinical bed. The arm was laid in a cushion to ensure a comfortable position and avoid movement artefacts.

Fig. 41a-b display the effect of BV changes on NAD(P)H AF signal during PORH test. The AF data clearly outline a reduction of NAD(P)H signal concurrent to the increase of BV shown in the LDF data during PORH response. This is attributed to the absorption of UV light by Hb that leads to artefacts on the NAD(P)H signal that make the evaluation of the temporal dynamics unreliable.

Fig. 42a-b display the effect of melanin on NAD(P)H AF signal during PORH test. The simultaneous LDF and AF traces clearly outline that while the colour of skin does not impact LDF signal, the intensity of NAD(P)H signal is reduced in subjects with dark skin because of the major amount of melanin absorbing UV light. However, while the reduction of the AF signal intensity may be a major problem for the absolute quantification of skin NAD(P)H concentrations, this does not seem an issue for evaluating the relative temporal dynamics of the fluorophore. Indeed, considering the constant amount of melanin present in the cutaneous tissue for the entire duration of the experiment, the degree of UV light absorbed by melanin is constant throughout the measurement allowing the detection of temporal fluctuations of the signal due to the biological turnover of the coenzyme. Therefore, as visible in Fig. 42a-b, also in this case the changes in blood volume seem to be the major factor leading to the introduction of artefacts in the temporal trace of NAD(P)H signal due to the continuous physiological fluctuations of BV.

Ratiometric approach for normalising NAD(P)H autofluorescence signal

The observations discussed above raised the need for implementing a normalisation method to correct NAD(P)H AF data with the purpose of reducing BV artefacts and obtaining acceptable time series reflecting the biological temporal dynamics of NAD(P)H more reliably. The method chosen for this purpose was the ratiometric correction, which has been previously employed for removing artefacts on NAD(P)H AF signal. The method consists in the 1:1 ratio between NAD(P)H AF and another variable affected by the same environmental artefacts, i.e. skin reflectance [85], to compensate for factors unrelated to NAD(P)H and obtain a dimensionless signal reflecting the dynamics of the fluorophore with more confidence. In this work, it has been taken advantage of the overlapping contributions in the UV spectrum of elastin (450 nm) and FAD^+ (550 nm) AF to perform a 1:1 ratiometric correction of NAD(P)H AF, as already described in equations 21-22 (section 2.2, paragraph 2.2.4, page 84).

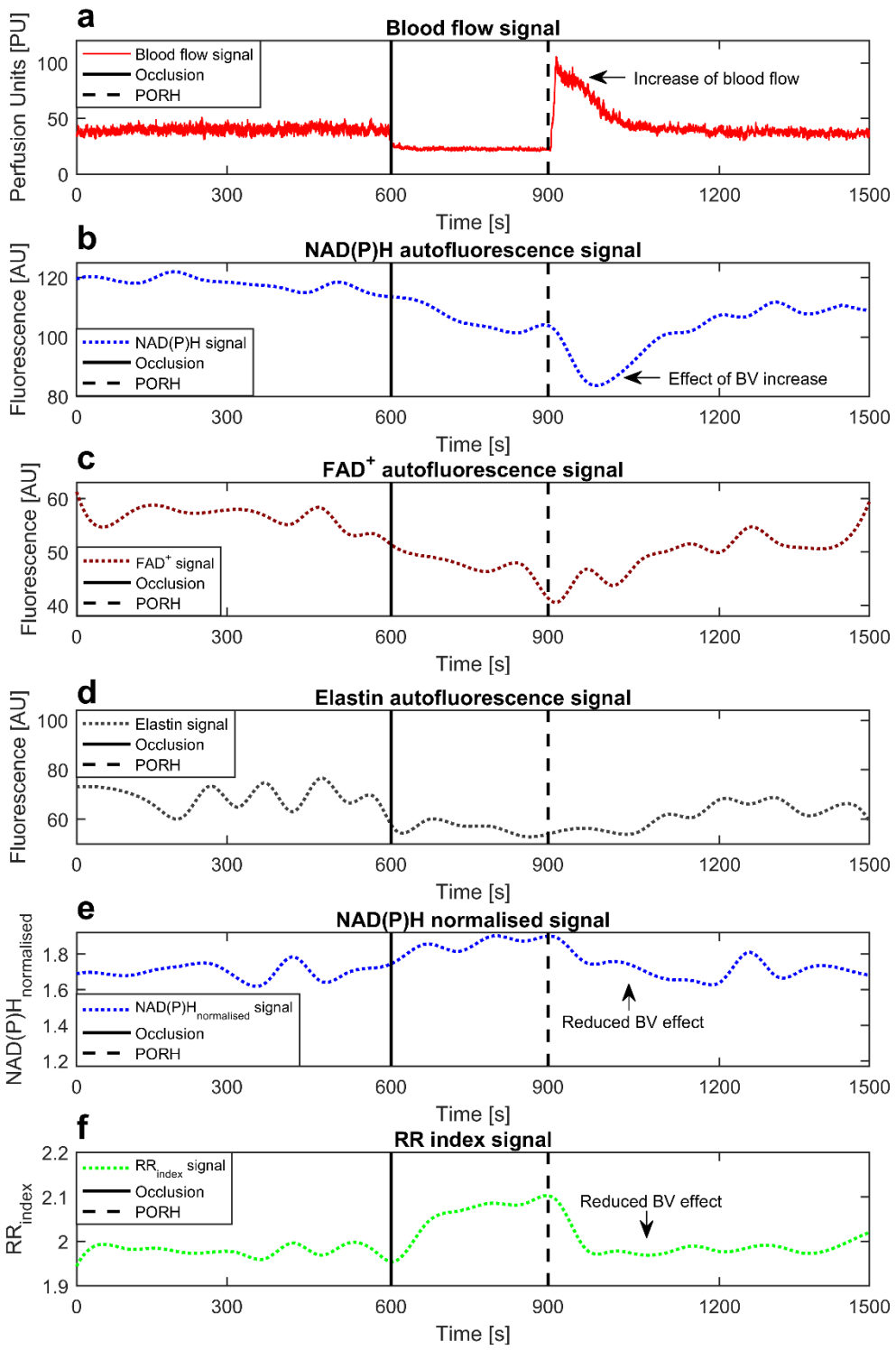

Fig. 41 Evaluation and correction of BV effects on NAD(P)H AF. Median (**a**) LDF signal and (**b**) NAD(P)H, (**c**) FAD^+ and (**d**) elastin reconstructed AF time series from the forearm of 16 subjects during a 25-min PORH test. Data are expressed in arbitrary units. A clear reduction in the intensity of NAD(P)H AF signal is visible during PORH response, associated with the increase of BV and absorption of UV light by Hb. (**e**) 1:1 ratiometric correction of NAD(P)H AF by elastin AF (dimensionless $NAD(P)H_{normalised}$, equation 21). (**f**) 1:1 ratiometric correction of NAD(P)H AF by FAD^+ AF (dimensionless RR_{index}, equation 22). The corrected signals were characterised by minimal effect of BV and temporal traces showing the expected trends for NAD(P)H and RR dynamics during PORH stimulation.

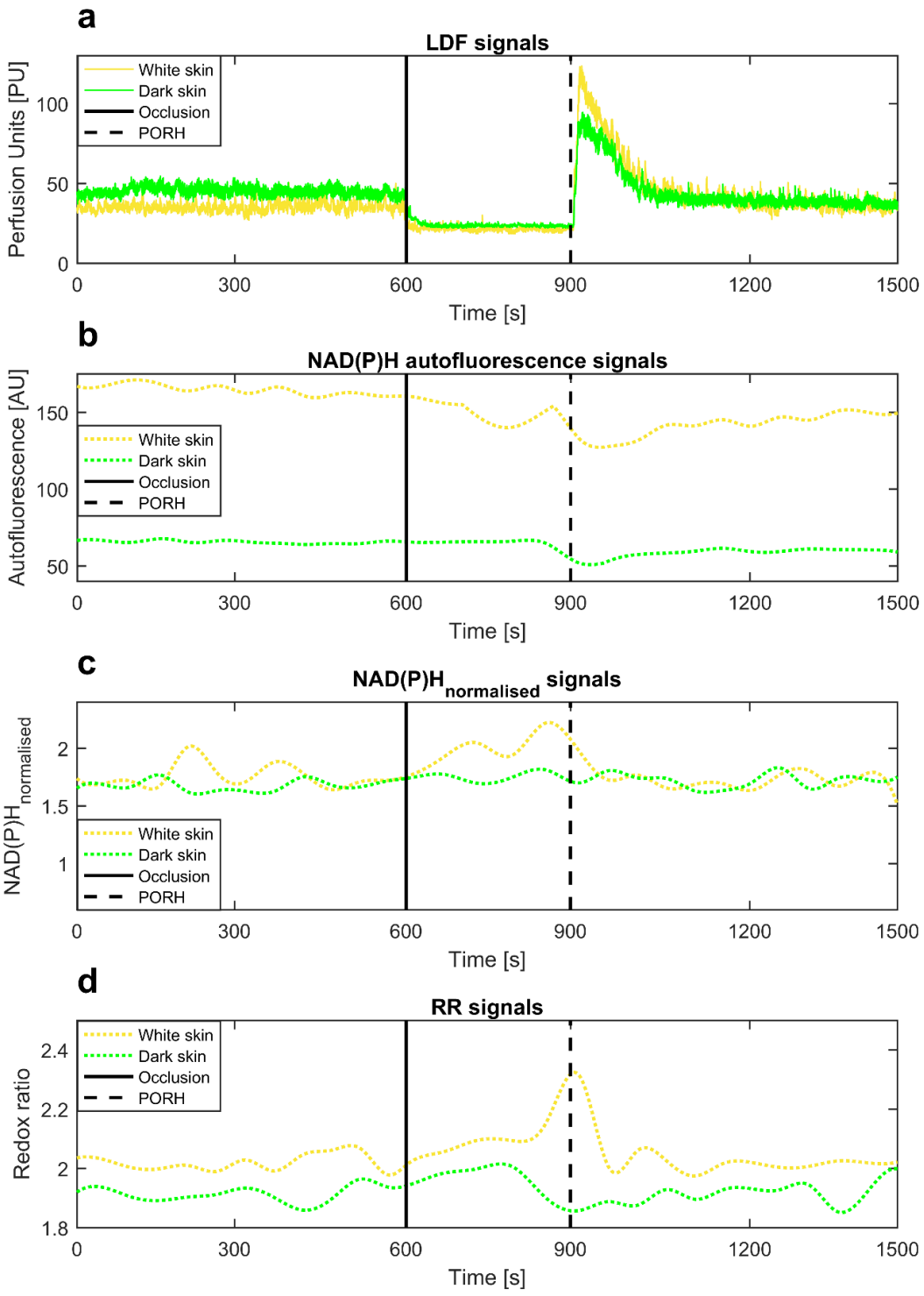

Fig. 42 Effects of melanin on NAD(P)H AF. Median (**a**) LDF and (**b**) reconstructed NAD(P)H AF signals from the forearm of 8 subjects with white skin (orange lines) and 8 subjects with dark skin (green lines) during a 25 min PORH test. Data are expressed in arbitrary units. LDF signal was not affected by skin melanin content, while the intensity of NAD(P)H signal was highly reduced in subjects with dark high-pigmented skin. (**c**) 1:1 ratiometric correction of NAD(P)H AF by elastin AF (dimensionless $NAD(P)H_{normalised}$, equation 21). (**d**) 1:1 ratiometric correction of NAD(P)H AF by FAD^+ AF (dimensionless RR_{index}, equation 22). The corrected signals displayed reduced BV effect and temporal traces comparable between subjects with different coloured skin.

Ratiometric correction of NAD(P)H AF signal by elastin autofluorescence

The reason for choosing the autofluorescence of elastin as correction factor is the structural nature of this protein, which is abundant in the dermal layer of the skin [46, 87]. The structural components of the cutaneous tissue are supposed to remain unchanged during the temporal period while NAD(P)H AF is measured. Thus, the correction of NAD(P)H autofluorescence peak by elastin AF represents an intra-subject compensation for environmental factors unrelated to NAD(P)H, i.e. absorption of UV light by Hb, and the corrected signal should reflect NAD(P)H temporal dynamics because of the unchanged amount of cutaneous elastin during the short time period of 25 min employed to perform the experiment. The AF emission of elastin after stimulation with UV light is between 400-450 nm, a spectral region that may contain also the overlapping contribution of collagen AF (emission between 390-460 nm) [46, 87]. However, collagen is also a structural protein abundant in the cutaneous tissue that should remain unchanged during the temporal collection of LFS UV spectra. Fig. 41e displays the dynamics of NAD(P)H AF signal during PORH test after 1:1 ratiometric correction by elastin AF. A reduction of BV effect compared to Fig. 41b is clearly shown, and the dynamics of the normalised signal seems to reflect more reliably the biological turnover of NAD(P)H during PORH test. Indeed, an increase of $NAD(P)H_{normalised}$ signal was observed during occlusion of blood flow, which can reflect the inhibition of ATP energy production through the oxidative phosphorylation because of reduced tissue oxygenation, uncoupling of the electron transport chain and accumulation of NAD(P)H [85]. In contrast, the moderate decrease of normalised NAD(P)H signal during PORH in this case may indicate the oxidation of NAD(P)H to $NAD(P)^+$ and reactivation of the aerobic production of ATP [85], rather than an artefact due to blood volume changes. The same results are shown in Fig. 42c, displaying that $NAD(P)H_{normalised}$ signal is characterised by reduced blood volume effect and is comparable between subjects with different coloured skin for the purpose of assessing the temporal oscillatory behaviour of NAD(P)H.

Ratiometric correction of NAD(P)H AF signal by FAD^+ autofluorescence

The estimation of the RR_{index} as the 1:1 ratio between NAD(P)H and FAD^+ AF emissions has been used in the past as correction method for both minimising the interfering effect of Hb and BV on the AF signal and providing specific information on the energetic metabolic dynamics of mitochondria [154]. Indeed,

RR_{index} is able to reflect specifically the activity of the mitochondrial electron transport chain and the degree of ATP energy production through the OXPHOS process [12, 85], thanks to the opposite response of reduced NAD(P)H and oxidised FAD^+ to changes in mitochondrial metabolic states [154]. However, care must be taken when interpreting RR_{index} data that may be variable depending on several factors in the environment of the biological system under investigation: kind of stimulus affecting the mitochondrial metabolism, absence or presence of oxygen, absence or presence of a specific disease. Moreover, because the efficiency in the detection of FAD^+ AF is much lower than NAD(P)H AF, the RR_{index} cannot be taken as value for performing absolute comparisons, unless the efficiency of FAD^+ autofluorescence detection is optimised relative to that of NAD(P)H autofluorescence. Therefore, evaluating the relative changes of RR_{index} over time concurrently to the assessment of other parameters (i.e. NAD(P)H, blood flow, etc.) may be more advantageous to gain reliable information on mitochondrial function. Fig. 41f displays the temporal dynamics of RR_{index} during PORH test. The signal seems to reflect reliably the mitochondrial metabolic dynamics associated with a temporary period of low oxygen intake and the hyperaemic response, with minimised effect of BV compared to Fig. 41b. A substantial growth of RR_{index} was observed during occlusion of blood flow, probably indicating a preferential biosynthesis of ATP energy through the glycolysis process due to low oxygen intake, accumulation of mitochondrial NAD(P)H and uncoupling of the electron transport chain. The baseline RR_{index} dynamics were restored during PORH, probably indicating the re-oxygenation of the tissue and the preferential production of ATP through the mitochondrial OXPHOS. Fig. 42d displays the comparison of the temporal dynamics of RR_{index} between subjects with dark and white skin during PORH test. Although the intensity of RR_{index} signal was slightly lower in individuals with dark skin, the signals seem to be comparable for the purpose of evaluating the temporal oscillatory dynamics of RR_{index} that was the main task of this research.

Based on the results discussed above, it can be concluded that the simultaneous assessment of LDF and LFS signals was an optimal approach allowing the characterisation of the effect of some factors unrelated to NAD(P)H (Hb and melanin) on the cutaneous autofluorescence signal. The artefacts associated to fluctuations in blood volume were minimised by performing a 1:1 ratiometric

correction of the autofluorescence signal, which provided acceptable results for a reliable assessment of the temporal dynamics of NAD(P)H and mitochondrial function allowing a reasonable explanation of the physiological processes reflected by LFS measurements. Therefore, this correction method was used in the final protocols implemented in this study for the characterisation and examination of the nonlinear oscillations of cellular energetic metabolism.

However, despite the ratiometric normalisation provided acceptable results for the purpose of assessing temporal oscillations of the autofluorescence signal, the implementation of more accurate normalisation methods is still challenging for the future. A promising approach might be the Monte Carlo modelling of skin LFS recordings to study the propagation of the UV light in the skin and its interaction with the different components of the cutaneous tissue, exploring possible novel correction techniques based on the findings from Monte Carlo investigations.

2.3.3 Implementation of continuous wavelet transform (CWT) analysis

In this work, the CWT method was employed to study the nonlinear dynamics of both LDF and $NAD(P)H_{normalised}$ or RR_{index} signals. Literature reports have already described applications of the CWT for processing the LDF cutaneous signal [60, 102, 103, 105, 106, 107], to monitor oscillatory vasomotor perturbations of the signal associated with the physiological activity of biological factors in the microcirculation (e.g. endothelial cells, vascular smooth muscle cells, sympathetic nerves). In contrast, the CWT method has never been used to process the *in-vivo* cutaneous NAD(P)H signal either in animal models or humans. Therefore, a novelty of the research work presented in this thesis is the first attempt to apply the CWT on $NAD(P)H_{normalised}$ or RR_{index} *in-vivo* cutaneous signals from mouse models and human individuals with the purpose of studying metabolic oscillations associated with the cyclic cellular redox reactions and energy metabolism.

Here, the CWT technique was implemented through Matlab R2015a (*The MathWorks Inc.*) software by using the principles (equations 4-12) that have been discussed in details in the section 1.8 (paragraph 1.8.2, page 54). Fig. 43 and Fig. 44 display examples of CWT time-frequency domain graphs and corresponding time-averaged spectra obtained from LDF and $NAD(P)H_{normalised}$ signals, respectively in mice and humans. A wavelet central frequency of 1 was used. The relative spectral energy e_i and amplitude a_i were extracted according

to the equations 9-12, to evaluate the contribution of each LDF or metabolic oscillator during specific microvascular tasks, e.g. iontophoresis or PORH and to compare data between different groups of mice or human subjects. The CWT of LDF signals showed results in agreement with the components reported in literature (Fig. 17). Similar oscillatory frequency intervals related to tissue and cells activity were found between mice and humans (Fig. 43 and Fig. 44):

- Myogenic oscillator, 50-150 × 10^{-3} Hz in mice, 52-145 × 10^{-3} Hz in humans.
- Neurogenic oscillator, 20-50 × 10^{-3} Hz in mice, 21-52 × 10^{-3} Hz in humans.
- Endothelial NO oscillator, 9-20 × 10^{-3} Hz in mice, 9.5-21 × 10^{-3} Hz in humans.
- Endothelial NO-independent oscillator, 5-9 × 10^{-3} Hz in mice, 5-9.5 × 10^{-3} Hz in humans. As discussed in the section 1.8 (paragraph 1.8.3, page 58), the physiological origin of this oscillator is unclear [102, 105]. However, the results from this dissertation support indirectly an association of this component with the EDHF endothelial pathway. For this reason, here this oscillator has been named as “Endothelial EDHF”. Details about this hypothesis are discussed in sections 3.3 (paragraph 3.3.1, page 132) and 4.4 (paragraph 4.4.2, page 177).

The cardiac and respiratory oscillators were characterised by higher frequency ranges in mice compared to human individuals, which is in agreement with faster heart and breath rates reported in literature for mice [155, 156]:

- Cardiac oscillator, 1350-5000 × 10^{-3} Hz in mice, 600-2000 × 10^{-3} Hz in humans.
- Respiratory oscillator, 150-1350 × 10^{-3} Hz in mice, 145-600 × 10^{-3} Hz in humans.

One of the goals of this work was the detection and study of metabolic oscillations *in-vivo*. This task was achieved by applying the CWT signal processing method on skin $NAD(P)H_{normalised}$ and RR_{index} reconstructed time series. As visible in Fig. 43b and Fig. 44b, the time-frequency domain graph of NAD(P)H time series was characterised by high wavelet energy in the slow frequency intervals, thus low-frequency fluctuations dominate the reconstructed trace. Despite the time resolution is poor in the low-frequencies, three distinct ranges of heterogeneous metabolic oscillations were clearly identified in both mice and humans. These components were defined as metabolic oscillator-1 (MO-1) (5-9.5 × 10^{-3} Hz), MO-2 (2.5-5 × 10^{-3} Hz), and MO-3 (1.5-2.5 × 10^{-3} Hz) (Fig. 43b and Fig. 44b).

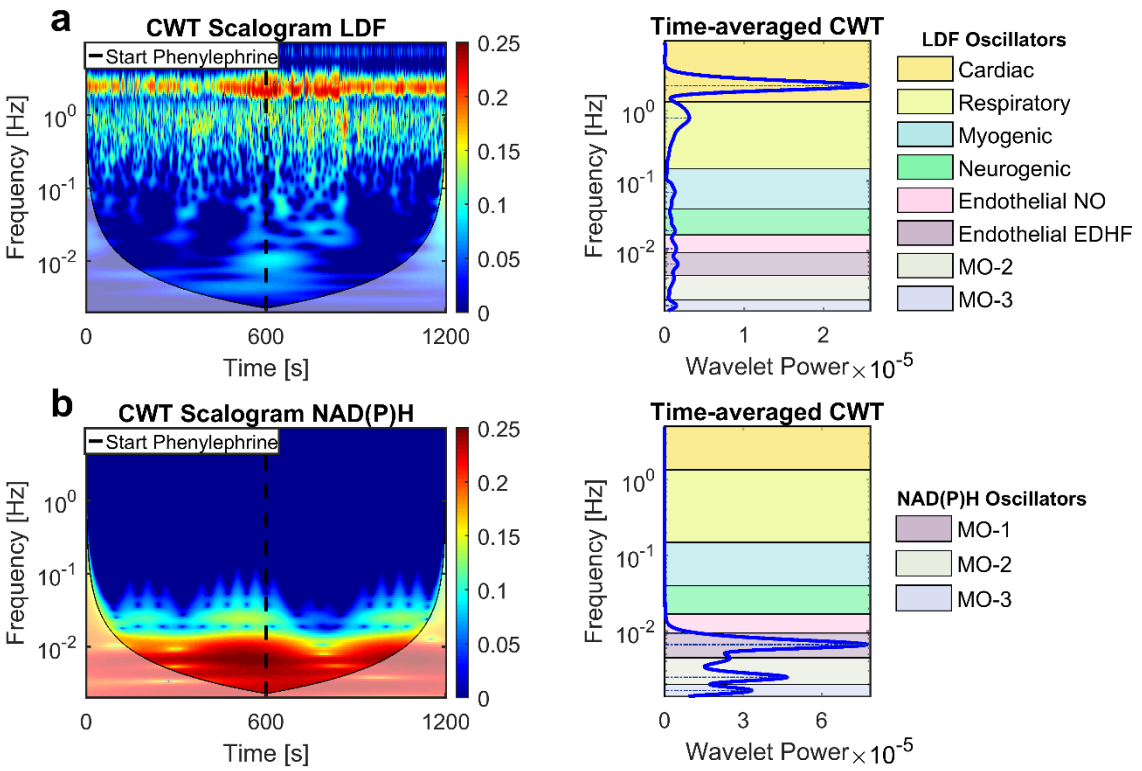

Fig. 43 CWT analysis of simultaneous LDF and NAD(P)H signals in mice. Data were collected for 20 min from the flank of a mouse while challenging micro-vessels by iontophoresis delivery of the vasoconstrictor drug PE (10 min). (**a**) Example of time-frequency domain scalogram and corresponding time-averaged CWT spectrum from LDF signal. The scalogram describes how the CWT power (energy, AU) is distributed in the time-frequency domain by using a gradient coloured map. The dark blue colour corresponds to low energy and the dark red to high energy. The graph shows a high power continuous band in the cardiac frequency range, confirming that data were collected correctly. Physiologically, the wavelet energy represents a measure of how much an oscillator defined by a frequency range contributes to blood flow signal at a specific time. The two transparent areas in the corners at the bottom of the graph represent sites outside of the "cone of influence" where data might not be reliable (frequencies < 5×10^{-3} Hz). The cone of influence is a "safe" time-frequency area where distortions of the CWT due to the finite time duration of the measured signal are irrelevant [157]. In contrast, the areas outside of the cone are close to the time limits of the signal, where the CWT suffers of boundary effects making the calculations from this time-frequency area inaccurate [157]. The time-averaged plot (right) allows to distinguish the wavelet amplitude peaks and energy (AUC of the peaks) of the specific physiological oscillators. The typical oscillators reported in literature were found: (I) cardiac, (II) respiratory, (III) myogenic, (IV) neurogenic, (V) endothelial NO-dependent, (VI) endothelial NO-independent (EDHF). Comparing the wavelet components of different LDF signals is powerful to distinguish healthy and diseased vascular conditions by quantifying the contribution of specific microvascular components. (**b**) Example of time-frequency domain scalogram and corresponding time-averaged CWT spectrum from NAD(P)H signal. Three low-frequency murine skin metabolic oscillators were characterised, which may reflect specific patterns of cellular ATP energy production that may vary depending on the health status of the tissue: Metabolic oscillator-1 (MO-1), MO-2 and MO-3.

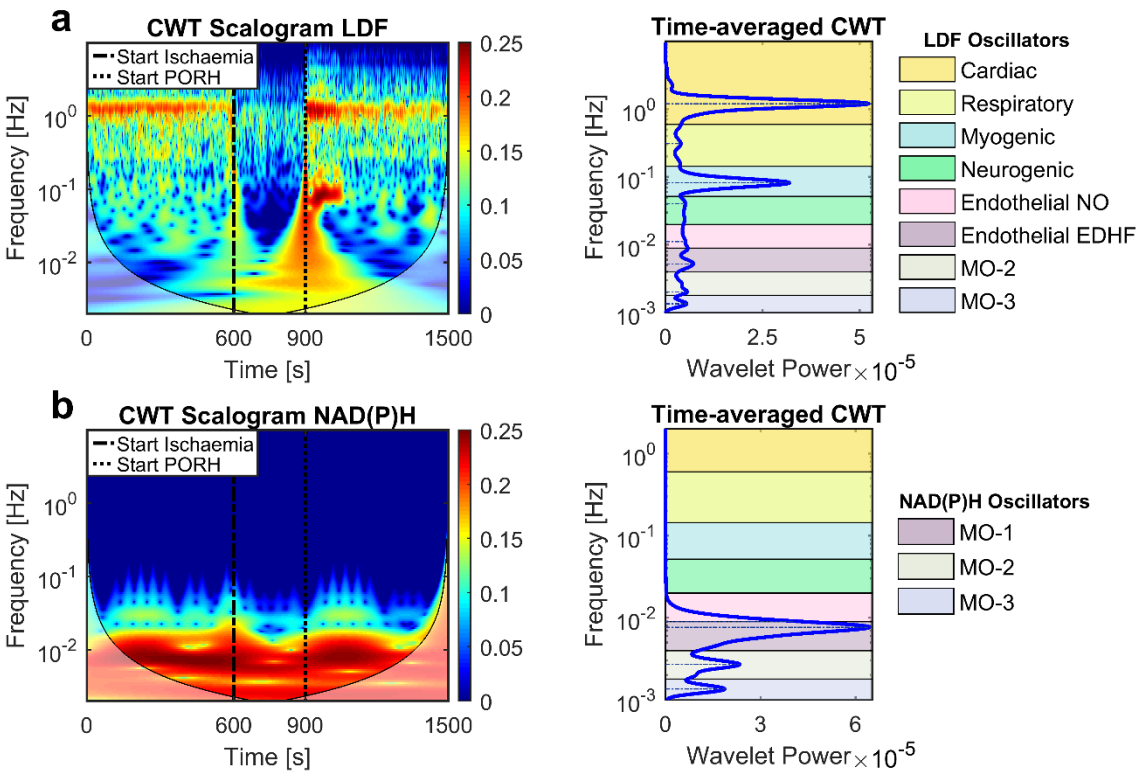

Fig. 44 CWT spectral analysis of simultaneous LDF and NAD(P)H signals in humans. Data were measured for 25 min from the human forearm during PORH test. (**a**) Time-frequency domain scalogram (left) and corresponding time-averaged CWT chart (right) from LDF signal. (**b**) CWT time-frequency domain scalogram and corresponding time-averaged spectrum from NAD(P)H reconstructed time series. The LDF scalogram displays a high-power band in the cardiac frequency range at baseline and during PORH, suggesting that data were collected correctly. Also in this case the typical LDF oscillators reported in literature were identified: (I) cardiac, (II) respiratory, (III) myogenic, (IV) neurogenic, (V) endothelial NO-dependent, (VI) endothelial NO-independent (EDHF). Moreover, three dominant human skin metabolic low-frequency oscillations contributing to NAD(P)H and RR signals were characterised for the first time, which may reflect specific dynamics of cellular ATP energy production that may be variable depending on the health status of the tissue: MO-1, MO-2, MO-3.

Although the CWT analysis allowed the detection of three distinct slow metabolic oscillators, only the study of the spectral wavelet peaks of the MO-1 is reported in this dissertation. The reason for this is that MO-2 and MO-3 frequency intervals fall in the time-frequency domain area outside of the cone of influence, where data might not be reliable (see Fig. 43 caption for more details on the cone of influence). Another metabolic oscillatory wavelet peak was also found in the frequency range 9.5-21 × 10^{-3} Hz which appears during PORH response in human subjects. This oscillatory component was simply defined as metabolic oscillator (MO). This is the first application of the CWT to characterise heterogeneous metabolic oscillations from live skin tissue.

Application of CWT analysis on signals reconstructed from simulated noise

An important aspect to consider when performing the CWT analysis is that the low-frequency regions of the CWT spectrum are characterised by the presence of a relevant background noise [118]. In this thesis, the characterisation of metabolic oscillations was performed especially from low-frequency regions of the CWT spectra of $NAD(P)H_{normalised}$ and RR_{index} signals. Therefore, an important aspect to address was verifying if the reconstructed metabolic signals represent a reliable measure containing some biological information or if they are composed exclusively by noisy artefacts resulting from the post-processing procedures applied on the raw autofluorescence data.

To verify if the $NAD(P)H_{normalised}$ and RR_{index} reconstructed signals were containing only noise or a combination of noise and biological information, a small simulation was run to show how the CWT analysis performs when raw data consist of simulated noise alone and to test the cross-correlation (CC) between signals reconstructed from the experimental data and signals reconstructed from simulated noise. The simulation was performed according to the following steps:

1. Representative $NAD(P)H_{normalised}$ and RR_{index} experimental data collected during a 25 min PORH test (each dataset made of 25 discrete temporal data points, one value per minute) were taken from 4 human subjects. For each dataset the mean and the standard deviation (SD) were measured over the experimental time series.
2. 4 data series (each of 25 points) were simulated by Matlab R2015a (*The MathWorks Inc.*) using Gaussian noise with the same mean and SD measured from the representative experimental data mentioned in the bullet point above. The noise was simulated according to the following formula,

   $$Simulated\ noise = [SD \times randn(n)] + Mean, \quad (24)$$

   where *SD* and *mean* are respectively the standard deviation and the mean of the experimental time series, *n* is the number of data points (25 in this case), and *randn* is the Matlab function to generate a random Gaussian distribution with *n* data points.
3. The cubic spline interpolation fitting described in paragraph 2.3.1 (page 96) was performed on both experimental and simulated data to reconstruct signals of $NAD(P)H_{normalised}$, RR_{index} and their respective simulated noise.

4. The spline-fitted data were passed into a cross-correlation analysis to evaluate what value is returned between pairs of simulated time series [$NAD(P)H_{normalised}$ versus its respective simulated noise, and RR_{index} versus its respective simulated noise] (Table 3). The cross-correlation analysis was performed using the Matlab function *crosscorr*.
5. The spline-fitted data were passed into the CWT analysis described at page 106, to assess how much the CWT spectrum varies over 4 repeats for $NAD(P)H_{normalised}$, RR_{index} and their respective noise, and to verify if the signals change differently in response to a biological stimulus (Fig. 45 and Fig. 46).

Table 3 reports the results concerning the cross-correlation analysis between signals reconstructed from the experimental data points and signals reconstructed from simulated noise. The analysis revealed very low cross-correlation values between $NAD(P)H_{normalised}$ or RR_{index} spline-fitted time series and their respective simulated noise. This is a good indication that the signals reconstructed by spline interpolation from the experimental data points are not made exclusively by noise but may still contain the biological information derived from the raw autofluorescence measurements.

Table 3 Cross-correlation analysis between metabolic and simulated noise signals. The cross-correlation analysis was performed between spline-fitted reconstructed time series obtained from 4 experimental datasets of $NAD(P)H_{normalised}$ (n=25) or RR_{index} (n=25) values acquired during a PORH test and 4 datasets of simulated Gaussian noise (n=25) generated using the same mean and SD of the experimental datasets. The cross-correlation analysis was run using the Matlab function *crosscorr*. CC = Cross-correlation. n = number of data points of each dataset used for the reconstruction of the signals by spline interpolation. -0.4 < CC values < 0.4 were considered as indicating low/absence of cross-correlation.

Simulation for $NAD(P)H_{normalised}$ data	**Mean**	**SD**	**CC value (experimental vs simulated noise spline-fitted data)**	**CC bounds**
Signal 1 (dimensionless)	1.798	0.141	-0.0810	± 0.011
Signal 2 (dimensionless)	1.923	0.329	-0.1580	± 0.011
Signal 3 (dimensionless)	1.795	0.105	-0.0330	± 0.011
Signal 4 (dimensionless)	1.725	0.097	0.1770	± 0.012
Mean signal over 4 repeats	1.810	0.168	-0.0238	± 0.011
Simulation for RR_{index} data	**Mean**	**SD**	**CC value (experimental vs simulated noise spline-fitted data)**	**CC bounds**
Signal 1 (dimensionless)	2.005	0.121	0.1630	± 0.012
Signal 2 (dimensionless)	2.043	0.114	0.0300	± 0.011
Signal 3 (dimensionless)	1.708	0.054	-0.0460	± 0.011
Signal 4 (dimensionless)	1.799	0.075	-0.1490	± 0.011
Mean signal over 4 repeats	1.888	0.091	-0.0005	± 0.011

Fig. 45 and Fig. 46 show respectively the comparison of wavelet analysis between NAD(P)H$_{normalised}$ or RR$_{index}$ time series and their respective simulated noise signals during all the stages of the PORH functional test: baseline (Fig. 45-46a), ischaemia (Fig. 45-46b) and post-occlusion (Fig. 45-46c).

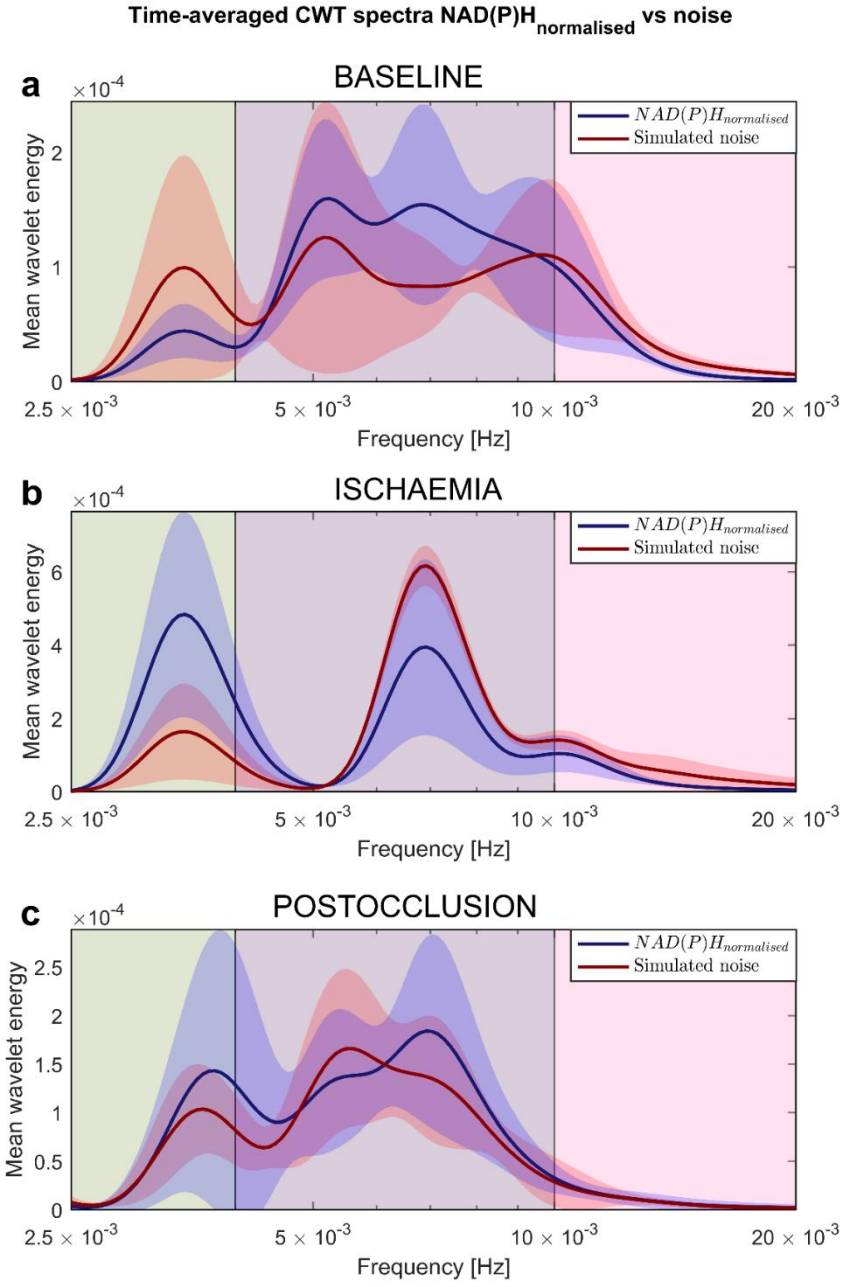

Fig. 45 Comparison of CWT spectra between NAD(P)H$_{normalised}$ signal and its respective simulated noise signal. Average spectra obtained from the CWT analysis of 4 NAD(P)H$_{normalised}$ signals (blue line) reconstructed by spline interpolation of raw autofluorescence data generated during a PORH functional test, and CWT analysis of 4 simulated noise signals (red line) generated using the same standard deviation and mean values of the raw autofluorescence data. (**a**) Baseline CWT spectra. (**b**) CWT spectra during occlusion of blood flow. (**c**) CWT spectra during PORH response. The shaded blue and red areas around the lines of the average spectra represent the range of variability (standard deviation over 4 repeats) of the CWT spectra.

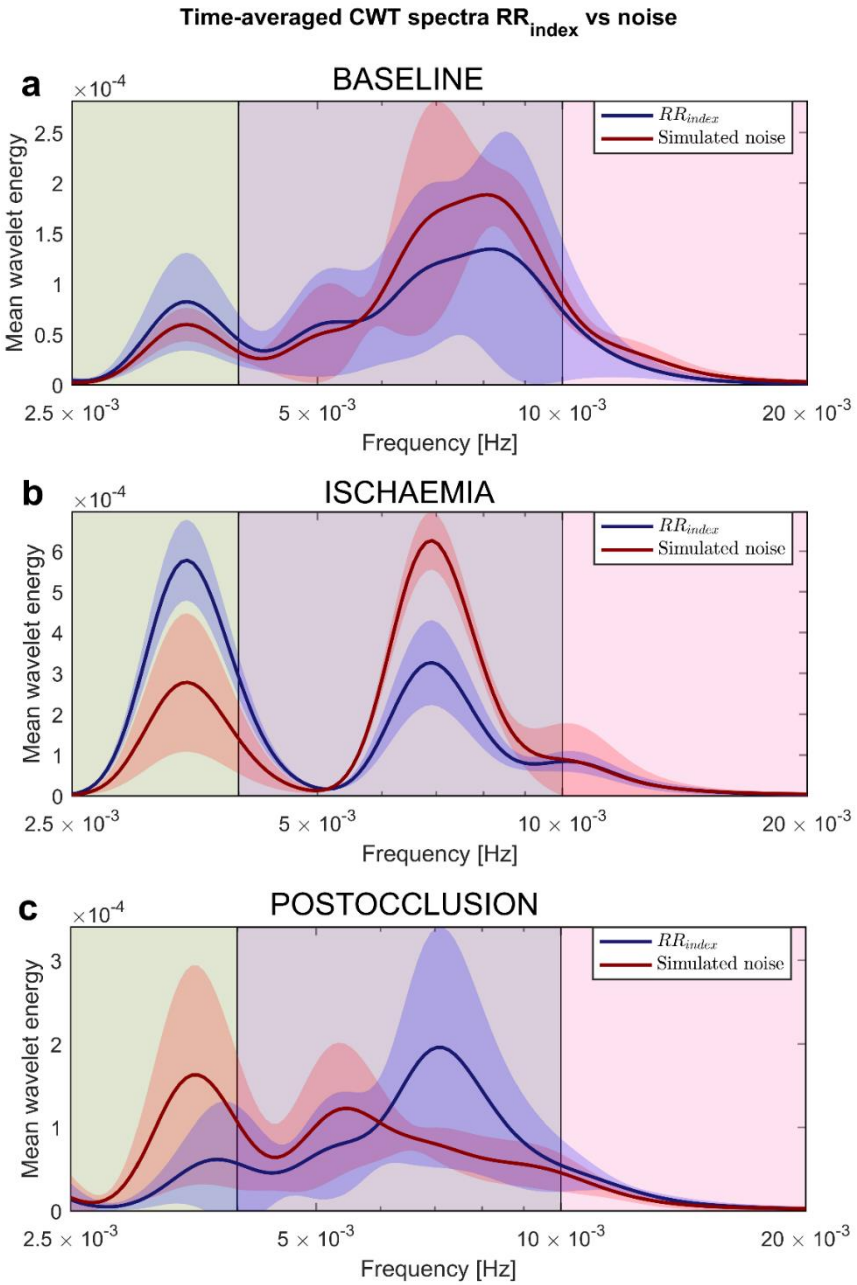

Fig. 46 Comparison of CWT spectra between RR$_{index}$ signal and its respective simulated noise signal. Average spectra obtained from the CWT analysis of 4 RR$_{index}$ signals (blue line) reconstructed by spline interpolation of raw autofluorescence data generated during a PORH functional test, and CWT analysis of 4 simulated noise signals (red line) generated using the same standard deviation and mean values of the raw autofluorescence data. (**a**) Baseline CWT spectra. (**b**) CWT spectra during occlusion of blood flow. (**c**) CWT spectra during PORH response. The shaded blue and red areas around the lines of the average spectra represent the range of variability (standard deviation over 4 repeats) of the CWT spectra.

Overall, the variability (SD of the spectrum over 4 repeats) of the CWT spectra from the biological signals and their simulated noise was spread with some degree of overlapping and some differentiated regions. Based on these observations, it could be assumed that the regions of the spectra showing a major

separation of the SD range may represent regions containing biological information. This is particularly true for some areas of the spectrum in the frequency range 5-9.5 × 10^{-3} Hz, especially during PORH response (Fig. 45c-46c) where it is visible a shift in the oscillatory peak between the biological metabolic signals and their respective noise, as well as a relevant difference in the distribution of the variability of the spectrum especially in the simulation associated with the RR_{index} signal. Based on the discussion above, it can be concluded that the reconstructed $NAD(P)H_{normalised}$ and RR_{index} signals contain both noisy and biological information, and following the application of the CWT analysis some regions of the spectrum are dominated by the noisy component and other regions by perturbations of biological origin, which are mainly manifested during the response to particular biological stimuli (in this case the PORH response).

2.3.4 Performing the wavelet phase coherence (WPCO) analysis

As discussed already in the section 1.8 (paragraph 1.8.7, page 61), the WPCO analysis provides information on the phase relationship between oscillators in the same frequency interval of two signals recorded simultaneously. The analysis returns values between 0 and 1, where $C_{\phi}(\omega_k) \approx 0$ indicates absence of phase coherence (no interaction), $C_{\phi}(\omega_k) \approx 1$ indicates complete coherence (full interaction), and $0 < C_{\phi}(\omega_k) < 1$ indicates partial coherence (partial interaction).

The main advantage of WPCO analysis is the possibility to gain information on the coupling/synchronisation between oscillators in time-frequency regions with relevant background noise. Another advantage is the chance to study the interaction between oscillators involved in the regulation of different biological mechanisms, i.e. in this dissertation the analysis was used to examine the interaction between cutaneous blood perfusion and NAD(P)H or RR metabolic oscillators. Specifically, the $C_{\phi}(\omega_k)$ between the MO-1 of metabolic time series and the endothelial EDHF oscillator of LDF signal, and between MO and the endothelial NO oscillators were examined because they are falling in the same frequency ranges. The analysis was performed through the WPCO Matlab code provided in the Lancaster University website http://py-biomedical.lancaster.ac.uk by the Stefanovska *et al.* research group. The code estimates the phase coherence according to the principles (equations 13-14) that were explained in section 1.8 (paragraph 1.8.7, page 61).

2.3.5 Examination of the complexity of LDF time series

Attractors of LDF time series were computed by using the software associated with the *LAKK-M* device (*LDF 3.1.1.404*), which allows the calculation of a set of parameters such as the fractal dimension (*D*), the Hurst index (*H*), the entropy (H_0), the information dimension (H_i) and the correlation dimension (D_2) according to the principles discussed in section 1.8 (paragraph 1.8.8, page 61).

2.4 Protocol for the assessment of microvascular and energy metabolism nonlinear dynamics in mouse models

2.4.1 Animals included in the study

Work on mouse models was conducted at the animal facility of the School of Medicine of the University of Dundee (Scotland). The study was approved by the local ethics committee (University of Dundee Ethical Review Process) and the experimental procedures were carried out according to the United Kingdom Home Office rules under the auspices of the Project Licence PPL N_o. 60/4265 and the Personal Licence N_o. IACEC4BB2. Animals included in the research were wild type (WT) (n=5) and nuclear factor erythroid 2–related factor 2 KO ($Nrf2^{-/-}$) female mice (n=6) on a C57Black/6 background aged 36-60 weeks. Mice were maintained under a 12:12-h light/dark cycle at 22 ± 1°C and 50% humidity, and were fed *ad libitum* on a standard rodent chow diet regime and water.

2.4.2 $Nrf2^{-/-}$ mouse model

The Nrf2 transcription factor is a key regulator of the cell redox state, involved in the resistance to oxidative stress by activating the cell antioxidant defence system [158]. Nrf2 KO leads to abnormal mitochondrial activity, altered redox status, increased oxidative stress, and has an impact on the functionality of the vascular system [158, 159]. Therefore, the rationale for using the $Nrf2^{-/-}$ strain was the chance to compare results between normal mice and a model characterised by altered functionality of the antioxidant defence that may impact the energetic metabolism and the cardiovascular system in the long term.

2.4.3 Skin preparation and anaesthesia

LFS and LDF techniques are sensitive to light absorption by hair and skin pigmentation. Therefore, a hair-free non-pigmented intact skin is required to obtain reliable measurements. Forty-eight hours prior to performing the

experiments, hair from the mice flanks was shaved using an electric shaver, and the residual hair was removed using a depilatory cream (*Veet*®, *Reckitt-Benckiser*). Before collecting measurements, mice were anaesthetised through a standard Boyle's Apparatus to prevent movement artefacts, and were laid on a heat mat at 37°C with the left flank facing the upper side (Fig. 47). A general light anaesthesia was maintained by delivering 1.5-2% isoflurane (*Abbott Laboratories*) in oxygen (1.5 L/min) through an inhalation nose cone (Fig. 47).

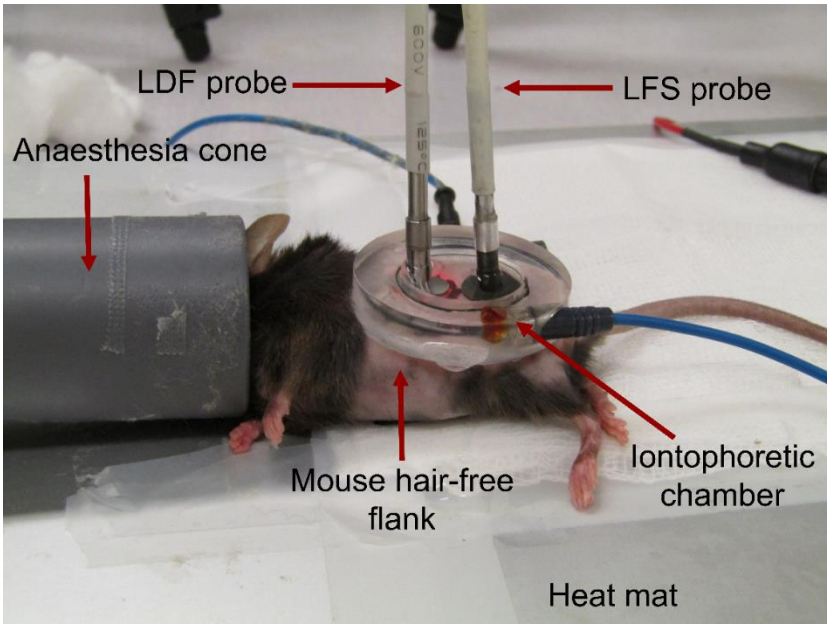

Fig. 47 Example of experimental setup for simultaneous recordings during iontophoresis. Anaesthetised mouse laid in a heat mat at 37 °C. Anaesthesia was maintained by delivering isoflurane through an inhalation nose cone. A 20 mm iontophoresis chamber was attached on the mouse flank by using a double-adhesive tape, and filled with a 2 ml solution of 1% PE. LFS and LDF probes were placed at two adjacent sites on the skin area inside the chamber to measure simultaneously autofluorescence, blood flow and oxygen saturation signals. The delivery of phenylephrine was induced by the application of a continuous 100 µA anodal current.

2.4.4 Iontophoresis

The principles of iontophoresis have been already discussed in the section 1.5 (paragraph 1.5.1, page 35). In this part of the work, iontophoresis was used to deliver phenylephrine (PE) and induce a local cutaneous vasoconstriction process. The reason for challenging skin micro-vessels by using this pharmacological agent was associated with the objective of studying the role of endothelium in vasomotion. Indeed, literature reports have described that PE is able to stimulate a vasomotion phenomenon specifically modulated by endothelium in rat small mesenteric artery, with the contribution of both NO and

EDHF signalling pathways [160]. Therefore, here a low dose 1% PE was delivered by iontophoresis for stimulating specifically an endothelium-mediated vasomotion phenomenon avoiding off-target effects. An iontophoresis chamber (*ION6* probe, *Moor Instruments Ltd*, UK) of 20 mm internal diameter was used, which was attached to the mouse flank using double-adhesive tape, and the reference electrode was placed underside of the animal to complete the circuit (Fig. 47). The experimental setup was completed by filling the chamber with a 2 ml solution of 1% PE, and placing the LFS and LDF probes at two adjacent sites on the skin area inside the chamber to measure simultaneously autofluorescence, blood flow and oxygen saturation parameters during the challenging test (Fig. 47). The delivery of PE was induced by the application of a continuous 100 µA anodal current through an iontophoresis controller (*MIC2*, *Moor Instruments Ltd*, UK) connected to the electrodes.

2.4.5 LDF, RS and LFS measurements

NAD(P)H autofluorescence, blood flow and oxygen saturation were measured simultaneously by using two single-point *LAKK-M* optical probes, one for LFS recordings and one for LDF/RS measurements. As described by Fig. 47, the probes were placed in two adjacent locations on the left flank of the mouse. The measurements were performed for 20 min, 10 min without application of electric current to determine the baseline oscillatory dynamics, and the remaining time during the delivery of phenylephrine. LDF/RS and LFS simultaneous recordings were collected according to the modalities explained in section 2.2 (paragraph 2.2.2 at page 75, and paragraph 2.2.4 at page 83 respectively). A total of 20 discrete UV spectra (1 spectrum per min) and a continuous LDF time series were sampled during the 20 min period of the iontophoresis test (Fig. 48a-b). NAD(P)H and RR time series were reconstructed from the discrete data points (Fig. 48a) by the methodology explained in section 2.3 (paragraph 2.3.1, page 96) for the study of metabolic oscillations.

2.4.6 Nonlinear dynamics analysis

CWT and WPCO analyses were performed on LDF, NAD(P)H and RR signals according to the methods discussed in section 2.3 (paragraph 2.3.3 at page 106, and paragraph 2.3.4 at page 114 respectively). Fig. 43 shows examples of CWT analyses of mouse LDF and NAD(P)H signals measured during delivery of PE.

2.4.7 Statistics

Statistical analysis was performed by R-Studio and Matlab R2015a software. The R-Studio package *Hmisc* was used to evaluate data normality by the Shapiro-Wilk test. All the analysed variables were normally distributed, thus correlations were evaluated by calculating the Pearson's correlation coefficient *r* which was estimated through the Matlab function *corr*. Statistical differences between baseline and phenylephrine time points were examined through the R-Studio software by using a paired t-test. Differences between mouse groups were assessed by unpaired t-test. All the analysis were considered significant at p-value < 0.05 with a statistical power of 0.8 which was calculated by R-Studio.

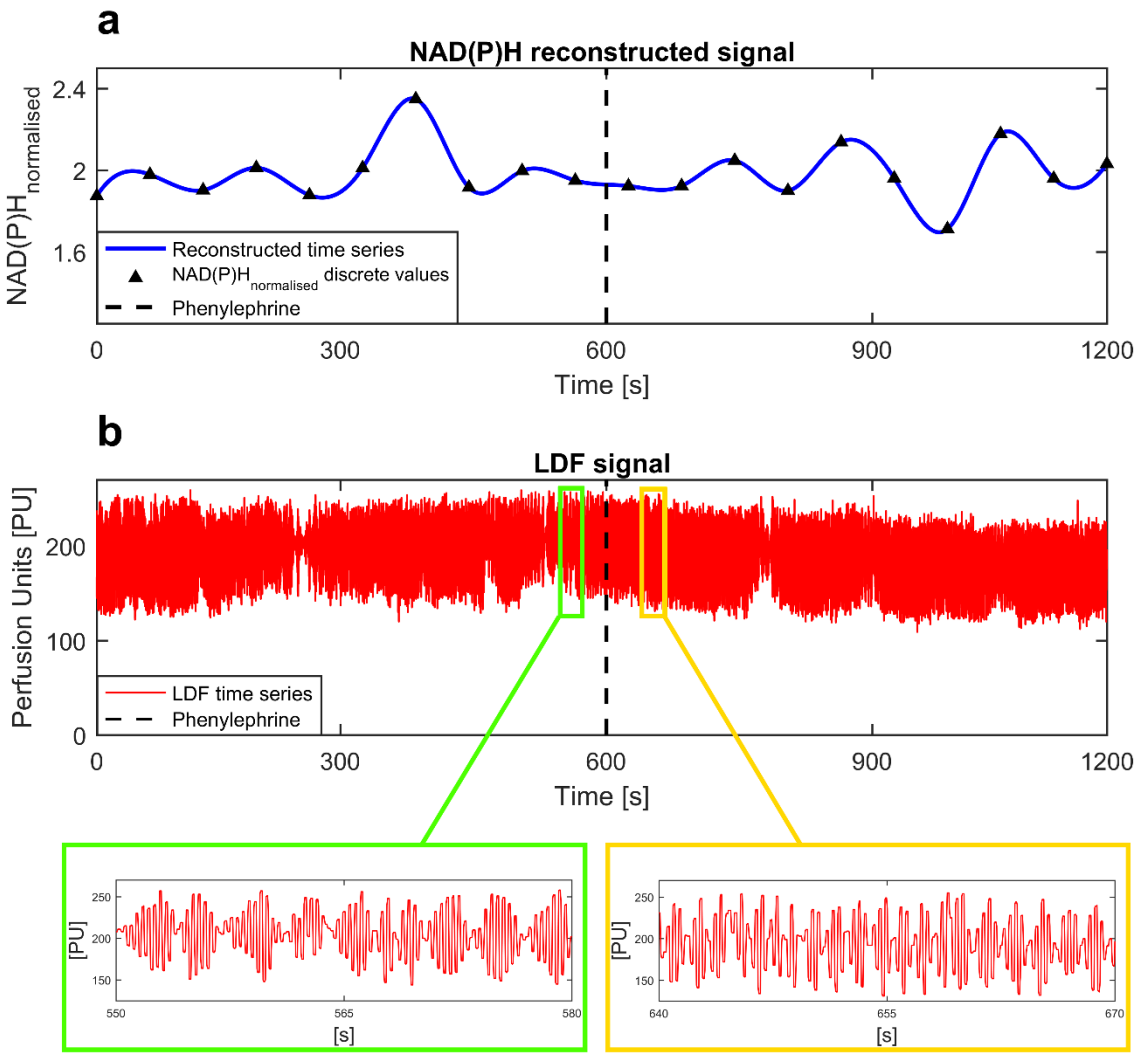

Fig. 48 Example of simultaneous data recordings from mouse flank during iontophoresis. (**a**) NAD(P)H 20-min signal reconstructed from 20 discrete data points collected during iontophoresis. Data are expressed in dimensionless units because the signal was reconstructed from the discrete $NAD(P)H_{normalised}$ values estimated according to equation 21. (**b**) 20-min LDF time series measured during iontophoresis. Data are expressed in perfusion arbitrary units (PU). The graph shows a slight reduction of blood perfusion at the beginning of phenylephrine delivery.

2.5 Protocol for the examination of microvascular and energy metabolism nonlinear dynamics in human individuals

2.5.1 Study population

The study on human subjects was approved by the Research Ethics Committee of the University of Dundee (UREC, Study Protocol N$_o$. 15064), according to the rules of the Declaration of Helsinki. The participants signed an informed consent form before being included in the research.

Fig. 49 displays a scheme of the recruitment process and allocation of the subjects to different study groups. A total of 70 volunteers were recruited among the students or staff members at the University of Dundee, which were divided in two groups: 48 non-smokers and 22 smokers. Sixteen non-smokers were allocated to a preliminary study group to evaluate the effect of blood volume and melanin on the autofluorescence measurements and implement an appropriate normalisation method. The data related to this preliminary study have been discussed previously in the paragraph 2.3.2 (page 99). The remaining volunteers were enrolled for the examination of skin microvascular and metabolic nonlinear dynamics and comparison of data between non-smokers and smokers. The inclusion criteria for non-smokers were the absence of hypertension, CVD or any pathological condition that may affect the vascular and respiratory systems. The inclusion criteria for smokers were smoking traditional cigarettes and absence of CVD or any pathological condition related to the respiratory system. Based on the criteria above, 3 non-smokers were excluded prior to the examination because of hypertensive conditions. Therefore, only 29 non-smokers and 22 smokers were tested according to the final protocol that will be discussed in the following paragraphs of this section. After the examination, 11 subjects (9 non-smokers and 2 smokers) were excluded from the data analysis mainly because of movement artefacts affecting LDF recordings or to match the age, gender and ethnicity distribution between the two groups. Indeed, as already discussed in the introduction (section 1.5, paragraph 1.5.2, page 37), the research studies related to skin blood perfusion must be designed ensuring that the individuals from different groups are matched for age and sex to allow obtaining comparable data. The reason is that in general elder subjects have impaired vascular reactivity compared to young individuals, and men and women may show physiological differences due to hormone level variations across the menstrual cycle.

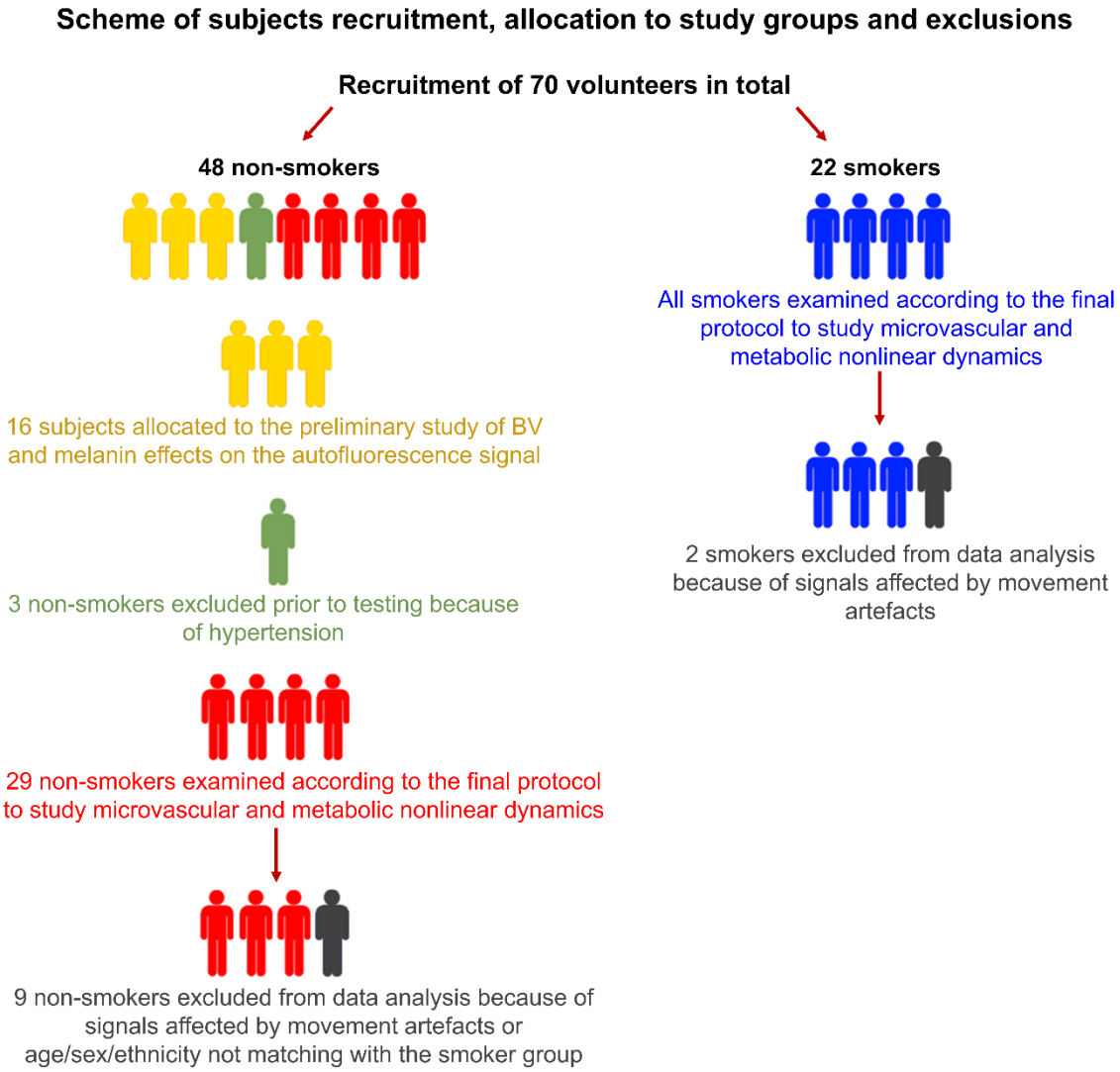

Fig. 49 Scheme of subjects' recruitment and design of study groups. 70 volunteers were enrolled in the project, divided in non-smoker (n=48) and smoker (n=22) groups. A part of non-smoking subjects (n=16) was allocated to a preliminary study for the implementation of a correction method of autofluorescence data aimed at reducing blood volume (BV) and melanin effects. The remaining subjects were allocated to the study of nonlinear dynamics of microcirculation and energy metabolism. Three non-smokers were excluded from the study prior to the examination due to hypertensive conditions. The experiments were performed on the remaining non-smokers (n=29) and smokers (n=22). Data from 9 non-smokers and 2 smokers were excluded from the study due to movement artefacts in the optical signals and to match the two groups according to age, gender and skin colour. The final groups were composed of 20 non-smokers and 20 smokers.

Additionally, in the section 1.7 (paragraph 1.7.2, page 50), it has been outlined that the content of melanin in the skin can affect AF measurements, thus the groups were matched also for ethnicity to avoid differences in the AF data related to a different degree of UV light absorption by melanocyte cells. The majority of the volunteers were of British ethnicity, and the remaining minority was composed

of Italian, Indian and Arabian ethnic groups, which were distributed equally and balanced between smoker and non-smoker groups.

All the points discussed above explain why in this study the allocation of the subjects in the smoker and non-smoker groups was not blinded, to ensure that optical data for the final comparison were not affected by differences associated with age, sex, colour of the cutaneous tissue and movement artefacts in the recorded signals. The groups employed for the final comparison were made of 20 smokers (42.6 ± 15.6 years old, 15 females and 5 males) and 20 non-smokers (41 ± 14 years old, 15 females and 5 males).

2.5.2 Preliminary arrangements and experimental setup

Preliminary arrangements. Subjects were tested between 11.00-13.00 hours. The room temperature was maintained constantly at 23 ± 1°C, and 20-30 min of acclimatisation were applied to allow body adaptation to the room environment. Food, drinks, and medications were avoided 4-6 hours before the test to prevent physiological changes due to diet habits or treatments that might had affected the results. Weight, height, blood pressure (BP) and skin temperature were measured before the test to check any correlation with vascular and autofluorescence data, and also to make sure that the differences between the two groups were mainly due to smoking rather than to differences in those general parameters. The BP was measured three times after the acclimatisation period using a traditional sphygmomanometer while the subject was resting on a clinical bed. The last two measurements were averaged to get the final BP value.
Experimental setup. Subjects were tested in resting supine position on a clinical bed and the data were collected from the volar surface of the left forearm. The tested arm was rested on a cushion to ensure a comfortable and static position during the analysis. The site of measurement was chosen avoiding areas with hair, huge veins and injured regions, and skin was disinfected using an alcohol strip before placing the probes. Two *LAKK-M* probes were placed in two adjacent sites for the simultaneous measurement of blood perfusion, oxygen saturation and autofluorescence. The probes were placed perpendicularly to the skin at 1/3 length of the left volar forearm by using tripods and adhesive tape. The probes were placed gently to avoid pressure artefacts. A pressure cuff was placed in the upper part of the tested arm for performing the PORH test while collecting LDF, RS and LFS measurements. In addition, arterial oxygen saturation (S_pO_2) was

monitored through a pulse oximeter probe placed in the index finger. An example of the experimental setup has been already shown in Fig. 40 of section 2.3 (paragraph 2.3.2, page 100) for the discussion of the effects of blood volume and melanin on NAD(P)H autofluorescence signal.

2.5.3 PORH test

The principles of PORH test have been already discussed in details in the section 1.5 (paragraph 1.5.1, page 34). In this part of the work, this technique was used for two reasons:

1. PORH represents an established challenging test for the evaluation of microvascular function.
2. PORH response is characterised by the induction of a vasomotion phenomenon involving several mediators (e.g. endothelial and smooth muscle cells, and the local sympathetic innervation).

Therefore, using this reactive test allowed to study both the applicability of nonlinear dynamic markers as putative CVD risk factors and their role in human cutaneous vasomotion.

The PORH test was performed in a time window of 25 min while measuring simultaneously blood perfusion, tissue oxygen saturation, arterial oxygen saturation and autofluorescence. During the first 10 min baseline measurements were collected. Then, blood flow was occluded through the brachial artery by inflating at 200 mmHg the pressure cuff placed in the upper left arm (Fig. 40) to induce ischaemia. After 5 min of occlusion the pressure of the cuff was released to monitor PORH response for 10 min.

2.5.4 LDF, RS and LFS recordings

Simultaneous NAD(P)H autofluorescence, blood perfusion and oxygen saturation measurements were collected during all the stages of PORH test by using two single-point *LAKK-M* optical probes. The recordings were performed according to the same modalities described in section 2.2 (paragraph 2.2.2 at page 75, and paragraph 2.2.4 at page 83 respectively). The measurements were collected for 25 min, 10 min to determine the baseline oscillatory dynamics, 5 min to monitor the parameters during the ischaemia stress condition, and 10 min during PORH response. A total of 25 discrete UV spectra (1 spectrum per min) and a continuous 25 min LDF trace were sampled simultaneously during the 25 min

period of the PORH test (Fig. 50a-b). NAD(P)H and RR time series were reconstructed from the discrete data points (Fig. 50a) by using the methodology explained in section 2.3 (paragraph 2.3.1, page 96) for the study of metabolic oscillations.

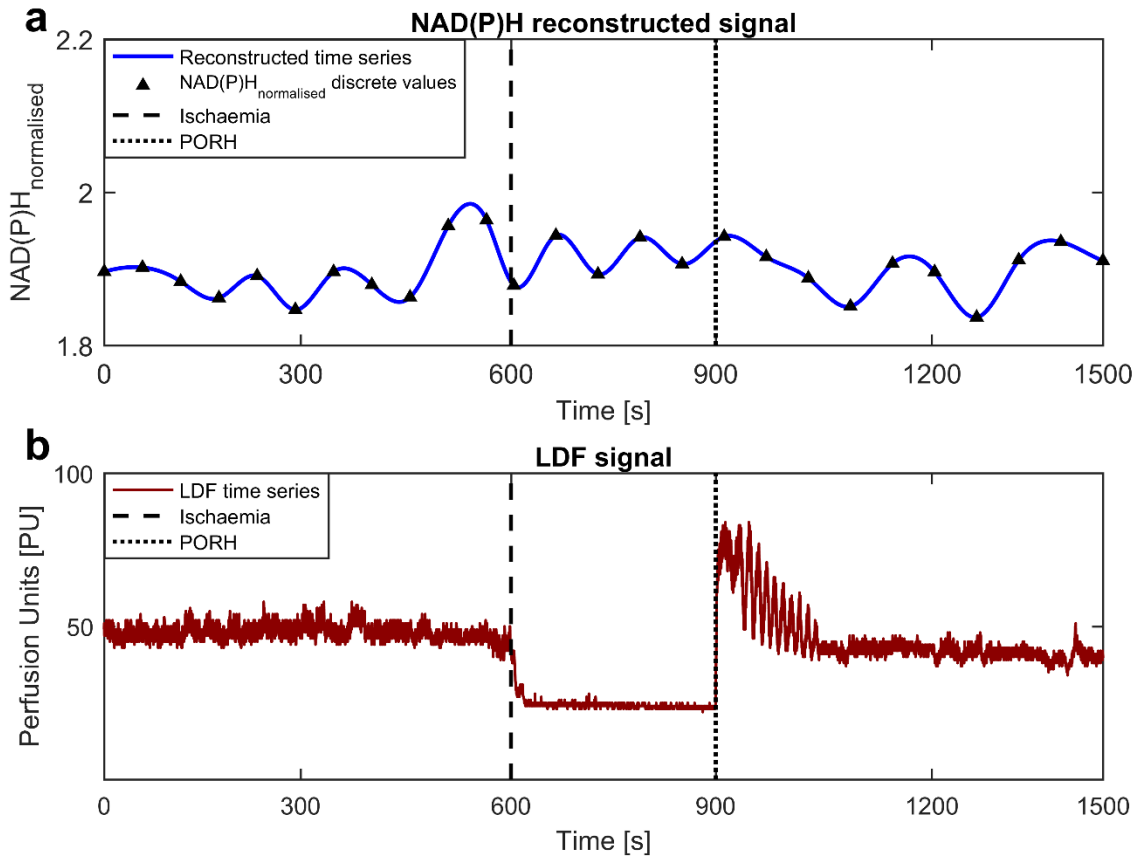

Fig. 50 Example of simultaneous data recordings from the human forearm during PORH. (**a**) NAD(P)H 25 min signal reconstructed from discrete data points collected during PORH test. Data are expressed in dimensionless units because the signal was reconstructed from the discrete $NAD(P)H_{normalised}$ values estimated according to equation 21. (**b**) 25 min LDF continuous signal measured during PORH test. Data are expressed in perfusion arbitrary units (PU). The graph shows clearly the typical PORH curve obtained after a period of arterial occlusion.

2.5.5 Nonlinear dynamics of LDF, NAD(P)H and RR time series

CWT and WPCO analyses were performed on LDF, NAD(P)H and RR time series according to the methods discussed in the section 2.3 (paragraph 2.3.3 at page 106, and paragraph 2.3.4 at page 114 respectively). Fig. 44 displays examples of wavelet analyses of human LDF and NAD(P)H signals measured during PORH functional test. The analysis of LDF attractors was performed by using the *LAKK-M* software *LDF 3.1.1.404* (*Spe Lazma Ltd*, Russia).

2.5.6 Tissue oxygenation dynamics

The simultaneous assessment of local cutaneous blood flow (I_m), oxygen saturation (SO_2), and arterial oxygen saturation (S_pO_2) in combination with the wavelet spectral analysis allowed the estimation of skin oxygen extraction (O_2ER) and oxygen consumption (VO_2). These variables provide information on the local transport and uptake of oxygen in the tissue. O_2ER represents a measure of the fraction of oxygen removed from the blood that diffuses from capillaries/arterioles to tissue, while VO_2 is a measure of tissue oxygen consumption or uptake.

The estimation of both O_2ER and VO_2 requires the calculation of the venous oxygen saturation (S_vO_2). The classic formula for the calculation of O_2ER is the following [161, 162],

$$O_2ER = \frac{(C_aO_2 - C_vO_2)}{C_aO_2}, \quad (25)$$

where C_aO_2 and C_vO_2 represent respectively the arterial and venous oxygen saturation in the blood expressed in (mL O_2/mL) [161]. The values of percentage SO_2 measured by RS method are proportional to the CO_2 (oxygen saturation expressed in mL) due the low variability of oxygen volume in the blood [161]. Therefore, equation 25 can be modified as follow [57, 161],

$$O_2ER = \frac{(S_aO_2 - S_vO_2)}{S_aO_2}. \quad (26)$$

Although SO_2 measured by RS method is closer to the venous oxygen saturation S_vO_2, overall it is representative of the average oxygenation of small arterioles and venules in the skin microcirculation. Therefore, the correct estimation of S_vO_2 requires the exclusion of the arterial contribution from SO_2. This can be achieved by calculating the SO_2 wavelet oscillations which allow to estimate correctly S_vO_2. Indeed, the arterial component of SO_2 is modulated by the absolute amplitude of the cardiac SO_2 wavelet oscillation $A_{cardiac}(SO_2)$, in contrast the venous contribution to SO_2 is modulated by the absolute amplitude of the respiratory SO_2 wavelet oscillation $A_{respiratory}(SO_2)$ [161]. Therefore, when the ratio between SO_2 cardiac and respiratory wavelet amplitudes $A_{cardiac}(SO_2)/A_{respiratory}(SO_2) \leq 1$, there is a predominant contribution of the venous component to oxygen saturation and S_vO_2 can be considered approximately equal to SO_2 [57, 161],

$$S_vO_2 = SO_2. \quad (27)$$

This situation is predominant in the cutaneous regions characterised by absence of arteriovenous anastomoses (AVAs), e.g. the forearm [57, 161]. The AVAs are microvascular functional structures characterised by the direct exchange of blood between arterioles and venules bypassing the capillaries [53, 54]. The microcirculation in AVAs containing regions is mainly depending on sympathetic vasomotor regulatory mechanisms, on the other hand free-AVAs regions are characterised by various vasomotor regulatory mechanisms of endothelial, sympathetic or myogenic origin [161].

Values of the ratio $A_{cardiac}(SO_2)/A_{respiratory}(SO_2) > 1$ indicate a predominant contribution of the arterial component to oxygen saturation [57, 161]. In this case, the venous oxygen saturation is estimated by normalising SO_2 for the size of the arterial contribution according to the following equation [57, 161],

$$S_vO_2 = \frac{SO_2}{A_{cardiac}(SO_2)/A_{respiratory}(SO_2)}. \quad (28)$$

This situation is predominant in skin regions characterised by the presence of AVAs, e.g. palmar surface of the fingers [57, 161].

In some cases the cardiac and/or the respiratory oscillators may be not expressed in the SO_2 wavelet spectrum, e.g. when there is synchronisation between oxygen saturation and blood flow oscillations in the endothelial, neurogenic and myogenic spectral intervals [57, 161]. In this case, the formulas for the calculation of S_vO_2 must be amended. If the synchronisation phenomenon involves endothelial and neurogenic oscillators, SO_2 represents the oxygenation of the afferent arterioles, thus it is roughly equal to the arteriolar oxygen saturation [161]. Therefore, S_vO_2 can be considered approximately equal to 0 which means that the oxygen extraction is maximal [161],

$$O_2ER = \frac{S_aO_2}{S_aO_2} = 1. \quad (29)$$

If the synchronisation phenomenon involves the myogenic or respiratory oscillators, S_vO_2 is approximately equal to SO_2 in the skin without AVAs, as shown in equation 27 [57, 161]. In contrast, in the regions with AVAs that are specifically controlled by the sympathetic innervation, S_vO_2 is equal to SO_2 only in the absence of the neurogenic oscillation [161]. In the presence of the neurogenic oscillation S_vO_2 is calculated taking into account the bypass index for the oxygen saturation $BI(SO_2)$ [57, 161],

$$S_vO_2 = \frac{SO_2}{BI(SO_2)}\,, \tag{30}$$

where *BI(SO_2)* is estimated according to equation 31, taking into consideration the components involved in the sympathetic vasomotor regulatory mechanisms,

$$BI(SO_2) = 1 + \frac{A_{neurogenic}(SO_2)}{A_{myogenic}(SO_2)}, \tag{31}$$

where $A_{neurogenic}(SO_2)$ and $A_{myogenic}(SO_2)$ are the absolute amplitudes of the neurogenic and myogenic SO_2 wavelet oscillations, respectively.

The formula for the calculation of oxygen consumption VO_2 by using arterial and venous oxygen saturation values is the following [161],

$$VO_2 = Q \cdot (S_aO_2 - S_vO_2), \tag{32}$$

where *Q* is the volume blood flow rate (mL/min x 100 g) and (S_aO_2 - S_vO_2) is the arteriovenous difference. Considering that the nutritive blood of arterioles and capillaries in the microcirculation contributes to the diffusion of oxygen in the tissue more than the blood in the venules, the perfusion rate value *Q* in equation 32 can be replaced by the nutritive blood perfusion value I_{mn} [161]. Thus the formula for the calculation of VO_2 is modified as follow [57, 161],

$$VO_2 = I_{mn} \cdot (S_aO_2 - S_vO_2). \tag{33}$$

The nutritive blood flow I_{mn} is estimated according to equation 34 [57, 161],

$$I_{mn} = \frac{I_m}{BI(I_m)}\,, \tag{34}$$

where I_m is blood perfusion, and *BI(I_m)* is the bypass index for blood perfusion estimated as shown in equation 35 for skin regions without AVAs, and as described in equation 36 for skin regions with AVAs [57, 161],

$$BI(I_m) = \frac{A_{max}(I_m)}{A_{myogenic}(I_m)}\,, \tag{35}$$

where $A_{max}(I_m)$ is the maximal LDF wavelet spectral amplitude in the frequency interval 5-150 x 10^{-3} Hz which reflects the activities of all the local microvascular components (endothelial, neurogenic and myogenic) that may be involved in the regulation of the vascular tone of free-AVAs regions, and $A_{myogenic}(I_m)$ is the wavelet amplitude of the myogenic LDF oscillator.

$$BI(I_m) = 1 + \frac{A_{neurogenic}(I_m)}{A_{myogenic}(I_m)}, \quad (36)$$

where $A_{neurogenic}(I_m)$ is the absolute wavelet amplitude of the neurogenic LDF oscillator [57]. In this case, the formula takes into account the components involved in the sympathetic vasomotor regulatory mechanism that is typical of AVAs cutaneous regions.

In this study, the amplitudes of SO_2 wavelet oscillators were extracted from *LAKK-M* SO_2 recordings by using the software provided with the device (*LDF 3.1.1.404*), and the amplitudes of LDF wavelet oscillators were computed as described in section 2.3 (paragraph 2.3.3, page 106).

Considering that the measurements were collected from a region without AVAs (volar forearm), S_vO_2 was mainly estimated by equation 27 and O_2ER according to equation 26, expressed in arbitrary units (AU). The oxygen consumption VO_2, expressed in AU, was calculated as shown in equation 33 by using I_{mn} values estimated according to equations 34-35.

2.5.7 Statistics

Statistical analysis was performed by R-Studio and Matlab R2015a software. The R-Studio package *Hmisc* was used to evaluate data normality by the Shapiro-Wilk test. Correlations were evaluated through the Matlab function *corr*, by calculating the Pearson's correlation coefficient *r* for normal variables and the Spearman's coefficient ρ for non-parametric variables. Statistical differences between PORH test time points were examined through R-Studio software by using paired t-test for normal variables and paired Wilcox-test for non-parametric variables. Differences between smokers and non-smokers were assessed by unpaired t-test or Wilcox-test, respectively for normal or non-parametric variables. All the analysis were considered significant at p-value < 0.05 with a statistical power of 0.8, which was calculated by R-Studio.

3 Nonlinear dynamics of microcirculation and cell energy metabolism in the *Nrf2*$^{-/-}$ mouse model

3.1 Introduction and aims

In the first part of this dissertation, it has been outlined the importance of investigating the nonlinear dynamics of both blood flow (LDF) and NAD(P)H cutaneous signals. Indeed, the wavelet spectral analysis of LDF time series reveals information on the functionality of specific microvascular components characterised by an oscillatory activity, i.e. endothelial and vascular smooth muscle cells. On the other side, the wavelet examination of NAD(P)H and redox ratio (RR) signals may be powerful to detect specific metabolic oscillations reflecting dynamic patterns of cellular ATP energy production.

Both LDF and metabolic oscillations may show different functional patterns between healthy or diseased vascular/metabolic conditions, or reflect the cellular and tissue mechanisms at the basis of vasomotion. Thus, the study of LDF and energy metabolism nonlinear dynamics could find powerful applications for the study of vasomotion and the prediction of CVD risk.

Based on the discussion above, the objectives of this part of the work were:

(1) Simultaneous characterisation of LDF oscillators and NAD(P)H and RR metabolic oscillations from mouse skin.
(2) Study of mouse cutaneous vasomotion with particular focus on the role of the endothelium and metabolic oscillators in the modulation of this phenomenon.
(3) Comparison of skin LDF and metabolic oscillators between normal mice and animals affected by oxidative stress, to test their potential use as predictors of vascular dysfunction associated with oxidative stress.

The work was carried out on two groups of animals: 5 control WT mice and 6 KO Nrf2$^{-/-}$ animals characterised by impaired antioxidant defence. The mice were tested from the skin of the left flank by evaluating the dynamics of microcirculatory and metabolic biomarkers during transdermal iontophoresis delivery of the vasoconstrictor drug phenylephrine (PE), which according to Okazaki *et al.* [160] is able to induce a vasomotion oscillatory phenomenon mediated specifically by NO and EDHF endothelial regulatory mechanisms.

3.2 General microcirculatory and cell energy metabolism biomarkers during iontophoresis administration of PE

3.2.1 Blood flow and oxygen saturation

Table 4 and Fig. 51a-b show the comparison of results between Nrf2$^{-/-}$ and WT mice related to the microcirculatory variables. Both groups showed a similar statistically significant decrease of blood flow ($p < 0.05$ WT, $p < 0.01$ Nrf2$^{-/-}$) during vasoconstriction stimulated by administration of PE with a stronger p-value in animals affected by oxidative stress. Oxygen saturation showed a minimal decrease during PE stimulation in both groups with non-statistical significance from baseline to post PE stimulation.

3.2.2 NAD(P)H and redox ratio (RR)

Both of NAD(P)H$_{normalised}$ and RR did not change significantly during PE stimulation either in WT or Nrf2$^{-/-}$ mice, as shown in Fig. 51c-d. However, the mean RR$_{index}$ (ratio NAD(P)H/FAD^{+}) was higher in WT mice compared to the knock-out animals ($p < 0.05$) (Table 4). This relevant difference confirmed that the phenotype of Nrf2$^{-/-}$ mice is characterised by an altered balance between mitochondrial NAD(P)H and flavins due to impairment of the molecular pathway involved in the antioxidant defence, increased amounts of ROS, and oxidative stress which may impact negatively the dynamics of cellular ATP production.

Table 4 Comparison of microvascular and metabolic variables between WT and Nrf2$^{-/-}$ mice. Data are presented as mean ± standard deviation (SD). PE = phenylephrine. I_m = Blood perfusion expressed in perfusion arbitrary units (PU). SO_2 = Oxygen saturation expressed in percentage arbitrary units (AU). NAD(P)H$_{normalised}$ = Reduced nicotamide adenine dinucleotide expressed in dimensionless units (equation 21). RR = Redox ratio expressed in dimensionless units (equation 22). Differences between WT and Nrf2$^{-/-}$ groups were calculated by unpaired t-test and are outlined by red asterisks. Differences between baseline and PE time points were calculated by paired t-test and are outlined by black asterisks. *p < 0.05, **p < 0.01.

	WT (n=5)		Nrf2$^{-/-}$ (n=6)	
Variable	**Baseline**	**PE**	**Baseline**	**PE**
I_m [PU]	174.0 ± 30.40	162.8 ± 26.80*	197.6 ± 20.50	184.0 ± 16.70**
SO_2 [%]	47.3 ± 9.60	44.9 ± 10.7	48.3 ± 9.60	45.5 ± 6.10
NAD(P)H$_{normalised}$	1.7 ± 0.2	1.7 ± 0.2	1.9 ± 0.2	1.8 ± 0.1
RR$_{index}$	*2.2 ± 0.1	*2.2 ± 0.1	*2.0 ± 0.1	*2.0 ± 0.1

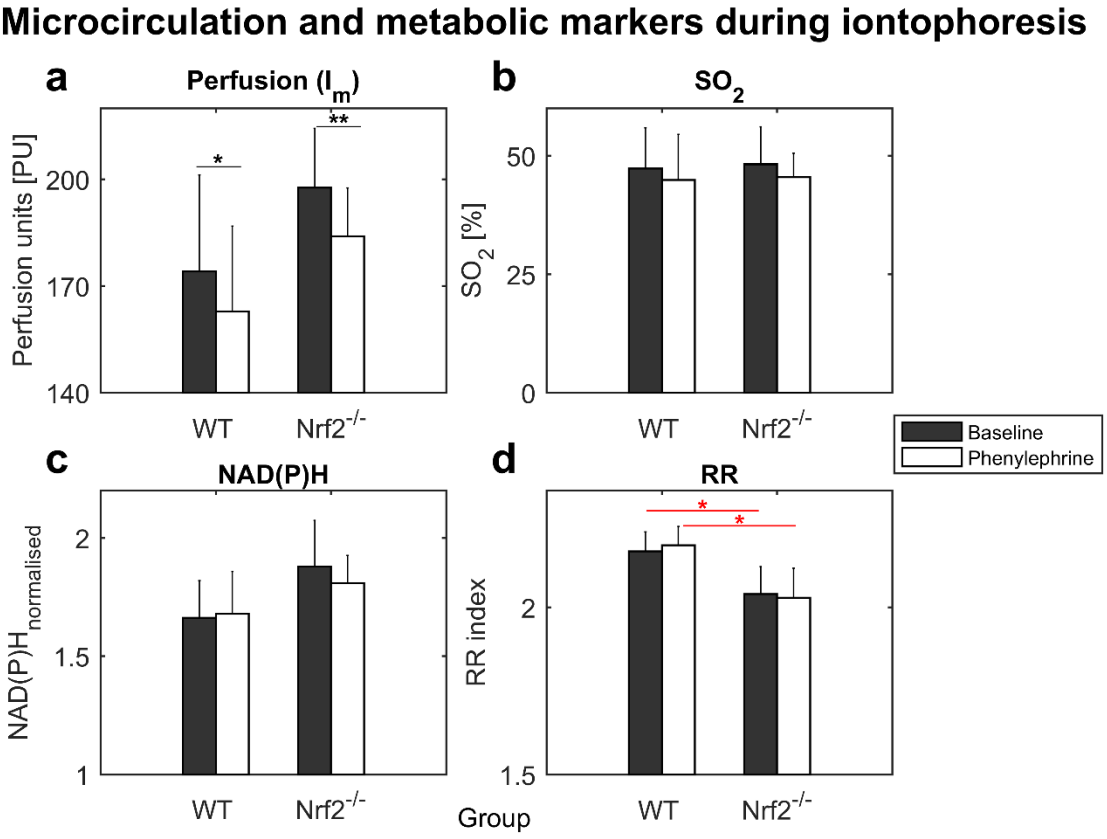

Fig. 51 Trends of microvascular and metabolic biomarkers during iontophoresis of PE. Graphic representation of the data reported in Table 4. (**a**) Blood perfusion (PU). (**b**) SO_2 (%). (**c**) $NAD(P)H_{normalised}$ (dimensionless units). (**d**) RR_{index} (dimensionless units). Data are presented as bar plots of the mean with error bars corresponding to two standard errors (SE) (~95% confidence interval). The black lines/asterisks refer to significant changes during PE stimulation. The red lines/asterisks refer to significant differences between WT (n=5) and Nrf2$^{-/-}$ (n=6) mice. Black bars = baseline. White bars = PE. The p-values were calculated by paired t-test to compare baseline and PE time points and unpaired t-test to compare animal groups. *p < 0.05, **p < 0.01.

3.3 Wavelet spectral analysis of LDF and metabolic signals measured during iontophoresis administration of PE

3.3.1 LDF oscillators in mice

Fig. 52 illustrates the median time-averaged LDF wavelet spectra from WT and Nrf2$^{-/-}$ mice during iontophoresis reactive test. The typical wavelet peaks of local cutaneous LDF physiological oscillators reported in the literature were characterised: endothelial NO-independent (EDHF), endothelial NO, neurogenic and myogenic. The specific features that characterise each LDF oscillator peak are the absolute energy E_i, the absolute amplitude A_i and the frequency location f of the peak, expressed in arbitrary units (AU) and hertz (Hz) respectively.

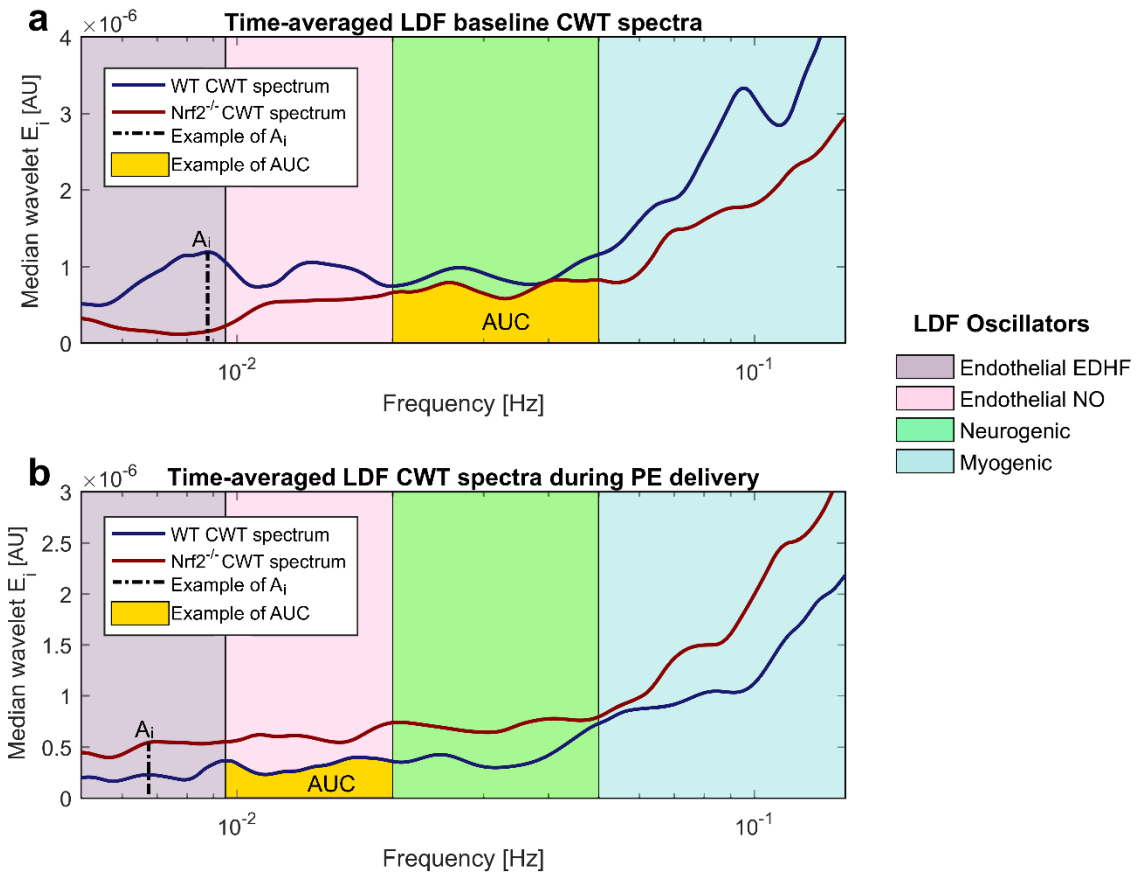

Fig. 52 Comparison of time-averaged blood flow CWT spectra during iontophoresis test. (**a**) Median CWT spectra of WT (n=5) and Nrf2$^{-/-}$ (n=6) mice at baseline. The dotted line indicates an example of amplitude A_i (maximal energy of the peak) located at a specific frequency f of the endothelial EDHF oscillator's interval. The yellow area (AUC of the peak) indicates an example of E_i (average energy underneath the peak) from the neurogenic oscillator's frequency range. (**b**) Median CWT spectra during transdermal iontophoresis delivery of phenylephrine (PE). The dotted line indicates an example of A_i located at a specific frequency f of the endothelial EDHF oscillator's range. The yellow area indicates an example of E_i from the endothelial NO oscillator's frequency interval. Both of E_i and A_i are expressed in arbitrary units (AU). The plots outline clearly differences in E_i, A_i and f of the LDF oscillatory peaks between the two groups of mice.

The graphs clearly outline differences between groups associated with the E_i, A_i or f of the various LDF oscillators. A_i is the maximum (peak) energy E_i in the frequency range of a specific oscillator, reflecting the maximal oscillatory activity in the frequency interval of interest. Instead, E_i (area under the curve of the peak) represents the total average energy in the frequency range of a specific oscillator, reflecting the overall oscillatory activity in the frequency interval under investigation. Although most of the times A_i and E_i trends are similar, sometimes the maximum oscillatory amplitude A_i reached during a specific task (e.g. response to PE) might not reflect the overall E_i trend in the interval of interest.

For this reason, the examination of both A_i and E_i provides a better overview of the data avoiding misinterpretations. In addition, the frequency location *f* of the oscillator's peak provides a different information compared to A_i and E_i, mostly reflecting the rate of the oscillatory activity rather than the magnitude of the oscillation. Thus, it is worth examining all of these three parameters (A_i, E_i, *f*) to gain a complete overview on the oscillatory activity of a specific wavelet oscillator.

Another important aspect to consider is that the absolute A_i and E_i wavelet data might not be reliable for comparing different animals because of the heterogeneous anatomy of the single-point analysed skin regions. The problem is addressed by using the relative wavelet amplitude a_i and energy e_i of each oscillator for comparisons between different groups of mice, which are dimensionless variables. The normalisation of A_i and E_i for obtaining the relative a_i and e_i has been discussed in the section 1.8 (paragraph 1.8.2, page 55) (equations 9-12). It is based on normalising the value of A_i or E_i extracted from the frequency interval of a specific oscillator by the A_i or E_i of the total wavelet spectrum, and by the number of frequencies in the interval of the oscillator. The experimental data of a_i, e_i, and *f* of the LDF oscillators' peaks characterised in this study for mice are reported in Table 5.

Characterisation of the endothelial EDHF oscillator

As discussed in section 1.8 (paragraph 1.8.3, page 58), the physiological origin of the endothelial NO-independent oscillator (5-9.5 × 10^{-3} Hz) is not clear. Although the endothelial origin of this oscillator has been proved [102, 105], in literature it has been reported that either the inhibition of the NO pathway by L-NMMA or inhibition of the PG pathways by aspirin does not affect the wavelet peak of this oscillator, suggesting a physiological origin related to a different endothelial mechanism that may be the EDHF [102, 105]. The results obtained in this thesis are in agreement with this hypothesis and support indirectly the possible EDHF origin of this oscillator. Indeed, Okazaki *et al.* [160] have reported that the vasoconstriction induced by PE in rat mesenteric artery is able to enhance a vasomotion phenomenon mediated specifically by NO and EDHF mechanisms but not by PG pathways. In this thesis a different microcirculatory bed (skin micro-vessels) from the mesenteric artery has been used, however, the results agree with what has been reported by Okazaki *et al.* [160]. Indeed, as displayed in Table 5, the wavelet components showing the most statistically

significant changes during PE administration were the endothelial NO oscillator (9-20 × 10^{-3} Hz) and the endothelial NO-independent (5-9 × 10^{-3} Hz) oscillator. Considering the recognised origin of the endothelial NO peak, by exclusion the high significant changes observed in the NO-independent interval after PE stimulation should be ascribed to the EDHF activity.

Table 5 Wavelet a_i, e_i and f of LDF oscillators during iontophoresis of PE. Data are presented as mean ± SD. Endo = Endothelial. NO = Nitric oxide. EDHF = Endothelial-derived hyperpolarizing factor. The relative a_i and e_i are expressed in dimensionless units. The frequency f is expressed in hertz (Hz). Differences between WT and Nrf2$^{-/-}$ groups were calculated by unpaired t-test and are outlined by red asterisks. Differences between baseline and PE time points were calculated by paired t-test and are outlined by black asterisks. *p < 0.05, **p < 0.01.

	WT (n=5)	
Variable	**Baseline**	**PE**
$a_{i\ Myogenic}$	(14.8 ± 6.60) × 10^{-3}	(9.70 ± 4.30) × 10^{-3}
$a_{i\ Neurogenic}$	(12.9 ± 7.60) × 10^{-3}	(5.50 ± 1.80) × 10^{-3}
$a_{i\ Endo\text{-}NO}$	(10.6 ± 4.40) × 10^{-3}	(6.00 ± 2.60) × 10^{-3}
$a_{i\ Endo\text{-}EDHF}$	(11.0 ± 2.30) × 10^{-3}	(6.10 ± 1.50) × 10^{-3} *
$e_{i\ Myogenic}$	(4.50 ± 1.50) × 10^{-3}	(3.20 ± 1.10) × 10^{-3}
$e_{i\ Neurogenic}$	(1.90 ± 0.80) × 10^{-3}	(1.00 ± 0.30) × 10^{-3} *
$e_{i\ Endo\text{-}NO}$	(1.10 ± 0.30) × 10^{-3}	(0.60 ± 0.20) × 10^{-3} **
$e_{i\ Endo\text{-}EDHF}$	*(0.70 ± 0.20) × 10^{-3}	(0.40 ± 0.10) × 10^{-3} **
$f_{Myogenic}$ [Hz]	(10.4 ± 1.30) × 10^{-2}	(9.30 ± 2.10) × 10^{-2}
$f_{Neurogenic}$ [Hz]	(2.80 ± 0.50) × 10^{-2}	(3.00 ± 0.70) × 10^{-2}
$f_{Endo\text{-}NO}$ [Hz]	(1.40 ± 0.10) × 10^{-2}	(1.50 ± 0.30) × 10^{-2}
$f_{Endo\text{-}EDHF}$ [Hz]	*(8.00 ± 0.60) × 10^{-3}	(6.90 ± 0.90) × 10^{-3} *
	Nrf2$^{-/-}$ (n=6)	
Variable	**Baseline**	**PE**
$a_{i\ Myogenic}$	(11.2 ± 2.40) × 10^{-3}	(12.4 ± 5.30) × 10^{-3}
$a_{i\ Neurogenic}$	(8.40 ± 1.90) × 10^{-3}	(8.40 ± 4.70) × 10^{-3}
$a_{i\ Endo\text{-}NO}$	(7.60 ± 3.90) × 10^{-3}	(9.50 ± 5.60) × 10^{-3} *
$a_{i\ Endo\text{-}EDHF}$	(7.10 ± 4.10) × 10^{-3}	(8.90 ± 4.00) × 10^{-3} *
$e_{i\ Myogenic}$	(3.40 ± 0.60) × 10^{-3}	(3.80 ± 1.10) × 10^{-3}
$e_{i\ Neurogenic}$	(1.30 ± 0.40) × 10^{-3}	(1.50 ± 0.80) × 10^{-3}
$e_{i\ Endo\text{-}NO}$	(0.80 ± 0.30) × 10^{-3}	(1.00 ± 0.50) × 10^{-3}
$e_{i\ Endo\text{-}EDHF}$	*(0.40 ± 0.20) × 10^{-3}	(0.60 ± 0.30) × 10^{-3} *
$f_{Myogenic}$ [Hz]	(9.20 ± 1.70) × 10^{-2}	(9.20 ± 1.60) × 10^{-2}
$f_{Neurogenic}$ [Hz]	(3.50 ± 1.00) × 10^{-2}	(4.00 ± 1.00) × 10^{-2}
$f_{Endo\text{-}NO}$ [Hz]	(1.40 ± 0.20) × 10^{-2}	(1.50 ± 0.20) × 10^{-2}
$f_{Endo\text{-}EDHF}$ [Hz]	*(6.30 ± 1.00) × 10^{-3}	(7.70 ± 0.80) × 10^{-3} *

Moreover, in literature it has been reported that EDHF plays a more important role than NO in the vaso-reactivity of small resistance arterioles [140, 163, 164]. The results have displayed changes that are more significant for the endothelial NO-independent frequency range (EDHF) compared to the endothelial NO interval (Table 5), which would confirm a major involvement of EDHF in the reactivity of small arterioles [140, 163, 164]. Finally, additional indirect proof of the possible EDHF origin of this oscillator is provided by experimental data that will be discussed in section 4.4 (paragraph 4.4.2, page 177), which describe the contribution of each LDF wavelet oscillator to the post-occlusive reactive hyperaemia (PORH) response in human subjects. For all the reasons discussed above, in this thesis the endothelial NO-independent oscillator was named as “Endothelial EDHF”.

Study of vasomotion dynamics and role of the endothelium in this phenomenon

Fig. 53-54 describe the trends of the relative a_i, e_i, and f of the LDF oscillators’ during iontophoresis reactive test. Blood flow oscillators were characterised by opposite dynamics in the two groups of mice during PE-induced vasomotion. Indeed, the values of the endothelial EDHF a_i, e_i and f increased in Nrf2$^{-/-}$ mice ($p < 0.05$) and decreased in the WT group ($p < 0.01$ or $p < 0.05$) after stimulation with PE. The endothelial NO component showed trends similar to those observed for the EDHF oscillation. However, statistical significance was found only for the decrease of amplitude/energy during delivery of PE in WT mice ($p < 0.01$), while the increase of NO a_i/e_i observed in the Nrf2$^{-/-}$ model was non-significant and could be due to the small number of tested animals. The neurogenic and myogenic oscillators showed also patterns similar to those of the endothelial oscillations. The e_i for the neurogenic oscillator was significantly reduced in WT mice during the response to PE ($p < 0.05$), with a non-significant trend for a reduction in the myogenic oscillator ($p=0.08$). Overall, these findings indicate different microvascular reactivity between the normal phenotype and a phenotype characterised by altered antioxidant defence. Moreover, the most relevant differences from a statistical point of view were observed for the endothelial oscillators, which are the most important factors associated with microvascular function. This suggests that the impairment of antioxidant defence may affect early the endothelial function of skin microcirculation.

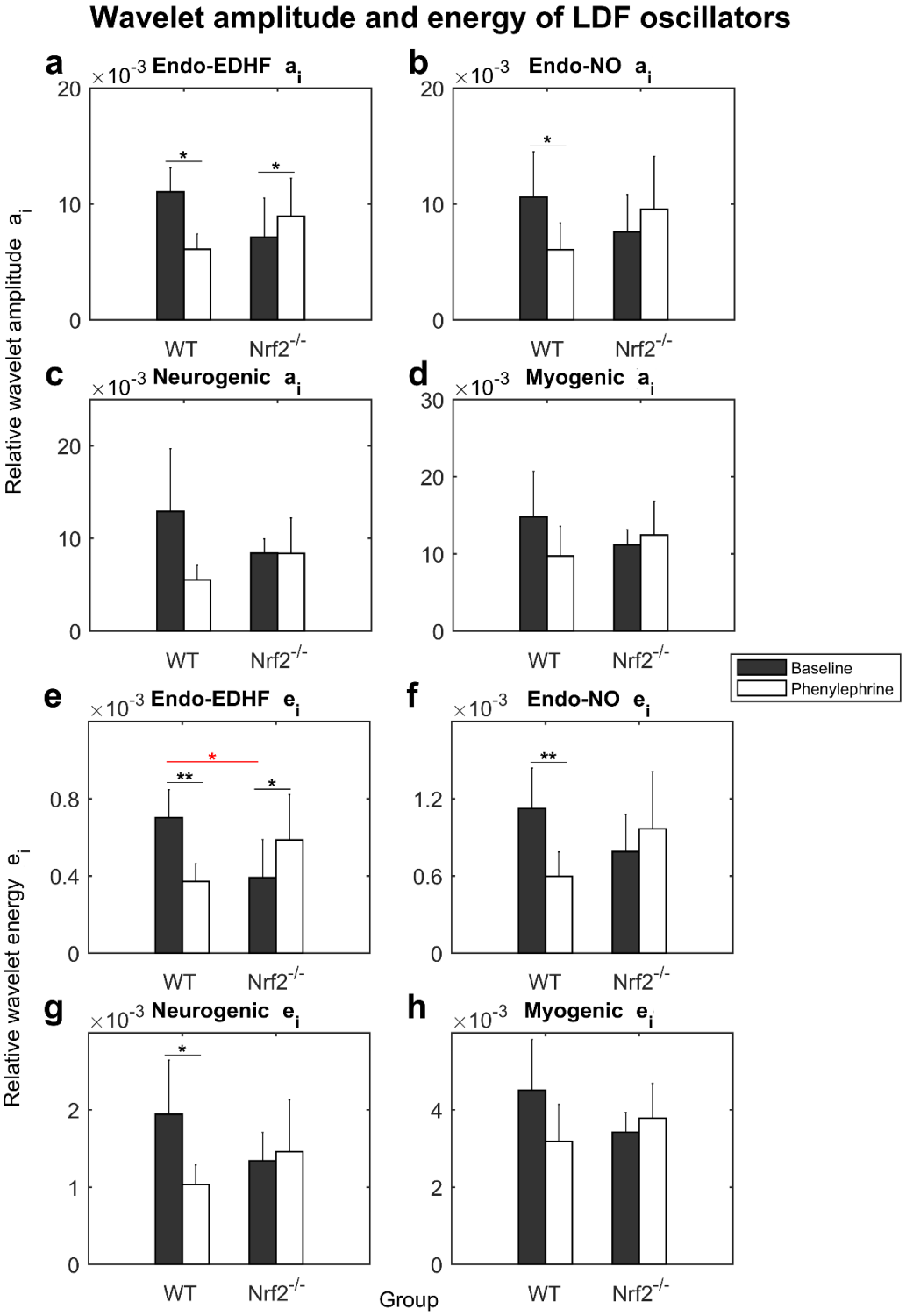

Fig. 53 Trends of a_i and e_i of LDF oscillators during iontophoresis. Graphic representation of the a_i and e_i data reported in Table 5. (**a**,**e**) Endothelial EDHF. (**b**,**f**) Endothelial NO. (**c**,**g**) Neurogenic. (**d**,**h**) Myogenic. Data are presented as bar plots of the mean with error bars corresponding to 2SE (~95% confidence interval). Both a_i and e_i are expressed in dimensionless units. The black lines/asterisks refer to significant changes during PE delivery. The red lines/asterisks refer to significant differences between WT (n=5) and Nrf2$^{-/-}$ (n=6) mice. Black bars = Baseline. White bars = PE. The p-values were estimated by paired or unpaired t-test to compare baseline and PE time points or WT and Nrf2$^{-/-}$ mice, respectively. *p < 0.05, **p < 0.01.

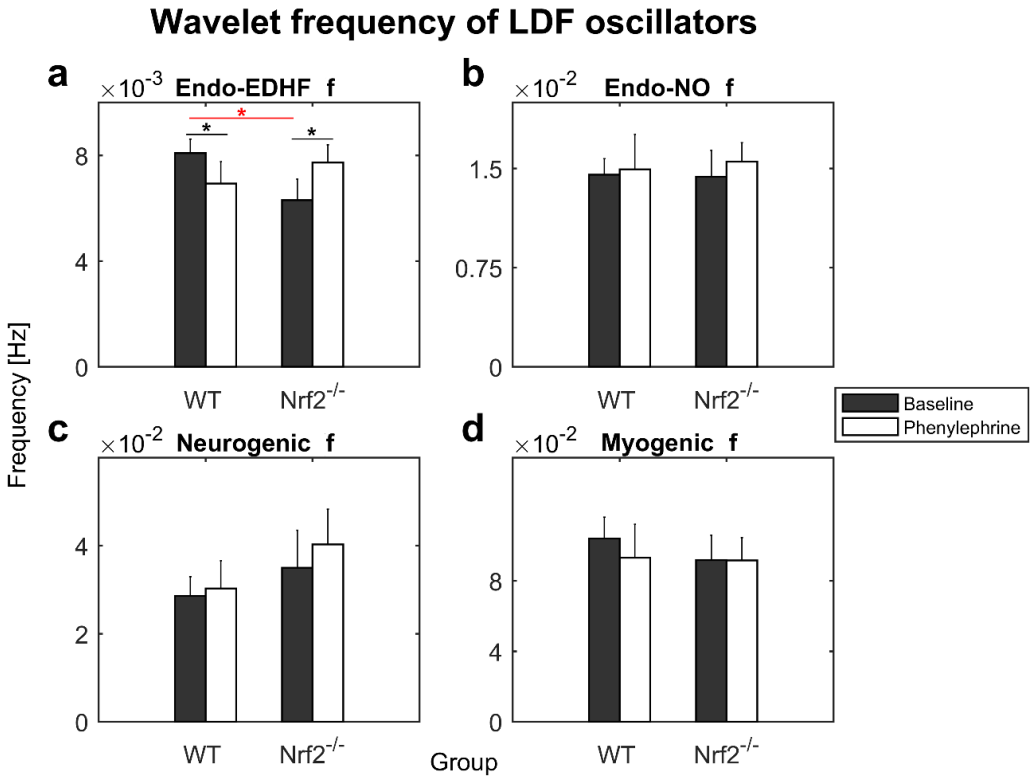

Fig. 54 Trends of LDF oscillators' peak frequency *f* during delivery of PE. Graphic representation of the frequency data reported in Table 5. (**a**) Endothelial EDHF. (**b**) Endothelial NO. (**c**) Neurogenic. (**d**) Myogenic. Data are presented as bar plots of the mean value with error bars corresponding to 2SE (~95% confidence interval). Data of *f* are expressed in hertz (Hz). The black lines/asterisks refer to significant changes during PE stimulation. The red lines/asterisks refer to significant differences between WT (n=5) and Nrf2$^{-/-}$ (n=6) groups. Black bars = baseline. White bars = PE. The p-values were calculated by paired t-test to compare baseline and PE time points, and by unpaired t-test to compare WT and Nrf2$^{-/-}$ groups. *p < 0.05.

According to literature reports related to the wavelet spectral analysis of LDF time series, in general the increase of wavelet amplitude/energy is associated with vasodilation dynamics [60, 102, 105, 107]. Based on this assumption, the expected trend for LDF oscillators during vasoconstriction should be a decrease of the oscillatory amplitude/energy, which is indeed what has been observed in this work for WT animals (Fig. 53). In contrast, although Nrf2$^{-/-}$ mice showed a decrease of blood flow during PE-induced vasoconstriction (Fig. 51), the wavelet amplitude/energy of LDF oscillators was increased in this group of mice (Fig. 53).

A possible explanation for this paradoxical response might be a vasomotion counter-mechanism to limit vasoconstriction by enhancing the vasodilation pathways modulated by the endothelium. A similar resistance mechanism to attenuate vasoconstriction has been already described in literature and is defined myoendothelial feedback [140], which is a bidirectional communication between

VSMCs and ECs enhanced after stimulation by vasoconstrictors, leading to the increase of Ca^{2+} in endothelial cells and the activation of both EDHF and NO signalling to moderate the constriction tone. A possible reason for the activation of this counter-regulatory mechanism in $Nrf2^{-/-}$ mice may be a counter-regulatory response to the impairment of antioxidant defence and the increase of oxidative stress, which are factors able to impact negatively the function of the endothelium and the overall pathways involved in microvascular reactivity. These observations may indicate a major tendency to constriction or a pre-existent vasoconstriction in the $Nrf2^{-/-}$ mice due to oxidative stress. However, this cannot be proved by evaluating the trends of blood flow, as shown in Fig. 51, which allows to account only the relative vasoconstriction induced by PE but does not allow to evaluate the presence of a pre-existent constriction status of micro-vessels.

Finally, it cannot be excluded that using higher concentrations of PE (> 1%) to induce stronger vasoconstriction also WT mice may show an increase of the LDF wavelet amplitudes/energies, reflecting the activation of a myoendothelial feedback and vasomotion to enhance vasodilation mechanisms, counteract the excessive constriction and maintain the normal skin perfusion and oxygenation.

Differences of LDF oscillators between normal and oxidative stress phenotypes

The most relevant statistically significant difference between groups was found for the endothelial EDHF oscillator, which showed greater wavelet energy ($p < 0.05$) and frequency ($p < 0.05$) in WT mice compared to $Nrf2^{-/-}$ at baseline (Table 5). This may indicate a general reduced basal activity of the EDHF vasodilator dynamics in $Nrf2^{-/-}$ mice due to impaired antioxidant defence and leading to major constriction of skin micro-vessels. Overall, also all the other oscillators (endothelial NO, neurogenic, myogenic) showed greater baseline amplitude/energy or *f* in WT compared to $Nrf2^{-/-}$ mice, suggesting a general reduced basal vasodilator potential in the knock-out animals, even though non-significant p-values were observed for these components (Table 5). Thus, LDF oscillators may be potential predictors of vascular dynamics associated with oxidative stress.

3.3.2 Metabolic oscillators in mice

Rationale for the study of metabolic oscillators in mouse models

NAD(P)H is a coenzyme involved in the cellular energy metabolism that is accumulated in the cells in the presence of oxidative stress. Monitoring the

relative amounts of NAD(P)H in the skin provides the potential to gain information on possible cell metabolic alterations associated with vascular/metabolic illness. Moreover, the estimation of the redox ratio (RR) index that is the balance between cellular NAD(P)H and flavins coenzymes provides specific information on mitochondrial function. NAD(P)H has an oscillatory time-dependent nature due to the continuous production and consumption of ATP energy in the cells [89].

As discussed in the paragraph 1.9.1 (page 64), monitoring the cellular oscillations of NAD(P)H levels may be powerful for the early prediction of metabolic dysfunction in the tissue that could be associated to the onset of many diseases (i.e. cancer or CVD) [89]. Metabolic oscillations have been studied from *in-vitro* or *ex-vivo* cell cultures, i.e., yeast [128, 129], cardiac myocytes [130] and β-cells [131, 132] by measuring the AF of NAD(P)H [128, 129, 130, 131, 133, 134]. Limited research on metabolic oscillations has been carried out also in live animals, i.e., detection of mitochondrial fast oscillations from rat skin salivary glands using intra-vital 2P microscopy [135], and study of circadian diurnal NAD(P)H oscillations from mouse stem cells of the basal epidermal skin layer by multiphoton FLIM method [136]. However, skin metabolic oscillations have never been investigated *in-vivo* in humans or mouse models by using AF single-point readouts, and no research has focused on the possible relationship between metabolic oscillators and skin microvascular reactivity or on the use of these nonlinear markers as predictors of risk for CVD. Based on the discussion above, the main novelties that the present work has added to the current knowledge are:

1. The application for the first time of the wavelet spectral analysis on skin NAD(P)H and RR signals obtained by label-free single-point autofluorescence readouts, to characterise *in-vivo* mouse skin metabolic oscillators.
2. The comparison for the first time of the dynamic patterns of skin metabolic oscillators between different animal groups to evaluate their potential applicability as CVD risk factors associated with oxidative stress.
3. The first attempt to study the role of metabolic oscillators in skin vasomotion by assessing their interaction/correlation with microvascular oscillators.

Characterisation of a slow metabolic oscillator from mouse skin

Fig. 55 shows the median time-averaged CWT spectra from $NAD(P)H_{normalised}$ and RR_{index} reconstructed signals of WT and $Nrf2^{-/-}$ mice during iontophoresis task.

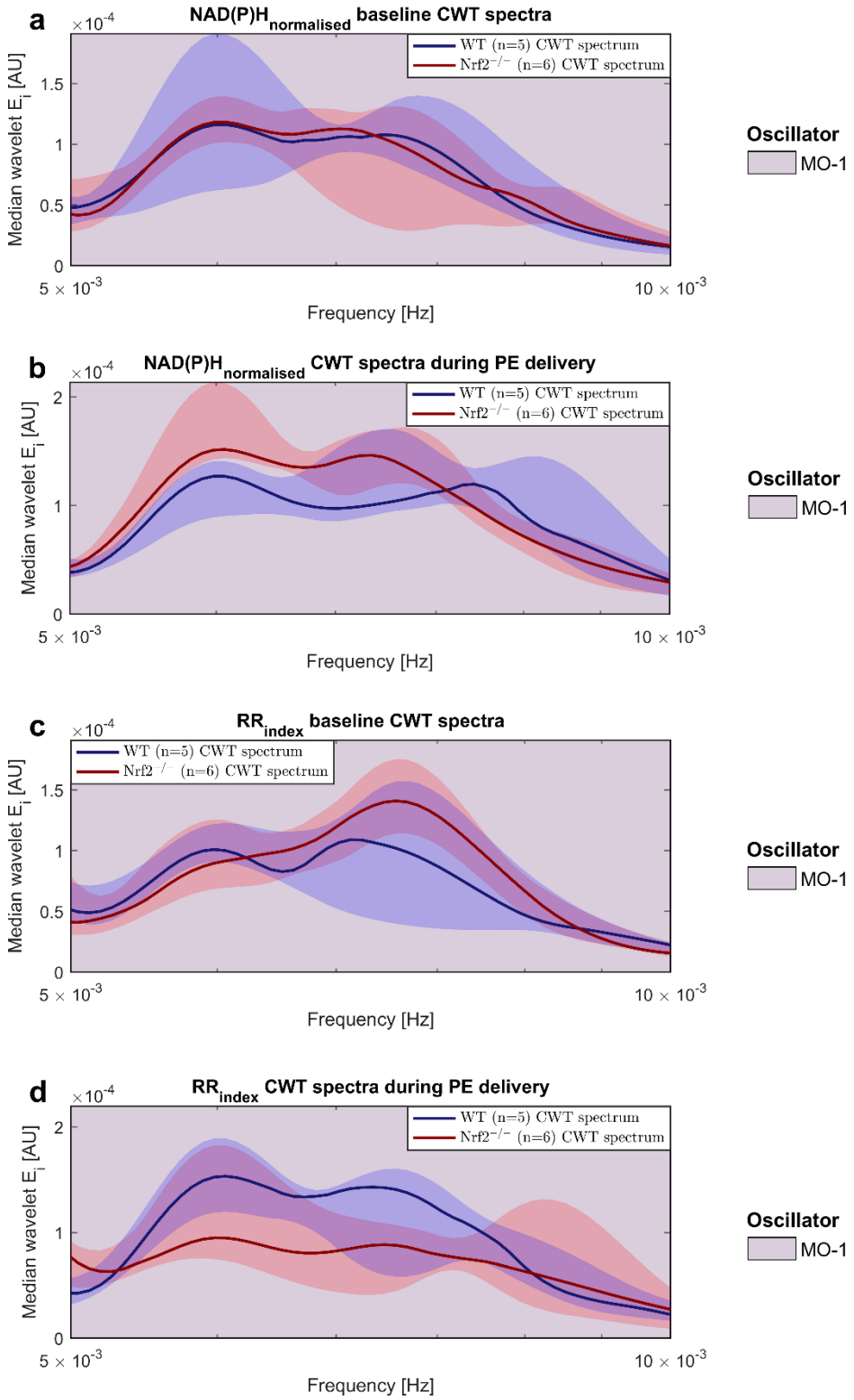

Fig. 55 Comparison of WT and Nrf2$^{-/-}$ NAD(P)H and RR CWT spectra during iontophoresis. (**a-b**) Median CWT NAD(P)H spectra of WT (n=5) and Nrf2$^{-/-}$ (n=6) mice during iontophoresis: (**a**) baseline and (**b**) PE response. (**c-d**) Median CWT RR spectra of WT (n=5) and Nrf2$^{-/-}$ (n=6) mice during iontophoresis: (**c**) baseline and (**d**) PE response. The shaded blue and red areas around the lines of the median spectra represent the inter-quartile range of the CWT spectra. MO-1 = Metabolic oscillator-1. Both E_i and A_i are expressed in AU. The plots show slight differences in the A_i, E_i and f of MO-1 peak between groups.

A relevant slow metabolic oscillation in the 5-9 × 10^{-3} Hz frequency range of NAD(P)H and RR signals was identified, named metabolic oscillator-1 (MO-1), which should reflect the biological cyclic turnover between the reduced and oxidised forms of NAD(P)H and $FADH_2$ coenzymes. The graphs outline some differences between groups associated with the absolute wavelet amplitude A_i and energy E_i of metabolic oscillators, especially for the RR MO-1 oscillator during both baseline and PE delivery time points.

Comparisons between groups were examined by evaluating the dimensionless relative amplitude a_i and energy e_i, which were estimated normalising the values of A_i and E_i extracted from the frequency interval of the MO-1 by the values of A_i and E_i derived from the total wavelet spectrum, and by the number of frequencies in the frequency interval of MO-1 (equations 9-12). Also the frequency location f of the MO-1 wavelet peak was compared between mice groups. The experimental data of a_i, e_i and f of the MO-1 are reported in Table 6.

Table 6 Wavelet a_i, e_i and f of NAD(P)H MO-1 and RR MO-1 during iontophoresis of PE. Data are presented as mean ± SD. NAD(P)H = Nicotamide adenine dinucleotide. RR = Redox ratio. MO-1 = Metabolic oscillator-1. The relative a_i and e_i are expressed in dimensionless units. The frequency f is expressed in hertz (Hz). Non-significant differences were found between WT and Nrf2$^{-/-}$ groups. Differences between baseline and PE time points were estimated by paired t-test and are outlined by black asterisks. *p < 0.05.

	WT (n=5)	
Variable	**Baseline**	**PE**
$a_{i\ NAD(P)H\ MO-1}$	(10.7 ± 2.70) × 10^{-3}	(11.7 ± 3.50) × 10^{-3}
$a_{i\ RR\ MO-1}$	(8.10 ± 4.40) × 10^{-3}	(12.4 ± 2.30) × 10^{-3} *
$e_{i\ NAD(P)H\ MO-1}$	(12.8 ± 1.40) × 10^{-3}	(16.1 ± 1.50) × 10^{-3} *
$e_{i\ RR\ MO-1}$	(11.7 ± 4.60) × 10^{-3}	(14.9 ± 2.50) × 10^{-3}
$f_{NAD(P)H\ MO-1}$ [Hz]	(6.10 ± 1.10) × 10^{-3}	(6.60 ± 0.60) × 10^{-3}
$f_{RR\ MO-1}$ [Hz]	(6.70 ± 1.10) × 10^{-3}	(6.40 ± 1.20) × 10^{-3}
	Nrf2$^{-/-}$ (n=6)	
Variable	**Baseline**	**PE**
$a_{i\ NAD(P)H\ MO-1}$	(9.60 ± 5.40) × 10^{-3}	(13.8 ± 5.50) × 10^{-3}
$a_{i\ RR\ MO-1}$	(11.2 ± 3.90) × 10^{-3}	(8.60 ± 4.20) × 10^{-3}
$e_{i\ NAD(P)H\ MO-1}$	(12.3 ± 4.60) × 10^{-3}	(15.8 ± 2.40) × 10^{-3}
$e_{i\ RR\ MO-1}$	(14.6 ± 3.90) × 10^{-3}	(12.0 ± 3.10) × 10^{-3}
$f_{NAD(P)H\ MO-1}$ [Hz]	(6.80 ± 1.40) × 10^{-3}	(6.30 ± 0.90) × 10^{-3}
$f_{RR\ MO-1}$ [Hz]	(6.30 ± 0.80) × 10^{-3}	(7.00 ± 1.30) × 10^{-3}

Biological meaning of NAD(P)H MO-1 and RR MO-1 dynamics

The interpretation of the data reported in Table 6 is difficult considering that this is the first attempt to investigate *in-vivo* metabolic oscillations detected by CWT spectral analysis. In general, from a biochemical point of view, NAD(P)H and RR oscillations reflect the oxido-reductive dynamics of the biological tissue, which consist in the continuous fluctuation of the cellular coenzymes NAD(P)H and $FADH_2$ from the reduced status to their respective oxidised forms ($NAD(P)^+$ and FAD^+) and vice-versa. These cyclic reactions are part of glycolysis (only NAD(P)H reactions) and oxidative phosphorylation (OXPHOS) (both NAD(P)H and FAD^+ reactions) cellular processes for the production of ATP energy, taking place in the cytoplasm and in the mitochondria cell compartments, respectively. Therefore, evaluating the metabolic oscillations makes it possible to gather information on the dynamics of cellular energetic metabolism. Based on the trends of MO-1 observed during human PORH test that will be discussed in section 4.4 (paragraph 4.4.3, page 184), as clue for mouse model data interpretation, it can be proposed the increase of MO-1 wavelet amplitude/energy as a general indicator of enhanced aerobic energy metabolism, and the decrease of the MO-1 amplitude/energy as indicator of a protective mechanism for the preferential production of cellular ATP through glycolysis in the presence of stress conditions.

Trends of the metabolic oscillator MO-1 during PE-induced vasomotion and differences between normal and oxidative stress phenotypes

Fig. 56 shows the trends of the relative wavelet amplitude a_i, energy e_i and frequency f of NAD(P)H MO-1 and RR MO-1 oscillators during iontophoresis of PE in mouse models. The data are partially in agreement with the interpretation of MO-1 trends proposed above. Indeed, a_i or e_i increased significantly in WT mice during PE challenge either for NAD(P)H MO-1 ($p < 0.05$) or RR MO-1 ($p < 0.05$) oscillators (Fig. 56a-d), indicating the maintenance of “normal” aerobic cellular energetic dynamics in the presence of a low-dose vasoconstriction stimulus. In contrast, although NAD(P)H MO-1 showed a “normal” response also in the $Nrf2^{-/-}$ mice, the a_i or e_i of RR MO-1 decreased in this group during PE-induced vasoconstriction (Fig. 56a-d). This finding may suggest a preferential production of part of the total ATP through glycolysis as protective mechanism to maintain a sufficient energy intake in response to oxidative stress and the consequent vasoconstriction, which are factors that may cause lower tissue

oxygenation. This would agree also with the more relevant vasomotion observed in Nrf2$^{-/-}$ mice compared to WT that has been explained in paragraph 3.3.1 (page 136) as a resistance mechanism to counteract vasoconstriction.

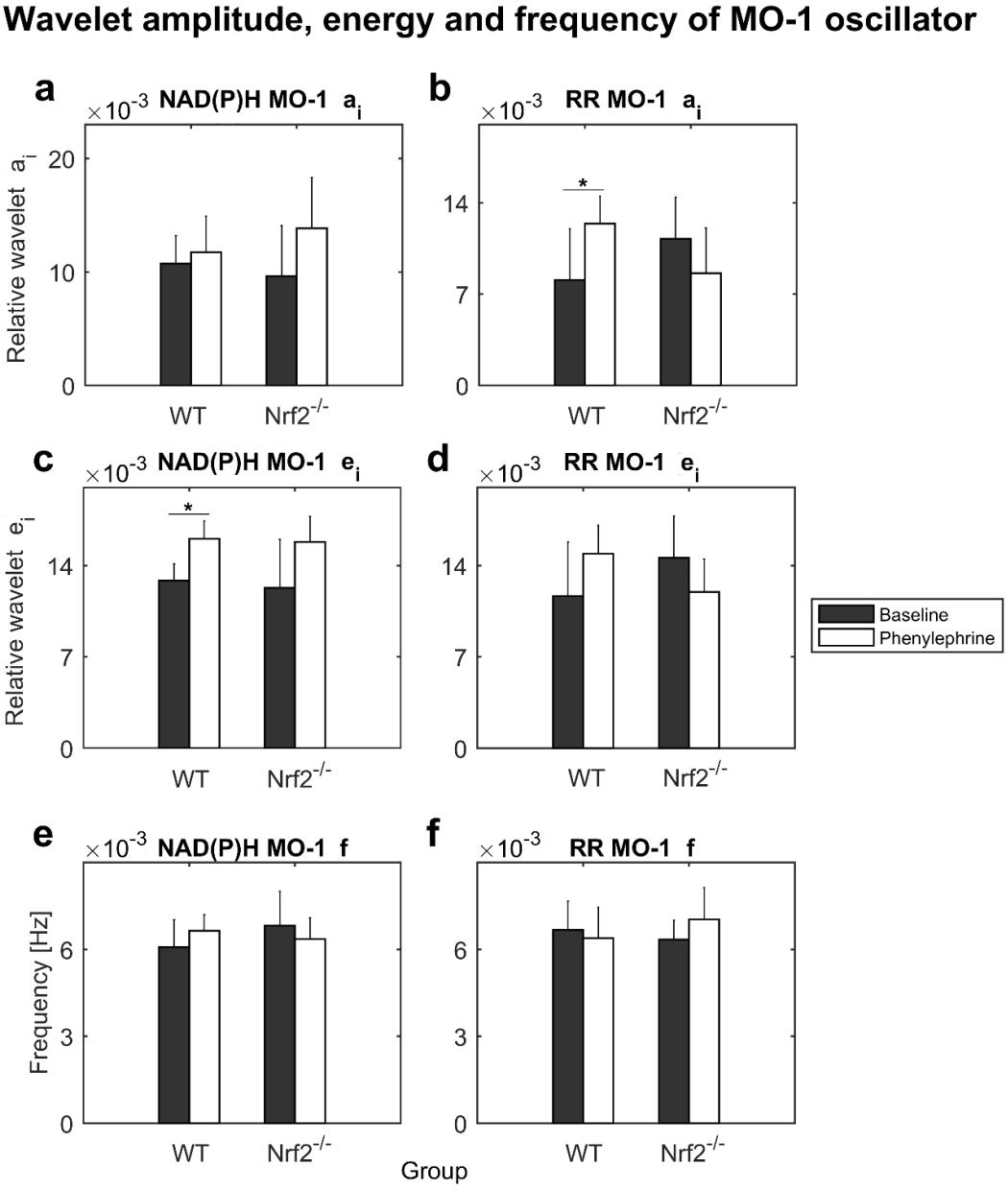

Fig. 56 Trends of the wavelet a_i, e_i and f of MO-1 during iontophoresis. Graphic representation of the data reported in Table 6. (**a**, **c**, **e**) NAD(P)H MO-1 wavelet data. (**b**, **d**, **f**) RR MO-1 wavelet data. NAD(P)H = Nicotamide adenine dinucleotide. RR = Redox ratio. MO-1 = Metabolic oscillator-1. Data are presented as bar plots of the mean value with error bars corresponding to 2SE (~95% confidence interval). Both a_i and e_i are expressed in dimensionless units. The frequency f is expressed in hertz (Hz). Non-significant differences were found between WT (n=5) and Nrf2$^{-/-}$ (n=6) mice. The black lines/asterisks refer to significant changes during PE stimulation. Black bars = baseline. White bars = PE. The p-values to compare baseline and PE time points were calculated by paired t-test. *p < 0.05.

However, the baseline wavelet energy/amplitude of RR MO-1 oscillator was found to be lower in WT animals compared with $Nrf2^{-/-}$ mice ($p = 0.097$). This finding would be in contrast with the hypothesis proposed above of lower wavelet amplitude/energy of RR MO-1 reflecting a protective mechanism to ensure suitable ATP production during oxidative stress. Indeed, in this case data might be misinterpreted as indicating the presence of higher basal oxidative stress in WT mice leading to lower baseline RR MO-1 oscillatory amplitude/energy and preferential production of ATP by glycolysis. These contrasting observations suggest that baseline wavelet data should be interpreted with caution, and a better approach for making reliable comparisons would be monitoring the changes of wavelet oscillators' dynamics in response to a challenging test (e.g. iontophoresis of PE or PORH).

The wavelet frequency of both NAD(P)H MO-1 and RR MO-1 oscillators did not show significant differences either between mouse groups or in relation to challenge of skin micro-vessels with iontophoretic delivery of PE (Fig. 56e-f).

In summary, the data have revealed different dynamics of metabolic oscillators between the two mice models, especially in relation to the RR MO-1 that was characterised by opposite trends in the two groups of animals during PE challenge showing greater differences compared to NAD(P)H MO-1. The reason why the RR MO-1 shows more relevant differences might be due to the fact that it reflects specifically the mitochondrial oxido-reductive dynamics. Indeed, the RR_{index} (dimensionless variable) was calculated as the $NAD(P)H/FAD^{+}$ ratio (equation 22) that is a measure of the mitochondrial activity and may undergo relevant changes when the cells switch towards a preferential anaerobic glycolytic metabolism taking place in the cytoplasm. In contrast, the autofluorescence of NAD(P)H itself may be less informative considering that the laser fluorescence spectroscopy (LFS) method does not allow to distinguish cytosolic and mitochondrial NAD(P)H, as well as the bounded (NADPH) and unbounded (NADH) forms of the coenzyme. Therefore, the oscillations of NAD(P)H in this case may reflect the overall cellular energetic dynamics rather than the oxido-reductive reactions of a specific cellular compartment.

In conclusion, the inter-group differences that were observed in relation to RR MO-1 dynamics may reflect an early alteration of cell energy metabolism in the $Nrf2^{-/-}$ mice due to oxidative stress. It cannot be excluded that this may explain

why the Nrf2$^{-/-}$ mice compared to WT have higher probability of developing metabolic illness (i.e. diabetes) in the presence of risk factors, i.e. high fat diet (HFD). Therefore, metabolic oscillators may be potential predictors of risk for metabolic dysfunction and the vascular complications derived from this condition.

However, the lack of antioxidant protection of the Nrf2$^{-/-}$ mice used in this work has not been fully tested, for example by challenging the mice with a significant oxidative stress load (i.e. treatment with HFD). Thus, because their baseline phenotype may not reveal the full picture on the dynamics of metabolic oscillators in response to oxidative stress, future work is required on larger groups of mice treated with HFD or affected by metabolic or vascular disorders to elucidate further these aspects. Another perspective is translating the research to human clinical studies to assess and validate metabolic oscillators as CVD risk factors.

3.4 Interactions and correlations between microvascular and metabolic oscillators in mice

The main goal of this section was investigating the possible link between metabolic and microvascular oscillators to gather information on the role of NAD(P)H and RR cellular nonlinear dynamics in the vasomotion process induced by administration of the α-adrenergic vasoconstrictor PE. In order to achieve this objective two kind of analyses were performed:

(1) The wavelet phase coherence (WPCO) analysis. The WPCO allows studying the degree of interaction between oscillators that reflect specific biological functions, with the potential of revealing the cooperation between these components for the regulation of particular biological mechanisms. For example, in this case the WPCO examination may be useful to detect interactions between metabolic and microvascular oscillators associated with PE-induced vasomotion, which may reflect dynamic patterns of cellular ATP production able to drive the regulation of the vascular tone in response to the given stimulus. Moreover, the analysis may potentially reveal different patterns of interaction in WT and Nrf2$^{-/-}$ mice due to the effect of oxidative stress and ROS on the mitochondrial energetic dynamics of Nrf2$^{-/-}$ animals.

(2) Analysis of correlations. The traditional analysis of correlations allows gathering more information than the WPCO on the association between

microvascular and metabolic oscillators. This is due to the fact that the WPCO is restricted to the study of phase relationship between oscillators that are located in the same frequency range, i.e. in this case it was possible investigating only the WPCO between MO-1 and the endothelial EDHF oscillators. Instead, the correlation analysis allows investigating the relationship between all the parameters that have been included in the study. Considering that the variables analysed in mouse models work were normally distributed, here the analysis of correlation was carried out by estimating the parametric Pearson's correlation coefficient *r*.

3.4.1 Phase coherence between metabolic and EDHF oscillators

The WPCO analysis is used to study the phase relationship $C\phi(\omega k)$ between oscillations in a specific frequency range of two signals measured simultaneously. The analysis allows gathering information on the degree of interaction/synchronisation between the oscillators under investigation, by returning coherence values ranging from 0 to 1 that respectively indicate absence of interaction and maximal interaction. In this work on animal models, the analysis was applied to examine the phase relationship between the endothelial EDHF oscillator of the LDF signal and the MO-1 of NAD(P)H ($C\phi(\omega k)_{NAD(P)H\ MO\text{-}1/EDHF}$) or RR ($C\phi(\omega k)_{RR\ MO\text{-}1/EDHF}$) reconstructed signals, which are located in the same frequency range (5-9 × 10^{-3} Hz). Table 7 displays the WPCO data of $C\phi(\omega k)_{NAD(P)H\ MO\text{-}1/EDHF}$ and $C\phi(\omega k)_{RR\ MO\text{-}1/EDHF}$ during an iontophoresis test. The table shows baseline phase coherence mean values for the analysed interactions between 0.74 and 0.79 in both WT and Nrf2$^{-/-}$ groups, indicating a relevant basal partial relationship between metabolic and microvascular endothelial oscillators. This finding might suggest a relevant interaction between cellular metabolic oscillatory processes and microvascular dynamics in the skin. However, because the WPCO analysis in this dissertation does not include the surrogate data testing described recently by Gruszecki *et al.* [165], the assumptions above on the degree of baseline coherence might not be reliable due to bias affecting the WPCO values at the low frequencies. Nonetheless, cautious comparisons of the differences between mouse groups and changes in response to PE stimulation can be made.

Differences of phase coherence between WT and oxidative stress phenotypes

Also in this case, as discussed in the previous section (paragraph 3.3.2, page 143), the RR MO-1 oscillator was more informative than NAD(P)H MO-1 showing relevant differences between WT and Nrf2$^{-/-}$ animals. Indeed, non-significant differences were found between groups (Table 7) or between baseline and PE iontophoresis time points (Fig. 57) for the $C\phi(\omega k)_{NAD(P)H\ MO\text{-}1/EDHF}$. In contrast, the $C\phi(\omega k)_{RR\ MO\text{-}1/EDHF}$ was significantly lower in the Nrf2$^{-/-}$ compared with WT mice at baseline ($p < 0.01$) (Table 7), indicating a major interaction between mitochondrial reactions and the EDHF vasodilation pathway in the WT group.

Table 7 Phase coherence between metabolic and EDHF oscillators during iontophoresis. Data are expressed as mean ± SD. *Cϕ(ωk)* = Wavelet phase coherence. PE = phenylephrine. MO-1 = Metabolic oscillator-1. EDHF = Endothelial-derived hyperpolarizing factor. NAD(P)H = Nicotamide adenine dinucleotide. RR = Redox ratio. Differences between groups were calculated by unpaired t-test and are outlined by red asterisks. Differences between baseline and PE time points were estimated by paired t-test and are outlined by black asterisks. **p < 0.01. *p < 0.05.

	WT (n=5)		Nrf2$^{-/-}$ (n=6)	
Variable	**Baseline**	**PE**	**Baseline**	**PE**
$C_\phi(\omega_k)_{NAD(P)H\ MO\text{-}1/EDHF}$	0.78 ± 0.03	0.76 ± 0.05	0.76 ± 0.05	0.79 ± 0.05
$C_\phi(\omega_k)_{RR\ MO\text{-}1/EDHF}$	**0.79 ± 0.04	0.76 ± 0.02*	**0.74 ± 0.06	0.78 ± 0.02**

The $C\phi(\omega k)_{RR\ MO\text{-}1/EDHF}$ changed significantly in both groups also during PE delivery, showing a decrease of coherence in WT mice ($p < 0.05$) and an increase of coherence in Nrf2$^{-/-}$ animals ($p < 0.01$) (Fig. 57b). Overall, these results outline a different interaction and coupling between RR MO-1 and the EDHF oscillators in WT mice compared to animals with altered redox conditions and impaired antioxidant defence. The multi-parametric integration of these data with the results obtained for the LDF oscillators highly indicates that the different phase interaction between metabolic and EDHF oscillators observed in WT and Nrf2$^{-/-}$ mice may be a factor determining the different microvascular reactivity to PE vasoconstriction stimulus found between the tested groups.

Phase coherence data may reflect the mechanisms of activation of EDHF

In summary, the wavelet phase coherence data have outlined a relevant degree of interaction between mitochondrial metabolic cyclic reactions (RR MO-1) and the EDHF endothelium-mediated vasodilation (EDHF oscillator), which may change depending on the presence of a specific phenotype (i.e. high oxidative stress) or the challenge with a particular stimulus (i.e. administration of PE).

The EDHF mechanism may be activated by different cellular pathways, including the electric signalling through gap junctions, chemical signalling through K^+ channels, or signalling pathways associated with the release of chemical metabolites, i.e. epoxyeicosatrienoic acids (EETs). Considering the metabolic origin of RR MO-1 oscillations, it could be hypothesised that the coherence between RR MO-1 and the EDHF oscillator may reflect the degree of activation of the EDHF mechanism mediated by metabolic factors such as EETs. However, these hypotheses are proposed based on indirect assumptions suggested by the integration of multi-parametric data. Therefore, as future perspective, further experiments are required to better clarify the physiological meaning of $C\phi(\omega k)_{RR\ MO\text{-}1/EDHF}$ and any possible link with the activation/inactivation of EDHF by EETs or through other cellular pathways (gap junctions or K^+ channels). This may be achieved by using the methodology implemented in this study in combination with the local administration of drugs for the specific inhibition of EETs biosynthesis, or for the inhibition of K^+ channels.

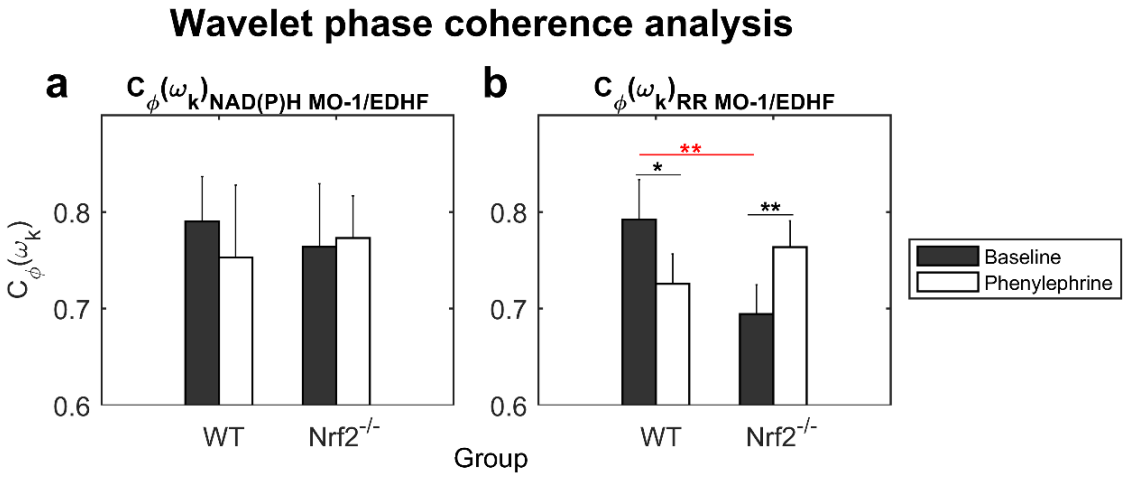

Fig. 57 Trends of phase coherence $C_\phi(\omega_k)$ between metabolic and EDHF oscillators during iontophoresis. Graphic representation of the data reported in Table 7. (**a**) Phase coherence between NAD(P)H MO-1 and EDHF oscillators. (**b**) Phase coherence between RR MO-1 and EDHF oscillators. NAD(P)H = Nicotamide adenine dinucleotide. MO-1 = Metabolic oscillator-1. EDHF = Endothelial-derived hyperpolarizing factor. RR = Redox ratio. Data are presented as bar plots of the mean value with error bars corresponding to 2SE (~95% confidence interval). The black lines refer to significant differences between baseline and PE time points. The red lines refer to significant differences between WT (n=5) and $Nrf2^{-/-}$ (n=6) mice. Differences between baseline and PE time points were calculated by paired t-test. Differences between mice groups were calculated by unpaired t-test. *p < 0.05, **p < 0.01.

3.4.2 Relevant correlations and role of the endothelium and metabolic oscillators in vasomotion

Correlations in the WT mouse model

Negative correlations were observed between the wavelet energy of NAD(P)H MO-1 and the wavelet energy of endothelial EDHF (r=-0.82, p < 0.01), endothelial NO (r=-0.77, p < 0.01), neurogenic (r=-0.71, p < 0.05) and myogenic (r=-0.68, p < 0.05) oscillators (Fig. 58).

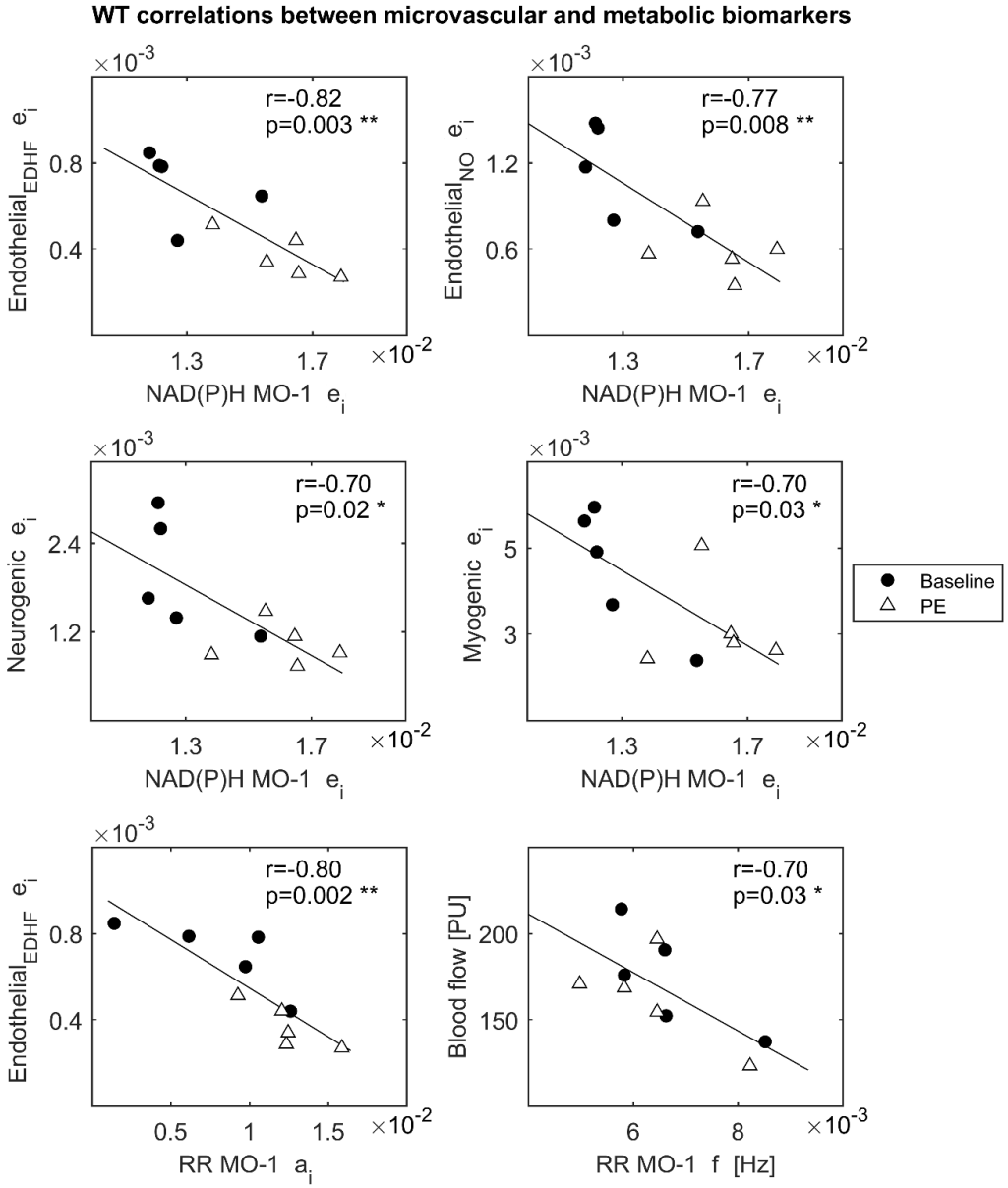

Fig. 58 Relevant correlations in the WT group. All the parameters analysed in this part of the work showed a Gaussian distribution. Thus, correlations were assessed by the calculation of the parametric Pearson's coefficient *r*. The analysis was performed using the function *corr* of Matlab R2015a (*The MathWorks Inc.*) software. The correlations were considered significant for p < 0.05 and values of *r* > 0.5 or < -0.5. Black dots = Baseline (n=5). White triangles = PE challenge (n=5). *p < 0.05, **p < 0.01.

The wavelet amplitude/energy of RR MO-1 also showed negative correlations with the energy/amplitude of endothelial EDHF (r=-0.84, $p < 0.01$), endothelial NO (r=-0.65, $p < 0.05$) and myogenic (r=-0.69, $p < 0.05$) oscillators, and with blood perfusion (r=-0.70, $p < 0.05$) (Fig. 58). None of these correlations between metabolic and microvascular oscillators were observed in the $Nrf2^{-/-}$ mice, except for the correlation between the energy/amplitude of RR MO-1 and blood perfusion which was positive in the KO mice (r=0.67, $p < 0.05$). These findings point to an involvement of the cellular oxido-reductive oscillatory processes in the vasomotor response enhanced by α-adrenergic stimulation. The results suggest a strong link between the cellular fluctuations of NAD(P)H involved in the production of ATP energy and the activation/inactivation of the microvascular pathways for the modulation of vascular tone. Indeed, the correlations indicate that during the response to a low-dose of PE in WT mice the energy/amplitude of microvascular oscillators decreases as the energy/amplitude of slow metabolic oscillators increases. This may reflect a change in the turnover between $NAD(P)^+$ and NAD(P)H promoting the decrease of the vasodilator activity mediated by EDHF and NO endothelial pathways, and inducing contraction of the smooth muscle and vasoconstriction.

Role of endothelium and metabolic oscillators in vasomotion

The fact that the strongest correlations were found for the EDHF and NO endothelial oscillators suggests an important role of endothelium in the modulation of small arterioles diameter during α-adrenergic stimulation, probably due to the direct targeting of ECs by PE. However, correlations were also found between metabolic oscillators and the neurogenic and myogenic wavelet components, suggesting a global involvement of all the microvascular components for the modulation of the vascular tone in response to an external vasoconstrictor stimulus. In this context, the EDHF could represent the key signalling pathway for the myoendothelial bidirectional communication by gap junctions or K^+ Ca^{2+}-dependent channels [140], which may promote Ca^{2+} fluctuations in VSMCs and vasomotion in response to primary Ca^{2+} oscillations of metabolic origin arising from ECs. These findings, could offer a novel mechanism for describing vasomotion. Indeed, in the literature vasomotion has always been described as a process mainly induced by the spontaneous pacemaker activity of VSMCs [111], originating from the interaction between

cellular cytosolic and membrane Ca^{2+} oscillations due respectively to the release of Ca^{2+} through the sarcoplasmic reticulum [110, 142, 143] and the opening activity of Ca^{2+} or K^{+} channels in the cell plasma membrane [110, 111, 144]. However, the results in this dissertation suggest that vasomotion may have a different origin depending on the nature of the stimulus affecting the microcirculation and the microvascular bed under investigation. For example in this case, a role of the endothelium in vasomotion of skin micro-vessels has been observed, which is in agreement with other studies in rat mesenteric artery that have proposed an important contribution of ECs to vasomotion [138, 139, 140].

Moreover, the outcomes of this study open a novel scenario for the elucidation of the cellular mechanisms at the basis of vasomotion. Indeed, the results have outlined a possible role of cellular metabolic oscillators for driving vasomotion in response to specific stimuli. Although in the past the existence of metabolic oscillators involved in the cellular origin of vasomotion has been proposed, this aspect has never been examined in depth [110, 111]. This is probably due to the underestimation of the role of endothelial cells in vasomotion, which according to the observations in this work seem to be the microvascular component mostly associated with slow metabolic oscillators. The hypothesis proposed in this work is supported further by recent studies that have proved the existence of cellular fluctuations of Ca^{2+} of glycolytic [89, 145, 146] or mitochondrial [129, 131, 134] metabolic origin. Therefore, the obtained results raise the interest for the further study of cellular mitochondrial and glycolytic oscillators as possible factors that may drive the Ca^{2+} oscillations at the basis of vasomotion. This would allow obtaining a more complete overview of the cellular mechanisms involved in vasomotion, including also the possible involvement of ECs and metabolic oscillations depending on the vascular bed under investigation and the kind of stimulus challenging the microcirculation. Furthermore, a shortcoming of the method used in this study is the under sampling of NAD(P)H autofluorescence spectra leading to the impossibility of tracing fast metabolic oscillations. Therefore, it cannot be excluded the existence of faster NAD(P)H oscillations of glycolytic and mitochondrial origin that may arise also from VSMCs, leading to Ca^{2+} oscillations and vasomotion events of metabolic origin mainly mediated by the smooth muscle.

Novel concept of vasomotion

According to the previous comments (pages 149-150), vasomotion could be defined as an adaptive mechanism of the microvascular tone in response to the energetic requirements of the surrounding tissue aimed at ensuring a suitable intake of nutrients (e.g. glucose) and oxygen for the production of ATP, rather than a spontaneous phenomenon due to the pacemaker activity of VSMCs. This definition may explain better several unclear aspects of vasomotion such as the contrasting fact that the oscillations of the vascular diameter might be associated with both healthy and diseased conditions [110, 111], and the primary involvement of ECs or VSMCs activity depending on the vascular bed under investigation or the stimulus affecting the microcirculation [110, 111]. Indeed, all of these aspects may be influenced by the nutritive and oxygen requirements and in general the molecular signalling in the environment (parenchymal tissue) surrounding the microvascular network, which may vary depending on the degree of oxygenation of the tissue, the presence of a particular pathology, and the kind of tissue/cells from which is arising the primary stimulus inducing the adaptation of microvascular tone. Based on these assumptions for example, in the presence of a pathology affecting blood vessels, e.g. hypertension, the primary stimulus for vasomotion may arise with high probability from the endothelium, which is the most internal microvascular layer at direct contact with the blood able to sense changes in blood pressure inducing the activation of the adaptive mechanisms for counteracting abnormal pressure conditions. In contrast, it could be supposed that pathologic conditions involving the cutaneous cells, e.g. melanoma cancer, may induce either vasomotion events mediated by VSMCs in the median layer of micro-arterioles that may communicate and receive signals from the surrounding tissue earlier than arteriolar ECs, or vasomotion events mediated by signals coming from the single-layer of ECs that constitutes the capillaries at direct contact with the diseased tissue. These examples could also explain why in some cases vasomotion is induced directly by VSMCs (especially for larger arteries) and in other cases is involving the modulation of ECs.

Moreover, in literature it has been reported that the factors released by microcirculatory ECs (NO, EDHF through EETs, etc.) could diffuse to the underlying parenchymal tissue exerting regulatory effects on mitochondrial metabolism, the production of ROS and inflammation [11, 166, 167]. Therefore,

considering that the autofluorescence signal analysed in this dissertation has a prevalent epidermal origin, the correlations found between metabolic oscillations and vasomotion may reflect the communication/interaction between the cutaneous tissue and the microcirculation to satisfy the metabolic demand of the organ in response to a specific stimulus, which in this case is the α-adrenergic stimulation induced by administration of PE.

Correlations in the Nrf2$^{-/-}$ model

No significant correlations were found between metabolic and microvascular oscillators in Nrf2$^{-/-}$ mice. This suggests that oxidative stress may impact the interaction between these factors, probably by affecting the dynamics of the cellular oxido-reductive processes due to the accumulation of reactive oxygen species. This could induce a switch towards regulatory mechanisms of the microvascular tone different from the normal physiological pathways involved in vascular reactivity, and may promote the onset of metabolic and cardiovascular disorders in the long term.

The most relevant correlations found in Nrf2$^{-/-}$ mice were associated with the wavelet frequency of the endothelial NO oscillator, which showed a positive correlation with the e_i of the NAD(P)H MO-1 (r=0.58, $p < 0.05$) oscillator, and a negative correlation with oxygen saturation SO_2 (r=-0.61, $p < 0.05$) (Fig. 59).

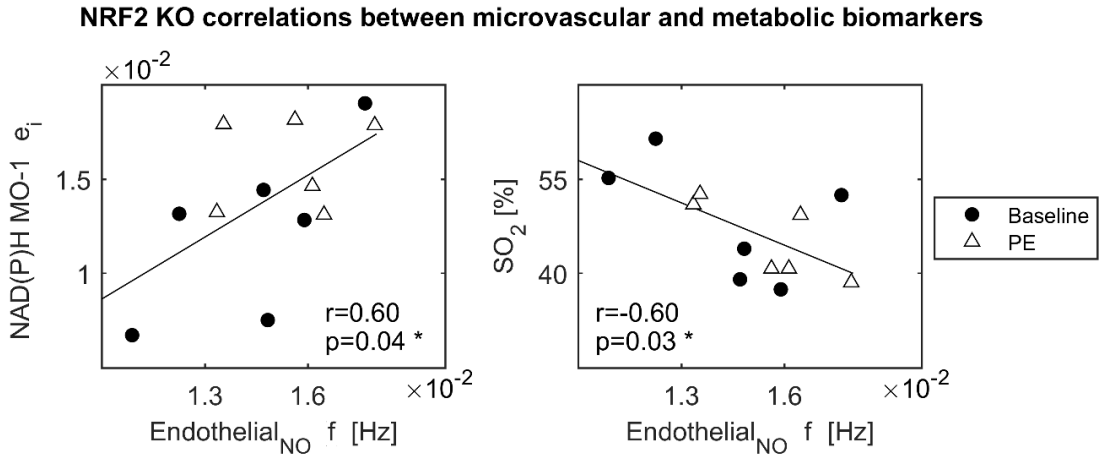

Fig. 59 Relevant correlations in the Nrf2$^{-/-}$ group. All the parameters analysed in this part of the work showed a Gaussian distribution. Thus, correlations were assessed by the calculation of the parametric Pearson's coefficient *r*. The analysis was performed using the function *corr* of Matlab R2015a (*The MathWorks Inc.*) software. The correlations were considered significant for $p < 0.05$ and values of $r > 0.5$ or < -0.5. Black dots = Baseline (n=6). White triangles = PE challenge (n=6). *$p < 0.05$.

Furthermore, oxygen saturation was also in a positive correlation with the phase shift ($\phi_{NAD(P)H\ MO\text{-}1}$ - $\phi_{Endothelial\ NO}$) between NAD(P)H MO-1 and the endothelial NO oscillators (r=0.60, $p < 0.05$). The phase shift was estimated as the difference between the ϕ extracted from the NAD(P)H MO-1 wavelet frequency interval, and the ϕ estimated from the endothelial NO wavelet frequency interval.

Considering that both SO_2 and the frequency of the endothelial NO oscillator did not show significant changes during stimulation with PE (Fig. 51 and Fig. 54, respectively), this set of correlations is probably indicating a general basic link between these variables in the Nrf2$^{-/-}$ mice rather than a correlation associated with the response to PE. More details on the possible meaning of these findings are provided below.

The NO pathway may be up-regulated in the skin microcirculation of Nrf2$^{-/-}$ mice to balance for dysfunction in the EDHF vasodilation mechanism

The correlations mentioned above might reflect a general overexpression of the eNOS (endothelial nitric oxide synthase) enzyme, which has been described previously in Nrf2$^{-/-}$ mice [159]. The up-regulation of eNOS leads to increase of NO production, probably to balance a dysfunction in other vasodilator signalling pathways as an attempt to preserve vascular function in blood vessels affected by oxidative stress [159]. The set of correlations found in this study may support this evidence. Indeed, according to the literature NADPH and molecular oxygen participate in the reaction for NO synthesis [168], and in this dissertation the increase of the endothelial NO wavelet frequency (might reflect augmentation of NO production) was found significantly correlated with the decrease of SO_2 (might reflect consumption of molecular oxygen) and the increase of NAD(P)H wavelet energy (might reflect the oxidation of NADPH in $NADP^+$). Moreover, the positive correlation of SO_2 with the phase shift between NAD(P)H MO-1 and endothelial NO oscillators supports further this hypothesis, indicating that as the coupling between NAD(P)H MO-1 and NO activities increases (reduction of phase shift) the amount of O_2 decreases, which may reflect NO production.

The correlation between augmented NO frequency and reduced SO_2 might reflect with high probability also the formation of peroxynitrite ($ONOO^-$) in response to oxidative stress and inflammation, due to a chemical reaction between the free radicals NO and superoxide anion ($O_2^{\bullet -}$) that are produced in relevant amounts in the presence of oxidative damage [169]. Considering that

peroxynitrite is a strong oxidant [169], this would explain also the increase of NAD(P)H wavelet energy probably associated with oxidation of the coenzyme.

As shown in the section 3.4 (paragraph 3.4.1, page 145), lower baseline phase coherence was observed between RR MO-1 and the EDHF oscillators in $Nrf2^{-/-}$ mice compared to WT (Table 7). This finding is explained as a probable lower baseline interaction between the EDHF and metabolic oscillators, which may reflect reduced basal vasodilator EDHF activity in $Nrf2^{-/-}$ compared to normal mice. Based on these findings, it could be speculated that the sustained NO activity/production suggested by the correlations discussed above may be a compensatory mechanism to counteract the reduced activity of EDHF, which is a dominant pathway in the peripheral microcirculation.

As future perspective, these hypotheses may be validated by performing the evaluation of microvascular dynamics concurrently with molecular biology analysis of eNOS expression in the skin region used for testing the microcirculation. This would allow checking if any correlation is present between the degree of expression of the eNOS enzyme and the wavelet frequency or amplitude/energy of the endothelial NO oscillator, the wavelet amplitude/energy of the NAD(P)H metabolic oscillator and the average SO_2.

These interesting findings suggest in general that the multi-parametric integration of non-invasive microvascular data obtained by laser techniques might have the potential of providing specific information on the degree of activation/inactivation of cellular molecular pathways involved in microvascular function. Therefore, in the future would be highly appropriate the combination of these kind of studies with parallel molecular biology investigations, which could help to decode the molecular signalling pathways at cellular level associated with specific features of the physics signals obtained from laser scans.

4 Nonlinear dynamics of microcirculation and cell energy metabolism in human individuals

4.1 Introduction and aims

In this part of the work, the nonlinear dynamics of microvascular and metabolic cutaneous signals were investigated in human subjects. The work was carried out on 40 volunteers divided in two groups: 20 smokers and 20 non-smokers. The subjects were tested from the forearm skin location by non-invasively evaluating the microcirculatory and metabolic biomarkers during a PORH test. The wavelet spectral analysis was applied on simultaneous LDF, NAD(P)H and RR time series to achieve the following objectives:

(1) Characterisation of blood flow oscillators and NAD(P)H and RR metabolic oscillations from human skin.
(2) Assessing the potential application of microvascular and metabolic oscillators as preclinical predictors of CVD risk in smokers.
(3) Study the relationship between metabolic oscillators and human vasomotion.
(4) Assessing the potential use of “attractors” as predictors of risk in smokers.

This chapter includes the analysis of a large amount of data, which could make it difficult to get an idea of what is the overall picture. Therefore, a brief summary of the main results will follow as a guide for the reader before going into details, to outline what are the sections/paragraphs describing the parameters that showed the major differences between controls and smokers, the most relevant findings related to the study of vasomotion, and the set of correlations and interactions taken into account to hypothesise the role of metabolic oscillators in human cutaneous PORH.

4.1.1 Summary of the best variables eligible as predictors of CVD risk

General microcirculation variables (section 4.3, paragraph 4.3.1, page 160)

Within the general microcirculatory variables assessed in the study, the baseline perfusion and the area under the curve (AUC) of PORH peak were the best factors outlining differences between smokers and controls. However, these variables showed less significant differences compared to the nonlinear biomarkers.

Tissue oxygenation dynamics (section 4.3, paragraph 4.3.2, page 162)

Within tissue oxygenation parameters, the oxygen consumption (VO_2) displayed a significant difference between the examined groups, with lower values in smokers during PORH response probably reflecting slower oxidative metabolism.

General metabolic variables (section 4.3, paragraph 4.3.3, page 163)

Within the general metabolic variables, $NAD(P)H_{normalised}$ showed slight differences between the two groups, with higher values in smokers probably reflecting higher oxidative stress.

LDF oscillators (section 4.4, paragraph 4.4.1, page 171)

The dynamic biomarkers of microcirculation displayed robust differences between the two groups. Specifically, the wavelet amplitude/energy of local microvascular oscillators (endothelial EDHF, endothelial NO, neurogenic and myogenic) was significantly higher in smokers, probably reflecting an adaptive hyperactive microvascular response to the early risk. The respiratory oscillator showed also robust differences with higher spectral energy in smokers, probably reflecting a greater resistance of peripheral skin arterioles compared to controls.

Metabolic oscillators (section 4.4, paragraph 4.4.3, page 187)

The dynamic biomarkers of cellular energy metabolism did not show significant differences, suggesting that healthy smokers are still characterised by an overall functioning cell energetic metabolism.

Attractors (section 4.6, paragraph 4.6.1, page 196)

Within the LDF attractors analysed in this study, the fractal dimension D, the correlation dimension D_2, and the information dimension H_i showed relevant differences between smokers and non-smokers. However, the interpretation of these parameters must be done with caution because they provide variable results depending on the kind of analysed signal and the health conditions of the subjects under examination. Therefore, more research is needed to characterise better the full picture of these markers.

4.1.2 Summary of the study of vasomotion and correlations/interactions between vascular and metabolic oscillators

Role of LDF oscillators in skin PORH (section 4.4, paragraph 4.4.2, page 176)

The analysis of the percentage increase of wavelet amplitude/energy of LDF oscillators allowed the characterisation of the contribution of each microvascular component to PORH vasomotion. The major contributor was the endothelial EDHF oscillator in agreement with what has been described in the literature [9].

Relevant correlations and role of metabolic oscillators in skin PORH vasomotion (section 4.5, paragraph 4.5.1 at page 189 and paragraph 4.5.2 at page 192)

The study of correlations and interactions (phase coherence) between metabolic oscillators and microvascular variables has revealed a role of the RR MO-1 oscillator in modulating the reactive hyperaemia peak concurrently with the EDHF oscillator. Specifically, the set of correlations suggests that during PORH the endothelial EDHF pathway could be activated preferentially through the release of EETs metabolic factors in healthy control subjects. On the other side, the exposure to tobacco may lead to impairment of EETs mechanism and preferential exogenous activation of EDHF by gap junctions or K^+ channels signalling.

4.2 General variables of the studied groups

Table 8 displays a summary of the exclusion and inclusion criteria adopted for the recruitment of control and smoking subjects.

Table 8 Inclusion and exclusion criteria. All the subjects were recruited ensuring the apparent absence of any pathological condition, especially CVD, diabetes and respiratory diseases.

Controls (n=20)		Smokers (n=20)	
Inclusion criteria	**Exclusion criteria**	**Inclusion criteria**	**Exclusion criteria**
Non-smoker	Smoker	Smoking traditional cigarettes	Non-smoker or smoking e-cigarettes
No CVD	CVD	No CVD	CVD
No diabetes	Diabetes	No diabetes	Diabetes
No respiratory disorders	Respiratory disorders	No respiratory disorders	Respiratory disorders
No hypertension	Hypertension	/	/

More details on the recruitment process and allocation of volunteers to the final study groups can be found in the section 2.5 (paragraph 2.5.1, page 119).The choice of examining healthy mild smokers was aimed at testing the potential

application of the nonlinear dynamic markers as preclinical predictors of cardiovascular risk, which could be eligible to trace the early stages of vascular dysfunction associated with smoke. The main clinical parameters of the control and smoker groups examined in this study are reported in Table 9.

Table 9 General parameters of the studied population. Data are presented as mean ± SD. The p-values were calculated by unpaired t-test. BMI = Body mass index. SBP = Systolic blood pressure. DBP = Diastolic blood pressure. T = temperature. S_pO_2 = Pulse oximetry arterial oxygen saturation. p = p-value. NA = Not applicable.

Variable	Controls (n=20)	Smokers (n=20)	p
Males	5	5	NA
Females	15	15	NA
Age [years]	41.0 ± 14.0	42.6 ± 15.6	0.70
Smoking/years	0	24.1 ± 14.4	NA
Cigarettes/day	0	12.4 ± 5.50	NA
Pack years	0	15.7 ± 12.8	NA
Weight [kg]	66.8 ± 12.1	70.6 ± 16.6	0.40
Height [cm]	168.1 ± 12.20	165.9 ± 8.30	0.50
BMI [kg/m^2]	23.5 ± 2.90	25.4 ± 4.90	0.15
SBP [mmHg]	120.9 ± 10.80	124.7 ± 15.20	0.40
DBP [mmHg]	78.1 ± 18.4	74.9 ± 10.2	0.50
Skin T [°C]	32.2 ± 1.80	31.8 ± 1.20	0.40
S_pO_2 [%]	98.0 ± 0.90	97.8 ± 1.20	0.70

The two groups were matched for age and sex. Smokers were aged 19 to 69 years, while non-smokers were 18 to 64 years old. The 75% of the study population was made of females. From one side this could be a disadvantage because data can be affected by a more variable physiology due to hormone level variations across the menstrual cycle. However, testing a major number of females can be an advantage to discover novel biomarkers of risk for women. Indeed, women are characterised by a different aetiology and incidence of CVD compared to men that frequently cannot be explained by traditional risk factors, thus more research is required to find novel biomarkers that could improve the assessment of risk for females.

Non-significant differences were observed between controls and smokers in relation to general variables such as weight, height, BMI (body mass index), BP (blood pressure), skin temperature and arterial oxygenation variables (Table 9). Therefore, the main feature distinguishing the tested groups was smoking. The

recruited smokers had a duration of smoking between 3 to 50 years, with an exposure to cigarette smoking between 1.5 to 40 pack years.

4.3 Results of PORH test

4.3.1 Blood flow and PORH response

Fig. 60 displays the comparison of the median blood perfusion signals from controls and smoker groups. The graph shows higher basal perfusion in healthy subjects compared to smokers. Moreover, the image shows that although the absolute perfusion peak during PORH response was slightly higher in smokers, the time course of the hyperaemic response represented by the area under the curve (AUC) of the peak was greater in control individuals.

Trends of blood perfusion during PORH test

The trends of the median blood perfusion during reactive hyperaemia test are shown in Fig. 61a. Both groups showed the expected trends related to PORH test stimulation. Blood perfusion was significantly reduced ($p < 0.001$) after blocking of blood flow from the brachial artery to induce an ischaemic low oxygenation condition, and increased significantly ($p < 0.001$) during the adaptive PORH response for the restoration of the physiological cutaneous perfusion after removal of the occlusion.

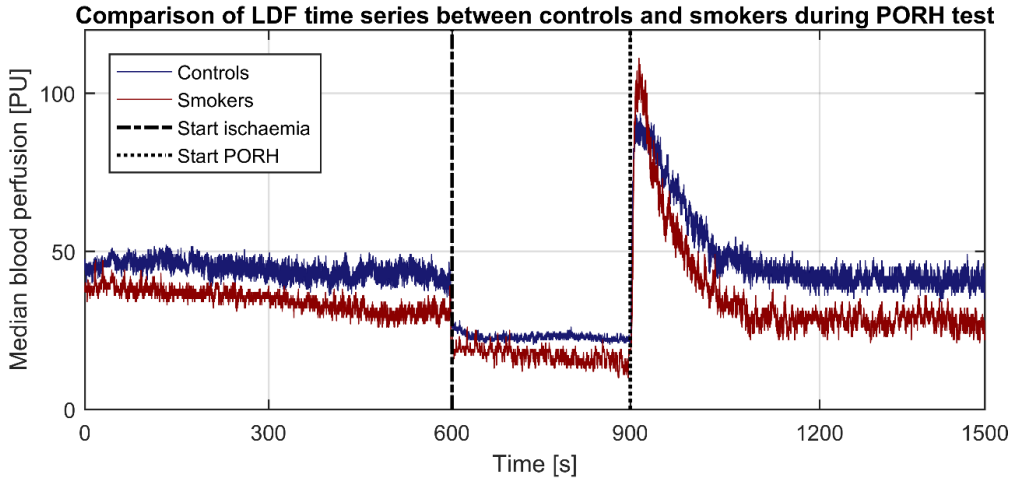

Fig. 60 LDF signals during PORH test. The graph shows the median blood perfusion signals from the forearm of non-smokers (blue line, n=20) and smokers (red line, n=20) during the PORH task: 10-min baseline, 5-min ischaemia, 10-min PORH response. Data are expressed in perfusion arbitrary units (PU). The chart shows the typical trend of PORH test for both groups, characterised by decrease of perfusion during occlusion of flow through the brachial artery and a massive increase of flow up to a peak during PORH response before the restoration of the basal perfusion.

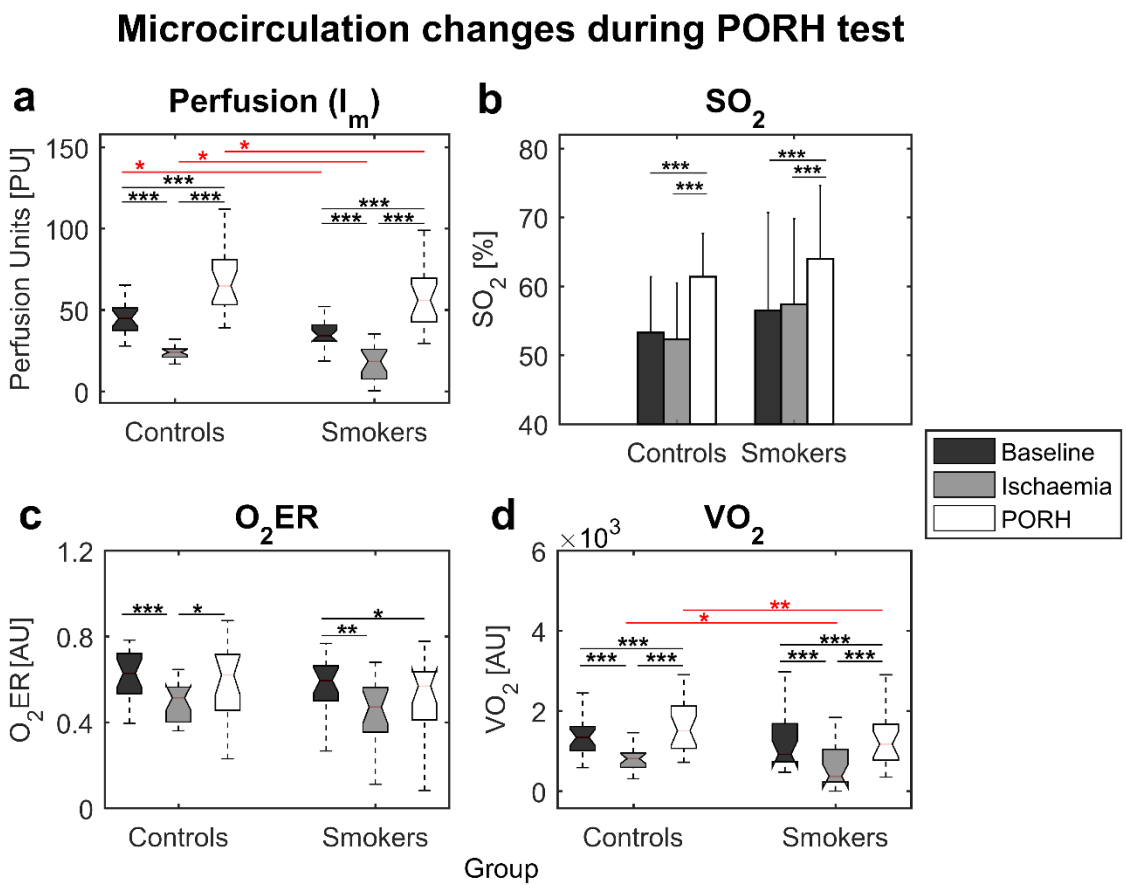

Fig. 61 Trends of microcirculatory and oxygenation parameters during PORH test. (**a**) Blood perfusion (PU). (**b**) SO_2 (%) (Oxygen saturation). (**c**) O_2ER (AU) (Oxygen extraction). (**d**) VO_2 (AU) (Oxygen consumption). Normal data are presented as bar plots of the mean with error bars corresponding to the SD. Non-parametric data are presented as boxplots. Black bars/boxplots = Baseline. Grey bars/boxplots = Ischaemia. White bars/boxplots = PORH. The black lines/asterisks refer to significant changes during PORH task that were estimated by paired t-test and Wilcox test, respectively for normal and non-parametric variables. The red lines/asterisks refer to significant differences between controls and smokers that were estimated by unpaired t-test and Wilcox test, respectively for normal and non-parametric variables. *p < 0.05, **p < 0.01, ***p < 0.001.

Differences of microcirculatory variables between groups

Table 10 shows the differences in blood perfusion and PORH response between controls and smokers. As reported in other studies [170, 171], the baseline blood perfusion was significantly lower ($p < 0.05$) in smokers compared to non-smokers (31.3% lower), indicating a reduced basal microcirculation under the effect of tobacco. The PORH response was assessed in terms of absolute flux peak, AUC of the flux peak, and time to reach the flux peak. The results are similar to those reported in the study by Noble *et al.* [172] from the sacrum skin location, showing non-significant differences between groups in relation to the maximum perfusion

peak or the time to reach the peak, while the AUC of the flux peak was significantly higher ($p < 0.05$) in the controls (16.4% higher).

Table 10 Comparison of blood perfusion and PORH response between controls and smokers. Data are presented as median (inter-quartile range). PU = Perfusion arbitrary units. AUC = Area under the curve. AU = arbitrary units. s = seconds. Differences between groups were evaluated by unpaired Wilcox test and are outlined by red asterisks. p = p-value. *p < 0.05.

Variable	Controls (n=20)	Smokers (n=20)	p
Baseline flux [PU]	44.9 (37.9-50.1)	34.2 (31.2-40.3)	*0.01
Absolute flux peak [PU]	106.0 (90.00-127.2)	117.5 (103.0-130.2)	0.60
AUC of the flux peak [AU]	11200 (9400-13900)	9600 (7400-11400)	*0.04
Time to peak [s]	13.8 (10.0-23.6)	11.3 (4.90-13.2)	0.10

The results agree with a better overall microvascular function in non-smokers compared to healthy mild smokers, confirming the early negative effect of tobacco on skin microvascular reactivity. However, the differences between groups were not large, probably due to the lower average age of the tested subjects compared to other studies (41 ± 14 years controls, 42.6 ± 15.6 years smokers), the major number of females enrolled in the study characterised by minor CVD risk, and the good health status of the individuals in the smoking group who were not suffering of cardiovascular, respiratory or metabolic disorders.

4.3.2 Tissue oxygenation

Trends of tissue oxygenation parameters during PORH test

Both groups showed similar trends of oxygen saturation (SO_2), oxygen extraction (O_2ER) and oxygen consumption (VO_2) during the stages of PORH test (Fig. 61b-d). The percentage SO_2 did not decrease significantly during ischaemia (Fig. 61b), indicating the ability to maintain tissue oxygenation during blocking of blood flow. SO_2 increased significantly ($p < 0.001$) during PORH compared to both ischaemia and baseline (Fig. 61b) due to reperfusion of the tissue. O_2ER is the ratio between the consumption and delivery of oxygen. O_2ER decreased significantly ($p < 0.001$ controls, $p < 0.01$ smokers) during ischaemia (Fig. 61c) due to the increased delivery of O_2 to tissue in response to hypoxic stress. O_2ER was normally restored during PORH in the controls with a significant increase ($p < 0.05$) compared to ischaemia (Fig. 61c). In contrast, smokers maintained a significantly reduced O_2ER ($p < 0.05$) during PORH compared to baseline (Fig. 61c), which may indicate a slower metabolic rate leading to longer time for

restoring the physiological aerobic metabolism. VO_2 was significantly reduced ($p < 0.001$) in both groups during ischaemia compared to baseline (Fig. 61d), due to anaerobic conditions reducing the conversion of O_2 in ATP. Finally, oxygen consumption increased significantly ($p < 0.001$) in both groups during PORH response (Fig. 61d), indicating the ability to restore the normal aerobic energy metabolism after the stress period.

Differences of tissue oxygenation variables between groups

The inter-group differences related to tissue oxygenation are summarised in Table 11. The SO_2 and O_2ER were not significantly different between smokers and controls. However, VO_2 was significantly higher in the controls during ischaemia ($p < 0.05$) and PORH ($p < 0.01$) time points, suggesting the ability of non-smokers to use and convert a major amount of oxygen in ATP energy compared to smokers during the response to hypoxic stress. Overall, the data show healthy tissue oxygenation conditions in both groups. However, the reduced VO_2 values in smokers compared to controls, and the decreased O_2ER during PORH time point compared to baseline in smokers might indicate a slower metabolism rate and reduced ability to convert oxygen in ATP, which may be due to early damage of the micro-vessels wall caused by the exposure to tobacco.

Table 11 Comparison of tissue oxygenation parameters between controls and smokers. The table reports the same data shown in Fig. 61b-d. Normal data are expressed as mean ± SD. Non-parametric data are expressed as median (inter-quartile range). (B) = Baseline. (IS) = Ischaemia. (P) = PORH. SO_2 = Oxygen saturation (%). O_2ER = Oxygen extraction (AU). VO_2 = Oxygen consumption (AU). p = p-values. Differences between groups related to normal and non-parametric variables were assessed respectively by unpaired t-test and Wilcox test and are outlined by red asterisks. *p < 0.05, **p < 0.01.

Variable	Controls (n=20)	Smokers (n=20)	p
(B) SO_2 [%]	53.3 ± 8.10	56.5 ± 14.2	0.100
(IS) SO_2 [%]	52.3 ± 8.20	57.4 ± 12.4	0.100
(P) SO_2 [%]	61.4 ± 6.30	64.0 ± 10.6	0.350
(B) O_2ER [AU]	0.63 (0.54-0.71)	0.60 (0.50-0.66)	0.200
(IS) O_2ER [AU]	0.51 (0.40-0.56)	0.47 (0.36-0.56)	0.400
(P) O_2ER [AU]	0.62 (0.47-0.71)	0.57 (0.42-0.64)	0.200
(B) VO_2 [AU]	1340 (1060-1600)	920 (770-1610)	0.100
(IS) VO_2 [AU]	810 (650-950)	370 (250-1040)	*0.020
(P) VO_2 [AU]	1510 (1090-2110)	1170 (780-1560)	**0.007

4.3.3 NAD(P)H and redox ratio (RR)

Trends of cellular metabolic biomarkers during PORH task

Fig. 62 describes the trends of the $NAD(P)H_{normalised}$ and RR_{index} dimensionless variables during the different steps of reactive hyperaemia functional test. All of the tested groups showed similar trends of $NAD(P)H_{normalised}$ and RR_{index}, indicating an overall normal cell energy metabolism also in the smoking cohort. Both of the variables increased significantly ($0.0001 < p < 0.01$) during the ischaemic hypoxic stress associated with the accumulation of the reduced NAD(P)H, and decreased significantly ($0.0001 < p < 0.05$) during PORH response due to the oxidation of NAD(P)H to $NAD(P)^+$ for the restoration of the physiological aerobic cell energy metabolism that is characterised by a more balanced turnover between the oxidised and reduced forms of the coenzyme.

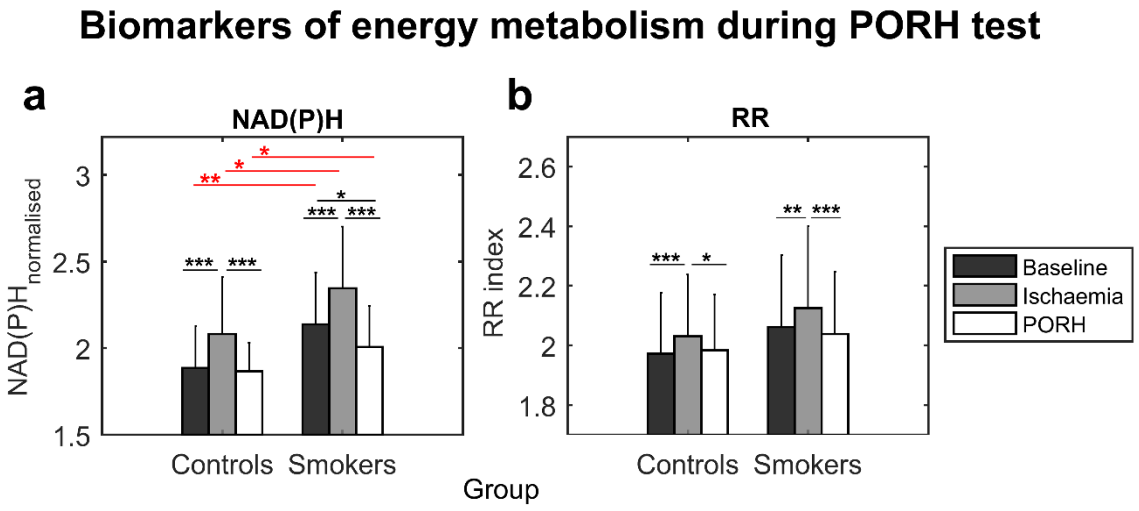

Fig. 62 Trends of biomarkers of cell energy metabolism during PORH. (**a**) $NAD(P)H_{normalised}$ (dimensionless units). (**b**) RR_{index} (dimensionless units). $NAD(P)H_{normalised}$ and RR are dimensionless ratiometric variables, which were calculated according to equations 21-22, respectively. Data are presented as bar plots of the mean with error bars corresponding to the SD. Black bars = Baseline. Grey bars = Ischaemia. White bars = PORH. The black lines/asterisks refer to significant changes during PORH task that were estimated by paired t-test. The red lines/asterisks refer to significant differences between controls and smokers groups that were estimated by unpaired t-test. *p < 0.05, **p < 0.01, ***p < 0.001.

Differences of metabolic biomarkers between groups

The inter-group differences related to biomarkers of energy metabolism are reported in Table 12. The relative amount of $NAD(P)H_{normalised}$ was significantly higher in smokers compared to controls at all the stages of the PORH test (baseline $p < 0.01$, ischaemia $p < 0.05$, PORH $p < 0.05$). This may indicate higher

degree of oxidative stress in smokers. However, non-significant differences were found in relation to the RR_{index}, suggesting that despite a slightly greater oxidative stress smokers presented a “normal” balance between NAD(P)H and FAD^+ ensuring a healthy mitochondrial energy metabolism.

Table 12 Comparison of $NAD(P)H_{normalised}$ and RR_{index} between controls and smokers. The table reports the same data shown in Fig. 62. Data are presented as mean ± SD. (B) = Baseline. (IS) = Ischaemia. (P) = PORH. $NAD(P)H_{normalised}$ = Reduced nicotamide adenine dinucleotide expressed in dimensionless units. RR = Redox ratio index expressed in dimensionless units. $NAD(P)H_{normalised}$ and RR were calculated according to equations 21 and 22, respectively. p = p-values. Differences between groups were examined by unpaired t-test and are outlined by red asterisks. *p < 0.05, **p < 0.01.

Variable	Controls (n=20)	Smokers (n=20)	p
(B) $NAD(P)H_{normalised}$	1.9 ± 0.2	2.1 ± 0.3	**0.006
(IS) $NAD(P)H_{normalised}$	2.1 ± 0.3	2.3 ± 0.3	*0.040
(P) $NAD(P)H_{normalised}$	1.9 ± 0.2	2.0 ± 0.2	*0.020
(B) RR_{index}	2.0 ± 0.2	2.1 ± 0.2	0.200
(IS) RR_{index}	2.0 ± 0.2	2.1 ± 0.3	0.200
(P) RR_{index}	2.0 ± 0.2	2.0 ± 0.2	0.400

4.4 Wavelet spectral analysis of LDF and reconstructed metabolic signals measured during PORH test

4.4.1 LDF oscillators in humans

Fig. 63 illustrates the median time-averaged LDF wavelet spectra from smokers and non-smokers during reactive hyperaemia task. The typical wavelet peaks of cutaneous LDF physiological oscillators reported in the literature were characterised: endothelial NO-independent (EDHF), endothelial NO, neurogenic, myogenic, respiratory and cardiac. The specific features that characterise each LDF oscillator peak are the absolute energy E_i, the absolute amplitude A_i and the frequency location f of the peak, expressed in arbitrary units (AU) and hertz (Hz) respectively. The graphs show differences between groups associated to A_i and E_i of blood flow oscillators. As explained already for the wavelet analysis of mice LDF signals (section 3.3, paragraph 3.3.1, page 131), the wavelet amplitude A_i reflects the maximal oscillatory activity in the frequency interval of interest, while the wavelet energy E_i reflects the overall oscillatory activity in the frequency interval under investigation.

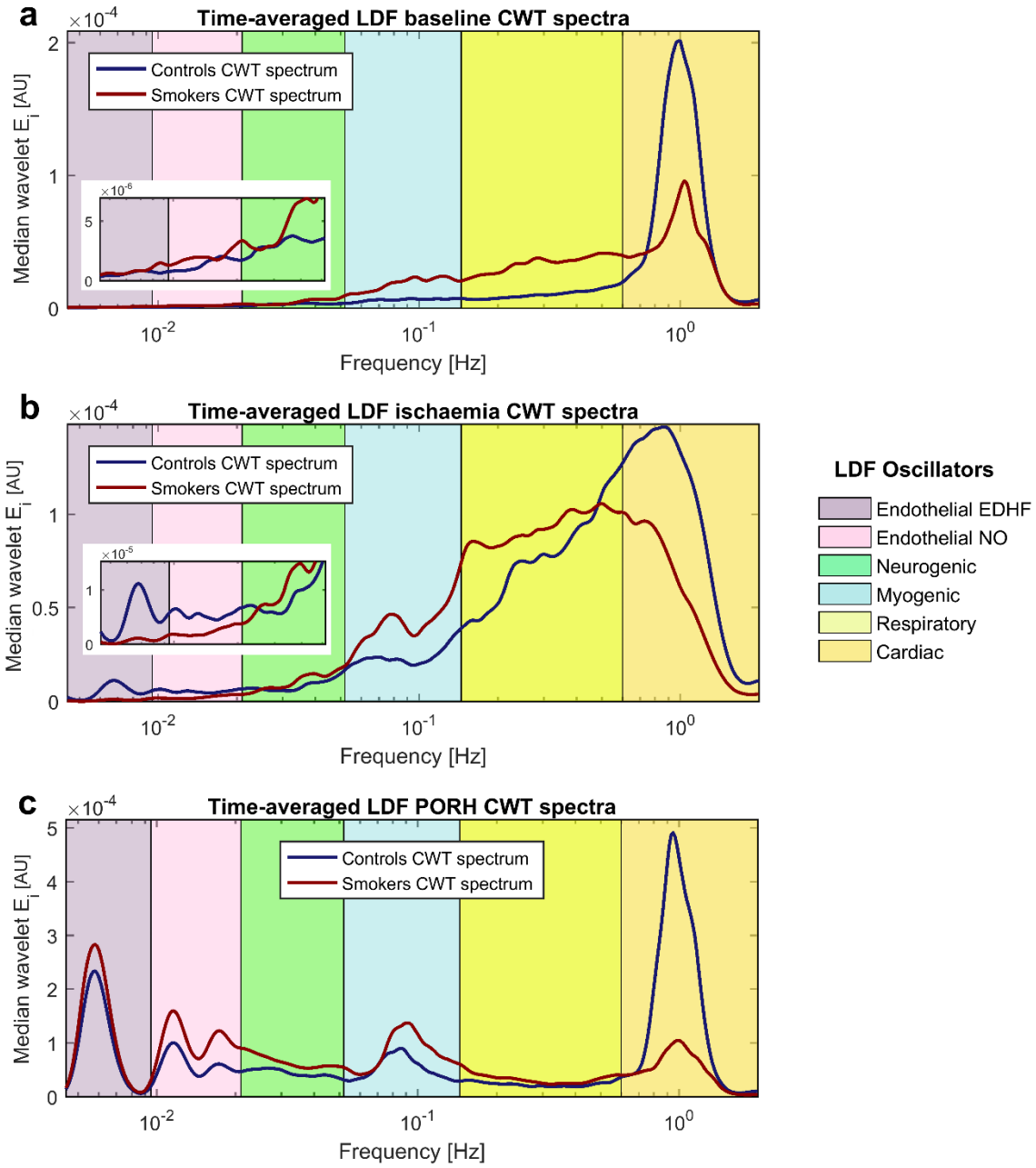

Fig. 63 Comparison of time-averaged blood flow CWT spectra during PORH test. (**a**) Median CWT spectra of controls and smokers at baseline. (**b**) Median CWT spectra during ischaemic stress. (**c**) Median CWT spectra during the hyperaemic response. The plots clearly outline differences in the amplitude A_i and energy E_i of the LDF oscillatory peaks between the two groups. Both of E_i and A_i are expressed in arbitrary units (AU).

Despite in general A_i and E_i trends are similar, sometimes the maximum oscillatory A_i reached during a specific task (e.g. PORH response) might not reflect the overall E_i trend in the interval of interest. For this reason, both parameters were examined for obtaining a better overview of the data avoiding misinterpretations. Moreover, the frequency location f of the oscillator's peak provides different information compared to A_i and E_i, mostly reflecting the rate of

the oscillatory activity rather than the magnitude of the oscillation. Thus, here all these three parameters (A_i, E_i, f) were taken into consideration to gain a complete overview on the oscillatory activity of each specific wavelet oscillator.

As discussed already in the section 3.3 (paragraph 3.3.1, page 132), the heterogeneous anatomy of the cutaneous locations employed for data collection does not allow making reliable comparisons of A_i and E_i between different groups of subjects. For this reason, comparison of wavelet data between controls and smokers was performed by estimating the relative wavelet amplitude a_i and energy e_i of each oscillator (equations 9-12), which are dimensionless variables.

Trends of LDF oscillators during ischaemia

Local microvascular oscillators (EDHF, NO, neurogenic and myogenic). Fig. 64 and Fig. 65 describe, respectively, the trends of the amplitude and energy of LDF oscillators at all the stages of the PORH test. During the 5 min period of ischaemia, a_i and e_i of the endothelial EDHF (Fig. 64-65a) and myogenic (Fig. 64-65d) oscillators increased significantly ($p < 0.01$ or $p < 0.001$) in the control group, and the increase of endothelial NO (Fig. 64-65b) and neurogenic (Fig. 64-65c) amplitudes/energies was close to statistical significance ($p=0.07$ and $p=0.06$, respectively). In contrast, none of the local components (endothelial, neurogenic, myogenic) showed substantial changes compared to baseline in smokers, except for the e_i of the myogenic oscillator (Fig. 65d) which increased significantly ($p < 0.01$) during ischaemia, reflecting an overall increase of VSMCs activity in response to the anoxic stress conditions. These findings might indicate a better local reactivity and adaptation of the cutaneous micro-vessels in non-smokers during anaerobic stress conditions. The rise in endothelial, myogenic and neurogenic activities observed in healthy individuals may be interpreted as a resistance mechanism against ischaemic damage, which might be impaired in smokers due to oxidative stress and the effect of tobacco.

Respiratory oscillator. The a_i and e_i of the respiratory component (Fig. 64-65e) increased significantly in both groups during ischaemia ($p < 0.001$ controls, $p < 0.05$ or $p < 0.001$ smokers). The respiratory oscillation of cutaneous LDF signal is correlated to the volumetric flow of second-order blood pressure wave of skin arterioles [173]. These fluctuations reflect the extrinsic modulation of peripheral arterioles resistance, exerted by coupling of the respiratory and cardiac systems via the autonomous nervous system or by the respiratory-dependent left cardiac

preload [173]. Thus, the increase of respiratory amplitude/energy during ischaemia might reflect the adaptation of skin arterioles resistance (increase of resistance) mediated by the coupling of the respiratory and cardiac systems in response to the increase of pressure induced by the occlusion of blood flow.

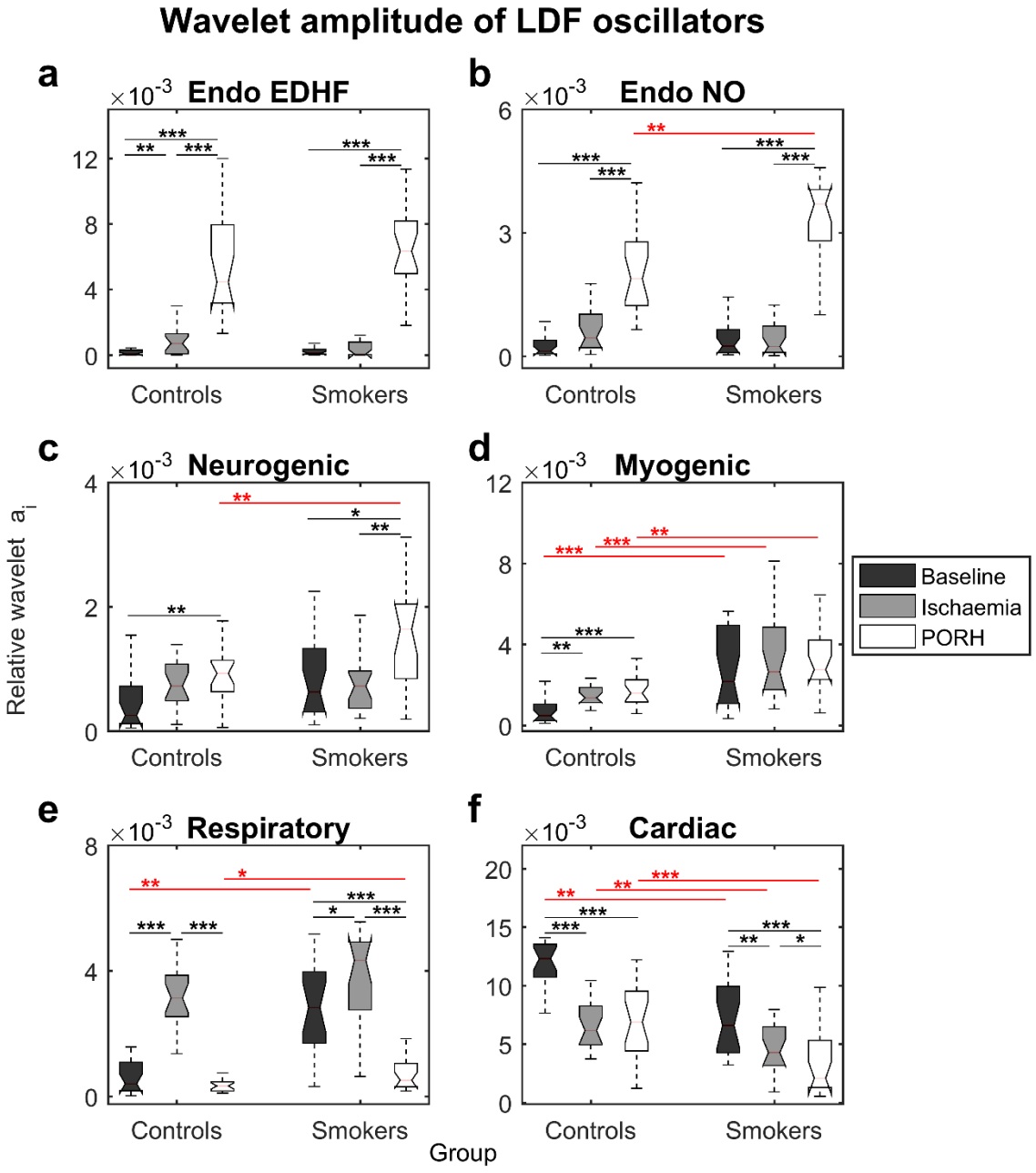

Fig. 64 Trends of the wavelet a_i of LDF oscillators during PORH test. (**a**) Endothelial EDHF, (**b**) Endothelial NO, (**c**) Neurogenic, (**d**) Myogenic, (**e**) Respiratory, and (**f**) Cardiac oscillators. Data are presented as boxplots. The relative wavelet amplitude a_i is expressed in dimensionless units. Black boxplots = Baseline. Grey boxplots = Ischaemia. White boxplots = PORH. The black lines/asterisks refer to significant changes during PORH task that were estimated by paired Wilcox test. The red lines/asterisks refer to significant differences between controls and smokers groups that were estimated by unpaired Wilcox test. *p < 0.05, **p < 0.01, ***p-value < 0.001.

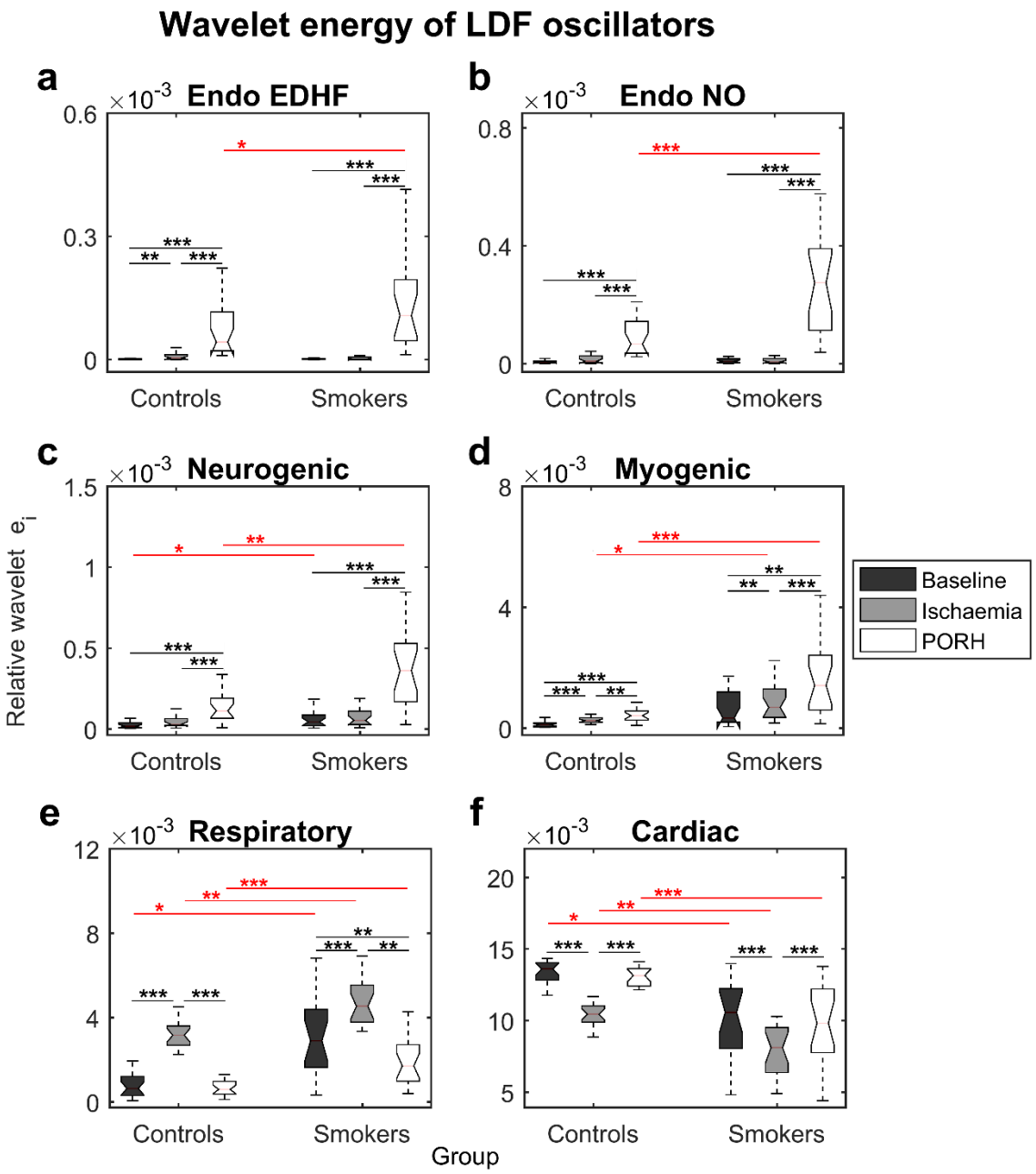

Fig. 65 Trends of the wavelet e_i of LDF oscillators during PORH test. (**a**) Endothelial EDHF, (**b**) Endothelial NO, (**c**) Neurogenic, (**d**) Myogenic, (**e**) Respiratory, and (**f**) Cardiac oscillators. Data are presented as boxplots. The relative wavelet energy e_i is expressed in dimensionless units. Black boxplots = Baseline. Grey boxplots = Ischaemia. White boxplots = PORH. The black lines/asterisks refer to significant changes during PORH task that were estimated by paired Wilcox test. The red lines/asterisks refer to significant differences between controls and smokers groups that were estimated by unpaired Wilcox test. *p < 0.05, **p < 0.01, ***p-value < 0.001.

Cardiac oscillator. The relative a_i and e_i of the cardiac component (Fig. 64-65f) decreased in both groups during ischaemia ($p < 0.001$ controls, $p < 0.01$ or $p < 0.001$ smokers). The cardiac oscillator of LDF cutaneous signal represents a flux motion component correlated to a volumetric flow of first order pressure waves,

reflecting cardiac actions [173], i.e. changes in the volume of blood pumped by the heart (cardiac output). Thus, the decrease of wavelet amplitude/energy probably reflects a reduction of the cardiac output due to the decrease in heart rate and increase in breathing rate observed during the period while the pressure cuff was inflated (ischaemia) (see the frequencies of the cardiac and respiratory oscillators in Table 13 at page 172).

Trends of LDF oscillators during PORH response

Local microvascular oscillators (EDHF, NO, neurogenic and myogenic). The a_i and e_i of the endothelial components showed similar trends in both groups during reactive hyperaemia response. A substantial increase of endothelial EDHF (Fig. 64-65a) and NO (Fig. 64-65b) amplitudes/energies was observed compared to both ischaemia ($p < 0.001$) and baseline ($p < 0.001$). These data confirm the high contribution of the endothelium to skin PORH response. The amplitude/energy of the neurogenic oscillation (Fig. 64-65c) increased in both groups compared to baseline ($p < 0.01$ or $p < 0.001$ controls, $p < 0.05$ or $p < 0.001$ smokers) and ischaemia ($p < 0.01$ smokers, $p < 0.001$ controls), confirming the contribution of the autonomic sympathetic system to the adaptation induced by PORH stimulus, through the transmission of impulses stimulating the activity of the innervated smooth muscle cells (VSMCs).

Both the amplitude and energy of the myogenic component (Fig. 64-65d) during PORH were significantly higher ($p < 0.001$) compared to baseline in healthy subjects, confirming the increased vasodilator activity of smooth muscle cells. In contrast, non-significant changes were found in the myogenic a_i (Fig. 64d) of smokers compared to both baseline and ischaemia time points. Considering that a normal PORH curve was observed for all the smokers tested in the study (Fig. 60), the unchanged myogenic amplitude cannot be interpreted as absence of vasodilator activity of VSMCs. As pointed out before, the wavelet amplitude represents the maximum peak response at a specific frequency interval. This means that in the myogenic frequency interval ($52\text{-}145 \times 10^{-3}$ Hz) of the smoking group, the maximal oscillatory activity was similar during baseline, ischaemia and PORH periods. However, to assess the whole activity in the myogenic range it is also necessary to evaluate the wavelet energy e_i, which represents the overall response in the frequency interval under investigation. The myogenic e_i in

smokers (Fig. 65d) showed a trend different from the a_i, characterised by a significant increase of energy during PORH response compared to both baseline ($p < 0.01$) and ischaemia ($p < 0.001$) time points. This observation demonstrates the importance of assessing both of the wavelet amplitude and energy to gain a complete overview of the data and avoid misinterpretations. Indeed, in this case the unchanged myogenic amplitude during all the stages of the functional test may reflect the same maximum activity peak reached at every stage of the reactive test (baseline, ischaemia, PORH). In contrast, the wavelet energy describes the overall myogenic activity which is increased during the vasodilator reactive hyperaemia response compared to both baseline and ischaemia.

Respiratory oscillator. The trend of the respiratory wavelet amplitude/energy (Fig. 64-65e) during PORH response was similar between the two groups, with a significant decrease compared to ischaemia ($p < 0.001$ or $p < 0.01$). The amplitude was significantly reduced also in relation to baseline in smokers ($p < 0.001$ or $p < 0.01$), while non-significant differences were found between baseline and PORH respiratory a_i and e_i in controls. These observations may reflect the extrinsic respiratory modulation to reduce the resistance of skin arterioles after the release of the pressure applied through the cuff, leading to vasodilation, reperfusion of the tissue and restoration of the basal microcirculation.

Cardiac oscillator. The cardiac amplitude a_i (Fig. 64f) during PORH was reduced compared to baseline in both groups (p-value < 0.001). Smokers showed also a decrease of the PORH cardiac amplitude compared to ischaemia (p-value < 0.05). These data are difficult to interpret. Indeed, as discussed above, during ischaemia the decrease of cardiac amplitude may reflect a reduction of the cardiac output due to the decrease in heart rate and increase in breathing rate observed after the inflation of the pressure cuff. Based on this, the expected trend after the release of the cuff's pressure would be an increase of the cardiac output instead, due to the restoration of a faster heart rate and slower breathing rate as observed in Table 13 (see the frequencies of the respiratory and cardiac oscillators during PORH compared to ischaemia). However, as previously discussed, the wavelet amplitude is referred to the maximal response in the frequency interval of interest and sometimes may not reflect the overall activity of the component under investigation. For this reason, it is advantageous to also assess the wavelet energy for gaining a better overview of the data and avoid

misinterpretations. Indeed, both groups showed a different trend of the cardiac e_i (Fig. 65f) compared to the a_i (Fig. 64f) during PORH response, characterised by a significant growth of energy compared to ischaemia ($p < 0.001$) indicating an overall increase of the cardiac output during PORH which was not reflected in the amplitude of the wavelet peak. Therefore, also in this case, as shown above for the myogenic oscillator, the examination of the wavelet energy allowed gathering information that was missing from the analysis of the amplitude.

Differences of LDF oscillators between controls and smokers

Table 13 reports the comparison of wavelet amplitude a_i, energy e_i and frequency location f of LDF oscillators' peaks between controls and smokers.

Table 13 Comparison of the wavelet a_i, e_i and f of LDF oscillators between groups. The table reports the same data of a_i **and** e_i shown in Fig. 64 and Fig. 65, and the frequency data of LDF oscillators. Data are presented as median (inter-quartile range). Both of a_i and e_i are expressed in dimensionless units, while f is expressed in hertz (Hz). (B) = Baseline. (IS) = Ischaemia. (P) = PORH. Endo = Endothelial. NO = Nitric oxide. EDHF = Endothelial-derived hyperpolarizing factor. Differences between controls and smokers were calculated by unpaired Wilcox test and are outlined by red asterisks. p = p-value. *p < 0.05, **p < 0.01, ***p < 0.001.

Wavelet amplitude a_i (dimensionless units)			
Variable	**Controls (n=20)**	**Smokers (n=20)**	**p**
(B) a_i Cardiac	12.3 (10.8-13.4) × 10^{-3}	6.60 (4.50-9.50) × 10^{-3}	**0.0060
(IS) a_i Cardiac	6.20 (5.10-8.10) × 10^{-3}	4.30 (3.20-6.50) × 10^{-3}	**0.0040
(P) a_i Cardiac	6.90 (4.60-9.30) × 10^{-3}	2.10 (1.30-4.50) × 10^{-3}	***0.0008
(B) a_i Respiratory	0.40 (0.20-1.10) × 10^{-3}	2.80 (1.70-4.00) × 10^{-3}	**0.0070
(IS) a_i Respiratory	3.10 (2.60-3.80) × 10^{-3}	4.30 (2.80-4.90) × 10^{-3}	0.1000
(P) a_i Respiratory	0.30 (0.20-0.40) × 10^{-3}	0.50 (0.30-1.00) × 10^{-3}	*0.0200
(B) a_i Myogenic	0.50 (0.30-1.00) × 10^{-3}	2.20 (1.10-4.90) × 10^{-3}	***0.0001
(IS) a_i Myogenic	1.40 (1.10-1.90) × 10^{-3}	2.60 (1.90-4.80) × 10^{-3}	***0.0005
(P) a_i Myogenic	1.60 (1.20-2.20) × 10^{-3}	2.80 (2.40-4.20) × 10^{-3}	**0.0010
(B) a_i Neurogenic	0.20 (0.10-0.70) × 10^{-3}	0.60 (0.30-1.30) × 10^{-3}	0.0800
(IS) a_i Neurogenic	0.70 (0.50-1.10) × 10^{-3}	0.70 (0.40-1.00) × 10^{-3}	0.9000
(P) a_i Neurogenic	0.90 (0.60-1.10) × 10^{-3}	1.60 (0.90-2.00) × 10^{-3}	**0.0030
(B) a_i Endo-NO	0.10 (0.06-0.40) × 10^{-3}	0.20 (0.09-0.60) × 10^{-3}	0.2000
(IS) a_i Endo-NO	0.40 (0.20-1.00) × 10^{-3}	0.20 (0.10-0.70) × 10^{-3}	0.2000
(P) a_i Endo-NO	1.90 (1.20-2.80) × 10^{-3}	3.70 (2.80-4.00) × 10^{-3}	**0.0010
(B) a_i Endo-EDHF	0.08 (0.03-0.30) × 10^{-3}	0.10 (0.07-0.30) × 10^{-3}	0.2000
(IS) a_i Endo-EDHF	0.70 (0.08-1.20) × 10^{-3}	0.07 (0.05-0.60) × 10^{-3}	0.2000
(P) a_i Endo-EDHF	4.50 (3.20-7.70) × 10^{-3}	6.30 (5.10-7.90) × 10^{-3}	0.3000

Wavelet energy e_i (dimensionless units)			
Variable	**Controls (n=20)**	**Smokers (n=20)**	**p**
(B) e_i Cardiac	13.6 (12.9-14.0) × 10^{-3}	10.6 (8.10-12.2) × 10^{-3}	*0.0100
(IS) e_i Cardiac	10.4 (9.90-11.0) × 10^{-3}	8.10 (6.70-9.50) × 10^{-3}	**0.0020
(P) e_i Cardiac	13.2 (12.5-13.6) × 10^{-3}	9.80 (7.80-11.9) × 10^{-3}	***0.0004
(B) e_i Respiratory	0.60 (0.30-1.10) × 10^{-3}	2.90 (1.60-4.30) × 10^{-3}	*0.0100
(IS) e_i Respiratory	3.20 (2.70-3.60) × 10^{-3}	4.50 (3.80-5.40) × 10^{-3}	**0.0080
(P) e_i Respiratory	0.60 (0.40-0.90) × 10^{-3}	1.70 (1.10-2.60) × 10^{-3}	***0.0004
(B) e_i Myogenic	0.10 (0.06-0.20) × 10^{-3}	0.30 (0.20-1.20) × 10^{-3}	0.0700
(IS) e_i Myogenic	0.20 (0.20-0.30) × 10^{-3}	0.70 (0.40-1.30) × 10^{-3}	*0.0300
(P) e_i Myogenic	0.40 (0.30-0.60) × 10^{-3}	1.40 (0.60-2.40) × 10^{-3}	***0.0006
(B) e_i Neurogenic	0.020 (0.001-0.040) × 10^{-3}	0.040 (0.020-0.090) × 10^{-3}	*0.0200
(IS) e_i Neurogenic	0.030 (0.020-0.060) × 10^{-3}	0.050 (0.030-0.100) × 10^{-3}	0.1000
(P) e_i Neurogenic	0.100 (0.070-0.200) × 10^{-3}	0.400 (0.200-0.500) × 10^{-3}	**0.0010
(B) e_i Endo-NO	0.003 (0.001-0.007) × 10^{-3}	0.008 (0.003-0.010) × 10^{-3}	0.1000
(IS) e_i Endo-NO	0.008 (0.004-0.030) × 10^{-3}	0.006 (0.003-0.020) × 10^{-3}	0.8000
(P) e_i Endo-NO	0.070 (0.040-0.100) × 10^{-3}	0.300 (0.100-0.400) × 10^{-3}	***0.0005
(B) e_i Endo-EDHF	0.0008 (0.0004-0.0020) × 10^{-3}	0.0020 (0.0006-0.0030) × 10^{-3}	0.2000
(IS) e_i Endo-EDHF	0.0040 (0.0006-0.0100) × 10^{-3}	0.0008 (0.0003-0.0040) × 10^{-3}	0.3000
(P) e_i Endo-EDHF	0.0400 (0.0200-0.1000) × 10^{-3}	0.1000 (0.0500-0.2000) × 10^{-3}	*0.0300

Wavelet frequency *f* (Hz)			
Variable	**Controls (n=20)**	**Smokers (n=20)**	**p**
(B) *f* Cardiac [Hz]	980 (860-1020) × 10^{-3}	1030 (925-1080) × 10^{-3}	0.3500
(IS) *f* Cardiac [Hz]	860 (780-950) × 10^{-3}	730 (590-800) × 10^{-3}	**0.0080
(P) *f* Cardiac [Hz]	965 (890-1000) × 10^{-3}	980 (890-1080) × 10^{-3}	0.6300
(B) *f* Respiratory [Hz]	260 (215-300) × 10^{-3}	310 (1840-360) × 10^{-3}	0.7300
(IS) *f* Respiratory [Hz]	440 (280-485) × 10^{-3}	390 (220-470) × 10^{-3}	0.3100
(P) *f* Respiratory [Hz]	240 (230-290) × 10^{-3}	275 (210-340) × 10^{-3}	0.7400
(B) *f* Myogenic [Hz]	75.0 (65.8-90.3) × 10^{-3}	84.6 (77.3-93.6) × 10^{-3}	0.4300
(IS) *f* Myogenic [Hz]	85.5 (74.3-129.4) × 10^{-3}	78.3 (76.9-81.0) × 10^{-3}	0.2500
(P) *f* Myogenic [Hz]	82.5 (76.9-89.2) × 10^{-3}	92.3 (83.5-103) × 10^{-3}	*0.0200
(B) *f* Neurogenic [Hz]	35.6 (29.0-39.8) × 10^{-3}	40.5 (34.4-41.8) × 10^{-3}	0.2800
(IS) *f* Neurogenic [Hz]	39.8 (30.7-41.6) × 10^{-3}	36.5 (29.0-37.8) × 10^{-3}	0.1200
(P) *f* Neurogenic [Hz]	27.9 (24.4-30.2) × 10^{-3}	35.0 (24.8-40.5) × 10^{-3}	0.0700
(B) *f* Endo-NO [Hz]	15.8 (14.2-17.7) × 10^{-3}	12.4 (11.1-17.2) × 10^{-3}	0.0800
(IS) *f* Endo-NO [Hz]	11.8 (10.1-13.6) × 10^{-3}	13.6 (10.1-17.4) × 10^{-3}	0.3400
(P) *f* Endo-NO [Hz]	15.3 (12.2-16.6) × 10^{-3}	15.5 (12.4-17.9) × 10^{-3}	0.8300
(B) *f* Endo-EDHF [Hz]	6.56 (4.97-6.80) × 10^{-3}	6.62 (4.97-7.26) × 10^{-3}	0.9600
(IS) *f* Endo-EDHF [Hz]	6.80 (6.77-6.80) × 10^{-3}	6.80 (6.68-6.80) × 10^{-3}	0.2500
(P) *f* Endo-EDHF [Hz]	5.15 (5.10-5.20) × 10^{-3}	5.96 (5.24-7.04) × 10^{-3}	***0.0003

Local microvascular LDF oscillators (EDHF, NO, neurogenic and myogenic). The wavelet energy e_i and frequency *f* of the endothelial EDHF component were greater ($p < 0.05$ and $p < 0.001$ respectively) in smokers during PORH response. The amplitudes/energies of the endothelial NO and neurogenic oscillators were significantly higher ($p < 0.01$ or $p < 0.001$) in smokers during PORH response. The myogenic amplitude/energy was greater in smokers during all the stages of the reactive test ($p < 0.001$ or $p < 0.05$ at baseline and ischaemia, $p < 0.01$ or $p < 0.001$ during PORH), and the myogenic frequency *f* was higher ($p < 0.05$) in smokers during PORH. These observations are in contrast with most of literature reports comparing the LDF spectral components between smokers and non-smokers. Greater values of endothelial, myogenic and neurogenic wavelet amplitudes/energies are generally associated with a better microvascular function. Therefore, in this case data may be misinterpreted as showing a better microcirculation in smokers, which is paradoxical. However, these contrasting observations may be explained by the lower average age of the tested subjects compared to most of the studies on smokers, and by the good health conditions of the smoker individuals enrolled in the research which were not affected by additional CVD risk factors (e.g. hypertension, high BMI, etc.). The greater amplitudes/energies observed in smokers might reflect an adaptive response to the early risk associated with tobacco while the blood vessels are still responsive. This may stimulate an increase of the endothelial NO levels as compensatory defence mechanism to the smoking stress.

Furthermore, enhanced non-specific sensitivity of the forearm's micro-vessels has been described in young healthy smokers compared to non-smokers during reactive hyperaemia, acetylcholine and SNP vasodilation stimuli [174, 175]. These reports are in agreement with the findings of this work, showing higher endothelium-dependent and endothelium-independent responses in healthy smokers compared to controls. The increase of endothelial activity in smokers was explained by Rangemark *et al.* [175] as a possible indirect consequence of the non-specific enhanced myogenic activity induced by cigarettes smoke, rather than a real better endothelial function.

Non-specific activation of myogenic vasodilation response due to smoking. The non-specific activation of myogenic response in the forearm's cutaneous

microcirculation of smokers, hypothesised by Rangemark *et al.* [175], may be stimulated in two ways:

(1) According to Vleeming *et al.* [176], cigarettes smoke or tobacco contain NO [176, 177]. Therefore, VSMCs may be targeted and activated non-specifically by the action of external NO contained in cigarettes smoke or tobacco.
(2) As reported by Vleeming *et al.* [176], the nicotine contained in tobacco is able to stimulate the activity of nicotinic acetylcholine receptors in endothelial cells. Thus, VSMCs may be targeted and activated non-specifically by the action of endogenous NO produced as consequence of the external effect of nicotine.

An objection to the mechanisms of activation proposed above may be that cigarettes smoke is inhaled through the respiratory system, thus the effect of exogenous NO and nicotine should impact only the respiratory airways. However, as reported by Bekö *et al.* [178], cigarettes smoke and nicotine can be absorbed directly from the skin reaching the dermal layer where the micro-vessels are located. Therefore, this would explain a local effect of NO and nicotine contained in cigarettes smoke on the cutaneous micro-vessels of the forearm.

The hypotheses proposed above may also explain the observations about the trend of myogenic wavelet a_i, which did not change significantly in smokers during all the stages of PORH test (Fig. 64d), as discussed previously. This is probably due to the hyperactivity of VSMCs induced non-specifically by NO and nicotine contained in tobacco and cigarettes smoke, which may cause the achievement of a maximal myogenic activity peak explaining the similar amplitude between baseline, ischaemia and PORH time points. Moreover, nicotine is able to activate also the peripheral autonomous nervous system [176], which may be another factor inducing the non-specific activation of VSMCs in smokers through the action of impulses transmitted by the sympathetic innervation. This may also explain why a higher amplitude of the neurogenic component was found in smokers compared to controls during PORH (Table 13).

According to the obtained results, it cannot be excluded that the hyperactive cutaneous microvascular reactivity observed in smokers may be an initial factor causing an imbalance between vasodilator and vasoconstrictor substances in the microcirculation, contributing to the onset of the skin micro-vessels endothelial damage and dysfunction observed especially in cohorts of chronic elder smokers.

These findings also outline that wavelet transform data could be misinterpreted. Indeed, although in general lower values of endothelial, myogenic and neurogenic wavelet amplitudes/energies represent hallmarks of vascular dysfunction, especially when comparing healthy vs diseased people or elder smokers vs healthy controls, this is not true when testing younger healthy smokers. In this case, the increase of wavelet amplitude/energy of local microvascular components may represent a hallmark of the early stages of vascular dysfunction, which could be used as biomarker for the prediction of risk at preclinical level.

Respiratory oscillator. The a_i or e_i of the respiratory wavelet component were significantly higher in smokers compared to controls during all the stages of the test ($p < 0.05$ or $p < 0.01$ baseline, $p < 0.01$ ischaemia, $p < 0.05$ or $p < 0.001$ PORH) (Table 13). As discussed before, the increase or decrease of amplitude/energy of the respiratory wavelet oscillation could be interpreted, respectively, as increase or reduction of skin arterioles resistance induced by the extrinsic respiratory modulation exerted via the autonomous nervous system or via the respiratory-dependent left cardiac preload [173]. Based on these assumptions the higher wavelet respiratory amplitude/energy observed in smokers at all the stages of PORH test may reflect an overall greater resistance of peripheral arterioles compared to controls. Increased arterioles resistance leads to constriction of vascular diameter and represents a CVD risk factor frequently associated with hypertension. Therefore, according to these findings the respiratory oscillator may represent a preclinical marker of risk reflecting the degree of arterioles resistance which is increased in healthy mild smokers.

Cardiac oscillator. The a_i of the cardiac wavelet component was higher in the control group during all the stages of the reactive test ($p < 0.01$ or $p < 0.05$ at baseline and ischaemia, $p < 0.001$ during PORH) (Table 13). Also the frequency of the cardiac oscillator was significantly higher ($p < 0.01$) in non-smokers during ischaemia, suggesting a greater heart rate in healthy individuals compared to smokers. These findings may indicate a higher basal cardiac output in healthy individuals leading to a better distribution of blood and oxygen in the tissue compared to smokers. This interpretation is also supported by the results discussed in Table 11 about oxygen consumption (VO_2). VO_2 is considered an indirect measure of the cardiac output [179] and greater values were found in the

control group compared to smokers ($p < 0.05$ during ischaemia, $p < 0.01$ during PORH), which indicates the ability of non-smokers to use and convert a major amount of oxygen in ATP energy. However, these data are contrasting with literature reports describing a higher cardiac output in smokers compared to non-smokers, generally associated to hypertension and increased heart rate [180, 181, 182, 183]. The contrasting results obtained in this dissertation probably may be explained by the healthy conditions of the tested groups (no CVD risk factors), which did not show significant differences in the basal BP (Table 9) and in the basal heart rate as shown indirectly by data related to the wavelet frequency *f* of the cardiac oscillator reported in Table 13. Therefore, in this case the "cardiac output" may just reflect the efficiency in blood perfusion and oxygen distribution rather than the presence of a particular pathologic condition.

4.4.2 Study of vasomotion by wavelet spectral analysis

The wavelet spectral analysis of LDF signal is a useful tool also for the study of vasomotion and the contribution of each physiological component to PORH response. According to literature, the major mediators of the vasodilator PORH cutaneous response are the sensory nerves and the EDHF mechanism. The sensory nerves contribute to the maximum perfusion peak response and time course (PORH AUC and time to peak) by a local reflex [184], while the EDHF acts through the action of the cytochromes P450 (CYPs) metabolites (e.g. EETs, epoxy-eicosatrienoic acids) [9]. The CYPs are oxidase enzymes of the electron transport chain, involved in the oxidation of NAD(P)H for transferring the electrons to the P450 heme cofactor during the OXPHOS process for the production of ATP. The implication of EDHF and CYPs supports the involvement of metabolic factors in the cutaneous reactive hyperaemic response, as proposed in the study by Kristensen *et al.* [185]. The major role of EDHF in the reactivity of skin micro-vessels is also supported by studies suggesting that NO is more implicated in the regulation of the vascular tone of larger arteries, while EDHF is more important for the control of the resistance of peripheral arterioles in the microcirculation [140, 186, 187, 188].

Although the contribution of the NO pathway to reactive hyperaemia in the skeletal muscle is relevant, its role in the cutaneous PORH seems to be minimal [9, 184], probably due to the fact that the small cutaneous blood vessels are less

dependent on NO and rely more on the EDHF pathway. Indeed, the inhibition of the eNOS (endothelial nitric oxide synthase) enzyme that is involved in the production of the endothelial NO does not block skin PORH response [9, 189, 190]. According to Medow *et al.* the cross-talk between NO and prostaglandins (PGs) pathways may be the cause reducing NO contribution during skin PORH, due to the inhibition of eNOS by the cyclooxygenases (COXs) or COX products involved in the PGs-mediated vasodilator mechanism [184].

PGs are involved in skeletal muscle hyperaemic response, while their role in the cutaneous PORH is not clear as there are contrasting reports and not robust evidences of their involvement [9, 184]. However, it cannot be excluded that the attenuation of NO contribution to cutaneous PORH mediated by COXs may be a consequence of PGs activation during the hyperaemic response. Indeed, the cross-talk between NO and PGs pathways is bidirectional, and it is thought that NO can interfere directly with PGs production and vice-versa [184]. Moreover, several studies have reported a reduction of the cutaneous PORH response after inhibition of PGs by aspirin or ibuprofen [191, 192], suggesting the involvement of these substances in skin hyperaemic response.

Finally, the involvement of the myogenic mechanism in both cutaneous and skeletal muscle PORH seems to depend on the duration of the occlusion. The myogenic activity is more relevant for reactive hyperaemic responses following ischemic periods below 3 minutes [185]. In contrast, prolonged occlusion periods exceeding 3 minutes lead to PORH responses involving the major activity of metabolic mediators (e.g. EDHF, CYPs) with a reduced contribution of the myogenic mechanism, which is in any case essential for the mechanical regulation of the vascular diameter to relax micro-vessels [185].

Contribution of blood flow LDF oscillators to vasomotion

In this study, the individual contribution of each physiological component to vasomotion was evaluated (1) by estimating the percentage relative growth of the wavelet amplitudes and energies during PORH compared to baseline (Table 14), and (2) by comparing the relative contribution of each oscillator to the total energy of the CWT baseline and PORH spectra (Table 15).

EDHF contribution. The results are in agreement with the major role of EDHF in the cutaneous reactive hyperaemia. Indeed, as shown in Table 14, EDHF was

the physiological factor showing the greatest percentage increase in wavelet amplitude and energy during PORH in both controls (76% increase of a_i, 61.3% rise of e_i) and smokers (68.7% increase of a_i, 55.3% increase of e_i).

Table 14 Percentage relative increase of wavelet a_i and e_i during PORH compared to baseline. Data are expressed as median (inter-quartile range). Endo = Endothelial. NO = Nitric oxide. EDHF = Endothelial-derived hyperpolarizing factor. Differences between controls and smokers were estimated by unpaired Wilcox test and are outlined by red asterisks. p = p-values. *p < 0.05, **p < 0.01.

Variable	Controls (n=20)	Smokers (n=20)	p
$a_{i\ Myogenic}$ increase [%]	4.60 (0.80-10.5)	0.30 (-0.20-2.20)	**0.001
$a_{i\ Neurogenic}$ increase [%]	1.30 (0.20-8.50)	1.40 (-0.01-6.60)	0.800
$a_{i\ Endo\text{-}NO}$ increase [%]	16.2 (7.10-21.0)	20.5 (9.20-35.0)	0.300
$a_{i\ Endo\text{-}EDHF}$ increase [%]	76.0 (57.8-88.7)	68.7 (57.6-91.0)	1.000
$e_{i\ Myogenic}$ increase [%]	4.30 (1.60-10.0)	1.25 (0.30-4.00)	0.700
$e_{i\ Neurogenic}$ increase [%]	6.30 (1.70-13.1)	4.90 (1.70-9.30)	*0.040
$e_{i\ Endo\text{-}NO}$ increase [%]	21.0 (11.6-28.0)	33.5 (16.5-38.3)	0.140
$e_{i\ Endo\text{-}EDHF}$ increase [%]	61.3 (48.4-79.2)	55.3 (48.2-79.5)	0.200

Table 15 Percentage relative contribution of each LDF oscillator to the total e_i of baseline and PORH median CWT spectra. Data are expressed as median (inter-quartile range). Endo = Endothelial. NO = Nitric oxide. EDHF = Endothelial-derived hyperpolarizing factor. Intra-group differences to compare baseline and PORH data were calculated by paired Wilcox test and are outlined by black asterisks. Inter-groups differences to compare controls and smokers data were estimated by unpaired Wilcox test and are outlined by red asterisks. p = p-value. *p < 0.05, **p < 0.01, ***p < 0.001.

Variable	Controls (n=20)		Smokers (n=20)	
	Baseline	PORH	Baseline	PORH
$e_{i\ Myogenic}$ [%]	76.9 (73.3-82.9)	64.3 (58.6-69.1)	87.4 (82.2-93.9)	65.9 (57.5-70.9)
$e_{i\ Neurogenic}$ [%]	18.7 (13.7-20.7)	20.0 (13.9-21.6)	10.1 (4.80-14.0)	18.3 (13.1-21.0)
$e_{i\ Endo\text{-}NO}$ [%]	2.80 (2.20-5.10)	9.60 (7.80-13.8)	1.40 (0.75-3.60)	11.1 (8.90-12.8)
$e_{i\ Endo\text{-}EDHF}$ [%]	0.90 (0.30-1.90)	6.40 (5.20-9.30)	0.30 (0.10-0.90)	5.60 (4.00-6.40)
Variable	Intra-group p (Baseline vs PORH)		Inter-groups p (Controls vs Smokers)	
	Controls	Smokers	Baseline	PORH
$e_{i\ Myogenic}$ [%]	0.0001***	< 0.0001***	0.001**	0.500
$e_{i\ Neurogenic}$ [%]	0.900	0.003**	0.001**	0.800
$e_{i\ Endo\text{-}NO}$ [%]	0.010*	0.002**	0.01*	0.500
$e_{i\ Endo\text{-}EDHF}$ [%]	0.002**	0.002**	0.06	0.070

These observations represent also a relevant indirect proof of the possible EDHF origin of the wavelet peak in the frequency interval 5-9.5 × 10^{-3} Hz, as it has been hypothesised and discussed in the results section of this dissertation related to the experimental work on mice (section 3.3, paragraph 3.3.1, page 132). The analysis of the relative contribution of each component to the total wavelet spectrum showed a statistically significant increase ($p < 0.01$) of the EDHF contribution to the total energy of PORH median CWT spectrum compared to baseline spectrum (increase from 0.9% to 6.4% in controls, and from 0.3% to 5.6% in smokers) (Table 15).

Endothelial NO and PGs contributions. The results related to the NO component showed a complex pattern of wavelet oscillatory peaks. As visible in Fig. 63c, the spectral interval related to NO activity was characterised by the presence of two wavelet peaks during PORH response in both smokers and healthy individuals. In the results discussed so far, the data from the maximum peak in this frequency interval have been presented as corresponding to endothelial NO activity. However, the presence of two peaks during PORH suggests a possible overlapping contribution of different components in the 9.5-21 × 10^{-3} Hz frequency range. This hypothesis would not be surprising, considering that the wavelet peak related to the activity of PGs has never been identified and this might be due to an overlap with the spectral region corresponding to NO activity. Indeed, most of the studies for the characterisation of the physiological origin of the endothelial wavelet peaks have been performed by using vasoactive agents for the stimulation of cholinergic receptors (e.g. ACh) [102, 105], which might not be sufficient to separate clearly the NO contribution from other molecular pathways (e.g. PGs) [9, 49, 184]. Moreover, as discussed above (page 176), according to literature the contribution of NO to cutaneous PORH is minimal [9, 184], and this may explain the appearance of an additional wavelet peak in the NO interval during PORH, which normally might be masked by the more prominent involvement of NO pathway in the modulation of vascular tone. The attenuation of NO contribution to cutaneous PORH has been suggested to be mediated by COXs as a consequence of PGs activation during the hyperaemic response [184]. Therefore, considering the bidirectional cross-talk between NO and PGs pathways, it would not be surprising an overlap of the wavelet peaks of these two endothelial molecular mechanisms at a similar frequency interval [184].

Furthermore, the results from this dissertation have suggested an EDHF origin of the wavelet component in the frequency interval 5-9.5 × 10^{-3} Hz, thus by exclusion, we could speculate a PGs origin of one of the two peaks appearing during PORH in the 9.5-21 × 10^{-3} Hz NO interval. However, further experiments are necessary to better clarify this aspect based on performing the wavelet analysis of LDF data recorded from the forearm in combination with PORH test and the non-invasive local delivery of inhibitors of PGs biosynthesis.

In view of the discussion above, in this research it is difficult to characterise precisely the contribution of the NO endothelial component to vasomotion because the origin of the two peaks observed in this frequency interval is ambiguous. Indeed, it is not clear which peak is associated with NO (probably the lower peak) and which peak may be related to another endothelial regulatory mechanism that is likely to be of PG origin. Considering that the wavelet energy is representative of the whole activity in the frequency interval of interest, it can be certainly stated that the cumulative percentage increase of wavelet energy during PORH related to the sum of NO pathway and another unknown endothelial mechanism (probably PGs) was 21% in the control group and 33% in smokers (Table 14), and the cumulative relative contribution to the total CWT spectrum increased during PORH from 2.8% to 9.6% in controls ($p < 0.05$) and from 1.4% to 11.1% in smokers ($p < 0.01$) (Table 15). These cumulative data suggest a lower contribution of NO and probably PGs to skin reactive hyperaemia compared to EDHF, confirming what has been reported in literature about the factors involved in cutaneous PORH.

Neurogenic and myogenic contributions. In this work, a non-significant percentage growth of the neurogenic (1.3% in controls, 1.4% in smokers) and myogenic (4.6% in controls, 0.3% in smokers) wavelet maximal amplitudes, and neurogenic (6.3% in controls, 4.9% in smokers) and myogenic (4.3% in controls, 1.25% in smokers) wavelet energies was observed during PORH response (Table 14). The relative neurogenic contribution to the total energy of the CWT spectrum was almost unchanged in the controls, and increased from 10.1% to 18.3% in smokers ($p < 0.01$) (Table 15). The relative myogenic contribution to the total e_i of the CWT spectrum was reduced from 76.9% to 64.3% in controls ($p < 0.001$), and decreased from 87.4% to 65.9% in smokers ($p < 0.001$) (Table 15). Overall, these observations are in contrast with most of literature reports

describing the sympathetic sensory nerves as major contributors to skin PORH peak. However, these findings may be explained by the 5 min ischaemia period that was applied during the functional test. Indeed, occlusion periods longer than 3 min stimulate a reactive hyperaemia response mainly mediated by metabolic factors [185], which may explain the larger variation observed in the spectral energy and contribution of the endothelial wavelet oscillators compared to neurogenic and myogenic oscillators. Nonetheless, data in Table 15 clearly display that the neurogenic and myogenic oscillators were the wavelet components showing the highest percentage contribution to the total energy of the CWT spectrum during both baseline and PORH time points. This outlines the crucial interaction between sympathetic nerves and VSMCs, which is essential for the mechanical vaso-relaxation of micro-vessels during the reactive hyperaemia process. Furthermore, smokers showed a statistically significant increase of the neurogenic contribution to the total CWT energy spectrum during PORH response that was not observed in controls. This finding is in agreement with a major activation of the peripheral autonomous nervous system in smokers favoured by tobacco, which may be one of the factors causing a non-specific activation of VSMCs responsible for the microvascular hyperactivity observed in smokers. This is confirmed further by a contribution of the myogenic oscillator to the total baseline CWT spectrum much higher in smokers (87.4%) compared to controls (76.9%) ($p < 0.01$) (Table 15).

4.4.3 Metabolic oscillators in humans

In the chapter 3 about mouse models work, it has been outlined how the examination of cellular oscillations of NAD(P)H concentration and of the RR_{index} may be powerful to detect specific dynamic patterns of ATP energy production that may reflect the switch of the tissue from a normal to a diseased phenotype. Here, the wavelet analysis was applied on NAD(P)H and RR signals obtained by single-point AF readouts to characterise for the first time *in-vivo* human cell metabolic oscillators, compare their dynamic patterns between controls and smokers to assess their potential use as CVD risk factors, and study their correlation with microvascular oscillators and vasomotion. Fig. 66 and Fig. 67 illustrate, respectively, the median time-averaged wavelet spectra from NAD(P)H and RR reconstructed signals of smokers and non-smokers during PORH test.

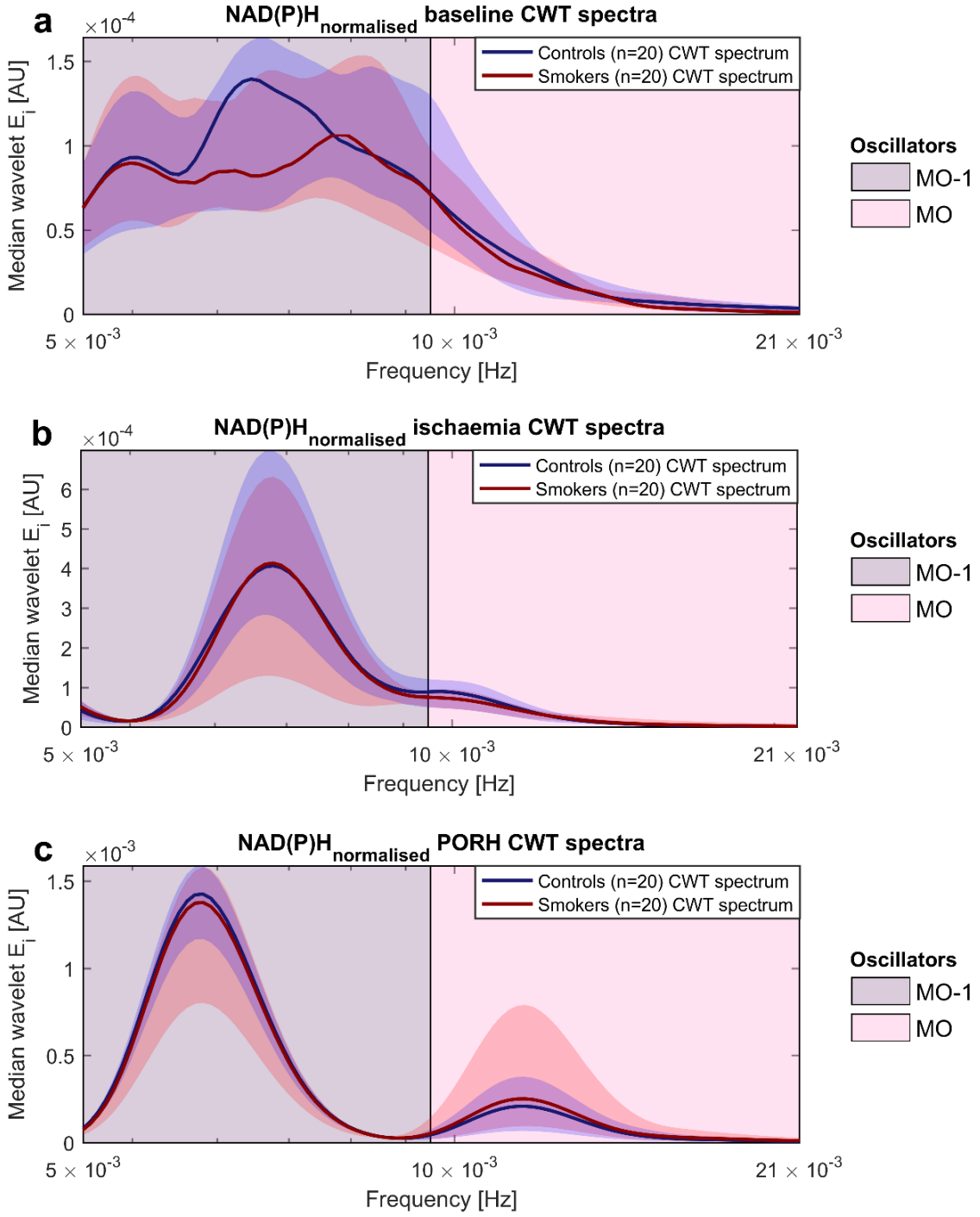

Fig. 66 Comparison of NAD(P)H signal CWT spectra during PORH task. Median CWT NAD(P)H spectra of controls and smokers during the stages of reactive hyperaemia test: (a) baseline, (**b**) ischaemia, (**c**) PORH response. The shaded blue and red areas around the lines of the median spectra represent the inter-quartile range of the CWT spectra. MO = Metabolic oscillator. MO-1 = Metabolic oscillator-1. Both A_i and E_i are expressed in arbitrary units (AU). The graphs show very slight differences in the absolute amplitude A_i and energy E_i of the metabolic oscillatory peaks between the two groups at baseline.

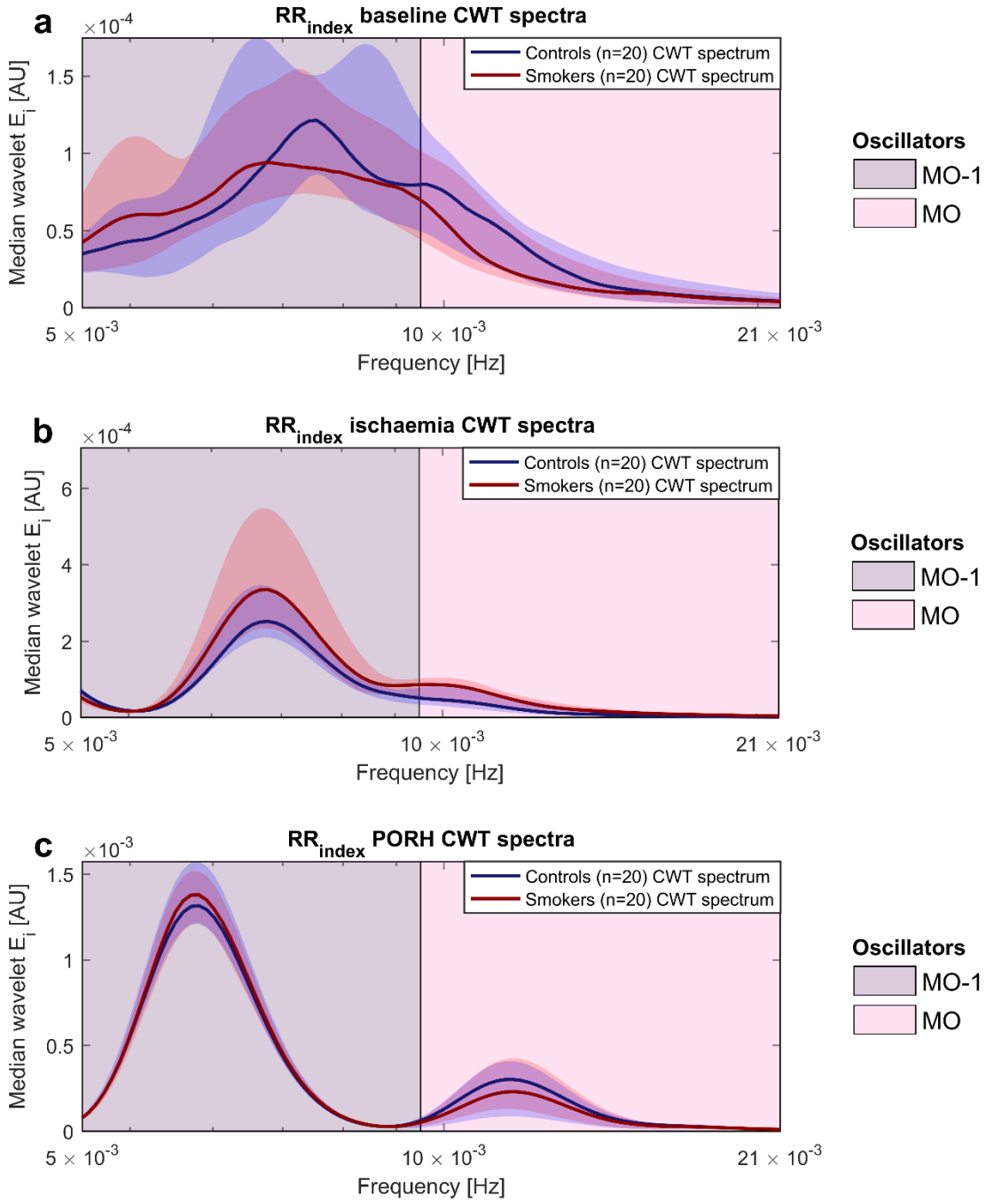

Fig. 67 Comparison of RR signal CWT spectra during PORH task. Median CWT RR spectra of controls and smokers during the stages of reactive hyperaemia test: (**a**) baseline, (**b**) ischaemia, (**c**) PORH response. The shaded blue and red areas around the lines of the median spectra represent the inter-quartile range of the CWT spectra. MO = Metabolic oscillator. MO-1 = Metabolic oscillator-1. . Both A_i and E_i are expressed in arbitrary units (AU). The graphs show slight differences in the absolute amplitude A_i and energy E_i of the metabolic oscillatory peaks between the two groups.

As shown in Fig. 66a-c and Fig. 67a-c, a relevant slow metabolic oscillation in the 5-9.5 × 10^{-3} Hz frequency range of NAD(P)H and RR signals was identified at all the stages of PORH test that was named metabolic oscillator-1 (MO-1). In

addition, a second metabolic oscillation appeared during PORH response (Fig 60c and 61c) that was called metabolic oscillator (MO). The graphs outline slight differences between groups associated with the absolute wavelet amplitude A_i and energy E_i of metabolic oscillators, especially for the RR MO-1 and RR MO oscillators. Comparisons between groups were examined by evaluating the relative dimensionless amplitude a_i and dimensionless energy e_i obtained by normalising A_i and E_i according to equations 9-12.

Trends of metabolic oscillators during ischaemia

Fig. 68 displays the trends of the wavelet amplitude and energy of MO-1 during the various steps of PORH test.

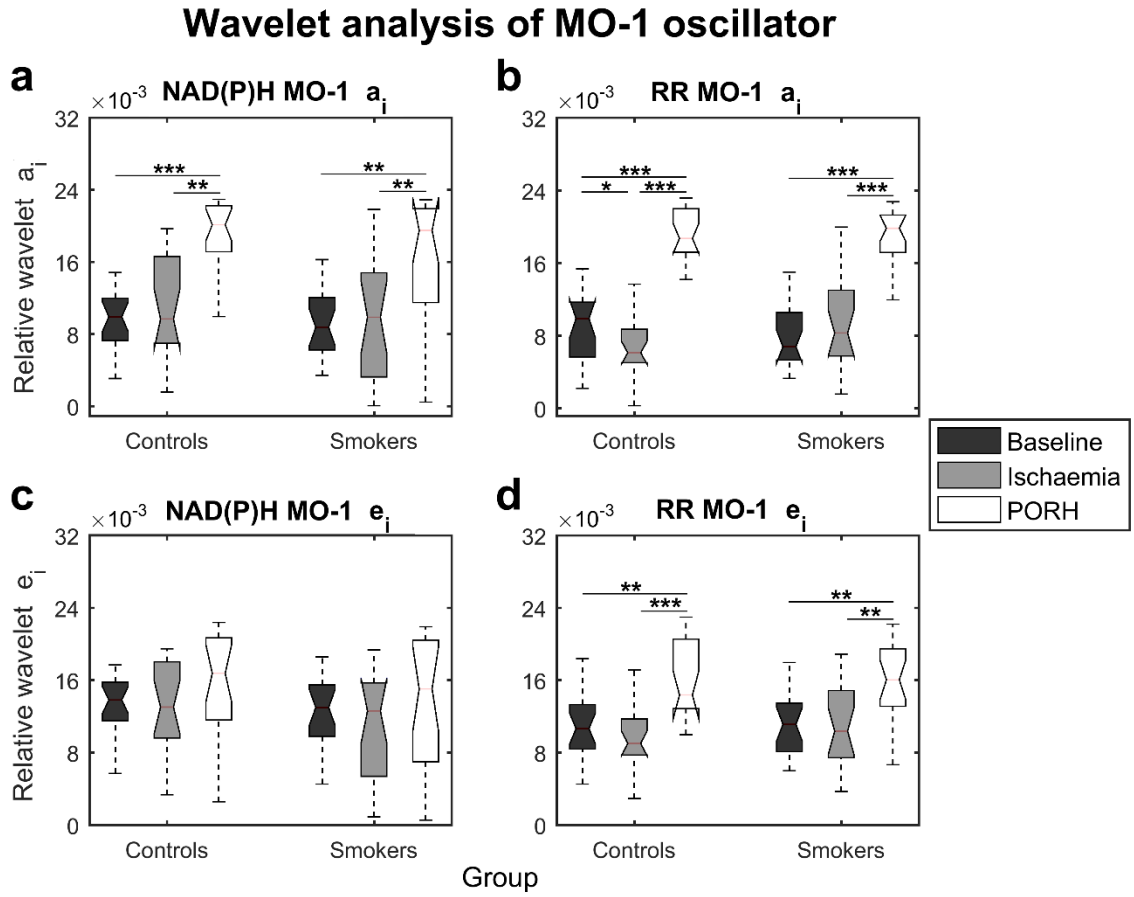

Fig. 68 Trends of the wavelet a_i and e_i of metabolic oscillator-1 (MO-1) during PORH test. (**a**) NAD(P)H MO-1 wavelet amplitude. (**b**) RR MO-1 wavelet amplitude. (**c**) NAD(P)H MO-1 wavelet energy. (**d**) RR MO-1 wavelet energy. Data are presented as boxplots. Both a_i and e_i are expressed in dimensionless units. Black boxplots = Baseline. Grey boxplots = Ischaemia. White boxplots = PORH. Non-significant differences were found between groups. The black lines/asterisks refer to significant changes during PORH task that were estimated by paired Wilcox test. *p < 0.05, **p < 0.01, ***p < 0.001.

During the 5 min period of ischaemia the amplitude of NAD(P)H MO-1 (Fig. 68a) did not change in both groups compared to baseline. In contrast, the amplitude of the RR MO-1 (Fig. 68b) decreased significantly in controls during the occlusion ($p < 0.05$) but did not change in smokers. A significant negative correlation (ρ=-0.55, p=0.01) was found in controls during ischaemia between the amplitude of RR MO-1 and the a_i of the myogenic LDF oscillator which was absent in smokers. Therefore, the decrease of RR MO-1 amplitude may partially reflect a protective mechanism against the ischemic damage in VSMCs, probably consistent in the attempt to reduce mitochondrial ROS production through uncoupling of the electron transport chain, reduction of $NAD(P)^+$ to NAD(P)H and switch towards an anaerobic glycolytic metabolism. As shown previously, the wavelet amplitude of the myogenic oscillator increased significantly during ischaemia in controls and did not change in smokers instead (Fig. 64d, page 167). Therefore, the data related to the RR MO-1 metabolic oscillator suggest that the activation of the myogenic mechanism during ischaemia may be sustained by ATP produced through the glycolysis process, and could represent an attempt to attenuate vasoconstriction and ensure the distribution of the remaining nutritive blood to the surrounding tissue. In contrast, this mechanism might be less efficient in smokers due to oxidative stress caused by cigarettes smoke. The wavelet energy of NAD(P)H MO-1 and RR MO-1 (Fig. 68c-d) did not show significant changes during ischaemia in both groups.

Fig. 69 displays the trends of the wavelet amplitude/energy of MO during the various steps of PORH test. Either the wavelet energy or amplitude of NAD(P)H and RR MO oscillators showed a decrease during ischaemia in both controls and smokers. However, in this case non-relevant correlations were found between the amplitude/energy of MO and specific blood flow oscillators, suggesting that MO trends probably provide a more general indication of cellular energy metabolism dynamics associated with aerobic and anaerobic conditions. For example, here the decrease of wavelet spectral power may reflect the general switch of cutaneous metabolism towards a glycolytic anaerobic metabolism due to hypoxic stress induced by occlusion of blood flow.

Trends of metabolic oscillators during PORH response

The amplitude of NAD(P)H MO-1 and RR MO-1 and the energy of RR MO-1 (Fig. 68) augmented in all groups during the hyperaemic response compared to both

baseline and ischaemia with significant p-values ($p < 0.01$ or $p < 0.001$). Overall, the increase of spectral amplitudes or energies may reflect the switch towards the normal aerobic metabolism during PORH, consistent with the oxidation of NAD(P)H to $NAD(P)^+$ for the production of ATP through the OXPHOS in the presence of oxygen. However, interesting correlations were found indicating that the RR MO-1 oscillator may partially provide specific information on the activation of the EDHF mechanism, which plays a major role in skin PORH response. These correlations will be discussed in details in the next section 4.5 (paragraph 4.5.2, page 192).

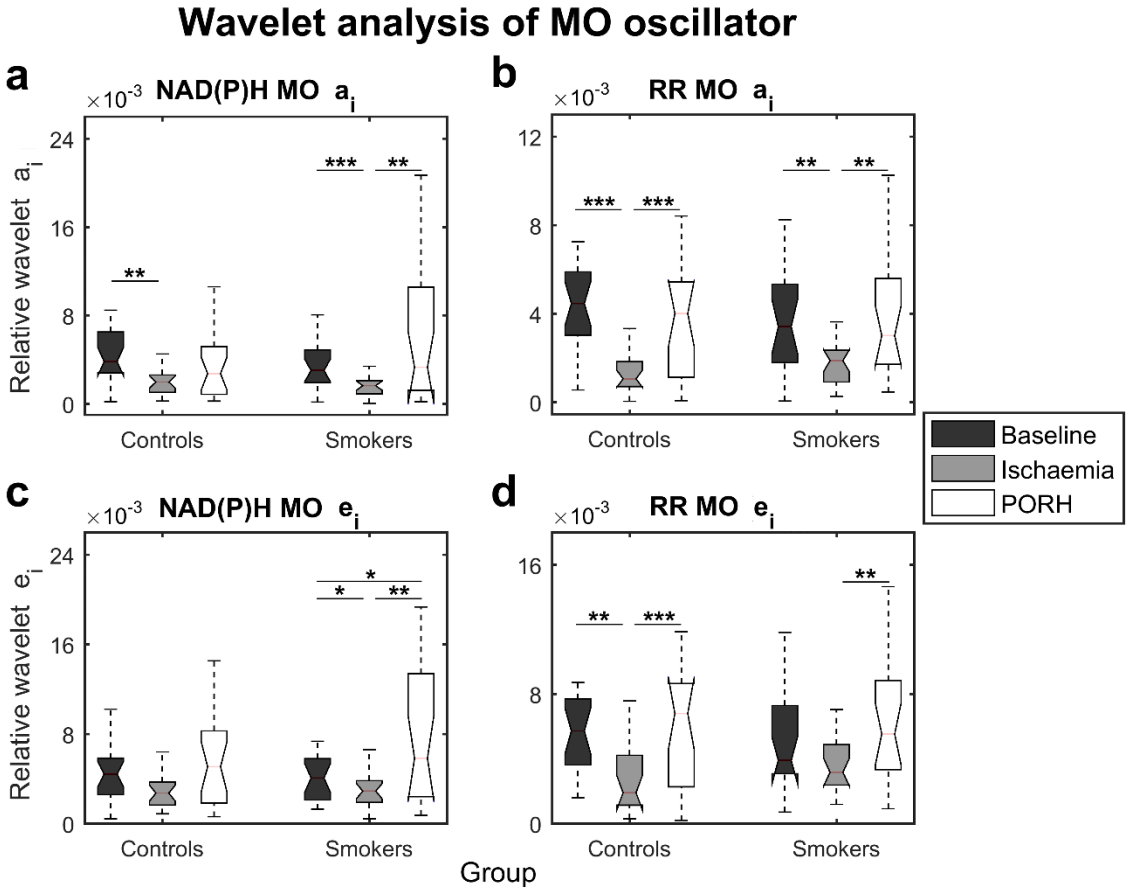

Fig. 69 Trends of the wavelet a_i and e_i of metabolic oscillator (MO) during PORH test. (**a**) NAD(P)H MO and (**b**) RR MO wavelet amplitudes. (**c**) NAD(P)H MO and (**d**) RR MO wavelet energies. Data are presented as boxplots. Both a_i and e_i are expressed in dimensionless units. Black boxplots = Baseline. Grey boxplots = Ischaemia. White boxplots = PORH. Non-significant differences were found between groups. The black lines/asterisks refer to significant changes during PORH task that were estimated by paired Wilcox test. *p < 0.05, **p < 0.01, ***p < 0.001.

The wavelet amplitude/energy of NAD(P)H and RR MO oscillators (Fig. 69) showed an increase during PORH compared to ischaemia but in general non-significant differences were observed between PORH and baseline time points in

both groups. These findings also suggest the hypothesis discussed previously of a more general meaning of MO trends, which in this case may simply reflect the restoration of the aerobic metabolism during PORH response compared to ischaemia, consistent with the oxidation of NAD(P)H to $NAD(P)^+$ for the production of ATP through the OXPHOS.

Differences of metabolic oscillators between smokers and controls

Table 16 shows the comparison of the wavelet amplitude, energy and frequency of MO-1 and MO between smokers and controls. Non-significant differences were found at all stages of the reactive test for all the variables. This indicates that healthy smokers in the average age around forties are characterised by overall functioning dynamics of the oxido-reductive metabolism ensuring an appropriate energy production. However, as will be discussed in section 4.5 (paragraph 4.5.2, page 192), the data reflect some differences in the correlations and interactions between microvascular and metabolic oscillations between non-smokers and smokers. This might indicate that cigarettes smoke causes initial changes in skin oxido-reductive dynamics and microvascular adaptive mechanisms, which may alter the balance of vasoactive substances and switch the pathways involved in microvascular reactivity leading to damage of the endothelium in the long term.

Table 16 Comparison of the wavelet a_i, e_i and f of metabolic oscillators between groups. The table reports the same data of a_i and e_i shown in Fig. 68 and Fig. 69, and the frequency data of metabolic oscillators. Data are expressed as median (inter-quartile range). Both a_i and e_i are expressed in dimensionless units, while f is expressed in hertz (Hz). (B) = Baseline. (IS) = Ischaemia. (P) = PORH. NAD(P)H = Nicotamide adenine dinucleotide. RR = Redox ratio. MO = Metabolic oscillator. Differences between controls and smokers were calculated by unpaired Wilcox test. Non-significant differences were found between the two groups p = p-value.

Wavelet a_i (dimensionless units)			
Variable	**Controls (n=20)**	**Smokers (n=20)**	**p**
(B) $a_{i\ NAD(P)H\ MO-1}$	9.90 (8.00-11.9) × 10^{-3}	8.80 (6.40-11.7) × 10^{-3}	0.7
(IS) $a_{i\ NAD(P)H\ MO-1}$	9.70 (7.40-16.6) × 10^{-3}	9.90 (3.30-14.5) × 10^{-3}	0.6
(P) $a_{i\ NAD(P)H\ MO-1}$	20.1 (17.4-22.2) × 10^{-3}	19.5 (11.7-21.8) × 10^{-3}	0.5
(B) $a_{i\ NAD(P)H\ MO}$	3.80 (2.80-6.40) × 10^{-3}	3.00 (2.00-4.70) × 10^{-3}	0.4
(IS) $a_{i\ NAD(P)H\ MO}$	2.00 (1.00-2.60) × 10^{-3}	1.70 (0.90-2.10) × 10^{-3}	0.3
(P) $a_{i\ NAD(P)H\ MO}$	2.70 (0.90-5.20) × 10^{-3}	3.30 (1.30-10.5) × 10^{-3}	0.5
(B) $a_{i\ RR\ MO-1}$	9.90 (5.80-11.6) × 10^{-3}	6.80 (5.30-10.5) × 10^{-3}	0.2
(IS) $a_{i\ RR\ MO-1}$	6.10 (5.20-8.60) × 10^{-3}	8.30 (5.90-12.8) × 10^{-3}	0.1
(P) $a_{i\ RR\ MO-1}$	18.7 (17.5-21.9) × 10^{-3}	19.8 (17.6-21.2) × 10^{-3}	0.8

(B) $a_{i\ RR\ MO}$	4.50 (3.10-5.70) × 10^{-3}	3.40 (2.00-5.30) × 10^{-3}	0.7
(IS) $a_{i\ RR\ MO}$	1.10 (0.70-1.80) × 10^{-3}	1.90 (1.00-2.30) × 10^{-3}	0.1
(P) $a_{i\ RR\ MO}$	4.00 (1.20-5.20) × 10^{-3}	3.00 (1.80-5.20) × 10^{-3}	0.8
Wavelet e_i (dimensionless units)			
Variable	**Controls (n=20)**	**Smokers (n=20)**	**p**
(B) $e_{i\ NAD(P)H\ MO-1}$	13.8 (11.7-15.8) × 10^{-3}	13.0 (9.90-15.4) × 10^{-3}	0.5
(IS) $e_{i\ NAD(P)H\ MO-1}$	13.0 (9.70-18.0) × 10^{-3}	12.6 (5.40-15.0) × 10^{-3}	0.5
(P) $e_{i\ NAD(P)H\ MO-1}$	16.8 (12.6-20.5) × 10^{-3}	15.0 (7.20-20.3) × 10^{-3}	0.5
(B) $e_{i\ NAD(P)H\ MO}$	4.40 (2.90-5.70) × 10^{-3}	4.10 (2.10-5.60) × 10^{-3}	0.5
(IS) $e_{i\ NAD(P)H\ MO}$	2.70 (1.70-3.50) × 10^{-3}	2.90 (1.90-3.80) × 10^{-3}	0.9
(P) $e_{i\ NAD(P)H\ MO}$	5.10 (1.90-8.20) × 10^{-3}	5.80 (2.60-13.3) × 10^{-3}	0.4
(B) $e_{i\ RR\ MO-1}$	10.7 (8.80-13.1) × 10^{-3}	11.1 (8.20-13.2) × 10^{-3}	0.9
(IS) $e_{i\ RR\ MO-1}$	9.00 (7.90-11.7) × 10^{-3}	10.4 (7.80-14.6) × 10^{-3}	0.3
(P) $e_{i\ RR\ MO-1}$	14.4 (13.2-20.5) × 10^{-3}	16.1 (13.8-19.3) × 10^{-3}	0.6
(B) $e_{i\ RR\ MO}$	5.70 (3.60-7.60) × 10^{-3}	3.90 (3.20-7.30) × 10^{-3}	0.4
(IS) $e_{i\ RR\ MO}$	1.90 (1.20-4.00) × 10^{-3}	3.20 (2.50-4.70) × 10^{-3}	0.06
(P) $e_{i\ RR\ MO}$	6.80 (2.40-8.40) × 10^{-3}	5.50 (3.50-8.40) × 10^{-3}	0.6
Wavelet *f* (Hz)			
Variable	**Controls (n=20)**	**Smokers (n=20)**	**p**
(B) $f_{NAD(P)H\ MO-1}$ [Hz]	6.74 (6.56-8.22) × 10^{-3}	6.68 (4.97-6.83) × 10^{-3}	0.25
(IS) $f_{NAD(P)H\ MO-1}$ [Hz]	6.80 (6.68-6.80) × 10^{-3}	6.80 (6.68-6.80) × 10^{-3}	0.42
(P) $f_{NAD(P)H\ MO-1}$ [Hz]	6.80 (5.15-7.04) × 10^{-3}	5.29 (5.15-6.92) × 10^{-3}	0.88
(B) $f_{NAD(P)H\ MO}$ [Hz]	9.45 (9.45-9.45) × 10^{-3}	9.45 (9.45-9.45) × 10^{-3}	0.95
(IS) $f_{NAD(P)H\ MO}$ [Hz]	9.78 (9.45-9.95) × 10^{-3}	9.95 (9.70-10.1) × 10^{-3}	0.12
(P) $f_{NAD(P)H\ MO}$ [Hz]	9.45 (9.45-9.45) × 10^{-3}	9.45 (9.45-9.45) × 10^{-3}	0.14
(B) $f_{RR\ MO-1}$ [Hz]	6.74 (6.65-8.37) × 10^{-3}	6.68 (6.56-7.07) × 10^{-3}	0.50
(IS) $f_{RR\ MO-1}$ [Hz]	6.80 (6.68-6.80) × 10^{-3}	6.80 (6.68-6.80) × 10^{-3}	0.42
(P) $f_{RR\ MO-1}$ [Hz]	6.80 (5.15-6.95) × 10^{-3}	6.80 (5.24-6.95) × 10^{-3}	0.61
(B) $f_{RR\ MO}$ [Hz]	9.45 (9.45-9.57) × 10^{-3}	9.45 (9.45-9.78) × 10^{-3}	0.82
(IS) $f_{RR\ MO}$ [Hz]	9.95 (9.45-10.1) × 10^{-3}	10.0 (9.70-10.1) × 10^{-3}	0.54
(P) $f_{RR\ MO}$ [Hz]	9.45 (9.45-9.45) × 10^{-3}	9.45 (9.45-9.45) × 10^{-3}	0.60

4.5 Interactions and correlations between microvascular and metabolic oscillators in human individuals

The main goal of this section was studying the possible link between metabolic and microvascular variables to gather information on the role of NAD(P)H and RR dynamics in the vasomotion process induced during PORH response. In order to achieve this objective two kind of analyses were performed:

(1) The wavelet phase coherence (WPCO) analysis, to detect specific interactions between metabolic and microvascular oscillators associated with PORH vasomotion, which may reflect dynamic patterns of cellular ATP production able to drive the regulation of the vascular tone in response to the given stimulus.

(2) Analysis of correlations. The traditional analysis of correlations allows gathering more information than the WPCO on the association between microvascular and metabolic oscillators. This is due to the fact that the WPCO is restricted to the study of phase relationship between oscillators that are located in the same frequency range, i.e. in this case it was possible investigating only the WPCO between MO-1 and the endothelial EDHF oscillators, and MO and the endothelial NO oscillators. Instead, the correlation analysis allows investigating the relationship between all the parameters that have been included in the study. Most of the variables analysed in human subjects were non-parametric, thus here the analysis of correlation was carried out by estimating the Spearman's correlation coefficient ρ.

4.5.1 Phase coherence between metabolic and endothelial oscillators

The WPCO analysis was used to study the interaction $C\phi(\omega k)$ between the MO-1 and the endothelial EDHF oscillators ($C\phi(\omega k)_{NAD(P)H\ MO\text{-}1/EDHF}$, $C\phi(\omega k)_{RR\ MO\text{-}1/EDHF}$), and between MO and the endothelial NO oscillators ($C\phi(\omega k)_{NAD(P)H\ MO/NO}$, $C\phi(\omega k)_{RR\ MO/NO}$) that are located in the same frequency intervals. Table 17 summarises the results of the WPCO analysis. The data show baseline coherence values for the analysed interactions between 0.66 and 0.75, suggesting a relevant basal partial relationship between metabolic and microvascular endothelial oscillators in agreement with data from mouse models (section 3.4, paragraph 3.4.1, page 145). This finding might suggest a relevant interaction between cellular metabolic oscillatory processes and microvascular dynamics in the human skin. However, because the WPCO analysis in this dissertation does not include the surrogate data testing described recently by Gruszecki *et al.* [165], the assumptions above on the degree of baseline coherence might not be reliable due to bias affecting the WPCO values in the low frequencies. Nonetheless, cautious comparisons of the differences between controls and smokers and between PORH time points can be made.

Table 17 Phase coherence between metabolic and endothelial oscillators during PORH test. Data are expressed as mean ± SD. *Cϕ(ωk)* = Wavelet phase coherence. (B) = Baseline. (IS) = Ischaemia. (P) = PORH. NAD(P)H = Nicotamide adenine dinucleotide. MO = Metabolic oscillator. EDHF = Endothelial-derived hyperpolarizing factor. NO = Nitric oxide. RR = Redox ratio. Differences between groups were calculated by unpaired t-test and are outlined by red asterisks. p = p-value. *p < 0.05.

Variable	Controls (n=20)	Smokers (n=20)	p
(B) $C\phi(\omega k)_{NAD(P)H\ MO\text{-}1/EDHF}$	0.73 ± 0.05	0.75 ± 0.04	0.30
(IS) $C\phi(\omega k)_{NAD(P)H\ MO\text{-}1/EDHF}$	0.82 ± 0.05	0.84 ± 0.04	0.50
(P) $C\phi(\omega k)_{NAD(P)H\ MO\text{-}1/EDHF}$	0.86 ± 0.04	0.86 ± 0.03	0.50
(B) $C\phi(\omega k)_{NAD(P)H\ MO/NO}$	0.66 ± 0.04	0.69 ± 0.05	0.10
(IS) $C\phi(\omega k)_{NAD(P)H\ MO/NO}$	0.74 ± 0.04	0.74 ± 0.06	0.60
(P) $C\phi(\omega k)_{NAD(P)H\ MO/NO}$	0.78 ± 0.05	0.77 ± 0.06	0.90
(B) $C\phi(\omega k)_{RR\ MO\text{-}1/EDHF}$	0.74 ± 0.05	0.74 ± 0.04	0.90
(IS) $C\phi(\omega k)_{RR\ MO\text{-}1/EDHF}$	0.83 ± 0.05	0.80 ± 0.03	0.50
(P) $C\phi(\omega k)_{RR\ MO\text{-}1/EDHF}$	0.88 ± 0.04	0.88 ± 0.04	1.00
(B) $C\phi(\omega k)_{RR\ MO/NO}$	0.66 ± 0.03	0.67 ± 0.04	0.50
(IS) $C\phi(\omega k)_{RR\ MO/NO}$	0.77 ± 0.04	0.70 ± 0.05	*0.02
(P) $C\phi(\omega k)_{RR\ MO/NO}$	0.79 ± 0.06	0.80 ± 0.06	0.60

Trends of phase coherence data during ischaemia

For all the interactions under investigation the phase coherence augmented with statistical significance ($p < 0.001$) during ischaemia in both groups (Fig. 70a-d), indicating an increase of interaction between the oscillators associated with the hypoxic stress. This may reflect the global cooperation between metabolic and endothelial components to activate protective mechanisms against the ischaemic damage in ECs and VSMCs, probably consistent with uncoupling of the electron transport chain, and preferential production of glycolytic ATP for sustaining the activation of vasodilator dynamics aimed at moderating vasoconstriction and ensure the distribution of the remaining nutritive blood to the surrounding tissue. This interpretation is supported also by data discussed previously showing the increase of both EDHF (Fig. 64-65a, pages 167-168) and myogenic (Fig. 64-65d, pages 167-168) wavelet amplitudes/energies in controls during ischaemia, indicating the activation of vasodilation dynamics to contrast vasoconstriction. However, the increase of EDHF wavelet energy was not observed for smokers, which could be consistent with less efficient activation of this mechanism as consequence of exposure to cigarettes smoke and increase of oxidative stress.

Trends of phase coherence data during PORH

Both groups showed a significant increase of phase coherence between MO-1 and EDHF up to 0.86 ($C\phi(\omega k)_{NAD(P)H\ MO\text{-}1/EDHF}$) and 0.88 ($C\phi(\omega k)_{RR\ MO\text{-}1/EDHF}$) during PORH compared to both baseline and ischaemia (Fig. 70a and Fig. 70c), indicating an additional increase of interaction between vascular and metabolic oscillators during cutaneous hyperaemic response. This may reflect the reactivation of the aerobic metabolism by oxidation of NAD(P)H in $NAD(P)^+$, and the concurrent and consequent activation of EDHF, NO, neurogenic and myogenic vasodilation mechanisms at the basis of the hyperaemic vasomotion, sustained by ATP energy produced through OXPHOS process.

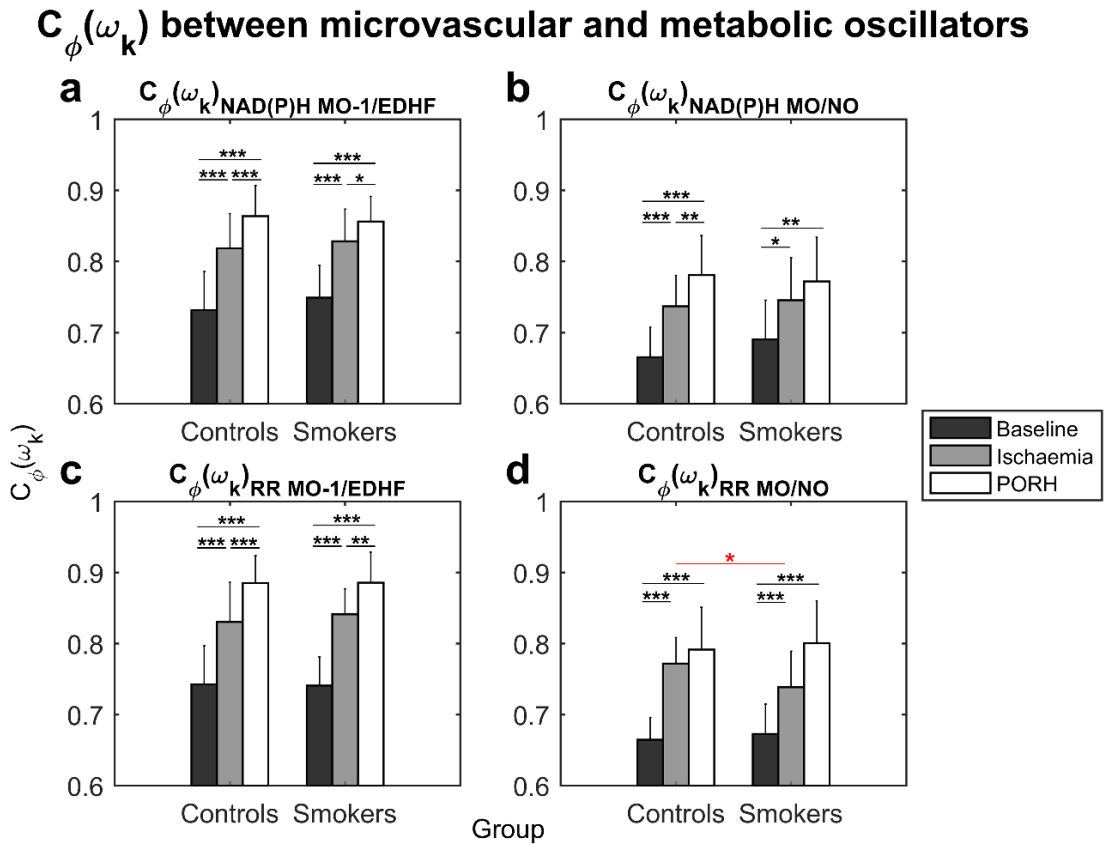

Fig. 70 Trends of phase coherence between metabolic and endothelial oscillators during PORH test. Bar plots of the data reported in Table 17. (**a**) Coherence between NAD(P)H MO-1 and EDHF oscillators. (**b**) Coherence between NAD(P)H MO and endothelial NO oscillators. (**c**) Coherence between RR MO-1 and EDHF oscillators. (**c**) Coherence between RR MO and endothelial NO oscillators. $C_\phi(\omega_k)$ = Phase coherence. NAD(P)H = Nicotamide adenine dinucleotide. MO = Metabolic oscillator. EDHF = Endothelial-derived hyperpolarizing factor. NO = Nitric oxide. RR = Redox ratio. Data are presented as bar plots of the mean with error bars corresponding to the SD. Differences between PORH time points were calculated by paired t-test and are outlined by black lines/asterisks. Differences between groups were calculated by unpaired t-test and are outlined by red lines/asterisks. *p < 0.05, **p < 0.01, ***p < 0.001.

The phase coherence between MO and endothelial NO oscillations (Fig. 70b and Fig. 70d) during PORH was higher than baseline with statistical significance ($p < 0.001$ or $p < 0.01$). However, overall non-significant differences were found between ischaemia and PORH time points. This suggests that the interaction between MO and NO oscillators is not relevant for the modulation skin PORH.

Differences of phase coherence between controls and smokers

Overall, non-significant differences of phase coherence values were found between the two groups, except for the phase coherence between RR MO and endothelial NO ($C\phi(\omega k)_{RR\ MO/NO}$) that was higher in controls during ischaemia ($p < 0.05$) (Table 17). This also suggest a slightly better endothelial-mediated response to hypoxia in controls compared to healthy smokers due to lower oxidative stress and absence of exposure to cigarettes smoke.

4.5.2 Relevant correlations and regulatory mechanism of PORH vasomotion

The analysis of correlations between the multiple parameters examined in this work outlined that the vasomotion mediated by EDHF during skin PORH response may be regulated through different mechanisms in smokers and non-smokers. In this context, the dynamics of RR MO-1 metabolic oscillator and its interaction with the EDHF oscillator may reflect the degree of activation of EDHF through the EETs pathway, which seems to contribute differently to vasomotion in smokers (less contribution) and non-smokers (more contribution). Before discussing in details the set of relevant correlations observed in this study, a brief description of the modalities of activation of the EDHF signalling is provided to allow a better understanding of the hypotheses proposed in this section.

Possible mechanisms for the activation of EDHF signalling

The EDHF released by ECs acts on VSMCs cells inducing hyperpolarisation and relaxation of the vascular tone. This mechanism can be activated through different pathways:

(1) Pathways implicating the hyperpolarisation of ECs and transmission of the signal to induce VSMCs hyperpolarisation by gap junctions or K^+ channels [193]. These mechanisms may involve also bidirectional feedbacks with signals transmitted from ECs to VSMCs and vice-versa [140].

(2) Pathways involving the production of chemical metabolic products released by ECs to target VSMCs and induce hyperpolarisation [193]. These

mechanisms mainly involve an endogenous unidirectional release of the metabolites from ECs to VSCMs.

One of the main mechanisms of activation of EDHF during cutaneous PORH is mediated by the production and release of the epoxyeicosatrienoic acids (EETs) metabolites from ECs to VSMCs [9, 193]. The cytochromes P450 (CYPs) enzymes are involved in EETs biosynthesis through the transfer of electrons from NAD(P)H to the P450 cofactor.

EDHF may be activated differently in smokers and controls during PORH

According to Cracowski *et al.* [193] the endothelial EDHF activity mediated by EETs contributes more to the time course of the cutaneous hyperaemic response (PORH AUC) rather than the hyperaemic peak. The experimental data from this dissertation are in agreement with this hypothesis, indeed a positive significant correlation was found between skin PORH AUC and the wavelet energy/amplitude of the EDHF oscillator in both the tested groups (ρ=0.50 and p=0.02 or p=0.01 in controls, ρ=0.50 and p=0.03 in smokers). Furthermore, the same degree of correlation was found between PORH AUC and the energy of the myogenic oscillator in smokers (ρ=0.50, and p=0.03) but not in controls. This observation supports the hypothesis that the more enhanced EDHF activity observed in healthy smokers compared to controls during cutaneous PORH (Table 13, page 172) may be an indirect consequence of a basal VSMCs hyper-stimulation caused by cigarettes smoke, which may enhance further EDHF by the bidirectional communication between VSMCs and ECs through gap junctions and K^+ channels in addition to the EETs endothelial metabolic mechanism.

The interaction between RR MO-1 and EDHF oscillators may reflect the degree of activation of the EETs pathway

The correlation analysis in the control group has also revealed a relationship between PORH AUC and the wavelet phase coherence between RR MO-1 and the EDHF oscillators (ρ=-0.75, p=0.0001). This correlation was absent in smokers. The phase coherence is a measure of the degree of interaction between oscillators in the same frequency range. Therefore, this observation indicates that in the control group the time course of PORH response is highly influenced by the degree of interaction between RR MO-1 and EDHF oscillators. The negative correlation (ρ=-0.75) indicates that PORH AUC is higher when the interaction

between EDHF and RR MO-1 oscillators is lower, which may be the case when these oscillators are involved in opposite interfering activities. For example, in biological terms this opposite activity may reflect the increase in production of EETs during PORH time course leading to EDHF activation, and in contrast the simultaneous conversion of NAD(P)H in $NAD(P)^+$ (lower NAD(P)H concentrations) required for both the biosynthesis of EETs and the reactivation of the OXPHOS. The activation of EDHF during PORH is confirmed by the increase of EDHF oscillator's wavelet amplitude/energy observed in Fig. 64-65a (pages 167-168), while the conversion of NAD(P)H to $NAD(P)^+$ might be partially reflected by the increase of RR MO-1 wavelet amplitude and the reduction of the relative amounts of NAD(P)H observed during PORH in Fig. 68b (page 184) and Fig. 62a (page 163), respectively.

RR MO-1 and EDHF oscillators have an opposite effect on the time employed to reach the hyperaemic blood perfusion peak

The hypotheses above are supported further by a set of correlations that were found exclusively in the control group, related to the time to reach the PORH peak. The time to peak was negatively correlated to the wavelet amplitude/energy ($-0.50 < \rho < -0.40$, $0.03 < p < 0.05$) of RR MO-1, while it was positively related to the wavelet amplitude/energy ($0.60 < \rho < 0.70$, $0.0009 < p < 0.0020$) of the EDHF oscillator, suggesting a concurrent opposite effect of RR MO-1 and EDHF oscillations on the determination of the time to reach the hyperaemic peak. Indeed, these correlations indicate that the aerobic mitochondrial activity restored during PORH response promotes a fast time to peak associated with the increase of RR MO-1 wavelet amplitude and conversion of NAD(P)H in $NAD(P)^+$. However, the simultaneous activation of EDHF mediated by EETs affects the hyperaemic response in an opposite way promoting an increase of the duration of PORH and time to achieve the peak. Therefore, the longer time to reach the peak and larger PORH AUC found in the control group may be due to a major activation of EDHF mediated by EETs compared to smokers.

Exposure to cigarettes smoke may impact negatively EETs pathway

The fact that the set of correlations discussed above was not found in smokers may support the hypothesis proposed above about lower activation of EETs during PORH in favour of other EDHF signalling mechanisms that do not involve

the conversion of NAD(P)H in $NAD(P)^+$ to activate EETs, and that can be promoted by exogenous factors (e.g. nicotine) stimulating the bidirectional communication between VSMCs and ECs through gap junctions and K^+ channels. Indeed, smokers showed higher relative concentrations of reduced NAD(P)H (Fig. 62a, page 163) during PORH compared to controls, which may account for lower conversion of NAD(P)H in $NAD(P)^+$ impacting negatively the EETs pathway. The lower production of EETs may be an effect of the exposure to cigarettes smoke and the consequent oxidative stress. Indeed, smoking and increased amounts of ROS have been reported as factors able to induce an impairment of EETs pathway associated with the aetiology of hypertension, heart failure, metabolic disorders, and the increase of endothelial dysfunction related to atherosclerosis [194]. Moreover, as shown previously, the wavelet frequency f of the EDHF oscillator during PORH was significantly higher ($p < 0.001$) in smokers compared to controls (Table 13, page 172), as well as the *f* of the myogenic oscillator (Table 13, page 172). Considering that the electric signalling is characterised by transmission rates faster than metabolic communication, these observations could be also a relevant indirect indication of a preferential activation of EDHF through gap junctions rather than EETs in smokers.

Future perspectives

Although the integration of multi-parameter findings in this thesis seems to support the interpretations above, further experiments should be performed to confirm the proposed hypotheses. Specifically, these aspects can be elucidated better by assessing RR MO-1 and EDHF oscillators in the forearm during PORH test combined with the local administration of inhibitors of EETs biosynthesis (fluconazole or sulfaphenazole [193]), and inhibitors of the EDHF mechanism mediated by KCa potassium channels, i.e. tetraethylammonium (TEA) [195]. Moreover, the study of these factors in subjects affected by different CVD risk factors (i.e. high BP, high BMI, high hypercholesterolemia, insulin resistance and diabetes) may allow the implementation of preclinical diagnostic applications of EDHF and RR MO-1 oscillators. Indeed, the results reported in this section suggest that the interaction between EDHF and RR MO-1 oscillators may be a nonlinear process reflecting the degree of dysfunction of the EETs pathway, which is a factor involved in the development of pathological conditions such as hypertension and metabolic disorders with cardiovascular implications [194].

4.6 Examination of LDF attractors as predictors of CVD risk

Brief summary on the definition of "attractors" and their use as markers of risk

The term "attractors" indicates a series of mathematical or physical variables able to describe the evolution of a dynamic system over time [122]. The computation of attractors for nonlinear signals describing a cardiovascular process, i.e. ECG, heart rate variability (HVR) or LDF, is considered a powerful approach for the prediction of vascular dysfunction [102]. Examples of attractors for this purpose are dimensional features of the signal, i.e. the fractal dimension (D) and the correlation dimension (D_2), parameters outlining the degree of order/disorder of a signal, e.g. entropy (H_0) and the information dimension (H_i), or factors defining the scaling properties of the signal, i.e. the Hurst exponent (H) [102]. Greater values of dimensional attractors and entropy correspond to a major complexity of the signal [102], while the Hurst index provides information on the persistence ($H > 0.5$) or anti-persistence ($H < 0.5$) of the signal which may indicate respectively a well-functioning or impaired vascular system. The analysis of complexity of BP and HVR signals has revealed greater fractal dimension and entropy in young compared to aged individuals, and in women compared to men [102]. Based on these observations, it has been proposed that a loss of complexity of cardiovascular signals may be associated with vascular dysfunction [116, 121].

4.6.1 Relevant differences of LDF attractors between smokers and controls

In this work, various attractors of LDF signal were estimated to understand their possible application for the prediction of skin microvascular dysfunction. Fig. 71 shows a 3D phase-space reconstruction of the median LDF signals from the controls and smokers groups tested in this study. The charts provide a portrait of the complex nonlinear structure of LDF signal in the phase-space during the steps of the PORH test. Differences related to the complex nonlinear dynamic patterns of the signal are visible between the tested groups at all the stages of PORH test, which could be used for the purpose of distinguishing healthy or impaired vascular conditions. This may be achieved by assessing the set of variables listed above (D, D_2, H_0, H_i, H) that provide a quantitative measure of the chaotic content and complexity of the signal. These parameters were estimated according to the principles described in paragraphs 1.8.8 (page 61) and 2.3.5 (page 115), by using the embedding dimensions m of the phase-space reconstructed attractor.

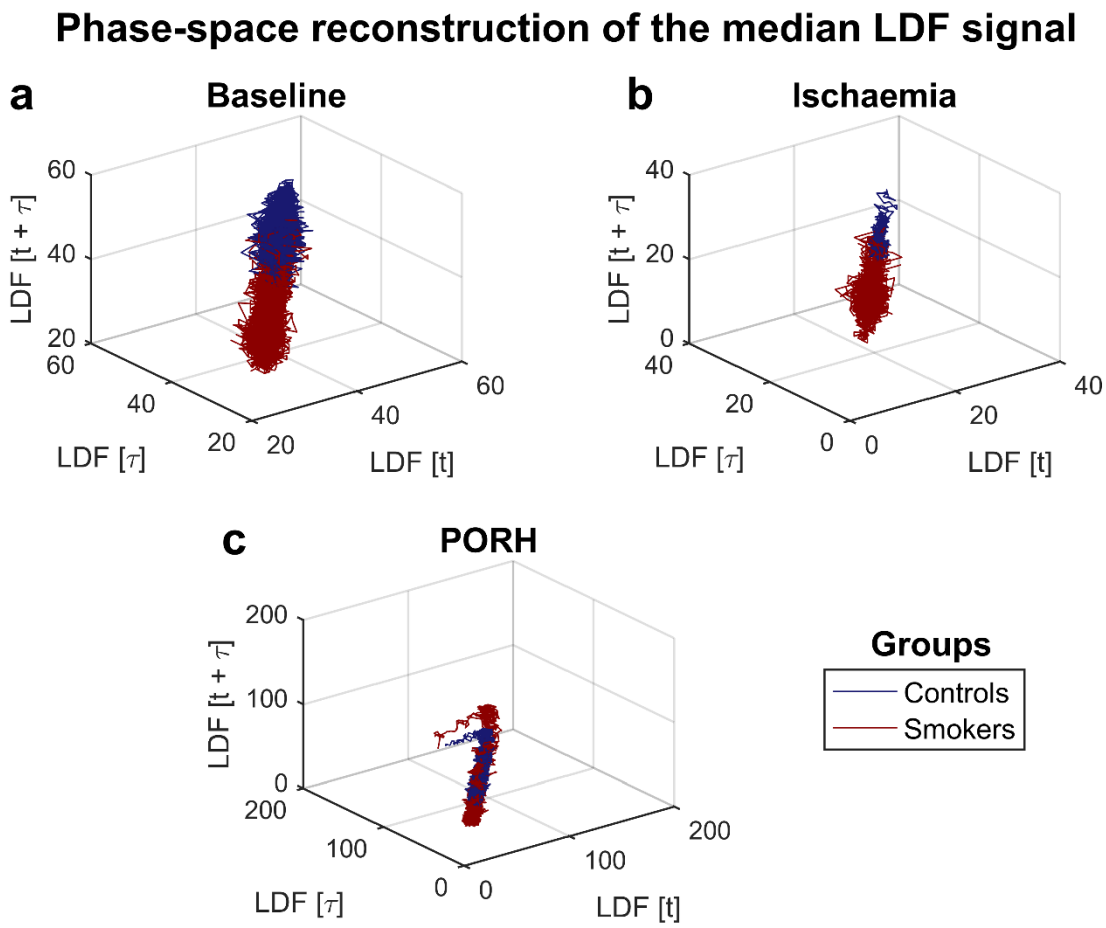

Fig. 71 3D graphic visualisation of the complexity of LDF signal during PORH test. Reconstruction of the attractors in the *m*-dimensional phase-space from the median LDF signal of non-smokers (dark blue line) and smokers (dark red line). (**a**) Baseline attractors. (**b**) Ischaemia attractors. (**c**) PORH attractors. The graphs clearly show differences in the complex nonlinear dynamics of LDF signal between non-smokers and healthy mild smokers at all the stages of the reactive functional task. The attractors were reconstructed according to the Takens method of delays [196, 197], by using an appropriate time lag τ estimated by calculating the first local minimum value from the graph of average mutual information (AMI). The optimal time lag for the analysed data was τ=1 for the controls' baseline time series (12000 samples), τ=3 for the smokers' baseline and ischaemia time series (12000 and 6000 samples respectively), τ=2 for the controls' ischaemia time series (6000 samples), τ=88 and τ=59 respectively for controls' and smokers' PORH time series (12000 samples). The number of embedding dimensions *m* of each attractor in the phase-space was calculated based on the optimal time lag chosen for each time series: 13 *m* for controls' baseline signal, 17 *m* for smokers' baseline signal, 20 *m* for controls' ischaemia signal, 24 *m* for smokers' ischaemia signal, 11 *m* for controls' PORH signal, 14 *m* for smokers' PORH signal. The embedding dimensions were used for the subsequent estimation of the quantitative parameters (D, D_2, H_0, H_i, H) defining the complexity of the attractors.

Table 18 displays the comparison of D, D_2, H_0, H_i, and H between controls and smokers during PORH test.

Table 18 Comparison of LDF attractors between smokers and controls. Normal data are expressed as mean ± SD. Non-parametric data are presented as media (inter-quartile range). (B) = Baseline. (IS) = Ischaemia. (P) = PORH. D = Fractal dimension. H = Hurst exponent. H_0 = Entropy. H_i = Information dimension. D_2 = Correlation dimension. Differences between groups are outlined by red asterisks and were estimated by unpaired t-test or Wilcox test, respectively for normal and non-parametric variables. p = p-value. *p < 0.05, **p < 0.01, ***p < 0.001.

Variable	Controls (n=20)	Smokers (n=20)	p
(B) *D*	1.08 ± 0.10	1.23 ± 0.08	***0.0006
(IS) *D*	1.17 ± 0.09	1.22 ± 0.06	0.0600
(P) *D*	1.17 ± 0.08	1.23 ± 0.05	**0.0060
(B) *H*	1.10 ± 0.40	1.10 ± 0.30	0.7000
(IS) *H*	0.70 ± 0.30	0.70 ± 0.40	0.9000
(P) *H*	1.20 ± 0.30	1.00 ± 0.20	**0.0070
(B) H_0	0.31 (0.30-0.34)	0.30 (0.28-0.33)	0.2000
(IS) H_0	0.19 (0.18-0.20)	0.24 (0.17-0.26)	0.7000
(P) H_0	0.36 (0.34-0.38)	0.35 (0.32-0.37)	0.3000
(B) H_i	0.021 (0.019-0.031)	0.016 (0.012-0.023)	***0.0007
(IS) H_i	0.013 (0.011-0.023)	0.006 (0.003-0.010)	**0.0030
(P) H_i	0.013 (0.011-0.015)	0.008 (0.007-0.010)	***0.0006
(B) D_2	1.50 (1.40-1.60)	1.60 (1.20-1.90)	0.7000
(IS) D_2	1.00 (0.80-1.21)	1.10 (0.60-1.60)	0.8000
(P) D_2	1.40 (1.30-1.40)	1.70 (1.30-1.80)	*0.0200

Differences of the fractal dimension attractor (D) between groups

The values of D were significantly greater in smokers compared to controls during both baseline ($p < 0.001$) and PORH response ($p < 0.01$). These results indicate a major fractal complexity characterising the blood flow dynamics in healthy smokers, suggesting that care must be taken when evaluating the attractors as predictors of vascular dysfunction. Indeed, although it has been reported in literature that lower complexity is associated with cardiovascular dysfunction [116, 121], this is not true for the groups of healthy subjects examined in this work. As discussed in paragraph 4.4.1 (page 173), smokers were characterised by hyperactive adaptive microvascular reactivity in response to the exposure to tobacco, which may be an early indicator of risk. Therefore, lower complexity

cannot be considered as an absolute indicator of cardiovascular dysfunction, and the interpretation of this parameter may vary depending on the analysed signal, and the risk factors and health status characterising the tested groups. For cutaneous LDF signals of healthy smokers, higher values of fractal dimension *D* may be an early indicator of vascular risk.

Differences of the correlation dimension attractor (D_2) between groups

The correlation dimension is an attractor providing variable results that may show different patterns and have different meanings depending on the kind of analysed signals. For example, the estimation of this parameter from HVR time series provided greater values for healthy subjects compared to individuals affected by cardiac arrhythmia (bigeminy) [196]. In this case, an increase in the complexity associated with the correlation dimension feature of the signal indicates optimal cardiovascular function. However, the estimation of the correlation dimension from ECG signals showed opposite results, with greater values of this parameter for diseased subjects affected by bigeminy [196]. Therefore, caution must be taken when presenting and interpreting data related to this attractor. In this work, D_2 was found significantly higher ($p < 0.05$) in smokers compared to controls during PORH response (Table 18). Thus, in the case of cutaneous LDF signals higher values of D_2 complexity may be an indicator of early microvascular dysfunction for healthy smokers.

Differences of entropy (H_0) and information dimension (H_i) between groups

These two attractors are strictly linked to each other, indeed the value of entropy is used for estimating the information dimension. However, the meaning of these variables is different, as entropy is a measure of the quantity of information required for the prediction of the future status of the dynamic system under investigation [102], while the information dimension represents a measure of the rate of temporal growth of the information contained in the dynamic system. In general, the increase of H_0 and H_i indicates a growth of the complexity of the dynamic system under investigation, less order and less predictability, even though the results obtained in this study suggest that attractors' data interpretation may vary depending on several factors and the increase of complexity is not always an indicator of cardiovascular dysfunction. Here, the comparison of entropy values between smokers and non-smokers did not show

significant differences between the two groups (Table 18). In contrast, the information dimension was significantly higher in controls at all the stages of PORH test, indicating a lower growth rate of information characterising the microvascular dynamics of smokers, which may be an early indicator of risk.

Differences of the Hurst index (H) attractor between groups

Although the Hurst exponent variable is denoted by *H*, this is not an entropy related measure. As explained in section 1.8 (paragraph 1.8.8, page 61) this attractor is related to the fractal dimension *D*. Here, the values of *H* were > 0.5 in both groups during all the stages of reactive hyperaemia (Table 18), indicating a persistent behaviour of LDF time series that is typical of signals reflecting an overall healthy vascular system. The value of *H* was significantly higher in controls compared to smokers during PORH response, even though this observation does not seem reliable for differentiating the two groups. Indeed, the correlation analysis, which will be discussed in the next paragraph, has revealed that the increase of *H* is associated with the presence of several risk factors, including also cigarettes smoke. Therefore, it was more likely to expect greater values of *H* in healthy smokers rather than in controls. Based on these observations, it can be concluded that this parameter is not reliable as predictor of CVD risk in healthy smokers.

4.6.2 Physiological meaning of LDF attractors

The attractors are parameters that define mathematical features of the analysed signal. To use these factors as biomarkers of CVD risk, a better understanding of the physiological processes reflected by these mathematical variables is required. The multi-parameter approach that was employed in this work allowed getting more insights on the physiological meaning of the attractors, which was examined by analysing their correlation with other parameters measured in the study, i.e. general clinical variables (BP, age, BMI, etc.), wavelet microvascular and metabolic oscillators, and tissue oxygenation data (SO_2, O_2ER and VO_2).

Physiological meaning of the fractal dimension D of LDF signal

Fractal dimension and systolic blood pressure (SBP). The most relevant correlations observed for the fractal dimension attractor indicate that the quantitative changes of *D* could reflect the regulation of the baseline systolic blood pressure (SBP). The control group showed a relevant negative correlation

between *D* and the SBP (r=-0.50, p=0.04), indicating that the increase of complexity is associated with lowering of systolic blood pressure in healthy subjects. In addition, the relevant negative correlation observed between the endothelial NO oscillator and SBP (ρ=-0.50, 0.01 < p < 0.03), and the positive correlation between EDHF (ρ=0.40, 0.001 < p < 0.002) or NO (0.40 < ρ < 0.50, 0.0001 < p < 0.0004) oscillators and the fractal dimension suggest that the endothelial modulation of microvascular tone may be a key factor involved in the control of SBP in healthy individuals. Indeed, these observations indicate that the increase of endothelial-mediated vaso-relaxation leads to growth of complexity of microvascular dynamics and lowering of SBP. Furthermore, the SBP showed a high negative correlation with the phase coherence between RR MO-1 and EDHF oscillators (r=-0.60, p=0.006), suggesting an important role of the interaction between mitochondrial oxido-reductive oscillatory reactions and microvascular endothelial modulation for the control of SBP. This observation is not casual, indeed in section 4.5 (paragraph 4.5.2, page 193) it has been emphasised that the phase coherence between RR MO-1 and EDHF may reflect the degree of activation of EETs-mediated EDHF, and the dysfunction of the EETs pathway has been described as a factor involved in the development of hypertension [194].

The set of correlations described above was absent in smokers, which may indicate an alteration of the normal pathways involved in the control of SBP and the switch towards different regulatory mechanisms leading to the development of pathological hypertensive conditions in the long term. This is confirmed by the fact that the basal SBP in smokers was negatively correlated with the neurogenic (ρ=-0.45, p=0.04), myogenic (ρ=-0.50, p=0.04), and NAD(P)H MO-1 (ρ=-0.50, 0.01 < p < 0.03) oscillators, while non-relevant correlations were found with the endothelial oscillators. These findings indicate a major involvement of different microvascular components in the regulation of SBP in smokers compared to controls, probably due to the direct negative effects of tobacco. Indeed, the myogenic and neurogenic microvascular components can be activated directly from exogenous factors contained in cigarettes smoke, such as nicotine that is able to enhance the neurogenic control by targeting cholinergic nicotinic receptors, and the external NO that can target directly VSMCs enhancing the myogenic mechanism. The non-specific activation of these factors may interfere with the control of SBP mediated by endothelial cells and enhance different

regulatory mechanisms. Further support to this hypothesis is provided by the relevant positive correlation found between SBP and the number of smoking years (r=0.70, p=0.001), and the negative correlation between the neurogenic (ρ=-0.50, 0.03 < p < 0.04) and myogenic (ρ=-0.50, p=0.03) oscillators and the number of smoking years. These correlations indicate that as the years of exposition to cigarettes smoke increase, the SBP growths as a consequence of the decrease of neurogenic and myogenic modulation, reflecting the impairment of the SBP control mechanisms typical of smokers which seems to rely on the activity of neurogenic/myogenic components.

Fractal dimension and microvascular dynamics. Additional correlations indicate that the quantitative changes of *D* values may reflect also the general degree of complexity of microvascular dynamics. Indeed, positive correlations were observed in the control group between *D* and EDHF (ρ=0.40, 0.001 < p < 0.002), endothelial NO (0.40 < ρ < 0.50, 0.0001 < p < 0.0004), neurogenic (ρ=0.40, 0.0005 < p < 0.0030), and myogenic (0.30 < ρ < 0.40, 0.002 < p < 0.009) microvascular oscillators. Overall, these findings show a global cooperation of the microvascular components to determine the complexity of flow dynamics in healthy subjects, and are in agreement with the general dogma associating the increase of complexity with an increase of vascular reactivity.

Physiological meaning of the correlation dimension D_2 of LDF signal

Correlation dimension and cardiac output. The quantitative increase of correlation dimension may reflect higher cardiac output. Indeed, relevant positive correlations were found in the healthy group between D_2 and some variables related to the cardiac output, such as the frequency *f* (ρ=0.45, p=0.0002) and amplitude/energy (0.60 < ρ < 0.70, p < 0.0001) of the cardiac oscillator, and the oxygen consumption VO_2 (0.30 < ρ < 0.40, 0.0004 < p < 0.0400). Several literature reports have described higher cardiac output associated to cardiovascular pathologic conditions characterised by increased heart rate [180, 181, 182, 183]. Therefore, D_2 may find application as biomarker of risk for cardiovascular illness related with changes in the heart rate.

Physiological meaning of the entropy H_0 of LDF signal

Entropy and cardiac output. The pattern of correlations that was found in this study in relation to H_0 suggests an association of the increase of entropy with

higher cardiac output. Indeed, both groups showed positive correlations of H_0 with oxygen consumption VO_2 ($0.30 < \rho < 0.50$, $0.0001 < p < 0.0400$) and the cardiac oscillator ($0.50 < \rho < 0.70$, $p < 0.0001$) suggesting an increase of entropy associated with higher cardiac output. As discussed above for the correlation dimension, the increase of cardiac output is associated to cardiovascular pathologic conditions characterised by increased heart rate [180, 181, 182, 183]. Therefore, also H_o may find application as biomarker of risk for cardiovascular illness related with changes in the heart rate.

Physiological meaning of the information dimension H_i of LDF signal

Information dimension and cardiac output. As observed for D_2 and H_0, also H_i showed positive correlations with oxygen consumption VO_2 (ρ=0.40, p=0.003) and the cardiac oscillator ($0.50 < \rho < 0.60$, $p < 0.0001$), indicating that the increase of information dimension values is associated with higher cardiac output. Therefore, also H_i may find application as biomarker of risk for cardiovascular illness related with changes in the heart rate.

Information dimension and microvascular dynamics. Additional correlations indicate that the quantitative changes of H_i values may reflect also the general degree of complexity of microvascular dynamics. Both groups showed negative correlations with the EDHF ($-0.35 < \rho < -0.60$, $0.0001 < p < 0.0060$), endothelial NO ($-0.30 < \rho < -0.50$, $0.0001 < p < 0.0400$), neurogenic ($-0.40 < \rho < -0.60$, $0.0001 < p < 0.0030$), and myogenic ($-0.30 < \rho < -0.60$, $0.0001 < p < 0.0200$) oscillators. This means that the increase of information dimension is associated with general reduced microcirculation.

Physiological meaning of the Hurst exponent H of LDF signal

Hurst exponent and energy metabolism. Most of the correlations found for *H* were related to metabolic factors. Indeed, *H* was positively correlated with the body mass index (BMI) (r=0.40, almost significant p=0.06) in the control group, and with NAD(P)H MO (ρ=0.30, $0.006 < p < 0.010$), RR MO ($0.40 < \rho < 0.50$, $0.0002 < p < 0.0070$) and NAD(P)H MO-1 (ρ=0.30, p=0.01) metabolic oscillators in both groups. Moreover, a relevant positive correlation was found between *H* and SBP (r=0.50, p=0.01) in controls. Overall, these observations suggest that the Hurst index of LDF signal may reflect dynamics related to energy metabolism

processes and their effect on the control of the systolic blood pressure. Thus, the increase of the *H* could be associated with hypertension and obesity.

Hurst exponent and smoking. Additionally, a positive correlation was found between *H* and the number of years of exposition to cigarettes smoke (r=0.50, p=0.02) in smokers. This indicates that increased values of *H* might be an indicator of risk for smokers, even though as discussed in paragraph 4.6.1 (page 200), *H* did not provide reliable differences between controls and healthy smokers.

5 Conclusions and future perspectives

5.1 Conclusions

5.1.1 Rationale and objectives of the study

Novel biomarkers for the non-invasive assessment of CVD risk

The peripheral skin microcirculation is a hallmark of the general health status of the cardiovascular system, which can be evaluated non-invasively by the combination of reactive tests and optical/laser methods to examine the functional dynamics and the degree of oxidative stress of skin micro-vessels. Many studies have characterised oscillators of skin blood flow signal that are potentially eligible as novel predictors of CVD risk. Furthermore, recently scientists have also focused on the study of the oxido-reductive dynamics of cell energy metabolism, detectable by analysing the oscillations of NAD(P)H autofluorescence. Metabolic oscillators may reflect specific patterns of ATP production related with normal or diseased vascular conditions, thus they may also be potential risk markers. Moreover, the concurrent evaluation of blood flow and NAD(P)H dynamics may outline specific links between microvascular and metabolic oscillators that could help to elucidate further the cellular mechanisms at the basis of vasomotion.

Objectives

The main goals of this research were:

(1) The first attempt to detect simultaneously blood flow and metabolic oscillators *in-vivo* and investigating their role and interaction in skin vasomotion.
(2) Assessing the potential use of cutaneous blood flow and metabolic oscillators as predictors of CVD risk associated with oxidative stress and smoke.

This was achieved by concurrent evaluation of the nonlinear dynamics of blood flow and metabolic NAD(P)H and RR signals measured from the skin of mouse models and human subjects by single-point autofluorescence readouts. Specific details on the protocols implemented in this study are reported in the sections 2.4 (mouse protocol, page 115) and 2.5 (human protocol, page 119). Additionally to the main objectives discussed above, the experiments carried out in this work allowed also the characterisation of the endothelial EDHF oscillator, as well as testing the potential use of the “attractors” and tissue oxygenation parameters (oxygen extraction, oxygen consumption) as predictors of risk in human subjects.

5.1.2 Mouse models results

Characterisation of the EDHF oscillator

In this work, the wavelet analysis of LDF signals from mice has provided indirect proof of the possible EDHF origin of the endothelial NO-independent oscillator (5-9.5 × 10^{-3} Hz). Indeed, according to literature the stimulation of micro-vessels with the vasoconstrictor drug PE induces a vasomotion process mediated by NO and EDHF endothelial mechanisms but not by PGs [160]. The results of this thesis showed that the most relevant changes during PE-induced vasomotion were related to the endothelial NO oscillator and the endothelial NO-independent oscillator that by exclusion may be considered of EDHF origin because the PGs origin of this oscillator has been already excluded by previous studies [102, 105].

Role of endothelium and metabolic oscillations in skin vasomotion

The analysis of nonlinear dynamics of the microcirculation in mouse models has revealed a key involvement of EDHF and NO endothelial components in PE-induced cutaneous vasomotion. A more pronounced vasomotion was observed in mice affected by oxidative stress, which was explained as a resistance mechanism to attenuate vasoconstriction already described in literature as myoendothelial feedback [140]. Relevant correlations were found between metabolic and microvascular oscillators in WT mice, suggesting an involvement of the oxido-reductive oscillatory processes in vasomotion dynamics. The strongest correlations were observed for the endothelial oscillators, indicating an important role of the interaction between endothelial and metabolic factors for the modulation of microvascular diameter. However, correlations were observed also between metabolic and neurogenic or myogenic oscillations, indicating a global involvement of all the microvascular components in PE-induced vasomotion.

These results raise attention on a possible role of cellular metabolic oscillators for driving vasomotion in response to specific stimuli, and may serve as stimulus to study further the cellular mitochondrial and glycolytic oscillators as possible factors that could drive the Ca^{2+} oscillations at the basis of vasomotion.

Finally, non-relevant correlations were found between metabolic and microvascular oscillators in knockout mice, indicating that oxidative stress affects the cooperation between these factors inducing the switch towards regulatory mechanisms of the vascular tone different from the physiological pathways, which may promote the onset of metabolic/cardiovascular illness in the long term.

LDF and metabolic oscillators as markers of risk related to oxidative stress?

The most relevant difference between WT and Nrf2$^{-/-}$ mice groups for blood flow oscillators was found in relation to the endothelial EDHF component, which was characterised by higher spectral energies in control mice. This indicates reduced baseline functioning of the EDHF vasodilation mechanism in the presence of oxidative stress which could be eligible as biomarker for the prediction of CVD risk. Also the other microvascular oscillators (endothelial NO, neurogenic and myogenic) displayed greater baseline energies in WT mice suggesting a general reduced baseline vasodilator potential in the presence of oxidative stress and the possible use of all the local microvascular oscillators as early biomarkers of risk.

The major differences between WT and Nrf2$^{-/-}$ groups in relation to metabolic oscillators were found for the RR MO-1. This oscillator displayed opposite trends between the two groups during PE stimulation, and the baseline "phase coherence" (interaction) between RR MO-1 and the EDHF vascular oscillator was found higher in WT mice compared to Nrf2$^{-/-}$ animals, indicating a different basal interaction between metabolic and endothelial oscillations in the presence of oxidative stress. Thus, RR MO-1 might be a potential preclinical indicator of risk for both metabolic and cardiovascular complications that might originate from oxidative stress conditions.

5.1.3 Human work results

Characterisation of the EDHF oscillator

The indirect suggestions from mice work of the EDHF origin of the wavelet peak in the 5-9.5 × 10^{-3} frequency interval was confirmed and supported further by human data. Indeed, the endothelial NO-independent oscillator displayed the greatest percentage increase of wavelet amplitude/energy during human PORH hyperaemic response compared to the other LDF oscillators. This observation highly supports the EDHF origin of this oscillator because the EDHF mechanism is considered in literature as the major contributor to skin PORH response [9].

Possible existence of an endothelial PGs oscillator?

The wavelet analysis of LDF signals from human subjects during PORH has revealed a complex pattern of oscillatory peaks in the frequency interval of the endothelial NO oscillator, which could be a clue for the characterisation of an oscillator associated with the PG endothelial pathways. Indeed, the spectral interval of the NO oscillator clearly displayed two oscillatory peaks during PORH

response. This observation may suggest a possible overlapping contribution of different components in the 9.5-21 × 10^{-3} Hz frequency range. The minimal contribution of NO to skin reactive hyperaemic response and the bidirectional cross-talk between NO and PGs endothelial mechanisms [9, 184] may be the reason for the appearance of an additional oscillatory peak during cutaneous PORH, which normally might be masked by the major activity of NO pathway in the regulation of microvascular tone. Therefore, it can be hypothesised a PGs origin of one of the two wavelet peaks appearing during skin hyperaemic response in the NO interval.

Role of the endothelium and metabolic oscillations in human vasomotion

The wavelet analysis of human LDF oscillators confirmed the primary role of the endothelial EDHF pathway and lower involvement of NO, PGs, neurogenic and myogenic modulatory mechanisms in skin PORH response to a 5 min ischaemia period. Indeed, the vasomotion response to occlusion periods > 3 min is mainly mediated by metabolic factors [185]. The set of correlations and interactions (phase coherence) found between microvascular and metabolic oscillators suggested that the endothelial EDHF pathway may be activated through different mechanisms in non-smokers and smokers during PORH. The correlations observed in controls suggested a more prominent activation of EDHF through the release of metabolic factors (EETs). In contrast, data from smokers suggested that the exposure to tobacco may impact this mechanism in favour of signalling pathways for the exogenous activation of EDHF by gap junctions or K^+ channels, probably due also to the higher degree of oxidative stress in smokers which is a factor leading to impairment of EETs production [194].

LDF and metabolic oscillators as predictors of CVD risk in smokers?

The wavelet LDF data displayed a hyperactive microvascular reactivity of local blood flow oscillators (endothelial, neurogenic, myogenic) in healthy smokers compared to non-smokers, which may be an early factor provoking an imbalance between vasodilator and vasoconstrictor agents contributing to the onset of the skin microvascular endothelial dysfunction observed in chronic elder smokers. These results indicate that wavelet data may be easily misinterpreted. Indeed, generally lower endothelial, myogenic and neurogenic wavelet energies are hallmarks of microvascular dysfunction when comparing healthy and diseased groups or elder smokers and controls but this is not true for healthy younger

smokers. Therefore, the increase of wavelet energy of local LDF oscillators may represent an early biomarker of CVD risk for healthy smokers. In this study, higher wavelet energies of the cardiac oscillator were found in the control group compared to smokers. Generally, higher values of the cardiac output are a hallmark of diseased conditions such as hypertension but in this case seemed to reflect a more efficient delivery and consumption of oxygen in controls compared to smokers. Thus, also data of the cardiac oscillator may be easily misinterpreted. The respiratory oscillator displayed clearly different patterns between the two groups with greater wavelet energy in smokers, which could reflect increased resistance of skin peripheral arterioles. This oscillator seems to be suitable for performing an early assessment of CVD risk for healthy smokers.

The metabolic oscillators did not show significant differences between the tested groups, indicating overall well-functioning oxido-reductive dynamics in healthy smokers that ensure a normal cell energy metabolism. Therefore, metabolic oscillators cannot be considered early biomarkers of risk for healthy smokers, even though differences were found in the trends of metabolic oscillators and correlations between metabolic and microvascular oscillators, which may indicate an impact of smoke in the mechanisms for the mediation of PORH response.

Tissue oxygenation biomarkers

The analysis of tissue oxygenation dynamics showed relevant differences in the oxygen consumption VO_2 that was lower in smokers compared to controls during both ischaemia and PORH tasks. This may reflect a slower metabolism rate and conversion of oxygen in ATP energy in smokers, due to early microvascular damage induced by exposure to nicotine. Therefore, VO_2 might be eligible as early biomarker of risk for healthy smokers. Non-significant differences were found for the oxygen extraction O_2ER parameter.

Evaluation of LDF attractors as predictors of CVD risk

The results of LDF attractors' analysis outlined that these parameters are variable factors which must be interpreted with caution. Indeed, according to the findings in this study, lower complexity cannot be considered as an absolute indicator of cardiovascular dysfunction and the meaning of the attractors may vary depending on the kind of analysed signal, the risk factors and the general health status characterising the groups of individuals under investigation.

The values of the fractal dimension *D* were significantly higher in smokers, indicating that increased fractal dimension of LDF signals could be an early indicator of CVD risk for healthy smokers. The correlation dimension D_2 showed significant differences between the analysed groups with higher D_2 values found for smokers during PORH, indicating a potential eligibility of this LDF attractor as predictor of CVD risk for healthy smokers. The LDF entropy attractor H_0 did not show relevant differences between groups, indicating that this attractor is not suitable for the preclinical prediction of risk in younger healthy smokers. The information dimension H_i was significantly lower in smokers compared to controls at all the stages of PORH test, indicating that decreased H_i may be an early indicator of risk for healthy smokers. Finally, the Hurst index attractor *H* did not show reliable differences, indicating that this LDF attractor is not suitable as early indicator of risk in healthy smokers.

5.2 Future perspectives

5.2.1 Improvement of the methodology

Detection of fast metabolic oscillations

A shortcoming of the method used in this work was the employment of reconstructed NAD(P)H and RR signals, allowing only the study of low-frequency metabolic oscillators due to the slow sampling frequency of the discrete autofluorescence spectra employed for the reconstruction of the signal. This aspect can be improved in the future reducing the sampling time to a spectrum every 6-7 s for the detection of fast metabolic oscillations up to 145×10^{-3} Hz.

Characterising fast metabolic oscillators may be useful for two reasons. First, it would allow studying the phase coherence (interactions) of myogenic or neurogenic oscillators with metabolic oscillators falling in their frequency ranges, which was not possible in this study. Secondly, fast metabolic oscillations may be associated with the activity of cells with higher glycolytic or mitochondrial metabolic rates. This could provide the opportunity for the study of a range of metabolic oscillations arising from different cell types during vasomotion.

Improvement of autofluorescence data normalisation

In this study, the negative effects of factors affecting autofluorescence signal (i.e. absorption of UV light by Hb) were addressed by applying ratiometric correction methods. The normalised signals were considered acceptable for the final

purpose of the work that was examing the oscillations of NAD(P)H over time. However, in the future a more precise correction may be achieved performing Monte Carlo modelling studies to trace specifically the path of the light through the cutaneous tissue and determine what the detected signal is accounting for.

Tracing the cellular origin of metabolic oscillators

Another point to address is the characterisation of the cellular origin of metabolic oscillators. Indeed, the skin includes a variety of heterogeneous cells, which are part of the different cutaneous layers (i.e. epidermis) or of functional structures (e.g. micro-vessels). The correlations between vascular and metabolic oscillators found in this work may be an indirect indication that (1) part of the skin metabolic oscillations are of microvascular origin, and that (2) vasomotion may be influenced also by metabolic dynamics related to the energetic requirements of the surrounding cutaneous tissue. The employment of imaging techniques for the spatial localisation of cutaneous NAD(P)H may better clarify these observations. Fluorescence lifetime imaging microscopy (FLIM) and multiphoton laser scanning microscopy (MPLSM) seem promising methods for this purpose.

Improvement of the wavelet phase coherence (WPCO) analysis

Although the potential for gathering information on the interaction between biological oscillators, the WPCO analysis from noisy regions of the wavelet spectrum (e.g. EDHF and RR MO-1 low-frequency ranges) may be affected by some bias. As future perspective, the interpretation of WPCO data may be improved by including the surrogate data testing described recently by Gruszecki *et al.* [165], making the assumptions on the degree of baseline coherence more reliable. Moreover, decomposition methods for the separation of the oscillators of interest from the original signal and the background noise may be implemented. The empirical mode decomposition (EEMD) may be an example of method useful for this purpose, to obtain time series of EDHF, NO, and slow metabolic oscillators separated from their original signal, which could be used to perform the WPCO analysis.

5.2.2 Direct characterisation of EDHF and PGs blood flow oscillators

EDHF oscillator

The experimental data from this study have suggested indirectly a possible EDHF origin of the endothelial NO-independent LDF wavelet oscillator. As future perspective, direct proof of this hypothesis may be provided in both mouse

models and human subjects. This may be achieved in mice by monitoring this wavelet oscillator during inhibition of the EDHF mechanism through a combination of the inhibitors of K^+ channels apamin and charybdotoxin (APA + ChTX) [198]. The same result can be obtained in human subjects by monitoring this wavelet oscillator during PORH in the presence/absence of inhibitors of the EDHF mechanism. Examples of substances that could be used for this purpose in humans are the fluconazole or sulfaphenazole inhibit the EDHF mechanism mediated by EETs metabolites [193], and the tetraethylammonium (TEA) for the inhibition of the EDHF mechanism mediated by KCa potassium channels [195].

PGs oscillator

The wavelet analysis of LDF oscillators during PORH test in human subjects has revealed the possible existence of an endothelial PGs oscillator peak in the same frequency range of the endothelial NO oscillator. As future perspective, this hypothesis may be tested directly by performing the wavelet analysis of LDF signals measured from the human forearm during PORH test in combination with the administration of inhibitors of PGs biosynthesis. Examples of pharmaceutical drugs that can be used for this purpose are aspirin [105, 191], ibuprofen [192], or micro-dialysis delivery of the non-specific inhibitor of COX ketorolac [184, 193].

5.2.3 Further study of vasomotion

Mouse vasomotion

The results from this study have outlined an important role of both endothelial and slow metabolic oscillators in the modulation of PE-induced vasomotion. As future perspective, the role of these oscillators and their interactions should be investigated for vasomotion processes induced by pharmacological agents different from PE (i.e. ACh), to obtain a full picture on the involvement of these factors in vasomotion. Additionally, the characterisation of fast metabolic oscillators may be useful to investigate their relationship with microvascular oscillations and their role in mouse vasomotion.

Human vasomotion

Human work has suggested that the phase coherence between EDHF and RR MO-1 oscillators may reflect the degree of activation/inactivation of the EETs pathway during PORH vasomotion. Moreover, the results suggest that the EDHF mechanism activated after a prolonged ischaemia period (> 3 min) might be mainly mediated by EETs metabolites. In contrast, in smokers the activity of EETs

metabolites may be reduced in favour of mechanisms of activation of EDHF involving gap junctions and K^+ channels. However, although the integration of multi-parameter findings in this dissertation seems to be consistent with these interpretations, further experiments should be performed to confirm these hypotheses. Specifically, all these aspects can be elucidated better by the assessment of metabolic and EDHF oscillators' dynamics in the forearm during PORH vasomotion in response to both ischaemic periods < 3 min and > 3 min, in combination with the local delivery of fluconazole or sulfaphenazole for the inhibition of EDHF signalling mediated by EETs [193], and TEA for the inhibition of the EDHF signalling mediated by KCa potassium channels [195]. Additionally, the characterisation of fast metabolic oscillators may be useful to investigate their relationship with microvascular oscillations and their role in human vasomotion.

5.2.4 Further exploration of the nonlinear markers of microcirculation and cell energy metabolism as predictors of CVD risk

Testing additional mouse phenotypes

In this work, the comparison of data between WT mice and the baseline phenotype of $Nrf2^{-/-}$ animals have outlined relevant differences for the local microvascular oscillators (especially the EDHF), the RR MO-1 metabolic oscillator, and the interaction (phase coherence) between EDHF and RR MO-1. However, the lack of antioxidant protection of the $Nrf2^{-/-}$ mice has not been fully tested with additional oxidative stress loads (e.g. treatment with high fat diet). Therefore, to reveal the full picture on the dynamics of microvascular and cell metabolic oscillators in response to oxidative stress, future studies are required on larger groups of mice under HFD regime. Moreover, the biomarkers should be tested also on animals affected by metabolic and cardiovascular illness to clarify further these aspects. Additionally, also the potential use of LDF attractors as predictors of risk associated with oxidative stress and vascular/metabolic illness may be tested in mouse models.

Testing microvascular and metabolic oscillators in human cohorts affected by risk factors different from smoking

The obtained results suggest that the applicability of microvascular and metabolic dynamic biomarkers as preclinical predictors of CVD risk may vary depending on the features of the tested subjects. The increase of wavelet energy of local microvascular oscillators and of the respiratory oscillator, oxygen consumption

(VO_2), and various attractors seem to be the promising early dynamic biomarkers of risk for healthy smokers. However, these nonlinear markers may acquire a different importance for cohorts of subjects with different risk factors. For example, comparing healthy normal-weight subjects with a cohort of healthy overweight individuals might evidence differences in the dynamics of metabolic oscillators as well as differences in local microvascular oscillators. Therefore, testing several cohorts of healthy subjects affected by risk factors different from smoke (e.g. high BMI, physical inactivity, family history of CVD, hypertension, etc.) may help to determine the specific patterns of dynamic biomarkers associated with each risk factor.

Testing the attractors in human cohorts affected by various risk factors or patients with CVD and respiratory illness.

The correlation analysis has revealed that the quantitative growth/decrease of the attractors may reflect multiple physiological processes, including changes in the cardiac output, control of the SBP, or microvascular and metabolic dynamics. Therefore, based on the results of the correlation analysis the following hypotheses may be tested in the future: (1) D and H as predictors of risk for hypertensive non-smokers or smokers. (2) D_2, H_0 and H_i as discrimination factors for patients with cardiovascular disorders characterised by increase of heart rate. (3) D and H_i as discrimination factors for patients affected by peripheral microvascular disease. (4) H as predictor of risk for subjects with high BMI, or as discriminatory factor for patients with metabolic disorders.

Adding the nonlinear dynamic biomarkers to existent risk functions

Finally, after the selection of the best microvascular and metabolic nonlinear dynamic biomarkers of risk, it would be appropriate the combination of these parameters to create an index usable for the preclinical prediction of risk or diagnostic purposes, and adding these factors to the existent risk functions. In addition, considering that this research was more focused on women and female mice, the potential biomarkers found in this study may be eligible as non-traditional risk factors for women who are characterised by a different aetiology and incidence of CVD compared to men that frequently cannot be explained by traditional risk factor.

References

[1] Balagopal, P. B. *et al.*, “Nontraditional risk factors and biomarkers for cardiovascular disease: mechanistic, research, and clinical considerations for youth: a scientific statement from the American Heart Association,” *Circulation,* 123(23), 2749-69 (2011).

[2] Kannel, W. B. and Gordan, T., “Evaluation of cardiovascular risk in the elderly: the Framingham study,” *Bull. N Y Acad. Med.*, 54(6), 573–591 (1978).

[3] D'Agostino, R. B., Pencina, M. J., Massaro, J. M. and Coady, S., “Cardiovascular Disease Risk Assessment: Insights from Framingham,” *Glob. Heart*, 8(1), 11-23 (2013).

[4] Flammer, A. J. *et al.*, “The assessment of endothelial function: from research into clinical practice,” *Circulation*, 126(6), 753-67 (2012).

[5] Cervantes Gracia, K., Llanas-Cornejo, D. and Husi, H. “CVD and oxidative stress,” *J. Clin. Med.*, 6(2), 22 (2017).

[6] den Uil, C. A. *et al.*, “The microcirculation in health and critical disease,” *Prog. Cardiovasc. Dis.*, 51(2), 161-70 (2008).

[7] Johnson, P. C., “Overview of the Microcirculation,” in *Microcirculation (Second Edition)*, Elsevier (2008).

[8] Braverman, I. M., “The cutaneous microcirculation,” *J. Investig. Dermatol. Symp. Proc.*, 5, 3-9 (2000).

[9] Roustit, M. and Cracowski, J. L., “Assessment of endothelial and neurovascular function in human skin microcirculation,” *Trends Pharmacol. Sci.*, 34(7), 373-84 (2013).

[10] Pries, A. R. *et al.*, “Coronary vascular regulation, remodelling, and collateralization:mechanisms and clinical implications on behalf of the working group on coronary pathophysiology and microcirculation,” *Eur. Heart J.*, 36, 3134–3146 (2015).

[11] Gutterman, D. D. *et al.*, “The Human Microcirculation – Regulation of Flow and Beyond,” *Circ. Res.*, 118(1), 157–172 (2016).

[12] Heikal, A. A., “Intracellular coenzymes as natural biomarkers for metabolic activities and mitochondrial anomalies,” *Biomark. Med.*, 4(2), 241-63 (2010).

[13] Heitzer, T. *et al.*, “Endothelial dysfunction, oxidative stress, and risk of cardiovascular events in patients with coronary artery disease,” *Circulation*, 104(22), 2673-8 (2001).

[14] Turner, J., Belch, J.J. and Khan, F., “Current concepts in assessment of microvascular endothelial function using laser Doppler imaging and iontophoresis,” *Trends Cardiovasc. Med.*, 18(4), 109-16 (2008).

[15] den Uil, C. A., “Impaired microcirculation predicts poor outcome of patients with acute myocardial infarction complicated by cardiogenic shock,” *Eur. Heart J.* , 31(24), 3032-9 (2010).

[16] Halcox, J. P. *et al.*, “Prognostic value of coronary vascular endothelial dysfunction,” *Circulation*, 106(6), 653-8 (2002).

[17] Cecchi, F. *et al.*, “Coronary microvascular dysfunction and prognosis in hypertrophic cardiomyopathy,” *N. Engl. J. Med.*, 349(11), 1027-35 (2003).

[18] van de Hoef, *et. al.*, “Physiological basis and long-term clinical outcome of discordance between fractional flow reserve and coronary flow velocity reserve in coronary stenoses of intermediate severity,” *Circ. Cardiovasc. Interv.*, 7(3), 301-11 (2014).

[19] Taqueti, V. R. *et al.*, “Interaction of impaired coronary flow reserve and cardiomyocyte injury on adverse cardiovascular outcomes in patients without overt coronary artery disease,” *Circulation*, 131(6), 528-35 (2015).

[20] Murthy, V. L. *et al.*, “Effects of sex on coronary microvascular dysfunction and cardiac outcomes,” *Circulation*, 129(24), 2518-27 (2014).

[21] van Kranenburg, M. *et. al.*, “Prognostic value of microvascular obstruction and infarct size, as measured by CMR in STEMI patients,” *JACC Cardiovasc. Imaging*, 7(9), 930-9 (2014).

[22] Rubinshtein, R. *et al.*, “Coronary microcirculatory vasodilator function in relation to risk factors among patients without obstructive coronary disease and low to intermediate Framingham score,” *Eur. Heart J.*, 31(8), 936-42 (2010).

[23] Patt, B.T. *et al.*, “Endothelial dysfunction in the microcirculation of patients with obstructive sleep apnea,” *Am. J. Respir. Crit. Care Med.*, 182(12), 1540-5 (2010).

[24] Rigo, F., *et al.*, “Diffuse, marked, reversible impairment in coronary microcirculation in stress cardiomyopathy: a Doppler transthoracic echo study,” *Ann. Med.*, 41(6), 462-70 (2009).

[25] Laguens, R. *et al.*, “Coronary microcirculation remodeling in patients with idiopathic dilated cardiomyopathy,” *Cardiology*, 119(4), 191-6 (2011).

[26] Prasad, A. *et al.*, “Abnormal coronary microvascular endothelial function in humans with asymptomatic left ventricular dysfunction*,” Am. Heart J.*, 146(3), 549-54 (2003).

[27] Paulus, W. J. and Tschöpe, C., “A novel paradigm for heart failure with preserved ejection fraction: comorbidities drive myocardial dysfunction and remodeling through coronary microvascular endothelial inflammation,” *J. Am. Coll. Cardiol.*, 62(4), 263-71 (2013).

[28] Holowatz, L. A., “Human cutaneous microvascular ageing: potential insights into underlying physiological mechanisms of endothelial function and dysfunction,” *J. Physiol.*, 586(14), 3301 (2008).

[29] Thijssen, D. H., Green, D. J. and Hopman, M. T., “Blood vessel remodeling and physical inactivity in humans,” *J. Appl. Physiol*. *(1985)*, 111(6), 1836-45 (2011).

[30] Miura, H., Toyama, K., Pratt, P. F. and Gutterman, D. D., “Cigarette smoking impairs Na+-K+-ATPase activity in the human coronary microcirculation,” *Am. J. Physiol. Heart Circ. Physiol.*, 300(1), H109-17 (2011).

[31] Feher, A., Chen, S. Y., Bagi, Z. and Arora, V., “Prevention and treatment of no-reflow phenomenon by targeting the coronary microcirculation,” *Rev. Cardiovasc. Med.*, 38-51, 15(1) (2014).

[32] Feng, J. *et al.*, “Calcium-activated potassium channels contribute to human coronary microvascular dysfunction after cardioplegic arrest,” *Circulation*, 118(14 Suppl), S46-51 (2008).

[33] Mohri, M. *et al.*, “Rho-kinase inhibition with intracoronary fasudil prevents myocardial ischemia in patients with coronary microvascular spasm,” J. Am. Coll. Cardiol., vol. 41(1), pp. 15-9, 2003.

[34] Medhora, M. *et al.*, “Epoxygenase-driven angiogenesis in human lung microvascular endothelial cells,” *Am. J. Physiol. Heart Circ. Physiol.*, 284(1), H215-24 (2003).

[35] Datla, S. R. *et al.*, “Important role of Nox4 type NADPH oxidase in angiogenic responses in human microvascular endothelial cells in vitro,” *Arterioscler. Thromb. Vasc. Biol.,* 27(11), 2319-24 (2007).

[36] Khan, F. *et al.*, “Relationship between peripheral and coronary function using laser Doppler imaging and transthoracic echocardiography,” *Clin. Sci. (Lond.)*, 115(9), 295-300 (2008).

[37] Katoh, A. *et al.*, “Coexistence of impairment of endothelium-derived nitric oxide and platelet-derived nitric oxide in patients with coronary risk factors,” *Circ. J.*, 66(9), 837-40 (2002).

[38] Al-Fiadh, A. H., “Retinal microvascular structure and function in patients with risk factors of atherosclerosis and coronary artery disease,” *Atherosclerosis*, 233(2), 478-84 (2014).

[39] Elherik, K., Khan, F. and McLaren, M., “Circadian variation in vascular tone and endothelial cell function in normal males,” *Clin. Sci.*, 102, 547–552 (2002).

[40] Hansell, J., Henareh, L., Agewall, S. and Norman, M., “Non-invasive assessment of endothelial function - Relation between vasodilatory responses in skin microcirculation and brachial artery,” *Clin. Physiol. Funct. Imaging*, 24(6), 317-22 (2004).

[41] Ijzerman, R. G. *et al.*, “Individuals at increased coronary heart disease risk are characterized by an impaired microvascular function in skin,” *Eur. J. Clin. Invest.*, 33(7), 536-42 (2003).

[42] Farkas, K. *et al.*, “Non-invasive assessment of microvascular endothelial function by laser Doppler flowmetry in patients with essential hypertension,” *Atherosclerosis*, 173(1), 97-102 (2004).

[43] Khan, F., Elhadd, T. A., Greene, S. A. and Belch, J. J., “Impaired skin microvascular function in children, adolescents, and young adults with type 1 diabetes,” *Diabetes Care*, 23(2), 215-20 (2000).

[44] Ramsay, J. E. *et al.*, “Enhancement of endothelial function by pregnancy: inadequate response in women with type 1 diabetes,” *Diabetes Care*, 26(2), 475-9 (2003).

[45] Tao, J. *et al.*, “Reduced arterial elasticity is associated with endothelial dysfunction in persons of advancing age: comparative study of noninvasive pulse wave analysis and laser Doppler blood flow measurement,” *Am. J. Hypertens.*, 17(8), 654-9 (2004).

[46] Drakaki, E. et al., “Laser-induced fluorescence and reflectance spectroscopy for the discrimination of basal cell carcinoma from the surrounding normal skin tissue,” *Skin Pharmacol. Physiol.*, 22(3), 158-65 (2009).

[47] Stoner, J. D., Angelos, M. G. and Clanton, T. L., “Myocardial contractile function during postischemic low-flow reperfusion: critical thresholds of NADH and O2 delivery,” *Am. J. Physiol. Heart Circ. Physiol.*, 286(1), H375-80 (2004).

[48] Noordzij, M. J. *et al.*, “Skin autofluorescence is increased in patients with carotid artery stenosis and peripheral artery disease,” *Int. J. Cardiovasc. Imaging*, 28(2), 431-8 (2012).

[49] Roustit, M. and Cracowski, J. L., “Non-invasive assessment of skin microvascular function in humans: an insight into methods,” *Microcirculation*, 19(1), 47-64 (2012).

[50] Whitton, J. and Everall, J., “The thickness of the epidermis,” *Brit. J. Dermatol.*, 89(5), 467-476 (1973).

[51] Fung, Y. C., “Biomechanics: Mechanical Properties of Living Tissues”, New York: Springer-Verlag, 2nd ed. (1993).

[52] Saeed, S., “Lookingbill & Marks' Principles of Dermatology,” *Am. J. Dermatopathol.*, 29(5), 496 (2007).

[53] Daly, S. M. and Leahy, M., “‘Go with the flow’: A review of methods and advancements in blood flow imaging,” J. Biophotonics, 6(3), 217-255 (2013).

[54] Wright, C. I., Kroner, C. I. and Draijer, R., “Non-invasive methods and stimuli for evaluating the skin's microcirculation,” *J. Pharmacol. Toxicol. Methods*, 54(1), 1-25 (2005).

[55] Elias, P. M., “Epidermal lipids, barrier function, and desquamation,” The *J. Invest. Dermatol.*, 80, 44 (1983).

[56] Agar, N. and Young, A. R., “Melanogenesis: a photoprotective response to DNA damage?,” *Mut. Res.*, 571, 121-132 (2005).

[57] Dunaev, A. V. *et al.*, “Investigating tissue respiration and skin microhaemocirculation under adaptive changes and the synchronization of blood flow and oxygen saturation rhythms,” *Physiol. Meas.*, 35(4), 607-21 (2014).

[58] Rogatkin, D. A. and Lapaeva, L. G., “Prospects for Development of Noninvasive Spectrophotometric Medical Diagnosis,” *Biomed. Eng.*, 37(4), 217-222 (2003).

[59] Kim, O. *et al.*, “Reflectance spectrometry of normal and bruised human skins: experiments and modeling,” *Physiol. Meas.*, 33(2), 159-75 (2012).

[60] Kvandal, P. *et al.*, “Regulation of human cutaneous circulation evaluated by laser Doppler flowmetry, iontophoresis, and spectral analysis: Importance of nitric oxide and prostaglandins,” *Microvasc. Res.*, 65(3), 160-171 (2003).

[61] Xu, M. and Wang, L.V., “Time-Domain Reconstruction for Thermoacoustic Tomography in a Spherical Geometry,” *IEEE Trans. Med. Imaging*, 21(7), 814-822 (2002).

[62] Wang, X. *et al.*, “Photoacoustic tomography of biological tissues with high cross-section resolution: Reconstruction and experiment,” *Med. Phys.*, 29, 2799 (2002).

[63] Xu, M. and Wang, L., “Universal back-projection algorithm for photoacoustic computed tomography,” Phys. Rev. E, 71(1), 16706 (2005).

[64] Wang, L. V., “Prospects of photoacoustic tomography,” Med. Phys., 35(12), 5758 (2008).

[65] Zhang, H. F., Maslov, K., Stoica, G. and Wang, L. V., “Functional photoacoustic microscopy for high-resolution and noninvasive in vivo imaging,” *Nat. Biotech.*, 24(7), 848-851 (2006).

[66] Maslov, K., Zhang, H. F., Hu, S. and Wang, L. V., “Optical-resolution photoacoustic microscopy for in vivo imaging of single capillaries,” *Opt. Lett.*, 33(9), 929-931 (2008).

[67] Podoleanu, A. G., “Optical coherence tomography,” *J. Microscopy*, 247, 209-219 (2012).

[68] Mogensens, M. and Jemec, G. B. E., “Diagnosis of Nonmelanoma Skin Cancer/Keratinocyte Carcinoma: A Review of Diagnostic Accuracy of Nonmelanoma Skin Cancer Diagnostic Tests and Technologies,” *Dermatol. Surg.*, 33(10), 1158-1174 (2007).

[69] Drexler, W. *et al.*, “In vivo ultrahigh-resolution optical coherence tomography,” *Opt. Lett.*, 24(17), 1221-1223 (1999).

[70] Fercher, A. F., Drexler, W., Hitzenberger, C. K. and Lasser, T., “Optical coherence tomography - principles and applications,” *Rep. Progr. Phys.*, 66(2), 239-303 (2003).

[71] Wang, X., Milner, T. and Nelson, J., “Characterization of fluid flow velocity by optical Doppler tomography,” *Opt. lett.*, 20(11), 1337-1339 (1995).

[72] Barton, J. and Stromski, S., “Flow measurement without phase information in optical coherence tomography images,” *Opt. Express*, 13(14), 5234-5239 (2005).

[73] Wang, R. K. *et al.*, “Three dimensional optical angiography,” *Opt. Express*, 15(7), 4083-4097 (2007).

[74] Enfield, J., Jonathan, E. and Leahy, M., “In vivo imaging of the microcirculation of the volar forearm using correlation mapping optical coherence tomography (cmOCT),” *Biomed. Opt. Express*, 2(5), 1184-1193 (2011).

[75] Jubran, A., “Pulse oximetry,” *Crit. Care*, 19(1), 272-278 (2015).

[76] Liu, H., Kohl-Bareis, M. and Huang, X., “Design of a tissue oxygenation monitor and verification on human skin,” *SPIE Proc.*, *Clinical and Biomedical Spectroscopy and Imaging II*, 80871Y (2011).

[77] Wallace, M. B., Wax, A., Roberts, D. N. and Graf, R. N., “Reflectance Spectroscopy,” *Gastrointest. Endosc. Clin. N. Am.*, 19(2), 233–242 (2009).

[78] Heusmann, H., Koelzer, J. G. and Mitic, G., “Characterization of female breasts in vivo by time-resolved and spectroscopic measurements in the near infrared spectroscopy,” *J. Biomed. Opt.*, 1, 425-34 (1996).

[79] Kohl-Bareis, M. *et al.*, “System for the Measurement of Blood Flow and Oxygenation in Tissue Applied to Neurovascular Coupling in Brain,” *Proc. SPIE*, 5859 (2005).

[80] Kohl-Bareis, M. *et al.*, “Physical model for the spectroscopic analysis of cortical intrinsic optical signals,” *Phys. Med. Biol.*, 45(12), 3749-3764, (2000).

[81] Huppert, T. J., Diamond, S. G., Franceschini, M. A. and Boas, D. A., “HomER: a review of time-series analysis methods for near-infrared spectroscopy of the brain,” *Appl. Opt.*, 48(10), D280-98 (2009).

[82] Jones, S., Chiesa, S. T., Chaturvedi, N. and Hughes, A. D., “Recent developments in near-infrared spectroscopy (NIRS) for the assessment of local skeletal muscle microvascular function and capacity to utilise oxygen,” *Artery Research*, 16, 25-33 (2016).

[83] Ballard, J. L., “Transcutaneous Oxygen Tension: Principles and Applications,” in *Noninvasive Vascular Diagnosis*, London, Springer (2007).

[84] Croce, A. C. and Bottiroli, G., “Autofluorescence spectroscopy and imaging: a tool for biomedical research and diagnosis,” *Eur. J. Histochem.*, 58:2461, 320-337 (2014).

[85] Mayevsky, A. and Rogatsky, G. G., “Mitochondrial function in vivo evaluated by NADH fluorescence: from animal models to human studies,” *Am. J. Physiol. Cell Physiol.*, 292(2), C615-40 (2007).

[86] Kollias, N. *et al.*, “Endogenous skin fluorescence includes bands that may serve as quantitative markers of aging and photoaging,” *J. Invest. Dermatol.*, 111(5), 776-80 (1998).

[87] Gillies, R., Zonios, G., Anderson, R. R. and Kollias, N., “Fluorescence excitation spectroscopy provides information about human skin in vivo,” *J. Invest. Dermatol.*, 115(4), 704-7 (2000).

[88] Rogatkin, D. A., Dunaev, A. V. and Lapaeva, L. G., “Metrological Support of Methods and Devices for Noninvasive Medical Spectrophotometry,” *Biomed. Eng.*, 44(2), 66-70 (2010).

[89] Lancaster, G., Suprunenko, Y. F., Jenkins, K. and Stefanovska, A., “Modelling chronotaxicity of cellular energy metabolism to facilitate the identification of altered metabolic states,” *Sci. Rep.*, 6:29584 (2016).

[90] Litvinova, K. S., Rogatkin, D. A., Bychenkov, O. A. and Shumskiy, V. I., “Chronic hypoxia as a factor of enhanced autofluorescence of endogenous porphyrins in soft biological tissues,” *Proc. SPIE 7547*, *Saratov Fall Meeting 2009: International School for Junior Scientists and Students on Optics, Laser Physics, and Biophotonics*, 75470D (2010).

[91] Dunaev, A. V. *et al.*, “Individual variability analysis of fluorescence parameters measured in skin with different levels of nutritive blood flow,” *Med. Engin. Phys.*, 37(6), 574-83 (2015).

[92] Mokrý, M. *et al.*, “Experimental Study on Predicting Skin Flap Necrosis by Fluorescence in the FAD and NADH Bands during Surgery,” *Photochem. Photobiol.*, 83(5), 1193-6 (2007).

[93] Coda, S. *et al.*, “Fluorescence lifetime spectroscopy of tissue autofluorescence in normal and diseased colon measured ex vivo using a fiber-optic probe,” *Biomed. Opt. Express*, 5(2), 515-38 (2014).

[94] Shah, A. T. *et al.*, “In Vivo Autofluorescence Imaging of Tumor Heterogeneity in Response to Treatment,” *Neoplasia*, 17(12), 862–870 (2015).

[95] Walsh, A. J. *et al.*, “Optical metabolic imaging identifies glycolytic levels, subtypes, and early-treatment response in breast cancer,” *Cancer Research*, 73(20), 6164-74 (2013).

[96] Skala, M. C. *et al.*, “In vivo multiphoton fluorescence lifetime imaging of protein-bound and free nicotinamide adenine dinucleotide in normal and precancerous epithelia,” *J. Biomed. Opt.*, 12(2), 024014 (2007).

[97] Levitt, J. A., Matthews, D. R., Ameer-Beg, S. M. and Suhling, K., “Fluorescence lifetime and polarization-resolved imaging in cell biology,” *Curr. Opin. Biotechnol.*, 20(1), 28-36 (2009).

[98] Blacker, T. S. *et al.*, “Separating NADH and NADPH fluorescence in live cells and tissues using FLIM,” *Nat. Commun.*, 5, 3936 (2014).

[99] Wu, Z. *et al.*, “Multi-Photon Microscopy in Cardiovascular Research,” *Methods*, S1046-2023(17), 30024-5 (2017).

[100] Balu, M. *et al.*, “In vivo multiphoton NADH fluorescence reveals depth-dependent keratinocyte metabolism in human skin,” *Biophys. J.*, 104(1), 258-67 (2013).

[101] Szulczewski, J. M. *et al.*, “In Vivo Visualization of Stromal Macrophages via label-free FLIM-based metabolite imaging,” *Sci. Rep.*, 6, 25086 (2016).

[102] Shiogai, Y., Stefanovska, A. and McClintock, P. V., “Nonlinear dynamics of cardiovascular ageing,” *Phys. Rep.*, 488(2-3), 51-110 (2010).

[103] Stefanovska, A., Bračič, M. and Kvernmo, H. D., “Wavelet analysis of oscillations in the peripheral blood circulation measured by laser Doppler technique,” *IEEE Trans. Biomed. Eng.*, 46(10), 1230-9 (1999).

[104] Lancaster, G. *et al.*, “Dynamic markers based on blood perfusion fluctuations for selecting skin melanocytic lesions for biopsy,” *Sci. rep.*, 5, 12825 (2015).

[105] Kvandal, P. *et al.*, “Low frequency oscillations of the laser Doppler perfusion signal in human skin,” *Microvasc. Res.*, 72(3), 120-127 (2006).

[106] Kvernmo, H. D. *et al.*, “Spectral analysis of the laser Doppler perfusion signal in human skin before and after exercise,” *Microvasc. Res.*, 56(3), 173-182 (1998).

[107] Kvernmo, H. D., Stefanovska, A., Kirkebøen, K. A. and Kvernebo, K., “Oscillations in the human cutaneous blood perfusion signal modified by endothelium-dependent and endothelium-independent vasodilators,” *Microvasc. Res.*, 3, 298-309 (1999).

[108] Landsverk, S. A. *et al.*, “Human skin microcirculation after brachial plexus block evaluated by wavelet transform of the laser Doppler flowmetry signal,” *Anesthesiology*, 105(3), 478-484 (2006).

[109] Stefanovska, A. and Bračič, M., “Physics of the human cardiovascular system,” *Contemp. Phys.*, 40:1, 31-55 (1999).

[110] Aalkjaer, C. and Nilsson, H., “Vasomotion: cellular background for the oscillator and for the synchronization of smooth muscle cells,” *Brit. J. Pharmacol.*, 144, 605-616 (2005).

[111] Pradhan, R. K. and Chakravarthy, V. S., “Informational dynamics of vasomotion in microvascular networks: a review,” *Acta Physiol.*, 201, 193-218 (2011).

[112] Traikov, L. *et al.*, “Subcutaneous Arteriolar Vasomotion Changes During and After ELF-EMF Exposure in Mice in Vivo,” *Environmentalis*, 25, 93-101 (2005).

[113] Lefer, D. J., Lynch, C. D., Lapinski, K. C. and Hutchins, P. M., “Enhanced vasomotion of cerebral arterioles in spontaneously hypertensive rats,” *Microvasc. Res.*, 39, 129-139 (1990).

[114] Bouskela, E., “Vasomotion frequency and amplitude related to intraluminal pressure and temperature in the wing of the intact, unanesthetized bat,” *Microvasc. Res.*, 37, 339-351 (1989).

[115] Bernjak, A., Clarkson, P. B., McClintock, P. V. and Stefanovska, A., “Low-frequency blood flow oscillations in congestive heart failure and after β1 blockade treatment,” *Microvasc. Res.*, 76, 224-232 (2008).

[116] Liao, F., O'Brien, W. D. J. and Jan, Y. K., “Assessing complexity of skin blood flow oscillations in response to locally applied heating and pressure in rats: implications for pressure ulcer risk,” *Physica A.*, 392(20) (2013).

[117] Stefanovska, A., Lotric, M. B., Strle, S. and Haken, H., “The cardiovascular system as coupled oscillators?,” *Physiol. Meas.*, 22(3), 535–550 (2001).

[118] Bandrivskyy, A., Bernjak, A., McClintok, P. and Stefanovska, A., “Wavelet phase coherence analysis: application to skin temperature and blood flow,” *Cardiovasc. Eng.*, 4, 89-93 (2004).

[119] Clemson, P., Lancaster, G. and Stefanovska, A., “Reconstructing time-dependent dynamics,” *Proc. IEEE*, 104(2), 223-241 (2016).

[120] Stefanovska, A. and Bračič, M., “Reconstructing cardiovascular dynamics,” *Control Engineering Practice*, 7, 161-172 (1998).

[121] Lipsitz, L. A. and Goldberger, A. L., “Loss of Complexity and Aging - Potential Applications of Fractals and Chaos Theory to Senescence,” *JAMA*, 267(13), 1806–1809 (1992).

[122] Frisbee, J. C. *et al.*, “Increased peripheral vascular disease risk progressively constrains perfusion adaptability in the skeletal muscle microcirculation,” Am. J. Physiol. Heart Circ. Physiol., 310(4), H488-H504 (2016).

[123] Carolan-Rees, G., Tweddel, A. C., Naka, K. K. and Griffith, T. M., “Fractal dimensions of laser doppler flowmetry time series,” *Med. Eng. Phys.*, 24(1), 71-76 (2002).

[124] Grassberger, P. and Procaccia, I., “Measuring the strangeness of strange attractors,” *Physica D: Nonlinear Phenomena*, 9(1-2), 189-208 (1983).

[125] Grassberger, P., “Generalized dimensions of strange attractors,” *Phys. Lett. A.*, 97(6), 227-230 (1983).

[126] Grassberger, P. and Procaccia, I., “Characterization of strange attractors,” *Phys. Rev. Lett.*, 50(5), 346-349 (1983).

[127] Grassberger, P. and Procaccia, I., “Estimation of the Kolmogorov entropy from a chaotic signal,” *Phys. Rev. A*, 28(4), 2591-2593 (1983).

[128] Reijenga, K. A., Bakker, B. M., van der Weijden, C. C. and Westerhoff, H. V., “Training of yeast cell dynamics,” *FEBS J.*, 272, 1616-1624 (2005).

[129] Olsen, L. F., Andersen, A. Z., Lunding, A., Brasen, J. C. and Poulsen, A. K., “Regulation of Glycolytic Oscillations by Mitochondrial and Plasma Membrane H+-ATPases,” *Biophys. J.*, 96, 3850-3861 (2009).

[130] Aon, M. A., Cortassa, S., Marbán, E. and O'Rourke, B., “Synchronized whole cell oscillations in mitochondrial metabolism triggered by a local release of reactive oxygen species in cardiac myocytes,” *J. Biol. Chem.*, 278, 44735-44744 (2003).

[131] Luciani, D. S., Misler, S. and Polonsky, K. S., “Ca2+ controls slow NAD(P)H oscillations in glucose-stimulated mouse pancreatic islets,” *J. Physiol.*, 572(2), 379-392 (2006).

[132] Chou, H. F., Berman, N. and Ipp., E., “Oscillations of lactate released from islets of Langerhans: evidence for oscillatory glycolysis in beta-cells,” *Am. J. Physiol.*, 262, E800-E805 (1992).

[133] Reijenga, K. A. *et al.*, “Control of glycolytic dynamics by hexose transport in Saccharomyces cerevisiae,” *Biophys. J.*, 80, 626-634 (2001).

[134] Aon, M. A. *et al.*, “Single and cell population respiratory oscillations in yeast: A 2-photon scanning laser microscopy study,” *FEBS Lett.*, 581, 8-14 (2007).

[135] Porat-Shilom, N. *et al.*, “In vivo tissue-wide synchronization of mitochondrial metabolic oscillations,” *Cell Rep.*, 9(2), 514-521 (2014).

[136] Stringari, C. *et al.*, “In vivo single-cell detection of metabolic oscillations in stem cells,” *Cell Rep.*, 10(1), 1-7 (2015).

[137] Boiteux, A., Goldbeter, A. and Hess, B., “Control of oscillating glycolysis of yeast by stochastic, periodic, and steady source of substrate: a model and experimental study,” *Proc. Nat. Acad. Sci.*, 72, 3829-3833 (1975).

[138] Mauban, J. R. and Wier, W. G., “Essential role of EDHF in the initiation and maintenance of adrenergic vasomotion in rat mesenteric arteries,” *Am. J. Physiol. Heart Circ. Physiol.*, 287, H608-H616 (2004).

[139] Rahman, A. *et al.*, “Antiphase oscillations of endothelium and smooth muscle [Ca2+]i in vasomotion of rat mesenteric small arteries,” *Cell Calcium*, 42, 536-547 (2007).

[140] Kapela, A., Nagaraja, S., Parikh, J. and Tsoukias, M., “Modeling Ca2+ Signaling in the Microcirculation: Intercellular Communication and Vasoreactivity,” *Crit. Rev. Biomed. Eng.*, 39(5), 435-460 (2011).

[141] Haddock, R. E, Hirst, G. D. and Hill, C. E., “Voltage independence of vasomotion in isolated irideal arterioles of the rat,” *Acta Physiol. Scand.*, 540, 219-229 (2002).

[142] Lee, C. H. et al., “Ca2+ oscillations, gradients, and homeostasis in vascular smooth muscle,” *Am. J. Physiol.*, 282, H1571-H1583 (2002).

[143] Peng, H. L. *et al.*, “Hypotesis for the initiation of vasomotion,” *Circ. Res.*, 88, 810-815 (2001).

[144] Oishi, H. *et al.*, “Role of membrane potential in vasomotion of isolated pressurized rat arteries,” *Life Sciences*, 71, 2239-2248 (2002).

[145] Merrins, M. J. *et al.*, “Direct measurements of oscillatory glycolysis in pancreatic islets β-cells using novel fluorescence resonance energy transfer (FRET) biosensors for pyruvate kinase M2 activity,” *J. Biol. Chem.*, 288, 33312-33322 (2013).

[146] Bertram, R. *et al.*, “Interaction of glycolysis and mitochondrial respiration in metabolic oscillations of pancreatic islets,” *Biophys. J.*, 92, 1544-1555 (2007).

[147] Dunaev, A. V. *et al.*, “Substantiation of medical and technical requirements for noninvasive spectrophotometric diagnostic devices,” *J. Biomed. Opt.*, 18(10), 107009 (2013).

[148] Rogatkin, D. A. *et al.*, “Multifunctional laser noninvasive spectroscopic system for medical diagnostics and metrological provisions for that,” *Proc. SPIE 7368*, *Clinical and Biomedical Spectroscopy*, 73681Y (2009).

[149] Bolognia, J. L., Jorizzo, J. L. and Rapini, R. P., “Dermatology”, Elsevier (2003).

[150] Gupta, A. *et al.*, “Ultraviolet Radiation in Wound Care: Sterilization and Stimulation,” *Adv. Wound Care (New Rochelle)*, 2(8), 422-437 (2013).

[151] Pasparakis, M., Haase, I. and Nestle, F. O., “Mechanisms regulating skin immunity and inflammation,” *Nat. Rev. Immunol.*, 14:(5), 289-301 (2014).

[152] Smirni, S. *et al.*, “Application of cmOCT and continuous wavelet transform analysis to the assessment of skin microcirculation dynamics,” *J. Biomed. Opt.*, 23(7), 076006 (2018).

[153] Smirni, S. *et al.*, “In-vivo assessment of microvascular functional dynamics by combination of cmOCT and wavelet transform,” *Proc. SPIE 10493*, *Dynamics and Fluctuations in Biomedical Photonics XV*, 104930P (2018).

[154] Huang, S., Heikal, A. A. and Webb, W. W., “Two-photon fluorescence spectroscopy and microscopy of NAD(P)H and flavoprotein,” *Biophys. J.*, 82, 2811–2825 (2002).

[155] Ho, D. *et al.*, “Heart rate and electrocardiography monitoring in mice,” *Curr. Protoc. Mouse Biol.*, 1, 123-139 (2011).

[156] Ewald, A. J., Werb, Z. and Egeblad, M., “Monitoring of Vital Signs for Long-Term Survival of Mice under anesthesia,” *Cold Spring Harb. Protoc.*, 2, pdb.prot5563 (2011).

[157] Iatsenko, D., McClintock, P. V. E. and Stefanovska, A., “Linear and synchrosqueezed time-frequency representations revisited: Overview, standards of use, resolution, reconstruction, concentration, and algorithms,” *Digit. Sig. Process.*, 42, 1-26 (2015).

[158] Hayes, J. D. and Dinkova-Kostova, A. T., “The Nrf2 regulatory network provides an interface between redox and intermediary metabolism,” *Trends Biochem Sci.*, 39(4), 199-218 (2014).

[159] Erkens, R. *et al.*, “Left ventricular diastolic dysfunction in Nrf2 knock out mice is associated with cardiac hyopertrophy, decreased expression of SERCA2a, and preserved endothelial function,” *Free Radic. Biol. Med.*, 89, 906-917 (2015).

[160] Okazaki, K., *et al.*, “Role of the endothelium-derived hyperpolarizing factor in phenylephrine-induced oscillatory vasomotion in rat small mesenteric artery,” *Anesthesiology*, 98, 1164-1171 (2003).

[161] Krupatkin, A., “Noninvasive estimation of human tissue respiration with wavelet-analysis of oxygen saturation and blood flow oscillations in microvessels,” *Fiziol. Cheloveka*, 38(4), 67-73 (2012).

[162] Kamkin, A. G. and Kamenskii, A. A., “Fundamental’naya i klinicheskaya fiziologiya (Basic and Clinical Physiology)”, Moscow: Akademiya (2004).

[163] Shimokawa, H. *et al.*, “The importance of the hyperpolarizing mechanism increases as the vessel size decreases in endothelium-dependent relaxations in rat mesenteric circulation,” *J. Cardiovasc. Pharmacol.*, 28(5), 703-11 (1996).

[164] Hwa, J. J., Ghibaudi, L., Williams, P. and Chatterjee, M., “Comparison of acetylcholine-dependent relaxation in large and small arteries of rat mesenteric vascular bed,” *Am. J. Physiol.*, 266(3 Pt 2), H952-8 (1994).

[165] Gruszecki, M. *et al.*, “Human subarachnoid space width oscillations in the resting state,” *Sci. Rep.*, 8, 3057 (2018).

[166] Brunori, M. *et al.*, “Nitric oxide and cellular respiration,” *Cell. Mol. Life Sci.*, 56(7-8), 549-57 (1999).

[167] Brookes, P. S. *et al.*, “Control of mitochondrial respiration by NO*, effects of low oxygen and respiratory state,” *J. Biol. Chem.*, 278(34), 31603-9 (2003).

[168] Förstermann, U. and Sessa, W. C., “Nitric oxide synthases: regulation and function,” *Eur. Heart J.*, 33, 829-837 (2012).

[169] Pacher, P., Beckman, J. S. and Liaudet, L., “Nitric oxide and peroxynitrite in health and disease,” *Physiol. Rev.*, 87(1), 315-424 (2007).

[170] Rossi, M. *et al.*, “Impact of long-term exposure to cigarette smoking on skin microvascular function,” *Microvasc. Res.*, 93, 46-51 (2014).

[171] Monfrecola, G. *et al.*, “The acute effect of smoking on cutaneous microcirculation blood flow in habitual smokers and nonsmokers,” Dermatology, 197(2), 115-8 (1998).

[172] Noble, M., Voegeli, D. and Clough, G. F., “A comparison of cutaneous vascular responses to transient pressure loading in smokers and nonsmokers,” *J. Rehabil. Res. Dev.*, 40(3), 283-8 (2003).

[173] Muck-Weymann, M. E. *et al.*, “Respiratory-dependent laser doppler flux motion in different skin areas and its meaning to autonomic nervous control of the vessels of the skin,” *Microvasc. Res.*, 52, 69-78 (1996).

[174] Hanna, S. T., “Nicotine effect on cardiovascular system and ion channels,” *J. Cardiovasc. Pharmacol.*, 47(3), 348-58 (2006).

[175] Rångemark, C. and Wennmalm, A., “Endothelium-dependent and -independent vasodilation and reactive hyperemia in healthy smokers,” *J. Cardiovasc. Pharmacol.*, 12, S198-201 (1992).

[176] Vleeming, W., Rambali, B. and Opperhuizen, A., “The role of nitric oxide in cigarette smoking and nicotine addiction,” *Nicotine Tob. Res.*, 4(3), 341-8 (2002).

[177] Alving, K., Fornhem, C., Weitzberg, E. and Lundberg, J. M., “Nitric oxide mediates cigarette smoke-induced vasodilatory responses in the lung,” *Acta Physiol. Scand.*, 146(3), 407-8 (1992).

[178] Bekö, G. *et al.*, “Measurements of dermal uptake of nicotine directly from air and clothing,” *Indoor Air.*, 27(2), 427-33 (2017).

[179] George, R. B., Matthay, M. A., Light, R. W. and Matthay, R. A., “Chest Medicine: Essentials of Pulmonary and Critical Care Medicine”, US: Lippincott Williams & Wilkins (2005).

[180] Hoyt, G. L., “Cigarette Smoking: Nicotine, Carbon Monoxide, and the Physiological Effects on Exercise Responses,” *Sport Sci. Rev.*, 22(1-2), 5-24 (2013).

[181] Irving, D. W. and Yamamoto, T., “Cigarette smoking and cardiac output,” *Br. Heart J.*, 25(1), 126-132 (1963).

[182] Tachmes, L., Fernandez, R. J. and Sackner, R. A., “Hemodynamic Effects of Smoking Cigarettes of High and Low Nicotine Content,” *Chest J.*, 74(3), 243-246 (1978).

[183] Omvik, P., “How smoking affects blood pressure,” *Blood Pressure*, 5(2), 71-7 (1996).

[184] Medow, M. S., Taneja, I. and Stewart, J. M., “Cyclooxygenase and nitric oxide synthase dependence of cutaneous reactive hyperemia in humans,” *Am. J. Physiol. Heart Circ. Physiol.*, 293, H425–H432 (2007).

[185] Kristensen, K. J. and Henriksen, O., “Excess cumulative blood flow and repayment during reactive hyperemia in human cutaneous tissue,” *Acta Physiol. Scand.*, 108, 1-6 (1980).

[186] Lenasi, H., “Assessment of Human Skin Microcirculation and Its Endothelial Function Using Laser Doppler Flowmetry,” in *Medical Imaging*, Okechukwu Felix Erondu, 271-296 (2011).

[187] Pohl, U. and deWit, C., “A Unique Role of NO in the Control of Blood Flow,” *News Physiol. Sci.*, 14, 74-80 (1999).

[188] Urakami-Harasawa, L. *et al.*, “Importance of endothelium-derived hyperpolarizing factor in human arteries,” *Clin. Invest.*, 100, 2793-2799 (1997).

[189] Wong, B. J., Wilkins, B. W., Holowatz, L. A. and Minson, C. T., “Nitric oxide synthase inhibition does not alter the reactive hyperemic response in the cutaneous circulation,” *J. Appl. Physiol.*, 95, 504–510 (2003).

[190] Zhao, J. L., Pergola, P. E., Roman, L. J. and Kellogg, D. L. J., “Bioactive nitric oxide concentration does not increase during reactive hyperemia in human skin,” *J. Appl. Physiol. (1985)*, 96(2), 628-32 (2004).

[191] Binggeli, C. *et al.*, “Statins enhance postischemic hyperemia in the skin circulation of hypercholesterolemic patients: a monitoring test of endothelial dysfunction for clinical practice?,” *J. Am. Coll. Cardiol.*, 42(1), 71-7 (2003).

[192] Carlsson, I., Sollevi, A. and Wennmalm, A., “The role of myogenic relaxation, adenosine and prostaglandins in human forearm reactive hyperaemia,” *J. Physiol.*, 389, 147-61 (1987).

[193] Cracowski, J. *et al.*, “Involvement of cytochrome epoxygenase metabolites in cutaneous postocclusive hyperemia in humans,” *J. Appl. Physiol.*, 114, 245–251 (2013).

[194] Bellien, J., Joannides, R., Richard, V. and Thuillez, C., “Modulation of cytochrome-derived epoxyeicosatrienoic acids pathway: A promising pharmacological approach to prevent endothelial dysfunction in cardiovascular diseases?,” *Pharmacol. Ther.*, 131, 1-17 (2011).

[195] Brunt, V. E. and Minson, C. T., “KCa channels and epoxyeicosatrienoic acids: major contributors to thermal hyperaemia in human skin,” *J. Physiol.*, 590(Pt 15), 3523–3534 (2012).

[196] Fojt, O. and Holcik, J., “Applying nonlinear dynamics to ECG signal processing. Two approaches to describing ECG and HRV signals.,” *IEEE Eng. Med. Biol. Mag.*, 17(2), 96-101 (1998).

[197] Takens, F., “Detecting Strange Attractors in Turbulence. Dynamical Systems and Turbulence”, Berlin: Springer (1981).

[198] Gaubert, M. L. et al., “Endothelium-derived hyperpolarizing factor as an in vivo back-up mechanism in the cutaneous microcirculation in old mice,” *J. Physiol.*, 585(Pt 2), 617-626 (2007).

Appendix

This section contains the manuscripts, part of this doctoral project, which have been published or submitted to peer-reviewed journals by July 2018.

I. In-vivo assessment of microvascular functional dynamics by combination of cmOCT and wavelet transform

This proceeding paper has been presented in San Francisco (US) at the *SPIE BiOS 2018, Dynamics and Fluctuations in Biomedical Photonics XV Conference* in January 2018, and published in February 2018. The content of the paper is related to additional experimental work that was carried out in collaboration with the *Tissue Optics and Microcirculation Imaging* group of the National University of Ireland Galway (NUIG), which was involved in this doctoral project as associated partner. The topic of the paper is the validation of the correlation mapping optical coherence tomography (cmOCT) imaging method for the concurrent assessment of microcirculation structure and microvascular functional dynamics (vasomotion), thanks to the combination with the post-occlusive reactive hyperaemia (PORH) challenging test and the continuous wavelet transform (CWT) spectral analysis.

II. Application of cmOCT and continuous wavelet transform analysis to the assessment of skin microcirculation dynamics

This is a full-length paper published in the *Journal of Biomedical Optics* (JBO) in July 2018. The content of this manuscript is an extended and completed version of the proceeding paper number I, containing additional data analyses and results from a major number of examined subjects.

III. In-vivo multi-parameter optical measurements show correlations between skin metabolic oscillations and vasomotion

This is a full-length paper submitted to the journal *Scientific Report*s in May 2018 and currently under peer review. The content of this manuscript is related to the results reported in the Chapter 3 of this thesis about the role of metabolic oscillators in mouse cutaneous vasomotion induced by α-adrenergic stimulation with phenylephrine (PE).

I. In-vivo assessment of microvascular functional dynamics by combination of cmOCT and wavelet transform

Salvatore Smirni[1], Michael P. MacDonald[1,2], Catherine P. Robertson[1], Paul M. McNamara[3], Sean O'Gorman[3], Martin J. Leahy[3,4] and Faisel Khan[1]

[1]School of Medicine, Ninewells Hospital, University of Dundee, Dundee, DD1 9SY, UK
[2]School of Science and Engineering, University of Dundee, Nethergate, Dundee, DD1 4HN, UK
[3]Tissue Optics and Microcirculation Imaging facility, National University of Ireland, Galway
[4]Royal College of Surgeons (RCSI), Dublin, Ireland

Full citation of the paper:
Salvatore Smirni, Michael P. MacDonald, Catherine P. Robertson, Paul M. McNamara, Sean O'Gorman, Martin J. Leahy, Faisel Khan, "In-vivo assessment of microvascular functional dynamics by combination of cmOCT and wavelet transform," *Proc. SPIE 10493, Dynamics and Fluctuations in Biomedical Photonics XV*, 104930P (2018); https://doi.org/10.1117/12.2289814

ABSTRACT

The cutaneous microcirculation represents an index of the health status of the cardiovascular system. Conventional methods to evaluate skin microvascular function are based on measuring blood flow by laser Doppler in combination with reactive tests such as post-occlusive reactive hyperaemia (PORH). Moreover, the spectral analysis of blood flow signals by continuous wavelet transform (CWT) reveals nonlinear oscillations reflecting the functionality of microvascular biological factors, e.g. endothelial cells (ECs). Correlation mapping optical coherence tomography (cmOCT) has been previously described as an efficient methodology for the morphological visualisation of cutaneous micro-vessels. Here, we show that cmOCT flow maps can also provide information on the functional components of the microcirculation. A spectral domain optical coherence tomography (SD-OCT) imaging system was used to acquire 90 sequential 3D OCT volumes from the forearm of a volunteer, while challenging the micro-vessels with a PORH test. The volumes were sampled in a temporal window of 25 minutes, and were processed by cmOCT to obtain flow maps at different tissue depths. The images clearly show changes of flow in response to the applied stimulus. Furthermore, a blood flow signal was reconstructed from cmOCT maps intensities to investigate the microvascular nonlinear dynamics by CWT. The analysis revealed oscillations changing in response to PORH, associated with the activity of ECs and the sympathetic innervation.
The results demonstrate that cmOCT may be potentially used as diagnostic tool for the assessment of microvascular function, with the advantage of also providing spatial resolution and structural information compared to the traditional laser Doppler techniques.

Keywords: microcirculation imaging; cmOCT; continuous wavelet transform; nonlinear dynamics; cardiovascular risk;

1. INTRODUCTION

1.1 Cutaneous microcirculation for the assessment of cardiovascular risk

The microcirculation is a network of tiny blood vessels distributed in all the tissues of the body, which ensure the normal perfusion of the organs, the maintenance of a normal blood pressure, and the exchange of nutritive substances and waste metabolites between blood and tissue[1,2]. Microvascular dysfunction is involved in the development of several diseases, such as cardiovascular complications of diabetes, cardiomyopathy, and hypertension[1]. Therefore, the evaluation of the microcirculation is a powerful modality for the assessment of cardiovascular disease (CVD) risk, which could find potential diagnostic applications[1]. Nonetheless, the examination of microvascular function *in-vivo* relies on invasive techniques such as coronary angiography[1]. This problem may be addressed by using non-invasive methodologies for the *in-vivo* examination of microcirculation from peripheral organs, i.e. skin[1,3,4]. Indeed, several studies have demonstrated that skin microcirculation reflects the health status of the coronary microvasculature[4], and could be used as biomarker of CVD risk. For this reason, over the past number of years, many non-invasive technologies have been developed for either the evaluation of skin microvascular function or the imaging of skin microvascular structure.

1.2 Examination of cutaneous microvascular function by Laser Doppler and LSCI

The conventional methods for the evaluation of skin microvascular function are laser Doppler or laser speckle contrast imaging (LSCI) in combination with functional tasks, e.g. post-occlusive reactive hyperaemia (PORH). Laser Doppler techniques are generally classified in laser Doppler flowmetry (LDF) and laser Doppler imaging (LDI), based on sensing the Doppler shift of red or infrared light backscattered by moving red blood cells (RBCs) for the calculation of the mean blood perfusion in small tissue areas[2,3,5,6]. LDF allows the continuous measurement of blood flow by a single-point laser probe in direct contact with the cutaneous tissue[5]. The application of spectral analytical methods, i.e. the continuous wavelet transform (CWT), on LDF time series is powerful to investigate the nonlinear dynamics of blood flow providing information on the function of biological microvascular factors, such as endothelial cells (ECs), vascular smooth muscle cells (VSMCs), and the microvascular sympathetic nerves[7,8]. Nonetheless, LDF has low reproducibility because of the heterogeneous structure of skin compared to the small area analysed by the single-point probe[2,3,5,6]. This shortcoming is addressed by LDI, a contactless method that employs a laser placed at a distance above the skin to generate two-dimensional perfusion maps covering a larger skin region[3,5,6]. However, LDI cannot be used for the study of flow nonlinear fluctuations due to the slow sampling frequency of discrete perfusion maps during the measurements[3]. LSCI is a contactless technique based on sensing the reduction of the speckle contrast pattern caused by moving RBCs when a laser beam hits the skin, for estimating a perfusion value proportional to RBCs velocity[5,6]. The advantage of LSCI is providing both temporal and spatial resolution, however the method has low penetration depth compared to laser Doppler, and is highly sensitive to movement artefacts[5,6]. Furthermore, both of laser Doppler and LSCI do not allow the visualisation of micro-vessels[2,5,6]. Laser Doppler and LSCI blood flow data are expressed in perfusion arbitrary units (PU), making it necessary the combination of measurements with reactive tasks for assessing the relative changes of flow while challenging blood vessels with a variety of stimuli[5,6]. An example of functional task is PORH, based on monitoring the blood perfusion increase induced by a temporary period of ischaemia obtained through the occlusion of flow in the brachial artery[5,6]. The occlusion is performed by using a pressure cuff placed on the upper part of the tested arm, and the microcirculation is generally monitored from the volar forearm or the fingertips[5,6].

1.3 Methods for the imaging of skin micro-vessels

The cutaneous micro-vessels can be imaged *in-vivo* by a variety of techniques based on optical microscopy, 3D photoacoustic imaging or optical coherence tomography (OCT). The optical microscopy methods, i.e. capillaroscopy, orthogonal polarisation spectral imaging (OPS) and sidestream dark-field imaging (SDF), are based on the use of a microscope provided with a light source (white or green polarised light) for the transmission of images to a videocamera[2,6]. Capillaroscopy allows mainly the imaging of the structural organisation of capillaries in skin sites with thinner epithelium (i.e. the nailfold)[2,9]. This method is limited by the generation of low-contrast images[6] and the requirement of invasive fluorescent dyes to visualise blood vessels from thicker skin regions[2,6]. OPS and SDF provide better resolution images than capillaroscopy thanks to the use of non-invasive green polarised light[2,10]. However, both the techniques are sensitive to motion and pressure artefacts[6] and the imaging is optimal only for thinner cutaneous areas, e.g. the sublingual tissue[2]. All the optical microscopy methods provide two-dimensional images with

ambiguous depth resolution leading to the impossibility of establishing the exact origin of the imaged microvascular layer[9,11]. This shortcoming has been solved by the implementation of techniques for the three-dimensional imaging of the microcirculation, such as 3D photoacoustic imaging and OCT[9,11]. The 3D photoacoustic imaging is a full light penetration depth method[12], employing low scattering ultrasound waves generated in all the directions by a pulsed laser light and absorbed by haemoglobin and melanin in the skin to provide contrast agents for the imaging of blood vessels[9,13,14]. Although photoacoustic imaging provides a full light penetration depth, the technique is characterised by low spatial resolution associated with the detection of ultrasound waves leading to poor structural images[9]. The development of photoacoustic microscopy (PAM) and optical resolution photoacoustic microscopy (OR-PAM) has allowed addressing the problem providing high-resolution images, even though this is still restricted to superficial capillaries[9]. Furthermore, photoacoustic imaging is limited by the use of a coupling medium at direct contact with the skin, which can affect the microcirculation and false the results[9]. OCT is a non-invasive method that uses a broadband near infrared light source placed at a distance above the skin to generate a low coherence gate for the selection of backscattered light from different tissue depths, providing two-dimensional and three-dimensional *in-vivo* morphological images[15]. OCT allows overcoming some shortcomings of photoacoustic imaging, by providing cross-sectional images comparable to conventional optical biopsies with high structural resolution in the order of micrometers[16,17]. However, OCT suffers of poor penetration depth compared to photoacoustic imaging[18].

1.4 Simultaneous assessment of microcirculation morphology and function

The advantage of laser Doppler and LSCI compared to the techniques for the visualisation of micro-vessels is the possibility to detect functional information that may be used for diagnostic purposes. Indeed, microvascular dysfunction is an early factor preceding the morphological damage to micro-vessels, which characterises the initial stages of cardiovascular pathologies[1,3]. However, LDI and LSCI are not suitable for a complete evaluation of the microcirculation because they do not allow micro-vessels visualisation and are characterised by uncertain spatial and depth resolution. For these reasons, many methods for the morphological imaging of the microcirculation have been implemented further to allow the simultaneous assessment of microvascular function and structure. For example, photoacoustic imaging may provide functional information associated to the oxygenation of the examined microvascular area, by tracing the light absorbed by haemoglobin at different wavelengths[19]. Additional examples are the improvements of OCT, adding contrast mechanisms based on the Doppler shift (DOCT)[20] and the speckle variance (svOCT)[21] principles to image blood flow, or by the development of data processing methods based on the discrimination of static and flow dynamic regions of the skin, i.e. Doppler optical micro-angiography (DOMAG)[22]. Nonetheless, the mentioned methods are not optimal for different reasons, such as angular dependence of the acquisitions leading to the production of incomplete flow maps (DOCT)[9,11], requirement of previous knowledge of the morphology to trace blood flow (svOCT)[9], and long post-processing time required for obtaining blood flow maps (DOMAG)[9]. To address these shortcomings, recently a novel technique for the *in-vivo* visualisation of micro-vessels named correlation mapping OCT (cmOCT) has been developed, which provides high-resolution structural maps of the microcirculation with potential to gain also functional information[9,11]. The technique is based on correlation coefficient statistics to detect blood flow from the OCT signal[9,11], by discriminating the moving scatters characterising the cutaneous areas containing active blood vessels and the stationary scatters in the skin locations lacking of blood vessels[9,11]. This is achieved by performing the cross-correlation analysis between adjacent two-dimensional B-frames of an OCT volume sampled from the skin, which returns high correlation coefficients for the static areas similar between different B-frames, and low correlation coefficients for the microvascular areas characterised by the presence of blood flow[9,11]. The correlation map generated from the analysis reveals the location of blood flow allowing the visualisation of the micro-vessels[9,11]. The benefits of cmOCT are the apparent angle independence of the method[11], the fact that it is not required the previous knowledge of the microvascular morphology to determine blood flow areas, and fast data processing to generate the flow maps[9].

1.5 Goal and findings of the research

Despite the suitability of cmOCT for the imaging of microvascular structure has been demonstrated[9,11], less proof is reported about the use of this method for the study of microvascular function. In this work, we show that cmOCT can be applied successfully for the study of microvascular function. We demonstrate that collecting many sequential low-resolution 3D OCT volumes from the human forearm during PORH functional task and processing the volumes by cmOCT it is possible to generate sequential blood flow maps

at several tissue depths clearly tracing the temporal changes of flow typical of PORH test. Furthermore, the intensity of cmOCT flow maps was used to reconstruct a continuous time series for the study of blood flow nonlinear fluctuations by the application of the CWT spectral analysis. The wavelet examination of the reconstructed signal revealed blood flow oscillations associated with the physiological activity of biological factors playing a fundamental role in microvascular function: oscillations related to endothelial vasodilatory mechanisms mediated by ECs, and the neurogenic oscillation that reflects the contribution of the microvascular sympathetic nerves to vasomotion. The CWT oscillators displayed changes in their spectral energy during reactive hyperaemia similar to those described in literature for the LDF signal. Therefore, our results demonstrate that cmOCT is suitable for the simultaneous evaluation of microcirculation structure and function. Next step will be the application of the technique to a larger number of subjects for testing the reproducibility of cmOCT and its applicability to clinical studies.

2. METHODS

2.1 Images acquisition

Data were collected from the volar forearm of a healthy woman aged 28, which signed an informed consent form. The experiment was performed in a laboratory room with controlled temperature (20 ± 1°C), allowing 15-20 min of acclimatisation of the subject. The scans were obtained from the left volar forearm while the volunteer was laying in a clinical bed. The tested arm was fixed by employing a house-designed soft support to ensure a static and comfortable position during the examination preventing motion artefacts. The location for the acquisitions was selected avoiding hairy and injured areas. A pressure cuff was fixed in the upper part of the arm for performing a PORH functional test during the acquisition of the images. PORH response was induced by blocking blood flow through the brachial artery by applying a pressure of 200 mmHg. A spectral domain (SD) OCT device (TEL2200C1, Thorlabs Inc., USA) was employed for imaging three-dimensional skin volumes. The system is provided with a superluminescent diode (SLD) with a center wavelength of 1300 nm, supporting a maximum imaging depth of 3.5 mm in non-scattering samples, an axial acquisition rate between 5.5 and 76 kHz, and an axial resolution of 5.5 µm in non-scattering samples. The sample arm contains a LSM003 (Thorlabs Inc., USA) scanning lens supporting a transverse resolution of 13 µm in air. An initial volume of 1.50 × 1.50 × 1.82 mm^3 was sampled from the forearm at a speed of 48 kHz with a sampling density of 1024 (length) × 1024 (width) × 512 (depth) pixels, to image the microvascular morphology of the examined location. The time employed for the acquisition of the structural volume was 50.9 s, which is too long for the evaluation of functional dynamics. Thus, the study of functional dynamics was performed by decreasing the scanning density to 256 × 256 × 512 pixels that can be acquired in ~6 s, allowing the fast collection of consecutive OCT volumes suitable for assessing microvascular function. Moreover, a fundamental requirement for visualising blood flow by cmOCT is a dense sampling below the lateral resolution of the consecutive 2D B-scans of the OCT volume, which guarantees a robust correlation between the motionless scatters of the adjacent B-scans. Thus, to ensure a spatial separation between the B-scans suitable for the cmOCT analysis the sampled area was reduced to 0.75 × 0.75 × 1 .82 mm^3, corresponding to a spatial separation of 2.9 µm. Although the possibility of acquiring each scan in ~6 s, the samples were collected at a rate of one volume every 16.6 s because the software associated with the OCT system (ThorImage OCT 4.3, Thorlabs Inc., USA) required around 10.6 s for saving each sample. In total, 90 consecutive low-resolution volumes were acquired from the forearm of the volunteer in a temporal period of ~25 min, while performing the PORH functional task. An initial 10 min collection of 36 OCT volumes was carried out to establish the blood flow at rest, then 18 volumes were collected for a 5 min occlusion period, and finally 36 volumes were collected for 10 min after the removal of the occlusion for tracking blood flow dynamic changes during PORH response.

2.2 cmOCT analysis

The cmOCT analysis to extract blood flow maps at different tissue depths from each OCT volume was carried out by using the Java algorithm implemented by Enfield *et al.*[9] and Jonathan *et al.*[11]. The algorithm is able to estimate the correlation coefficients between consecutive two-dimensional B-frames extracted from the OCT volume, by calculating the cross-correlation of a square grid from the first B-scan 1 (I_1) to the same grid from the adjacent B-scan 2 (I_2), as follow,

$$cmOCT(x,y) = \sum_{p=0}^{M} \sum_{q=0}^{N} \frac{\left[I_1(x+p,y+q)-\overline{I_1(x,y)}\right]\left[I_2(x+p,y+q)-\overline{I_2(x,y)}\right]}{\sqrt{(I_1(x+p,y+q)-\overline{I_1(x,y)})^2 (I_2(x+p,y+q)-\overline{I_2(x,y)})^2}} \quad (1)$$

where M and N define the dimension of the grid, and $\bar{I}$ is the mean intensity of the grid. The grid is shifted along all the pixels of the B-frames to generate a 2D map with correlation coefficients between 0 and 1. The low correlation regions are displayed as bright areas representing blood flow, while the high correlation regions associated to the motionless scatters of the tissue are displayed as dark background areas of the map. A 7 × 7 kernel dimension of the grid was used to produce the cmOCT maps, which ensures a good sensitivity to blood flow without loss of spatial resolution due to kernal size. The maps were generated as maximum intensity projection (MIP) images, which allow a better visualisation of microvascular structure and the detection of the maximum flow intensity. To study micro-vessels from different cutaneous microvascular layers, the flow maps were produced from different depths of the OCT volumes, i.e. in the *en face* plane. This was achieved by determining the location of skin surface from the structural images, and employing the superficial region as a reference to determine the various depths of the underlying tissue. The typical anatomic morphology of cutaneous microcirculation was visualised, characterised by the presence of capillaries at a depth of 80-180 µm (dermal-epidermal junction) and horizontal micro-vessels at a depth of 300-400 µm (dermal plexus).

2.3 Reconstruction of blood flow time series

To test the suitability of cmOCT for the study of microvascular flow nonlinear dynamics by CWT spectral analysis, a continuous time series of blood flow was reconstructed from the cmOCT maps. First, the average image intensity was extracted by Matlab R2015a software from 90 sequential flow maps produced at the cutaneous depth of 300-400 µm during PORH test. Then, the intensity values were used as discrete data points to reconstruct a continuous signal, covering the 25 minutes time used in the experiment for collecting the volumes. The reconstruction was performed by piecewise cubic spline interpolation using Matlab R2015a, applying a temporal interval of 16.6 s between each pair of discrete data points that corresponds to the sampling frequency employed during the collection of the OCT volumes. The spline interpolation is a mathematical procedure to approximate a function by interpolating equally spaced discrete data points of the function. The technique uses a low-degree piecewise polynomial named spline, which reduces the interpolation error compared to the normal polynomial interpolation. The method is advantageous for the approximation of a function over large intervals, which is not optimal by using a single polynomial that would require a large degree of the approximating polynomial introducing oscillatory artefacts (Runge's phenomenon) during the interpolation process. The spline interpolation addresses this problem by subdividing the interval [a,b] where the function f is continuous in smaller sub-intervals, and approximating f in every sub-interval by the use of low-degree polynomial pieces that define a composite spline function s. In this study, a third-degree cubic natural spline was used which allows the reconstruction of continuous processes reproducing the smooth curvature of the function to be approximated. As displayed by equation 2, the cubic spline function employs four terms to define a piecewise cubic polynomial between each pair of data points,

$$p_3(x) = ax^3 + bx^2 + cx + d\ , \tag{2}$$

where p_3 is the piecewise cubic polynomial, and a, b, c and d are the four coefficients defining p_3. The final curve is the result of the sum of many pieces reconstructed between each pair of data points. The reconstruction was carried out by employing the *cftool* instrument in Matlab R2015a, which allows performing the cubic spline interpolation by entering the vectors of time and experimental data points. Specifically, we have used a time vector of 90 time points defining an acquisition rate of each flow measurement every 16.6 s and a vector containing the 90 flow intensity values extracted from the sequential cmOCT maps. The values of the continuous signal obtained from the reconstruction were saved for the subsequent application of the CWT analysis. As discussed previously, a benefit of spline interpolation is that the approximation process does not produce oscillatory artefacts. Thus, applying this technique we have ensured that the results of the subsequent CWT analysis were representative of the real fluctuations of microvascular flow detected by cmOCT, without the effect of artefacts introduced during the reconstruction. However, a shortcoming of spline interpolation is the low accuracy in the reconstruction of the right and left ends of the function, due to the presence of a single known data point at each extremity. To prevent the generation of artefacts at the extremities of the reconstructed signal, the curve was broken off at the left and right tips ensuring that the beginning and termination of the signal were corresponding respectively to the initial and final experimental data points. Finally, it should be clarified that in this work, the spline interpolation was not employed as a numerical analysis to fit a model but the method was used

as a technical procedure to obtain a continuous signal, which is a compulsory requirement to allow performing the CWT spectral analysis.

2.4 CWT spectral analysis

The continuous wavelet transform technique allows the study of microvascular flow nonlinear dynamics, revealing the contribution of specific components in the microcirculation (i.e. ECs, VSMCs, and sympathetic nerves) to the temporal dynamic changes of flow. The method is advantageous for the analysis of the oscillatory behaviour of signals showing heterogeneous oscillations over a large range of frequencies, e.g. the LDF signal, providing a good time-frequency resolution[7,8]. Here, the CWT was used for analysing the dynamic fluctuations of a blood flow signal reconstructed from the cmOCT maps generated at a skin tissue depth of 300-400 µm, to prove that cmOCT can provide functional microvascular information related to vasomotion. The method allowed the detection of fluctuations in the frequency ranges 21-52 × 10^{-3} Hz, 9.5-21 × 10^{-3} Hz and 5-9.5 × 10^{-3} Hz that respectively reflect the neurogenic activity of sympathetic nerves, the ECs activity nitric oxide (NO)-dependent, and the ECs activity NO-independent[8]. The myogenic oscillation related to VSMCs function was not detected because the OCT volumes were sampled at a frequency of each volume every 16.6 s, restricting the study to fluctuations up to ~60 × 10^{-3} Hz that is not enough to cover the entire myogenic frequency range located between 52-145 × 10^{-3} Hz [8]. The CWT analysis was implemented by using Matlab R2015a, according to the principles described by Stefanovska *et al.*[7,8]. The method is based on the employment of a set of non-orthogonal basic functions $\Psi_{s,t}$ providing a large frequency window scaled and shifted along the time domain for the extraction of the CWT ensuring an optimal time-frequency resolution[8]. The functions $\Psi_{s,t}$ for the calculation of the CWT of blood flow signals is obtained according to equation 3, by using a Morlet mother wavelet ψ scaled in the temporal domain by a factor s and a center time t, providing a window size suitable for the analysis of highly time-varying signals[8],

$$\Psi_{s,t}(u) = |s|^{-1/2}\ \psi\left(\frac{u-t}{s}\right), \tag{3}$$

where the Morlet mother wavelet ψ is estimated as displayed in equation 4 [8],

$$\psi(u) = \frac{1}{\sqrt{\pi}} e^{-iu} e^{-u^2/2}. \tag{4}$$

The CWT spectrum of a signal $g(u)$ is then extracted as shown in equation 5 [8],

$$\tilde{g}(s,t) = \int_{-\infty}^{\infty} \overline{\Psi}_{s,t}\ (u) g(u) du, \tag{5}$$

where $\overline{\Psi}$ is a complex conjugate of the basic window function removing any dependence of the technique from frequency scales, and $\tilde{g}(s,t)$ is the CWT spectral function defined by the scale s and time t [8]. The obtained CWT spectrum is characterised by a power/energy distributed at various frequencies, indicating the amount of signal located at specific frequencies at the time t. Explained in physiological terms, the CWT energy indicates the contribute of each microvascular oscillator (i.e. ECs) associated with a specific frequency range to blood flow changes at a precise time that for example may be the stage of a reactive test. Monitoring the changes of the CWT energy from specific frequency intervals allows the assessment of the function of specific microvascular components with potential clinical diagnostic applications.

3. RESULTS

3.1 Visualisation of skin microcirculation morphology

A first three-dimensional OCT volume was acquired from a 1.50 × 1.50 × 1.82 mm^3 area in the volar forearm of the volunteer to visualise the microcirculation morphology. The acquisition was performed in 50.9 s employing 1024 × 1024 A-scans, and the MIP flow maps were extracted at different tissue depths by cmOCT analysis. Figure 1 shows the structural *enface* MIPs at three different tissue depths obtained from the volunteer, displaying the classical cutaneous microvascular morphology described by Enfield *et al.*[9].

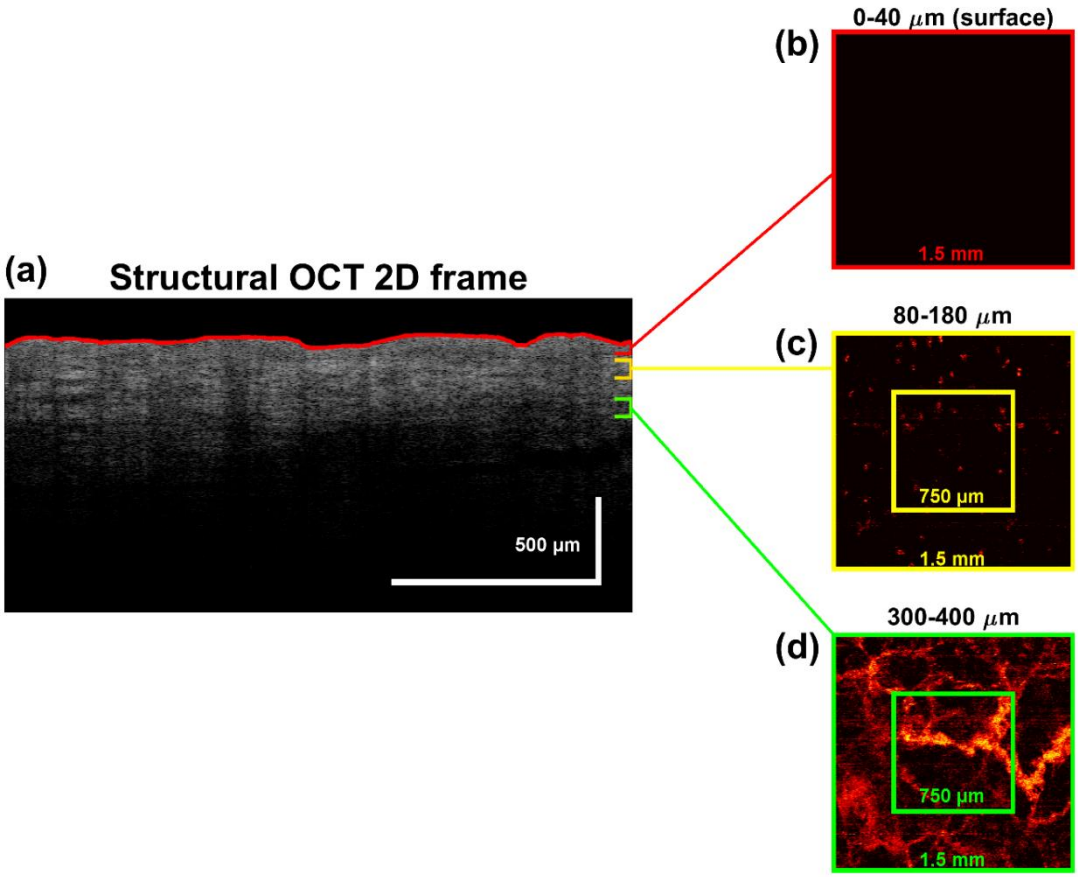

Figure 1 Morphological visualisation of skin micro-vessels from the forearm. (a) 2D structural B-scan from a 1.50 × 1.50 × 1.82 mm^3 OCT volume. The red area outlines the epidermis surface, the yellow region defines the dermal-epidermal junction, and the green area marks a part of the dermal plexus. **(b)** *Enface* 1.50 × 1.50 mm^2 MIP of the epidermis (0-40 µm). **(c)** *Enface* 1.50 × 1.50 mm^2 MIP of the dermal-epidermal junction (80-180 µm) where the capillaries are located. The smaller yellow square marks the 750 × 750 $µm^2$ region selected to study capillaries function. **(d)** *Enface* 1.50 × 1.50 mm^2 MIP of the dermal plexus (300-400 µm) characterised by a horizontal network of micro-vessels. The smaller green square marks the 750 × 750 $µm^2$ area selected to study arterioles/venules function.

Figure 1 (a) shows a structural 2D B-frame of the OCT volume, displaying a longitudinal view of the locations from which the cmOCT maps were produced. Figure 1 (b) displays the MIP *enface* map from the epidermis (0-40 µm) that, as expected, was characterised by absence of micro-vessels. Figure 1 (c) shows the MIP generated from a depth of 80-180 µm (dermal-epidermal junction), displaying the presence of micro-vessels with vertical direction corresponding to the capillary loops originated from the ascending blood vessels of the dermal layer, and appearing as red points in a black background. Figure 1 (d) shows an *enface* MIP of the skin at a depth of 300-400 µm (dermal plexus), displaying a network of arterioles and venules orientated horizontally from which, respectively, the nutritive substances are transferred to the capillaries and the waste metabolites to the venous system. To study microvascular function from 80-180 µm and 300-400 µm tissue depths, an *enface* plane of 0.75 × 0.75 mm^2 was selected from the structural images to perform sequential temporal acquisitions of 3D OCT volumes during reactive hyperaemia task. Figure 1 (c) and (d) illustrate the 750 × 750 $µm^2$ areas selected for monitoring capillaries and arterioles/venules functional dynamics, respectively marked by yellow and green squares.

3.2 Examination of blood flow functional dynamics from cmOCT maps

Ninety low-resolution volumes of the 0.75 × 0.75 × 1.82 mm^3 yellow/green regions shown in Figure 1 (c-d) were collected from the forearm of the volunteer during a 25 min PORH test, sampling each volume every 16.6 s. First, 36 samples were collected during a 10 min resting period, then 18 samples were acquired during a 5 min occlusion of blood flow, and finally 36 samples were collected in a 10 min period after the removal of the occlusion for monitoring flow changes during PORH response. The volumes were processed by cmOCT to obtain consecutive flow maps at 80-180 µm and 300-400 µm cutaneous depths for tracing, respectively, the flow dynamics of capillaries (Figure 2) and arterioles/venules (Figure 3).

Figure 2 and Figure 3 display the *enface* MIPs obtained from 24 volumes of the total 90 temporal samples, which represent the most important stages of PORH test. Although the quality of the maps was not optimal compared to the morphological images, they clearly traced the flow changes typical of PORH reactive task. The capillaries did not show relevant flow changes during occlusion (Figure 2, occlusion 1-8) compared to the flow at rest (Figure 2, baseline 1-8), while the micro-vessels in the dermal plexus showed a relevant decrease and disappearance of flow during occlusion (Figure 3, occlusion 1-8) compared to the flow at rest (Figure 3, baseline 1-8). These findings may indicate the delivery of the residual blood flow from arterioles to capillaries during the occlusion period, ensuring the feeding of the epidermis during ischaemia. On the other hand, a relevant growth of the flow typical of the hyperaemic response was observed during PORH either for the capillaries or the dermal micro-vessels (Figures 2-3, porh 1-8), related to the vascular reactivity for the restoration of a normal blood flow after removal of the occlusion. These findings prove that cmOCT allows tracking the microcirculatory dynamics and may be used for the investigation of microvascular function.

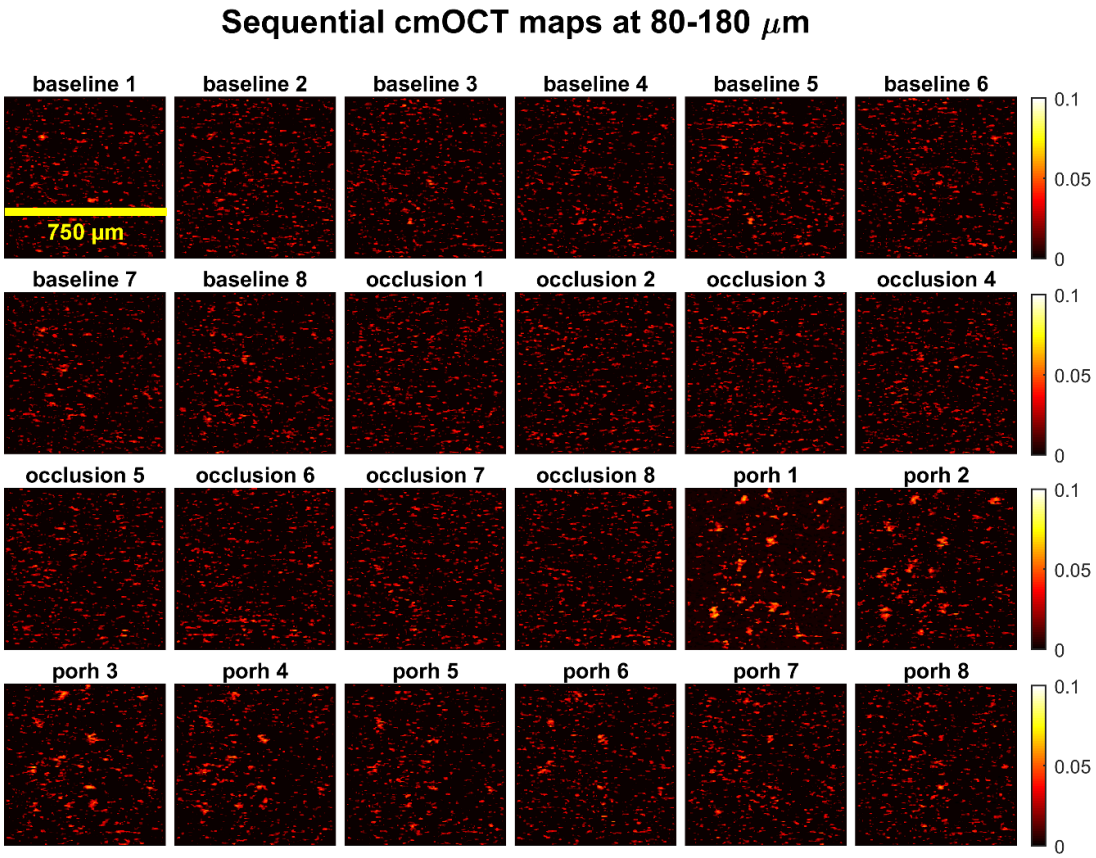

Figure 2 Consecutive cmOCT flow maps obtained at a depth of 80-180 µm from OCT volumes collected during PORH task. Temporal *enface* MIPs from the 750 × 750 µm^2 yellow region marked in Figure 1 (c) for the examination of capillaries microvascular function. The MIPs were generated from 0.75 × 0.75 × 1.82 mm^3 volumes collected every 16.6 s with a sampling density of 256 × 256 A-scans. The baseline 1-8 maps illustrate the flow detected at baseline before the application of the occlusion, the occlusion 1-4 and 5-8 maps correspond respectively to the flow detected after the beginning of the occlusion and before the end of the occlusion, and the porh 1-8 maps show the flow detected during the hyperaemic response.

3.3 Reconstruction of blood flow signal from cmOCT maps

To demonstrate further the applicability of cmOCT for the study of microvascular function, the cmOCT maps were employed for tracing the nonlinear dynamics of blood flow to detect the oscillatory activity of microvascular components contributing to the rhythmic vaso-relaxation induced by PORH stimulation. The task was achieved by reconstructing a continuous flow signal from the intensities of the sequential temporal cmOCT maps and processing the obtained time series by CWT spectral analysis. The reconstruction process was a fundamental step to allow performing the CWT analysis, which is a technique applicable only on continuous time-varying signals. Figure 4 shows the blood flow time series obtained by using the mean intensity values extracted from the 90 sequential cmOCT maps generated at a depth of 300-400 µm as

discrete data points to reconstruct a curve covering the 25 min period of the reactive test. The reconstruction was performed by piecewise cubic spline interpolation method that is advantageous because no oscillatory artefacts are introduced between each pair of discrete data points during the reconstruction process. The curve in Figure 4 clearly outlines the classic flow trend of the reactive hyperaemia task, showing a decrease of blood flow during the ischaemic period, and a relevant increase of flow during PORH vasodilation response up to a maximal peak before the gradual restoration of the baseline flow. This is a further proof that cmOCT is suitable for the study of functional dynamics.

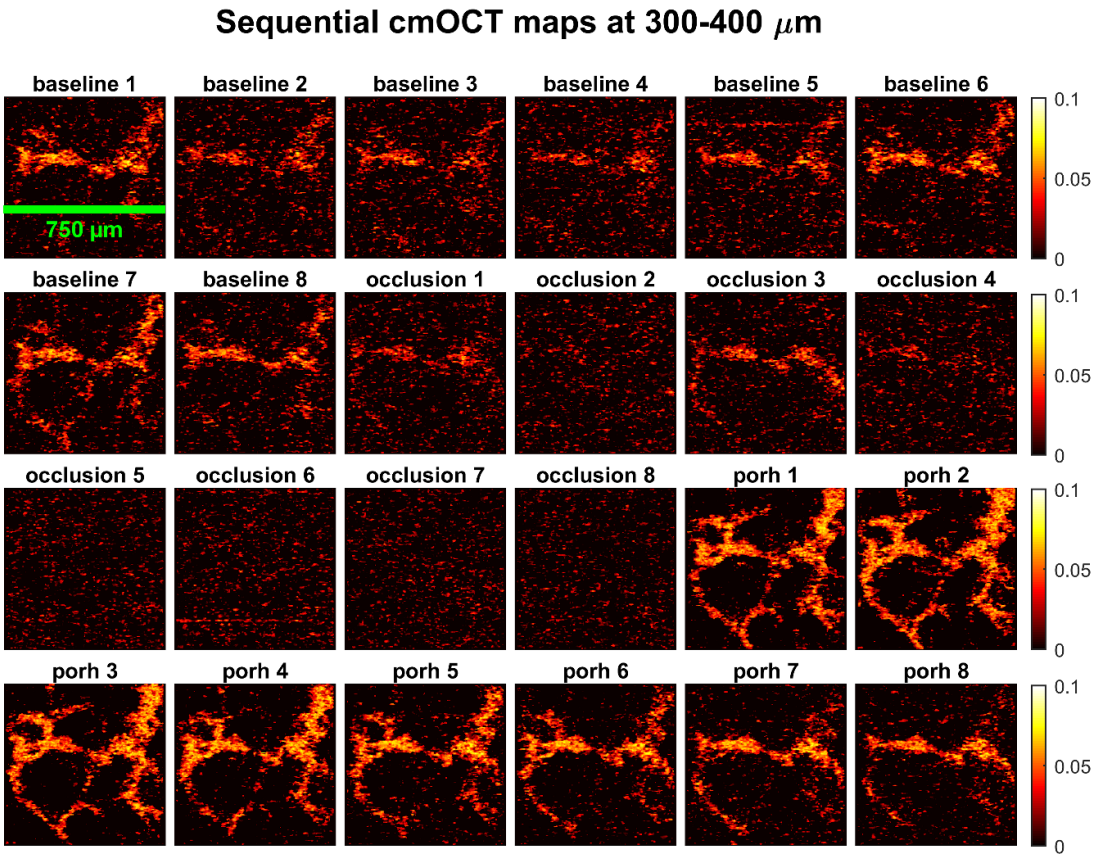

Figure 3 Consecutive cmOCT flow maps obtained at a depth of 300-400 µm from OCT volumes collected during PORH task. Temporal *enface* MIPs from the 750 × 750 µm^2 green region marked in Figure 1 (d) for the examination of arterioles/venules microvascular function. The MIPs were generated from 0.75 × 0.75 × 1.82 mm^3 volumes collected every 16.6 s with a sampling density of 256 × 256 A-scans. The baseline 1-8 maps illustrate the flow detected at baseline before the application of the occlusion, the occlusion 1-4 and 5-8 maps correspond respectively to the flow detected after the beginning of the occlusion and before the end of the occlusion, and the porh 1-8 maps show the flow detected during the hyperaemic response.

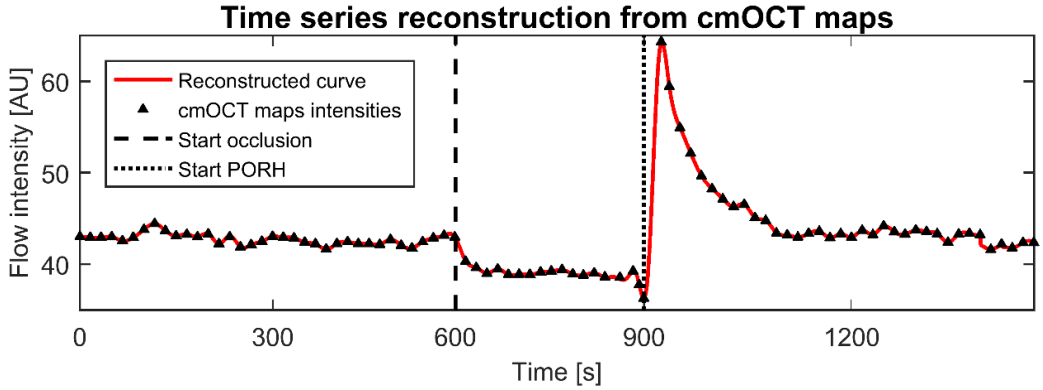

Figure 4 Reconstruction of a continuous blood flow signal from cmOCT maps. Blood flow curve reconstructed by piecewise cubic spline interpolation of the discrete average intensity values obtained from 90 sequential cmOCT maps produced at a cutaneous depth of 300-400 µm. A time interval of 16.6 s was applied between each pair of discrete data points to cover the 25 min period of the PORH functional task. The flow is expressed in arbitrary units (AU).

3.4 CWT spectral analysis of the blood flow signal reconstructed from cmOCT maps

The CWT analysis of the signal reconstructed from cmOCT maps revealed oscillations in the frequency ranges 21-52 × 10^{-3} Hz, 9.5-21 × 10^{-3} Hz and 5-9.5 × 10^{-3} Hz, which respectively reflect the neurogenic modulation of microvascular tone mediated by the sympathetic nerves, and the regulation of microvascular tone mediated by ECs through NO-dependent and NO-independent pathways[8]. Figure 5 displays the CWT analysis of the reconstructed flow signal shown in Figure 4. Figure 5 (a) displays the CWT scalogram chart that shows a gradient coloured map representing the distribution of the wavelet energy of the signal in the time-frequency domain. The dark blue regions represent the lowest energies and the dark red areas the highest energies. The chart clearly outlines the growth of energy during PORH response in all the identified oscillatory frequency intervals, reflecting the endothelial and sympathetic modulatory mechanisms activated during vasodilation. The time-averaged CWT spectrum in Figure 5 (b) distinguishes the maximum wavelet energy peaks at various frequency intervals corresponding to the specific microvascular oscillators (neurogenic, ECs NO-dependent, ECs NO-independent). This allows tracking the activity of each oscillator and making comparisons between different individuals, by extracting values of the maximal energy (amplitude), the overall energy (area under the curve), and the frequency from each wavelet peak during the different stages of PORH task. For example, in Figure 5 (b) an increase of the amplitude and energy of all the oscillators was clearly observed during PORH response (black line) compared to occlusion (red line) and baseline (blue line). These data are in agreement with the results reported for the spectral analysis of LDF signals measured during PORH functional test[23]. Indeed, the growth of energy reflects the vasodilation modulated by ECs, VSMCs and the neurogenic control to allow the reperfusion of the cutaneous tissue after an occlusion period. The CWT spectral analysis showed results in agreement with the current techniques for the examination of microvascular nonlinear fluctuations. Therefore, this is an additional evidence of the suitability of cmOCT for monitoring microvascular function.

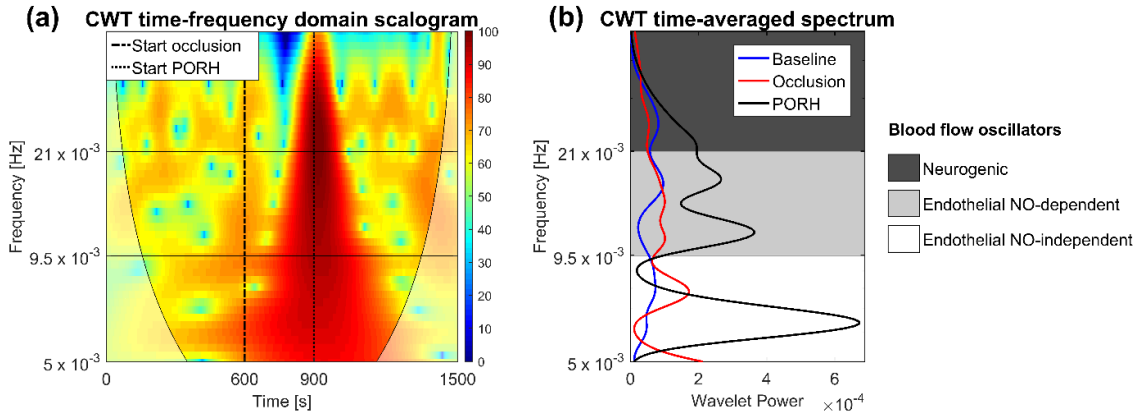

Figure 5 CWT spectral analysis of a blood flow signal reconstructed from cmOCT maps produced at a depth of 300-400 µm. (a) CWT scalogram displaying the distribution of the wavelet power in the time-frequency domain represented by a coloured gradient map ranging from dark blue (low power) to dark red (high power). The coloured areas in the scalogram are part of the "cone of influence", which is a time-frequency region where distortions of the wavelet transform due to the finite duration of the signal are irrelevant[24]. In contrast, the transparent regions in the corners at the bottom of the chart are regions outside of the cone in proximity of the time edges of the signal, where the CWT is characterised by boundary effects making the calculations from these areas uncertain[24]. **(b)** Time-averaged CWT spectra estimated for all the steps of PORH functional task. The graphs discriminate the CWT maximum amplitude peak and overall energy (area under the curve of the peak) related to each specific microvascular oscillator. The neurogenic (21-52 × 10^{-3} Hz), ECs NO-dependent (9.5-21 × 10^{-3} Hz), and ECs NO-independent (5-9.5 × 10^{-3} Hz) oscillators were detected.

4. DISCUSSION AND CONCLUSIONS

In this study, we have shown that cmOCT method allows the simultaneous imaging of skin microcirculation morphology and monitoring of microvascular function. Although the resolution of the functional temporal cmOCT maps was low, they allowed tracking the overall microvascular dynamics with spatial resolution at various tissue depths, showing results similar to those reported for the conventional techniques employed to study microvascular function (i.e. LDF). This is demonstrated by the blood flow trend typical of PORH reactive test observed on the cmOCT maps (Figures 2-3), and also reflected on the reconstructed flow signal displayed in Figure 4. Furthermore, additional evidence was provided by the identification of dynamic microvascular oscillators characterising the reconstructed signal associated with biological components in

the microcirculation (Figure 5), which displayed trends of the wavelet spectral energy similar to those reported for the spectral analysis of LDF time series recorded during PORH test. The CWT analysis did not allow the detection of the myogenic oscillator related to the activity of VSMCs, which are implicated in the mechanical modification of micro-vessels diameter during vasomotion. This was due to the long time required by the ThorImage software (Thorlabs Inc., USA) for saving the OCT volumes during the acquisition of the images, allowing a scanning rate of one volume every 16.6 s that was not sufficient to detect the myogenic oscillation. The use of a more powerful computer in the future may help to improve the performance of the software, allowing a faster data storage to increase the sampling frequency and detect the myogenic oscillator. Overall, the findings from this study suggest that cmOCT may be used as a tool for the study of microvascular function with possible diagnostic applications. However, further experiments in a larger number of subjects are required to demonstrate the robustness of the method and the eligibililty for clinical studies. In addition, the combination of cmOCT with the CWT spectral analysis may find several applications. For example, this may help to establish the contribution of each microvascular bed to vasomotion and clarify which layer is more involved in cutaneous PORH response, by comparing the spectral analysis of cmOCT blood flow signals reconstructed from different skin tissue depths. Another application may be the examination of endothelial function for diagnostic purposes by comparing the endothelial wavelet energy between healthy individuals and patients affected by cardiovascular disease (CVD).

ACKNOWLEDGMENTS

The research leading to these results has received funding from the People Programme (Marie Curie Actions) of the European Union's Seventh Framework Programme (FP7/2007-2013) under REA grant agreement n° 608133. The experiments were performed at the Tissue Optics and Microcirculation Imaging facility of the National University of Ireland, Galway (NUIG) that was involved as associated academic partner in the Marie Curie PHOQUS research programme co-ordinated by the University of Dundee (Scotland).

REFERENCES

[1] Gutterman, D. D., Chabowski, D. S., Kadlec, A. O., Durand, M. J., Freed, J. K., Aissa, K. A. and Beyer, A. M., "The Human Microcirculation – Regulation of Flow and Beyond", Circ. Res., 118(1), 157–172 (2016).

[2] den Uil, C. A., Klijn, E., Lagrand, W. K., Brugts, J. J., Ince, C., Spronk, P. E. and Simoons, M. L., "The microcirculation in health and critical disease", Prog. Cardiovasc. Dis., 51(2), 161-70 (2008).

[3] Turner, J., Belch, J. J. and Khan, F., "Current concepts in assessment of microvascular endothelial function using laser Doppler imaging and iontophoresis", Trends Cardiovasc. Med., 18(4), 109-16 (2008).

[4] Khan, F., Patterson, D., Belch, J. J., Hirata, K. and Lang, C. C., "Relationship between peripheral and coronary function using laser Doppler imaging and transthoracic echocardiography", Clin. Sci. (Lond.), 115(9), 295-300 (2008).

[5] Roustit, M. and Cracowski, J. L., "Assessment of endothelial and neurovascular function in human skin microcirculation", Trends Pharmacol. Sci., 34(7), 373-84 (2013).

[6] Roustit, M. and Cracowski, J. L., "Non-invasive assessment of skin microvascular function in humans: an insight into methods", Microcirculation, 19(1), 47-64 (2012).

[7] Stefanovska, A., Bračič, M. and Kvernmo, H. D. "Wavelet analysis of oscillations in the peripheral blood circulation measured by laser Doppler technique", IEEE Trans. Biomed. Eng., 46(10), 1230-9 (1999).

[8] Shiogai, Y., Stefanovska, A. and McClintock, P. V., "Nonlinear dynamics of cardiovascular ageing", Phys. Rep., 488(2-3), 51-110 (2010).

[9] Enfield, J., Jonathan, E. and Leahy, M., "In vivo imaging of the microcirculation of the volar forearm using correlation mapping optical coherence tomography (cmOCT)", Biomed. Opt. Express, 2(5), 1184-1193 (2011).

[10] Daly, S. M. and Leahy, M., "'Go with the flow': A review of methods and advancements in blood flow imaging", J. Biophotonics, 6(3), 217-255 (2013).

[11] Enock, J., Enfield, J. and Leahy, M. J., "Correlation mapping method for generating microcirculation morphology from optical coherence tomography (OCT) intensity images", J. Biophotonics, 4, 583-587 (2010).

[12] Wang, L. V., "Prospects of photoacoustic tomography", Med. Phys., 35(12), 5758 (2008).

[13] Xu, M. and Wang, L. V., "Time-Domain Reconstruction for Thermoacoustic Tomography in a Spherical Geometry", IEEE Trans. Med. Imaging, 21(7), 814-822 (2002).

[14] Wang, X., Xu, Y. and Xu, M., "Photoacoustic tomography of biological tissues with high cross-section resolution: Reconstruction and experiment", Med. Phys., 29, 2799 (2002).

[15] Podoleanu, A. G., "Optical coherence tomography", J. Microsc., 247, 209-219 (2012).

[16] Mogensens, M. and Jemec, G. B. E., "Diagnosis of Nonmelanoma Skin Cancer/Keratinocyte Carcinoma: A Review of Diagnostic Accuracy of Nonmelanoma Skin Cancer Diagnostic Tests and Technologies", Dermatol. Surg., 33(10), 1158-1174 (2007).

[17] Drexler, W., Morgner, U., Kärtner, F. X., Pitris, C., Boppart, S. A., Li, X. D., Ippen, E. P. and Fujimoto, J. G., "In vivo ultrahigh-resolution optical coherence tomography", Optics Letters, 24(17), 1221-1223 (1999).

[18] Fercher, A. F., Drexler, W., Hitzenberger, C. K. and Lasser, T., "Optical coherence tomography - principles and applications", Rep. Progr. Phys., 66(2), 239-303 (2003).

[19] Zhang, H. F., Maslov, K., Stoica, G. and Wang, L. V., "Functional photoacoustic microscopy for high-resolution and noninvasive in vivo imaging", Nature Biotechnology, 24(7), 848-851 (2006).

[20] Wang, X., Milner, T. and Nelson, J., "Characterization of fluid flow velocity by optical Doppler tomography", Optics letters, 20(11), 1337-1339 (1995).

[21] Barton, J. and Stromski, S., "Flow measurement without phase information in optical coherence tomography images", Optics Express, 13(14), 5234-5239 (2005).

[22] Wang, R. K., Jacques, S. L., Ma, Z., Hurst, S., Hanson, S. R. and Gruber, A., "Three dimensional optical angiography", Optics Express, 15(7), 4083-4097 (2007).

[23] Rossi, M., Pistelli, F., Pesce, M., Aquilini, F., Franzoni, F., Santoro, G. and Carrozzi, L., "Impact of long-term exposure to cigarette smoking on skin microvascular function", Microvasc. Res., 93, 46-51 (2014).

[24] Iatsenko, D., McClintock, P. V. E. and Stefanovska, A., "Linear and synchrosqueezed time-frequency representations revisited: Overview, standards of use, resolution, reconstruction, concentration, and algorithms", Digital Signal Processing, 42, 1-26 (2015).

II. Application of cmOCT and continuous wavelet transform analysis to the assessment of skin microcirculation dynamics

Salvatore Smirni[1,*], Michael P. MacDonald[1,2], Catherine P. Robertson[1], Paul M. McNamara[3], Sean O'Gorman[3], Martin J. Leahy[3,4] and Faisel Khan[1]

[1]School of Medicine, Ninewells Hospital, University of Dundee, Dundee, DD1 9SY, UK
[2]School of Science and Engineering, University of Dundee, Nethergate, Dundee, DD1 4HN, UK
[3]Tissue Optics and Microcirculation Imaging facility, National University of Ireland, Galway
[4]Royal College of Surgeons (RCSI), Dublin, Ireland
*Corresponding author: Salvatore Smirni, University of Dundee, E-mail addresses: salvatore.smirni@gmail.com or s.z.smirni@dundee.ac.uk

Full citation of the paper:
Salvatore Smirni, Michael P. MacDonald, Catherine P. Robertson, Paul M. McNamara, Sean O'Gorman, Martin J. Leahy, Faisel Khan, "Application of cmOCT and continuous wavelet transform analysis to the assessment of skin microcirculation dynamics," *Journal of Biomedical Optics* 23(7), 076006 (2018); https://doi.org/10.1117/1.JBO.23.7.076006

ABSTRACT

Correlation mapping optical coherence tomography (cmOCT) is a powerful technique for the imaging of skin micro-vessels structure, based on the discrimination of the static and dynamic regions of the tissue. Although the suitability of cmOCT to visualize the microcirculation has been proved in humans and animal models, less evidence has been provided about its application to examine functional dynamics. Therefore, the goal of this research was validating the cmOCT method for the investigation of microvascular function and vasomotion.
A spectral domain optical coherence tomography (SD-OCT) device was employed to image 90 sequential three-dimensional OCT volumes from the forearm of 12 volunteers during a 25 minutes post-occlusive reactive hyperaemia (PORH) test. The volumes were processed using cmOCT to generate blood flow maps at selected cutaneous depths. The maps clearly trace flow variations during the PORH response for both capillaries and arterioles/venules microvascular layers.
Continuous blood flow signals were reconstructed from cmOCT maps to study vasomotion by applying wavelet transform spectral analysis, which revealed fluctuations of flow during PORH, reflecting the regulation of microvascular tone mediated by endothelial cells and sympathetic nerves. The results clearly demonstrate that cmOCT allows the generation of functional information that may be used for diagnostic applications.

Keywords: cmOCT; skin microvascular function; vasomotion; wavelet transform; nonlinear dynamics.

1. INTRODUCTION

1.1 Conventional methods for the assessment of skin microvascular function

The examination of the microcirculation is a promising tool for the establishment of novel biomarkers of cardiovascular disease (CVD) risk, which may help to improve the diagnosis, prognosis and early preclinical assessment of vascular pathologies[1]. However, the direct assessment of the microcirculation *in-vivo* is limited by the requirement of invasive methods based on catheterization, e.g. coronary angiography and intracoronary Doppler[1]. In contrast, the examination of the microcirculation from peripheral organs,

i.e. skin, represents a better modality to investigate microvascular function based on the use of non-invasive imaging laser technologies[1,2,3].

The conventional methods for the evaluation of skin microvascular function are laser Doppler and laser speckle contrast imaging (LSCI) in combination with reactive tests. Laser Doppler techniques rely on the detection of the Doppler shift of red or infrared light backscattered by moving erythrocytes for the estimation of the average blood flow in small tissue volumes[2,4,5]. Within these methods, laser Doppler flowmetry (LDF) is used for the continuous monitoring of microvascular perfusion through single-point laser probes in direct contact with the skin[5]. An advantage of LDF is the high temporal data acquisition that allows studying the nonlinear fluctuations of blood flow[6]. This can be achieved by applying the continuous wavelet transform (CWT) spectral analysis on LDF time series[7,8], which reveals indirectly the activity of specific biological factors in the microcirculation, e.g. endothelial cells (ECs), vascular smooth muscle cells (VSMCs) and the local sympathetic innervation. However, relevant limitations of laser Doppler and LSCI are the impossibility to visualize blood vessels and the expression of data in arbitrary units making it possible only relative assumptions based on the combination of perfusion measurements with reactive tests[4,5,6]. An example of a widely used reactive test for the examination of human cutaneous microcirculation is the post-occlusive reactive hyperaemia (PORH), which evaluates the increase in blood perfusion from the forearm or fingertips after a temporary period of ischaemia stimulated by artificial occlusion of the brachial artery[5,6].

1.2 Techniques for the examination of cutaneous microvascular structure

Skin microvascular structure can be visualized *in-vivo* by several methods based on optical microscopy, 3D photoacoustic imaging or optical coherence tomography (OCT). A common relevant limitation of the optical microscopy techniques is the generation of 2D images with uncertain depth resolution[9,10]. 3D photoacoustic imaging is based on the generation of pressure acoustic waves in all the directions employing a pulsed laser light absorbed by chromophores in the skin that act as contrast agents to visualize micro-vessels[11,12]. The main benefit of photoacoustic imaging is the full light penetration depth[13]. However, the method suffers from poor spatial resolution, even though this aspect has been improved by implementing the optical resolution photoacoustic microscopy (OR-PAM)[9]. Moreover, the method requires a coupling medium in direct contact with the tissue, which is a drawback for several applications, i.e. image-guided brain surgery[14,15], wounds/burns assessment[16] and ophthalmology[14,15]. This might also be a limitation to assess the activity of skin micro-vessels, which is sensitive to the local cutaneous temperature[17] and may be affected by the temperature of the coupling medium. However, the recent implementation of contact-free PAM[18,19,20] is promising to overcome this shortcoming. Additionally, some limits of photoacoustic imaging have been solved with the further implementation of OCT method to allow micro-vessels imaging. OCT is a non-invasive contactless technology employing a broadband near infrared light source to provide a low coherence gate for the selection of backscattered light from different tissue depths, producing *in-vivo* 2D and 3D structural images[21]. The main advantage of OCT is the generation of cross-sectional images comparable to conventional optical biopsies with micrometer-level structural resolution[22,23]. However, the technique is limited by low penetration depth (~1-2 mm)[24].

1.3 Concurrent evaluation of microvascular structure and function

Although the visualization of microvascular structure is powerful for the detection of specific organisational patterns or damage to the microvasculature that may be associated with CVD, laser Doppler and LSCI are still the preferential choice for the examination of skin microvascular function. The reason is that functional abnormalities in the microcirculation precede structural changes and clinical manifestations, thus representing a hallmark of the early stages of the pathology suitable for the preclinical prediction of CVD risk[1,2]. However, laser Doppler and LSCI are limited by both ambiguous spatial and depth resolution. Therefore, the ideal tool for a complete assessment of the microcirculation would be a technology providing simultaneous functional and structural information. Extensions of OCT utilize the Doppler shift (DOCT)[25] and the speckle variance (svOCT)[26] principles for providing a contrast mechanism to visualize blood flow, or processing techniques relying on the separation of static areas and flow dynamic regions of the tissue, i.e. Doppler optical microangiography (DOMAG)[27]. The combination of OMAG with the PORH reactive test has been described previously as an optimal method for providing quantitative functional data of the human peripheral skin microcirculation[28].

Another technique for the *in-vivo* imaging of the microcirculation is correlation mapping OCT (cmOCT). This method employs correlation coefficient statistics to determine blood flow from the intensity of the reflected OCT signal[9,10], taking advantage of the time-varying speckle of moving scatters in skin regions containing active blood vessels and the constant reflectance of the stationary scatters in the bulk tissue lacking of blood vessels[9,10]. Therefore, the correlation map obtained from the cross-correlation analysis is able to visualize the location of blood flow[9,11]. The advantages of cmOCT compared to DOCT, svOCT and DOMAG respectively are the apparent angle independence of the technique[10], non-requirement of previous

knowledge of the structure to determine flow regions, and very fast data processing to obtain the flow maps[9]. However, cmOCT is limited by high decorrelation caused by noisy background regions in the images, which can be misinterpreted as blood flow signal. This necessitates the use of a binary mask to suppress these regions[9] leading to reduced quality images compared to those generated with OMAG or svOCT techniques.

1.4 Aims of the study

The objectives of this research were providing evidence on the potential application of cmOCT for assessing microvascular function, and demonstrating for the first time that OCTA techniques are suitable to monitor vasomotion and the activity of specific biological factors of the microcirculation. This was achieved by generating sequential cmOCT blood flow maps from the human forearm at different cutaneous depths during a 25 min PORH reactive test, and applying the CWT spectral analysis on continuous blood flow signals reconstructed from cmOCT maps.

The results displayed that cmOCT is able to detect functional flow dynamics and vasomotion oscillatory patterns reflecting the activity of the microvascular endothelium and local sympathetic innervation. Our results demonstrate that the study of microvascular function by OCTA techniques is not restricted only to the general observation of flow dynamics but can be extended for gaining information on the behaviour of specific biological components in the microcirculation network.

2. METHODS

2.1 Study population

The experiments were performed on 8 women and 4 men with an average age of 33 ± 10 years old, which signed an informed consent form according to the rules of the Declaration of Helsinki. The measurements were collected in the morning time in a laboratory with a constant temperature (20 ± 1 °C), allowing at least 15-20 min of acclimatisation of the subjects. The volunteers were asked to observe a fasting period of 4-6 hours prior to the examination to avoid physiological differences related to nutritional habits. The measurements were performed from the left volar forearm maintained at heart level, while the volunteer was laying in supine position in a clinical bed. A custom-built soft support was used to fix the arm, ensuring a static and comfortable position during the test to avoid bias in the experimental data due to movement artefacts (Fig. 1). The skin site for the measurements was chosen while avoiding hairy and injured regions. A pressure cuff was placed in the upper part of the left arm for performing the PORH test during the acquisition period of the images. The occlusion of the brachial artery to stimulate PORH response was induced by inflating the pressure cuff at 200 mmHg.

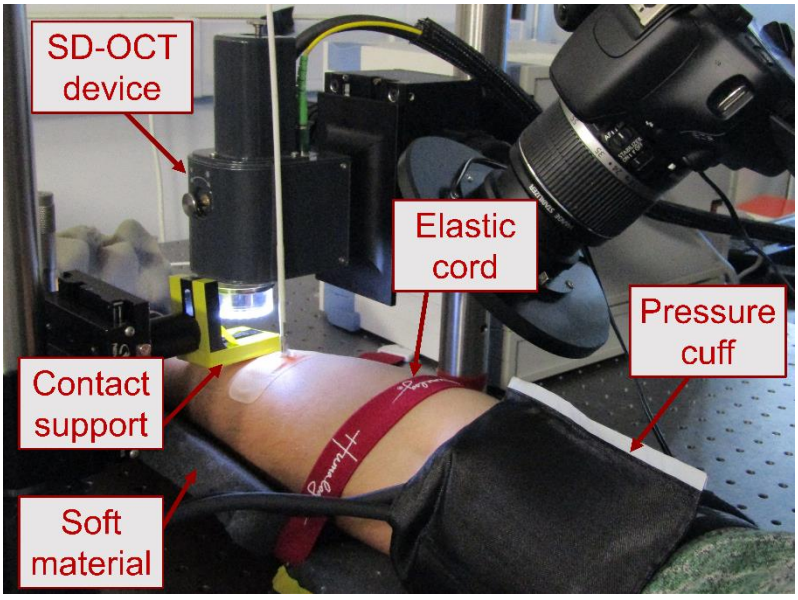

Fig. 1 Experimental setup. A custom-built mount was used to immobilize the arm as much as possible during testing. A contact support was applied in the skin surface with gentle pressure to stabilize the scan location between data sets avoiding mismatches. The OCT probe was placed above the contact support to collect data from the chosen region. The image shows also additional equipment (a LDF optical probe and a camera) that is not relevant for the research presented in this work.

2.2 OCT device for images acquisition

A commercial OCT system (TEL2200C1, Thorlabs Inc., USA) was used for imaging 3D volumes of the cutaneous tissue. This spectral domain (SD) device consists of a superluminescent diode (SLD) with a center wavelength of 1300 nm, which supports an imaging depth up to 3.5 mm (in non-scattering samples), an axial scan rate from 5.5 to 76 kHz, and an axial resolution of 5.5 µm in air. The sample arm contains a LSM003 (Thorlabs Inc., USA) scanning lens providing a transverse resolution of 13 µm in air. Fig. 1 displays the experimental setup employed to collect OCT data. For each volunteer tested in the study, an initial 3D volume of 1.50 × 1.50 × 1.82 mm^3 was acquired at a speed of 48 kHz with a scanning density of 1024 (length) × 1024 (width) × 512 (depth) pixels, to visualize the microvascular structure of the volar forearm. The time employed for the acquisition of the structural volume was ~51 s, which is too long for the assessment of blood flow functional dynamics. For this reason, the examination of microvascular dynamics was performed by reducing the sampling density to 256 × 256 × 512 pixels that can be acquired at a temporal rate of ~6 s, allowing the fast scanning of sequential 3D volumes suitable for the assessment of microvascular function. However, an important requirement for visualizing blood flow by cmOCT is a dense sampling below the lateral resolution of the adjacent B-frames of the OCT volume, which ensures a strong correlation between the stationary scatters of consecutives B-scans. Therefore, to maintain a spatial separation between the B-frames suitable for the cmOCT analysis the size of the sampled area was reduced to 0.75 × 0.75 × 1.82 mm^3, which means a spatial separation of 2.9 µm. Although the possibility of performing each scan in ~6 s, the volumes were acquired with a sampling frequency of one volume every 16.6 s because the software provided with the OCT device (ThorImage OCT 4.3, Thorlabs Inc., USA) required ~10.6 s for saving each volume. In total, 90 sequential low-resolution volumes were acquired from the forearm of each volunteer in a time window of ~25 min, while performing the PORH reactive test. An initial 10 min acquisition of 36 volumes was performed to determine the baseline flow, then 18 volumes were recorded for a 5 min ischaemia period stimulated by blocking blood flow through the brachial artery, and finally 36 volumes were acquired for further 10 min to monitor flow dynamic changes during the hyperaemic response.

2.3 cmOCT data processing

The cmOCT analysis to generate blood flow maps at different depths from each 3D OCT volume was performed by employing the same in-house designed Java algorithm and principles described by Enfield *et al.*[9] and Jonathan *et al.*[10]. The software is able to perform the correlation analysis between consecutive adjacent 2D B-scans extracted from the 3D OCT volume, by estimating the cross-correlation of a square grid from the first B-scan 1 (I_1) to the same grid from the adjacent B-scan 2 (I_2), according to the following formula,

$$cmOCT(x,y) = \sum_{p=0}^{M} \sum_{q=0}^{N} \frac{\left[I_1(x+p,y+q)-\overline{I_1(x,y)}\right]\left[I_2(x+p,y+q)-\overline{I_2(x,y)}\right]}{\sqrt{\left(I_1(x+p,y+q)-\overline{I_1(x,y)}\right)^2\left(I_2(x+p,y+q)-\overline{I_2(x,y)}\right)^2}} \quad (1)$$

where M and N represent the size of the square grid, and $\bar{I}$ the average intensity value of the grid. The grid is shifted along all the pixels of the B-scans to produce a two-dimensional map with correlation coefficients between 0 and 1, associated respectively with low and high correlation. The low correlation areas (coefficient < 0.6) in the map are shown as bright coloured regions representing blood flow, while the strong correlation sections (coefficient > 0.6) related to the stationary bulk of the tissue appear as the background of the image.

A 7 × 7 kernel size of the grid was employed to generate the correlation maps, which represents an optimal compromise of producing good sensitivity to blood flow without loss of spatial resolution due to kernal size. As mentioned in the introduction, the cmOCT maps are affected by a background noise with low correlation coefficients between consecutive B-scans that makes the identification of the flow regions difficult. The noise was removed by processing the correlation maps with a structural mask, produced from the original OCT structural images by the application of a kernel blur and binary threshold. The maps were presented as maximum intensity projection (MIP) images, which allow at the same time a better visualization of micro-vessels morphology and location, and the detection of the maximum flow intensity. To examine blood vessels from different skin microvascular beds (capillaries and arterioles/venules), the cmOCT maps were extracted from different depths (80-180 µm, 180-280 µm, 300-400 µm) of the OCT volumes, i.e. in the *enface* plane. This was obtained by determining the position of skin surface from the structural images, and using the superficial location as a reference to establish the various depths of the underlying tissue.

2.4 Reconstruction of blood flow time series

The CWT spectral analysis for the study of vasomotion can be applied exclusively on continuous time-varying signals. Therefore, to investigate the nonlinear dynamics by wavelet analysis, continuous time series of microvascular blood flow at different tissue depths were reconstructed from the cmOCT maps using the same methodology previously described by our group[29]. First, the average blood flow was estimated from each of the 90 sequential MIP maps generated at different tissue depths during the reactive hyperaemia test. This was achieved by calculating the mean value across the ROI of each map. Then, the mean values of flow extracted from the sequential MIP maps were employed as discrete data points to reconstruct a continuous curve, covering the 25 min time window used in the experiment. The reconstruction was performed by piecewise cubic spline interpolation[29] method using the *cftool* instrument in Matlab R2015a. Specifically, we have created a vector containing the 90 sequential average values of blood flow extracted from the cmOCT maps, and a time vector defining an interval of 16.6 s between each pair of discrete data points corresponding to the sampling frequency adopted during the temporal acquisition of the 3D OCT volumes. More details on the principles of spline interpolation can be found in our previous publication[29].

2.5 CWT spectral analysis

The continuous wavelet transform is a widespread method for the investigation of blood flow fluctuations, revealing the contribution of specific biological components in the microcirculation to the nonlinear dynamic changes of microvascular flow. In this work, the application of CWT on blood flow signals reconstructed from the cmOCT maps allowed the identification of oscillations in the frequency intervals 21-52 × 10^{-3} Hz, 9.5-21 × 10^{-3} Hz and 5-9.5 × 10^{-3} Hz. According to the literature[8,30], these oscillations reflect respectively the activity of local sympathetic nerves, the ECs activity nitric oxide (NO)-dependent and the ECs activity NO-independent.

The CWT analysis was performed according to the principles described by Stefanovska *et al.*[7,8,30]. The method is based on the use of the Morlet mother wavelet function ψ scaled by a factor s and a time t to provide an adequate frequency window, which is shifted along the time domain of the analysed signal for obtaining an optimal time-frequency resolution[7,8,30]. The CWT spectrum of a signal $g(u)$ is calculated as follow[7,8,30],

$$g(s,t) = \frac{1}{\sqrt{s}} \int_{-\infty}^{\infty} \psi \left(\frac{u-t}{s}\right) g(u) du, \tag{2}$$

where $g(s, t)$ is the wavelet spectral function defined by s and t. The obtained spectrum is characterized by a power/energy distributed at various frequencies, which is a measure of how much of the signal is located at a specific frequency range of an oscillator at the time t.

In this work, a central frequency f of the Morlet wavelet equal to 1 was used[30], noting that the scale parameter s and f were related according to the following equation[30], $s=1/f$. Specifically, a logarithmic scale array of 346 scales ranging from 0.5 to 200 with Morlet factor 1.03 was used, which corresponds to a frequency interval between 5-2000 × 10^{-3} Hz. The minimum size of the time window used in the study was ~200 s to allow the investigation of the slowest oscillations of interest (frequencies up to 5 × 10^{-3} Hz). A time scale of minutes is sufficient to detect oscillatory phenomena with a period of 200 s. However, while for periodic signals a single period is sufficient to observe the phenomenon under investigation, this is not true for nonlinear quasiperiodic time series, i.e. blood flow signals[8]. In this case the period of a specific phenomenon fluctuates constantly, thus the trace should be long enough to contain at least several periods[8]. For this reason, here a 25 min time window was used for data collection to sample a sufficient number of periods for observing oscillations up to 5 × 10^{-3} Hz.

3. RESULTS

3.1 Visualization of microvascular structure

To select the cutaneous areas for the study of functional dynamics, an initial 3D OCT volume was acquired from a 1.50 × 1.50 × 1.82 mm^3 region in the volar forearm of each volunteer to visualize microvascular structure. The acquisition was performed in ~51 s employing 1024 × 1024 A-scans, and the MIP flow maps were obtained at different tissue depths by cmOCT data processing using a 7 × 7 kernel grid. Fig. 2 shows examples of structural *enface* MIPs at three different depths obtained from a volunteer, describing the typical skin microvascular structure reported by Enfield *et al.*[9], even if in this case the size of the analysed region was smaller.

Fig. 2a displays a structural 2D B-scan of the OCT volume, showing a longitudinal view of the tissue regions from which the MIPs were generated. The depths were selected by using the skin surface, marked with a green line, as a reference for the estimation of the specific microvascular beds. Fig. 2b illustrates the MIP map from the epidermal surface at 0-40 μm that, as expected, does not show any flow region due to

the absence of blood vessels. Fig. 2c displays the MIP generated from the dermal-epidermal junction, which is located around a depth of 80-180 µm. The image shows small blood vessels with vertical orientation corresponding to the finger-like capillary loops arising from the ascending micro-vessels of the dermal layer and appearing as coloured spots in the blue background. The function of the capillary loops is the nourishment of the epidermal layer that is lacking of blood vessels. Fig. 2d represents a MIP projection of the skin layer around 300-400 µm corresponding to the dermal plexus. This microvascular bed is characterized by a network of arterioles and venules with horizontal orientation from which, respectively, the nutrients are delivered to the capillaries and the waste products directed to the venous system. To study the microvascular dynamics from the dermal-epidermal junction and dermal plexus regions, an *enface* plane of 0.75 × 0.75 mm^2 was selected from the structural images to perform sequential temporal acquisitions of 3D OCT volumes during PORH test. Fig. 2c-d show examples of 750 × 750 µm regions selected for the study of capillary loops and arterioles/venules functional dynamics, respectively marked by yellow and red squares.

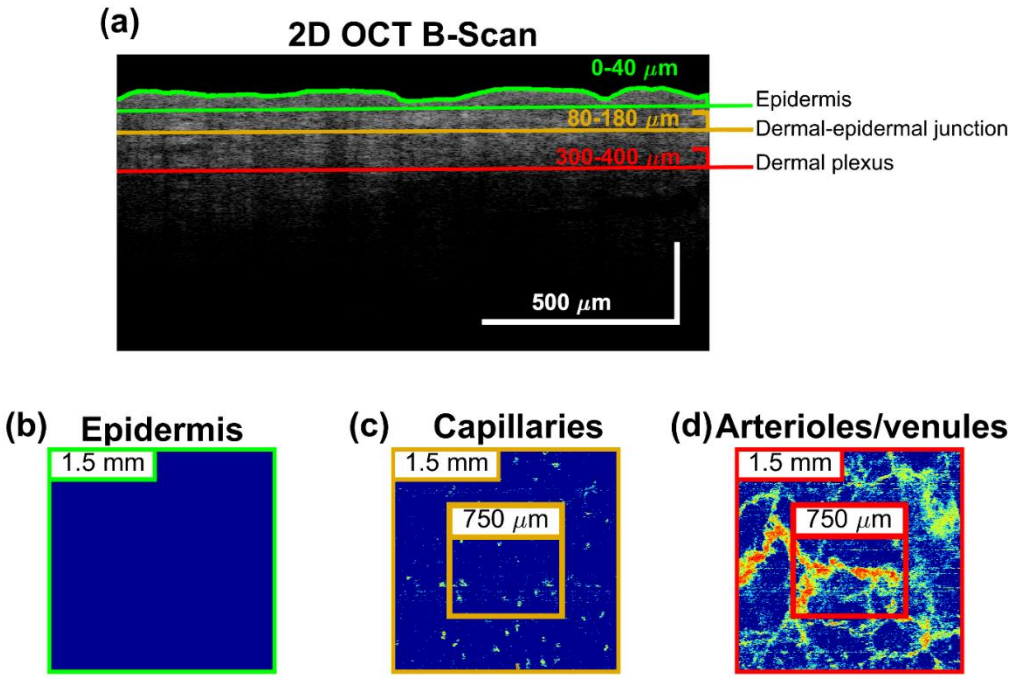

Fig. 2 Structural visualization of cutaneous micro-vessels from the volar forearm. (a) 2D structural B-frame from a 1.50 × 1.50 × 1.82 mm^3 3D OCT volume. The region marked in green indicates the epidermal surface (0-40 µm), the yellow area represents roughly the location of the dermal-epidermal junction (80-180 µm) and the red region outlines a part of the dermal plexus (300-400 µm). **(b)** *Enface* MIP projection of the epidermal surface at 0-40 µm. **(c)** *Enface* MIP projection of the dermal-epidermal junction around 80-180 µm where the capillary loops are located. The small yellow square indicates the 750 × 750 µm area chosen for the study of capillaries functional dynamics. **(d)** *Enface* MIP projection of the dermal plexus at a depth of 300-400 µm characterized by a horizontal network of micro-vessels. The small red square outlines the 750 × 750 µm region chosen for the study of arterioles/venules functional dynamics.

3.2 Assessment of flow dynamics from cmOCT maps

Ninety sequential volumes (256 × 256 × 512 pixels, 0.75 × 0.75 × 1.82 mm^3) of the small yellow/red area selected in Fig. 2c-d were acquired from each volunteer during a 25 min PORH functional test at a sampling rate of 16.6 s. The first 36 volumes were acquired during a 10 min resting period to determine the baseline flow, 18 volumes were collected during a 5 min occlusion of blood flow through the brachial artery, and 36 volumes were acquired for 10 min after the removal of the occlusion for monitoring blood flow changes during PORH response. The volumes were processed by cmOCT to obtain sequential flow maps of the dermal-epidermal junction (80-180 µm) and dermal plexus (300-400 µm) regions for tracking the temporal flow changes of capillaries (Fig. 3a) and arterioles/venules (Fig. 3b), respectively.

For simplicity, in Fig. 3a-b are displayed only the cmOCT maps extracted from 12 volumes of the total 90 temporal samples, which represent the key steps of the reactive test. The maps were characterised by residual background noise represented by small snow-like dots (see the ISCHAEMIA MIPs in Fig. 3a-b), which may be confused and misinterpreted as capillary blood flow at the 80-180 µm depth. Nonetheless, the relevant increase of flow observed in specific points of the MIP maps at 80-180 µm during PORH response (Fig. 3a, PORH 1-4) was helpful to identify the specific regions of the images containing the capillaries.

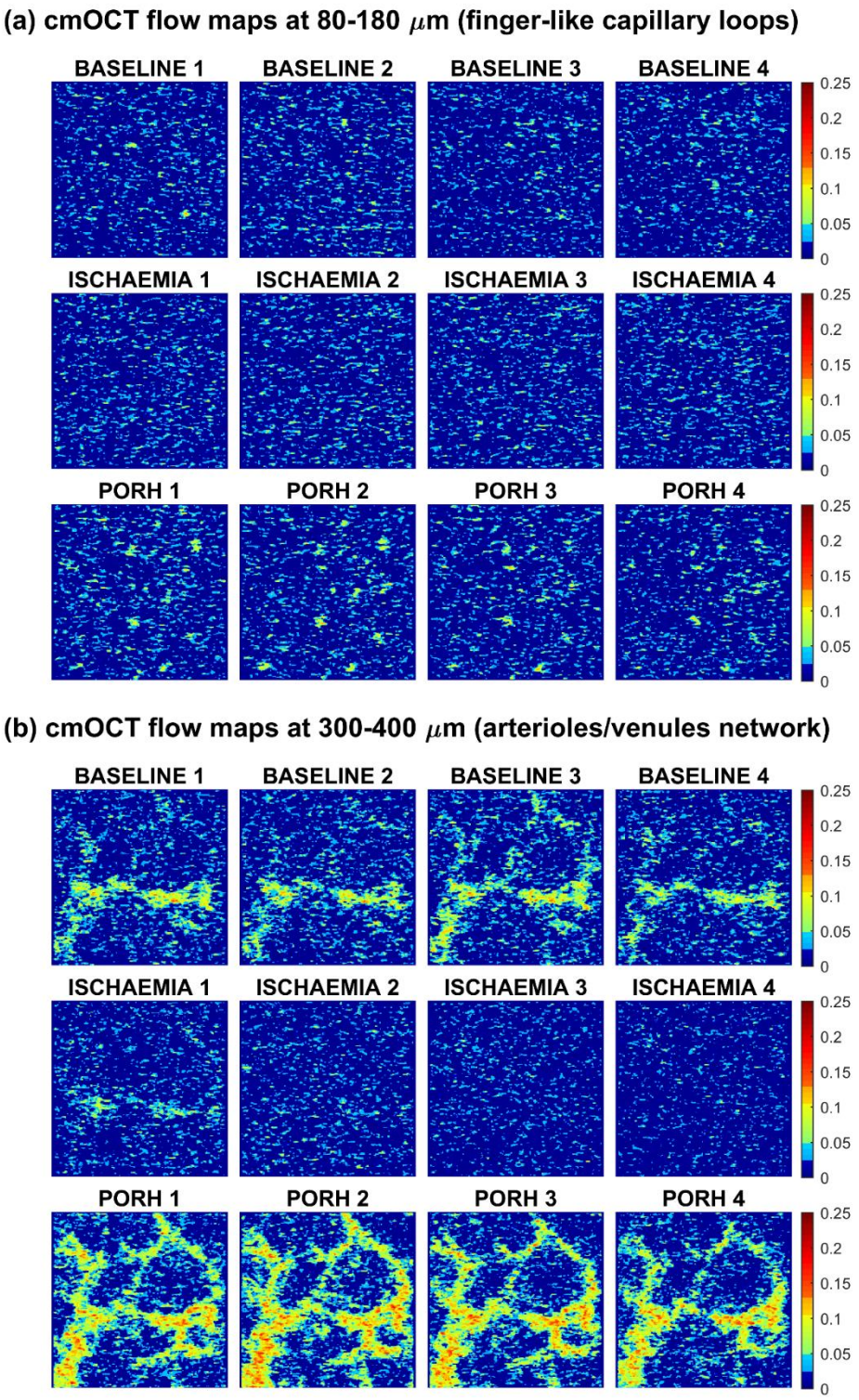

Fig. 3 Sequential cmOCT flow maps generated at different tissue depths from the OCT volumes acquired during PORH test. (a) Temporal *enface* MIPs from the 750 × 750 µm yellow area selected in Fig. 2c for the study of skin capillaries microvascular dynamics at a depth of 80-180 µm. **(b)** Temporal *enface* MIPs from the 750 × 750 µm red area selected in Fig. 2d for the study of cutaneous arterioles/venules microvascular dynamics at a depth of 300-400 µm. The maps were obtained from 0.75 × 0.75 × 1.82 mm^3 volumes sampled every 16.6 s with a scanning density of 256 × 256 A-scans. The BASELINE 1-4 MIPs describe the flow at rest detected prior to the occlusion stage of the PORH functional test, the ISCHAEMIA 1-2 and 3-4 MIPs refer respectively to the flow detected immediately after the beginning of the occlusion process and before the removal of the occlusion, and the PORH 1-4 MIPs outline the flow detected during PORH response. The images contain residual background noise, which is clearly visible in the ISCHAEMIA MIPs at both 80-180 µm and 300-400 µm cutaneous depths.

Additionally, because all the MIPs were characterised by the same degree of background noise at all the stages of the reactive test, this made it possible monitoring reliably the relative dynamic changes of blood flow over time. Indeed, although the images were characterized by poor resolution and residual background noise compared to the structural images, they clearly outlined the temporal flow changes associated with the different stages of the functional task. In details, the capillaries did not show relevant changes during occlusion (Fig. 3a, ISCHAEMIA 1-4) compared to baseline (Fig. 3a, BASELINE 1-4), while the network of blood vessels in the dermal plexus displayed a clear reduction and disappearance of blood flow during occlusion (Fig. 3b, ISCHAEMIA 1-4) compared to baseline (Fig. 3b, BASELINE 1-4). These observations probably reflect the delivery of the residual flow from arterioles to capillaries during the 5 min ischaemia period, ensuring the nourishment of the epidermal tissue under hypoxic stress conditions. In contrast, a massive increase of flow intensity typical of the hyperaemic response was detected during PORH for both capillaries and arterioles/venules (Fig. 3a-b, PORH 1-4), associated with the vessels reactivity for the restoration of a normal microcirculation after removal of the occlusion. These results demonstrate that cmOCT is suitable for tracking the general microvascular functional dynamics.

3.3 Reconstruction of time series from cmOCT maps

In this study, the cmOCT flow maps were also employed to detect the key contribution of biological components in the microcirculation to the rhythmic variations in vessels diameter (vasomotion) in response to PORH stimulus. The goal was achieved by reconstructing continuous time series of blood flow at different depths from the intensities of the sequential temporal cmOCT maps (see paragraph 2.4 in methods for more details), and processing the reconstructed signals with the CWT spectral analysis that is a widespread method for the study of microvascular oscillations. Fig. 4a displays an example of continuous time series obtained by using the average flow extracted from 90 sequential cmOCT MIP maps as discrete data points for the reconstruction of a curve covering the 25 min period of the PORH test. The method employed for the reconstruction process was the piecewise cubic spline interpolation that is advantageous because no oscillation artefacts are introduced between each pair of discrete data points. This means that the obtained time series reflects the real dynamics of the process under investigation. The reconstructed curve in Fig. 4a clearly shows the typical trend of the reactive hyperaemia test, characterized by a reduction of blood flow during ischaemia and a massive increase of flow during PORH response reaching a peak before the gradual restoration of the normal microcirculation. This is a further confirmation that cmOCT is able to detect microvascular functional dynamics.

For each volunteer enrolled in the study, the microvascular flow was reconstructed from cmOCT maps generated at three different depths: 80-180 µm (dermal-epidermal junction), 180-280 µm (upper dermal plexus), and 300-400 µm (median dermal plexus). Fig. 4b-c display respectively the absolute and relative average reconstructed blood flow at the selected depths for the 12 tested individuals. As shown in Fig. 4b, the absolute flow reflects the increasing density of blood vessels in the deepest layers of the cutaneous tissue. Indeed, the absolute flow intensity was greater in the deepest microvascular beds at all the stages of PORH test. The relative average blood flow in Fig. 4c, expressed as a function of the baseline, provides a more reliable comparison of flow dynamics from different tissue depths in response to the reactive test. The graph shows the same findings discussed for Fig. 3a-b, consistent with the maintenance of a normal flow in the capillaries and a gradual reduction of the flow intensity going deeper in the tissue during ischaemia. This may reflect the delivery of the residual flow from the deeper arterioles network to the upper capillaries for feeding the epidermis during ischaemia. In contrast, PORH response was characterized by higher flow intensity and peak response in the deepest vascular beds, reflecting the path of flow directed from the deepest network of arterioles to the superficial capillaries and a major vasodilator response in the deepest layers associated with greater size and density of micro-vessels.

3.4 CWT spectral analysis of the flow signal reconstructed from cmOCT maps

The study of vasomotion at different tissue depths was performed applying the CWT spectral analysis on the reconstructed time series. The method allowed the identification of oscillations in the frequency ranges 21-52 × 10^{-3} Hz (neurogenic), 9.5-21 × 10^{-3} Hz (endothelial NO-dependent) and 5-9.5 × 10^{-3} Hz (endothelial NO-independent)[8,30]. Fig. 5 illustrates an example of CWT analysis of the blood flow signal reconstructed from a tissue depth of 180-280 µm. Fig. 5a displays the CWT scalogram graph that describes the distribution of the wavelet power of the signal in the time-frequency domain, visualized as a gradient coloured map. The graph clearly shows an increase of power (increase of brightness) during PORH response in all the oscillatory frequency ranges under investigation, reflecting the activation of the endothelial and sympathetic control mechanisms associated with vasodilation. The time-averaged spectrum in Fig. 5b discriminates the maximum wavelet power peaks at various frequency intervals corresponding to the specific blood flow oscillators. This allows monitoring the activity of each oscillator and making comparisons between different subjects, by extracting values of the maximum amplitude A_i and energy E_i (area under the curve) from each wavelet peak during the various steps of the reactive test. For instance, in

Fig. 5b an increase of the wavelet maximum amplitude and power of all the oscillators was clearly observed during PORH (black line) compared to ischaemia (dark red line) and baseline (dark blue line).

Fig. 6 displays the median time-averaged CWT spectra obtained from the 12 healthy volunteers, by wavelet analysis of the cutaneous flow signals reconstructed at 80-180 µm (yellow line), 180-280 µm (blue line) and 300-400 µm (red line) tissue depths. The CWT spectral power was normalized as a function of the minimum baseline power, to compare the relative spectral energy between different cutaneous depths during PORH test. All the wavelet oscillators showed greater power with increasing depth at all the stages of the reactive hyperaemia task (Fig. 6a-c): baseline, ischaemia, and PORH. These observations may be explained by a major number of micro-vessels involved in vasomotion in the deepest cutaneous layers due to greater vessels density.

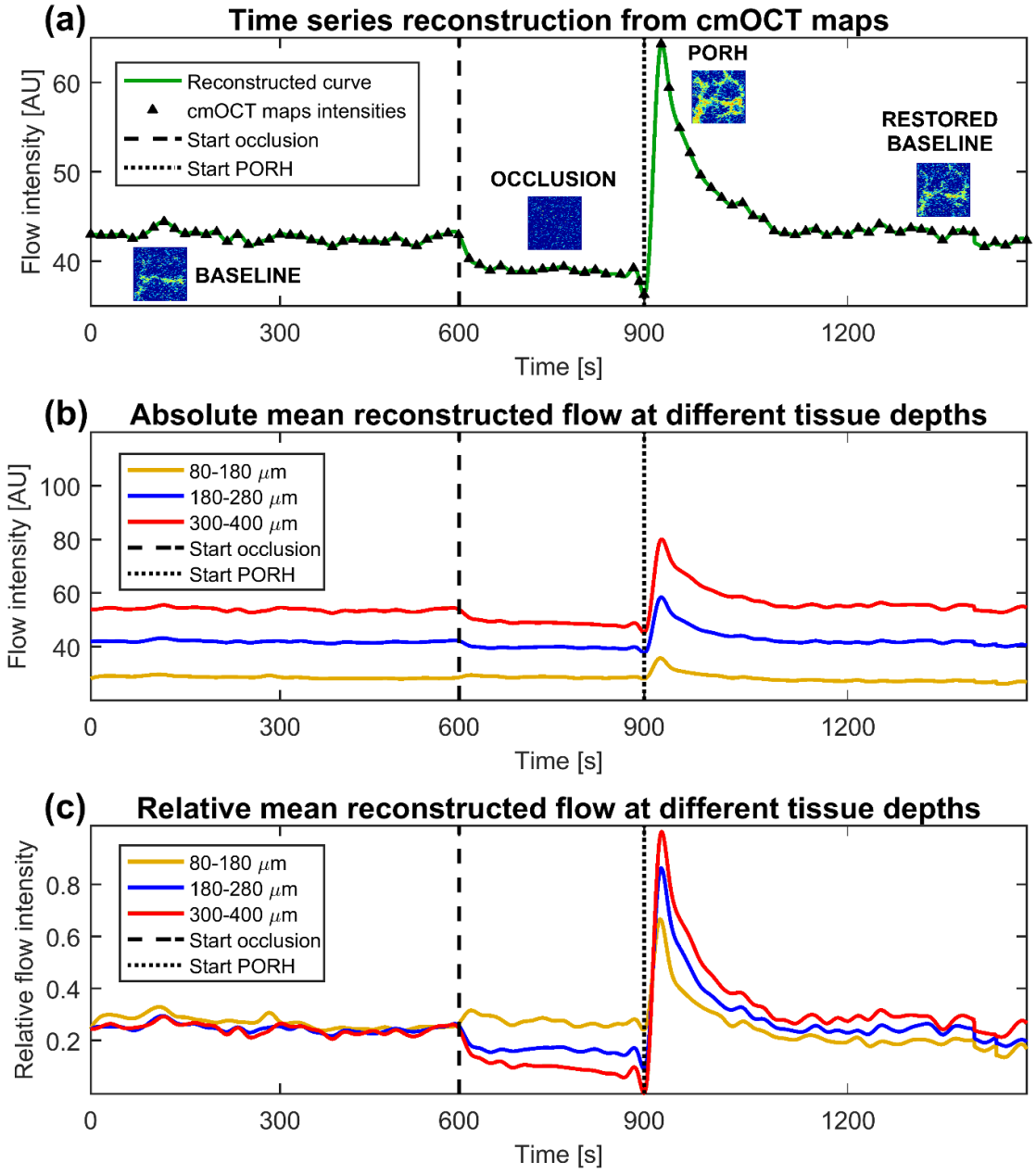

Fig. 4 Reconstruction of continuous time series from cmOCT maps. (a) Example of curve reconstruction by piecewise cubic spline interpolation of the discrete average flow values estimated from the ROI of the 90 sequential cmOCT MIP maps generated at a tissue depth of 300-400 µm. A time interval of 16.6 s between each pair of data points was applied to cover the 25 min period of the PORH test. The flow is expressed in arbitrary units (AU). **(b)** Average absolute blood flow from 12 healthy subjects during reactive hyperaemia test reconstructed at three different tissue depths. The flow is expressed in AU. **(c)** Average relative blood flow from 12 healthy volunteers during PORH test reconstructed at three different depths. The flow is expressed as a function of baseline.

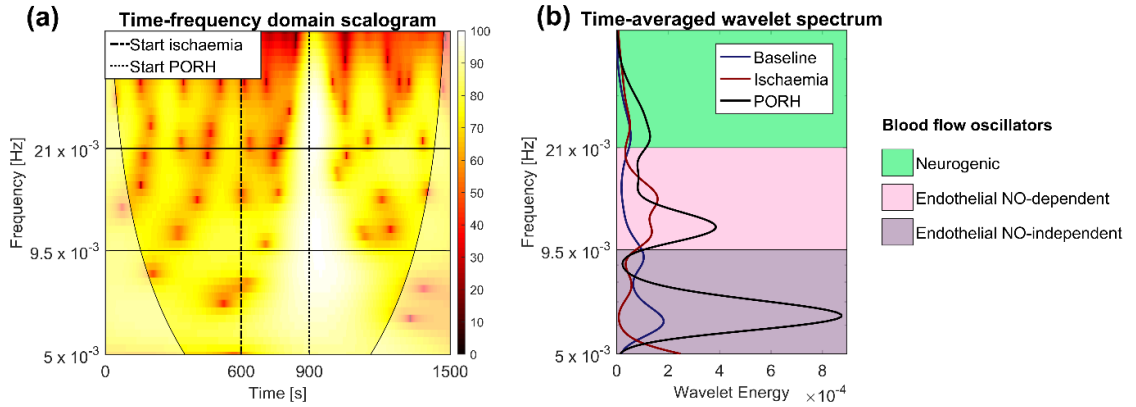

Fig. 5 CWT analysis of a continuous blood flow signal reconstructed from cmOCT maps generated at a depth of 180-280 µm. (a) CWT scalogram showing the distribution of the wavelet power in the time-frequency domain using a coloured map ranging from dark (low energy) to bright (high energy) colours. The coloured areas in the scalogram outline the "cone of influence", which is a time-frequency area where distortions of the CWT due to the limited duration of the time series are not relevant[31]. In contrast, the transparent areas at the bottom-right and bottom-left of the graph represent regions external to the cone in proximity of the time edges of the signal, where the wavelet transform is characterized by boundary effects making the estimations from these regions ambiguous[31]. **(b)** Time-averaged wavelet spectra computed for all the stages of the reactive hyperaemia test. The plots distinguish the CWT maximal amplitude peak and energy (area under the curve of the peak) associated with each specific blood flow oscillator. The neurogenic (21-52 × 10^{-3} Hz), ECs NO-dependent (9.5-21 × 10^{-3} Hz), and ECs NO-independent (5-9.5 × 10^{-3} Hz) oscillators were identified.

The wavelet energy E_i and amplitude A_i of all the oscillators, extracted from the time-averaged CWT spectra according to the principles described by Shiogai *et al.*[8], were significanty increased during PORH response compared to baseline for all the analysed tissue dephts (Table 1), which is in agreement with the results reported for the spectral analysis of LDF signals recorded during the hyperaemic challenge[32].

Although OCTA methods are flow-based imaging tools not suitable to monitor the architecture of blood vessels, the increase of blood perfusion observed in this study during PORH response should reflect vasodilation dynamics. Indeed, literature reports have demonstrated that the increase of flow observed during cutaneous PORH is mediated by the activation of vasodilator mechanisms regulated through the major activity of the endothelium and the sympathetic nerves[5]. This is also supported by the results of the wavelet spectral analysis of cmOCT blood flow signals discussed in Table 1. The wavelet analysis is a method suitable for the indirect detection of vasomotion dynamics by its application on blood flow signals that do not contain architectural information, i.e. LDF signal[7,8,30]. Therefore, the increase of wavelet spectral power observed for the endothelial and neurogenic oscillators should reflect indirectly the rythmic vaso-relaxation process mediated by ECs, VSMCs and sympathetic nerves for the fast reperfusion of the tissue after an ischaemic period. Damages to the microvascular endothelium may impact negatively the hyperaemic response with a reduction of the endothelial-mediated vasodilation, which can be reflected in the wavelet spectrum as a reduced increase of the endothelial wavelet power.

Mechanisms at the basis of the vasomotor perturbations of skin blood flow signal. The endothelial and neurogenic oscillators and the myogenic oscillation, which was not detected in this study, are classified as low-frequency dynamic patterns of flow motion associated with local vasomotor phenomena occurring on the time scale of blood distribution to the tissue surrounding micro-vessels[8,33]. These slow vasomotor rhythms cause changes in the vascular diameter as part of the local regulation of microvascular flow, and they are reflected in the blood flow signal as naturally occurring perturbations representing a correlation of volumetric flow to a third-order blood pressure wave[33]. The vasoconstriction or vasodilation induced by these regulatory rhythms has an effect on red blood cells (RBCs) velocity with a consequent decrease or increase of velocity leading to lower or higher blood perfusion to tissue[34], respectively. These oscillatory phenomena have been detected also on capillary blood flow, as confirmed by our results (Fig. 6), probably reflecting the degree of vasomotion in the terminal arterioles connected to the capillary loops[34].
The mechanism at the basis of the vasomotor perturbations of blood flow signal is the mechanical contraction or relaxation of VSMCs, due respectively to depolarization or hyperpolarization induced by cellular rhythmic fluctuations of Ca^{2+} concentrations throughout voltage-dependent channels in the plasma membrane and sarcoplasmic reticulum[35,36]. This process may be modulated through different regulatory mechanisms (Fig. 7), which are characterised by a different oscillatory rhythm reflected by the low-frequency vasomotor waves detected in the blood flow signal:

(1) *Myogenic mechanism* (52-145 × 10^{-3} Hz), based on spontaneous contraction/relaxation of VSMCs in response to changes of the intra-arteriolar blood pressure[8,34,35].
(2) *Neurogenic mechanism* (21-52 × 10^{-3} Hz), based on a feedback between VSMCs and the local sympathetic or parasympathetic innervation[34]. The nerves are activated by changes in the intravascular pressure and/or tissue perfusion[34], which cause the release of substances targeting VSMCs to regulate the vascular diameter[8].
(3) *Endothelial mechanisms* (5-21 × 10^{-3} Hz), based on a feedback between VSMCs and ECs[8,34]. The activity of ECs may be stimulated by the concentration of metabolic mediators in the blood or by the shear stress[8,37], which cause the release of vasoactive substances modulating the relaxation/contraction of VSMCs.

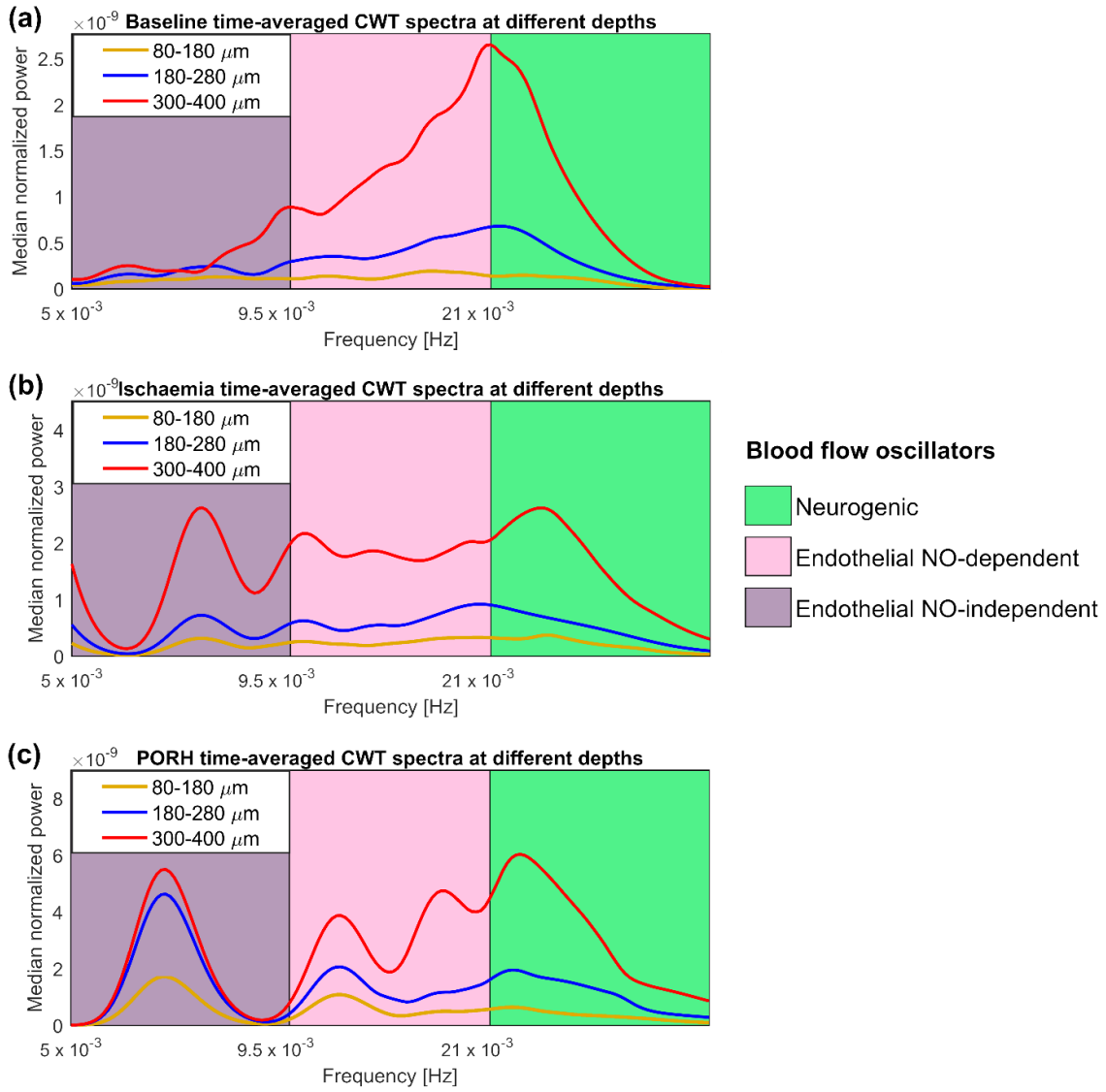

Fig. 6 Median relative time-averaged CWT spectra of reconstructed flow signals from 12 healthy subjects during PORH test. (a) Baseline median CWT spectra of blood flow time series reconstructed from cmOCT maps generated at 80-180 µm, 180-280 µm and 300-400 µm. **(b)** Median CWT spectra during ischaemia. **(c)** Median CWT spectra during PORH response. All the spectra were normalized by the respective minimum baseline spectral power to compare the relative increase of wavelet energy during the hyperaemic response between different cutaneous depths.

Physiological origin of the endothelial NO-independent oscillator. Table 2 reports the percentage relative increase of the wavelet power for each oscillator analysed in this study. The endothelial NO-independent oscillator showed the greatest percentage increase of energy at all depths, suggesting a fundamental role of this component in the vasomotion phenomenon associated with cutaneous hyperaemic response. The origin of this oscillator is uncertain because the endothelial NO-independent modulation may be mediated by different mechanisms such as the endothelial-derived hyperpolarizing factor (EDHF) or prostaglandins (PGs) cellular pathways (Fig. 7). However, the inhibition of PGs mechanism by aspirin did not alter the

oscillatory peak in the endothelial NO-independent range[38], suggesting a more likely EDHF origin of this oscillator. Moreover, spectral LDF data obtained at our laboratories from animal models and human subjects, which will be published elsewhere, also suggest an EDHF origin of the wavelet component in the 5-9.5 × 10^{-3} Hz, and for these reasons we have named this oscillator as EDHF. This hypothesis is supported further in this work because the EDHF mechanism is considered as a major mediator of the cutaneous microvascular PORH response[5], and the endothelial NO-independent component was indeed the oscillator displaying the greatest percentage increase of wavelet power during reactive hyperaemia (Table 2).

Overall, the CWT spectral analysis of time series reconstructed from cmOCT flow maps showed results in agreement with the current methods to assess microvascular flow nonlinear oscillations. Therefore, this supports the powerful application of cmOCT and all the OCTA techniques for the study of microcirculation nonlinear dynamics, allowing the investigation of the activity of key factors involved in vasomotion either for elucidating the mechanisms underlying this phenomenon or for clinical diagnostic applications.

Table 1 Comparison of the amplitude and power of the wavelet oscillators between baseline and PORH time points. The variables were non-parametric, thus data are expressed as median (inter-quartile range). The amplitude A_i represents the maximum wavelet power in the interval of interest, while the energy E_i is the overall wavelet power in the frequency range under investigation. The comparison was performed at all the analysed depths: 80-180 µm, 180-280 µm, 300-400 µm. The p-values (p) were estimated by paired Wilcox test performed using the software R-Studio. ***p < 0.001. ECs = Endothelial cells. NO = Nitric oxide. EDHF = Endothelial-derived hyperpolarizing factor.

80-180 µm (n=12)	**Baseline**	**PORH**	**p**
A_i Neurogenic	6.10 (5.20-11.0) × 10^{-5}	3.80 (2.20-4.00) × 10^{-3}	< 0.001***
A_i ECs NO-dependent	7.10 (6.00-10.3) × 10^{-5}	4.70 (3.40-5.10) × 10^{-3}	< 0.001***
A_i ECs NO-independent (EDHF)	5.50 (4.30-7.50) × 10^{-5}	4.90 (3.90-6.70) × 10^{-3}	< 0.001***
E_i Neurogenic	7.20 (4.40-13.7) × 10^{-7}	3.70 (3.40-5.00) × 10^{-6}	< 0.001***
E_i ECs NO-dependent	6.60 (5.10-8.00) × 10^{-7}	2.60 (2.30-3.10) × 10^{-6}	< 0.001***
E_i ECs NO-independent (EDHF)	1.50 (1.40-1.90) × 10^{-7}	0.90 (0.70-1.20) × 10^{-6}	< 0.001***
180-280 µm (n=12)	**Baseline**	**PORH**	**p**
A_i Neurogenic	12.4 (7.50-14.1) × 10^{-5}	3.10 (2.00-4.20) × 10^{-3}	< 0.001***
A_i ECs NO-dependent	10.0 (7.80-12.0) × 10^{-5}	3.30 (2.70-5.00) × 10^{-3}	< 0.001***
A_i ECs NO-independent (EDHF)	5.20 (3.90-7.70) × 10^{-5}	4.40 (3.40-7.80) × 10^{-3}	< 0.001***
E_i Neurogenic	10.3 (6.70-13.0) × 10^{-7}	4.30 (3.60-5.20) × 10^{-6}	< 0.001***
E_i ECs NO-dependent	9.60 (7.50-10.0) × 10^{-7}	2.00 (1.40-3.20) × 10^{-6}	< 0.001***
E_i ECs NO-independent (EDHF)	1.70 (1.20-2.10) × 10^{-7}	0.80 (0.60-1.40) × 10^{-6}	< 0.001***
300-400 µm (n=12)	**Baseline**	**PORH**	**p**
A_i Neurogenic	6.10 (5.00-8.80) × 10^{-5}	2.70 (1.70-4.30) × 10^{-3}	< 0.001***
A_i ECs NO-dependent	7.20 (5.30-8.70) × 10^{-5}	3.20 (2.00-4.10) × 10^{-3}	< 0.001***
A_i ECs NO-independent (EDHF)	5.20 (4.50-5.80) × 10^{-5}	3.80 (2.80-8.00) × 10^{-3}	< 0.001***
E_i Neurogenic	10.5 (7.80-12.9) × 10^{-7}	4.90 (3.00-6.30) × 10^{-6}	< 0.001***
E_i ECs NO-dependent	6.00 (4.70-7.00) × 10^{-7}	2.20 (1.50-3.10) × 10^{-6}	< 0.001***
E_i ECs NO-independent (EDHF)	1.60 (1.40-1.90) × 10^{-7}	0.70 (0.50-1.40) × 10^{-6}	< 0.001***

Table 2 Percentage increase of wavelet power. Data are reported as mean ± standard deviation (SD), and reflect the percentage growth of the CWT spectral energy of each analysed oscillator during PORH response compared to baseline. The percentage increase was estimated for all the dephts under investigation.

Wavelet oscillators	**80-180 µm (n=12)**	**180-280 µm (n=12)**	**300-400 µm (n=12)**
E_i Neurogenic **increase [%]**	29.7 ± 13.3	16.2 ± 10.2	17.0 ± 12.2
E_i ECs NO-dependent **increase [%]**	28.6 ± 11.2	26.6 ± 11.4	37.2 ± 16.1
E_i ECs NO-independent (EDHF) **increase [%]**	41.6 ± 21.2	57.1 ± 18.2	45.8 ± 24.2

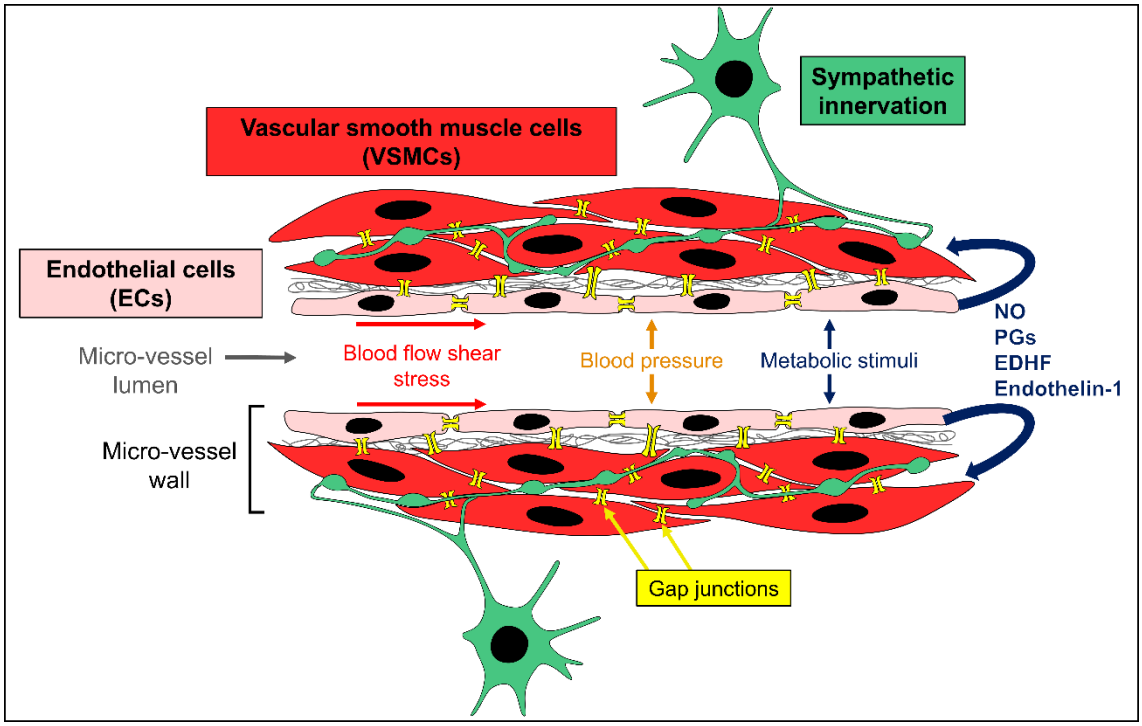

Fig. 7 Mechanisms causing the vasomotor perturbations of blood flow signal. The slow vasomotor waves of skin microvascular flow are caused by changes in the vascular diameter mediated through three main mechanisms occurring with different rhythms: (1) The spontaneous myogenic contraction/relaxation of VSMCs in the micro-vessel wall induced by changes in the intra-arteriolar blood pressure[8,34,35]. (2) The neurogenic feedback between the local nerves and VSMCs stimulated by changes in intra-arteriolar blood pressure or blood perfusion[34], which cause the release of substances from the nerves modulating the contraction/relaxation of VSMCs[8]. (3) The myoendothelial feedback between the ECs and VSMCs[8,34]. The activity of ECs may be stimulated by changes in the concentration of metabolic substances in the blood or by shear stress[8,37], which cause the release of vasoactive agents to modulate VSMCs tone, i.e. NO, PGs, EDHF (mediated by release of metabolites), endothelin-1 or electric signals, e.g. EDHF (mediated by gap junctions signalling). The endothelial oscillations of blood flow signal may reflect the rate of release of vasoactive agents targeting VSMCs, or the rhythmic response of a cellular oscillator in the VSMCs (e.g. Ca^{2+}) to these substances[37]. NO = Nitric oxide. PGs = Prostaglandins. EDHF = Endothelial-derived hyperpolarizing factor.

4. DISCUSSION AND CONCLUSIONS

In this work, we have demonstrated that cmOCT is a suitable non-invasive method for the concurrent visualization of microcirculation structure and assessment of microvascular functional dynamics. Although the resolution of the functional OCT images generated in this research was not optimal, the cmOCT temporal maps allowed to trace clearly the overall flow dynamics with spatial resolution at different selected depths, providing results that reproduce reliably the same patterns observed with the conventional methods for the study of microvascular function. This is extensively proved by the typical reactive hyperaemia trend observed on the reconstructed time series from different tissue depths (Fig. 4), which showed dynamic patterns reflecting the spatial distribution of micro-vessels in the various cutaneous layers. Therefore, the results demonstrate that the technique provides functional information from the flow maps even when the visualization of blood vessels is not optimal. However, this may represent a limit when the goal of the study is focusing on the functional analysis of a specific micro-vessel selected from the cmOCT maps, especially when the size of the vessel is small. In this case, the visualization of micro-vessels in the sequential cmOCT maps may be improved by the choice of a better compromise during the acquisition of the OCT volumes between the sampling density, the speed of acquisition and the size of the sampled volumes, to ensure at the same time a fast scanning rate and a spatial separation between the B-frames avoiding an excessive oversampling that may lead to the mask of smaller blood vessels in the final cmOCT map.

Our results also demonstrate that cmOCT is suitable for the study of vasomotion. Indeed, dynamic oscillators associated with biological components of the micro-vessels were detected by wavelet analysis of cmOCT blood flow signals (Fig. 5-6), which showed spectral power patterns comparable to those observed for LDF signals during PORH vasomotion response (Fig. 6 and Tables 1-2). However, we were not able to detect the myogenic CWT oscillation associated with the spontaneous activity of VSMCs, which represent an important microvascular component involved in the mechanical constriction and enlargement of vessels diameter. This was due to an additional time of 10.6 s during the acquisition of each OCT volume

employed by the ThorImage software (Thorlabs Inc., USA) for saving the data, extending the time of each scan from 6 s to 16.6 s that is not enough to sample the myogenic oscillation (52-145 × 10^{-3} Hz)[8]. The problem may be addressed in the future by using a more powerful computer to maximise the performance of the software ensuring a faster data storage.

Although other OCTA methods such as OMAG may also be suitable for the application of the wavelet analysis and the study of vasomotion, in this work we used cmOCT because it was a readily accessible technique at our facilities providing some benefits. Indeed, in order to detect vasomotion dynamics a fast acquisition time is necessary and the use of cmOCT was advantageous because only the intensity information is needed, allowing a faster data collection at such short time intervals compared to OMAG which uses complex OCT signals requiring the acquisition of both the intensity and the phase. Moreover, because a very large amount of volumes was sampled over time, the employment of cmOCT, which is a lower computationally intensive technique compared to the competing OCTA methods, allowed a quick reduction in size of the overall data volume.

Finally, an important aspect to consider when studying the microcirculation is that the functional impairment of micro-vessels precedes any morphological change, thus representing a hallmark of the early stages of CVD. Therefore, our results outline the eligibility of cmOCT and in general all the OCTA methods as preclinical diagnostic tools for the assessment of CVD risk, with the advantage of providing non-invasive acquistitions from an easy accessible region such as the cutaneous microvascular tissue that represents a surrogate marker reflecting the health status of the central vascular system. The size of the region imaged in this study to track functional dynamics was 750 × 750 μm. Imaging such a small area was advantageous to allow the fast collection of OCT volumes for monitoring the nonlinear dynamics of skin microvascular flow, and to make wavelet data comparable with those reported for LDF that is the conventional technique used in combination with CWT analysis for the indirect assessment of skin vasomotion dynamics. Indeed, LDF probes provide functional data from quite small regions of ~1 × 1 mm. Although the data generated in this work display that functional information can be extracted by imaging small regions of the skin, this is an obvious shortcoming from a clinical perspective that does not allow to draw relevant clinical conclusions and may lead to variable results due to the heterogeneous structure of the cutaneous tissue. Therefore, this point must be addressed before translating the method to any clinical research study. A possible solution may be the acquisition of OCT volumes at a speed faster than the 48 kHz used in this work, which would allow to enlarge the size of the imaged region maintaining a suitable sampling frequency (16.6 s or below) for tracking vasomotion dynamics.

The experiments were carried out successfully from a group of 12 healthy individuals, showing that the technique can be applied easily on large groups of subjects providing quite reproducible results. Therefore, the future perspective is the extension of the method to clinical studies for the exploration of potential diagnostic applications to monitor the onset and progression of cardiovascular disease.

ACKNOWLEDGMENTS

The research leading to these results has received funding from the People Programme (Marie Curie Actions) of the European Union's Seventh Framework Programme (FP7/2007-2013) under REA grant agreement n° 608133. The study was performed in collaboration between the School of Medicine of the University of Dundee (Scotland) and the Tissue Optics and Microcirculation Imaging group of the National University of Ireland, Galway (NUIG) that was involved as associated academic partner in the Marie Curie PHOQUS research programme co-ordinated by the University of Dundee. This study represents the expanded and completed version of a conference proceeding work[29] presented in San Francisco (US) at the SPIE BiOS 2018, *Dynamics and Fluctuations in Biomedical Photonics XV* Conference.

CONFLICT OF INTERESTS

The authors declare no financial interests or potential conflict of interests in the manuscript.

REFERENCES

[1] Gutterman, D. D. *et al.*, "The Human Microcirculation – Regulation of Flow and Beyond," *Circ. Res.*, 118(1), 157–172 (2016).

[2] Turner, J., Belch, J. J. and Khan, F., "Current concepts in assessment of microvascular endothelial function using laser Doppler imaging and iontophoresis," *Trends Cardiovasc. Med.*, 18(4), 109-16 (2008).

[3] Khan, F. *et al.*, "Relationship between peripheral and coronary function using laser Doppler imaging and transthoracic echocardiography," *Clin. Sci. (Lond.)*, 115(9), 295-300 (2008).

[4] den Uil, C. A. *et al.*, "The microcirculation in health and critical disease," *Prog. Cardiovasc. Dis.*, 51(2), 161-70 (2008).

[5] Roustit, M. and Cracowski, J. L., "Assessment of endothelial and neurovascular function in human skin microcirculation," *Trends Pharmacol. Sci.*, 34(7), 373-84 (2013).

[6] Roustit, M. and Cracowski, J. L., "Non-invasive assessment of skin microvascular function in humans: an insight into methods," *Microcirculation*, 19(1), 47-64 (2012).

[7] Stefanovska, A., Bračič, M. and Kvernmo, H. D., "Wavelet analysis of oscillations in the peripheral blood circulation measured by laser Doppler technique," *IEEE Trans. Biomed. Eng.*, 46(10), 1230-9 (1999).

[8] Shiogai, Y., Stefanovska, A. and McClintock, P. V., "Nonlinear dynamics of cardiovascular ageing," *Phys. Rep.*, 488(2-3), 51-110 (2010).

[9] Enfield, J., Jonathan, E. and Leahy, M., "In vivo imaging of the microcirculation of the volar forearm using correlation mapping optical coherence tomography (cmOCT)," *Biomed. Opt. Express*, 2(5), 1184-1193 (2011).

[10] Enock, J., Enfield, J. and Leahy, M. J., "Correlation mapping method for generating microcirculation morphology from optical coherence tomography (OCT) intensity images," *J. Biophotonics*, 4, 583-587 (2010).

[11] Xu, M. and Wang, L. V., "Time-Domain Reconstruction for Thermoacoustic Tomography in a Spherical Geometry," *IEEE Trans. Med. Imaging*, 21(7), 814-822 (2002).

[12] Wang, X. *et al.*, "Photoacoustic tomography of biological tissues with high cross-section resolution: Reconstruction and experiment," *Med. Phys.*, 29, 2799 (2002).

[13] Wang, L. V., "Prospects of photoacoustic tomography," *Med. Phys.*, 35(12), 5758 (2008).

[14] Tian, C. *et al.*, "Non-Contact Photoacoustic Imaging Using a Commercial Heterodyne Interferometer," *IEEE Sens. J.*, 16(23), 8381-8388 (2016).

[15] Rousseau, G., Blouin, A. and Monchalin, J. P., "Non-contact photoacoustic tomography and ultrasonography for tissue imaging," *Biomed. Opt. Express*, 3(1), 16-25. (2012).

[16] Zhang, H. F. *et al.*, "Imaging acute thermal burns by photoacoustic microscopy," *J. Biomed. Opt.*, 11(5), 054033 (2006).

[17] Abraham, P. *et al.*, "Effect of skin temperature on skin endothelial function assessment," *Microvasc. Res.*, 88, 56-60 (2013).

[18] Yao, J., "When pressure meets light: detecting the photoacoustic effect at the origin," *Light: Science & Applications*, 6, e17062 (2017).

[19] Dong, B., Sun, C. and Zhang, H. F., "Optical Detection of Ultrasound in Photoacoustic Imaging," *IEEE Trans. Biomed. Eng.*, 64(1), 4-15 (2017).

[20] Hajireza, P. *et al.*, "Non-interferometric photoacoustic remote sensing microscopy," *Light: Science & Applications*, 6, e16278 (2017).

[21] Podoleanu, A. G., "Optical coherence tomography," *J. Microscopy*, 247, 209-219 (2012).

[22] Mogensens, M. and Jemec, G. B. E., "Diagnosis of Nonmelanoma Skin Cancer/Keratinocyte Carcinoma: A Review of Diagnostic Accuracy of Nonmelanoma Skin Cancer Diagnostic Tests and Technologies," *Dermatol. Surg.*, 33(10), 1158-1174 (2007).

[23] Drexler, W. *et al.*, "In vivo ultrahigh-resolution optical coherence tomography," *Opt. Lett.*, 24(17), 1221-1223 (1999).

[24] Fercher, A. F. *et al.*, "Optical coherence tomography - principles and applications," *Rep. Progr. Phys.*, 66(2), 239-303 (2003).

[25] Wang, X., Milner, T. and Nelson, J., "Characterization of fluid flow velocity by optical Doppler tomography," *Opt. Lett.*, 20(11), 1337-1339 (1995).

[26] Barton, J. and Stromski, S., "Flow measurement without phase information in optical coherence tomography images," *Opt. Express*, 13(14), 5234-5239 (2005).

[27] Wang, R. K. *et al.*, "Three dimensional optical angiography," Opt. Express, 15(7), 4083-4097 (2007).

[28] Choi, W. J., Wang, H. and Wang, R. K., "Optical coherence tomography microangiography for monitoring the response of vascular perfusion to external pressure on human skin tissue," *J. Biomed. Opt.*, 19(5), 056003 (2014).

[29] Smirni, S. *et al.*, "In-vivo assessment of microvascular functional dynamics by combination of cmOCT and wavelet transform," *Proc. SPIE 10493, Dynamics and Fluctuations in Biomedical Photonics XV*, 104930P (2018).

[30] Lancaster, G. *et al.*, "Dynamic markers based on blood perfusion fluctuations for selecting skin melanocytic lesions for biopsy," *Sci. Rep.*, 5, 12825 (2015).

[31] Iatsenko, D., McClintock, P. V. E. and Stefanovska, A., "Linear and synchrosqueezed time-frequency representations revisited: Overview, standards of use, resolution, reconstruction, concentration, and algorithms," *Digit. Sig. Process.*, 42, 1-26 (2015).

[32] Rossi, M. *et al.*, "Impact of long-term exposure to cigarette smoking on skin microvascular function," *Microvasc. Res.*, 93, 46-51 (2014).

[33] Mück-Weymann, M. E. *et al.*, "Respiratory-dependent laser-Doppler flux motion in different skin areas and its meaning to autonomic nervous control of the vessels of the skin," *Microvasc. Res.*, 52(1), 69-78 (1996).

[34] Kastrup, J., Bülow, J. and Lassen, N. A., "Vasomotion in human skin before and after local heating recorded with laser Doppler flowmetry. A method for induction of vasomotion," *Int. J. Microcirc. Clin. Exp.*, 8(2), 205-15 (1989).

[35] Stefanovska, A. and Bračič, M., "Physics of the human cardiovascular system," *Contemp. Phys.*, 40(1), 31-55 (1999).

[36] Aalkjaer, C. and Nilsson, H., "Vasomotion: cellular background for the oscillator and for the synchronization of smooth muscle cells," *British J. Pharmacol.*, 144, 605-616 (2005).

[37] Kvernmo, H. D. *et al.*, "Oscillations in the human cutaneous blood perfusion signal modified by endothelium-dependent and endothelium-independent vasodilators," *Microvasc. Res.*, 57(3), 298-309 (1999).

[38] Kvandal, P. *et al.*, "Low frequency oscillations of the laser Doppler perfusion signal in human skin," *Microvasc. Res.*, 72(3), 120-127 (2006).

AUTHORS PROFESSIONAL BIOGRAPHIES

Salvatore Smirni
Salvatore Smirni is a Marie Curie ESR fellow at the University of Dundee, specialized in multidisciplinary research at the cutting-edge between biomedicine and physics with particular focus on the nonlinear dynamics of skin microcirculation and cell energy metabolism. He received his BSc in Biology and MSc in Molecular Biotechnologies respectively from the University of Catania and University of Pisa. In 2018, he obtained a PhD in Biophotonics at the University of Dundee.

Michael P. MacDonald
Michael P. MacDonald is a Reader in Physics and Medicine at the University of Dundee. His research interests cover the application of optical imaging, sensing and manipulation to the Life Sciences and Medicine. He joined Dundee in 2007 from the University of St. Andrews, received his MSc and PhD in Laser Physics at the University of Bern and his BSc from the University of Strathclyde.

Catherine P. Robertson
Catherine P. Robertson has received her BSc in Physics from the University of Dundee in 2018. The work of her dissertation was focused on laser measurement of non-linear dynamics of beta-carotene in the skin microcirculation. She has also contributed to research in the area of medical imaging and biophysics.

Paul M. McNamara
Paul M. McNamara received his PhD in biophotonics from the University of Limerick in 2013, specializing in tissue viability (TiVi) imaging and full-field optical coherence tomography. He is a postdoctoral researcher at the Tissue Optics and Microcirculation Imaging Group at NUI Galway and head of Application Research Ireland for Compact Imaging Ireland, Ltd. His research interests include wearable devices and biophotonics applications in low-resource settings.

Sean O'Gorman
Sean O'Gorman is a graduate researcher at the TOMI lab, NUI Galway. He specializes in multiple reference optical coherence tomography (MR-OCT) with a particular interest in angiography and liveness detection. His early research work is centred on cmOCT angiography of the nail fold capillary plexus.

Martin J. Leahy
Martin J. Leahy is Chair of Applied Physics at NUI Galway where he leads the Tissue Optics and Microcirculation Imaging Group. His group invented the Heart Rate App, correlation mapping OCT, nano-sensitive OCT and depth encoded super-resolution microscopy. He chairs the biannual international Biophotonics and Imaging Graduate Summer School in Ireland and is a JBO Letters Editor.

Faisel Khan
Faisel Khan is Professor of Cardiovascular Sciences at the University of Dundee Medical School. He has a multidisciplinary, collaborative research programme with a major "bench to bedside" focus on translational research. He has published over 120 peer reviewed research papers. He is a Member of the Royal Society of Medicine Council of Vascular Medicine and serves on the Editorial Board for The European Journal of Vascular Medicine, Microcirculation and International Angiology.

III. In-vivo multi-parameter optical measurements show correlations between skin metabolic oscillations and vasomotion

Salvatore Smirni[1,*], Alison D. McNeilly[1], Michael P. MacDonald[1,2], Rory J. McCrimmon[1] & Faisel Khan[1,*]

[1]School of Medicine, Ninewells Hospital, University of Dundee, Scotland, UK
[2]School of Science and Engineering, University of Dundee, Scotland, UK
*Corresponding authors: salvatore.smirni@gmail.com
f.khan@dundee.ac.uk

Arterioles in the cutaneous microcirculation frequently display an oscillatory phenomenon defined vasomotion, consistent with periodic diameter variations in the micro-vessels associated with particular physiological or abnormal conditions. The driving mechanisms at cellular level underlying the fluctuations of vascular diameter and their physiological role have not been completely elucidated. Various mechanisms were demonstrated, based on cell Ca^{2+} oscillations determined by the activity of channels in the plasma membrane and sarcoplasmic reticulum cellular compartments. However, the possible engagement in vasomotion of cell metabolic oscillations of mitochondrial or glycolytic origin has been poorly explored. Metabolic oscillations associated with the production of ATP energy were previously described in cells. Nevertheless, little focus has been committed to the investigation of these fluctuations *in-vivo*. We present a method to characterise low-frequency metabolic oscillations from live mouse skin, based on the combination of fluorescence spectroscopy and wavelet transform signal processing technique. Furthermore, the relationships between metabolic and microvascular oscillators during phenylephrine-induced vasoconstriction were examined. Relevant correlations were found in normal mice, while animals with altered antioxidant defence presented a different oscillatory behaviour and set of correlations. These evidences raise interest in the possible metabolic origin of Ca^{2+} oscillations driving arterioles motion in specific physiological conditions.

Introduction

The term vasomotion indicates rhythmic oscillations of blood vessels diameter responsible for changes in the vascular tone and blood perfusion to tissue[1,2]. The physiological role of these oscillations is unclear, with contrasting studies supporting the development of vasomotion in both diseased and healthy conditions[2]. The origin of the oscillations is mainly determined by the local contraction and relaxation of vascular smooth muscle cells (VSMCs), which act as synchronised pacemakers in the vessels wall[1,2,3]. Although in several arteries (e.g. rat aorta) the oscillations may depend exclusively on the activity of VSMCs[1], in other vascular beds (i.e. rat mesenteric artery) the most internal layer of blood vessels (endothelium) plays an important modulatory role during arterial motion[4,5]. Vasomotion is more prominent in small resistance micro-vessels[2] such as skin arterioles that represent an optimal sample for the *in-vivo* examination of this phenomenon reflecting the general health conditions of the cardiovascular system[6].

Non-invasive observation of skin vasomotion can be achieved by direct methods measuring vessels diameter, e.g. intravital video-microscopy[3,7,8], or by indirect techniques such as Laser Doppler Flowmetry (LDF) based on monitoring the heterogeneous fluctuations of microvascular blood perfusion signal[2]. The combination of LDF with wavelet transform signal processing analysis has revealed oscillations in the human cutaneous microcirculation that relate to physiological phenomena: myogenic (52-145 × 10^{-3} Hz), neurogenic (21-52 × 10^{-3} Hz), endothelial nitric oxide (NO)-dependent (9.5-21 × 10^{-3} Hz), and endothelial NO-independent (5-9.5 × 10^{-3} Hz)[4,9].

For the explanation of the cellular mechanisms causing the oscillations of vessels diameter observed during vasomotion, three different kinds of cellular oscillators have been proposed as possible drivers of this phenomenon: cytosolic oscillator, membrane oscillator and metabolic oscillator[1,2]. The importance of the cooperation between cytosolic and membrane oscillators to enhance the VSMCs synchronisation responsible for vasomotion has been largely explored and recognised[1,2,10,11,12,13]. They act inducing Ca^{2+} fluctuations in VSMCs, respectively through the oscillatory release of Ca^{2+} from the sarcoplasmic reticulum[1,11,12], and via the opening activity of voltage-dependent Ca^{2+} channels and large-conductance K^{+} channels of the plasma membrane[1,2,13]. Furthermore, Ca^{2+} and membrane potential oscillations have been described in endothelial cells (ECs), suggesting that in some vascular beds (i.e. rat mesenteric artery) in response to specific stimuli (e.g. α-adrenergic stimulation) a primary oscillation from ECs and the interaction with VSMCs might be essential for vasomotion[14,15,16].

A third hypothesised driving mechanism is the presence of a metabolic oscillator represented by oscillations in the activity of the glycolytic enzyme phosphofructokinase (PFK) that cause fluctuations in glycolysis, ATP levels and in the activity of plasma membrane ion channels and membrane potential[17,18,19]. This mechanism has never been considered important because of limited experimental evidence for the involvement of PFK in glycolytic and Ca^{2+} fluctuations[1,2]. However, recent studies have strongly suggested the participation of PFK in reactions responsible for glycolysis and Ca^{2+} oscillations[20,21,22], with a possible driving effect exerted *in-vivo* by external glucose availability and uptake[22,23,24,25]. Furthermore, metabolic mitochondrial oscillations have also been reported, mainly associated with fluctuations of the mitochondrial membrane potential $\Delta\Psi_m$ that may be mediated by calcium[26,27,28]. The external oxygen required for sustaining the electron transport chain has been proposed as the driving force for the mitochondrial oscillator[22]. All these evidences suggest that the energetic and oxygen tissue requirements might stimulate vasomotion phenomena associated with Ca^{2+} oscillations of metabolic origin, which may involve the intercellular communication between heterogeneous groups of cells (e.g. ECs, VSMCs and cells of the tissue surrounding blood vessels).

Metabolic oscillations have been studied in different cell types, i.e. yeast *Saccharomyces cerevisiae*[23,26], cardiac myocytes[29], β-cells[28,30], and can be detected indirectly by measuring the fluctuations in the autofluorescence of the intermediate product of energy metabolism NAD(P)H (nicotamide adenine dinucleotide). However, there are limited studies describing metabolic oscillations in live tissue. Mitochondrial fast oscillations have been reported *in-vivo* in rat, and detected by intravital two-photon (2P) microscopy measurements of NAD(P)H[31]. Nevertheless, to our knowledge, the slow metabolic NAD(P)H oscillations described in many *in-vitro* or *ex-vivo* cell studies[20,28] have not been investigated *in-vivo*.

In the present study, we have utilised skin tissue from live mice to simultaneously measure NAD(P)H and microvascular blood flow respectively by laser fluorescence spectroscopy (LFS) and LDF, under physiological conditions and during α-adrenergic stimulation with the vasoconstrictor drug phenylephrine (PE). Data were processed by continuous wavelet transform (CWT) spectral analysis to characterise heterogeneous oscillations of NAD(P)H and LDF signals. We found low-frequency oscillations of NAD(P)H autofluorescence with periods of ~2.4 min, ~5 min and ~10 min. To our knowledge, this is the first study in live skin tissue of slow NAD(P)H oscillations previously described in cells. Furthermore, we found relevant correlations between metabolic and vasomotion oscillations suggesting a link between these processes. Therefore, our results support the idea of vasomotion as a dynamic process in the context of a metabolically active microvascular network involving the cooperation of different cell types and vascular segments[2,16], and a possible driving mechanism of metabolic origin.

Results

Nrf2$^{-/-}$ (*Nuclear factor-erythroid 2 p45-related factor 2*) knockout (KO) model. Experiments were performed on 5 wild type (WT) control and 6 Nrf2$^{-/-}$ mice. The Nrf2 transcription factor is a key regulator of the cell redox state, involved in the resistance to oxidative stress by activating the cellular antioxidant defence[32]. Nrf2 knockout leads to abnormal mitochondrial activity, altered redox status, increased oxidative stress, and has an impact on cardiovascular dynamics[32,33]. We used the Nrf2$^{-/-}$ strain to investigate the differences in metabolic and vascular dynamics between normal mice and animals with impaired antioxidant defence that may favour the development of metabolic and cardiovascular disorders. Fig. 1 shows the experimental setup (Fig. 1a), and examples of simultaneous LFS and LDF signals (Fig. 1c-d) from the flank of a mouse at baseline (10 min) and during vasoconstriction induced by local administration of PE (10 min). Because of the small number of animals available in the study, the experiments were repeated in duplicate for each mouse and the average value of each variable between the two experiments was taken as final value for data analysis. Data of all the variables analysed in this study are summarised in Table 1 at the end of the results section.

Microvascular biomarkers. Results of blood perfusion and oxygen saturation (SO_2) are shown in Fig. 2a-b. Blood perfusion decreased to a similar degree in WT (p=0.046) and Nrf2$^{-/-}$ (p=0.007) mice during PE-induced vasoconstriction, however, a stronger p-value was found in KO mice. SO_2, measured by reflectance spectroscopy (RS), was similar between groups and decreased slightly following vasoconstriction without statistical significance.

Metabolic biomarkers. LFS skin irradiation by UV light stimulates the autofluorescence emission of multiple fluorophores, including NAD(P)H (490 nm), flavin adenine dinucleotide (FAD^+, 550 nm) and elastin (450 nm) (Fig. 1b). Although the NAD(P)H central emission peak represents the highest contribution to the spectrum, we took advantage of the overlapping contributions from FAD^+ and elastin, respectively to estimate the redox ratio (RR) index and to normalise NAD(P)H fluorescence:

$$\mathrm{RR} = \frac{\mathrm{NAD(P)H}_{\,\mathrm{amplitude}}}{FAD^{+}_{\mathrm{amplitude}}} \tag{1}$$

$$\mathrm{NAD(P)H}_{\mathrm{normalised}} = \frac{\mathrm{NAD(P)H}_{\,\mathrm{amplitude}}}{\mathrm{Elastin}_{\,\mathrm{amplitude}}} \tag{2}$$

RR is a measure of the mitochondrial redox state, reflecting the mitochondrial balance between the reduced NAD(P)H and the oxidised FAD^+ coenzymes. Comparing this index between WT and Nrf2$^{-/-}$ mice should provide discriminatory data, confirming that the Nrf2$^{-/-}$ phenotype is characterised by altered mitochondrial function due to impaired antioxidant defence and higher oxidative stress. NAD(P)H autofluorescence was normalised by elastin's fluorescence peak to reduce blood volume effects (see more details in the supplementary information online). During each experiment, 20 UV spectra were collected in 20 min at a rate of a spectrum every minute, 10 at baseline and 10 during PE administration. RR and $NAD(P)H_{normalised}$ values were estimated from each spectrum and used to reconstruct continuous signals (Fig. 1c) for applying the CWT spectral analysis. Fig. 2c-d describe the average trends of $NAD(P)H_{normalised}$ and RR signals. $NAD(P)H_{normalised}$ did not show significant statistical differences between groups, while RR was significantly lower in Nrf2$^{-/-}$ mice (p=0.016) confirming that KO animals were affected by altered redox state and higher oxidative stress.

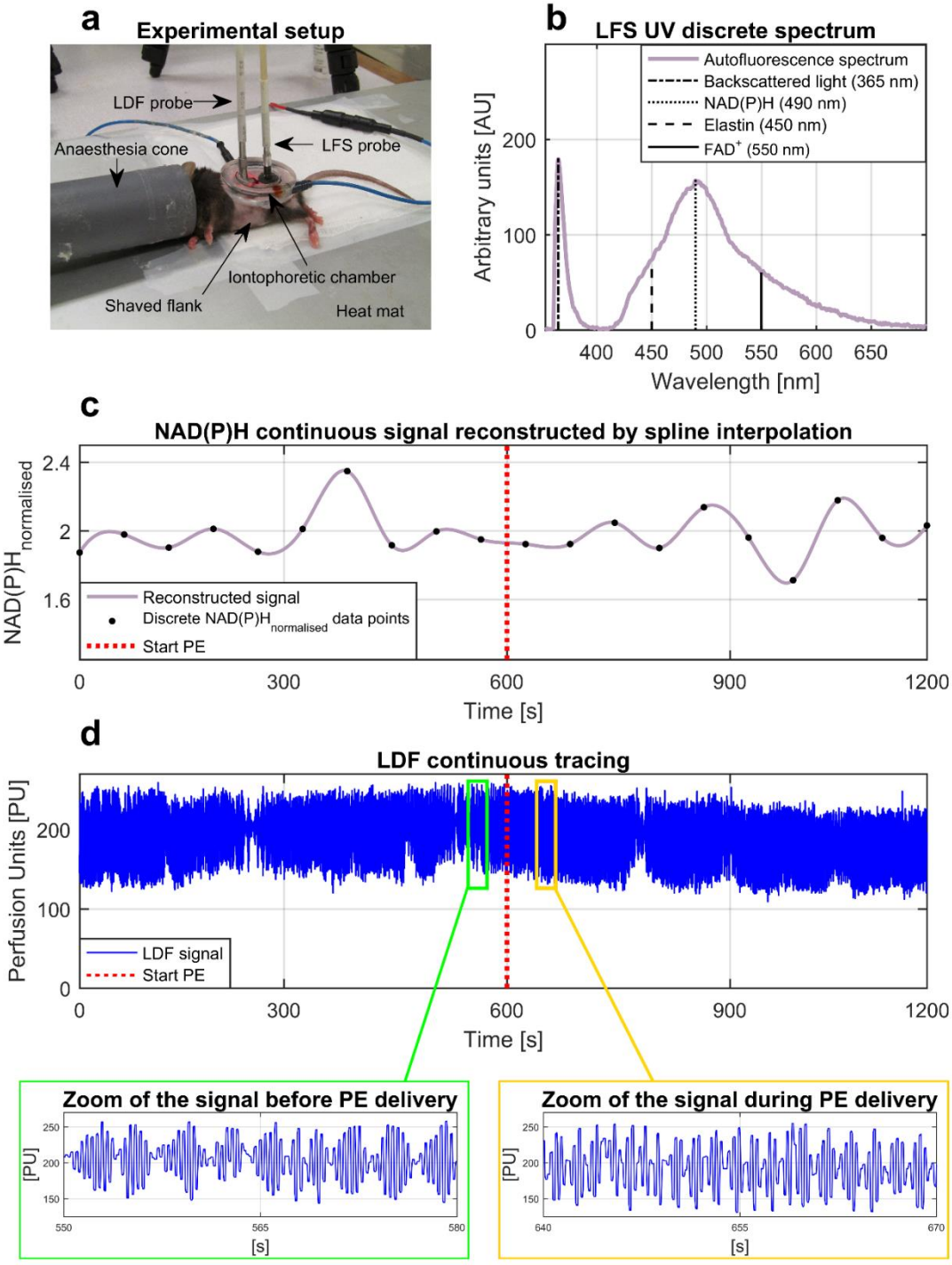

Fig. 1 Example of data collection from mouse skin. (**a**) Experimental setup for simultaneous LFS and LDF recordings during local transdermal administration of 1% phenylephrine by iontophoresis method. The reason for using PE is that, according to Okazaki *et al.*[5], this vasoactive agent is able to stimulate a vasomotion phenomenon mediated by endothelial cells. Thus, the use of PE provided the opportunity to study at the same time the role of the endothelium in vasomotion and its relationship with metabolic oscillations. (**b**) Example of single UV discrete autofluorescence spectrum measured by LFS. (**c**) Example of 20 min NAD(P)H continuous signal reconstructed by piecewise cubic spline interpolation of $NAD(P)H_{normalised}$ values extracted from 10 baseline UV spectra and 10 UV spectra collected during PE administration. (**d**) Example of 20 min blood flow continuous tracing measured by LDF during iontophoresis test.

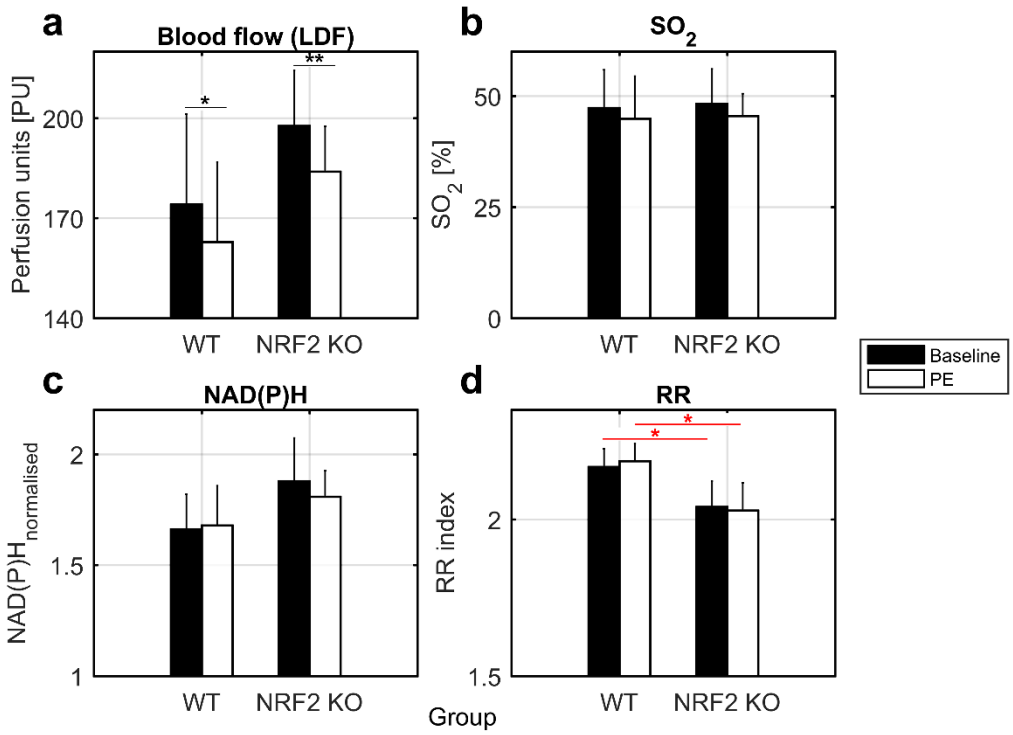

Fig. 2 General trends of microvascular and metabolic biomarkers. (**a**) Average blood flow (PU). (**b**) Average oxygen saturation (%). (**c**) Average NAD(P)$H_{normalised}$ (dimensionless). (**d**) Average RR index (dimensionless). The software R-Studio was used to perform the statistical analyses. The Shapiro-Wilk test revealed normal distributions for all the variables, thus data are reported as bar plots of the mean values. Error bars are referred to two standard errors (SE), corresponding approximately to a 95% confidence interval (CI). Black bars = Baseline. White bars = PE administration. WT = Control mice. NRF2 KO = Knockout mice. Black lines/asterisks = Significant changes during delivery of PE estimated by paired t-test. Red lines/asterisks = Significant differences between mice groups estimated by unpaired t-test. The t-test was considered significant at p (p-value) < 0.05 with a statistical power of 0.8 determined by R-Studio. *p < 0.05, **p < 0.01.

Reproduction of the LDF oscillators reported in the literature. Vasomotion oscillations were assessed by combining LDF and CWT techniques[4,34,35,36,37,38,]. We found oscillatory frequency intervals related to tissue/cell activity similar to those reported in human studies: myogenic (50-150 × 10^{-3} Hz), neurogenic (20-50 × 10^{-3} Hz), endothelial NO-dependent (9-20 × 10^{-3} Hz), endothelial NO-independent (5-9 × 10^{-3} Hz) (Fig. 3a). In contrast, cardiac (1350-5000 × 10^{-3} Hz) and respiratory (150-1350 × 10^{-3} Hz) components showed higher frequency ranges (Fig. 3a), confirming the faster heart and breathing rates expected for mice[39,40]. Although the magnitude of the oscillations could be reduced due to the effects of anaesthesia[41], we used a light isoflurane anaesthesia to avoid major systemic effects on the circulation. Additionally, all mice were scanned under the same conditions thus making it possible to compare differences between groups.

CWT allows the identification of two oscillators reflecting ECs activity. While the biological link between the 9-20 × 10^{-3} Hz oscillator and the endothelial NO mechanism has been demonstrated[37], the origin of the 5-9 × 10^{-3} Hz oscillator (endothelial NO-independent) is ambiguous. However, our results and literature reports suggest indirectly an association with the endothelial-derived hyperpolarizing factor (EDHF) vasodilation mechanism, thus here we will refer to the endothelial NO-independent component as EDHF. The reasons supporting this hypothesis are explained in the supplementary information online.

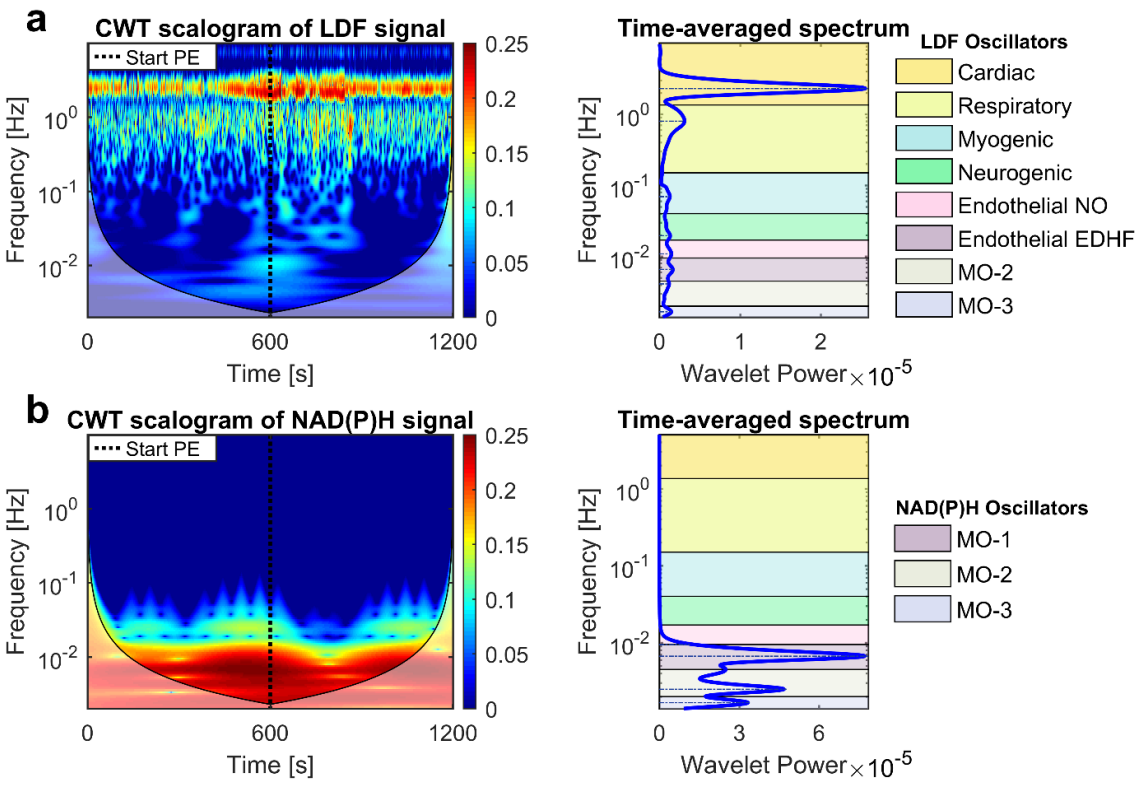

Fig. 3 CWT data processing of LDF and NAD(P)H signals. (**a**) Example of CWT scalogram (left) and corresponding time-averaged spectrum (right) from LDF signal. The scalogram describes the distribution of the wavelet spectral power/energy in the time-frequency domain using a gradient coloured map ranging from dark blue (low energy) to dark red (high energy). The chart displays a high-energy continuous band in the cardiac frequency interval, confirming that data were collected correctly. Physiologically, the wavelet energy represents a measure of how much a physiological component defined by a specific frequency interval contributes to blood flow signal at a specific time. The two transparent regions at the bottom-right and bottom-left of the scalogram represent regions outside of the "cone of influence" where data might not be reliable (frequencies < 5×10^{-3} Hz). The cone of influence is a time-frequency region where distortions of the CWT due to the finite temporal period of the measured signal are not relevant[42]. Instead, the areas outside of the cone are close to the time limits of the time series, where the wavelet transform is affected by boundary effects making the calculations from this time-frequency region imprecise[42]. The time-averaged spectrum (right graph) allows discriminating the wavelet energy peaks of the different oscillators at specific frequency intervals. As shown by the coloured tags in the legend, we identified the typical oscillators reported in literature: (I) cardiac, (II) respiratory, (III) myogenic, (IV) neurogenic, (V) endothelial NO-dependent, (VI) endothelial NO-independent (EDHF). Comparing the wavelet components between mice groups is powerful to distinguish healthy and diseased vascular conditions by quantifying the contribution of specific biological components. (**b**) Example of CWT analysis of the NAD(P)H reconstructed signal. Three low-frequency metabolic oscillators were characterised: Metabolic oscillator-1 (MO-1), MO-2 and MO-3. These oscillators might reflect specific dynamic patterns of ATP energy production in the cutaneous tissue, which may be variable depending on the presence of healthy or diseased conditions. In this study, we focused on the dynamics of MO-1 because MO-2 and MO-3 intervals are located outside of the cone of influence where data might be inaccurate.

Characterisation of metabolic fluctuations. *In-vivo* metabolic oscillations were detected by CWT analysis of NAD(P)H and RR reconstructed signals. Fig. 3b shows an example of CWT scalogram and the corresponding time-averaged spectrum from NAD(P)H signal. High spectral energy was found in the low-frequency ranges, thus slow oscillators dominate the reconstructed tracing. Although time resolution is scarce in the low frequencies, we clearly identified three heterogeneous oscillatory intervals defined metabolic oscillator-1 (MO-1) (5-9 × 10^{-3} Hz), metabolic oscillator-2 (MO-2) (2.5-5 × 10^{-3} Hz), metabolic oscillator-3 (MO-3) (1.5-2.5 × 10^{-3} Hz). However, we will discuss only results of MO-1 because MO-2 and MO-3 frequency ranges fall largely at the edges of the cone of influence region in the CWT scalogram, where data might not be reliable[42] (see caption of Fig. 3 for more details).

LDF oscillators' changes during vasomotion and comparison between groups. Fig. 4 describes the quantitative results of the relative spectral energy e_i and frequency f extracted from the time-averaged wavelet peak of each LDF oscillator. The relative e_i, to allow comparisons between groups, was obtained by normalising the absolute energy extracted from the peak of each oscillator (E_i, area under the curve) by the total absolute energy E_{tot} of the wavelet spectrum and the number of frequencies in the interval of the oscillator. The spectral e_i and frequency of the EDHF endothelial oscillator were significantly greater in WT mice at baseline (energy p=0.03, frequency p=0.005). The EDHF energy and frequency changed significantly in both groups during PE stimulation following opposite trends. The values increased in Nrf2$^{-/-}$ mice (energy p=0.01, frequency p=0.02) and decreased in controls (energy p=0.008, frequency p=0.04). The endothelial NO oscillator displayed the same trends observed for the EDHF oscillation. However, we found statistical significance only for the decrease of energy during phenylephrine delivery in WT mice (p=0.008). The neurogenic and myogenic components showed patterns similar to those of the endothelial oscillations. The energy was reduced in normal mice after PE administration, with a good p-value for the neurogenic oscillator (p=0.04) and a p-value close to statistical significance for the myogenic component (p=0.08). We evaluated also the relative maximal amplitude a_i of the wavelet peaks, estimated by normalising the absolute amplitude A_i of each oscillator by the total amplitude A_{tot} of the wavelet spectrum and the number of frequencies in the interval of the oscillator. The data of a_i are summarised in Table 1 and displayed the same patterns found for e_i but with lower statistical significance.

These results outline opposite microvascular reactivity to PE in WT and Nrf2$^{-/-}$ mice, especially for the endothelial components that are key factors determining microvascular function. This suggests that oxidative stress may affect endothelial function and the overall cardiovascular dynamics in the long term.

In general, the increase of LDF oscillators' spectral energy reflects vasodilation dynamics[4,36,38,43], thus the expected oscillatory pattern during mild vasoconstriction (1% PE) should be a decrease of e_i, as observed in WT animals. In contrast, Nrf2$^{-/-}$ mice displayed an increase of LDF oscillators' e_i during phenylephrine administration. The reason for this behaviour might be the activation of an endothelial-mediated vasomotion resistance mechanism to attenuate vasoconstriction defined myoendothelial feedback[16], consistent with the alternation of vasoconstriction and vasodilation induced respectively by simultaneous targeting of VSMCs with PE and EDHF/NO endothelial signalling. The cause for the activation of this mechanism may be a general major vasoconstriction in micro-vessels affected by oxidative stress. We cannot exclude that also WT mice may activate this mechanism in response to higher vasoconstriction stimuli (PE > 1%).

Metabolic oscillations' changes and comparison between groups. Data of the spectral e_i, a_i and f of NAD(P)H MO-1 and RR MO-1 wavelet peaks are summarised in Fig. 5a-c. Only WT mice showed a statistically significant increase of NAD(P)H MO-1 e_i (p=0.01) and RR MO-1 a_i (p=0.04) during PE delivery. The baseline RR MO-1 amplitude a_i was lower in WT compared to Nrf2$^{-/-}$ mice with a p-value approaching statistical significance (p=0.097). Differences in frequencies were not relevant.

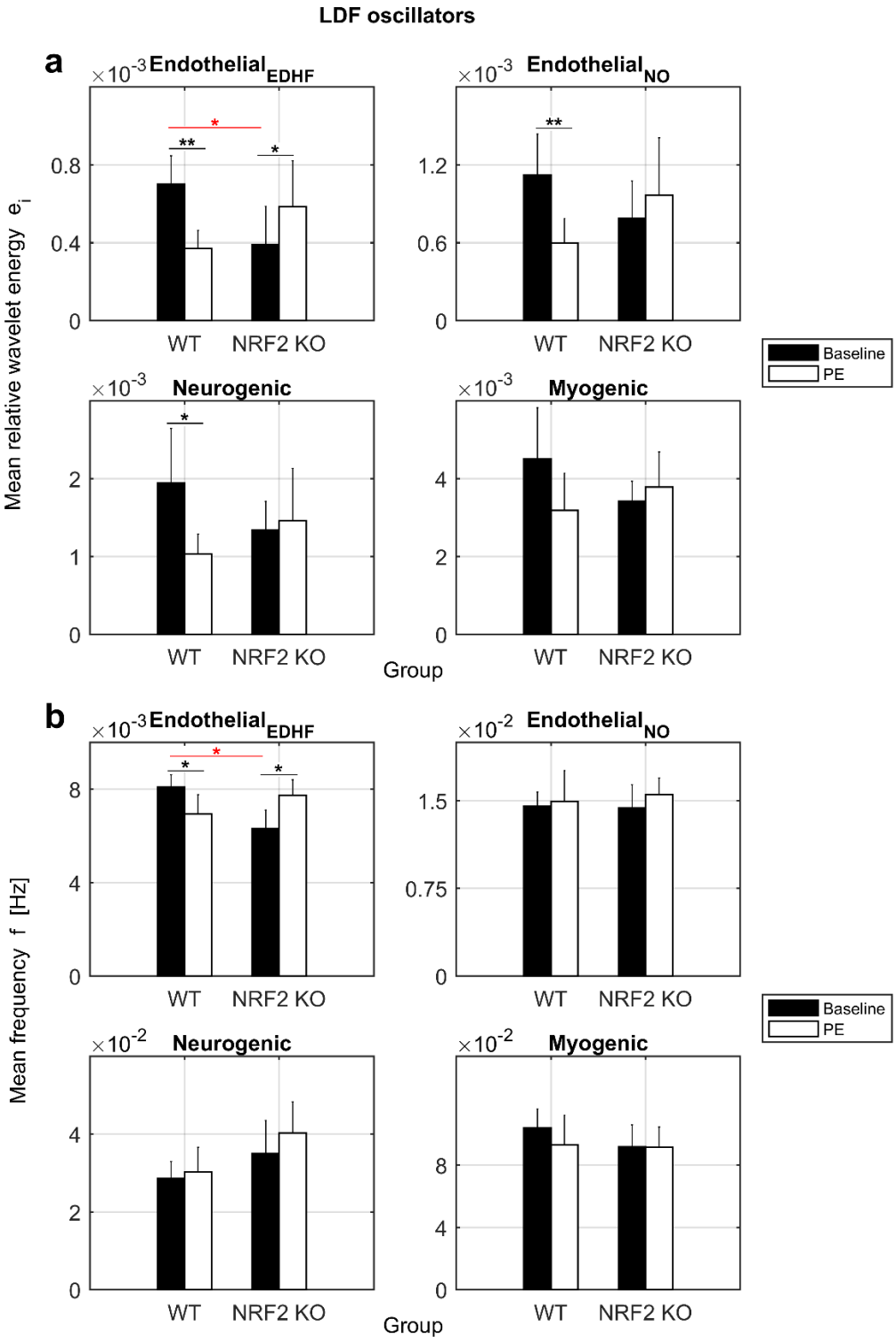

Fig. 4 Results of LDF oscillators. (**a**) Mean relative energy e_i (dimensionless units) of the wavelet peaks. (**b**) Mean frequency f (Hz) of the wavelet peaks. The software R-Studio was used to perform all the statistical analyses. The Shapiro-Wilk test revealed normal distributions for all the variables, thus data are reported as bar plots of the mean values. Error bars are referred to two standard errors (SE), corresponding approximately to a 95% confidence interval (CI). Black bars = Baseline. White bars = PE administration. WT = Control mice. NRF2 KO = Knockout mice. Black lines/asterisks = Significant changes during administration of PE estimated by paired t-test. Red lines/asterisks = Significant differences between mice groups estimated by unpaired t-test. The t-test was considered significant at $p < 0.05$ with a statistical power of 0.8 determined by R-Studio. *$p < 0.05$, **$p < 0.01$.

NAD(P)H and RR oscillations reflect the cellular oxido-reductive dynamics, consistent with the turnover between the oxidised and reduced forms of NAD(P)H and $FADH_2$ coenzymes as part of the cyclic reactions for the production of ATP energy during glycolysis and oxidative phosphorylation (OXPHOS) processes. The results of the spectral analysis outline different dynamics of metabolic oscillators in WT and $Nrf2^{-/-}$ mice, especially for the RR MO-1. Considering that RR reflects mitochondrial function, the major discriminatory power of RR MO-1 may indicate abnormal mitochondrial energetic dynamics in $Nrf2^{-/-}$ mice due to increased amounts of reactive oxygen species (ROS) affecting the electron transport chain.

Wavelet phase coherence (WPCO). The WPCO analysis allows investigating the phase relationship $C\phi(\omega k)$ between oscillations in a specific frequency range of two signals measured simultaneously. We used WPCO to explore the phase interaction between the endothelial EDHF oscillator and the MO-1 of NAD(P)H ($C\phi(\omega k)_{\text{NAD(P)H MO-1/EDHF}}$) or RR ($C\phi(\omega k)_{\text{RR MO-1/EDHF}}$) signals, which fall in the same low-frequency interval (5-9 × 10^{-3} Hz). Because our analysis does not include the surrogate data testing described recently by Gruszecki *et al.*[44], we cannot make reliable assumptions on the degree of coherence at rest due to bias affecting the low frequencies. However, we can cautiously compare differences between mice phenotypes and changes in response to PE stimulation. Non-significant differences were found for the $C\phi(\omega k)_{\text{NAD(P)H MO-1/EDHF}}$ (Fig. 5d). In contrast, baseline $C\phi(\omega k)_{\text{RR MO-1/EDHF}}$ was significantly lower in $Nrf2^{-/-}$ mice (p=0.005), and changed significantly in both groups during PE administration showing a decrease in the WT (p=0.01) and an increase in the KO (p=0.003) (Fig. 5d). These results outline again a major discriminatory power of RR MO-1 compared to NAD(P)H MO-1, suggesting that oxidative stress may impact the interaction/coupling between mitochondrial reactions and the EDHF vasodilation mechanism affecting vascular reactivity to PE.

Relevant correlations in WT mice. Fig. 6a displays the correlations between microvascular and metabolic variables observed in WT mice. We found strong negative correlations between the EDHF e_i and both NAD(P)H MO-1 e_i (r=-0.82, p=0.003) and RR MO-1 a_i (r=-0.80, p=0.002). NAD(P)H MO-1 e_i showed also high negative correlations with the energy of endothelial NO (r=-0.77, p=0.008), neurogenic (r=-0.70, p=0.02) and myogenic (r=-0.70, p=0.03) oscillators, and the RR MO-1 a_i was negatively related to blood perfusion (r=-0.70, p=0.03). None of these correlations were observed in $Nrf2^{-/-}$ mice. These results outline a robust association between the oxido-reductive fluctuations of NAD(P)H and $FADH_2$ involved in ATP biosynthesis and the activation/inactivation of microvascular regulatory mechanisms. Indeed, the correlations indicate that in response to 1% PE the spectral energy of vascular oscillators decreases as the energy of slow metabolic oscillators increases. This may reflect a change in the turnover between $NAD(P)^+$ and NAD(P)H promoting the inhibition of EDHF/NO endothelial-mediated vasodilation, and the enhancement of VSMCs-mediated vasoconstriction.

Relevant correlations in $Nrf2^{-/-}$ mice. The main correlations in knockout animals were related to the wavelet frequency *f* of the endothelial NO oscillator, which was positively correlated with NAD(P)H MO-1 e_i (r=0.60, p=0.04) and negatively correlated with SO_2 (r=-0.60, p=0.03) (Fig. 6b). These correlations might reflect the overexpression of the endothelial nitric oxide synthase (eNOS) enzyme described previously in $Nrf2^{-/-}$ mice[33], leading to major production of NO probably to balance for dysfunction in other vasodilation pathways preserving vascular function in vessels affected by oxidative stress[33]. The correlations may be consistent with this evidence because both NADPH and molecular oxygen participate in the reaction for NO biosynthesis[45]. Therefore, the increase of endothelial NO frequency correlated with the decrease of SO_2 and the increase of NAD(P)H MO-1 e_i might reflect respectively growth of NO production, consumption of molecular oxygen and oxidation of NADPH in $NADP^+$. We could speculate that a sustained NO production may compensate for dysfunction in the EDHF vasodilator activity that was found significantly lower at baseline in mice affected by oxidative stress compared to WT (Fig. 4a).

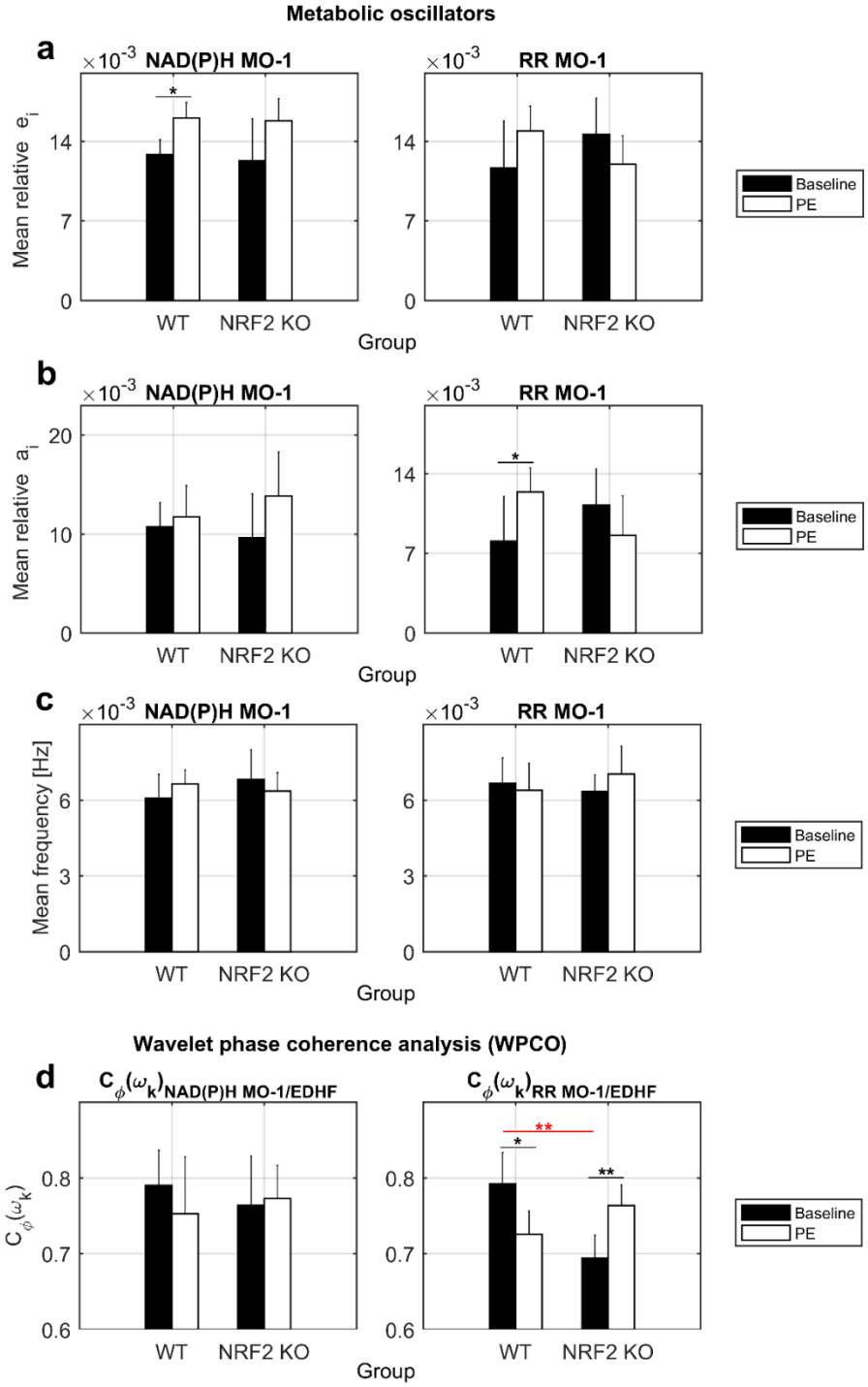

Fig. 5 Results of metabolic oscillators and WPCO analysis. (**a**) Mean energy e_i (dimensionless units), (**b**) mean amplitude a_i (dimensionless units), and (**c**) mean frequency f (Hz) of NAD(P)H and RR MO-1 wavelet peaks. (**d**) Average phase coherence $C\phi(\omega k)$ between NAD(P)H or RR MO-1 and the endothelial EDHF oscillator. The WPCO analysis is useful to study the phase relationship between low-frequency oscillators, which cannot be performed using the analysis of synchronisation due to the noisy background in the slow CWT components. The Shapiro-Wilk test revealed normal distributions for all the variables, thus data are reported as bar plots of the mean values. Error bars are referred to two SE, corresponding to a 95% CI. Black bars = Baseline. White bars = PE delivery. WT = Control mice. NRF2 KO = Knockout mice. Black lines/asterisks = Significant changes during delivery of PE estimated by paired t-test. Red lines/asterisks = Significant differences between groups estimated by unpaired t-test. The t-test was considered significant at $p < 0.05$. *$p < 0.05$, **$p < 0.01$.

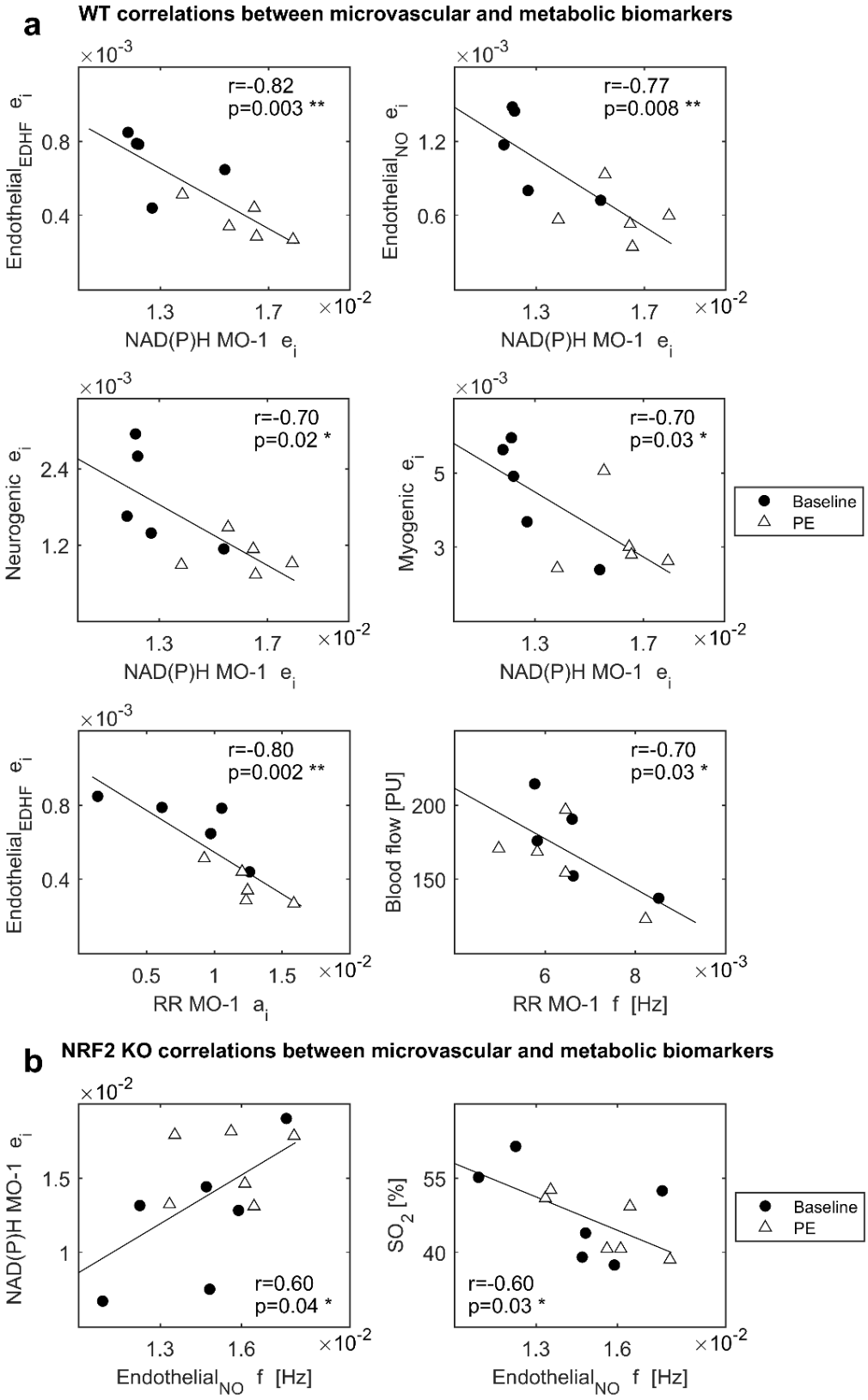

Fig. 6 Main correlations in WT and Nrf2$^{-/-}$ mice. (**a**) Relevant correlations in the WT group. (**b**) Relevant correlations in the KO group. All the variables tested in this study were normally distributed. Therefore, correlations were evaluated by estimation of the parametric Pearson's coefficient *r* using the function *corr* of MATLAB R2015a software. The correlations were considered relevant for $p < 0.05$ and values of the coefficient $r > 0.5$ or < -0.5. Black dots = Baseline. White triangles = PE administration. *$p < 0.05$, **$p < 0.01$.

Table 1. Average values of all the variables included in the study. Data are presented as mean ± Standard Deviation (SD).

PARAMETERS	WT (Mean ± SD)		Nrf2$^{-/-}$ (Mean ± SD)	
Variable name	Baseline	Phenylephrine	Baseline	Phenylephrine
Blood Perfusion [PU]	174.0 ± 30.40	162.8 ± 26.80	197.6 ± 20.50	184.0 ± 16.70
SO_2 [%]	47.3 ± 9.60	44.9 ± 10.7	48.3 ± 9.60	45.5 ± 6.10
$NAD(P)H_{normalised}$	1.7 ± 0.2	1.7 ± 0.2	1.9 ± 0.2	1.8 ± 0.1
Redox Ratio (RR)	2.2 ± 0.1	2.2 ± 0.1	2.0 ± 0.1	2.0 ± 0.1
$e_{i\ \text{Endothelial EDHF}}$	(0.7 ± 0.2) × 10^{-3}	(0.4 ± 0.1) × 10^{-3}	(0.4 ± 0.2) × 10^{-3}	(0.6 ± 0.3) × 10^{-3}
$e_{i\ \text{Endothelial NO}}$	(1.1 ± 0.3) × 10^{-3}	(0.6 ± 0.2) × 10^{-3}	(0.8 ± 0.3) × 10^{-3}	(1.0 ± 0.5) × 10^{-3}
$e_{i\ \text{Neurogenic}}$	(1.9 ± 0.8) × 10^{-3}	(1.0 ± 0.3) × 10^{-3}	(1.3 ± 0.4) × 10^{-3}	(1.5 ± 0.8) × 10^{-3}
$e_{i\ \text{Myogenic}}$	(4.5 ± 1.5) × 10^{-3}	(3.2 ± 1.1) × 10^{-3}	(3.4 ± 0.6) × 10^{-3}	(3.8 ± 1.1) × 10^{-3}
$a_{i\ \text{Endothelial EDHF}}$	(11.0 ± 2.30) × 10^{-3}	(6.10 ± 1.50) × 10^{-3}	(7.10 ± 4.10) × 10^{-3}	(8.90 ± 4.00) × 10^{-3}
$a_{i\ \text{Endothelial NO}}$	(10.6 ± 4.40) × 10^{-3}	(6.00 ± 2.60) × 10^{-3}	(7.60 ± 3.90) × 10^{-3}	(9.50 ± 5.60) × 10^{-3}
$a_{i\ \text{Neurogenic}}$	(12.9 ± 7.60) × 10^{-3}	(5.50 ± 1.80) × 10^{-3}	(8.40 ± 1.90) × 10^{-3}	(8.40 ± 4.70) × 10^{-3}
$a_{i\ \text{Myogenic}}$	(14.8 ± 6.60) × 10^{-3}	(9.70 ± 4.30) × 10^{-3}	(11.2 ± 2.40) × 10^{-3}	(12.4 ± 5.30) × 10^{-3}
$f_{\text{Endothelial EDHF}}$ [Hz]	(8.0 ± 0.6) × 10^{-3}	(6.9 ± 0.9) × 10^{-3}	(6.3 ± 1.0) × 10^{-3}	(7.7 ± 0.8) × 10^{-3}
$f_{\text{Endothelial NO}}$ [Hz]	(1.4 ± 0.1) × 10^{-2}	(1.5 ± 0.3) × 10^{-2}	(1.4 ± 0.2) × 10^{-2}	(1.5 ± 0.2) × 10^{-2}
$f_{\text{Neurogenic}}$ [Hz]	(2.8 ± 0.5) × 10^{-2}	(3.0 ± 0.7) × 10^{-2}	(3.5 ± 1.0) × 10^{-2}	(4.0 ± 1.0) × 10^{-2}
f_{Myogenic} [Hz]	(10.4 ± 1.30) × 10^{-2}	(9.30 ± 2.10) × 10^{-2}	(9.20 ± 1.70) × 10^{-2}	(9.20 ± 1.60) × 10^{-2}
$e_{i\ \text{NAD(P)H MO-1}}$	(12.8 ± 1.40) × 10^{-3}	(16.1 ± 1.50) × 10^{-3}	(12.3 ± 4.60) × 10^{-3}	(15.8 ± 2.40) × 10^{-3}
$e_{i\ \text{RR MO-1}}$	(11.7 ± 4.60) × 10^{-3}	(14.9 ± 2.50) × 10^{-3}	(14.6 ± 3.90) × 10^{-3}	(12.0 ± 3.10) × 10^{-3}
$a_{i\ \text{NAD(P)H MO-1}}$	(10.7 ± 2.70) × 10^{-3}	(11.7 ± 3.50) × 10^{-3}	(9.60 ± 5.40) × 10^{-3}	(13.8 ± 5.50) × 10^{-3}
$a_{i\ \text{RR MO-1}}$	(8.10 ± 4.40) × 10^{-3}	(12.4 ± 2.30) × 10^{-3}	(11.2 ± 3.90) × 10^{-3}	(8.60 ± 4.20) × 10^{-3}
$f_{\text{NAD(P)H MO-1}}$	(6.1 ± 1.1) × 10^{-3}	(6.6 ± 0.6) × 10^{-3}	(6.8 ± 1.4) × 10^{-3}	(6.3 ± 0.9) × 10^{-3}
$f_{\text{RR MO-1}}$	(6.7 ± 1.1) × 10^{-3}	(6.4 ± 1.2) × 10^{-3}	(6.3 ± 0.8) × 10^{-3}	(7.0 ± 1.3) × 10^{-3}
$C\phi(\omega k)_{\text{NAD(P)H MO-1/EDHF}}$	0.78 ± 0.03	0.76 ± 0.05	0.76 ± 0.05	0.79 ± 0.05
$C\phi(\omega k)_{\text{RR MO-1/EDHF}}$	0.79 ± 0.04	0.76 ± 0.02	0.74 ± 0.06	0.78 ± 0.02

Discussion

In this work, cutaneous vasomotion and cell metabolic oscillations were examined simultaneously from live mice. A vasomotion phenomenon specifically mediated by NO and EDHF endothelial mechanisms[5] was stimulated through administration of low-dose phenylephrine. Comparisons between Nrf2$^{-/-}$ mice affected by oxidative stress and WT controls revealed an opposite behaviour of vascular oscillations in the two models, indicating an effect of oxidative stress on microvascular reactivity. The most relevant differences were found especially for the endothelial EDHF oscillator, and vasomotion was more prominent in KO mice probably due to the activation of the myoendothelial feedback[16] vascular modulation in response to oxidative stress.

We characterised a low-frequency metabolic oscillator (MO-1) of NAD(P)H and RR signals that displayed different dynamics in WT and Nrf2$^{-/-}$ models, probably reflecting an alteration of the mitochondrial energetic processes due to oxidative stress. Relevant correlations were found in WT mice between metabolic and microvascular oscillators, highly suggesting an involvement of the cellular processes associated with fluctuations of NAD(P)H concentrations (i.e. OXPHOS and glycolysis) in microvascular reactivity. These correlations were absent in Nrf2$^{-/-}$ mice suggesting an influence of oxidative stress on the interaction/coupling between cell metabolic reactions and microvascular regulatory mechanisms.

Our findings indicate indirectly that cell metabolic oscillators may have an important role in modulating vasomotion in response to specific stimuli at least for oscillatory processes endothelium-mediated. Therefore, this raises interest in the study of cell mitochondrial and glycolytic oscillators to elucidate further the mechanisms driving the Ca^{2+} oscillations at the basis of vasomotion. Despite ECs seemed the microcirculation component mostly associated with slow metabolic oscillators, metabolic fluctuations were also correlated with neurogenic and myogenic components indicating a global cooperation of multiple factors during vasomotion with higher/lower contributions depending on the type of stimulus and vascular bed. In the context of skin microcirculation, primary metabolic Ca^{2+} oscillations coming from ECs and the

EDHF may represent the key drivers and regulatory factors for vasomotion. Based on our results, vasomotion can be considered an adaptive mechanism directed by the energetic requirements/stimuli in the environment surrounding blood vessels aimed at ensuring an optimal intake of nutrients (i.e. glucose) and oxygen for the production of ATP energy, rather than a process leading exclusively to the spontaneous pacemaker activity of VSMCs. This definition could help addressing better several controversial aspects, i.e. the observation of vasomotion in both healthy and diseased conditions[1,2], or the primary involvement of ECs or VSMCs in different vascular beds[1,2]. These contrasting observations may be the result of variable energetic requirements of different tissues depending on the degree of nutrition/oxygenation, the presence of a particular pathology, and the cell types involved.

The methodology used in this work can be easily translated for the concurrent study of metabolic and microvascular dynamics in humans and the exploration of metabolic oscillators as cardiovascular risk factors for diagnostic purposes. The use of LFS to monitor NAD(P)H provided some advantages, i.e. label-free minimally invasive nature of the measurements, convenient combination of LFS and LDF probes for simultaneous recordings, portability of the technology. However, there are limitations leading to the discrete nature of LFS measurements, necessity to reconstruct NAD(P)H signals to characterise the oscillators, and the inability to trace the specific cellular origin of the oscillations. Furthermore, the technique was restricted to the investigation of low-frequency fluctuations due to discrete slow sampling of the spectra. More advanced technologies for the *in-vivo* imaging of NAD(P)H, i.e. fluorescence lifetime imaging microscopy (FLIM) and multiphoton laser scanning microscopy (MPLSM), allow a better monitoring and discrimination between glycolytic and mitochondrial NAD(P)H, with high spatial-temporal resolution at cell level[31,46,47,48,49,50,51]. Combining these methods with CWT can help studying both slow and fast NAD(P)H oscillators. Nevertheless, these technologies still require further implementation for the application on humans and for providing continuous NAD(P)H recordings, they are expensive and lacking of portability and device design for combining with the LDF probe to study simultaneously metabolic and microvascular oscillators.

Methods

Animals. Animal work was conducted at the School of Medicine of the University of Dundee, after gaining approvals by the local ethics committee (Licence protocol n. 60/4265). Animals included in the research were WT (n=5) and $Nrf2^{-/-}$ (n=6) female mice on a C57Black/6 background aged 36-60 weeks. Mice were maintained under a 12:12-h light/dark cycle at 22 ± 1°C and 50% humidity, and were fed *ad libitum* on a standard rodents chow diet regime and water.

Skin preparation and anaesthesia. LFS and LDF techniques are sensitive to light absorption by hair and skin pigmentation. Therefore, a hair-free non-pigmented intact skin is required to obtain reliable measurements. Forty-eight hours prior to performing the experiments, hair from the mice flanks was shaved using an electric shaver, and the residual hair was removed using depilatory cream (Veet®, Reckitt-Benckiser). Before collecting measurements, mice were anaesthetised through a standard Boyle's Apparatus to prevent movement artefacts and were laid on a heat mat at 37°C, as described previously by us[52]. A light anaesthesia was maintained by delivering 1.5-2% isoflurane (Abbott Laboratories) in oxygen (1.5 L/minute) through an inhalation nose cone (Fig. 1a).

Iontophoresis. Iontophoresis allows the local delivery of vasoactive drugs in the skin microcirculation without inducing systemic effects. The drug is transferred transdermally by the unidirectional movement of ions in a solution, through a continuous current generated by a reference electrode and a platinum electrode incorporated in a ring-shaped chamber[52,53]. We used an iontophoresis chamber (ION6 probe, Moor Instruments, UK) of 20 mm internal diameter attached to the mouse flank using double-adhesive tape, and a reference electrode placed

underside the animal. The chamber was filled with a 2 ml 1% phenylephrine solution, and LFS and LDF probes were placed at two adjacent sites on the skin area inside the chamber (Fig. 1a). LFS/LDF signals were measured simultaneously for 20 min, 10 min without application of electric current (baseline), and 10 min during delivery of PE by applying a continuous 100 μA anodal current through a controller (MIC2, Moor Instruments, UK) connected to the electrodes.

Laser Fluorescence Spectroscopy. LFS employs a low-power laser (1-5 mW) for the *in-vivo* excitation of cell endogenous fluorophores, i.e. NAD(P)H, allowing the detection of autofluorescence emission peaks proportional to the tissue concentration of the biomarkers[54,55,56]. We assessed skin NAD(P)H autofluorescence with a single-point LFS probe (LAKK-M, Spe Lazma, Russia) provided with irradiating and detection sensors at a distance of ~1 mm for targeting a tissue volume of ~1 mm^3. Discrete 10 seconds autofluorescence spectra were sampled from the mouse flank by a 365 nm UV excitation light (1 mW) at a rate of one spectrum every minute during iontophoresis. The spectra were processed by MATLAB R2015a to extract the amplitudes of NAD(P)H (490 nm), FAD^+ (550 nm), and elastin (450 nm) peaks (Fig. 1b). The redox ratio and normalised NAD(P)H autofluorescence were estimated respectively according to equations 1 and 2. For the study of NAD(P)H and RR oscillations by CWT, 20 min continuous signals were reconstructed from the discrete data points (Fig. 1c) using the piecewise cubic spline interpolation method that we have previously described for reconstructing blood flow signals[57]. More details on signals reconstruction and NAD(P)H autofluorescence normalisation are provided in the supplementary information online.

Laser Doppler Flowmetry. LDF allows the indirect measurement of blood perfusion by sensing the Doppler-shift in wavelength generated when a monochromatic and coherent light is backscattered by moving blood cells[4,9,36,37,39,53]. We measured skin blood flow using a laser Doppler flowmeter (LAKK-M, Spe Lazma, Russia) provided with a probe identical to the LFS probe described above, which was calibrated with a fluoroplastic oscillating disk simulating Brownian motion. A 20 min LDF signal was measured during iontophoresis (Fig. 1d) using a 1064 nm laser with sampling frequency of 20 Hz. The multifunctional probe was also provided with 630 nm and 532 nm lasers, which allowed measuring the percentage skin oxygen saturation (SO_2) according to the reflectance spectroscopy principles[58].

Continuous Wavelet Transform. The CWT method is largely employed to analyse blood perfusion vasomotion dynamics in the time-frequency domain[34,37], providing optimal frequency resolution for low frequencies and good time resolution for high frequencies. We employed this method to investigate heterogeneous oscillations of LDF, NAD(P)H and RR signals, using a CWT with scaling factor *s*, time *t*, Morlet wavelet function ψ and central frequency 1 [35,36,37]:

$$g\ (s,t) = \frac{1}{\sqrt{s}} \int_{-\infty}^{\infty} \varphi \left(\frac{u-t}{s}\right) g(u) du \qquad (3)$$

CWT and the extraction of the spectral energy E_i[36], amplitude A_i[36] and frequency f [36] from the time-averaged wavelet peaks were performed using MATLAB R2015a. Fig. 3 shows examples of CWT scalograms and corresponding time-averaged spectra from LDF and NAD(P)H signals.

Wavelet phase coherence. The WPCO analysis provides information on the phase relationship $C\phi(\omega k)$ between oscillators in the same frequency interval of two signals recorded simultaneously[59]. The analysis returns values between 0 and 1, where $C\phi(\omega k) \approx 0$ indicates absence of coherence, $C\phi(\omega k) \approx 1$ complete coherence, and $0 < C\phi(\omega k) < 1$ partial coherence[59]. We investigated the coherence between MO-1 of metabolic signals and the LDF EDHF oscillator that are located in the same frequency range. The analysis was performed through the WPCO code provided in the Lancaster University website http://py-biomedical.lancaster.ac.uk by Professor Aneta Stefanovska research group, which estimates $C\phi(\omega k)$ according to the principles described by Bandrivskyy *et al.* and Clemson *et al.*[59,60].

Acknowledgments
The research leading to these results has received funding from the People Programme (Marie Curie Actions) of the European Union's Seventh Framework Programme (FP7/2007-2013) under REA grant agreement n° 608133.

Author contributions
F.K and M.P.M supervised the entire study jointly. S.S designed the experimental work in collaboration with F.K. S. S performed all the experiments, data analysis, and drafted the manuscript. A.D.M trained S.S in performing specific experimental procedures on mouse models according to the current regulations, and supervised the experimental work. Experiments were performed under R.J.M's project licence (protocol n. 60/4265). All authors edited, commented and approved the manuscript.

Additional Information
Supplementary information accompanies this paper.

Competing financial interests
The authors do not have competing financial interests to declare.

References

1. Aalkjaer, C. & Nilsson, H. Vasomotion: cellular background for the oscillator and for the synchronization of smooth muscle cells. *Br. J. Pharmacol.* **144,** 605-616 (2005).
2. Pradhan, R. K. & Chakravarthy, V. S. Informational dynamics of vasomotion in microvascular networks: a review. *Acta Physiol. (Oxf.).* **201(2),** 193-218, doi: 10.1111/j.1748-1716.2010.02198.x (2011).
3. Traikov, L., Ushiyama, A., Lawlor, G., Sasaki, R. & Ohkubo, C. Subcutaneous arteriolar vasomotion changes during and after ELF-EMF exposure in mice in vivo. *Environmentalis.* **25(2-4),** 93-101, doi:10.1007/s10669-005-4271-0 (2005).
4. Kvandal, P., Stefanovska, A., Veber, M., Kvernmo, H. D. & Arvid, K. K. Regulation of human cutaneous circulation evaluated by laser Doppler flowmetry, iontophoresis, and spectral analysis: importance of nitric oxide and prostaglandins. *Microvasc. Res.* **65(3),** 160-171 (2003).
5. Okazaki, K. *et al.* Role of the endothelium-derived hyperpolarizing factor in phenylephrine-induced oscillatory vasomotion in rat small mesenteric artery. *Anesthesiology*. **98(5),** 1164-1171 (2003).
6. Khan, F., Patterson, D., Belch, J. J., Hirata, K. & Lang, C. C. Relationship between peripheral and coronary function using laser Doppler imaging and transthoracic echocardiography. *Clin. Sci. (Lond.).* **115(9),** 295-300, doi: 10.1042/CS20070431 (2008).
7. Lefer, D. J., Lynch, C. D., Lapinski, K. C. & Hutchins, P. M. Enhanced vasomotion of cerebral arterioles in spontaneously hypertensive rats. *Microvasc. Res.* **39(2),** 129-139, doi: 10.1016/0026-2862(90)90065-Y (1990).
8. Bouskela, E. Vasomotion frequency and amplitude related to intraluminal pressure and temperature in the wing of the intact, unanesthetized bat. *Microvasc. Res.* **37(3),** 339-351 (1989).
9. Bernjak, A., Clarkson, P. B., McClintock, P. V. & Stefanovska, A. Low-frequency blood flow oscillations in congestive heart failure and after β1 blockade treatment. *Microvasc. Res.* **76(3),** 224-232, doi: 10.1016/j.mvr.2008.07.006 (2008).
10. Haddock, R. E., Hirst, G. D. & Hill, C. E. Voltage independence of vasomotion in isolated irideal arterioles of the rat. *J. Physiol.* **540(Pt1),** 219-229 (2002).
11. Lee, C. H., Poburko, D., Kuo, K. H., Seow C. Y. & Van Breemen, C. Ca(2+) oscillations, gradients, and homeostasis in vascular smooth muscle. *Am. J. Physiol. Heart Circ. Physiol.* **282(5),** H1571-H1583 (2002).
12. Peng, H. L., Matchkov, V., Ivarsen, A., Aalkjaer, C. & Nilsson, H. Hypotesis for the initiation of vasomotion. *Circ. Res.* **88(8),** 810-815 (2001).
13. Oishi, H. *et al.* Role of membrane potential in vasomotion of isolated pressurized rat arteries. *Life Sci.* **71(19),** 2239-2248 (2002).

14 Mauban, J. R. & Wier, W. G. Essential role of EDHF in the initiation and maintenance of adrenergic vasomotion in rat mesenteric arteries. *Am. J. Physiol. Heart Circ. Physiol.* **287(2),** H608-H616 (2004).

15. Rahman, A., Hughes, A., Matchkov, V., Nilsson H. & Aalkjaer, C. Antiphase oscillations of endothelium and smooth muscle [Ca2+]i in vasomotion of rat mesenteric small arteries. *Cell Calcium.* **42(6),** 536-547 (2007).

16. Kapela, A., Nagaraja, S., Parikh, J. & Tsoukias, M. Modeling Ca2+ signaling in the microcirculation: intercellular communication and vasoreactivity. *Crit. Rev. Biomed. Eng.* **39(5),** 435-460 (2011).

17. Siegel, G., Ebeling, B. J. & Hofer, H. W. Foundations of vascular rhythm. *Ber. Bunsenges. Phys. Chem.* **84(4),** 403-406, doi: 10.1002/bbpc.19800840422 (1980).

18. Siegel, G. Principles of vascular rhythmogenesis. In *Vasomotion and Quantitative Capillaroscopy* (eds. Messmer, K., Hammersen, F.) *Prog. Appl. Microcirc.* **3,** 40-62, doi: 10.1159/000409285 (Basel, Karger, 1983).

19. Siegel, G. *et al.* Autorhytmicity in blood vessels: its biophysical and biochemical bases. In *Rhythms in Physiological Systems* (eds. Haken, H., Koepchen, H. P.) *Springer Series Synergetics.* **55,** 35-60, doi: 10.1007/978-3-642-76877-4_3 (Springer, Berlin, Heidelberg, 1991).

20. Merrins, M. J., Van Dyke, A. R., Mapp, A. K., Rizzo, M. A. & Satin, L. S. Direct measurements of oscillatory glycolysis in pancreatic islets β-cells using novel fluorescence resonance energy transfer (FRET) biosensors for pyruvate kinase M2 activity. *J. Biol. Chem.* **288(46),** 33312-33322, doi: 10.1074/jbc.M113.508127 (2013).

21. Bertram, R., Satin, L. S., Pedersen, M. G., Luciani, D. S. & Sherman, A. Interaction of glycolysis and mitochondrial respiration in metabolic oscillations of pancreatic islets. *Biophys. J.* **92(5),** 1544-1555 (2007).

22. Lancaster, G., Suprunenko, Y. F., Jenkins, K. & Stefanovska, A. Modelling chronotaxicity of cellular energy metabolism to facilitate the identification of altered metabolic states. *Sci. Rep.* **6,** 29584, doi: 10.1038/srep29584 (2016).

23. Reijenga, K. A., Bakker, B. M., van der Weijden, C. C. & Westerhoff, H. V. Training of yeast cell dynamics. *FEBS J.* **272(7),** 1616-1624 (2005).

24. Reijenga, K. A. *et al.* Control of glycolytic dynamics by hexose transport in Saccharomyces cerevisiae. *Biophys. J.* **80(2),** 626-634 (2001).

25. Boiteux, A., Goldbeter, A. & Hess, B. Control of oscillating glycolysis of yeast by stochastic, periodic, and steady source of substrate: a model and experimental study. *Proc. Nat. Acad. Sci. U S A.* **72(10),** 3829-3833 (1975).

26. Olsen, L. F., Andersen, A. Z., Lunding, A., Brasen, J. C. & Poulsen, A. K. Regulation of glycolytic oscillations by mitochondrial and plasma membrane H+-ATPases. *Biophys. J.* **96(9),** 3850-3861, doi:10.1016/j.bpj.2009.02.026 (2009).

27. Aon, M. A., Cortassa, S., Lemar, K. M., Hayes, A. J. & Lloyd, D. Single and cell population respiratory oscillations in yeast: A 2-photon scanning laser microscopy study. *FEBS Lett.* **581(1),** 8-14 (2007).

28. Luciani, D. S., Misler, S. & Polonsky, K. S. Ca2+ controls slow NAD(P)H oscillations in glucose-stimulated mouse pancreatic islets. *J. Physiol.* **572(Pt 2),** 379-392 (2006).

29. Aon, M. A., Cortassa, S., Marbán, E. & O'Rourke, B. Synchronized whole cell oscillations in mitochondrial metabolism triggered by a local release of reactive oxygen species in cardiac myocytes. *J. Biol. Chem.* **278(45),** 44735-44744 (2003).

30. Chou, H. F., Berman N. & Ipp., E. Oscillations of lactate released from islets of Langerhans: evidence for oscillatory glycolysis in beta-cells. *Am. J. Physiol.* **262(6 Pt 1),** E800-E805 (1992).

31. Porat-Shilom, N. *et al.* In vivo tissue-wide synchronization of mitochondrial metabolic oscillations. *Cell Rep.* **9(2),** 514-521, doi:10.1016/j.celrep.2014.09.022 (2014).

32. Hayes, J. D. & Dinkova-Kostova, A. T. The Nrf2 regulatory network provides an interface between redox and intermediary metabolism. *Trends Biochem. Sci.* **39(4),** 199-218, doi: 10.1016/j.tibs.2014.02.002 (2014).

33. Erkens, R. *et al.* Left ventricular diastolic dysfunction in Nrf2 knock out mice is associated with cardiac hyopertrophy, decreased expression of SERCA2a, and preserved endothelial function. *Free Radic. Biol. Med.,* **89,** 906-917, doi:10.1016/j.freeradbiomed.2015.10.409 (2015).

34. Bračič, M. & Stefanovska, A. Wavelet-based analysis of human blood-flow dynamics. *Bull. Math. Biol.* **60(5),** 919-935 (1998).
35. Lancaster, G. *et al.* Dynamic markers based on blood perfusion fluctuations for selecting skin melanocytic lesions for biopsy. *Sci. Rep.* **5,** 12825, doi: 10.1038/srep12825 (2015).
36. Shiogai, Y., Stefanovska, A. & McClintok, P. V. Nonlinear dynamics of cardiovascular ageing. *Phys. Rep.* **488(2-3),** 51-110 (2010).
37. Stefanovska, A., Bračič, M. & Kvernmo, H. D. Wavelet analysis of oscillations in the peripheral blood circulation measured by laser Doppler technique. *IEEE Trans. Biomed. Eng.* **46(10),** 1230–1239 (1999).
38. Kvandal, P. *et al.* Low frequency oscillations of the laser Doppler perfusion signal in human skin. *Microvasc. Res.* **72(3),** 120-127 (2006).
39. Ho, D. *et al.* Heart rate and electrocardiography monitoring in mice. *Curr. Protoc. Mouse Biol.* **1,** 123-139 (2011).
40. Ewald, A. J., Werb Z. & Egeblad, M. Monitoring of vital signs for long-term survival of mice under anesthesia. *Cold Spring Harb. Protoc.* **2,** pdb.prot5563, doi: 10.1101/pdb.prot5563 (2011).
41. Landsverk, S. A., Kvandal, P., Bernjak, A., Stefanovska, A. & Kirkeboen, K. A. The effects of general anesthesia on human skin microcirculation evaluated by wavelet transform. *Anesth. Analg.,* **105(4),** 1012-1019 (2007).
42. Iatsenko, D., McClintock, P. V. E. & Stefanovska, A. Linear and synchrosqueezed time-frequency representations revisited: overview, standards of use, resolution, reconstruction, concentration, and algorithms. *Digit. Sig. Process.* **42,** 1-26, doi: 10.1016/j.dsp.2015.03.004 (2015).
43. Kvernmo, H. D., Stefanovska, A., Kirkebøen, K. A. & Kvernebo, K. Oscillations in the human cutaneous blood perfusion signal modified by endothelium-dependent and endothelium-independent vasodilators. *Microvasc. Res.* **57(3),** 298-309 (1999).
44. Gruszecki, M. *et al.* Human subarachnoid space width oscillations in the resting state. *Sci. Rep.* **8,** 3057, doi: 10.1038/s41598-018-21038-0 (2018).
45. Förstermann, U. & Sessa, W. C. Nitric oxide synthases: regulation and function. *Eur. Heart J.* **33(7),** 829a-837d, doi: 10.1093/eurheartj/ehr304 (2012).
46. Szulczewski, J. M. *et al.* In vivo visualization of stromal macrophages via label-free FLIM-based metabolite imaging. *Sci. Rep.* **6,** 25086, doi: 10.1038/srep25086 (2016).
47. Shah, A. T., Diggins, K. E., Walsh, A. J., Irish, J. M. & Skala, M. C. In vivo autofluorescence imaging of tumor heterogeneity in response to treatment. *Neoplasia* **17(12),** 862–870, doi:10.1016/j.neo.2015.11.006 (2015).
48. Wu, Z. *et al.* Multi-photon microscopy in cardiovascular research. *Methods.* **130,** 79-89, doi: 10.1016/j.ymeth.2017.04.013 (2017).
49. Walsh, A. J. *et al.* Optical metabolic imaging identifies glycolytic levels, subtypes, and early-treatment response in breast cancer. *Cancer Res.* **73(20),** 6164-74, doi: 10.1158/0008-5472 (2013).
50. Balu, M. *et al.* In vivo multiphoton NADH fluorescence reveals depth-dependent keratinocyte metabolism in human skin. *Biophys. J.* **104(1),** 258-67, doi: 10.1016/j.bpj.2012.11.3809 (2013).
51. Breunig, H. G., Studier, H. & König, K. Multiphoton excitation characteristics of cellular fluorophores of human skin in vivo. *Opt. Express.* **18(8),** 7857-71, doi: 10.1364/OE.18.007857 (2010).
52. Belch, J. J. *et al.* Longitudinal assessment of endothelial function in the microvasculature of mice in-vivo. *Microvasc. Res.* **85,** 86-92, doi: 10.1016/j.mvr.2012.10.008 (2013).
53. Turner, J., Belch, J. J. & Khan, F. Current concepts in assessment of microvascular endothelial function using laser Doppler imaging and iontophoresis. *Trends Cardiovasc. Med.* **18(4),** 109-16, doi: 10.1016/j.tcm.2008.02.001 (2008).
54. Mayevsky, A. & Rogatsky, G. G. Mitochondrial function in vivo evaluated by NADH fluorescence: from animal models to human studies. *Am. J. Physiol. Cell Physiol.* **292(2),** C615-40 (2007).
55. Croce, A. C. & Bottiroli, G. Autofluorescence spectroscopy and imaging: a tool for biomedical research and diagnosis. *Eur. J. Histochem.* 58(4), 2461, doi: 10.4081/ejh.2014.2461 (2014).

56. Heikal, A. A. Intracellular coenzymes as natural biomarkers for metabolic activities and mitochondrial anomalies. *Biomark. Med.* **4(2),** 241-63, doi: 10.2217/bmm.10.1 (2010).

57. Smirni, S. *et al.* In-vivo assessment of microvascular functional dynamics by combination of cmOCT and wavelet transform. *Proc. SPIE 10493, Dynamics and Fluctuations in Biomedical Photonics XV.* **104930P,** doi: 10.1117/12.2289814 (2018).

58. Wallace, M. B., Wax, A., Roberts, D. N. & Graf, R. N. Reflectance Spectroscopy. *Gastrointest. Endosc. Clin. N. Am.* **19(2),** 233–242, doi: 10.1016/j.giec.2009.02.008 (2009).

59. Bandrivskyy, A., Bernjak, A., McClintok, P. & Stefanovska, A. Wavelet phase coherence analysis: application to skin temperature and blood flow. *Cardiovasc. Eng.* **4(1),** 89-93, doi: 10.1023/B:CARE.0000025126.63253.43 (2004).

60. Clemson, P., Lancaster, G. & Stefanovska, A. Reconstructing time-dependent dynamics. *Proc. IEEE,* **104(2),** 223-241, doi: 10.1109/JPROC.2015.2491262 (2016).

Supplementary information

In-vivo multi-parameter optical measurements show correlations between skin metabolic oscillations and vasomotion

Salvatore Smirni[1,*], Alison D. McNeilly[1], Michael P. MacDonald[1,2], Rory J. McCrimmon[1] & Faisel Khan[1,*]

[1]School of Medicine, Ninewells Hospital, University of Dundee, Scotland, UK
[2]School of Science and Engineering, University of Dundee, Scotland, UK
*Corresponding authors: salvatore.smirni@gmail.com
f.khan@dundee.ac.uk

Biological origin of the LDF endothelial nitric oxide (NO)-independent wavelet oscillator

The physiological origin of the endothelial NO-independent wavelet oscillator (5-9.5 × 10^{-3} Hz) of skin LDF signals has not been completely elucidated. The endothelial origin of this oscillator has been proved by experiments showing relevant changes of its wavelet amplitude during the cutaneous administration of acetylcholine (ACh) [1, 2], a vasoactive agent able to stimulate multiple endothelial-mediated vasodilation mechanisms including NO, prostaglandins (PGs) and the endothelial-derived hyperpolarizing factor (EDHF) pathways. Moreover, blocking both NO or PGs mechanisms respectively by administration of L-NMMA (N^G-monomethyl-l-arginine) and aspirin did not affect the endothelial NO-independent oscillation [1, 2]. These evidences suggest indirectly a more likely biological link of this oscillator with an endothelial vasodilator mechanism different from NO and PGs that could be with high probability the EDHF pathway. The results that we have presented in this paper might support indirectly this hypothesis. Indeed, according to Okazaki *et al.* [3], the vasoconstriction stimulated by administration of phenylephrine (PE) in rat mesenteric artery is able to enhance a vasomotion phenomenon mediated specifically by NO and EDHF mechanisms but not by PGs. Even if in this work we have tested micro-vessels different from the rat mesenteric artery (skin micro-vessels), the results seem to agree with what has been reported by Okazaki *et al.* [3]. Indeed, as we have discussed in Figure 4 of this paper, the oscillators showing the most statistically significant changes during PE stimulation were the endothelial NO and endothelial NO-independent components. Considering that the NO origin of the 9-20 × 10^{-3} Hz oscillation has been already recognised [4], by exclusion, the high significant changes that we found in the 5-9 × 10^{-3} Hz interval after PE stimulation should be ascribed to the EDHF activity.

Furthermore, according to the literature EDHF plays a more important role than NO in the reactivity of small resistance arterioles [5, 6, 7, 8]. Our results, discussed in Figure 4 of the manuscript, have displayed changes that are more significant for the endothelial NO-independent frequency range compared to the endothelial NO interval, which would support an EDHF origin of this oscillator and its major involvement in the reactivity of small arterioles [5, 6, 7, 8].

Additional indirect proof of the possible EDHF origin for the endothelial NO-independent oscillator was also provided by experimental data that we have obtained from human subjects. We have measured blood flow signals by LDF method from the forearm of 40 individuals during a 25 min post-occlusive reactive hyperaemia (PORH) functional test, using the same LDF single-point probe employed in this study (LAKK-M, Spe Lazma, Russia) that we have already described in the methods section. All of the tested subjects signed an informed consent form before performing the experiment, as part of a research project approved by the University of Dundee Research Ethics Committee (UREC, Study n. 15064) according to the guidelines of the declaration of Helsinki. The PORH test was divided in three main steps (supplementary **Figure S1**):

(1) Measurement of the LDF signal for 10 min at rest (baseline).
(2) Blocking blood flow through the brachial artery for 5 min, by inflating a pressure cuff placed in the upper part of the tested arm at 200 mmHg. This step is characterised by a massive decrease of LDF signal because of a temporary ischaemia condition induced by the occlusion of flow.
(3) Release of the cuff's pressure and monitoring for 10 min the PORH response stimulated by the previous occlusion of flow. PORH response is consistent with a massive increase of blood flow up to

a peak for the fast reperfusion of the cutaneous tissue after a temporary period of occlusion, and the subsequent restoration of the basal blood flow.

All the LDF signals collected during PORH stimulation from the 40 tested subjects were processed by continuous wavelet transform (CWT) spectral analysis to determine the contribution of each LDF oscillator to skin PORH response. The CWT analysis was performed according to the same methodology that we have already discussed in the methods section of this paper. The results have revealed a median percentage increase of wavelet amplitude/energy during PORH compared to baseline much higher for the endothelial NO-independent (EDHF) oscillator (58.3-72.3%) compared to the other LDF oscillators (supplementary **Table S1**). According to the literature, the EDHF mechanism is the major mediator contributing to human skin PORH response [9], thus considering that the endothelial NO-independent wavelet peak showed the highest contribution to the cutaneous hyperaemic response our findings represent a robust indirect proof of the EDHF origin of this oscillator. As future perspective, direct proof may be provided from either mouse models or humans by monitoring the behaviour of this LDF wavelet oscillator during the inhibition of the EDHF vasodilation mechanism. This task can be achieved in mouse models by blocking EDHF through a combination of the inhibitors of K^+ channels apamin (APA) and charybdotoxin (ChTX) [10]. Examples of pharmacological agents that might be applied for the same purpose in human skin are the fluconazole or sulfaphenazole for blocking locally the EDHF mechanism mediated by the epoxyeicosatrienoic metabolites (EETs) [11], and the tetraethylammonium (TEA) for the local inhibition of the EDHF mechanism mediated by KCa channels [12].

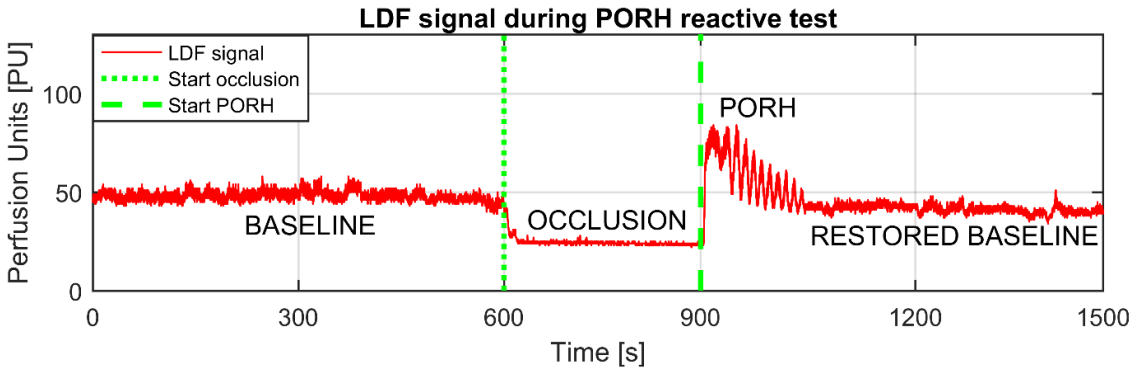

Figure S1. Example of LDF signal collected from the human forearm during PORH test. Data are expressed in perfusion arbitrary units (PU). The graph shows the typical trend of LDF signal during a 25 min PORH test. The first 10 min represent the baseline blood flow. Then the pressure cuff was inflated at 200 mmHg to induce an ischaemia period of 5 min characterised by decrease of flow. Finally, the pressure of the cuff was released to monitor PORH response and the restoration of resting blood flow for 10 min.

Table S1. Percentage increase of the relative wavelet amplitude a_i and energy e_i of LDF oscillators during skin PORH response. The Shapiro-Wilk test performed by R-Studio software has revealed non-parametric distributions for all the variables. Thus, data are reported as median (inter-quartile range). n = Number of tested subjects. The increase of wavelet amplitude/energy was evaluated as percentage growth during PORH response compared to baseline.

PARAMETERS	n=40
Variable name	Median (inter-quartile range)
$e_{i\ \text{Endothelial EDHF}}$ increase [%]	58.3 (48.3-79.3)
$e_{i\ \text{Endothelial NO}}$ increase [%]	27.2 (14.0-33.1)
$e_{i\ \text{Neurogenic}}$ increase [%]	5.60 (1.70-11.2)
$e_{i\ \text{Myogenic}}$ increase [%]	5.50 (0.90-7.00)
$a_{i\ \text{Endothelial EDHF}}$ increase [%]	72.3 (57.7-89.8)
$a_{i\ \text{Endothelial NO}}$ increase [%]	18.3 (8.10-28.0)
$a_{i\ \text{Neurogenic}}$ increase [%]	1.30 (0.10-7.50)
$a_{i\ \text{Myogenic}}$ increase [%]	2.40 (0.50-6.00)

Reconstruction of NAD(P)H and RR continuous time series by piecewise cubic spline interpolation

In this work, the *in-vivo* investigation of metabolic oscillations from mice skin was achieved by the application of the CWT spectral analysis on NAD(P)H and RR_{index} signals. Considering that the CWT can be applied only on continuous time series, the reconstruction of NAD(P)H and RR_{index} signals from discrete UV autofluorescence spectra was a key step to allow the characterisation of metabolic oscillations. The reconstruction was performed in two steps by using the software Matlab R2015a, according to the same methodology previously described by us for the reconstruction of continuous blood flow signals from discrete data points [13]. First, the discrete values of $NAD(P)H_{normalised}$ (equation 2 in the manuscript) and RR_{index} (equation 1 in the manuscript) were extracted from the 20 sequential UV autofluorescence spectra measured over time during iontophoresis test. Finally, the values were used as discrete data points to reconstruct a continuous curve covering the whole 20 min period used in the experiment for acquiring the spectra. The reconstruction was performed by piecewise cubic spline interpolation, applying an interval of 1 min between each pair of data points that corresponds to the sampling frequency adopted during the temporal collection of the spectra.

The spline interpolation technique is a mathematical procedure based on the use of a piecewise low-degree polynomial called spline for the approximation of a continuous function *g* by interpolating equally spaced discrete data points of the function [13]. The main advantage of this technique is the accurate approximation of a function over large intervals, avoiding and reducing errors during the interpolation process, i.e. the introduction of oscillatory artefacts between each pair of data points (Runge's phenomenon) which is typical of interpolation processes performed by using a single high-degree polynomial [13]. The spline interpolation process consists in subdividing the interval [a, b] where *g* is continuous in smaller sub-intervals, and approximating *g* in each sub-interval using low-degree polynomial pieces that define a composite spline function *s* [13]. In this work, we used a cubic (third-degree) spline function which is suitable for reconstructing continuous natural processes, and requires four terms to define a piecewise polynomial between each pair of data points, as displayed by the supplementary **equation S1** [13],

$$p_3(x) = ax^3 + bx^2 + cx + d, \quad \text{(S1)}$$

where p_3 is the piecewise third-degree polynomial, and *a*, *b*, *c* and *d* are the four terms defining p_3. The final curve resulting from the cubic spline interpolation process is made of a number of pieces reconstructed between each pair of data points equal to *1-n*, where *n* is the number of data points [13]. Therefore, considering that the number of $NAD(P)H_{normalised}$ and RR_{index} discrete values used in this study during the interpolation process was 20, we have obtained NAD(P)H and RR_{index} reconstructed curves made of 19 pieces (supplementary **Figure S2**).

Considering that the cubic spline interpolation method does not introduce oscillatory artefacts in the reconstructed signal [13], by using this technique we have ensured that the results of the subsequent CWT spectral analysis were reflecting the real oscillatory behaviour of NAD(P)H and RR_{index} detected by autofluorescence recordings. Nonetheless, a limit of this technique is poor accuracy in the reconstruction of the right and left extremities of the signal [13]. Thus, to avoid artefacts at the edges of the signal the time series was cut at the extremities making sure that the starting and ending points of the curve were corresponding respectively to the first and last experimental discrete data points [13].

Normalisation of NAD(P)H to reduce blood volume and skin pigmentation effects

As already explained in the methods section of this paper, we have evaluated the relative changes of NAD(P)H concentrations and mitochondrial function (RR_{index}) from live mice skin by ratiometric normalisation of NAD(P)H fluorescence, respectively by the autofluorescence of the structural protein elastin (450 nm) and of the coenzyme FAD^+ (550 nm). The reason for the normalisation was reducing the effect of blood volume and cutaneous melanin on NAD(P)H autofluorescence signal for obtaining a more accurate assessment of cellular metabolic oscillations over time. Indeed, a major problem when evaluating the UV autofluorescence from *in-vivo* skin is that the signal is highly affected by artefacts due to absorption of UV light by cutaneous chromophores, i.e. haemoglobin (Hb) in the blood of micro-vessels and melanin pigmentation [14, 15]. This is clearly visible in supplementary **Figure S3a-b** and supplementary **Figure S4a-b**, which show respectively the effects of blood volume changes and melanin on the reconstructed NAD(P)H autofluorescence signal obtained from measurements collected using the LAKK-M probe (Spe Lazma Ltd, Russia).

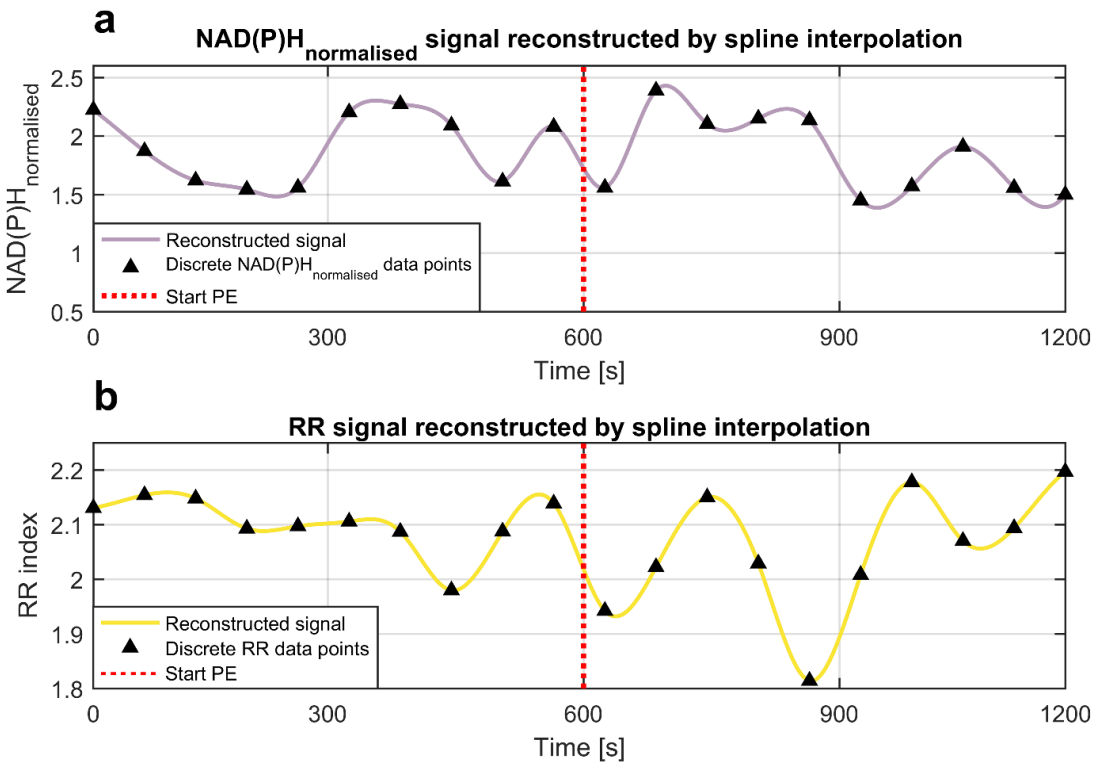

Figure S2. Examples of signals reconstructed by cubic spline interpolation of discrete data points. (**a**) 20 min NAD(P)H signal reconstructed using $NAD(P)H_{normalised}$ values extracted from 20 sequential discrete UV autofluorescence spectra measured from the flank of a mouse during a 20 min iontophoresis test. (**b**) 20 min RR_{index} continuous signal obtained using RR_{index} values estimated from 20 sequential discrete UV autofluorescence spectra measured from the flank of a mouse during a 20 min iontophoresis test. An interval of 1 min was applied between each pair of data points, which corresponds to the sampling frequency used for the temporal acquisition of the UV spectra (1 spectrum per minute). Both the reconstructed signals are made of 19 pieces (n-1, where n is the number of discrete data points) with the starting and ending points of the curve corresponding to the first and last experimental data points used for the reconstruction to avoid the presence of oscillatory artefacts at the extremities of the time series.

Supplementary **Figure S3** displays the trends of simultaneous median LDF (**Figure S3a**) and reconstructed NAD(P)H autofluorescence (**Figure S3b**) signals that we have measured from the forearm of human subjects (n=16) during a 25 min PORH test. The graphs clearly show a massive decrease of NAD(P)H autofluorescence signal intensity concurrent to the increase of blood flow/volume during PORH response. This observation clearly outlines the negative effect of blood volume changes on NAD(P)H signal due to absorption of UV light by Hb, which makes the measurements unreliable for the evaluation of NAD(P)H oscillations over time.

Supplementary **Figure S4** displays the trends of simultaneous median LDF (**Figure S4a**) and reconstructed NAD(P)H autofluorescence (**Figure S4b**) signals that we have measured from the forearm of subjects with dark skin (n=8) and white skin (n=8) during a 25 min PORH test. The graphs clearly show that while the colour of skin does not affect LDF measurements, the intensity of NAD(P)H autofluorescence signal is highly reduced in individuals with dark skin that is characterised by a major content of melanin pigmentation. However, while melanin absorption may represent a major problem for the evaluation of the absolute quantitative concentrations of NAD(P)H, also in this case the effect of blood volume seems to be the major obstacle for making a reliable assessment of the relative oscillatory changes of NAD(P)H over time which was the main goal of this work.

A widespread method used for the correction of NAD(P)H UV autofluorescence artefacts is the 1:1 ratio with another variable affected by the same artefacts, e.g. skin reflectance signal [14], in order to compensate for NAD(P)H unrelated factors obtaining a normalised signal which should reflect more reliably the relative temporal trends of NAD(P)H. In this work, we did not have the chance to measure skin

reflectance signal, thus we have taken advantage of the overlapping contributions in the UV spectrum of elastin and FAD^+ autofluorescence to perform 1:1 ratiometric corrections of NAD(P)H autofluorescence.

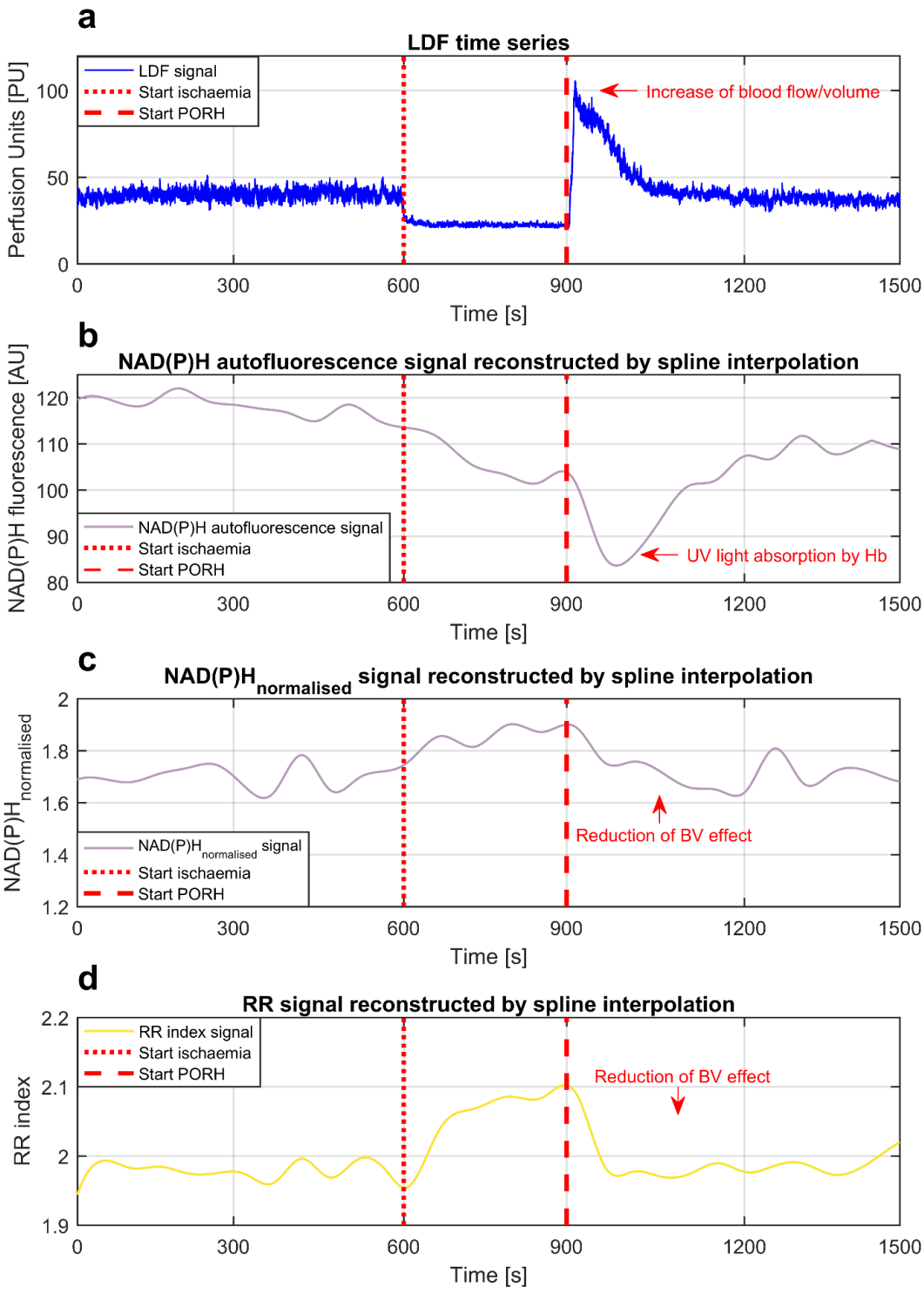

Figure S3. Correction of NAD(P)H autofluorescence signal to reduce blood volume effects. Examples of simultaneous median (**a**) LDF (PU) and (**b**) reconstructed NAD(P)H autofluorescence (AU) signals measured from the forearm of 16 human subjects during a 25 min PORH test. The graphs clearly display the absorption of UV light by Hb affecting NAD(P)H autofluorescence signal during PORH response due to increase of blood perfusion/volume. (**c**) 1:1 ratiometric normalisation of NAD(P)H signal by the autofluorescence of the structural protein elastin [$NAD(P)H_{normalised}$ expressed in dimensionless units]. (**d**) 1:1 ratiometric normalisation of NAD(P)H signal by the autofluorescence of FAD^+ coenzyme (RR_{index} expressed in dimensionless units). Normalised signals reflect more reliably the trends of NAD(P)H and mitochondrial oxido-reductive dynamics expected during PORH functional test.

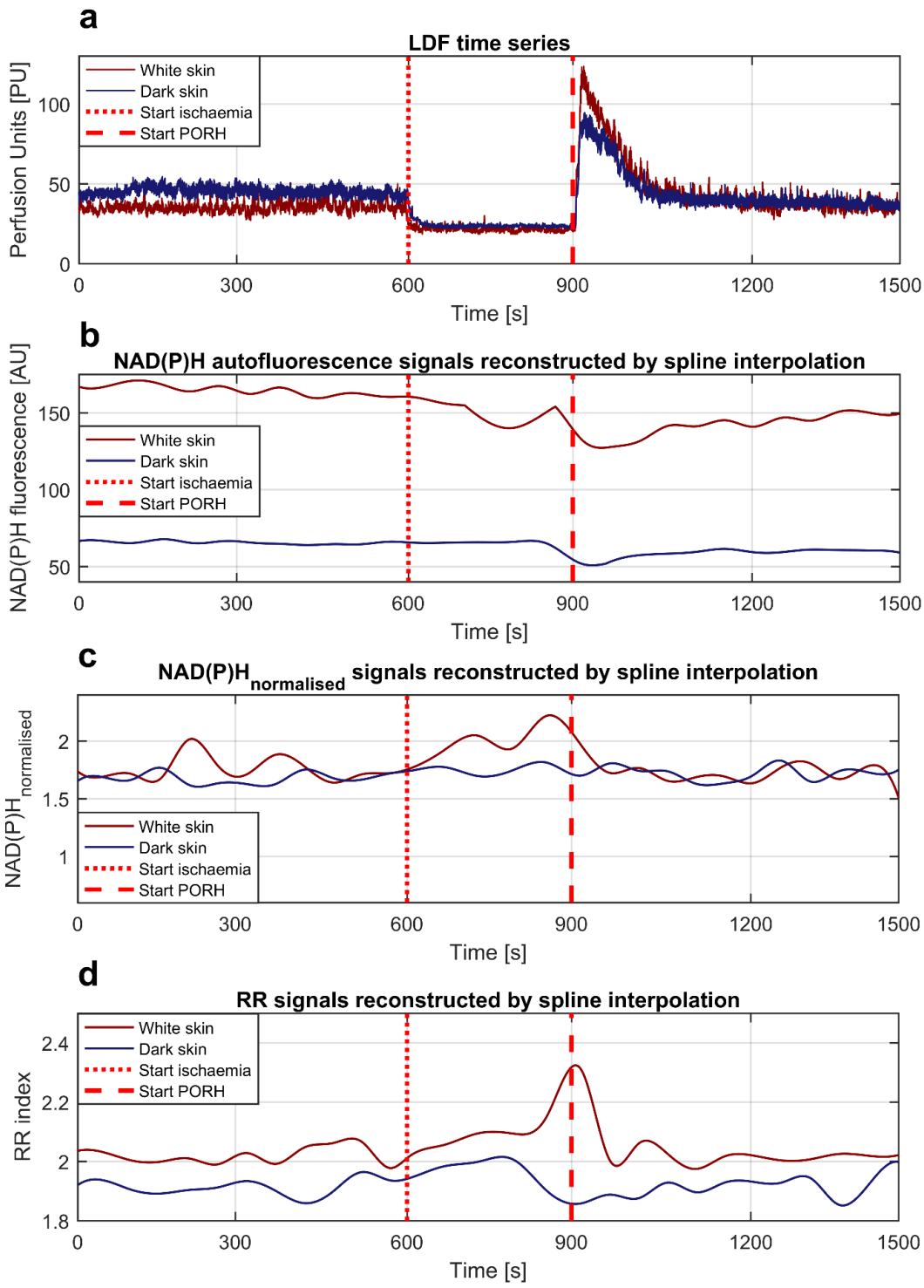

Figure S4. Effects of melanin pigmentation on NAD(P)H autofluorescence signal. Examples of simultaneous median (**a**) LDF (PU) and (**b**) reconstructed NAD(P)H autofluorescence (AU) signals measured from the forearm of 8 subjects with white skin (dark red lines) and 8 individuals with dark skin (dark blue lines) during a 25 min PORH test. The graphs clearly display that the LDF signal is not affected by different amounts of cutaneous melanin pigmentation. In contrast, the intensity of NAD(P)H autofluorescence signal was highly reduced in subjects with dark skin due to the major content of melanin absorbing UV light. (**c**) 1:1 ratiometric normalisation of NAD(P)H signals by the autofluorescence of the structural protein elastin [$NAD(P)H_{normalised}$ expressed in dimensionless units]. (**d**) 1:1 ratiometric normalisation of NAD(P)H signal by the autofluorescence of FAD^+ coenzyme (RR_{index} expressed in dimensionless units). Normalised signals were characterised by reduced blood volume effect reflecting more reliably the trends of NAD(P)H and mitochondrial oxido-reductive dynamics expected during PORH functional test, and seemed to be suitable for making acceptable comparisons of temporal oscillatory dynamics between subjects with different skin pigmentation.

Elastin is an abundant structural component in the connective tissue of the dermal cutaneous layer [15, 16]. The reason for using the autofluorescence of this protein as correction factor is that being a structural component it should maintain a constant amount in the cutaneous tissue during the temporal period employed for the collection of autofluorescence data. Therefore, normalising the autofluorescence by elastin represents an intra-subject compensation for micro-environmental factors unrelated to NAD(P)H, i.e. Hb and melanin absorption, and the resulting signal should be more representative of NAD(P)H temporal dynamics considering the constant amounts of elastin in the tissue during the temporal acquisition of UV spectra. The autofluorescence emission wavelength of elastin after excitation with UV light is between 400-450 nm and could be affected by an overlapping contribution of collagen autofluorescence (390-460 nm) [15, 16]. However, considering that also collagen is a structural component abundant in the dermal connective tissue this should not represent a major problem because also this protein should present constant amounts in the skin during the temporal window employed for acquiring the UV spectra. **Figure S3c** shows the trend of NAD(P)H signal during PORH test after normalisation by elastin autofluorescence. The graph clearly displays a reduction of blood volume effect compared to **Figure S3b**, and a temporal trend of NAD(P)H which seems to reflect more reliably the relative changes in the concentrations of this coenzyme during PORH test. Indeed, $NAD(P)H_{normalised}$ signal increased during the 5 min occlusion of blood flow, probably reflecting the uncoupling of the electron transport chain and the inhibition of ATP production through the oxidative phosphorylation (OXPHOS) mitochondrial process due to reduced intake of oxygen and accumulation of reduced NAD(P)H [14]. In contrast, the moderate decrease of NAD(P)H during PORH response in this case may reflect the oxidation of NAD(P)H in $NAD(P)^+$ due to the restoration of a normal aerobic metabolism and increased production of ATP [14] rather than an artefact due to Hb absorption. Similar results are shown in **Figure S4c** demonstrating that $NAD(P)H_{normalised}$ signal is not affected by skin pigmentation and seems more reliable to compare the temporal oscillatory behaviour of NAD(P)H between cutaneous samples with different amounts of melanin.

The estimation of the redox ratio (RR_{index}) by normalising NAD(P)H autofluorescence for the fluorescence of the coenzyme FAD^+ provided also optimal results. This index is a measure of the balance between the reduced form of NAD(P)H and the oxidised FAD^+, which reflects specifically the activity of the mitochondrial electron transport chain and the degree of ATP energy production through the OXPHOS process [14, 17]. The interpretation of RR_{index} values may vary depending on the kind of stimulus affecting mitochondrial function, the degree of oxygenation, or the presence of particular pathologic conditions (e.g. cancer). **Figure S3d** displays the trend of RR_{index} during PORH functional test, which seems to reflect reliably the changes of mitochondrial activity associated with a temporary ischaemia period and PORH response. The relevant increase of RR_{index} during ischaemia may reflect a preferential production of ATP through the glycolysis process in the presence of lower tissue oxygenation, due to accumulation of mitochondrial NAD(P)H and uncoupling of the electron transport chain. In contrast, the restoration of the baseline RR_{index} trend observed during PORH response may reflect the reactivation of the aerobic metabolism, oxidation of NAD(P)H in $NAD(P)^+$ and increase of ATP production through the OXPHOS cycle**.** **Figure S4d** displays the comparison of RR_{index} trends between subjects with dark coloured skin and individuals with white skin. The signals showed a trend similar to the RR_{index} signal in **Figure S3d**, reflecting the oxido-reductive mitochondrial dynamics expected during PORH test. Although the values of RR_{index} were slightly higher in the group of individuals with white skin, the signals seem to be comparable for an acceptable evaluation of the temporal RR_{index} oscillatory dynamics that was the main goal of this work.

The concurrent multi-parametric monitoring of LDF and autofluorescence signals during PORH test was helpful to optimise the correction of autofluorescence data, allowing the easy detection of non-physiological responses affecting NAD(P)H autofluorescence (i.e. effect of UV light absorption by Hb) and a better explanation of the physiological processes reflected by NAD(P)H signal. The application of the ratiometric normalisation approach provided time series with an acceptable degree of reliability for the evaluation of temporal metabolic oscillations, thus we decided to apply the same correction method on mice data presented in this work. Nonetheless, although the correction techniques used in this study allowed performing an acceptable evaluation of NAD(P)H oscillations, the development of more accurate, successful, and practical correction methods is still challenging. A promising approach for the future that

we are pursuing is the Monte Carlo modelling of skin autofluorescence measurements to determine the interaction of the UV light with the cutaneous tissue, and the path of the photons detected by the single-point probe used for the measurements. This approach may help to characterise and quantify better the effects of blood volume and melanin on the autofluorescence signal and the implementation of more precise correction methods.

Spatial resolution of LFS measurements and cellular origin of the metabolic oscillators

A shortcoming of laser fluorescence spectroscopy (LFS) is the inability to quantify the contribution of specific groups of cells to the detected autofluorescence signal, due to the uncertain spatial resolution of the measurements and the heterogeneous structure of skin. Indeed, the cutaneous tissue includes cells from different layers (e.g. epidermal cells) and functional components such as micro-vessels (i.e. endothelial cells and vascular smooth muscle cells). Therefore, this makes it difficult also the characterisation of the cellular origin of the metabolic oscillators investigated in this work.

According to the literature, The 365 nm UVA wavelength has a penetration depth incorporating the human upper dermal skin layer [18, 19], where capillaries and arterioles are located. In mice, the epidermis is thinner than in humans [20], thus the UVA light should target the core of the dermal layer. This suggests that a relevant part of the detected autofluorescence signal is derived from the microcirculation network, which was the main tissue of interest in this research. The relevant correlations that we have found in this work between microvascular and metabolic oscillations may represent an indirect proof that part of skin metabolic oscillations is of microvascular origin, even though the correlations could also reflect the activation of vasomotion in response to the energetic/nutritive requirements and oscillatory stimuli coming from other cutaneous cell types (e.g. epidermal cells).

Finally, according to ongoing Monte Carlo modelling studies that we are performing in collaboration with a research group of the University of St. Andrews (Scotland, UK), the penetration depth of the UV laser of the device used in this study (LAKK-M, Spe Lazma Ltd, Russia) is around 200 µm (supplementary **Figure S5**). This evidence would support both an epidermal and a dermal origin of skin autofluorescence stimulated by UV light.

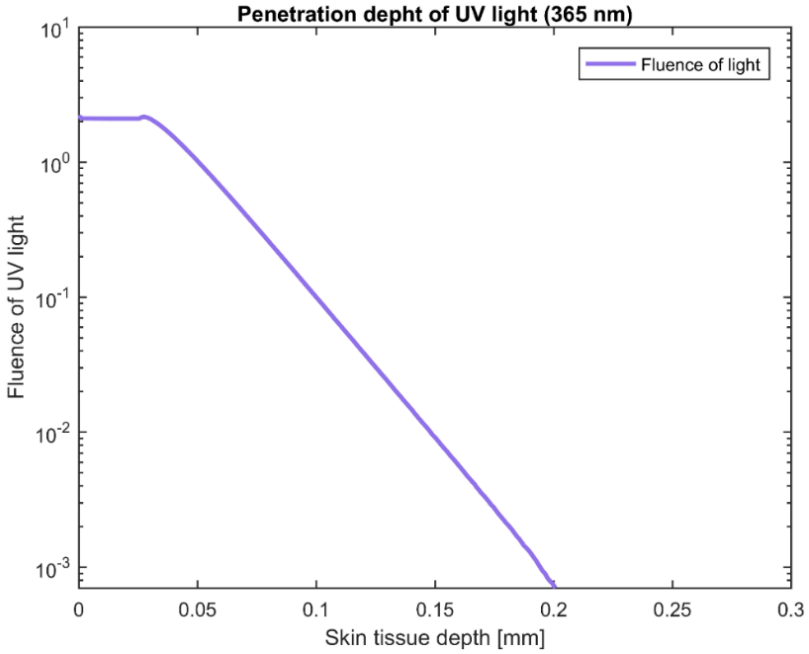

Figure S5. Monte Carlo modelling of LAKK-M UV laser (365 nm) penetration depth. The propagation of UV light was simulated in a five layers cutaneous model composed of stratum corneum, epidermis, papillary dermis, reticular dermis and hypodermis. Each layer was populated with various skin natural absorbers and scatterers: water, fat, oxy-Hb, deoxy-Hb, eumelanin, pheomelanin, bilirubin, β-carotene and a baseline absorber. A penetration depth of ~0.2 mm was predicted, which should correspond to the upper dermis of human skin and the median dermis of mouse skin. Data were kindly provided by Mr Lewis McMillan and Dr Kenneth Wood from the Astronomy group at the University of St. Andrews (Scotland, UK).

References

[1] Shiogai, Y., Stefanovska, A. & McClintok, P. V. Nonlinear dynamics of cardiovascular ageing. *Phys. Rep.* **488(2-3)**, 51-110 (2010).

[2] Kvandal, P. *et al.* Low frequency oscillations of the laser Doppler perfusion signal in human skin. *Microvasc. Res.* **72(3)**, 120-127 (2006).

[3] Okazaki, K. *et al.* Role of the endothelium-derived hyperpolarizing factor in phenylephrine-induced oscillatory vasomotion in rat small mesenteric artery. *Anesthesiology*. **98(5)**, 1164-1171 (2003).

[4] Stefanovska, A., Bračič, M. & Kvernmo, H. D. Wavelet analysis of oscillations in the peripheral blood circulation measured by laser Doppler technique. *IEEE Trans. Biomed. Eng.* **46(10)**, 1230–1239 (1999).

[5] Kapela, A., Nagaraja, S., Parikh, J. & Tsoukias, M. Modeling Ca2+ signaling in the microcirculation: intercellular communication and vasoreactivity. *Crit. Rev. Biomed. Eng.* **39(5)**, 435-460 (2011).

[6] Shimokawa, H. et al. The importance of the hyperpolarizing mechanism increases as the vessel size decreases in endothelium-dependent relaxations in rat mesenteric circulation. *J. Cardiovasc. Pharmacol.* **28(5)**, 703-11 (1996).

[7] Hwa, J. J., Ghibaudi, L., Williams, P. & Chatterjee, M. Comparison of acetylcholine-dependent relaxation in large and small arteries of rat mesenteric vascular bed. *Am. J. Physiol.* **266(3 Pt 2)**, H952-8 (1994).

[8] Lenasi, H. Assessment of Human Skin Microcirculation and Its Endothelial Function Using Laser Doppler Flowmetry. In *Medical Imaging* (ed. Erondu, O. F.). 271-296, doi: 10.5772/27067 (IntechOpen, 2011).

[9] Roustit, M. & Cracowski, J. L. Assessment of endothelial and neurovascular function in human skin microcirculation. *Trends Pharmacol. Sci.* **34(7)**, 373-84, doi: 10.1016/j.tips.2013.05.007 (2013).

[10] Gaubert, M. L. et al. Endothelium-derived hyperpolarizing factor as an in vivo back-up mechanism in the cutaneous microcirculation in old mice. *J. Physiol.* **585(Pt 2)**, 617-626 (2007).

[11] Cracowski, J. et al. Involvement of cytochrome epoxygenase metabolites in cutaneous postocclusive hyperemia in humans. *J. Appl. Physiol.* **114(2)**, 245–251, doi: 10.1152/japplphysiol.01085.2012 (2013).

[12] Brunt, V. E. & Minson, C. T. KCa channels and epoxyeicosatrienoic acids: major contributors to thermal hyperaemia in human skin. *J. Physiol.* **590(15)**, 3523–3534, doi:10.1113/jphysiol.2012.236398 (2012).

[13] Smirni, S. *et al.* In-vivo assessment of microvascular functional dynamics by combination of cmOCT and wavelet transform. *Proc. SPIE 10493*, *Dynamics and Fluctuations in Biomedical Photonics XV*. **104930P**, doi: 10.1117/12.2289814 (2018).

[14] Mayevsky, A. & Rogatsky, G. G. Mitochondrial function in vivo evaluated by NADH fluorescence: from animal models to human studies. *Am. J. Physiol. Cell Physiol.* **292(2)**, C615-40 (2007).

[15] Drakaki, E. *et al.* Laser-induced fluorescence and reflectance spectroscopy for the discrimination of basal cell carcinoma from the surrounding normal skin tissue. *Skin Pharmacol. Physiol.* **22(3)**, 158-65, doi: 10.1159/000211912 (2009).

[16] Gillies, R., Zonios, G., Anderson, R. R. & Kollias, N. Fluorescence excitation spectroscopy provides information about human skin in vivo. *J. Invest. Dermatol.* **115(4)**, 704-7 (2000).

[17] Heikal, A. A. Intracellular coenzymes as natural biomarkers for metabolic activities and mitochondrial anomalies. *Biomark. Med.* **4(2)**, 241-63, doi: 10.2217/bmm.10.1 (2010).

[18] Bolognia, J. L., Jorizzo, J. L. & Rapini, R. P. *Dermatology*. (Elsevier, 2003).

[19] Gupta, A., Avci, P., Dai, T., Huang, Y. Y. & Hamblin, M. R. Ultraviolet radiation in wound care: sterilization and stimulation. *Adv.. Wound Care (New Rochelle)*. **2(8)**, 422-437 (2013).

[20] Pasparakis, M., Haase, I. & Nestle, F. O. Mechanisms regulating skin immunity and inflammation. *Nat. Rev. Immunol.* **14(5)**, 289-301, doi: 10.1038/nri3646 (2014).